New biomarkers of in vitro cell electropermeabilization and ofskin toxicities in cancer patients using non-invasive and label-freeoptical techniques (Raman microspectroscopy and terahertzmicroscopy)

Antoine Azan

To cite this version:

Antoine Azan. New biomarkers of in vitro cell electropermeabilization and ofskin toxicities in cancer patients using non-invasive and label-freeoptical techniques (Raman microspectroscopy and terahertzmicroscopy). Optics / Photonic. Université Paris Saclay (COmUE), 2017. English. NNT : 2017SACLS122 . tel-01565648

HAL Id: tel-01565648
https://theses.hal.science/tel-01565648

Submitted on 20 Jul 2017

NNT : 2017SACLS122

Thèse de doctorat de l'Université Paris-Saclay préparée Université Paris-Sud

Ecole doctorale n°569
Innovation thérapeutique du fondamental à l'appliqué
Spécialité de doctorat : Pharmacotechnie et biopharmacie
par

Antoine AZAN

New biomarkers of *in vitro* cell electropermeabilization and of skin toxicities in cancer patients using non-invasive and label-free optical techniques (Raman microspectroscopy and terahertz microscopy)

Thèse présentée et soutenue à Villejuif, le 16 juin 2017.

Composition du Jury :

Mme.	Arlette Baillet-Guffroy	Professeur Université Paris-Saclay	(Présidente du jury)
M.	Josep Sulé-Suso	Professeur Keele University	(Rapporteur)
M.	Vincent Couderc	Directeur de recherche CNRS	(Rapporteur)
M.	Tadej Kotnik	Professeur University of Ljubljana	(Examinateur)
M.	Gerwin Puppels	Maître de conférence Erasmus MC	(Examinateur)
M.	Ali Tfayli	Maître de conférence Université Paris-Saclay	(Examinateur)
M.	Lluis M. Mir	Directeur de recherche CNRS	(Directeur de thèse)
Mme.	Marie Breton	Chercheur CNRS	(Co-directrice de thèse)
Mme.	Corinne Laplace-Builhé	Ingénieur de Recherche Gustave Roussy	(Invitée)

Á Isabelle et Axel.

Remerciements

Tout d'abords, je souhaiterais remercier mon directeur de thèse, Lluis M. Mir, pour sa disponibilité, ses précieux conseils scientifiques et son enthousiasme à tout épreuve. Je remercie également ma codirectrice de thèse, Marie Breton. Son pragmatisme sans concession a permis de maintenir le cap lors des tumultes rencontrées. Ce binôme d'encadrant a largement contribué au bon déroulement de ce doctorat.

Je tiens à remercier l'ensemble de mon jury: Pr. Arlette Baillet-Guffroy - présidente du jury, Pr. Josep Sulé-Suso et Pr. Vincent Couderc - rapporteurs, Pr. Tadej Kotnik, Dr. Gerwin Puppels et Dr. Ali Tfayli - examinateurs, et enfin Dr. Corinne Laplace-Builhé - invitée. Je garderai un très bon souvenir de ma soutenance.

Cette thèse aurait été difficilement réalisable sans le soutien de l'ensemble des membres de l'équipe de vectorologie physique de l'UMR 8203: Franck, Tomás, Jean-Rémi, Caterina, Iris, Sandra, Adeline et Florian; ainsi que les anciens membres de cette équipe: Léa, Marie-Amélie, Christophe, Isabelle et Hanna. J'ai une pensée spéciale pour Aude qui a pris le temps de me présenter le laboratoire et ses activités de recherche. Son enthousiasme communicatif a fortement influencé mon choix de faire mon doctorat à l'UMR 8203. Un grand merci à Isabelle Croquison, gestionnaire du laboratoire, qui m'a plus qu'assister dans mes innombrables démarches administratives. Je tiens à féliciter chaleureusement Lucie Descamps qui a du "survivre" à ma première expérience d'encadrant de stage. Je remercie également le reste de l'UMR 8203, en particuliers Ludivine, Charles et Alexandre, pour la sympathique et chaleureuse ambiance qui règne au sein du laboratoire.

En outre je tiens à remercier l'ensemble des collaborateurs avec lesquels j'ai eu l'occasion de travailler au cours de ce doctorat. J'ai eu beaucoup de chance de travailler avec vous: Valérie Untereiner, Olivier Piot, Lyla Lauvergne, Cyril Gobinet, Ganesh Sockalingum et Louis Liu de l'université Reims Champagne-Ardennes pour m'avoir laissé "jouer" avec leur microscope Raman; Gerwin Puppels, Peter Caspers, Tom Bakker Schut, Senada Koljenović, Vincent Noordhoek Hegt, Elisa Barroso et Inês Santos d'Erasmus MC pour les très bons moments passés ensemble à Rotterdam; Martin Van der Wolf and Kevin Stoutent de RiverD International B.V. pour leur support technique sur le "skin anlyzer"; les équipes médicales de Gustave Roussy: Caroline Robert, Alexander Eggermont, Benjamin Besse, David Planchard, Christine Mateus, Emilie Routier, Céline Boutros, Séverine Roy, Nyam Kamsu Kom, Gorana Tomasic, Emilie Lanoy, Matthieu Texier, Angelo Paci et Atmane Seck pour m'avoir permis de découvrir l'univers hospitalier; Marianne Grognot et Guilhem Gallot de l'école Polytechnique pour m'avoir initié à la microscopie térahertz; et enfin Brigitte Attal-Trétout et Michaël Scherman de l'ONERA pour m'avoir initié à la photonique vibrationelle.

Je n'oublie évidemment pas la plateforme d'imagerie de Gustave Roussy avec qui j'ai beaucoup échangé lors de ce doctorat et qui contribue grandement à faire avancer la recherche.

Cette expérience de doctorat n'aurait pas été la même sans ma mission d'enseignement à l'I.U.T. d'Orsay et de Ville d'Avray dont je remercie les membres de l'équipe pédagogique pour leur accueil et le temps qu'ils m'ont accordé.

Les activités en dehors du laboratoire m'ont permis de bien vivre ces années de doctorat. Ainsi, j'adresse un petit clin d'oeil aux membres du CRAO et je souhaite une longue vie à Orang Outang. De même, je remercie les amis villejuifois pour tous les moments partagés au Pacha. J'ai également une pensée spéciale pour les camarades rencontrés sur les bancs de l'ENSERG, il y a maintenant 13 ans.

Je ne peux terminer ces remerciements sans mentionner ma famille: mes parents, mes frères et leurs familles respectives pour leur soutien dans cette réorientation professionnelle et finalement ma compagne et mon fils: mes précieux compagnons de voyage.

Contents

Abbreviations

AFM	Atomic force microscopy
ATP	Adenosine triphosphate
ATR	Attenuated total internal reflection
AUC	Area under the curve
CCD	Charge coupled device
CRS	Coherent Raman scattering
CARS	Coherent anti-stokes Raman scattering
DHE	Dihydroethidium
DOPC	1,2-Dioleoyl-sn-glycero-3-phosphocholine
ECT	Electrochemotherapy
EGT	Electrogenetransfer
EMSC	Extended multiplicative signal correction
EPN	Electropermeabilization
ESOPE	European standard operating procedures of ECT
FGP	Fingerprint
FN	False negative
FP	False positive
FRAP	Fluorescence recovery after Photobleaching
FITC	Fluorescein isothiocyanate
GFP	Green fluorescent protein
GUV	Giant unilamellar vesicle
hMSC	Human mesenchymal stem cell
haMSC	Human adipose-derived mesenchymal stem cell
HCA	Hierarchical clustering analysis
HVT	High voltage
HWN	High wavenumber
KMCA	K-means clusters analysis
LD	Linear discriminant
LDA	Linear discriminant analysis
LOOCV	Leave-one out cross validation
LSCM	Laser-scanning confocal microscopy
LV	Latent variable
LVT	Low voltage
MAPK	Mitogen-activated protein kinase
MD	Molecular dynamics
MSC	Multiplicative signal correction
NA	Numerical aperture
NIR	Near-infrared
NMF	Natural moisturizing factor
nsPEF	Nanosecond pulsed electric field
PC	Principal component
PCA	Principal component analysis
PEF	Pulsed electric field
PhC	Phosphatidylcholine
PhE	Phosphatidylethanolamine

PhS	Phosphatidylserine
PI	Propidium iodide
PIP_2	$Phosphatidylinositol_{4,5}$-biphosphate
PLS	Partial least-square regression
PMT	Photomultiplier
PSF	Point spread function
RF	Random forest
ROC	Receiver operating characteristics
siRNA	Small interefering RNA
SC	Stratum corneum
SERS	Surface-enhanced Raman spectroscopy
SHG	Second harmonic generation
SM	Sphingomyelin
SNR	Signal-to-noise ratio
SRG	Stimulated Raman gain
SRL	Stimulated Raman loss
SRS	Stimulated Raman scattering
SVD	Singular value decomposition
SVM	Support vector machine
THz	Terahertz
TIRF	Total internal reflection fluorescence
TKI	Tyrosine kinase inhibitor
TMP	Transmembrane potential
TN	True negative
TP	True positive
TPF	Two-photon fluorescence
UV	Ultraviolet
VE	Viable epidermis

1

Preface

This research work mainly deals with the investigation of the interaction between pulsed electric fields (PEFs) and biological cells by means of different biophotonics instrumentations, such as confocal Raman microspectroscopy, terahertz (THz) microscopy and fluorescence microscopy. Confocal Raman microspectroscopy and THz microscopy are biophotonics techniques able to provide detailed information about the molecular composition of cells in a non-invasive and label-free way. The use of these biophotonics technique are relevant because the monitoring of the impact of PEFs on the molecular composition of cells is a hot topic in the electropermeabilization (EPN) community. As a side project of the investigation of the underlying mechanisms of cell EPN, we report a clinical study in order to detect *in patients* the skin toxicity induced by targeted anticancer therapies thanks to confocal Raman microspectroscopy.

Chapter 2 consists in a large presentation of biophotonics techniques. A special focus has been done on Raman microspectroscopy which is the dominant instrumentation technique used in this research work. The third chapter is a state of the art of cell EPN including a description of the plasma membrane, the underlying mechanisms of cell EPN and the EPN-based biomedical applications. Chapter 4 focuses on the contribution of biophotonics techniques to improve the understanding of cell EPN. Chapter 5 introduces the research hypothesis and objectives of this doctorate. In the sixth chapter, the results of this research work are presented via five articles. Four articles concerns the EPN topic, the last one is about skin toxicity. Two articles have already been published and three are about to be submitted. Finally, discussion and perspectives of this research work will conclude the manuscript (chapter 7 and 8 respectively in english and french language). In the annexe, a contribution to a book edited by Dr. Julita Kulbacka is included.

2

Biophotonics technique

Biophotonics is defined as an emerging multidisciplinary research area, embracing all light-based technologies applied to the life sciences and medicine [1]. Biophotonics term is the combination of the Greek syllables “bio” which means life and “phos” standing for light. Biophotonics consists in all methodologies and technologies based on light, from ultraviolet (UV) to THz region, and the interaction with any biological materials. In this research work, Raman microspectroscopy was the main biophotonics instrumentation used. Thus, first a large presentation of Raman microspectroscopy will be done. Others biophotonics techniques, such as fluorescence-based microscopy, will be also presented.

2.1 Raman microspectroscopy

In this section, the Raman-based optical technique will be detailed.

Notations

As in many domains in physics, specific conventions to the vibrational-based methods are used for the notation of the probed physical and optical properties. The wavenumber ω is related to the wavelength λ and the frequency ν of the light by the equation 2.1. Wavenumber is the reference unit in vibrational spectroscopy and is commonly expressed in cm^{-1}.

$$\omega = \frac{1}{\lambda} = \frac{\nu}{c} \tag{2.1}$$

where ω is the wavenumber, λ is the wavelength, ν is the frequency and c is the speed of light in the air.

The magnitude of the Raman signal is called “Raman Intensity” and is related to the photon counts on a photon detector. Raman Intensity is expressed in “Arbitrary Units”.

2.1.1 Raman effect: Principle and history

In 1928, Sir Chandrasekhara Venkata Raman (Fig. 2.1), an Indian physicist, discovered “a new radiation” [2]. Sir Raman demonstrated that when light interacts with a transparent material, a new scattered light is detected with a wavelength shift. This light/matter interaction is now called the “Raman effect”. Sir Raman has been rewarded by the Nobel Prize in Physics for this major discovery in 1930, only 2 years after the publication.

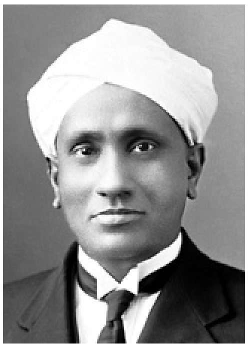

Fig. 2.1 Picture of Sir Chandrasekhara Venkata Raman

The Raman effect is defined as an inelastic scattering of photons when a sample is exposed to light. In opposition to the elastic scattering also known as the Rayleigh scattering [3], the frequency of the scattered light is shifted in comparison to the wavelength of the excitation light. This frequency shift is related to the chemical composition of the sample through its vibrational footprint (Fig. 2.2). Therefore, by measuring the frequency shift between the excitation wave and the scattered photons, the chemical composition of the sample can be assessed in a non-invasive and label-free way. The light/matter interaction induces the scattering of photons called “Stokes photons” and “anti-Stokes photons”. Fig. 2.2-B illustrates the energy transfer inducing the photons scattering at a frequency related to the vibrational frequency.

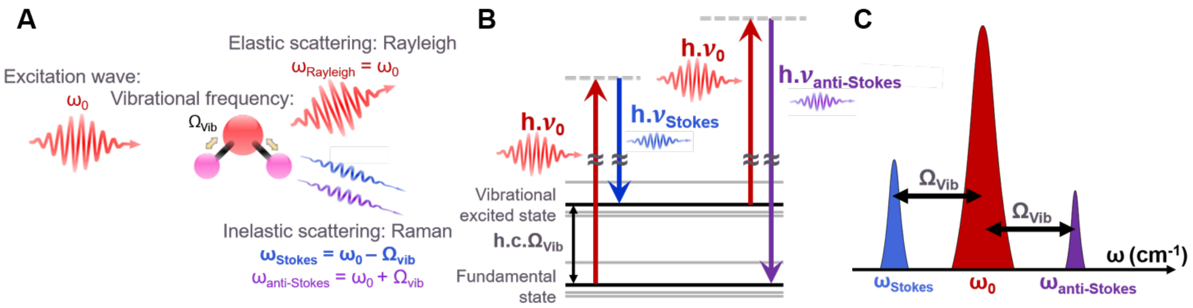

Fig. 2.2 Principle of the Raman effect. A - Scheme of the elastic and the inelastic scattering of photons. B - Jabłoński diagram associated to the Raman effect. C - Spectral distribution of the photons.

The wavenumber of the Stokes ω_{Stokes} or anti-Stokes $\omega_{anti-Stokes}$ photon is equal to the wavenumber of the excited beam ω_0 modulated by the vibrational frequency of the sample Ω_{Vib}. These relations are presented in equations 2.2 and 2.3.

$$\omega_{Stokes} = \omega_0 - \Omega_{Vib} \tag{2.2}$$

$$\omega_{anti-Stokes} = \omega_0 + \Omega_{Vib} \tag{2.3}$$

where ω_{Stokes} is the wavenumber of the Stokes photon, $\omega_{anti-Stokes}$ is the wavenumber of the anti-tokes photon, ω_0 is the wavenumber of the lase and Ω_{Vib} is the vibrational footprint frequency.
As mentioned previously, Raman spectroscopy can probe the vibrational modes of a sample. Each vibrational mode is attributed to a specific chemical bond and to a specific vibrational wavenumber (Fig. 2.3).

Fig. 2.3 Examples of three vibrational modes of water (H_2O) (with the courtesy of Michaël Scherman, ONERA/DMPH).

In most cases, the molecular composition of the sample is complex. Hundreds of different chemical bounds are part of the sample. Thus, the sample can be described by a vibrational footprint which is the envelop of the individual vibrational modes of the chemical bounds in the sample [4]. Fig. 2.4 shows the vibrational footprint, also called the Raman signature, of bulk water at room temperature and its Gaussian decomposition in the OH-stretching vibrational modes [5]. This vibrational footprint is directly related to the biochemical composition of the sample. Moreover, the magnitude of a Raman peak is related to the concentration of the corresponding molecules and the peak bandwidth to its local environment including for example the solvent.

2.1.2 The underlying mechanisms of the Raman effect

Since the discovery of Sir Raman, the physical mechanisms underlying this light/matter interaction have been studied in detail and are now well established [6–8]. The physical origin of the Raman signal comes from the polarizability of the sample under an electromagnetic radiation, in this case the laser beam. The polarizability is related to the faculty of the electron cloud of the nucleus to acquire an electric dipole under an electromagnetic radiation. The relationship between the electric dipole and the polarizability of a sample under an electromagnetic radiation is described by equation 2.4.

$$P(t) = \alpha(t) \cdot E_0 \cdot \cos(\omega_0 \cdot t + \varphi) \tag{2.4}$$

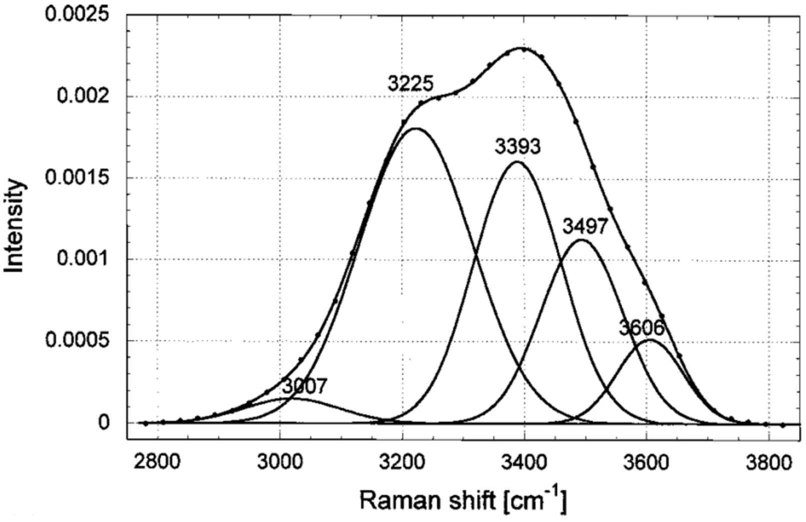

Fig. 2.4 Raman signature of bulk water at room temperature and its Gaussian decomposition in the OH-stretching vibrational modes. From [5].

where $P(t)$ is the electric dipole, $\alpha(t)$ is the polarizability, E_0 is the magnitude of the electromagnetic radiation, ω_0 is the pulsation of the electromagnetic radiation and φ is the phase of the electromagnetic radiation.
Since the electrons are bound to the nucleus, the motion of the nucleus can affect the oscillatory motion of the electrons. The polarizability is therefore perturbed by the presence of an intrinsic nuclear motion. At a certain nuclear coordinate, the polarizability can be expanded in a Taylor series (equation 2.5).

$$\alpha(t) = \alpha_0 + Q(t) \cdot \left(\frac{\partial \alpha}{\partial Q}\right)_0 + \ldots \tag{2.5}$$

where $\alpha(t)$ is the polarizability of the sample, $Q(t)$ is the nuclear coordinate and α_0 is the first derivative of $\alpha(t)$. If the nuclear motion is considered as a classic harmonic oscillator at a pulsation ω_ν and a magnitude Q_0 , the nuclear coordinate can be expressed by equation 2.6.

$$Q(t) = Q_0 \cdot \cos(\omega_\nu \cdot t) \tag{2.6}$$

where $Q(t)$ is the nuclear coordinate, Q_0 is the magnitude of the nuclear motion and ω_ν is the pulsation of the nuclear motion.

The electric dipole can then be expressed by equations 2.7 and 2.8.

$$P(t) = \alpha_0 \cdot E_0 \cdot \cos(\omega_0 \cdot t + \varphi) + Q_0 \cdot E_0 \cdot \left(\frac{\partial \alpha}{\partial Q}\right)_0 \cdot \cos(\omega_0 \cdot t + \varphi) \cdot \cos(\omega_\nu \cdot t) + \ldots \tag{2.7}$$

where $P(t)$ is the electric dipole, α_0 is the first derivative of $\alpha(t)$, $\left(\frac{\partial \alpha}{\partial Q}\right)_0$ is the second derivative of $\alpha(t)$, E_0 is the magnitude of the electromagnetic radiation, Q_0 is the magnitude of the nuclear motion, ω_0 is the pulsation of the electromagnetic radiation, ω_ν is the pulsation of the nuclear motion, φ is the phase of the electromagnetic radiation.

$$\begin{aligned} P(t) = {} & \alpha_0 \cdot E_0 \cdot \cos(\omega_0 \cdot t + \varphi) + \frac{1}{2} \cdot Q_0 \cdot E_0 \cdot \left(\frac{\partial \alpha}{\partial Q}\right)_0 \cdot \cos((\omega_0 - \omega_\nu) \cdot t + \varphi) \\ & + \frac{1}{2} \cdot Q_0 \cdot E_0 \cdot \left(\frac{\partial \alpha}{\partial Q}\right)_0 \cdot \cos((\omega_0 + \omega_\nu) \cdot t + \varphi) + \ldots \end{aligned} \tag{2.8}$$

where $P(t)$ is the electric dipole, α_0 is the first derivative of $\alpha(t)$, $\left(\frac{\partial\alpha}{\partial Q}\right)_0$ is the second derivative of $\alpha(t)$, E_0 is the magnitude of the electromagnetic radiation, Q_0 is the magnitude of the nuclear motion, ω_0 is the pulsation of the electromagnetic radiation, ω_ν is the pulsation of the nuclear motion, φ is the phase of the electromagnetic radiation.

The first term of equation 2.8 describes the elastic Rayleigh scattering. The second term is attributed to the Stokes photons of the inelastic scattering and the third term to the anti-Stokes photons of the inelastic scattering. Therefore, it appears that the Raman scattering occurs if a molecular vibration can change the polarizability of a molecule under an electromagnetic radiation. The existence of the Stokes and anti-Stokes photons depends on the term $\left(\frac{\partial\alpha}{\partial Q}\right)_0$ which is associated to the selection rules for a Raman-active vibration. The selection rules can be described by equation 2.9 and based on the group theory and the symmetry properties of the molecule [9].

$$\left(\frac{\partial\alpha}{\partial Q}\right)_0 \neq 0 \tag{2.9}$$

The intensity of the Stokes photons can be calculated by equation 2.10:

$$I(\omega_{Stokes}) = N \cdot z \cdot \sigma(\omega_{Stokes}) \cdot I_0 \tag{2.10}$$

where I is the intensity of the Stokes photons, (ω_{Stokes}) is the wavenumber of the Stokes photons, N is the molecular density, z is the length of the observed segement of the laser beam, σ is the cross-section which is proportional to $|\left(\frac{\partial\alpha}{\partial Q}\right)_0|^2$ and I_0 is the intensity of the laser [10].
The cross-section depends on many parameters including the wavelength of the laser beam. The intensity of the anti-Stokes photons can be calculated from equation 2.10 by replacing ω_{Stokes} by $\omega_{antiStokes}$.

Concerning the molecular density, based on the distribution of Maxwell-Boltzmann [11, 12], the ratio between the average number of particles in the vibrational excited states of energy $N_{excited}$ and the average number of particles in the fundamental states of energy $N_{fundamental}$ can be estimated thanks to equation 2.11.

$$\frac{N_{excited}}{N_{fundamental}} \propto \exp\frac{-h \cdot c \cdot \Omega_{vib}}{k_B \cdot T} \tag{2.11}$$

where h is the Planck constant, c is the speed of light in the air, k_B is the Boltzmann constant and T is the temperature in Kelvin.
Therefore, the average number of particles in the vibrational excited states is lower than the average number of particles in the fundamental states due to the energy gap. This explains why the intensity of the anti-Stokes signal is lower than the intensity of the Stokes signal. This ratio between the intensity of the Stokes and the anti-Stokes signal has been used to monitor the temperature of a sample in a non-invasive way [13]. It has to be mentioned that this spontaneous inelastic process is rare. The Raman signal intensity is typically 10^{10} times lower than the fluorescence signal intensity. Hence, highly sensitive instrumentation has been designed in order to acquire the Raman signature of samples with a good signal-to-noise ratio (SNR).

2.1.3 Raman microspectroscopy instrumentation

Raman instrumentation has now reached a mature state. In most of equipments, the architecture is nearly the same. Basically, a spectroscope is coupled to a confocal microscope. That is why the term microspectroscope is also used. The laser beam is focused on the sample through an objective with a high numerical aperture. The scattered light is also collected with an objective. In the case of a backward detection, the same objective is used to excite the sample and to collect the scattered light. Some optical filters are necessary to remove the non-specific light. A pinhole allows to improve the spatial resolution of the system by making it confocal. In order to analyse the spectral composition of the collected light, the light is diffracted on a cooled charge coupled device (CCD) camera via a diffraction grating. Each column of the CCD is related to a specific wavelength of the collected light (Fig. 2.5).

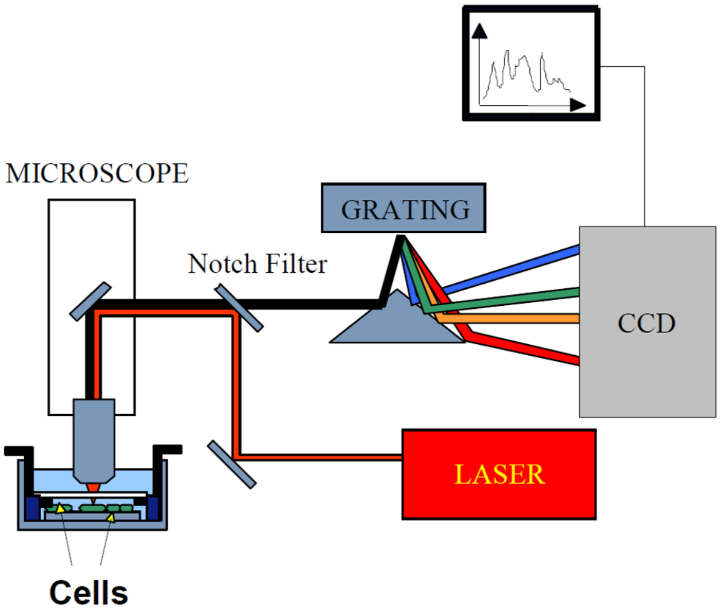

Fig. 2.5 Schematic representation of an experimental set-up for Raman microspectroscopy measurements of cells. In this case, the backward scattered light is collected. From [14].

The spatial resolution of the equipment depends on the combination of the characteristics of the objective and the pinhole size. For example, a 100 X water-immersion objective with a numerical aperture of 1.0 and a pinhole size fixed to 100 µm provides a lateral resolution (XY) of 1 µm and an in-depth resolution (Z) of 1 µm. The spectral resolution depends mainly on the diffraction grating, the number of pixel of the CCD camera and the laser wavelength. The classical spectral resolution is approximately 1 cm^{-1}. The sample can be placed on an XY piezoelectric stage to perform cartographies. Therefore, it is possible to acquire hyperspectral images in which each pixel of the image is a spectrum. An hyperspectral image may be represented as a spectra data cube or hypercube with two spatial dimensions (pixel coordinates x and y) and a third dimension which is the spectral dimension (Fig. 2.6).

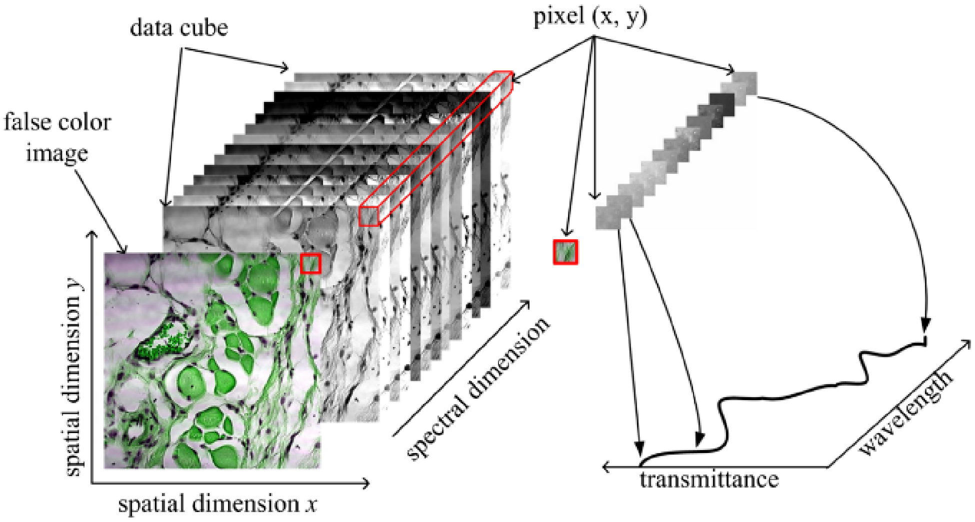

Fig. 2.6 Hyperspectral image represented as a spectral data cube with two spatial dimensions (pixel coordinates x and y) and one spectral dimension. From [15].

Many suppliers have commercialized high-performance and user-friendly equipment (Fig. 2.7). The equipment includes several lasers, objectives and diffraction gratings in order to be versatile. The software may also include data processing tools for an analysis of the results in real time.

Fig. 2.7 Example of commercially available Raman equipment: Renishaw - inVia Raman Microscope. From `http://sciences.usca.edu/chemistry/chad/instrumentation.htm`.

The ultimate goal in instrumentation is to acquire a signal with the optimum SNR. To do so, the selection of the wavelength of the laser is a critical point. The Raman signal intensity is known to increase with a decrease in the wavelength. The detector performance is also greatter at shorter wavelengths as illustrated in Fig. 2.8. But sample damages and autofluorescence increase at shorter wavelengths [16]. Generally, the recommended laser wavelengths to acquire the Raman signature of biological samples are from 532 to 785 nm. A quantitative and qualitative study demonstrated that the optimum laser wavelength for breast calcification detections with transmission Raman spectroscopy is between 790 and 810 nm . Recently, new CCD cameras have been developed allowing the acquisition of spectra with a Near-InfraRed (NIR) excitation beam [17]. As mentioned in equation 2.10, the Raman intensity is proportional to the laser intensity. Thus, increasing the laser power will increase the Raman signal. It is therefore necessary to check that the sample is not damaged by the laser. Typical laser powers for biological samples are around tens of milliwatt.

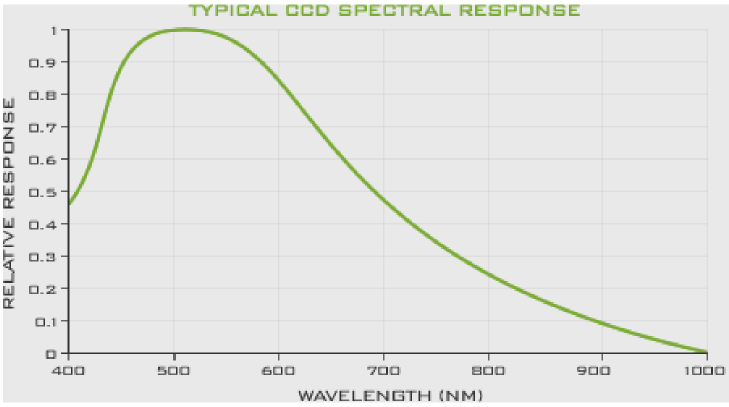

Fig. 2.8 Typical CCD spectral response. From `http://www.looptechnology.com`.

A Raman microspectroscope device may also include a system for the polarization of the laser beam. This might be particularly useful to enhance specific vibrational modes in the case of materials such as carbon nanotubes [18].

Many technical improvements of the CCD camera, the optical elements and the laser beam have been allowed to improve the SNR and thus to speed up the Raman acquisition. Nowadays, classical acquisition times for *in vitro* studies are about 60 seconds. For *in vivo* studies, the molecular concentrations are usually higher and the acquisition time can be below one second. In order to characterize the heterogeneity of a sample, multiple acquisitions are necessary. One of the limitation of a confocal Raman microspectroscope is the point-by-point scanning. In order to overcome this limitation and get access to dynamical processes, the line-scanning technology has been developed. The principle is detailed in Fig. 2.9. Instead of performing the acquisition at a single point, the laser beam is expanded in a line by a cylindrical lens. Therefore, the Raman acquisition is performed line-by-line, instead of point-by-point. The exposure times have been reduced from 130 minutes to 3 minutes in the case of the analysis of HeLa cancer cells [19].

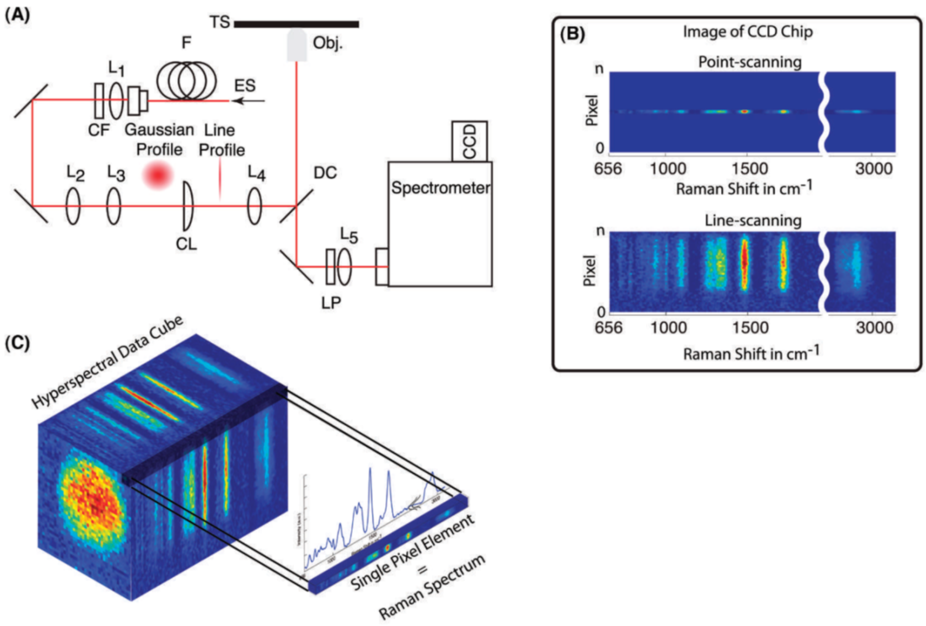

Fig. 2.9 Line-scanning configuration Raman spectroscope. A - Expansion of laser beam along one axis by a cylinder lend. B - Differences between CCD images of Raman-scattered photon obtained by point scanning and line-scanning Raman scattering. C - By scanning an expanded line across the sample, the rapid acquisition of hyperspectral data cubes containing spectral as well as temporal information on the biochemical state of cell is facilitated. From [16].

Raman systems including optical fiber probes have been designed in order to use Raman spectroscopy for biomedical applications [20–22]. A typical example of a Raman probe is shown in Fig. 2.10. A multicore fiber is generally used in order to limit the coupling between the high power laser beam and the low intensity Raman signal.

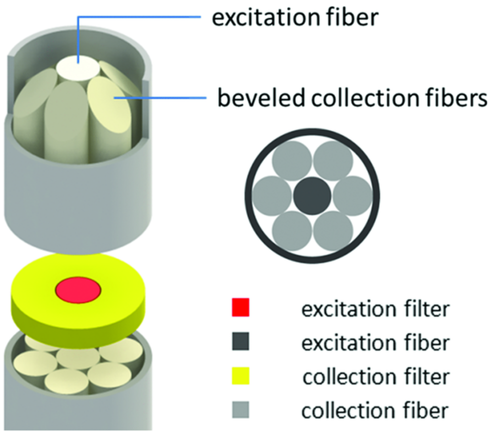

Fig. 2.10 Internally filtered six-around-one Raman probe with bevelled collection fibers for beam shaping. Core diameters are 400 µm for the excitation and 300 µm for the collection fibers respectively. From [22].

Before any measurement, Raman systems need to be calibrated in order to correct any distortions due to the instrumentation response. The distortions can be in wavenumber or/and in intensity. The instrumentation calibration needs to be performed for each configuration of the equipment. Incorrect calibration of the system may have an impact on the outcome of the study [23]. Moreover, the instrumentation calibration allows to combine

Raman measurements from different equipments [24]. The 519 cm^{-1} band of a silicon sample or a neon lamp are commonly used to calibrate Raman microspectroscope [25]. Bocklitz *et al.* suggested a calibration protocol for Raman spectra recorded with difference excitation wavelengths [26].

In the case of biological samples such as cells, experimental precautions may also contribute improve the SNR of the measurements. The substrate used must be chosen carefully in order to minimize the background signal. Kerr *et al.* showed that calcium fluoride substrates provide low background signal [27]. At a specific excitation wavelength (532 nm), a thin film of aluminium substrate (1 000 - 1 500 nm thickness) can be also considered as a good substrate for Raman spectroscopy experiments. In the case of an *in vitro* study, the buffer solution will also contribute to the non-specific signal. Physiological serum (NaCl 154 mM)can be considered as a good buffer due to its low Raman signal and its biocompatibility.

2.1.4 Specific Data process for Raman images

2.1.4.1 Pre-processing methods

The Raman signal is suffering of many sources of interference, such as sample autofluorescence, buffer solution or cosmic rays. A pre-processing step is necessary to extract the targeted signal from the measured signal 2.11 [28]. By performing a multivariable data analysis on a raw data set and on the same pre-processed data set, it has been demonstrated that the pre-processing allows to enhance the results [29]. The interference information of the substrate is clearly identified in the pre-processed images, which is not the case in the raw images. The uniformity within the same image and the differentiation capability across the different time points are emphasized by pre-processing the data.

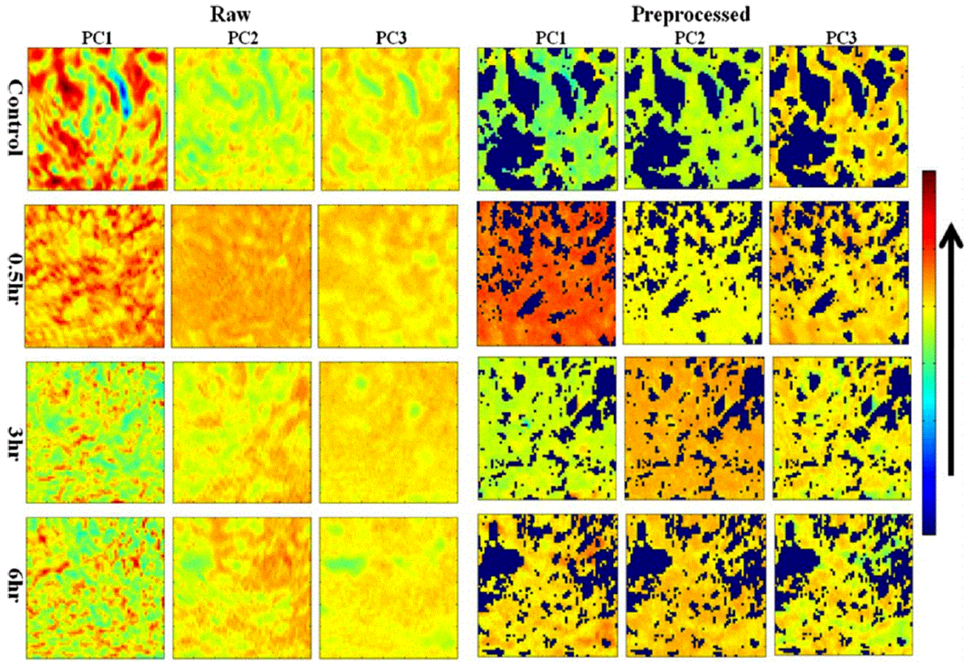

Fig. 2.11 Principal component scores of raw and preprocessed Raman images of mouse liver exposed to acetaminophen with different exposure time. Dark blue regions in the pre-processed images indicate the presence of glass substrate. From [29].

The following section will detail some pre-processing methods commonly used in Raman spectroscopy.

CCD detectors are known to be sensitive to electromagnetic radiation originating from high energy particles. The Raman measurements may contain thus spikes from cosmic rays hitting the CCD detector. The cosmic ray artefacts are easy to identify by their sharp and intense features superimposed to the Raman signal (Fig.2.12).

Several techniques are available to remove this unwanted signal. Cosmic ray artefacts are known to be non-reproducible in time. By performing two consecutive acquisitions and a correlation between the two acquisitions, the spikes can be identified and removed by a low order polynomial extrapolation at the Raman shift around the spike. Many filtering methods have been designed ([30]) and now the commercially available Raman systems include a spike removal procedure in their software. In the specific case of hyperspectral images, the similarity between neighbouring pixels of the spectrum can be used as a measure for the presence of cosmic spike artefacts [31].

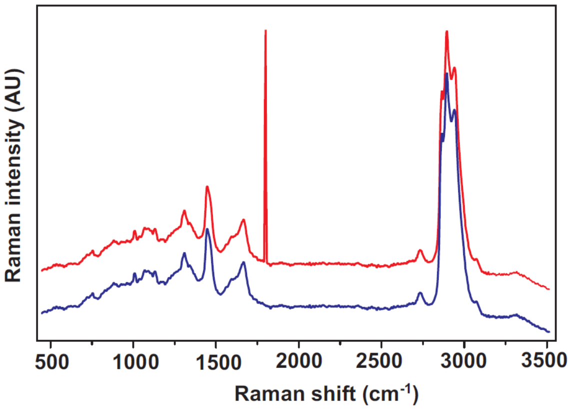

Fig. 2.12 Example of a cosmic ray correction of a Raman spectra. Red trace - Raman spectrum obtained from the cerebellum of Syrian hamster showing a strong cosmic ray feature around 1 795 cm^{-1}. Blue - the corrected Raman spectrum. From [28].

Smoothing the spectra allows to remove the high frequency noise contribution from the signal. Although many filters exist [32, 33], the Savitzky-Golay smoothing is the most popular method in vibrational spectroscopy [34]. The principle is to replace each value of the spectrum with a new value which is obtained from a polynomial fit of the 2n+1 neighbouring points. Fig.2.13 displays a typical example of a Savitzky-Golay smoothing.

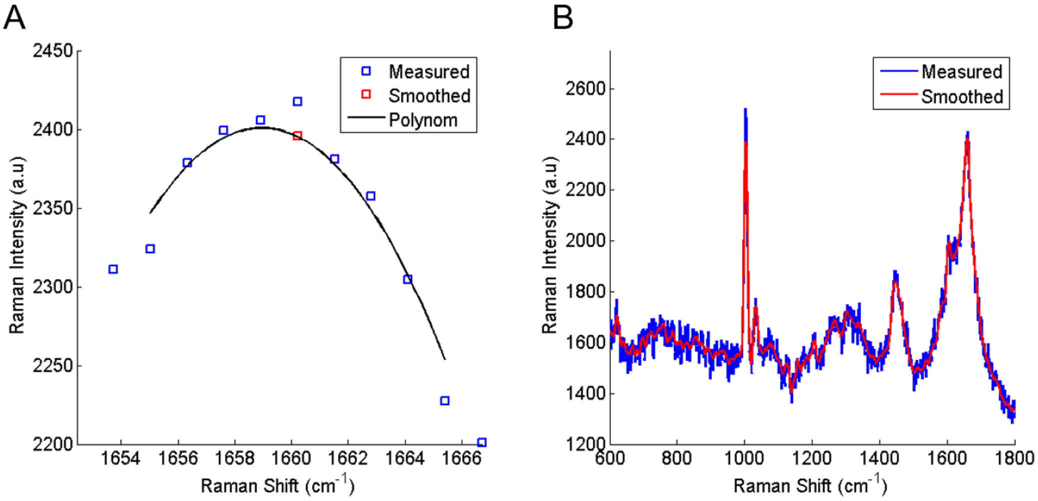

Fig. 2.13 Example of a Savitzky-GOlay smoothing. A - Savitzky-Golay smoothing example with an 8-points window and a 2^{nd} order polynomial fitting. B - Comparison between a measured spectrum and a smoothed spectrum.

The in-depth resolution of Raman equipments do not allow to acquire only the signal coming from a thin sample. The sources of contamination are multiple: sample autofluorescence, substrate, buffer solution, paraffin... The removal of the contaminant signal is a critical point in order to perform quantitative analyses. Many algorithms have been developed so as to perform intelligent background corrections [35, 36]. Automated methods are available to subtract a known contaminant spectrum in a measured Raman spectrum [37]. Tfayli *et al.* [38] designed a specific algorithm to perform digital dewaxing of paraffin for skin biopsy samples (Fig. 2.14).

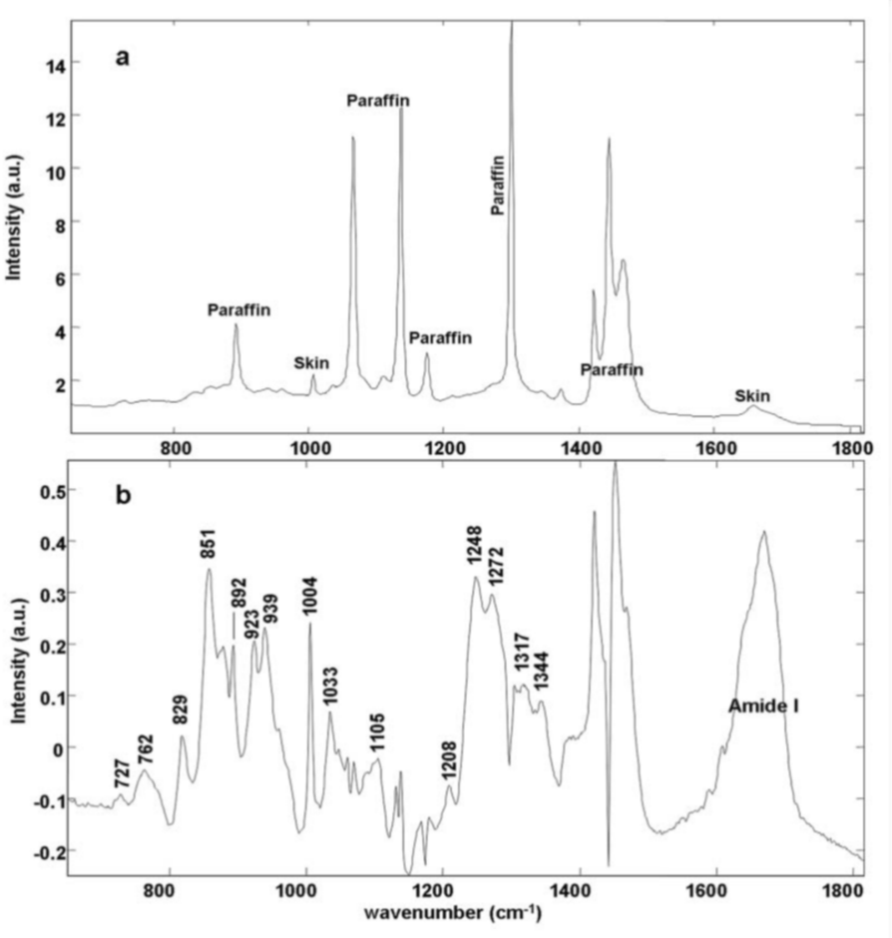

Fig. 2.14 Digital dewaxing of paraffin in skin biopsy sample. A - Raw Raman spectrum of paraffin-embedded skin. B - The corresponding spectrum after elimination of the computed signal of paraffin. Adapted from [38].

Finally, the last step of the pre-processing is the normalisation. There is a high variability in the amount of signal in a spectral data set. The origins of this variability are various, for instance: the laser intensity fluctuations, the reproducibility of the laser focusing, the concentration of molecules at the laser spot ... In order to be able to compare quantitatively and qualitatively the spectra, a normalisation step is required. Different methods are possible with their own advantages and disadvantages. The normalisation methods can be classified in two main groups. The first group requires only information from the spectrum to perform the normalisation. Generally, the normalisation methods of this group are performed after the baseline removal. The second group requires extra information such as reference spectra or the order of the polynomial used to remove the baseline.

In the following, a non-exhaustive list of normalisation methods belonging to these two groups are presented:

Peak normalisation: A very simple method is to normalize each spectrum of the data set to the magnitude of a specific peak, for instance the phenylalanine ring breathing mode at 1 003 cm^{-1} [39]. This method is based on the hypothesis that the chemical compound associated to the selected peak is relatively constant in comparison with the other chemical compounds. This hypothesis needs to be strictly checked before selecting this normalization process.

Area under the curve normalisation: This method aims to respect the relative band magnitude of the peaks in the whole spectrum. The individual spectrum is divided by its area under the curve (AUC). This method is pretty simple and commonly used [40].

Vector normalisation: The spectra are mean-centered (meaning that each spectrum is offset in order to have a mean value equal to zero) and then divided by the square root of the sum of the mean-centered intensities squared. Thus, the sum of all mean-centered intensities values squared equals one.

Standard normal variate: It is a similar technique to the vector normalisation except that the standard deviation is equal to one instead of the sum of all mean-centered intensities values squared [41].

The second group is of normalisation methods are model-based pre-processing techniques [42]. Historically, multiplicative signal correction (MSC) has been developed in the 1980s by Martens *et al.* [43, 44] for near-infrared spectroscopic measurements in the food industry. Later, this pre-processing technique has been improved and extended [45, 46]. Nowadays, extended multiplicative signal correction (EMSC) is one of the most popular pre-processing technique used in vibrational spectroscopy. Basically, EMSC considers that the measured spectrum is a linear combination of interference spectra (provided by the operator), a polynomial baseline (associated to the autofluorescence) and the useful signal. For each spectrum of the data set, EMSC calculates a new linear combination of the previously listed contributors to the signal in order to fit with a reference spectrum. Hence, the interference spectra can be removed easily and the useful signal is normalized to a unique reference. EMSC is known to be non-sensitive to the baseline as shown in Fig. 2.15.

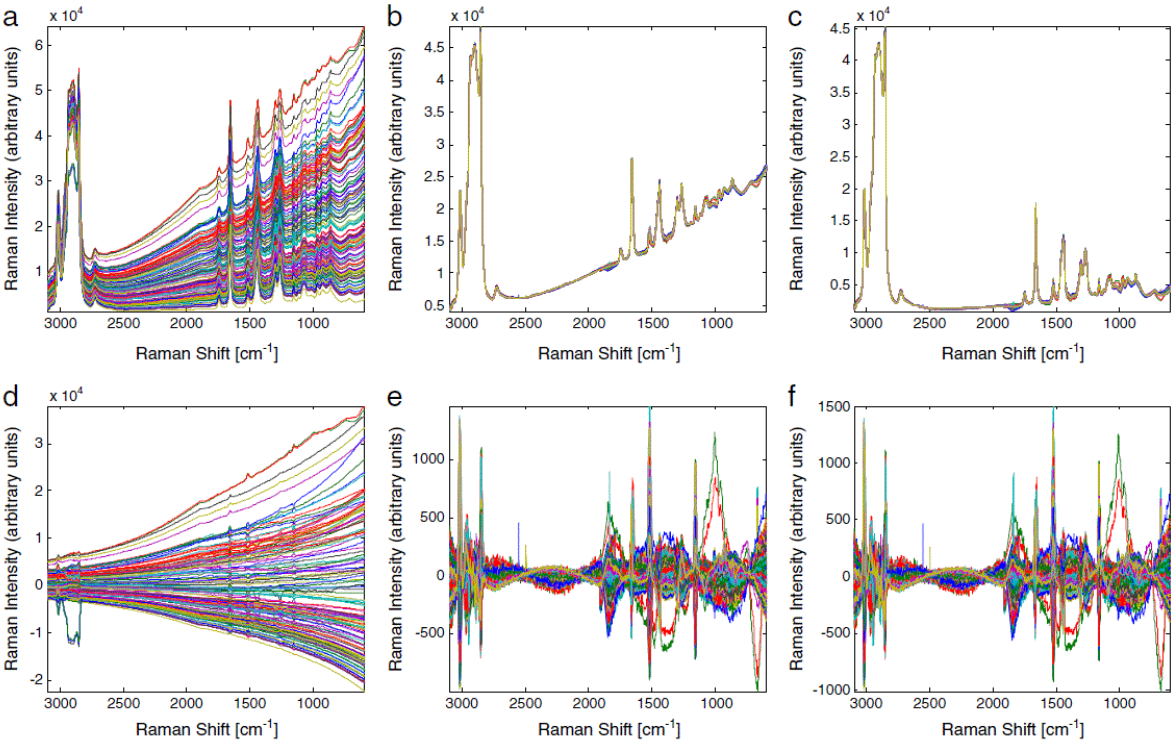

Fig. 2.15 EMSC illustration from Raman spectra of salmon oils. a - Raw Raman spectra. b - EMSC pre-processed spectra using a reference spectrum with strong slope (the mean Raw spectra was used as the reference spectrum). c - EMSC pre-processed spectra using a reference spectrum with reduced slope. d - f Corresponding mean-centered data sets. Adapted from [42].

Afseth *et al.* compared quantitatively and qualitatively different pre-processing methods on four Raman data sets [47]. As expected, the authors suggested to remove the baseline before a normalisation step. In a second study, the same group demonstrated that the EMSC algorithm strongly reduces the replicate variance in comparison with the other pre-processing methods (Fig. 2.16).

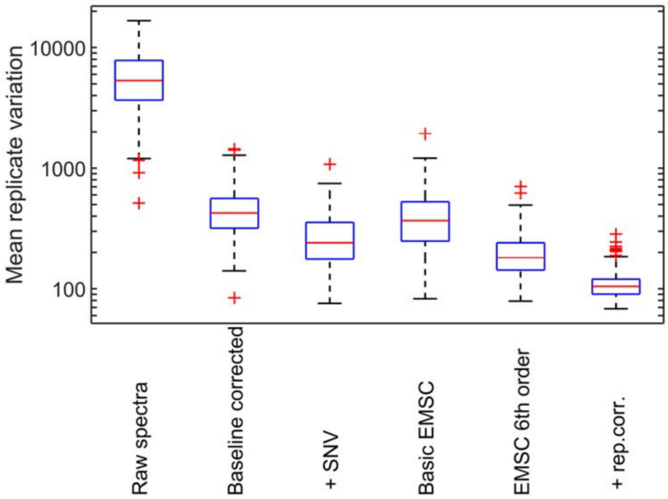

Fig. 2.16 Quantitative comparison of the replicate variation of different pre-processing methods. Variation is measured as the mean of the standard deviation of each Raman shift for a replicate set. Adapted from [47].

Finally, the impact on the discriminative power of different pre-processing methods was analysed by Heraud *et al.* [48]. In this case, EMSC was the pre-processing method providing the best overall discriminative power.

A Raman data set can contain hundreds of spectra and thus is a rich but complex data set. In the case of bio-systems such as cells or tissues, the heterogeneity is important and may hide the useful information, for instance the impact of a drug on the Raman signatures of cells. As presented before, many pre-processing methods allow to remove the various interference signals. A high performance data analysis technique is necessary to extract specifically the targeted information.

2.1.4.2 Univariate data analysis technique

A basic data analysis [49]. Difference between two mean spectra of different groups, first and second order derivative, peak magnitude or peak position, curve fitting are part of these univariate data analysis techniques. However, none of the spectroscopic measurements depends on a single variable. Therefore, more complex and powerful data analysis techniques are mandatory.

2.1.4.3 Multivariate data analysis technique

This section aims to present the different multivariate data analysis techniques that have been used for decades in Raman spectroscopy [28, 29, 50].

A Raman spectrum is generally made of hundreds of wavenumbers (variables) in order to have a good spectral resolution. A Raman data set may contain over one hundred measured spectra (observations). Thus, the dimension of a Raman data set is huge and requires a specific statistical data analysis technique to extract meaningful information. Generally, the spectroscopic measurements may be divided into two parts as shown in equation 2.12.

$$Observation = RelevantSignal + Noise \tag{2.12}$$

The relevant signal is considered as the signal related to the scientific question targeted. The noise signal is considered as an unspecific signal such as autofluorescence signal or interference signals. The multivariate data analysis technique aims to separate the relevant signal from the noise part by using intrinsic variable correlations and thus reducing the dimension of the data set. The concept of variance is very important as “directions with maximum variance” are almost directly related to the structural part of the relevant signal [51].

These multivariate techniques, also called chemometrics [52, 53], are also commonly used in many other domains such as mass spectrometry [54], bio-impedance [55, 56] or finance [57].

Multivariate techniques can be divided in two groups:

Unsupervised methods: These methods perform statistical analyses without any supervision or complementary information. Principal components analysis (PCA), K-means clustering analysis (KMCA) or hierarchical clustering analysis (HCA) are examples of unsupervised methods.

Supervised methods: These methods take into considering label information to perform the statistical analysis. Hence the data set is invested based on this contextual information. Partial-Least square regression (PLS), linear discriminant analysis (LDA) or support vector machine (SVM) are examples of supervised methods.

Principal components analysis

PCA is an unsupervised multivariable technique commonly used in Raman spectroscopy. PCA allows to represent the original data set in a space with lower dimensions than the original space, but with a limited information loss [58–60]. This transformation is done by calculating the eigenvectors and eigenvalue of the covariance matrix from the data set. The eigenvectors of the new coordinate space are termed principal components (PC). The eigenvector with the highest eigenvalue gives rise to the first PC (PC1) representing the direction of the greatest variance of the data. PC2 is the eigenvector with the second highest eigenvalues. And so on .... PCA is be illustrated by the Fig. 2.17.

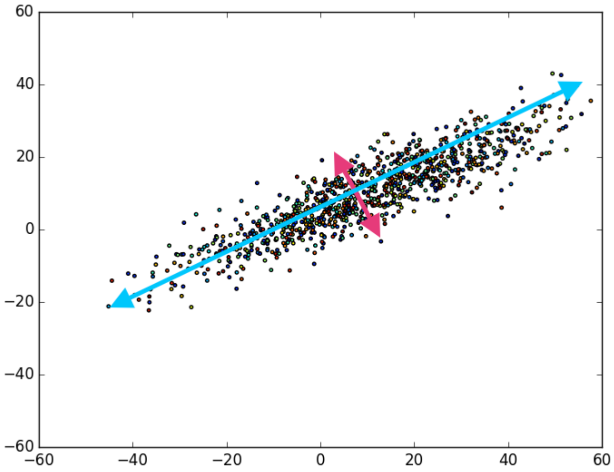

Fig. 2.17 Illustration of PCs determined by PCA. Adapted from http://austingwalters.com/pca-principal-component-analysis/.

From a mathematical point of view, let's assume that a Raman data set is composed of m measured spectra and that each spectrum is composed of n wavenumbers. Thus the data set can be represented as a [m x n] matrix called X. By determining the eigen decomposition of the X matrix by Singular Value Decomposition (SVD) method [61], it is possible to express the X matrix as:

$$X = U \cdot \Sigma \cdot W^T + E \tag{2.13}$$

where U is a [m x r] matrix with the first r eigenvectors of the matrix XX^T, W is a [n x r] matrix with the first r eigenvectors of X^TX, Σ is a small diagonal [r x r] matrix containing the first r singular values of X and E is the residual [m x n] matrix. In the case of the PCA, U corresponds to the PC score vectors and the matrix product $\Sigma \cdot W^T$ to the matrix of PC loading vectors. In the case of the discrimination of two groups by Raman spectroscopy, PCA allows to extract the spectral features associated to the targeted question. Fig. 2.18 shows how easily secondary and primary cell types can be discriminated thanks to PCA [62].

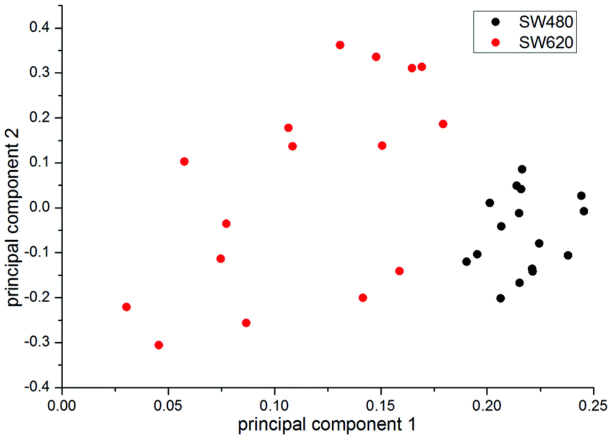

Fig. 2.18 PCA plot of the Raman spectra of 16 secondary tumor cells (SW480 in black) and 16 primary tumor cells (SW620 in red.) Adapted from [62].

PCA can also be used to extract not only spectral but spatial information from a data set and thus perform Raman imaging. In the study by [50], Raman signatures of a mixture of acetylsalicylic acid, stearic acid and starch are acquired. After PCA, the first three PCs have been associated to the three chemical species. PC1 was associated to acetylsalicylic acid, PC2 to stearic acid and PC3 to cellulose. By plotting the PC score of PC1, PC2 and PC3, PCA allows to extract the spatial distribution of the chemical species (Fig. 2.19).

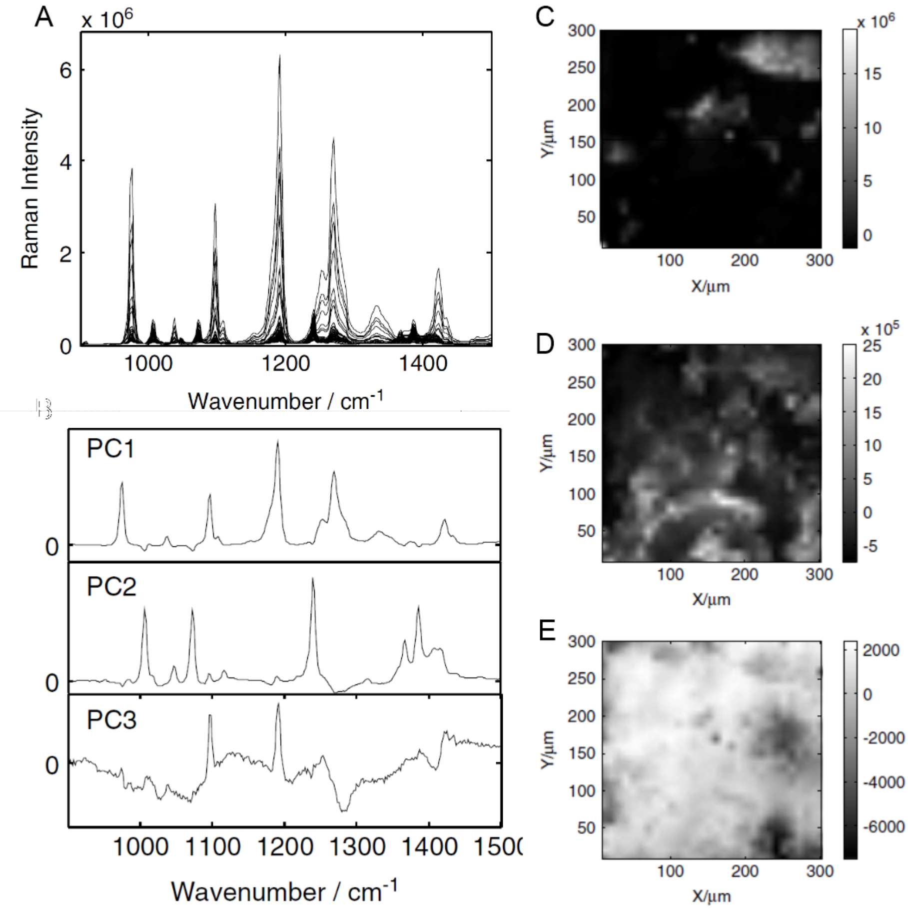

Fig. 2.19 Illustration of PCA mapping. A - Raman spectra of the tablet containing acetylsalicylic acid, stearic acid and starch. B - Loadings of the first three PCs. C-D Score of the first three PCs. Adapted from [50].

PCA is also used to remove the noise contribution by selecting only the first PCs. Multivariate analysis is also commonly used to perform classification, discrimination or clustering of groups in a data set. In this case, supervised methods are necessary. Many techniques are existing. Some of them are presented in the following paragraph.

Clustering Analysis

Another unsupervised method is based on clustering analysis [63, 64]. The goal of these algorithms is to find clusters in the Raman data set in order to extract the most relevant biochemical information. The clustering process is based on the calculation of a distance metric, for instance an euclidian distance, in order to quantify the similarities in the spectral data set. The clusters are defined in order to maximize the distance metric between two clusters (inter-cluster distance) and minimize the distance metric between the members of one cluster (intra-cluster distance). Many algorithms exist and have been used in Raman spectroscopy such as KMCA [65, 66] or HCA [67, 68]. In the case of HCA, the clustering is hierarchically meaning that the spectra are clustered two by two based on the metric distance. These sub-clusters are then clustered again two by two with the same criterion and so on until all the data are attributed to a unique cluster. The HCA result is commonly represented by a dendrogram which is a tree diagram where the spectra and sub-clusters are identified by a node. The distance between the nodes is related to the difference in the distance metric between the 2 nodes, termed heterogeneity (Fig. 2.20).

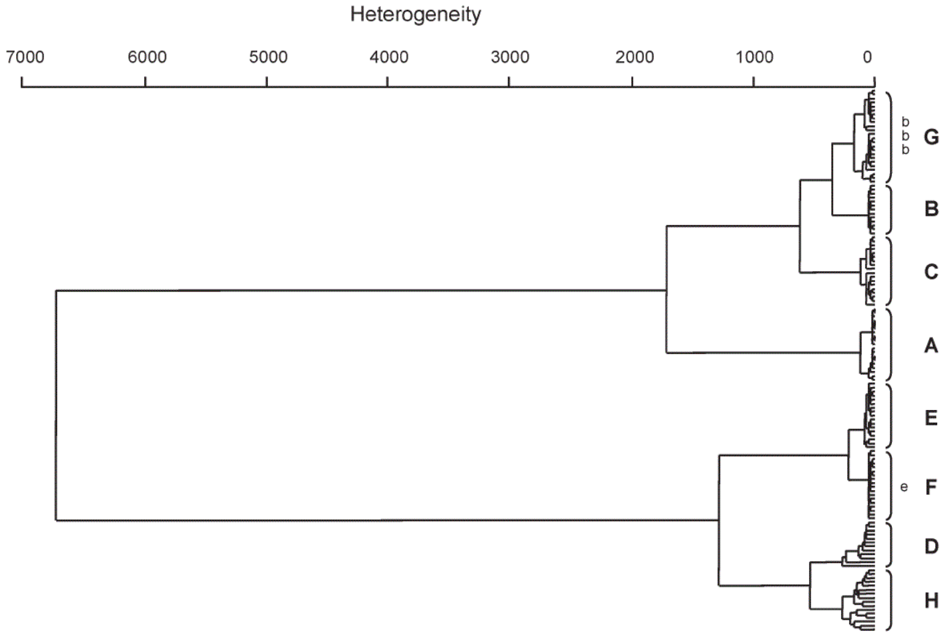

Fig. 2.20 The dendrogram of HCA applied to a Raman data set combining spectra from bacterial bulk samples of A - Staphylococcus cohnii DSM 6669, B - Staphylococcus cohnii DSM 6718, C - Staphylococcus cohnii DSM 6719, D - Staphylococcus cohnii DSM 20260, E - Staphylococcus warneri DSM 20036, F - Staphylococcus warneri DSM 20316, G - Staphylococcus. epidermidis ATCC 35984 and H - Staphylococcus. epidermidis DSM 1798. Adapted from [67].

Fig. 2.21 shows an example of HCA performed on an HeLa cell characterized by Raman spectroscopy. The average Raman spectrum of the first cluster displays obvious spectral patterns related to the nucleic acids.

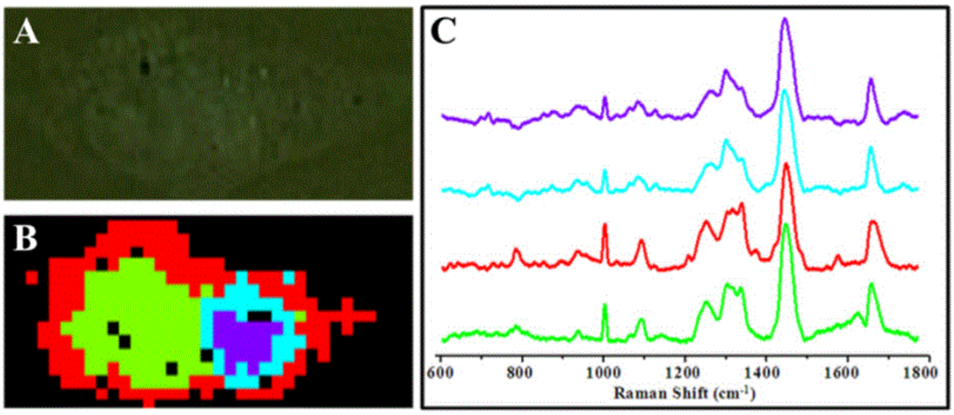

Fig. 2.21 HCA of Raman image from HeLa cell. A - White-light image. B - Corresponding Raman image of four clusters obtain using HCA multivariate technique. Black regions indicate low SNR spectra (mostly buffer and substrate). C - Average Raman spectra of the four clusters. Adapted from [29].

Partial Least Square regression

PLS calculates a linear regression model of the data set based on predictor variables [69]. PLS is similar to PCA except that the transformation is done in order to find a linear relation between the data matrix and the predictor variables. If we assume that Y is a [p x m] matrix, composed of p predictors variables for the m Raman spectra and that X is a [m x n] data set matrix made of m Raman spectra composed of n wavenumber points, the X^TY matrix is subjected to SVD to determine Latent Variables (LVs) which are used to predict the response variables [29]). In comparison SVD is performed on X^TX to determine the PCs in the case of PCA. PLS has been used to predict the concentration of components in samples. For instance, the concentration of glucose, cholesterol, triglyceride, urea, total protein and albumin in Raman spectra of patient's serum as shown in Fig. 2.22.

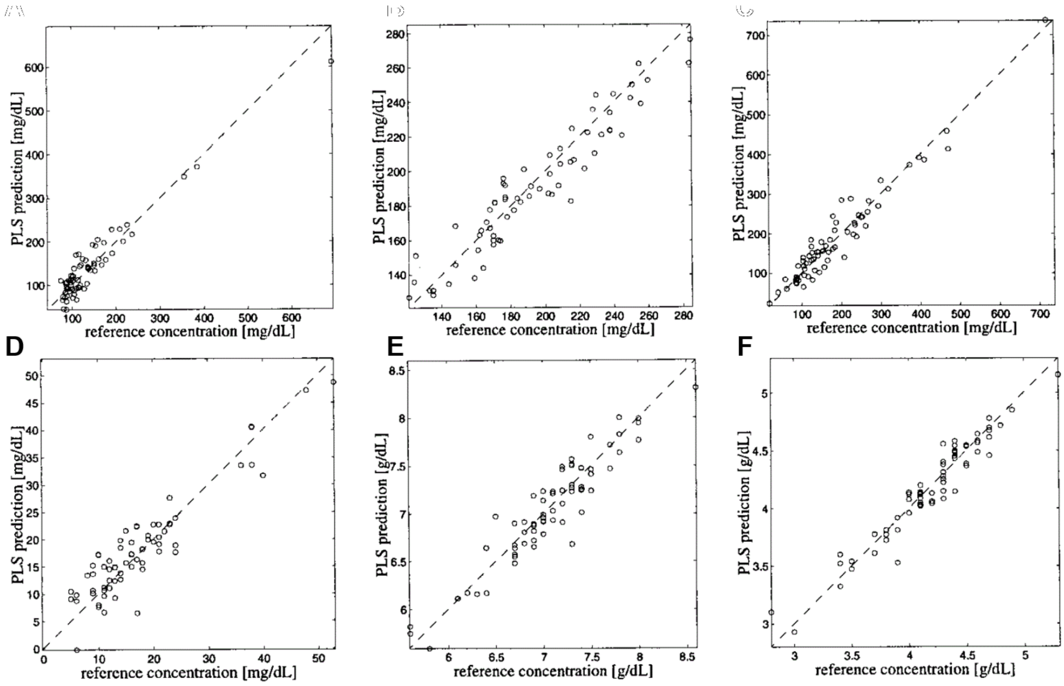

Fig. 2.22 PLS prediction of analyte concentration in serum. A - glucose. B - cholesterol. C - triglyceride. D - urea. E - total protein. F - albumin. Adapted from [70].

Linear Discriminant Analysis

The aim of LDA, also called Fisher's linear Discriminant analysis, is to design a model which will be able to discriminate different classes in the data set with the optimal discriminative power [71]. In our case, a model is a Raman spectrum which will characterize the variance associated to the different classes in the model. To do so, each spectrum needs to be labelled with its specific class. That is why it is a supervised method. LDA is commonly coupled with PCA [72, 73] or PLS [74, 75] in order to design a model based on selected PCs or LVs. The linear discriminant (LD) model will be a linear combination of the selected PCs or LVs that maximizes the ratio of between-class to within class scatter (Fig. 2.23).

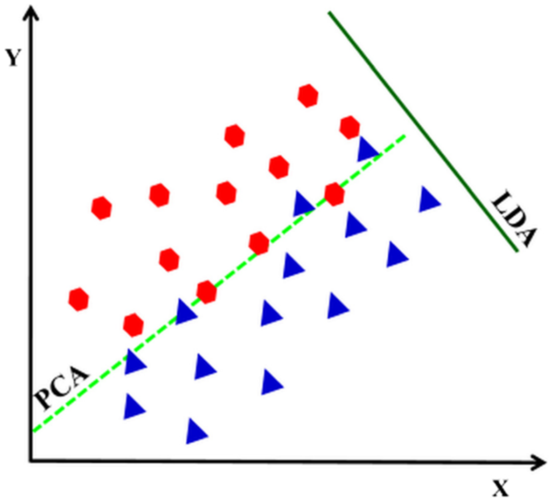

Fig. 2.23 Schematic representation of the axes found using PCA and LDA for a two-class data set [29].

LDA can also be used for multiclass discrimination [76]. The power of LDA is that biochemical information can be easily extracted from the LD which is a Raman spectrum. Spectral features can be identified as related to a reference Raman spectra. One of the major limitation of LDA is that the discriminant model has to be linear, meaning that non-linear discrimination is not possible. To overcome this limitation, other classification algorithms have been developed such as Support Vector Machines.

Support Vector Machine

SVM identifies the optimal hyperplane to discriminate the different classes [77, 78]. To discriminate two groups, several hyperplanes can be considered with different margins between the hyperplane and the elements. By an iterative process, SVM aims to find the hyperplane with the maximum margins (Fig. 2.24).

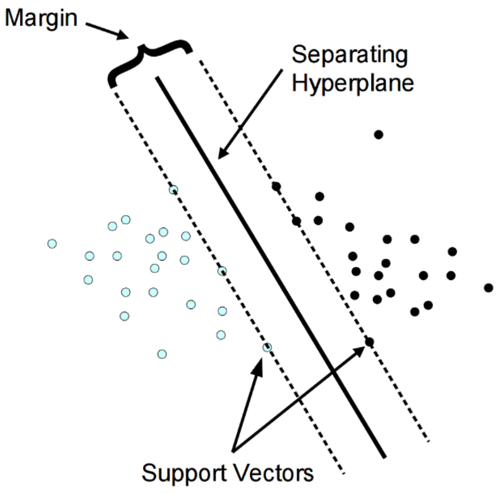

Fig. 2.24 SVM classification. From [79].

Moreover, SVM is able to rearrange the data with kernels methods into a new multidimensional space where the data are now linearly separable (Fig. 2.25). SVM has been used in Raman spectroscopy to classify tissues [80, 81]. The SVM method allows a better discriminative power than the LDA method [81–83]. The major drawback of SVM is the difficulty to interpret the discriminant model from a biochemical point of view, which can be easily done with an LDA method.

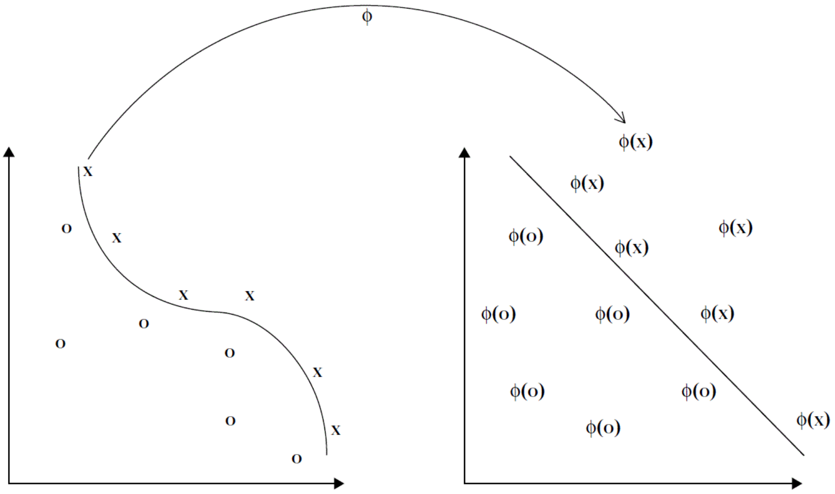

Fig. 2.25 The function embeds the data into a feature space where the nonlinear pattern now appear linear. The kernel computes inner products in the feature space directly from the inputs. From [84].

Random Forest

Random Forest (RF) is one of the latest multivariate supervised methods proposed by Breiman [85]. This algorithm is based on a learning strategy used to identify the most accurate pattern in order to design the discriminative model. The pattern recognition will provide the spectral bands which are statistically the most relevant to perform the discrimination between the two groups. The decrease in Gini index will provide the most relevant wavenumbers to discriminate between the groups (Fig. 2.26). RF can be used for classification or regression [86]. RF is now more and more used in Rama spectroscopy studies [87, 88].

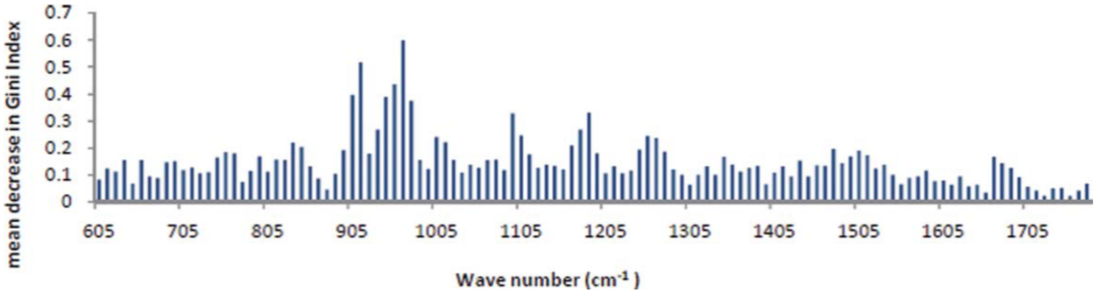

Fig. 2.26 Gini index plots in the case of the determination of protein fold class. Adapted from [89].

2.1.4.4 Performance metrics

When the goal is to discriminate two groups in a data set, it is important to quantify the discrimination performance. Performance metrics are explained in Fig. 2.27. Let's assume a data set is composed of a positive group and a negative group. After the multivariate data analysis, a score is attributed to each data point. A data point is classified as positive by the discriminant model if its score is above a threshold value. Respectively, a data point is classified as negative by the discriminant model if its score is below a threshold value. Therefore, correct classification and misclassification can be quantified based on the performance metrics defined below:

True Positive (TP): Number of data which are originally positive and are classified as positive (score above the threshold value).

True Negative (TN): Number of data which are originally negative and are classified as negative (score below the threshold value).

False Positive (FP): Number of data which are originally negative but classified as positive (score above the threshold value).

False Negative (FN): Number of data which are originally positive but classified as negative (score below the threshold value).

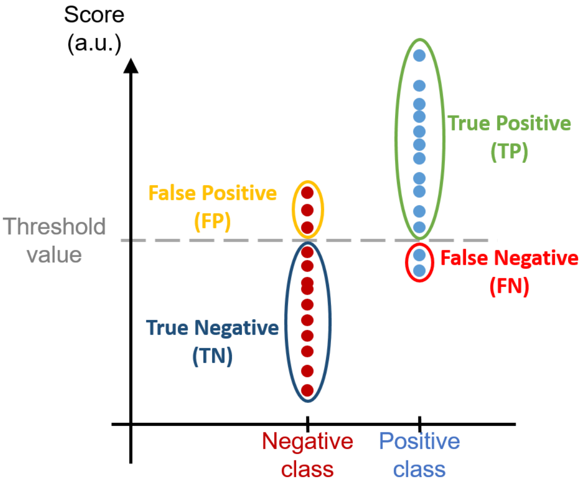

Fig. 2.27 Illustration of discrimination and performance metrics.

The performances metrics are defined by the following equations:

$$Sensitivity = \frac{TP}{TP + FN} \tag{2.14}$$

$$Specificity = \frac{TN}{TN + FP} \tag{2.15}$$

$$PositivePredictiveValue = \frac{TP}{TP + FP} \tag{2.16}$$

$$FalsePositiveRate = \frac{FP}{TP + FP} \tag{2.17}$$

$$NegativePredictiveValue = \frac{TN}{TN + FN} \tag{2.18}$$

$$Accuracy = \frac{TP + TN}{TP + TN + FN + FP} \tag{2.19}$$

The performance metrics listed above are depending on the threshold value. Receiver operating characteristics (ROC) curve is used to determine the ability of the discriminative model to discriminate the two groups [90]. In the ROC curve, the specificity and 1-sensitivity values are used as the axis. These performance metrics are calculated for a threshold from the minimum score value to the maximum score value. Basically it will indicate how the discrimination performance is sensitive to the threshold value. Fig. 2.28 shows different ROC curve for different discriminative models. From the ROC curves, the AUC can be calculated. The AUC is mathematically the area under the curve of the ROC curve [91]. A 100 % AUC is associated to an ideal discriminative model. A 50 % AUC is an inefficient discriminative model. A discrimination by flip-flopping a coin has an AUC of 50 %. The Youden Index has been introduced to determine an optimal threshold to discriminate the two groups [92].

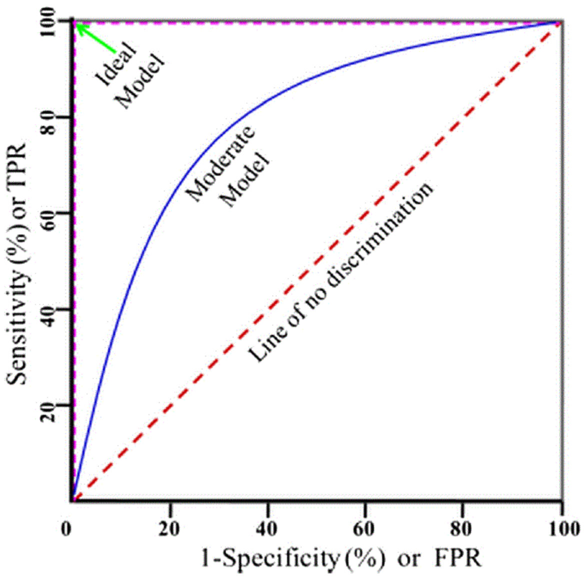

Fig. 2.28 Illustration of a ROC curve and three levels of performance. Adapted from[29].

Validation of statistical models

Cross-validation is the typical statistical method used to quantify the accuracy of the model designed on a limited data set and to evaluate the discriminative power of this model applied to a new and future data set [93, 94]. To do so, the measured data set is split in two sub-data sets. The first one is called "training data set" and is used to build the discriminative model. The second is called " testing data set" and is used to test the discriminative power of the model. This technique is particularly relevant in the case of disease diagnosis by applying the discriminative designed model on a new data set. Cross-validation allows to indicate if the discriminative model is overfitted or not. An overfitted discriminative model will have a strong discriminative power on the training data used but will have a low discriminative power on the testing data set (Fig. 2.29).

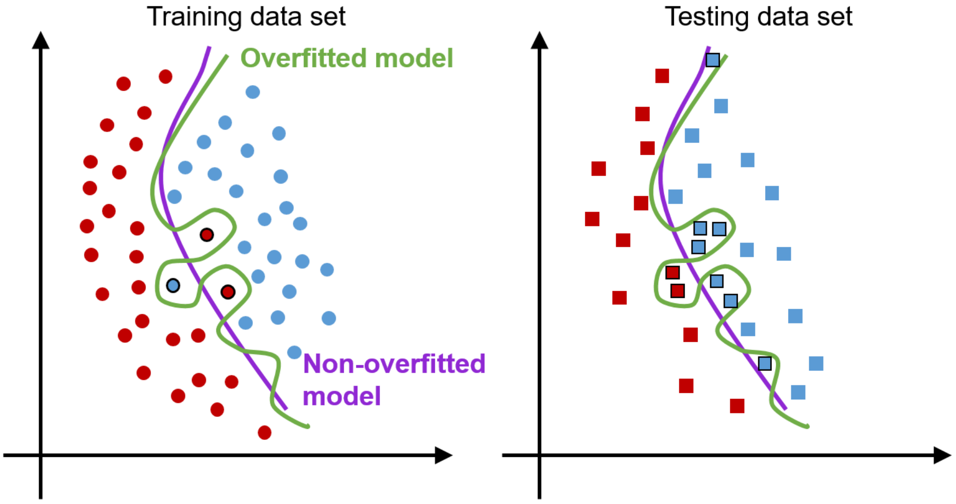

Fig. 2.29 Overfitting example. Blue points belongs to the positive class. Red points belong to the negative class. The overfitted model is displayed in green. The non-overfitted model is displayed in violet. In the case of the non-overfitted model, three data are misclassified in the training data set and all the data are correctly classified in the validation data set. In the case of the overfitted model, all the data are correctly classified and nine data are misclassified..

Different cross-validation techniques have been used in Raman spectroscopy among them k-fold cross validation [95] consists in splitting the data set into k sub-data set with similar size. The first k-1 sub-data set is used as the training data set to build the discriminative model. The last sub-data set is used as the testing data set to evaluate the discriminated model. This operation is repeated k times in order to have each sub-data set to be used in both training and testing data set. Leave-one out cross validation (LOOCV) is a particular example of a k-fold cross validation where k equals the number of data. LOOCV is commonly used in Raman spectroscopy studies [96, 97]. One of the limitation of this cross-validation technique is that the number of iteration depends on the size of the data set. To overcome this limitation, the bootstrap technique performs a similar algorithm but includes a randomization of the data set before performing the splitting step. Thus, much more combination of training and testing data are available providing more statistical power to the analysis. This technique has been recently used in Raman spectroscopy [75].

2.1.5 Raman microspectroscopy for biology

Raman microspectroscopy has been used for decades to study materials [98, 99]and liquids [100, 101]. As mentioned previously, gas thermometry is also commonly performed in a non-invasive way via Raman microspectroscopy [13]. Many reviews are available and detail the opportunities of Raman microspectroscopy in the biomedical domain [102–106]. In this section, some representative examples of the extensive literature are reported.

2.1.5.1 Investigations on biological cells

In 1990, Puppels *et al.* reported, in the review Nature, the first Raman signature of living cells without any damage induced by the laser [107]. Fig. 2.30 shows a typical example of the Raman signature of living cells, the MLE-12 mouse lung cells in this case.

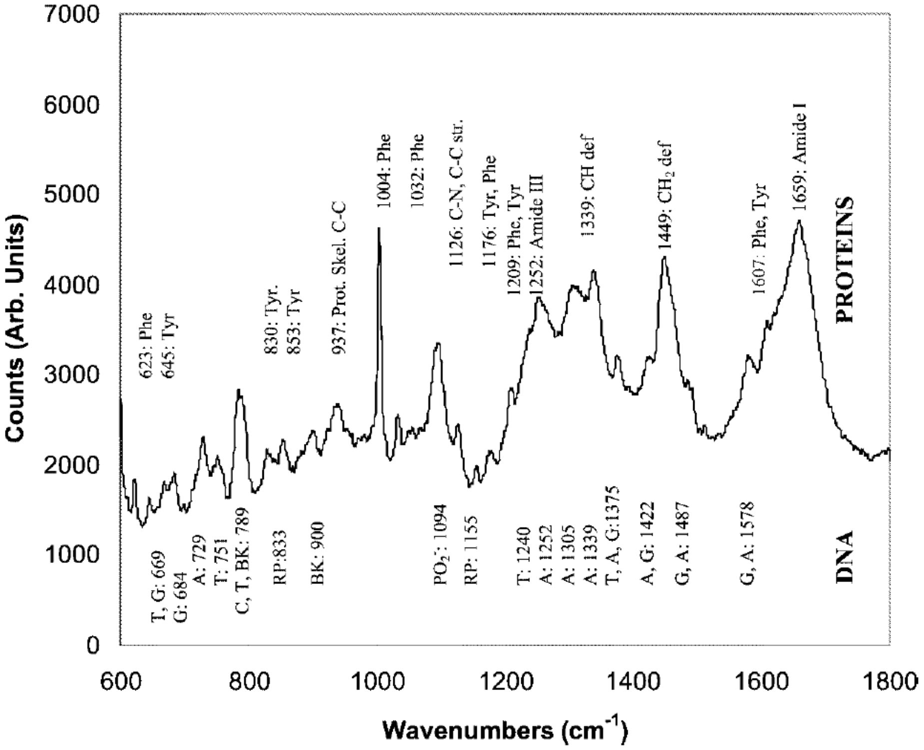

Fig. 2.30 Typical Raman signature of living MLE-12 mouse lung cells. From [14].

The Raman signature provides detailed information about the molecular composition of the cells. As shown in Fig. 2.31, the Raman signatures of living cells consists in the combination of the Raman signature of the major biopolymers that are present into the cells: proteins, lipids, DNA and RNA.

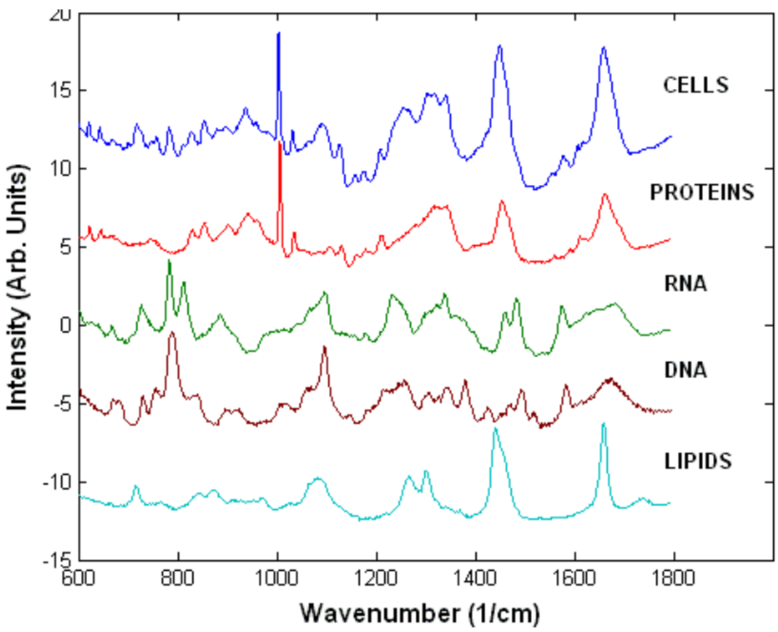

Fig. 2.31 Typical Raman spectrum of a cell and of the main biopolymers found in cells. From [108].

The determination of the protein secondary structure into the cells was a hot topic in the beginning of the 2000s [109]. The amide I band around 1650 cm^{-1} and the amide III band around 1250 cm^{-1} are the most appropriate spectral bands to obtain detailed information about the protein secondary structure. The amide I and amide III band are known to be associated respectively with the C=O and C-N stretching modes of the peptide bond between two amino acids, respectively. These chemical bonds of the peptide bond are highly sensitive to the different protein secondary structures: α-helix, β-sheet, ... As shown in Fig. 2.32, the different types of secondary structures are characterized by different peak positions and shapes in the amide I band. Many studies acquired the Raman signature of reference proteins with secondary structures previously determined by X-ray crystallography [110–112] in order to associate accurately the amide I band and the protein secondary structure. These studies revealed that the peak position of the α-helix secondary structure is slightly higher than the peak position associated to the β-sheet secondary structure. This is due to the hydrogen-bonding strengths which are weaker in β-sheets secondary structure due to their flexibility and tendency to twist [113].

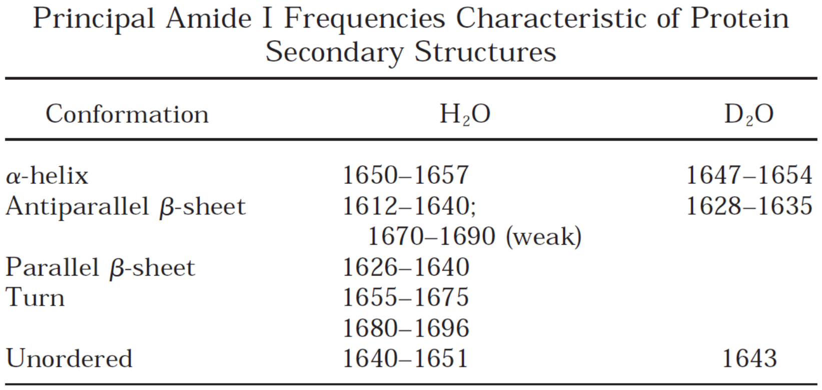
Principal Amide I Frequencies Characteristic of Protein Secondary Structures

Conformation	H_2O	D_2O
α-helix	1650–1657	1647–1654
Antiparallel β-sheet	1612–1640; 1670–1690 (weak)	1628–1635
Parallel β-sheet	1626–1640	
Turn	1655–1675 1680–1696	
Unordered	1640–1651	1643

Fig. 2.32 : Principal Amide I frequencies characteristics of protein secondary structures. From [113].

The nucleic acids are also one of the major contributors to the Raman signature of the cells. The main Raman peaks of nucleic acids are found at 1095 cm^{-1} (PO_2^- stretching), 788 cm^{-1} (O-P-O backbone in DNA), 813 cm^{-1} (O-P-O backbone in RNA), 782 cm^{-1} (thymine, cytosine and uracil) and 1578 cm^{-1} (guanine and adenine) [14]. These bands provide an accurate quantification of DNA into blood cells with an error below 10 % in comparison with a quantification based on the genome size [114]. The lipids are also easy to monitor by confocal Raman microspectroscopy when acquiring living cells. The main bands are around 1450 cm^{-1} with the CH bending vibrational modes and CH_2, CH_3 stretching mode around 2850 cm^{-1}. The degree of unsaturation of acyl chains is accessible with the 1660 cm^{-1} vibration attributed to C=C stretching mode [115]. The band attribution is a critical point in order to accurately determine the molecular composition of the cells. Nevertheless, the peak positions may shift about 5 cm^{-1} from one cell type to another making the interpretation of the spectra more difficult. A tentative band assignment for the human embryonic stem cells is reported in Fig. 2.33. Over the last years, a large data base of biological molecules has been built [116] and allows to get accurate biochemical information of the cells when taking into account the potential peak position shifts. It can be noticed that the Raman signature of biological samples can be splitted into two spectral bands: fingerPrint (FGP) and high wavenumber (HWN). The FP spectral band is between 600 and 1900 cm^{-1}; while the HWN band is between 2800 and 3800 cm^{-1}. From 2000 to 2800 cm^{-1}, the Raman signature of biological samples is extremely low and is only attributed to the sample autofluorescence. This “empty” band can be usefully used to target specific external compounds which are active in this spectral band.

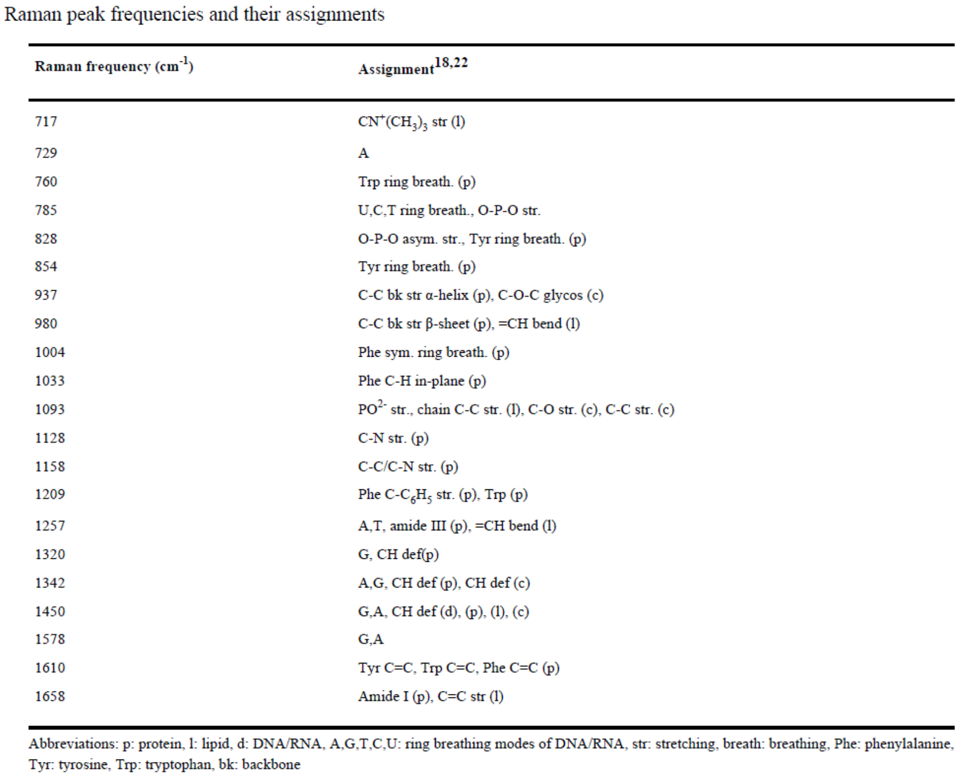

Raman peak frequencies and their assignments

Raman frequency (cm^{-1})	Assignment[18,22]
717	$CN^+(CH_3)_3$ str (l)
729	A
760	Trp ring breath. (p)
785	U,C,T ring breath., O-P-O str.
828	O-P-O asym. str., Tyr ring breath. (p)
854	Tyr ring breath. (p)
937	C-C bk str α-helix (p), C-O-C glycos (c)
980	C-C bk str β-sheet (p), =CH bend (l)
1004	Phe sym. ring breath. (p)
1033	Phe C-H in-plane (p)
1093	PO^{2-} str., chain C-C str. (l), C-O str. (c), C-C str. (c)
1128	C-N str. (p)
1158	C-C/C-N str. (p)
1209	Phe C-C_6H_5 str. (p), Trp (p)
1257	A,T, amide III (p), =CH bend (l)
1320	G, CH def(p)
1342	A,G, CH def (p), CH def (c)
1450	G,A, CH def (d), (p), (l), (c)
1578	G,A
1610	Tyr C=C, Trp C=C, Phe C=C (p)
1658	Amide I (p), C=C str (l)

Abbreviations: p: protein, l: lipid, d: DNA/RNA, A,G,T,C,U: ring breathing modes of DNA/RNA, str: stretching, breath: breathing, Phe: phenylalanine, Tyr: tyrosine, Trp: tryptophan, bk: backbone

Fig. 2.33 Tentative band assignment of human embryonic stem cells. From [117].

Nowadays, many reviews are detailing the large possibilities offered by this non-invasive and label-free optical technique to contribute to a better understanding of the cellular metabolism [16, 108, 118]. In the next paragraph, we are going to present some examples of *in vitro* studies.

Monitoring the cell cycle

In 2008, Swain *et al.* demonstrated that the cell cycle can be monitored by Raman microspectroscopy on human osteosarcoma living cells [119]. The cells were previously synchronized in G0/G1, S or G2/M cell cycle phases by serum starvation and chemical-based protocols. As expected, a relative increase in signal from the nucleic acids and the proteins were noticed from G0/G1 phase to G2/M phase (Fig. 2.34-A). An accuracy of 97 % was obtained by LDA data analysis in LOOCV when discriminating the G0/G1-phase cells from the G2/M-phase cells. The classification accuracy was lower for the cells synchronized in S phase with the two others cell cycle phases (Fig. 2.34-B).

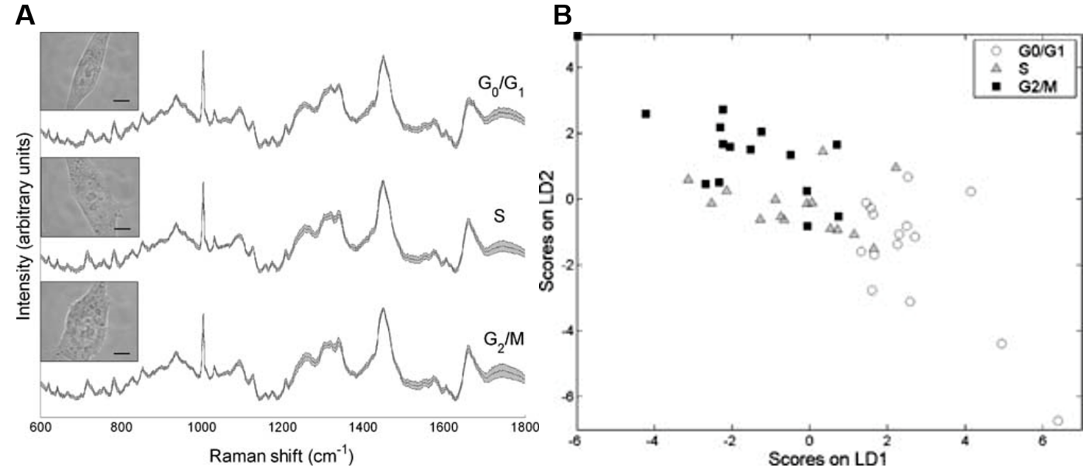

Fig. 2.34 Monitoring the cell cycle via Raman microspectroscopy. A - Mean Raman signature of living cells at different phase in the cell cycle. B - LD score plot to discriminate the different phase cell populations. Adapted from [119].

Living vs dead cells

In a different cell type (human lung derived cell A549), modifications in DNA vibrational modes (782, 788 and 1095 cm^{-1}) were also noticed when comparing the Raman signature of living cells versus the Raman signature of dead cells [120]. Fig. 2.35 shows that the peak at 788 cm^{-1}, relative to DNA O-P-O backbone modes, decreases by 80 % in the spectrum of the dead cells in comparison to the living cells.

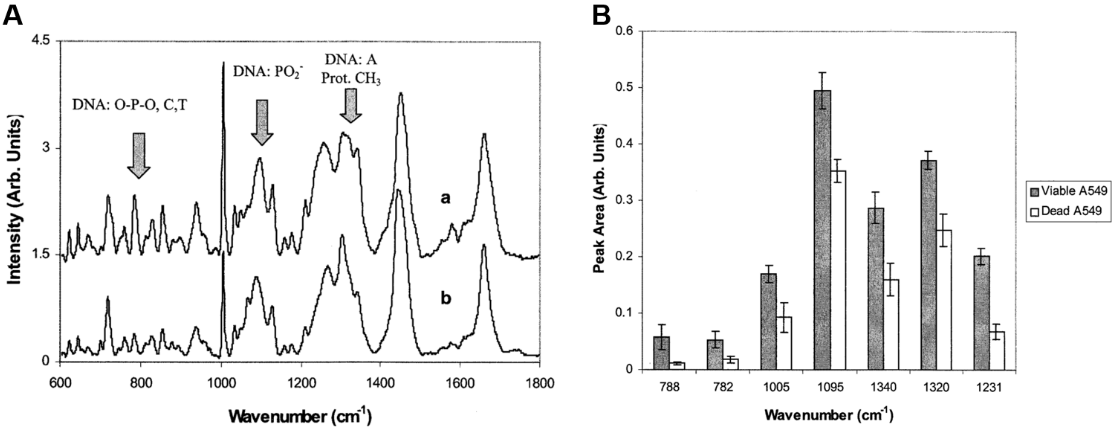

Fig. 2.35 Raman analysis of viable and dead A549 cells. A - Raman spectra of viable (spectrum a) and dead (spectrum b) A549 cells. B - The spectral differences between viable and dead A548 cells. Adapted from[120].

Pharmacology in cells

Raman microspectroscopy has also been used to study drug delivery systems in biological samples [121]. For instance erlotinib, a tyrosine kinase inhibitor currently used as a targeted therapy to treat non-small-cell lung cancer [122, 123], is well-suited to be monitored by Raman microspectroscopy because it contains an acetylene function group. The acetylene stretching vibrates at 2095 - 2140 cm^{-1}, which is the region free of cellular vibrational modes. The pharmacodynamics of erlotinib into the cells have been studied by monitoring this spectral band [124]. Spectral differences were noticed between the spectrum of pure erlotinib spectrum and the spectrum of erlotinib into the cells, suggesting that the cells metabolized the drug.

Stem cells differentiation

Stem cells have the ability to differentiate into other cell types (Fig. 2.36) [125–127]. Being able to control the stem cell differentiation process is a promising technique for the regenerative medicine [128]. Having a confirmation of the stem cell differentiation is though necessary. The chemical composition of cells may be used as an accurate biomarker for monitoring the stem cell differentiation process. The stem cell differentiation takes several days.

This slow dynamic process is easily accessible by confocal Raman microspectroscopy. Many reviews are available on this hot topic [117, 129, 130].

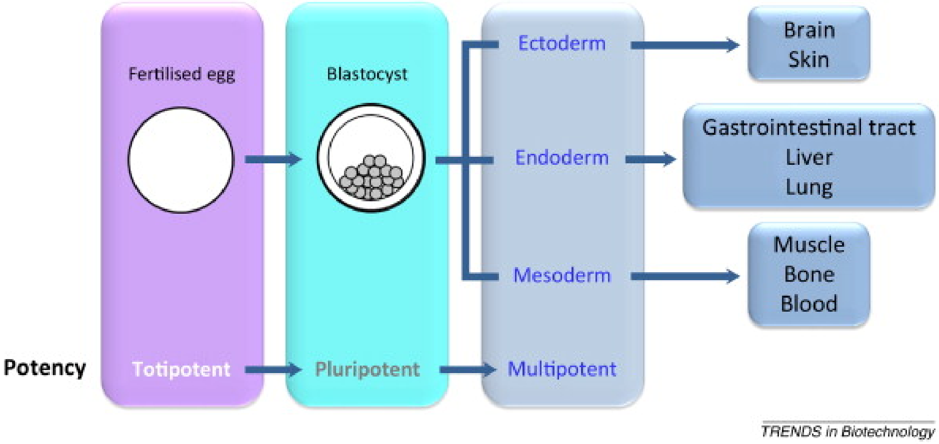

Fig. 2.36 The different stages in stem cell development. The pluripotent embryonic stem cells are represented by grey circles. From [130].

Pascut *et al.* monitored the cardiac differentiation of human embryonic stem cells [131]. Based on multivariable data analysis, a spectrum specific of the cardiac differentiation was determined. The molecular interpretation of this spectrum has shown that the carbohydrates play a key role in the differentiation process. The spectral maps of this biomarker showed that the dynamics of the differentiation process present a key time point at day 7.

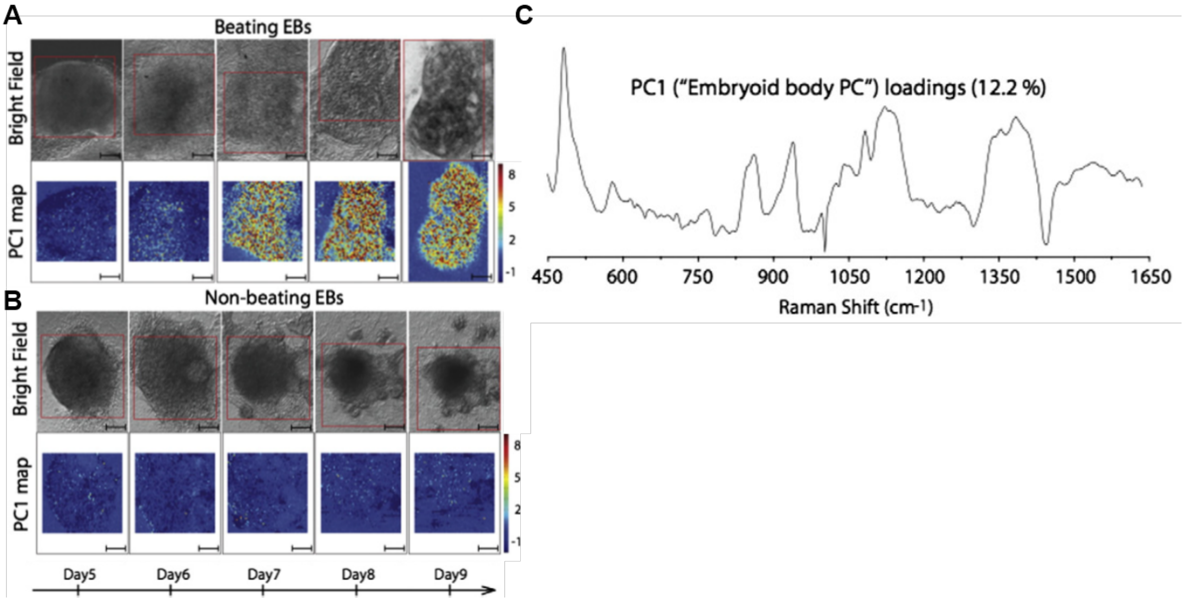

Fig. 2.37 Monitoring of embryonic stem cells cardiac differentiation by Raman microspectroscopy. A - Time-course of Raman spectral maps of beating embryonic body (positive condition). B - Time-course of Raman spectral maps of non-beating embryonic body negative condition). C - Loading of "Embryoid body principal component". Adapted from [131].

Another study demonstrated obvious changes in the Raman signature of human Mesenchymal Stem Cell (hMSCs) during the osteogenic differentiation process [132]. Raman biomarkers were identified and associated to the apparition of mineral species that are similar to what is expected in native bone (Fig.2.38).

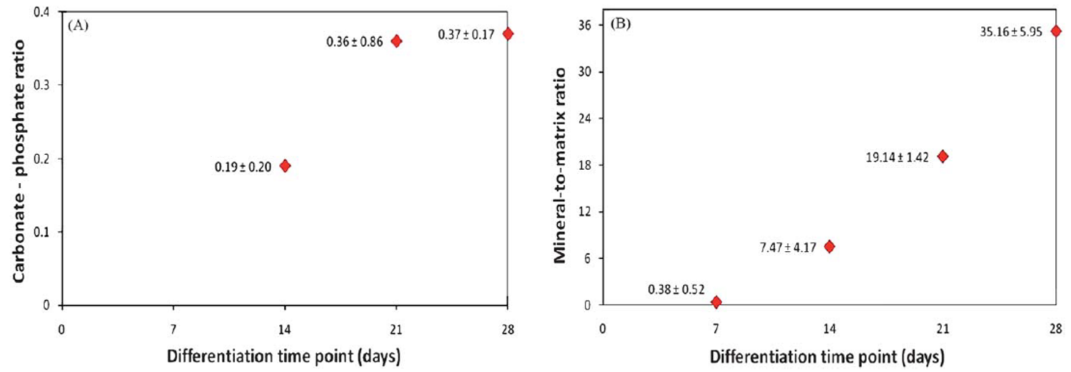

Fig. 2.38 hMSC differentiation process. A - Carbonate-to-phosphate ratio (CO_3^{2-}, 1070 cm^{-1}; PO_4^{3-}, 960 cm^{-1}) from hMSCs cultured in osteogenic media for 28 days. B - Mineral-to-matrix ratio (PO_4^-, 960 cm^{-1}; Hydroxyproline, 850 cm^{-1}) from hMSCs cultured in osteogenic media for 28 days. Adapted from [132].

Many other studies confirmed that Raman microspectroscopy is an adequate non-invasive and label-free optical technique to monitor stem cell differentiation process in different cell types [117, 133, 134].

Cell type identification

Raman microspectroscopy is able to discriminate and classify two liver cancer cells HepG2 and SK-Hep1 [135]. Fig. 2.39 shows the obvious discrimination results of HCA, an unsupervised multivariable data analysis technique. In this study, a classification by SVM algorithm in 10-fold cross-validation allows to classify the two cells types with a prediction accuracy of 93 %. The differences in the Raman signature between the proliferating HepG2 cells and the non-proliferating HepG2 cells were also assessed with an accuracy of 98 %. A similar study has been performed on human thyroid cell lines with good discriminative results [136]. Another study went further by demonstrating the possibility of Raman microspectroscopy to identify different cell types from a mixed cancer cell populations [137].

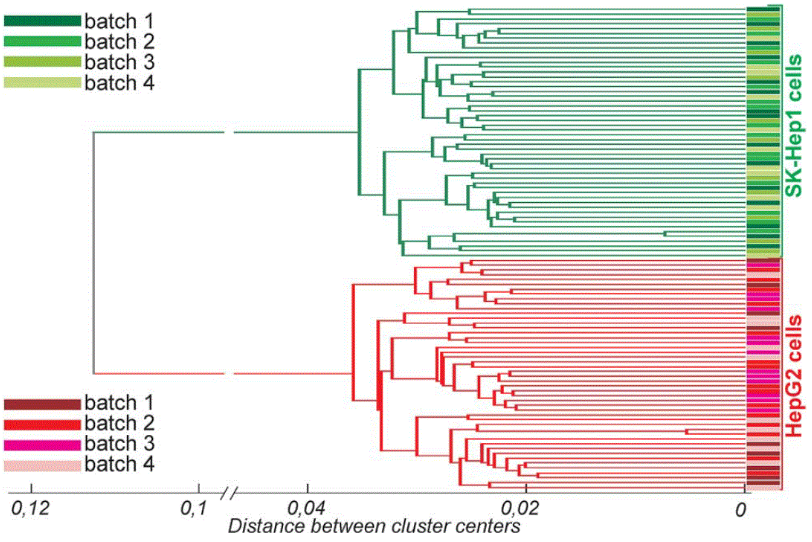

Fig. 2.39 Dendrogram from HCA of Raman spectra showing the clustering of HepG2 (n=48) and SK-Hep (n=52) cells with assigned sub-clusters. The batches of the cell are marked in different colours . From [135].

Fixed cells vs living cells

The Raman signal is known to be a weak signal. So, long exposure times (almost one minute) are necessary to acquire a spectrum. This major drawback limits the access to dynamical processes. Fixing the sample is one of the solution in order to have the opportunity to perform long-term acquisitions and to get a complete map of the Raman signature of the sample. But the fixation procedure is not without effects on the Raman signature. Draux and colleagues demonstrated that three fixation procedures modify notably the Raman signature in comparison with the living cells [138]. Mainly, the vibrational modes of DNA, RNA and proteins were affected by the fixation procedure. The formalin-fixation process was the one recommended to limit the impact on the Raman signature.

2.1.5.2 Investigations on tissue samples

The great potential of Raman microspectroscopy to target biomedical questions has now been proven [105, 139, 140]. Nevertheless, Raman microspectroscopy is not yet part of the routine clinical workflow, many Raman microspectroscopy clinical studies have been done since 2000 especially in order to improve the diagnosis of disease such as cancer. The absence of standardized protocols compatible with the clinics might explain the slow entrance of Raman microspectroscopy into the clinical workflow [141].

Cancer diagnosis
In the clinics, the diagnosis of cancer disease is not performed by Raman microspectroscopy. In most cases, the diagnosis of cancer disease is performed based on the histopathology. Although histopathology is the gold standard technique to detect cancer tissue, it has the major drawback to be performed *ex vivo*, meaning after a biopsy of the suspected lesion, and to be time consuming due to the preparation of the sample (fixation, cutting thin slices and staining) and the analysis by the pathologist. Performing optical diagnosis via Raman microspectroscopy seems to be a good alternative, but a carefully conducted study needs to be performed in order to quantify accurately the discriminative power of this optical technique [142]. Many studies of cancer diagnosis in different organs were performed in the last decades [104, 143, 144]. In the following, some examples will be presented. Caspers *et al.* demonstrated that confocal Raman microspectroscopy is able to determine with a high accuracy the molecular concentration of many compounds, such as water and natural moisturing factor (NMF) [145]. By acquiring the Raman signature in the HWN spectral band of the skin, the water concentration can be determined by a simple band ratio. This biomarker is accessible with an acquisition time of around 1 second. Recently, Barroso *et al.* used this biomarker to discriminate squamous cell carcinoma from healthy tissue in the case of oral cancer [146]. On 14 patients, this biomarker allowed to classify fresh surgically resected tongue in the two groups with a discriminative power of 98 %. The threshold of water concentration was fixed to 69 % to achieve this discriminative power. In a second study, it was observed that the water concentration changes across the tumour border towards the healthy surrounding tissue on freshly excised samples [147]. The transition from a high water concentration (76 %) to a low water concentration (54 %) is associated to the transition from tumour tissue to the healthy surrounding tissue. This transition takes place over a distance between 4 to 6 mm to the tumour border which fits with the 5 mm of resection margin required by the surgical procedure in this case (Fig. 2.40).

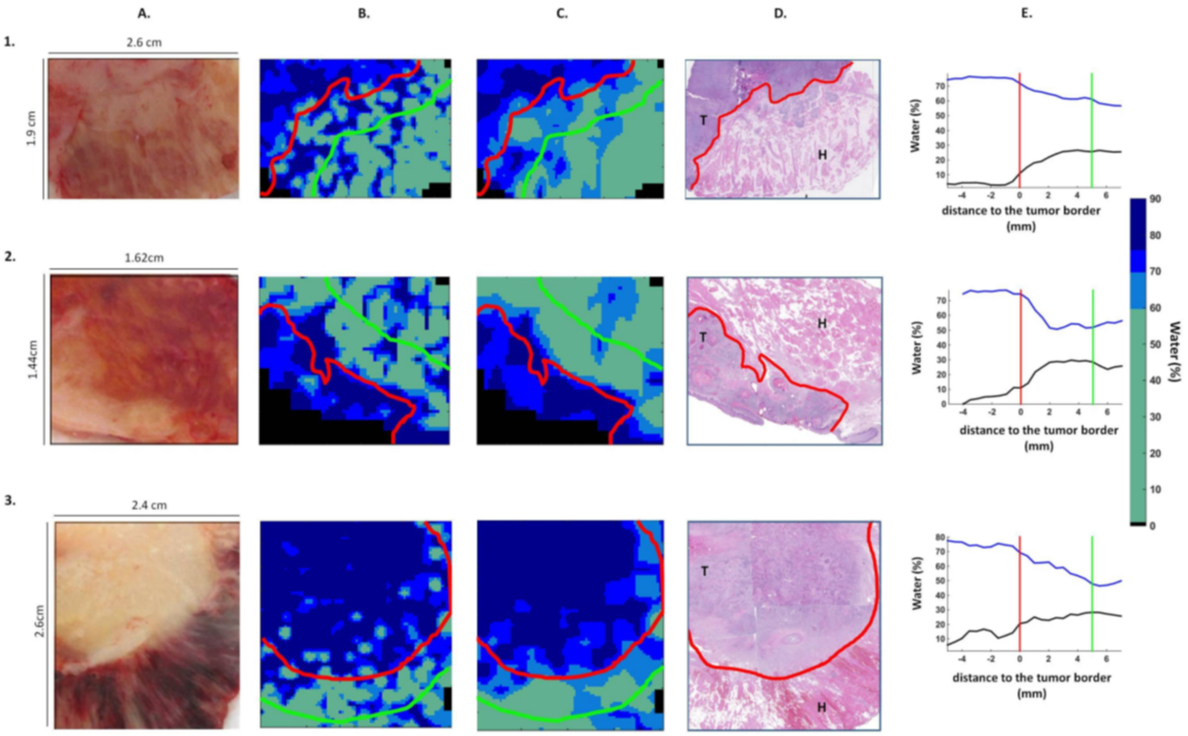

Fig. 2.40 1-3: Examples of the data obtained by the means of mapping experiments on 3 Raman tissue sections from 3 patients. Column A-Photograph of the measured fresh tissue surface. Column B-Raman water map with indication of tumour border (red: based on final histopathology shown in column D) and adequate surgical margin (green). Column C-Averaged Raman water map with indication of tumour border (red: based on final histopathology shown in column D) and adequate surgical margin (green). Column D-H&R stained section obtained from the measured tissue surface with the tumour border (red), tumour (T), healthy surrounding tissue (H) indicated by pathologist. Column E-Graphs showing water concentration as function of the distance to the tumor border. Blue line: Average water concetration calculated per 0.5 mm distance interval. Black line: Standard deviation of the water concentration, per 0.5 mm distance interval. The red line at 0 mm represents the tumor border and the green line represents a distances of 5 mm from tumor border. Adapted from [147].

Discrimination of breast cancer by Raman microspectroscopy has also been studied. Haka and colleagues demonstrated, *ex-vivo* [148] and then *in-vivo* [149], that collagen and fat might be used as biomarkers to discriminate malign from benign lesions with an accuracy of 93 % (Fig. 2.41).

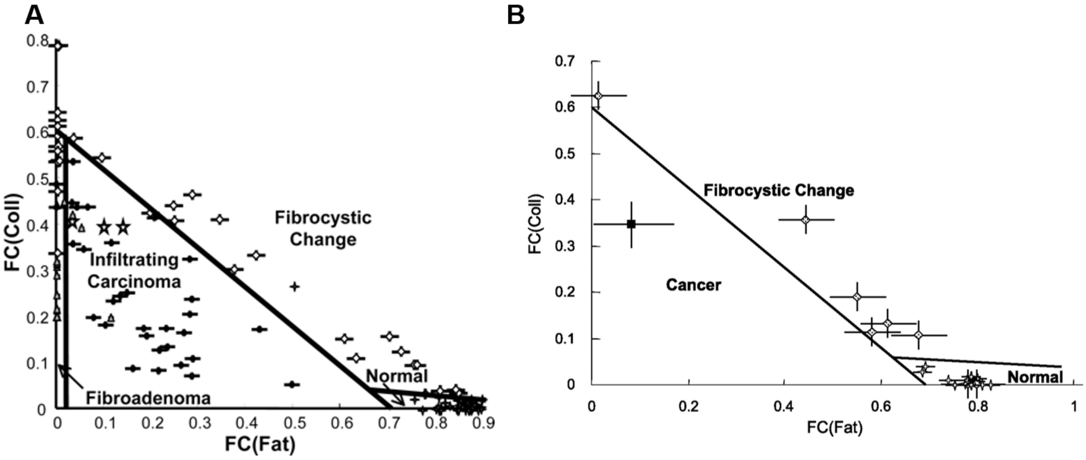

Fig. 2.41 Discrimination between cancer and healthy tissue in the case of breast cancer. A - Scatter plot displaying the fat and collagen content for the *ex-vivo* Raman spectra [148]. B - Scatter plot displaying the fat and collagen content for the *in-vivo* Raman spectra. From [149].

Harris *et al.* reviewed the cancer diagnosis via Raman microspectroscopy in the case of head and neck cancer [150]. Two similar studies report that the identification of squamous cell carcinoma on *ex vivo* larynx tissue section performed via Raman microspectroscopy was obtained with a specificity of around 90 % [151, 152]. The spectral changes associated to the malignancy were related to the proteins conformation and the increase in nucleic acid bases. Recently, Singh *et al.* performed oral cancer diagnosis based on Raman microspectroscopy on *in-vivo* tissue sample with an accuracy of around 95 % without cross-validation and 85 % with cross-validation [153]. Due to a high concentration in melanin, the acquisition of Raman signature of melanoma suffered from a strong autofluorescence signal. Santos *et al.* used a laser in the near-infrared (around 1000 nm) and a low-noise InGaAs detector to acquire the Raman signature of pigmented lesion with a reasonable SNR [17]. Fig. 2.42 shows that this experimental set-up was able to discriminate melanoma and benign melanocytic lesions with an accuracy of 77 % in LOOCV [154]. *In-vivo* measurements were also performed with a fibre probe. The discrimination results were of 73 % and 85 % in the case of, respectively, basal cell carcinoma and squamous cell carcinoma [155].

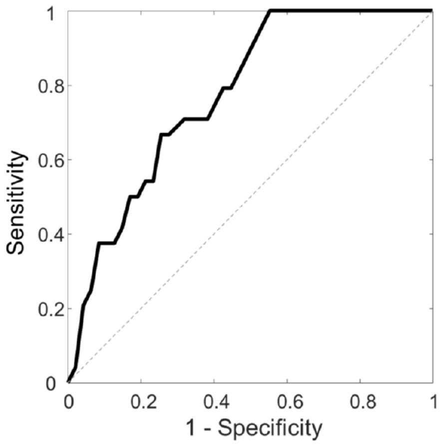

Fig. 2.42 ROC curve of discrimination of melanoma using PCA-LDA classification model with lean-one sample-out cross validation method. From [154].

In the case of brain tumors, Kast and colleagues succeeded to identify normal grey matter and whitte mater from pathologic glioblastoma and necrosis in *ex-vivo* tissues [156]. The area under the ROC curve was 96 % for grey matter and 98 % for white matter. A group in Montreal has designed a handheld contact Raman probe to investigate the use of Raman microspectroscopy for intraoperative brain cancer detection (Fig. 2.43). The study reported an accurate detection of grade 2 to 4 gliomas during human brain cancer surgery [157] . The discrimination performance between cancer cell-invaded brain and normal brain was over 90 % in sensitivity and specificity. The most significant differences between the spectra of normal and cancer tissues were attributed to cholesterol, proteins and nucleic acids. The authors demonstrated that the detection limit of the equipment was 17 cancer cells/0.0625 mm^2.

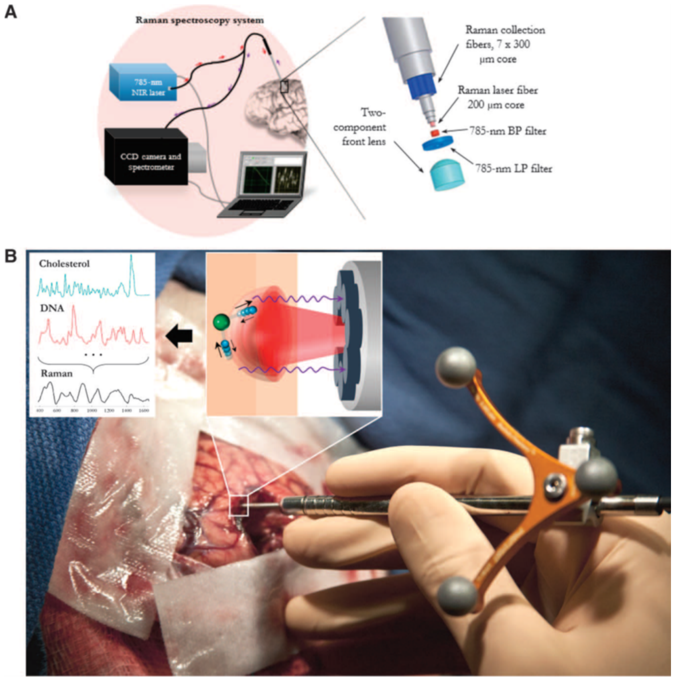

Fig. 2.43 The handheld contact fibre optic probe for Raman microspectroscopy. A - Experimental setup diagram. B - The probe was used to interrogate brain tissue during surgery. Adapted from [157].

Cancer disease has been diagnosed via confocal Raman microspectroscopy with good discriminative performances on other organs such as the bladder [158] or the œsophagus [97]. As for brain cancer, a fibered Raman system allows an access to deep seated tissue [22, 159]. These promising results confirm the efficiency of Raman microspectroscopy to perform an optical diagnosis in a non-invasive, label-free and fast way. Nevertheless, the maturity of the discriminant models still highly differs between the different organs.

2.2 Other Raman-based instrumentations

As mentioned previously, one of the major limitations of Raman microspectroscopy is its very weak signal which induces a low time resolution due to long exposure times (about 60 seconds to acquire the Raman signature of a cell). The low Raman signal is mainly due to the fact that it is generated by a spontaneous excitation. Many other Raman-based microspectroscopy techniques have been designed in order to significantly increase the signal and thus to improve the time resolution. The exhaustive presentation of these optical techniques is out of the scope of this manuscript. However, we will briefly introduce the main Raman-based techniques.

2.2.1 Coherent Raman scattering microscopy

Coherent anti-stokes Raman scattering (CARS) and stimulated Raman scattering (SRS), are two coherent Raman scattering techniques that allow the acquisition of images at a specific vibrational mode of interest [10, 160, 161]. Coherent Raman scattering microscopy is based on the Raman effect. Thus, it is a non-invasive and label-free optical technique which give access to the molecular composition of the sample [162, 163]. Fig. 2.44 illustrates the chemical specificity of SRS microscopy on Drosophila cells. Coherent Raman microscopes are generally confocal microscopes. By selecting the appropriate vibrational mode to be probed, the spatial distribution of amino-acids, lipids or proteins is easily accessible. The spatial resolution is similar to the one achieved in confocal microscopy, about hundreds of nanometres. For instance, single nanodiamonds with a radius between 60 to 200 nm have been detected into HeLa cells [164]. Thanks to a high SNR, video-rate microscopy has been achieved on *in vivo* samples, thus allowing the monitoring of dynamic metabolic processes [165, 166].

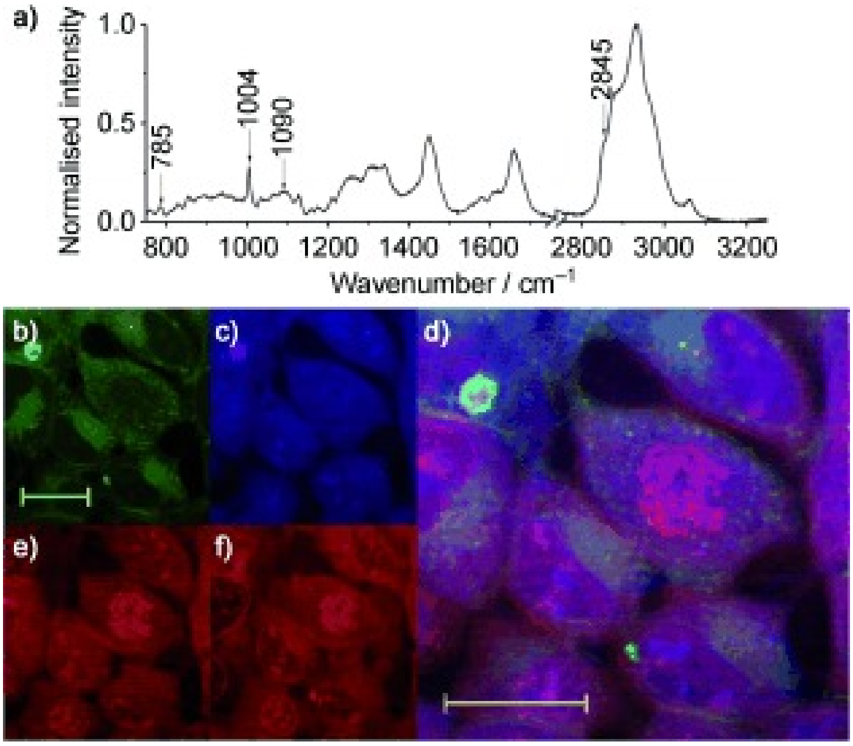

Fig. 2.44 a) Raman spectrum of a Drosophila cell. b–f) SRS images of a salivary gland cells from Drosophila melanogaster, via the stimulated Raman loss detection scheme. b) Lipid-specific image taken at 2845 cm^{-1}, c) Amide I band at 1655 cm^{-1}, e) nucleic acids at 785 cm^{-1} and f) 1090 cm^{-1}. d) Multicolor image generated by combining images (b)–(e). The scale bar is 20 µm. Each image has the size of 512 Ö 512 pixels. From [167].

CARS is a four-wave mixing and non-linear process in which a pump, Stokes and probe photon interact with the sample in order to generate an anti-Stokes photon at a specific frequency (Fig. 2.45-A). Generally the pump and probe photons derive from the same laser beam. Hence the anti-Stokes wavenumber is equal to (equation 2.20):

$$\omega_{anti-Stokes} = 2 * \omega_{Pump} - \Omega_{Stokes} \tag{2.20}$$

where $\omega_{anti-Stokes}$ is the wavenumber of the anti-Stokes photons, ω_{Pump} is the wavenumber of the pump photons and ω_{Stokes} is the wavenumber of the Stokes photons

The CARS intensity depends linearly on the Stokes laser intensity and quadratically on the pump laser intensity. Coherent excitation is the key point to increase the Raman signal by 8 orders of magnitude. To induce coherent excitation, the difference in wavenumbers between the pump and the Stokes photons has to match with a vibrational mode present in the sample. This resonant condition has to be fulfilled in order to generate the CARS signal. Fig. 2.45 illustrates the generation of the CARS signal in a resonant and a non-resonant process. Finally, a phase-matching condition has to be fulfilled in order to create a CARS signal in the appropriate direction, meaning the direction of the detection system [160, 161]. The CARS signal is generated by the creation of anti-Stokes photons and the CARS images are acquired by the detection of anti-Stokes photons at each pixel by a sensitive photomultiplier. It is possible to acquire hyperspectral CARS images, meaning a CARS spectrum at each pixel of the image, by simultaneously exciting several vibrational modes using a laser with a multiple frequency content such as a supercontinuum laser [168].

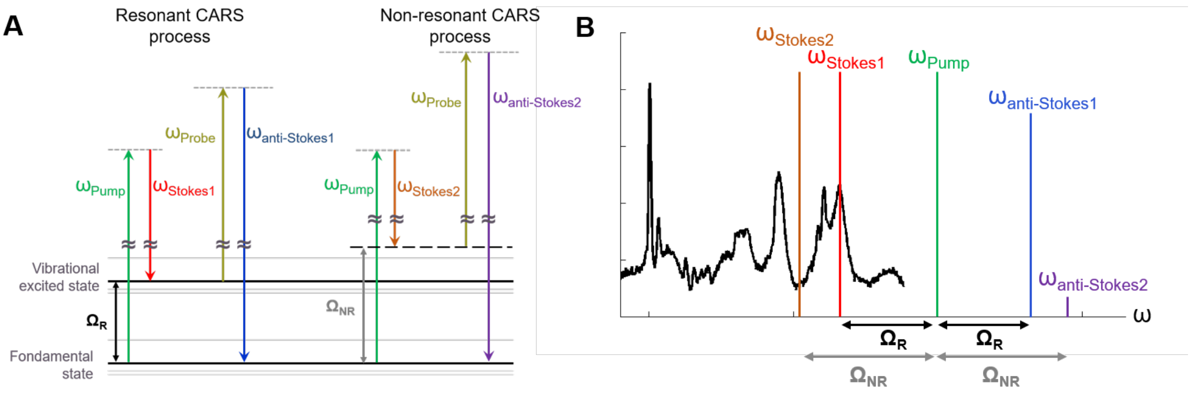

Fig. 2.45 Scheme of the CARS process. A - Energy diagram for a resonant (Ω_R) and a non-resonant (Ω_{NR}) CARS process. B – Wavenumbers representation of the different photons on a Raman spectrum for a resonant and a non-resonant CARS process.

CARS images may suffer from a non-resonant background due to electronic transitions. The removal of the contribution of the non-resonant background in CARS images requires a specific data image processing. Many phase retrieval algorithms have been developed specifically for CARS images [169, 170]. Fig. 2.46 illustrates the effect of data processing on a CARS spectrum.

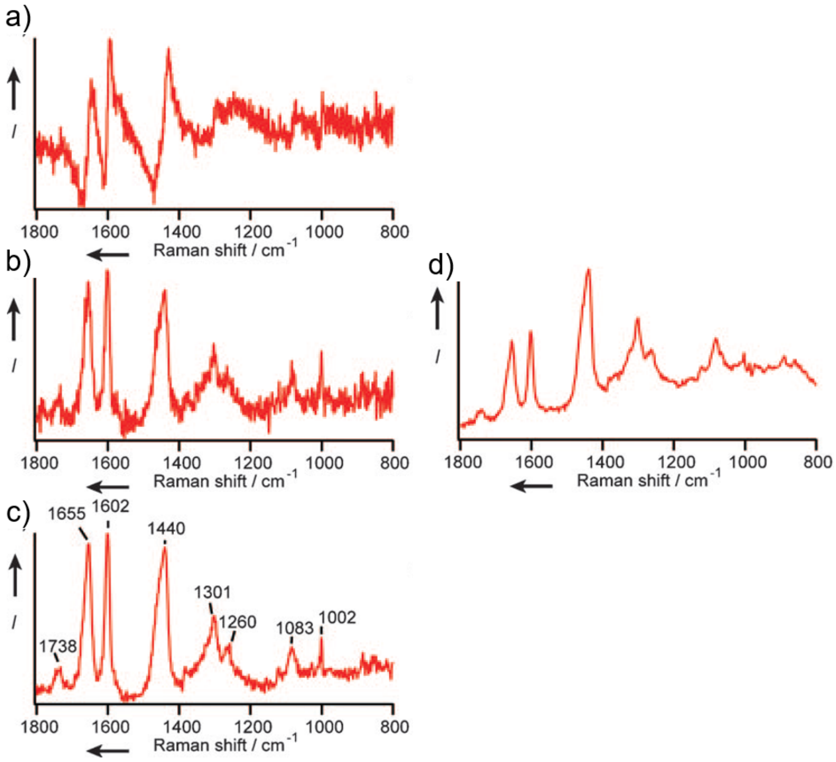

Fig. 2.46 a) Typical CARS spectrum in the fingerprint region of a living budding yeast cell; b) Phase retrieval CARS spectrum by maximum entropy method; c) Phase retrieval CARS spectrum after a singular value decomposition analysis; d) spontaneous Raman spectrum. The exposure times for the measurement of the CARS and spontaneous Raman spectra were 50 ms and 300 s, respectively. Adapted from [171].

SRS microscopy aims at performing coherent Raman scattering microscopy or microspectroscopy without the contribution of the non-resonant background. The absence of the non-resonant background is due to the acquisition of the signal. Unlike CARS microscopy which can be performed via an epi-detection, SRS is a transmission light imaging technique [172, 173]. SRS is based on the detection of the intensity of the pump or the Stokes beam after having crossed the sample. When the Stokes and the pump beams are both focused at the same time and the same location, the pump beam intensity collected after the sample is lower than only the pump beam was focused on the sample. This loss in the pump intensity is called stimulated Raman loss (SRL). Respectively, when the Stokes and the pump beams are both focused at the same time and the same location, the Stokes beam intensity collected after the sample is higher than when only the Stokes beam was focused on the sample. This gain in the Stokes beam intensity is called stimulated Raman gain (SRG). SRL or SRG are detected via a photodiode by the modulation of either the Stokes or the pump beam. The detection of SRL or SRG is synchronized with the modulation of the pump or the Stokes beam via a lock-in amplifier (Fig. 2.47). SRG and SRL signals are not suffering from the contribution of non-resonant background. In this case, no phase retrieval algorithm is necessary.

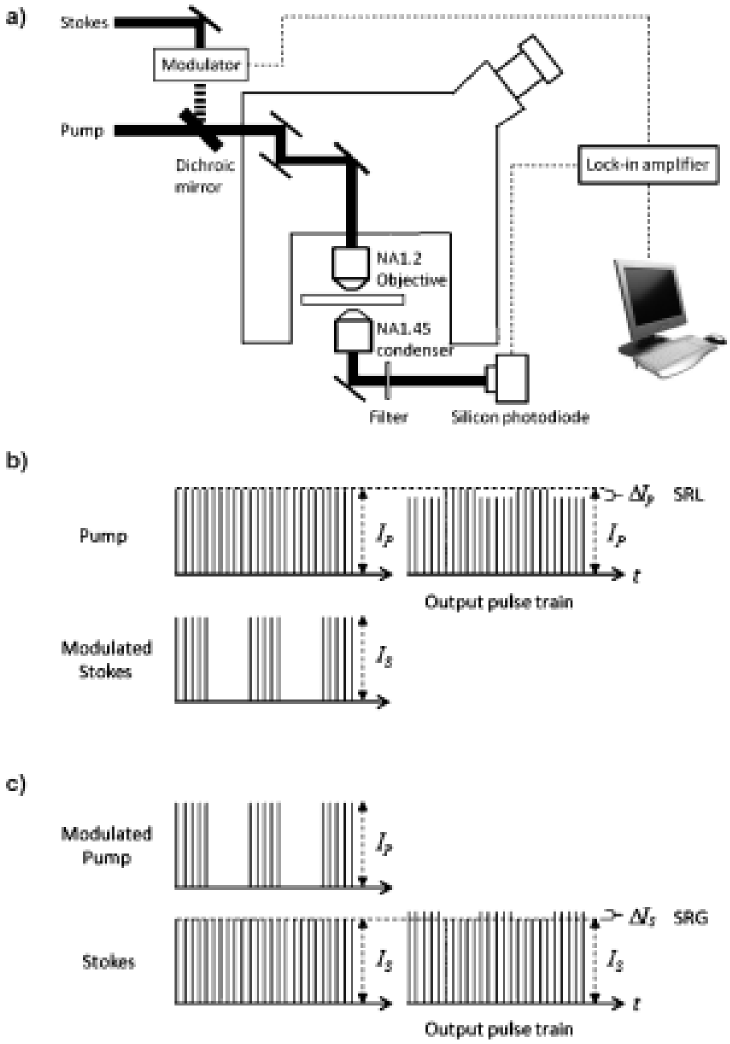

Fig. 2.47 a) Experimental setup of the stimulated Raman loss (SRL) microscope. For SRG, the pump beam is modulated instead of the Stokes beam and a photodetector is used instead of a silicon photodetector because of its better responsivity at 1064 nm. b) Detection scheme of SRL. The Stokes beam is modulated at 10.4 MHz, where the resulting amplitude modulation of the pump beam due to the stimulated Raman loss can be detected. c) Detection scheme of SRG. The pump beam is modulated at 10.4 MHz, where the resulting amplitude modulation of the Stokes beam due to the stimulated Raman gain can be detected. Adapted from [167].

Many SRS and CARS microscopy studies have been performed on live cells and revealed that the lipid droplets were mainly made of unsaturated lipids [174, 175]. The dynamics of the uptake of surfactant in mammalian cells which is known to lead to cell lysis has also been investigated thanks to CARS microscopy [176]. This study demonstrated that the surfactant is detected inside the cells mainly after 20 minutes of incubation. These dynamics fit with a major decrease in the cellular metabolic activity observed after 20 minutes of incubation. SRS microscopy has allowed to follow the cell cycle in a label-free manner by monitoring the DNA of HeLa cells [167].

Although coherent Raman scattering microscopy is a much less mature technology than Raman microspectroscopy, the first commercially available confocal CARS microscope was proposed by Leica a few years ago (Fig. 2.48).

Fig. 2.48 Leica SP8 CARS microscope (from `http://www.leica-microsystems.com/`)

2.2.2 Surface-enhanced Raman scattering microscopy

Surface-enhanced Raman scattering (SERS) gives an enhancement of up to 10^6 in scattering efficiency over spontaneous Raman scattering. It consists in the generation of an enhanced electric field in the proximity of a metallic nanostructure thanks to a localized surface plasmon resonance process [177]. The mechanisms of the plasmon surface resonance process are not described here, but details can be found in two reviews published about 10 years ago [178, 179]. The SERS instrumentation is exactly the same as a Raman microscope. For SERS, the sample has to be in contact with the metallic nanostructure to enhance the Raman signal. The key point of SERS is to assure the proximity between the metallic nanostructure and the sample to study. Therefore, functionalized SERS surfaces have been designed in order to optimize the interactions between the SERS surface and the sample. SERS flow cytometry has also been designed and allows to discriminate two populations of cells based on their Raman signatures with a time resolution of around 100 µs per spectrum [180].

2.3 Fluorescence microscopy

Among the large palette of biophotonics techniques, fluorescence microscopy is the most commonly used in life sciences. Fluorescence microscopy is based on the use of a fluorescent molecule, called fluorochrome or fluorophore, and the detection of its fluorescence signal by a light microscope. Depending on the properties of the fluorochrome, fluorescence microscopy enables the study of diverse cellular structures and/or processes [181]. For instance, Fig. 2.49 illustrates a Normal African Green Monkey Kidney Fibroblast cell with three different fluorochromes labelling the nucleus, the mitochondria and the cytoskeleton.

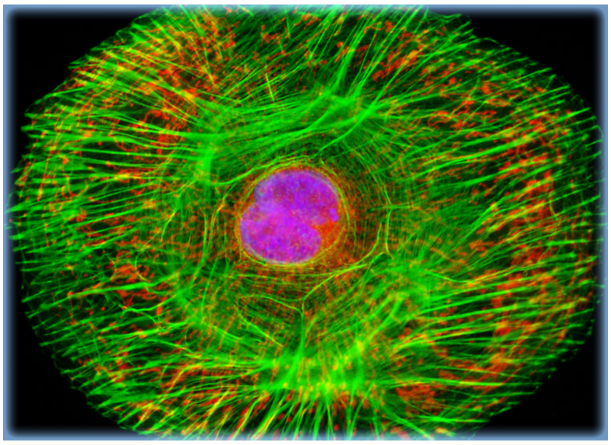

Fig. 2.49 Normal African Green Monkey Kidney Fibroblast Cell (CV-1 Line). Multilabelling: MitoTracker Red CMXRos, DAPI, and Alexia Fluor 488 conjugated to phalloidin, which target respectively mitochondria, DNA in the cell nuclei, and F-actin. From `http://www.olympusmicro.com/primer/techniques/fluorescence/gallery/cells/agmindex.html`.

2.3.1 Physical bases of the fluorescence phenomenon

Fluorescence is based on the interaction of light with specific fluorescent molecules. These molecules have the ability to generate photons with a specific wavelengths within nanoseconds after the absorption of a photon with a shorter wavelength. Thus, the fluorescence signal is delimited in duration and in wavelength [182, 183].

The fluorescence phenomenon has been detailed thanks to quantum physics (Figure 3). When fluorescent compounds in their ground state absorb the energy of the exciting light, an energetic transition towards a virtual excited state occurs (Fig. 2.50-B, step 2). The spontaneous relaxation to the ground state of the fluorescent molecules induces the emission of photons (emission light) (Fig. 2.50-B, step 4) [184]. The Jabłoński diagram in Fig. 2.50-B illustrates the electronic states and the energetic transitions occurring [185]. The difference between the exciting and the emitted wavelength is known as the Stokes shift and is the critical property of fluorescence [186].

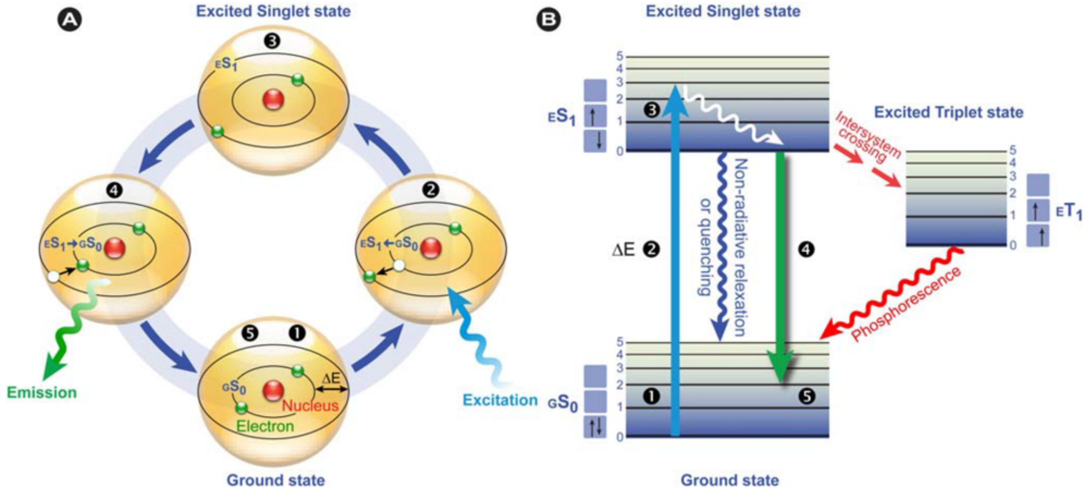

Fig. 2.50 Fluorescence principle. A - Schematic representation of the fluorescence phenomenon in the classical Bohr model. B - Jabłoński diagram of fluorescence. Adapted from [187].

The optical properties of fluorescent molecules are generally described by their excitation (also called absorption) and their emission spectra. The excitation spectrum is related to the ability of the molecule to absorb the light at a specific wavelength. The emission spectrum describes the ability of the molecule to generate fluorescence light at a specific wavelength from at specific excitation. In Fig. 2.51, typical absorption/excitation and emission spectra of two different fluorophores are displayed.

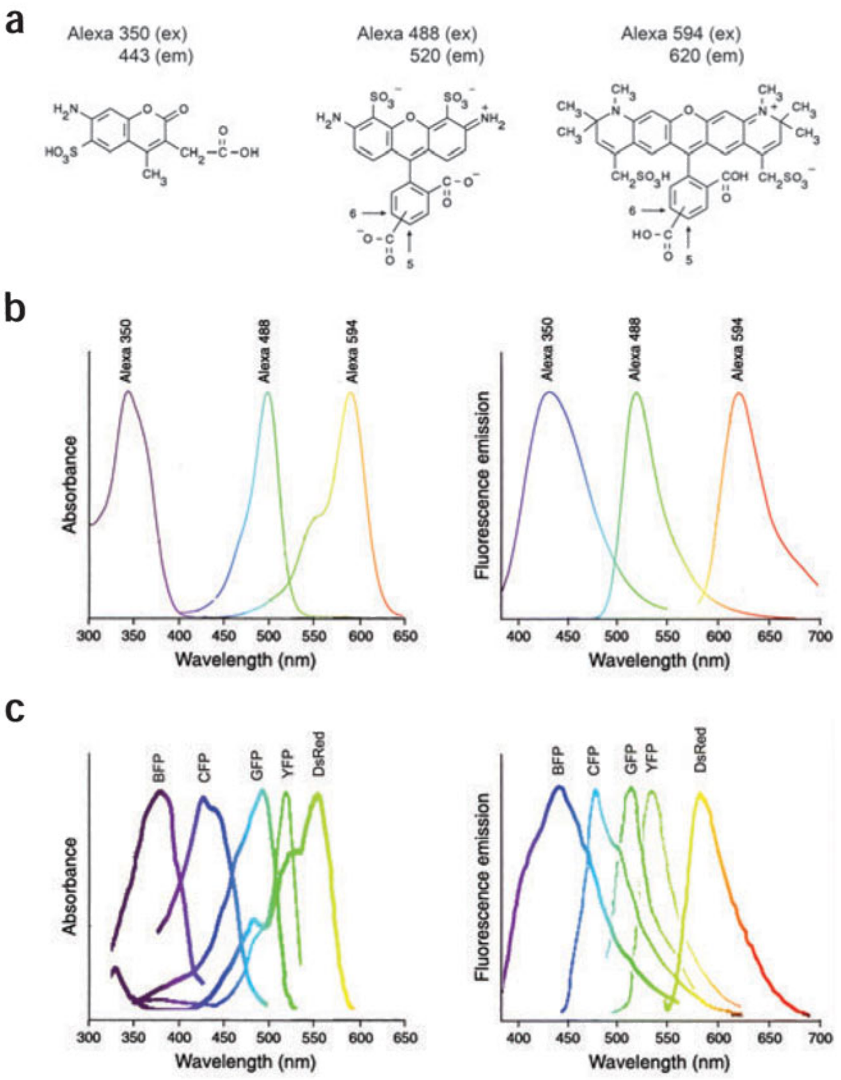

Fig. 2.51 Typical absorption/excitation and emission spectra of two different fluorescent dyes. A – *cis*-Parinaric acid. B – BODIPY 650/665-X.The different between the excitation and the emission maxima is called the “Stokes shift”. Adapted from [183].

2.3.2 Fluorochrome

A myriad of fluorochromes are now available from commercial providers and some chemistry teams are specialized in the design of customized fluorochromes [188–190]. This variety of possibilities is definitely one of the major advantages of fluorescence microscopy.

Chemical fluorescent dyes are small molecules, ranging from 300 to 1000 Da, that become highly fluorescent when they are in an appropriate molecular environment. For instance, nucleus staining dyes are generally DNA intercalating molecules whose quantic fluorescence efficiency is increased 20 to 30 fold when the dye interacts with DNA. Fig. 2.52 lists the main chemical fluorescent dyes used for nuclear staining. Many other fluorescent dyes label the cytoskeleton, the membrane or the intracellular calcium concentration, or give the opportunity to monitor specific cell metabolism [191, 192].

	Ex/Em (nm)	DNA	RNA	cell permeablity
DAPI	358/461	+++	−	semi-permeant
Hoechst 33258	352/461	+++	−	permeant
BO-PRO-1	462/509	+	++	impermeant
YO-PRO-1	491/509	+++	+	impermeant
SYBR Green I	494/512	++	−	impermeant
PicoGreen	502/523	+	−	impermeant
SYTOX Green	504/523	+++	−	impermeant
TO-PRO-1	515/531	+	+	impermeant
POPO-3	534/570	+++	+++	impermeant
PI	535/617	+++	++	impermeant
YO-PRO-3	612/631	+++	±	impermeant
TO-TO-3	642/660	++	+++	impermeant
TO-PRO-3	642/661	+++	±	impermeant

DAPI (4',6-diamidino-2-phenylindole), PI (propidium iodide).

Fig. 2.52 Chemical fluorescent dyes for nuclear staining. From [192].

The cloning of the gene encoding for the green fluorescent protein (GFP) of the jellyfish Aequoria Victoria opened new avenues. Indeed, this protein exhibits a bright green fluorescence when exposed to light from blue to ultraviolet range [193]. The opportunity to label most of the proteins was made possible by the genetic fusion of the GFP gene with the coding sequences of the targeted proteins. Since then, fluorescent proteins have been widely used to investigate protein locations and functions [194, 195].

Another classical technique to perform specific fluorescent stainings is the immunofluorescent staining [196]. This versatile technique is able to detect the biomolecules in the cells that can be targeted by specific antibodies. Antibodies are non-permeant molecules so it is necessary to previously permeabilize the plasma membrane. Generally, this technique requires to fix the sample prior to the staining, hence it is unsuitable for live-imaging. Two methods have been designed to perform immunofluorescent staining. The direct method uses fluorochrome-labelled antibodies. The antibodies targeting the protein is itself fluorescent. The indirect method requires two antibodies. A primary non-fluorescent antibody targeting the protein and a secondary fluorescent antibody labelling the primary antibody [192].

It is possible to perform multi-labelling on the same sample if signal interferences between the excitation and emission spectra of the different fluorescent molecules are avoided. Multilabelling can also be performed through the combination of the different fluorescent staining methods listed above (Fig. 2.53).

Excitation (nm):	800 (2 photon)	488	432	568	637
Emission (nm):	410-490	500-530	555-565	580-620	>660
Fluorophore:	Hoechst	GFP	QD565	ReAsH	Cy5
Targeting:	direct affinity	genetic	immuno	genetic	immuno
Target:	DNA	α-tubulin	giantin	β-actin	Cytochrome c
Structure:	nuclei	microtubules	golgi	stress fibers	mitochondria

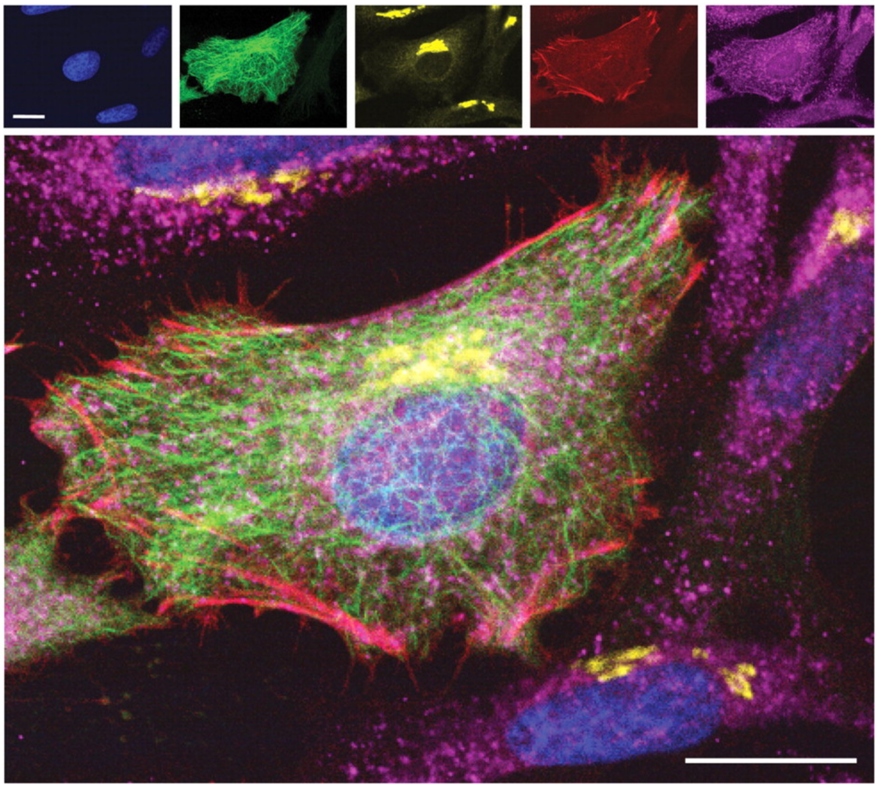

Fig. 2.53 Parallel application of targeting methods and fluorophores. HeLa cells transfected with GFP–α-tubulin and tetracysteine–β-actin were stained with ReAsH. After fixation, cells were immunolabeled for the Golgi matrix protein giantin with quantum dots and for the mitochondrial enzyme cytochrome c with Cy5 as indicated. DNA was stained with Hoechst 33342. Images were acquired from Z planes that best represent each structure using excitation and emission wavelengths as indicated in the table. Individual channels are false-colored (middle) and merged (bottom). Scale bars, 20 µm. From [195].

Fluorescence microscopy requires some precautions for relevant image acquisition. Fluorescence microscopy use labels (the fluorochromes) which may impact the cell metabolism. Above a certain concentration threshold, fluorochromes may be cytotoxic and trigger undesired cell metabolism [197]. In principle, a fluorophore can infinitely cycle between ground and excited states. Thus the fluorescence signal should not suffer from any irreversible decrease in intensity. In practice, permanent bleaching occurs after a certain exposure time. The bleaching phenomenon starts after a certain time after the first excitation by light. This time is highly depend on the fluorophore. For stable fluorophores, the number of cycles before permanent bleaching is estimated between 10000 and 40000 cycles [186].

2.3.3 Wide-field fluorescence microscopy

Fluorescence microscopy aims at specifically detecting the emission light signal from the fluorochrome. The fluorescence microscope architecture is based on three optical filters as illustrated in Fig. 2.54. The exciting filter allows to deliver the light at an appropriate wavelength compatible with the excitation spectrum of the fluorescent molecule used. The exciting light is focused on the sample thanks to an objective. In the case of an epi-illumination fluorescence microscope, the same objective is used to collect the backscattered light which comprises the light emitted from the fluorescent dye, the reflected excitation light and any other interference light such as autofluorescence. The dichroic filter allows to split the emitted light and the reflected excited light. Finally, the emission filter specifically selects the wavelength in agreement with the emission spectrum of the fluorophore. Via an appropriate optical pathway, this useful signal is focused to a CCD camera and/or to the eyepiece of the microscope for direct visualization.

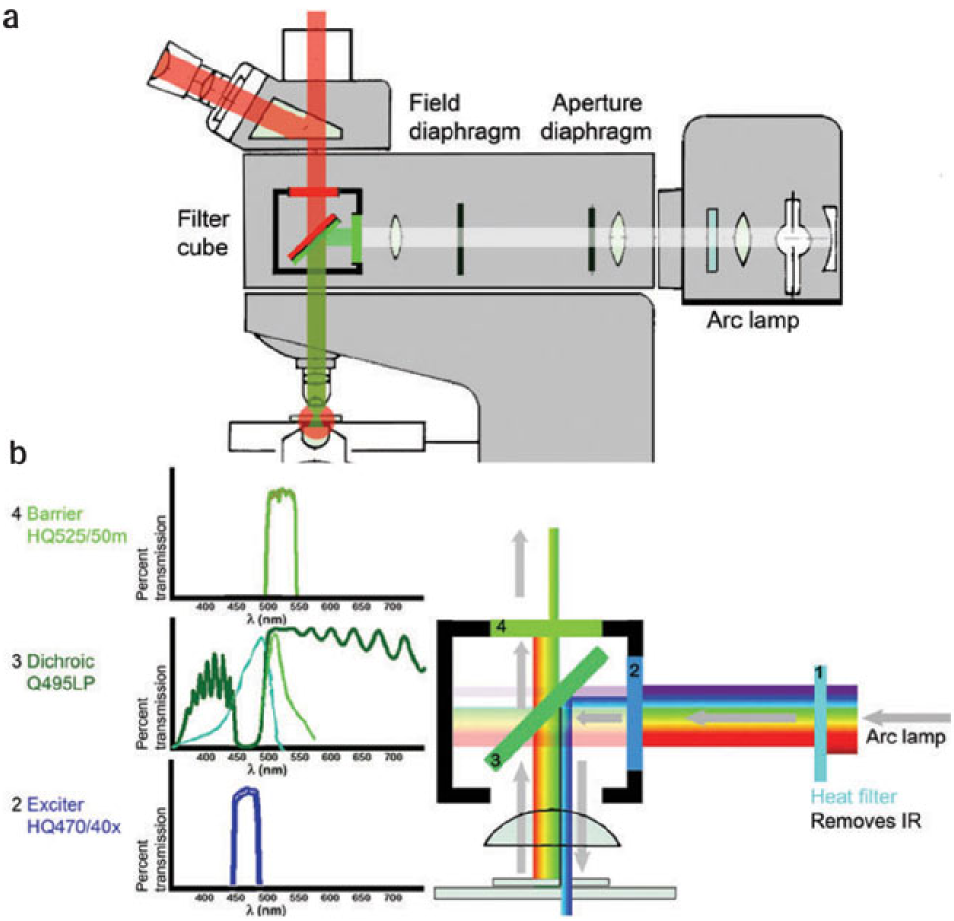

Fig. 2.54 The fluorescence microscope. (a) Epi-illumination fluorescence microscopes use the objective both to illuminate and image the specimen. Shown is an upright microscope with the specimen-supporting slide at the bottom. The light source, in this case an arc lamp, sends full-spectrum light to the specimen by way of a fluorescence 'cube' that selectively illuminates the specimen with a wavelength that excites a particular fluorophore (shown, green light to excite rhodamine). The red fluorescence that is excited sends photons in all directions and a fraction is collected by the objective and sent through the cube to the eye or camera port above. The cube has two filters, the dichroic mirror and barrier filter, to prevent the exciting wavelengths from reaching the detector. (b) The details of a cube designed by Chroma Technologies to excite and detect EGFP. The three main components (labelled 2, 3 and 4) have specific spectral features that are ideal for GFP. Note that the dichroic mirror (3) splits reflection and transmission right between the absorption and emission peaks of the GFP, which are superimposed in blue and light green, respectively. Adapted from [186].

Wide-field fluorescence microscopy is the basic instrumentation. It has a limited spatial resolution Rxy based on the Ernst Abbe's diffraction law, equation 2.21

$$R_{xy} \approx \frac{0.61 * \lambda}{NA} \tag{2.21}$$

where λ is the wavelength of the excitation light and NA is the numerical aperture of the objective.

For a typical objective of NA=0.8 and an excitation light at 475 nm, the lateral spatial resolution is 362 nm. The in-depth resolution is much weaker because all the emission light from the sample is integrated in the z dimension. In order to monitor internal organelles of cells, the spatial resolution of wide-field microscopy is a serious limitation. Thus many technical improvements have been developed in order to significantly improve the spatial resolution.

2.3.4 Confocal fluorescence microscopy

2.3.4.1 Laser-scanning confocal microscopy

Laser-scanning confocal microscopy (LSCS) significantly improves the spatial resolution in comparison with wide-field microscopy. The in-depth resolution is improved by eliminating the out-of-focus light from the images. The x-y resolution is also improved by the scanning process.

Fig. 2.55 illustrates the general architecture of a LSCM. First, a laser beam is used to focus light on the sample with the smallest spot possible. The spatial distribution of the beam into the sample is called the point spread function (PSF). The lateral resolution of the PSF defines the x-y spatial resolution and is given by the equation 2.22):

$$R_{xy} = \frac{1.22 * \lambda}{NA} \tag{2.22}$$

where λ is the wavelength of the excitation light and NA is the numerical aperture of the objective.

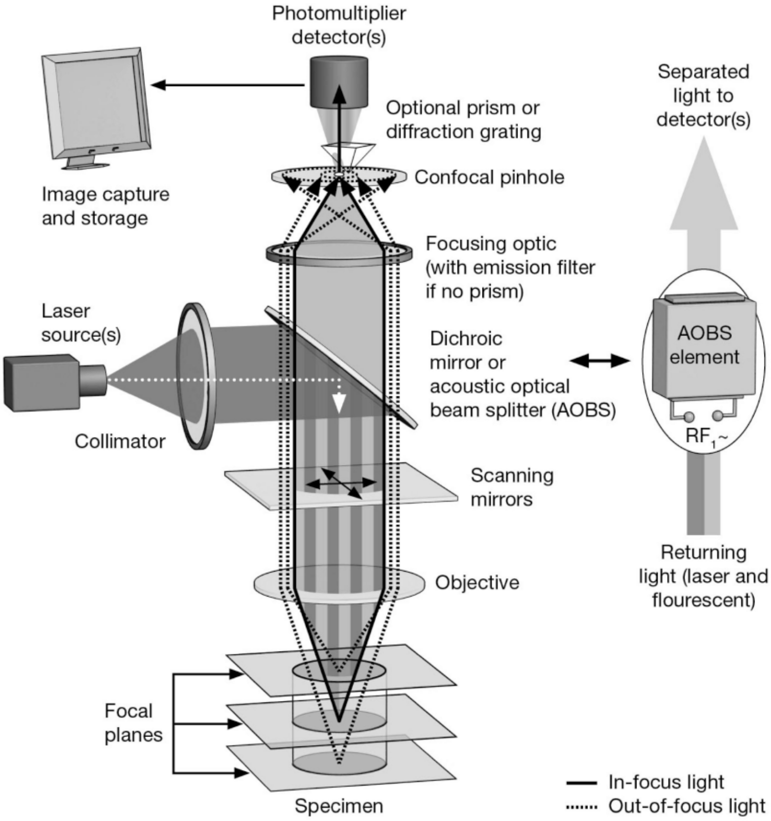

Fig. 2.55 Basic architecture of a laser-scanning confocal microscope. From [182].

Fig. 2.56-B compares the PSFs of wide-field and confocal microscopes. The lateral spatial resolution is significantly improved by the use of a laser in comparison with the lamps used in wide-field microscopy. The in-depth resolution is improved by the addition of a confocal pinhole aiming to remove the signal contribution from the out-of-focus light. The smaller is the pinhole, the better is the z resolution but the lower is the signal intensity. Fig. 2.56-C and D shows the evolution of the SNR and of the depth of focus for different pinhole sizes. As the pinhole decreases the general signal intensity that comes from one signal spot, a highly sensitive photomultiplier is required to collect the light signal and to convert it into digital information. The acquisition of an image is performed by scanning the whole sample point-by-point.

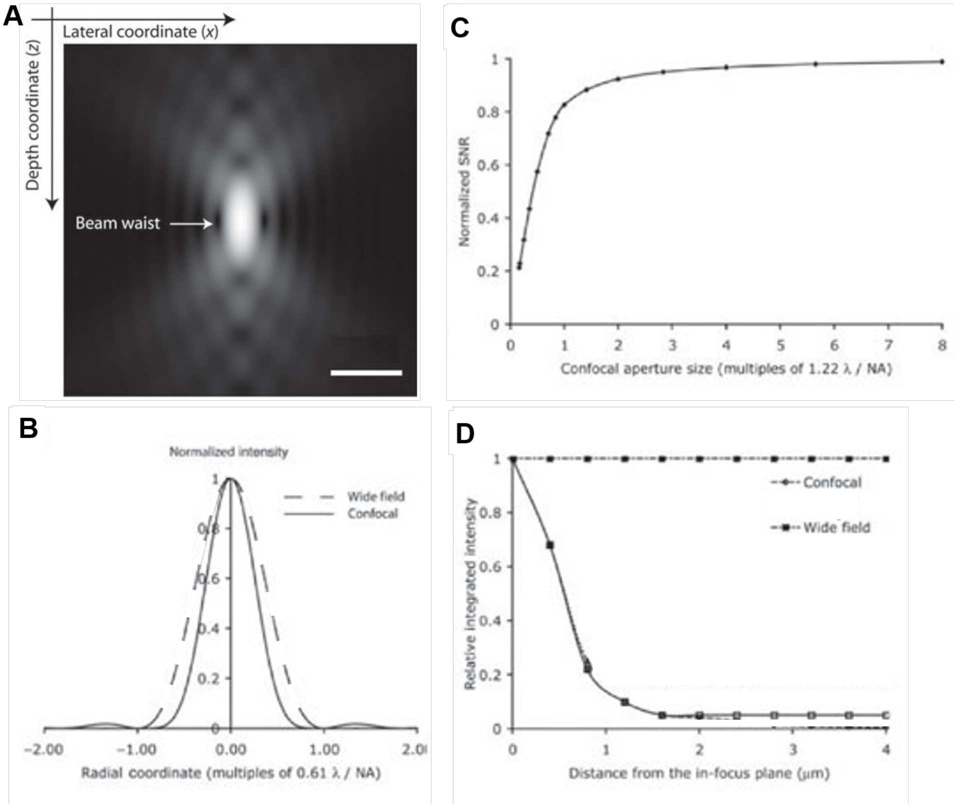

Fig. 2.56 A - Light distribution near the location of the confocal scanning spot for a 100 X, 1.4 NA oil-immersion lens and an excitation wavelength of 530 nm (brightness in log-scale with three decades). Bar, 0.5 µm. B - PSF of the wide-field and confocal microscopes. C - SNR in the confocal microscope with finite aperture normalized such that with a fully open–aperture SNR = 1. D - Background rejection in multiple-aperture confocal scanning microscopy. Graph of overall intensity due to a horizontal thin layer of fluorescence as a function of the distance from focus. For the wide-field microscope the intensity does not change with the distance from the in-focus plane. For the single-aperture confocal microscope it decreases in inverse proportion to the square of the distance from focus. Close to the in-focus plane, the intensity decreases as in the confocal microscope. At more distant planes, the intensity remains constant as in the wide-field microscope. The figure shows this behaviour for apertures that are 1.25 µm and 2.5 µm apart (when projected to the specimen). The further apart the apertures are, the stronger the background rejection. Adapted from [198].

Fig. 2.57 illustrates the significant improvement of the quality image between wide field and confocal microscopy.

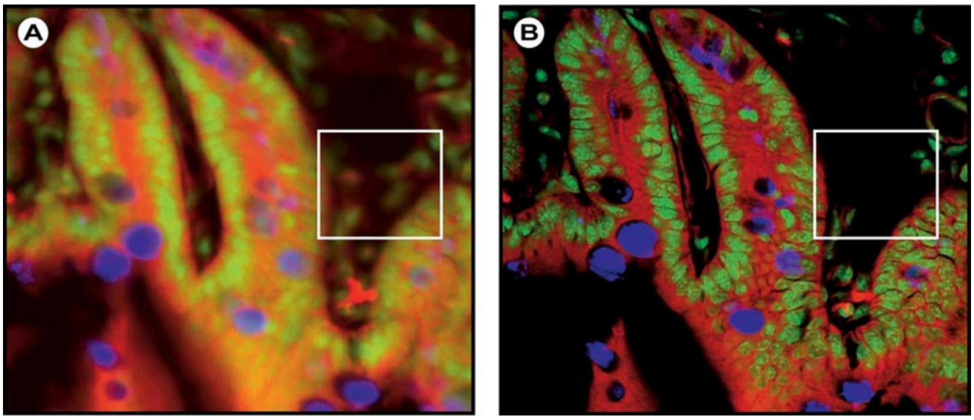

Fig. 2.57 Confocal (B) versus wide field (A) microscopy of a triple-labelled cell aggregate from a mouse intestine section. Notice that the out of focus signal in the wide field image causes additional structures to appear (white box). Adapted from [183].

2.3.4.2 Fluorescence recovery after photobleaching microscopy

Fluorescence recovery after photobleaching microscopy (FRAP) is a powerful tool to investigate molecule mobility in cells. In a typical FRAP experiment, the fluorescent molecule is present into the cellular compartment targeted (Fig. 2.58-A). Then, an irreversible photobleaching of a small ROI is performed by high intensity illumination (Fig. 2.58-C). The diffusion of the surrounding non-bleached fluorescent molecules into the bleached ROI leads to a recovery of fluorescence with a particular velocity, which is recorded at classical laser power.

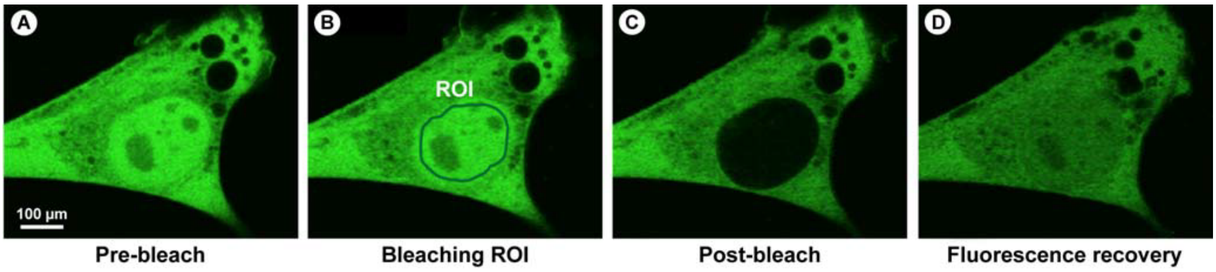

Fig. 2.58 Example of a FRAP experiment performed on a myoblast cell line expressing GFP-myosin III. Adapted from [183].

The analysis of the signal recovery allows the quantification of the diffusion coefficient of the probed molecules and the ratio of the mobile to immobile molecules (Fig. 2.59). FRAP is suitable for the investigation of many biological processes such as: lipids or proteins lateral diffusion in membranes (Poo and Cone 1974), nuclear protein dynamics [199], cytoskeletal dynamics [200] or cell adhesion [201].

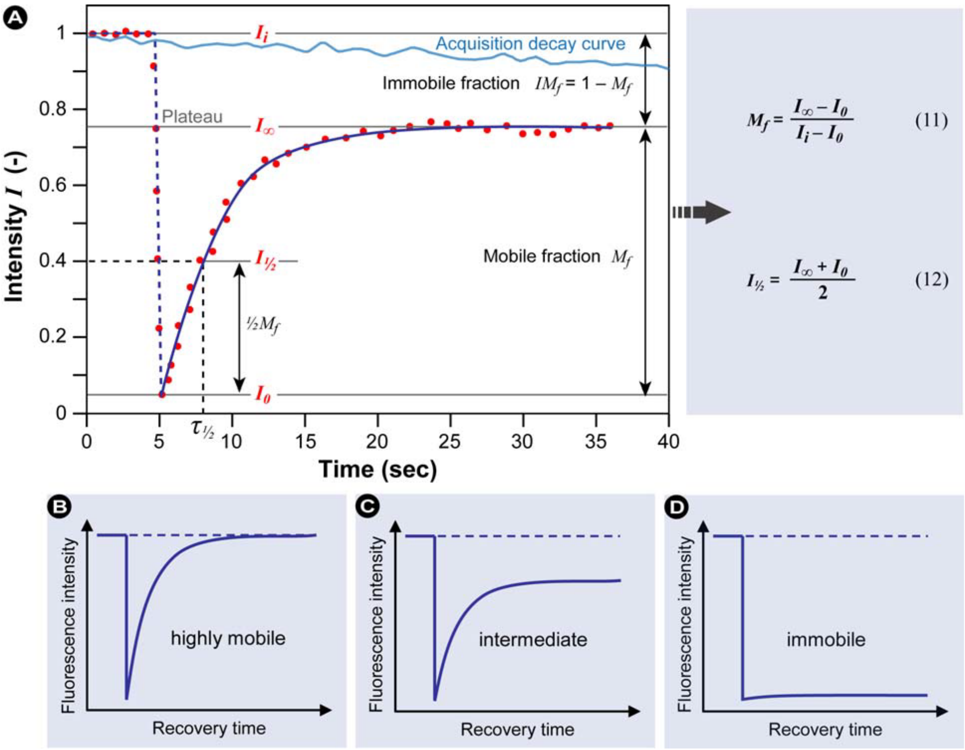

Fig. 2.59 Analysis of a typical FRAP curve. (A) From the initial (pre-bleach) fluorescence intensity (I_i), the signal drops to a particular low value (I_0) as the high intensity laser beam bleaches fluorochromes in the ROI. Over time the signal recovers from the post-bleach intensity (I_0) to a maximal plateau value (I_∞). From this plot, the mobile fraction (Mf), immobile fraction (IMf), the half of the mobile fraction $\frac{I}{2}$ and corresponding time $\frac{\tau}{2}$ (the time for the exchange of half the mobile fraction between bleached and unbleached areas) can be calculated (Light blue line: reference natural photobleaching curve to correct for fluorescence loss during data acquisition). The information from the recovery curve (from I_0 to I_∞) can be used to determine the diffusion constant and the binding dynamics of fluorescently labeled molecules. Based on different recovery profiles, the molecule mobility can be classified as (B) highly mobile with virtually no immobile fraction, (C) intermediately mobile with an immobile fraction, or (D) immobile. Adapted from [183].

2.3.4.3 Multipoint-scanning confocal microscopy

Multipoint scanning confocal microscopy, which is based on spinning disk microscopy, is an upgrade of LSCM aiming to speed up the frame acquisition rate. The speed limitation of LSCM originates from the point-by-point acquisition. The opportunity to perform multipoint scanning at the same time increases significantly the frame rate from about 30 frame/s in LSCM to 360 frame/s in spinning disk microscopy [202]. Fig. 2.60 illustrates the design of a spinning disk microscope. The design of the spinning disk by Yokogawa Corp is the key point of the performance of spinning disk microscopy. The spinning disk consists in a 20000 pinholes arranged in a series of nested spirals on a disk allowing to perform multi point illumination of the sample. Due to the pinhole arrangement, one complete image required 12 rotations of the spinning disk. The pinhole arrangement aims to limit as much as possible any crosstalk between neighbouring pinholes. [198, 203]. On the contrary to LSCM, the pinhole size is not adjustable and thus the in depth resolution is fixed.

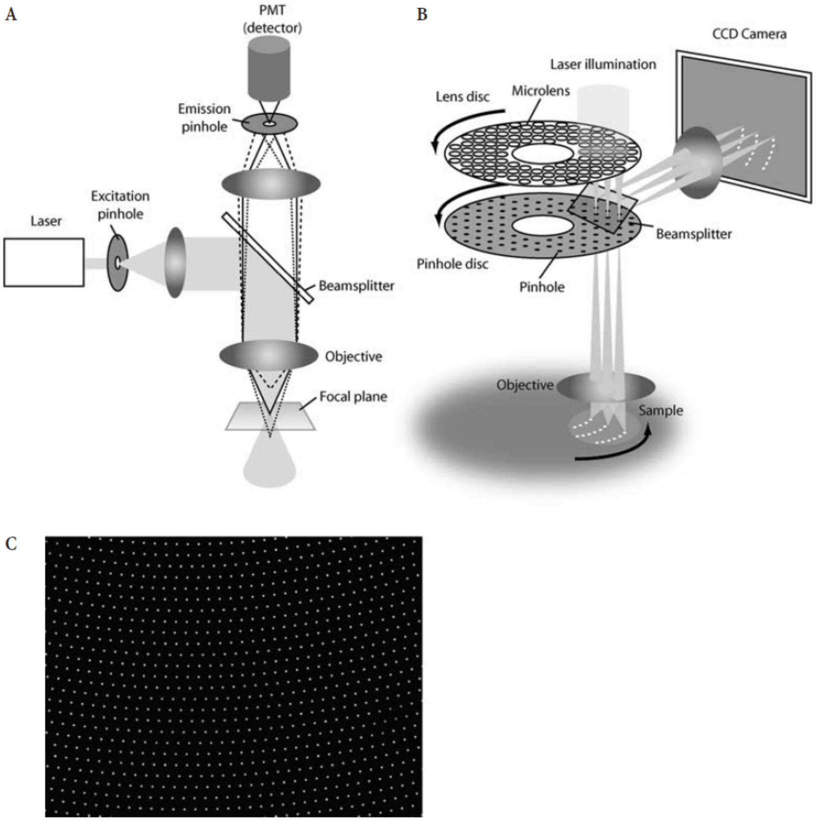

Fig. 2.60 Operating principles of single and multi-beam scanning confocal microscopes: A schematic drawing of a single beam scanning confocal microscope; B schematic drawing of a multi-beam scanning confocal microscope (Yokogawa CSU 10); C the constant pitch helical pinhole pattern of the Yokogawa spinning disk in the image field. During rotation of the disk, the pinholes evenly sweep the whole field of view. From [203].

2.3.5 Total internal reflection fluorescence microscopy

Total internal reflection fluorescence (TIRF) microscopy aims to improve the in depth resolution of the wide field microscope. TIRF microscopy is based on the generation of the signal on a limited optical section at the interface between the substrate and the sample [204, 205]. Thus, an evanescent wave is generated by focusing the laser with a critical angle able to induce evanescent waves (Fig. 2.61).

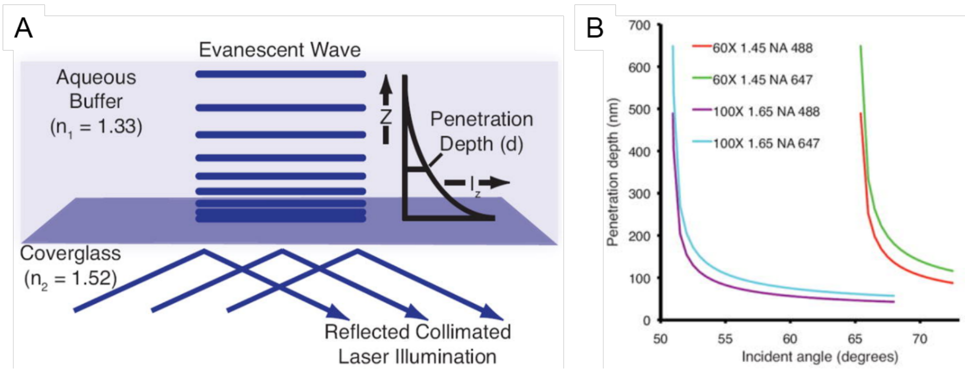

Fig. 2.61 The evanescent wave. (A) The incident angle can be described using a coordinate system arranged to display all three orthogonal directions. The x-y plane represents the interface between the coverglass and the cell cytosol. The plane of incidence is the x-z plane, which is parallel to the excitation light beam. (B) Penetration depth according to the incident angle for different objectives and excitation wavelengths. Adapted from [204].

In order to generate an evanescent wave, the incident angle of the laser illumination has to overcome a critical angle to the normal of the coverglass. This critical angle is determined thanks to the Snell Descartes law and is given by equation 2.23:

$$\theta_c = \sin(\frac{n_1}{n_2})^{-1} \tag{2.23}$$

where n_1 is the refractive index of the aqueous buffer and n_2 the refractive index of the coverglass.

The evanescent wave is generated at the surface of the coverglass and its intensity exponentially decreases along the z axis. The penetration depth of the evanescent wave depends on the incident angle of the laser beam and is equal to equation 2.24:

$$d_p = \frac{\lambda}{4 * \pi * \sqrt{n_1^2 * \sin(\theta_1)^2 - n_1^2}} \tag{2.24}$$

where d_p is the penetration depth of the evanescent wave, λ is the wavelength of the incident laser beam, θ_1 is the incident angle of the incident laser beam, n_1 is the refractive index of the aqueous buffer and n_2 the refractive index of the coverglass.

The penetration depth fixes the z resolution of the TIRF microscope. TIRF microscopy is suitable to investigate cell processes at the interface with the coverglass. Fig. 2.62 shows a comparison of a HeLa cell image acquired by standard epifluorescence microscopy and by TIRF microscopy.

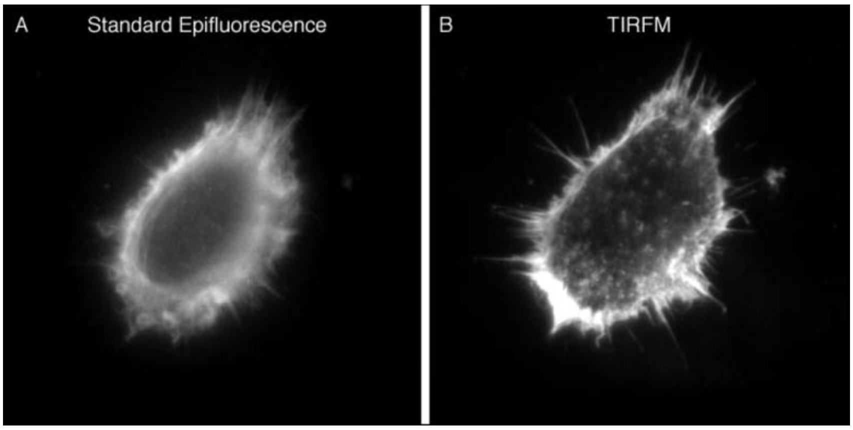

Fig. 2.62 Information revealed by TIRF microscopy (B) compared to standard epifluorescence microscopy (A). HeLa cells were cultured on 18 mm round 1.78 RI coverslips. Post fixation with 4 % paraformaldehyde, rhodamine-conjugated phalloidin was used to visualize F-actin. The cell was imaged in HBSS using a 100X 1.65 NA objective and 1.78 RI immersion liquid. Both images were taken at the same plane with the same exposure settings. From [204].

2.4 Terahertz microscopy

Terahertz (THz) waves lie between the microwave (< 10 GHz) and mid-infrared (> 10 THz) in the electromagnetic spectrum (Fig. 2.63). Its unique position between photonics and RF technologies has long restrained THz technologies development, each field reaching its limits when approaching this frequency range. As a result, a so called "Terahertz (technologic) Gap" is still observable today. Current well-established application range from astronomy to semi-conductors physics. Since the beginning of the century, an important interest in its application to biochemistry and biology has risen. We will focus on THz instrumentation for biomolecules and biological samples investigations.

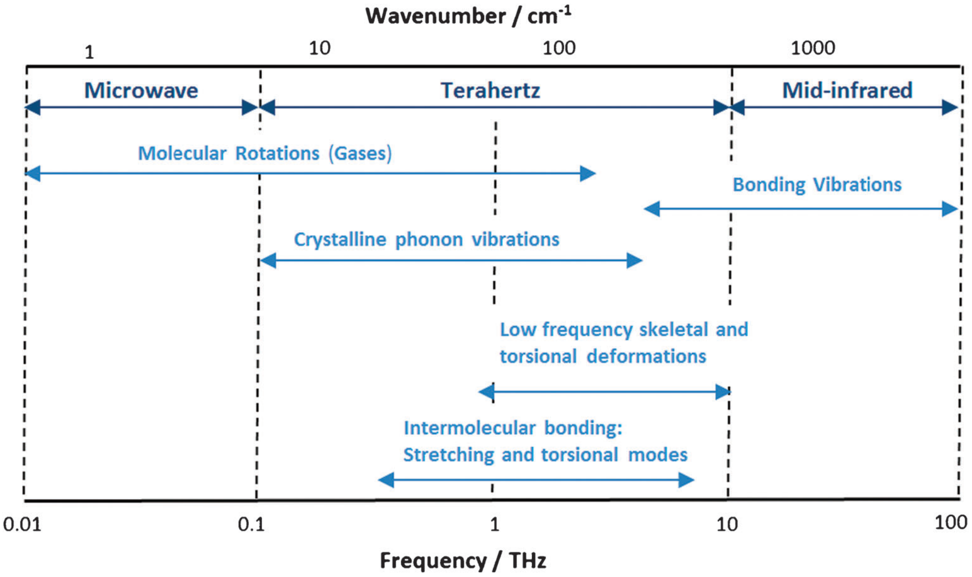

Fig. 2.63 Molecular modes and activity in the terahertz region of the electromagnetic spectrum. From [206].

According to the energy associated to the electromagnetic wave in the THz region (between 0.5 and 50 meV), THz waves mainly interact with low-frequency biomolecules deformations, and intermolecular bonding such as Van der Waals and hydrogens bonds. THz waves are therefore sensitive to molecular composition, with spectral fingerprints for solid form of drugs [207]. In hydrated states, the profusion of intermolecular modes swipe away spectral fingerprints but gives an overall sensitivity to conformation, hydration state and molecular abundance.

Because of THz waves high sensitivity to intermolecular mode (especially hydrogen bonding) they are extremely sensitive to polar molecules such as water for instance. This strong absorption of THz waves by water (over 200 cm^{-1} at 1 THz) has a major impact in the perspectives of the study of biological samples which are mainly composed of water. On one hand, it represents an obstacle to signal penetration and detection. On the other hand, it leads to an incredible sensitivity to any change of the water state, quantity and/or composition.

This optical technique also has the major advantage to be non-invasive and label free [208]. Due to the low frequency of THz waves in comparison with visible light waves, THz microscope offers a relative low spatial resolution, between 50 µm and 500 µm [209–211].

In the last 20 years, the discrimination between cancer and normal tissue has been performed thanks to THz microscope on *ex vivo* samples (Fig. 2.64) and even more recently in *in vivo* conditions [212]. The use of THz microscope to monitor cancer tissue fits with Raman microspectroscopy study showing that water concentration can be used as a biomarker of cancer tissue [147]. Another recent approach based on the same contrast mechanism shows that THz microscopy can be used for assessing *in vivo* burn wounds seriousness and healing [213].

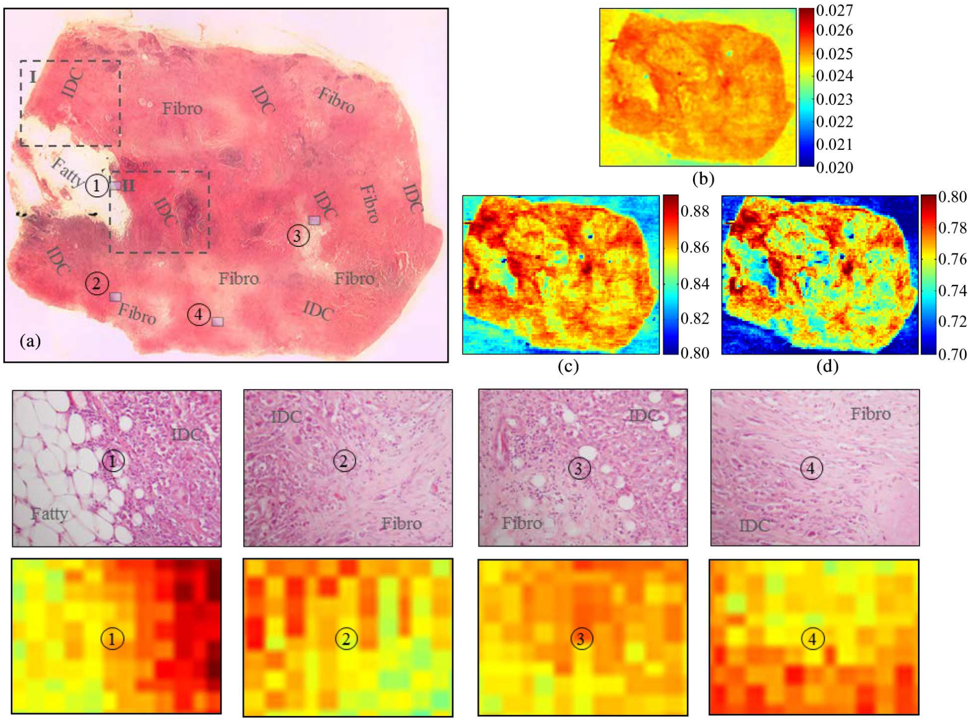

Fig. 2.64 THz image of sample 1, 40-year-old Caucasian woman diagnosed with poorly differentiated infiltrating ductal carcinoma (IDC). (a) Low-power pathology image used for correlation. Selected locations of high-power pathology of borders between regions are denoted by 1 between fatty and IDC and by 2, 3, and 4 between IDC and fibro. (b) THz time-domain image. (c) THz frequency-domain image at 1.5 THz. (d) THz frequency-domain image at 2.0 THz. THz images in (b)–(d) are scanned at 200 µm. High-power pathology images at 100× magnification are shown for 1, 2, 3, and 4 borders compared to the frequency-domain images at 1.5 THz using 50 µm scanning step size. From [211].

Thanks to THz waves sensitivity to water and its solutes, THz instrumentation has been used to detect biomolecules state and concentration (DNA or RNA [214, 215]), proteins [216], sugars [217] and microorganisms [218] non-invasively and without any labelling protocol. Cells in culture have much less signal than tissues. In 2014, Shiraga *et al.* published the first detection of eukaryotic cells in physiological condition [219]. The contrast mechanism behind this detection was later demonstrated to originate from the asymetric proteins/water repartition between inside and outside the cells.

Different geometry illumination are currently under investigation to maximize the SNR for biological samples. Overall, reflexion geometry is increasingly preferred in biomedical applications, to avoid thickness dependency and signal loss [220]. The attenuated total internal reflection illumination geometry provides the advantage to generate THz signal only at the interface between the substrate and cells attached above via an evanescent wave with a thickness of tens of µm (depending on the wavelength, indexes and reflection angle involved). This illumination geometry allows to focus on the cells, increase sensitivity and limit water absorption [221].

Although THz microscopy is still under development, this optical technique is promising due to its non-invasiveness and the absence of label.

3
Electropermeabilization

EPN is based on the interaction between PEF and biological cells, especially the plasma membrane In order to understand this bio-electromagnetic interaction, it is necessary to present into details the plasma membrane structure, physiology and functions.

3.1 Plasma membrane

Plasma membrane is crucial to the cell life (Fig. 3.1). First, it defines the boundaries of the cell and maintains the essential differences between the cytosol and the extracellular environment [222]. Then, it regulates selectively the exchanges between the outside and the inside of the cell in order to maintain the activity of cell metabolism [223]. This thick structure (about 5 nm) is universal to all living cells. Despite its small thickness, it is a complex and dynamic structure which is involved in many critical cellular processes [224, 225]. In this section, we will first present a brief historical overview of the research conducted on the plasma membrane. Then, we will focus on its chemical composition, its structure and finally its role in cell metabolism.

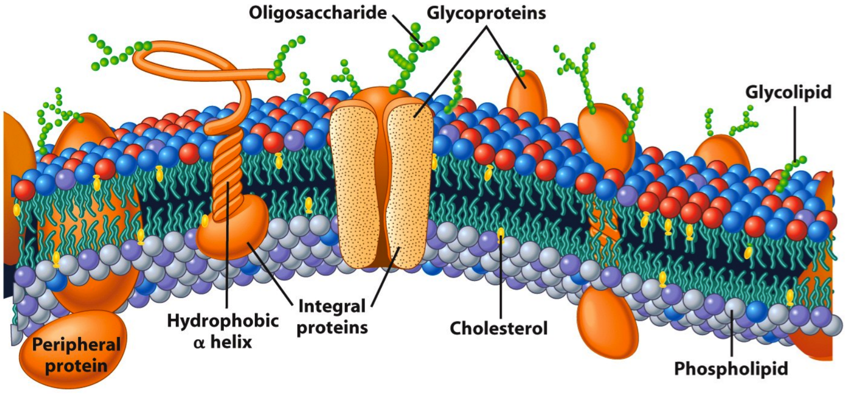

Fig. 3.1 A current representation of the plasma membrane. From [226].

3.1.1 Historical view

An exhaustive history about the progress on the knowledge on plasma membrane has been published by Lombard [227] and Singer [228]. This section is just a brief historical overview about cell membrane understanding.

In 1665, Hooke was the first one to observe individual cells on a piece of cork thanks to light microscopy [229]. Two centuries later, Schleiden and Schwann developed the "Cell Theory" which identify the cells as the basic unit of all organisms [230, 231]. At that time, the membrane was just considered as a secondary structure resulting from the hardening of the cell surface (Fig. 3.2).

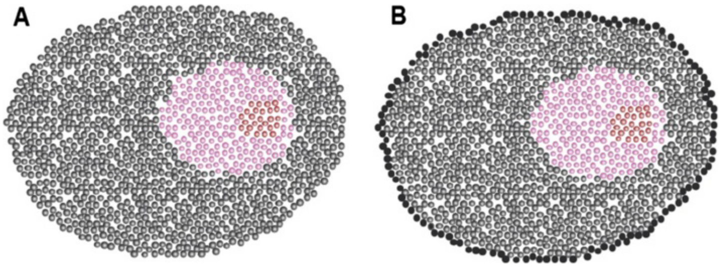

Fig. 3.2 XIX$^{\text{th}}$ century doubts about the existence of membranes. A - In this vision, the cell is devoid of any membrane and all the properties of the cell are defined by the activity of the protoplasmic colloid. B - The cell is surrounded by an external layer (membrane) of which the nature is distinct from the rest of the protoplasm. Yet, in this view, the inside of the cell remains a colloid. From [227].

During the second half of the XIX$^{\text{th}}$ century, many scientists worked on the effect of osmotic pressure on cells

[232–235]. The studies performed led to the concept of cell membrane that was suggested for the first time by Overton in 1895 [236]. In the early XX$^{\text{th}}$ century, the existence of a cell membrane was commonly admitted by the scientific community and supported by several experimental proofs [237, 238]. But it was necessary to wait until 1953 to have a direct visualisation of a cell membrane thanks to the electron microscopy studies of Chapman *et al.* [239–241].

In 1925, Gorter and Grandel demonstrated that the molecular structure of membrane was based on a lipid bilayer [242]. This significant result was obtained by comparing the surface of extracted lipids to the surface of the cells. The ratio between the surface of extracted lipids and the surface of the cells was equal to 2:1. Thus, the authors concluded that the cell was surrounded by a bilayer lipid membrane with the hydrophobic components towards the inside of the membrane and the hydrophilic components at its external parts. The lipid bilayer structure was in agreement with the thickness studies, as it was estimated to be around 5 nm [243, 244]. On the contrary, it was also established that proteins were also part of the membrane [245]. Therefore, the "paucimolecular model" suggested that a protein layer was superposed over the lipid layer (Fig. 3.3-A). In the years following the publication of this model, many experiments challenged it. First, it was demonstrated that the protein-lipid ratio was between 1:4 and 1:5 [246]. Based on this ratio and the proteins size, the surface theoretically covered by a protein layer was not sufficient to entirely cover the lipid layer. Several studies revealed that the secondary structures of the membrane proteins were α-helices rather than β-sheets [247, 248]. The α-helix conformation of the membrane proteins supported the idea that proteins cross the membrane instead of surrounding it. Thermodynamic calculations demonstrated that a bilayer containing a mixture of lipids and proteins was more stable than the superposition of two protein and lipid layers [249]. Based on the criticisms of the paucimolecular model, Singer and Nicolson proposed the fluid mosaic model which is now considered as the best model to describe the structure of cell membrane [250]. This model considered the cell membrane as a lipid bilayer including proteins crossing the membrane (Fig. 3.3-B). The experimental demonstration of the membrane fluidity by Frye and Edidin was in agreement with the fluid mosaic model [251]. Since then, the fluid mosaic model has been updated [252] but never replaced by a new model. We will see in a next section that the membrane structure plays a key role in the membrane functions.

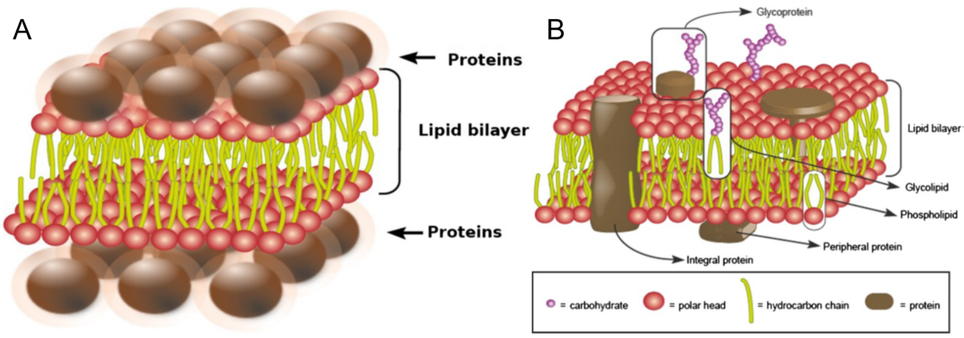

Fig. 3.3 Time evolution of the structure model of cell membrane. A - Paucimolecular model with a lipid bilayer coated with proteins on both sides, from [253]. B – Fluid mosaic model from [250]. Adapted from [227].

3.1.2 Molecular composition

The molecular composition of the plasma membrane has been extensively studied. It is well known that the plasma membrane is made of lipids, proteins and carbohydrates [254]. As described by the fluid mosaic model, the lipids are arranged in a bilayer and the proteins are embedded into the bilayer, except for a proteins at the surface of the plasma membrane. Despite this universal structure, the molecular composition of the membrane depends on the organism and the cell type.

3.1.2.1 Lipids

Lipids are amphipathic molecules with both hydrophilic and hydrophobic properties. Lipids constitute about 40% of the plasma membrane mass. There are about 5.10^6 lipid molecules for a 1 μm^2 area of plasma membrane [255]. In eukaryotic cells, phospholipids and cholesterol represent respectively about 60 % and 40 % of the total lipids present into the plasma membrane [254]. The structure of phospholipid molecules consists in two nonpolar hydrophobic fatty acid "tails" and one polar hydrophilic "head" with a phosphate group. The tail contains typically between 14 and 24 carbon atoms [222]. Most of the phospholipids in the cell membrane are phosphoglycerides since they possess a glycerol group which links the fatty acid chain to the hydrophilic head. The fatty acid chains are linked through ester bonds to adjacent carbon atoms of the glycerol group which is part of the head group. Among the phosphoglyceride group, phosphatidylcholine (PhC), phosphatidylethanolamine (PhE), phosphatidylserine (PhS) and sphingomyelin (SM) are the main phospholipids present into the plasma membrane (Fig. 3.4). PC represents more than 50 % of the phospholipids in typical eukaryotic membranes. A phospholipid is considered as unsaturated when at least one double bond is present in the tail. The presence of *cis* double bond creates an angle in the carbonyl chain which plays a key role in the membrane fluidity [256]. Thanks to their amphiphilic characteristic, phospholipids spontaneously form a lipid bilayer when they are in water solution which gives a highly stable structure [223]. The bilayer structure is maintained by hydrophobic interactions between lipids.

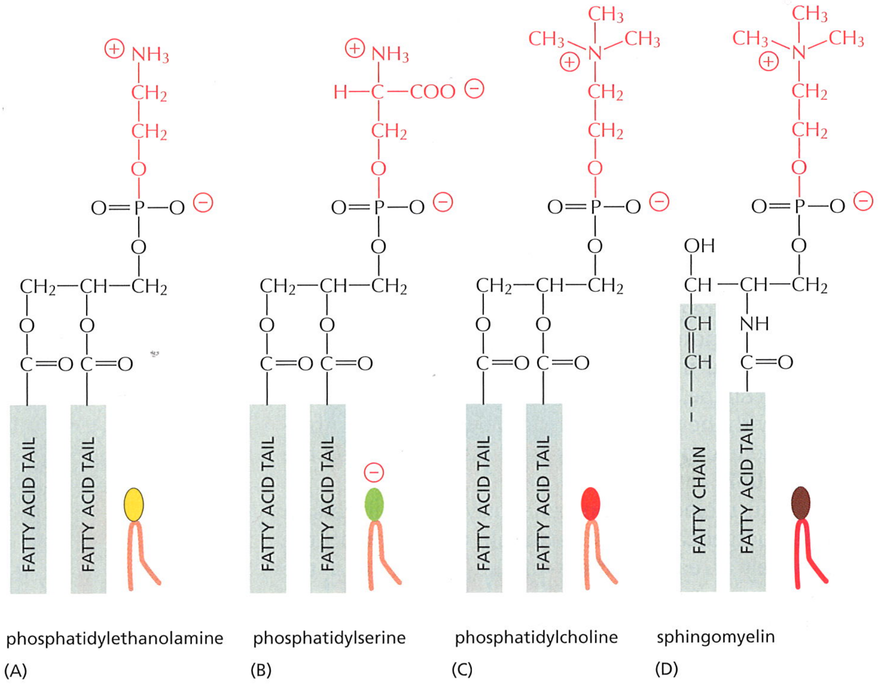

phosphatidylethanolamine (A)

phosphatidylserine (B)

phosphatidylcholine (C)

sphingomyelin (D)

Fig. 3.4 Four major phospholipids in mammalian plasma membranes. Adapted from [222].

In addition to phospholipids, the plasma membrane of animal cells contains a large amount of cholesterol (Fig. 3.5). In plant cells and yeast, respectively phytosterol and ergosterol are equivalent to cholesterol. Cholesterol is a sterol made of a rigid ring structure attached to a single polar hydroxyl group and a short nonpolar hydrocarbon chain. Cholesterol plays a key role in the physicochemical properties of the membrane, especially its fluidity [257]. In cell membrane, cholesterol interacts with other lipids based on the umbrella model [258]. Indeed, the hydroxyl group of cholesterol forms the hydrophilic headgroup facing the external medium and the tail points toward the interior of the bilayer. The hydroxyl group is too small to shield the hydrophobic ring structure of cholesterol from water molecules. Hence, the large headgroup of the closest phospholipids complete the shielding by covering the hydroxyl group, like umbrellas. The condensed complex model is another cholesterol-lipid interaction model with similar characteristics [259].

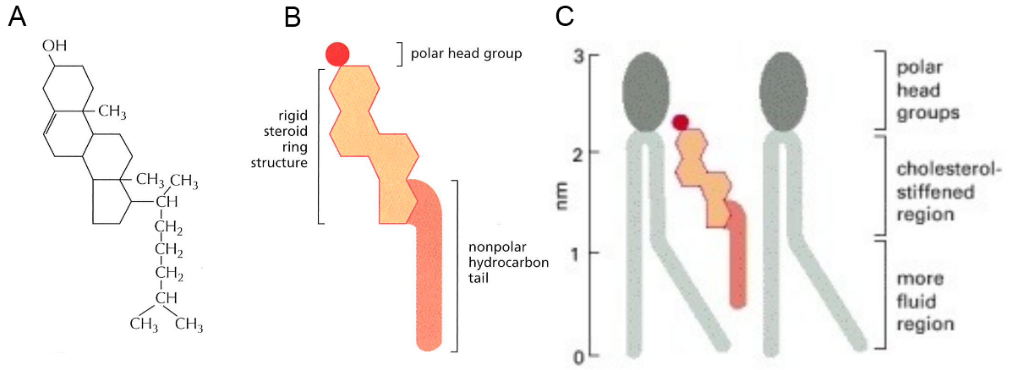

Fig. 3.5 The structure of cholesterol. Cholesterol is represented (A) by a formula, (B) by a schematic drawing. C Scheme of the interaction between cholesterol and two phospholipids. From [222].

Even if other cell membranes (endoplasmic reticulum membrane or mitochondria membrane) are out of the focus of this section, it has to be mentioned that the lipid composition of the membrane differs between the internal organelles membranes and the plasma membrane (Fig. 3.6).

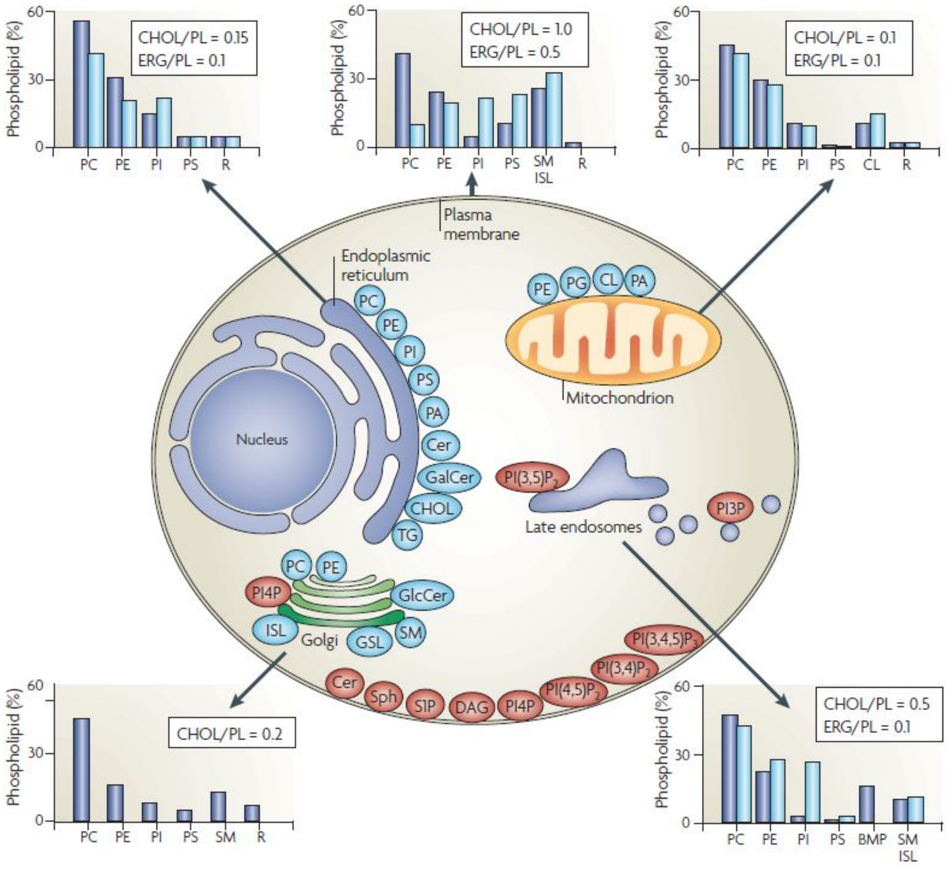

Fig. 3.6 Lipid synthesis and steady-state of cell membranes The lipid compositional data (shown in graphs) are expressed as a percentage of the total phospholipid (PL) in mammals (blue) and yeast (light blue).The molar ratio of cholesterol (CHOL; in mammals) and ergosterol (ERG; in yeast) to phospholipid is also included. The figure shows the site of synthesis of the major phospholipids (blue) and lipids that are involved in signalling and organelle recognition pathways (red). PC : phosphatidylcholine, PE: phosphatidylethanolamine, PI: phosphatidylinositol, PS: phosphatidylserine, SM: sphingomyelin, PA: phosphatidic acid, Cer: ceramide, GalCer: galactosylceramide, TG: triacylglycerol, GSL: glycosphingolipids, ISL: inositol sphingolipid, DAG: diacylglycerol, CL: cardiolipin, PG: phosphatidylglycerol, BMP: bis(monoacylglycero)phosphate, PI4P: phosphatidylinositol-4-phosphate, PI(4,5)P$_2$: phosphatidylinositol-(4,5)-bisphosphate, PI(3,5)P$_2$: phosphatidylinositol-(3,5)-bisphosphate, phosphatidylinositol-(3,4,5)-trisphosphate, R: remaining lipids, S1P: sphingosine-1-phosphate and Sph: sphingosine. Adapted from [260].

3.1.2.2 Proteins

Proteins represent about 50 % in mass of the plasma membrane. Membrane proteins are much heavier than lipids. Thus, there are many more lipid molecules than protein molecules in the plasma membrane. Typically, the molar ratio of protein to lipids is around 1/50 [222].

Membrane proteins can be associated with a lipid bilayer in different manners. Transmembrane proteins (Fig. 3.7 – 1, 2 and 3) are amphiphilic molecules which are thus inserted in the membrane. The hydrophobic regions of the transmembrane proteins interact with the hydrophobic tails of the lipids in the interior of the membrane. The hydrophilic regions are in contact with water outside of the membrane. Their secondary structure (α-helix or β-sheet) contributes also to stabilize the transmembrane proteins into the membrane. These transmembrane proteins are called integral membrane proteins. Another class of membrane proteins are the lipid-anchored proteins (Fig. 3.7 – 4, 5 and 6). This proteins are placed inside (cytosol) or outside (external medium) of the membrane but are associated with the membrane by an amphiphilic α-helix or a covalent bond to the lipid chain. Finally, peripheral membrane proteins are proteins taht can be attached to the membrane thanks to covalent bonds with integral proteins. Membrane proteins can be associated to other membrane proteins to form large and complex structures. For instance, the Photosystem II complex from cyanobacteria, with a 240 kDa molecular weight, contains 19 proteins subunits and over 60 transmembrane helices [261].

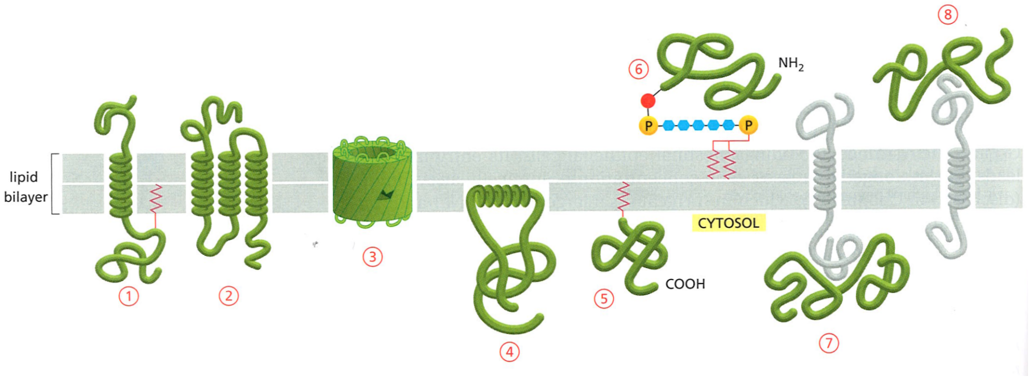

Fig. 3.7 Various way in which membrane proteins associate with the lipid bilayers. 1 – single α helix, 2 – multiple α helices, 3 – rolled up β sheet. 4 – one side of the membrane, 5 – anchored in the membrane by an α helix, 6 – attached by covalent bond with the lipid chain, 7 and 8 – attached by noncovalent bonds. From [222].

3.1.2.3 Carbohydrates

Carbohydrates are the third major component of cell membranes by representing about 10 % of the molecules in the plasma membrane. They are present specifically on the outer surface of the plasma membrane [222]. They are covalently linked to proteins or lipids to form respectively glycoproteins ir glycolipids [226]. Carbohydrates are key part of the distinctives cellular markers. These markers are highly involved in cell-cell recognition in the framework of the immune system response [262].

3.1.3 Structure of the plasma membrane

3.1.3.1 A fluid mosaic model

The fluid mosaic model was presented by Singer and Nicolson in 1972 [250]. It is now well established that the plasma membrane is a highly dynamic system. Hence, FRAP experiments allowed to measure the coefficient of diffusion of lipids and proteins into biological membranes [263]. This diffusion coefficient, which was measured at around 10^{-12} m^2/s, depends on the molecular composition of the plasma membrane and thus can differ between two cell types [264]. By considering a cell as a sphere with a 20 µm diameter, 2.6 minutes are necessary for a lipid to diffuse all around the cell surface. In the case of a pure lipid bilayer, the diffusion coefficient of lipids is about 10 times higher than the one in the plasma membrane. The presence of cholesterol decreases the lateral coefficient diffusion of lipids [265]. The membrane configuration, meaning planar bilayer or giant liposome, also affects the diffusion coefficient of lipids [266]. The fluidity of the membrane is also associated with other lipid movements such as rotation, flexion or rarely flip-flop (Fig. 3.8). Like lipids, membrane proteins can laterally diffuse into the membrane with a diffusion coefficient between 10^{-15} and 10^{-14} m^2/s [267]. The diffusion coefficient of proteins is much lower than the one of lipids mainly because of the large size of proteins and the protein-protein interactions.

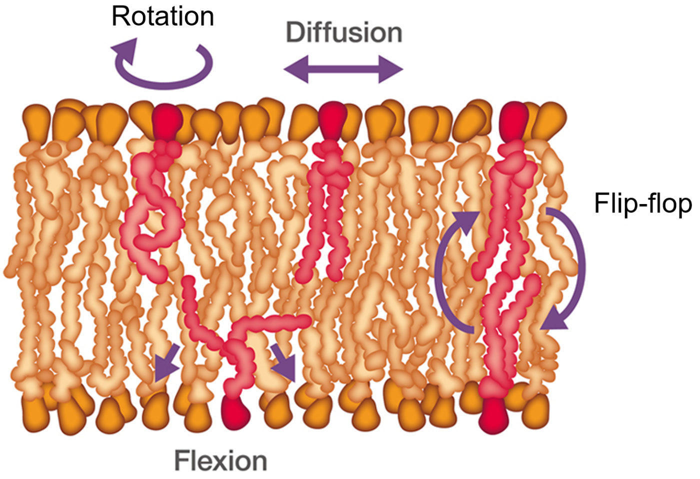

Fig. 3.8 Representation of the different movement of lipids possible in the cell membrane. Adapted from `http://csls-text3.c.u-tokyo.ac.jp/active/11_01.html`.

The membrane fluidity depends on many parameters such as the chemical composition of the membrane or the temperature. Fig. 3.9 illustrates the different physical states of a lipid bilayer in aqueous medium. Each physical state is characterized by a specific molecular order. The gel phase, also called solid-ordered phase, is associated with a two-dimensional triangular lattice arrangement of lipids [268]. The hydrocarbon tails are elongated at the maximum. As a consequence, the lipid network is extremely compact and the membrane fluidity is reduced. The carbonyl tails may be tilted with respect to the membrane normal plane. The fluid phase, also called liquid-disordered phase, consist in a higher lipid disordered phase. The membrane fluidity, for instance the lateral and rotational movements of lipids, is favoured in this phase [269].

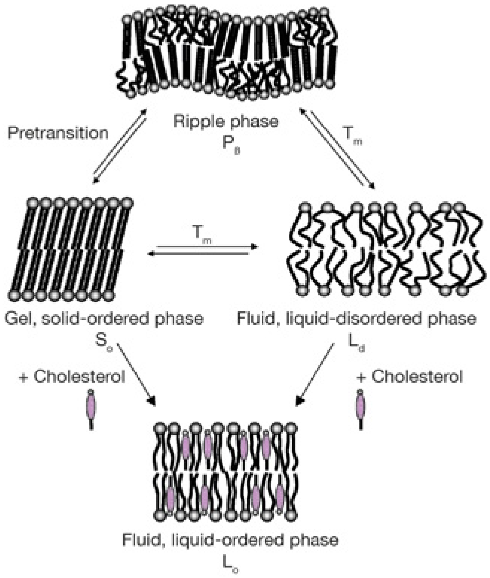

Fig. 3.9 Scheme illustrating the different physical states adopted by a lipid bilayer in aqueous medium. From [269].

A change in the temperature or the cholesterol concentration can induce a transition between the gel phase and the fluid phase (Fig. 3.10). The length and the number of insaturation of the carbonyl tails also impact the phase diagram of the lipid bilayer [226]. Thus, the phase transition depends on the temperature and the chemical composition of the membrane [257].

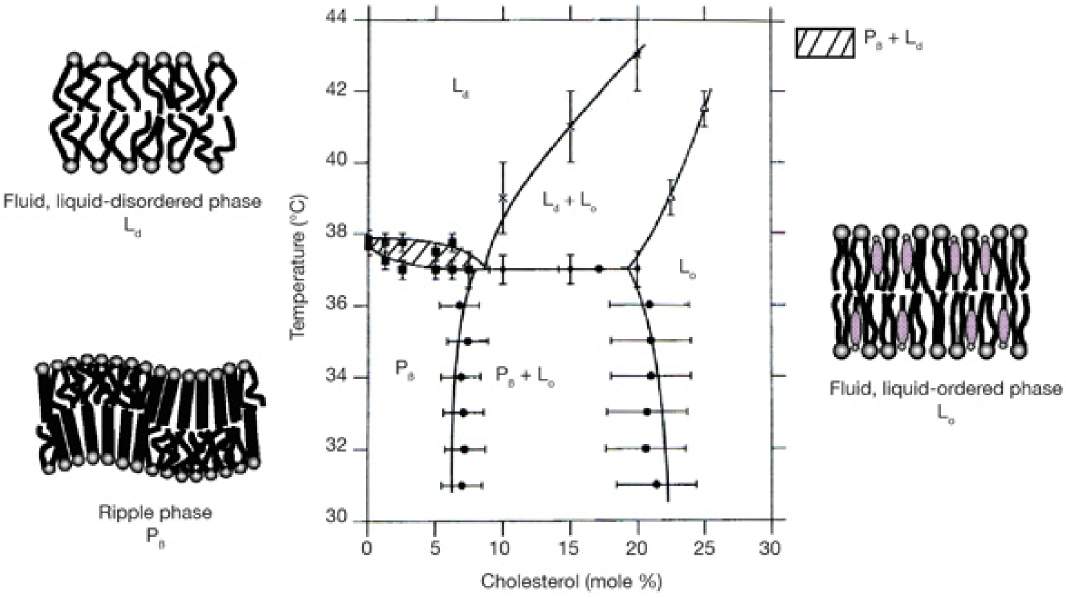

Fig. 3.10 Partial phase diagram for a mixture of cholesterol and chain-predeuteriated dipalmitoylphosphatidylcholine in excess water. From [269].

As underlined by the fluid mosaic model, the cell membrane is not a homogeneous structure. The cell membrane is composed of many microdomains containing lipid patches with specific lipid compositions and physical phase (Fig. 3.11). Lipid rafts are one of the principal lipid microdomains present in cell membrane [270]. Lipid rafts contain high concentrations of cholesterol and saturated phospholipids [271]. Lipid rafts play a key role in the regulation of signal transduction by driving the intracellular trafficking of proteins [225]. These lipid rafts are about 26 ± 13 nm thick and are highly dynamic with a lifetime of about 1 minute. Steinman and colleagues showed that about one hour is necessary to entirely recycle the plasma membrane by endocytosis and exocytosis for macrophage cells [272].

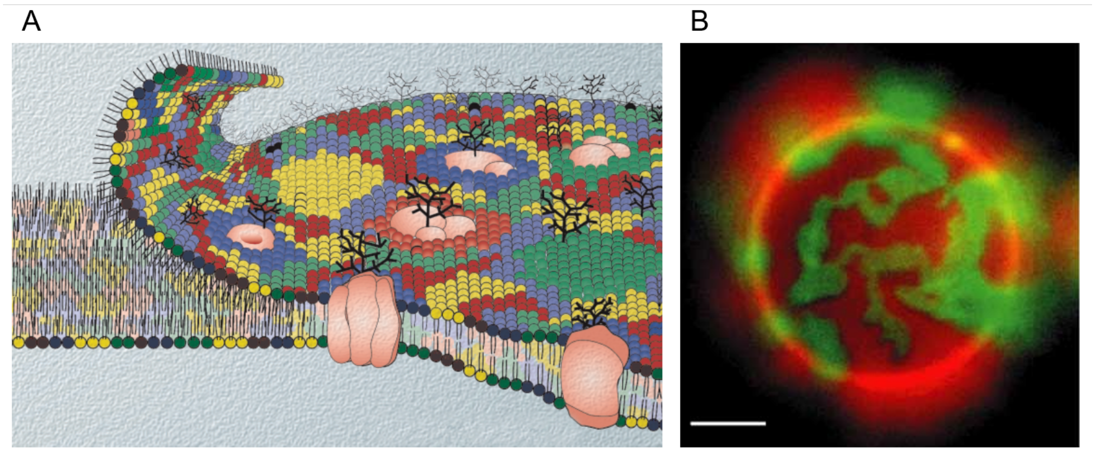

Fig. 3.11 The lipid domains in a cell membrane. A – Cartoon. Different lipid species are shown in different colours. B - Fluorescence image. The red fluorescence from DiIC18 dye corresponds to the ordered lipids whereas the green fluorescence lipid from BODY PI) corresponds to the fluid lipids. From [273].

3.1.3.2 An asymmetric membrane

Due to its curvature, the cell membrane has to be asymmetric in its chemical composition. For instance, all anionic lipids face the cytoplasm; whereas most lipids with large glycosylated headgroups are exposed to the extracellular environment [274]. Cholesterol seems to be more abundant in the outer leaflet than in the inner leaflet (Fig. 3.12). These differences in the chemical composition have an impact on the physical properties of the membrane. But membranes are also functionally asymmetric. The inner leaflet of the membrane contains the proteins involved in the intracellular trafficking; whereas the outer leaflet contains proteins in charge of the defence mechanisms [275].

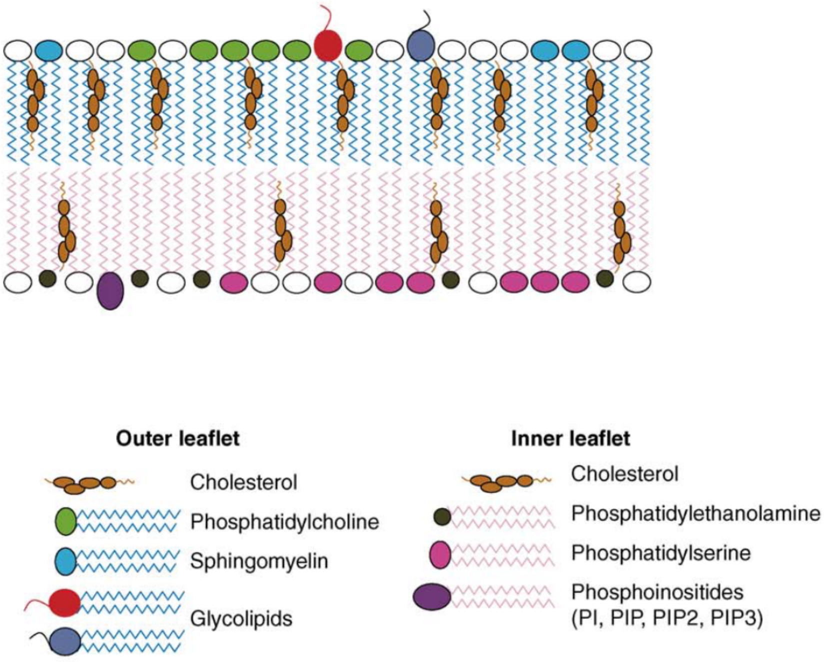

Fig. 3.12 Decomposition of the lipids found in the inner and the outer leaflet of the plasma membrane. From [274].

The membrane curvature is not just a passive consequence of the chemical composition of the cell. Dynamical cellular metabolisms such as membrane trafficking affect dramatically the membrane curvature which play a key role in growth, division and movement of the cell [276].

3.1.4 Role in the cell metabolism

First, plasma membrane defines the boundaries of the cell. It acts as a selective barrier in order to regulate the internal chemical composition of the cells. The transport of molecules across the plasma membrane can be done by either passive or active processes. Due to the lipid bilayer structure of the membrane, the physicochemical properties of molecules define the ability to cross spontaneously or not this biological barrier (Fig. 3.13). For instance, small uncharged molecules, such as O_2 or CO_2, or uncharged polar molecules can diffuse across the plasma membrane. Hydrophobic molecules can also cross the plasma membrane. On the contrary, the plasma membrane is impermeable to charged molecules, such as ions, and large uncharged nonpolar molecules [255]. Concerning the ions, it is well known that many critical cellular processes, such as mitochondrial metabolism [277], mechanical transduction [278] or differentiation [279], are regulated by ion concentrations. The intracellular and extracellular ion concentrations differ a lot (Table 3.1). In order to maintain the appropriate amount of ions inside the cell, it is necessary to accurately regulate the ion exchange between the intracellular and the extracellular compartments. Thus, specific structures, such as ion channels, allow ions to cross the plasma membrane by an active process [280]. Many other molecular exchanges occur though the membrane. For instance, metabolic factors or nutrients are regularly internalized in order to provide these essential molecules to the cell metabolism. On the other side, toxic substances are excluded from the interior of the cell to preserve cell viability [281]. Membrane trafficking is the active process necessary to perform the plasma membrane crossing of these molecules [282]. Endocytosis and exocytosis are crucial steps in order to internalize or externalize large molecules [283].

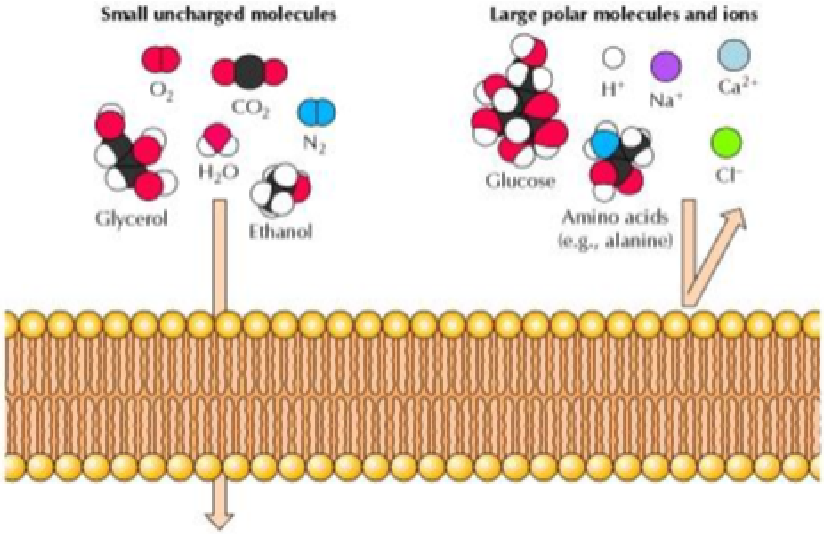

Fig. 3.13 Permeability of phospholipids bilayer for different type of molecules. From [255].

Ion	K^+	Na^+	Mg^{2+}	Ca^{2+}	Cl^+	HCO_3^-
$C_{\text{intracellular}}$ (mM)	60	7-12	5	10^{-4} - 10^{-5}	4 - 7	8
$C_{\text{extracellular}}$ (mM)	4	144	1 - 2	2	120	26 - 28

Table 3.1 Intracellular and extracellular concentration of ions in eukaryotic cells. From [284].

The plasma membrane is also involved in signal transduction in order to initiate a precise cellular response to an external stimulus; for instance, the induction of apoptosis by anticancer drugs [285]. Many membrane proteins are receptors to external ligand in order to initiate a signal transduction into the cell . The main membrane receptors are the G proteins-coupled receptors [286], the tyrosine kinase receptors [287], the ion channels and the lipid rafts [288]. Mechanical properties of the cell depend directly on the plasma membrane. It interacts strongly with the cytoskeleton to control cell shape, to stabilize attachments to others cells or to the substrate and to regulate cell movement [289].

3.1.5 Resting transmembrane potential

As mentioned before, there are large gradients for K+ and Na+ across the plasma membrane due to the differences in intracellular and extracellular concentrations. A cell can maintain this large gradients of ions thanks to the activity of the Na^+-K^+-ATPase, a primary active ion pump. This ion pump requires ATP to take 3 Na^+ ions out of the cell and 2 K^+ into the cell [290]. Fig. 3.14 illustrates the mechanism of the sodium-potassium pump. First, the binding of 3 intracellular Na^+ ions induces a phosphorylation by ATP of the cytoplasmic face of the pump. A conformational change in the protein is triggered and induces the transfer across the membrane of the 3 Na^+ ions. Then, the binding of 2 K^+ ions on the extracellular surface of the pump induces a reverse process, meaning a dephosphorylation of the pump and a return to its original conformation. This conformation change results in the release of the 2 K^+ ions into the cytoplasm. This process is equivalent to a final transfer of one positive charge from the cytoplasm to the extracellular medium and allow the cell to maintain its resting transmembrane potential.

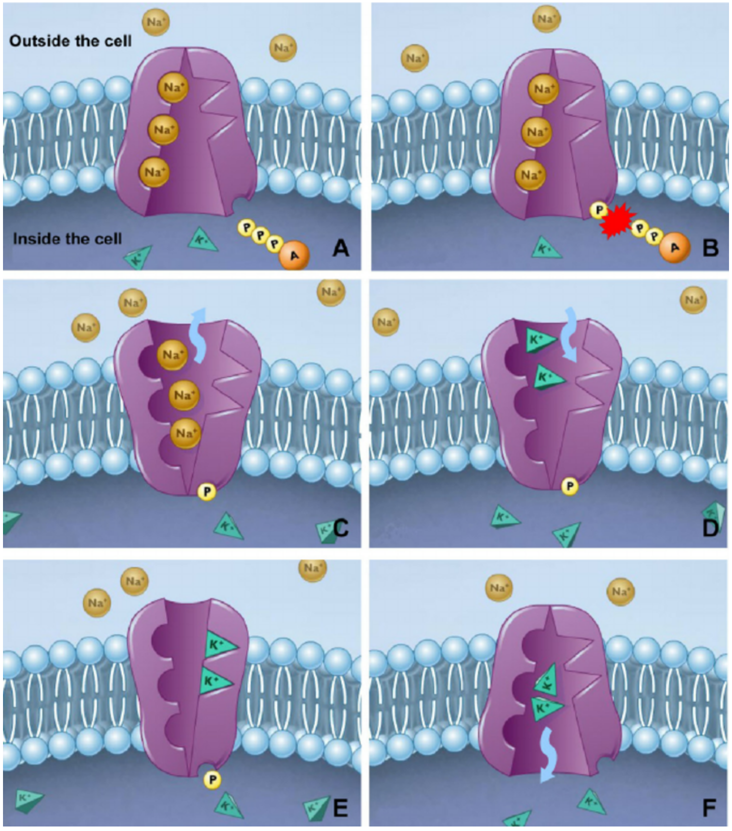

Fig. 3.14 The sodium-potassium exchange pump mechanism. From [291].

The resting transmembrane potential is between -10 to -70 mV depending on the cell type. This membrane potential is involved in many cellular processes such as action potentials in neuron cells [292] and differentiation in stem cells [293].

3.2 Electropermeabilization

Although the plasma membrane is a barrier, several methods are now available to deliver non-permeant molecules of interest into the cells and overcome this biological barrier. The vectorization of molecules, such as drugs or DNA, can be performed thanks to physical agents, chemical agents or biological agents (Fig. 3.15). Laser beams [294, 295], ultrasounds [296, 297], accelerated particles [298, 299] and magnetic fields [300, 301] are commonly used to vectorize non-permeant molecules into the cells [302].

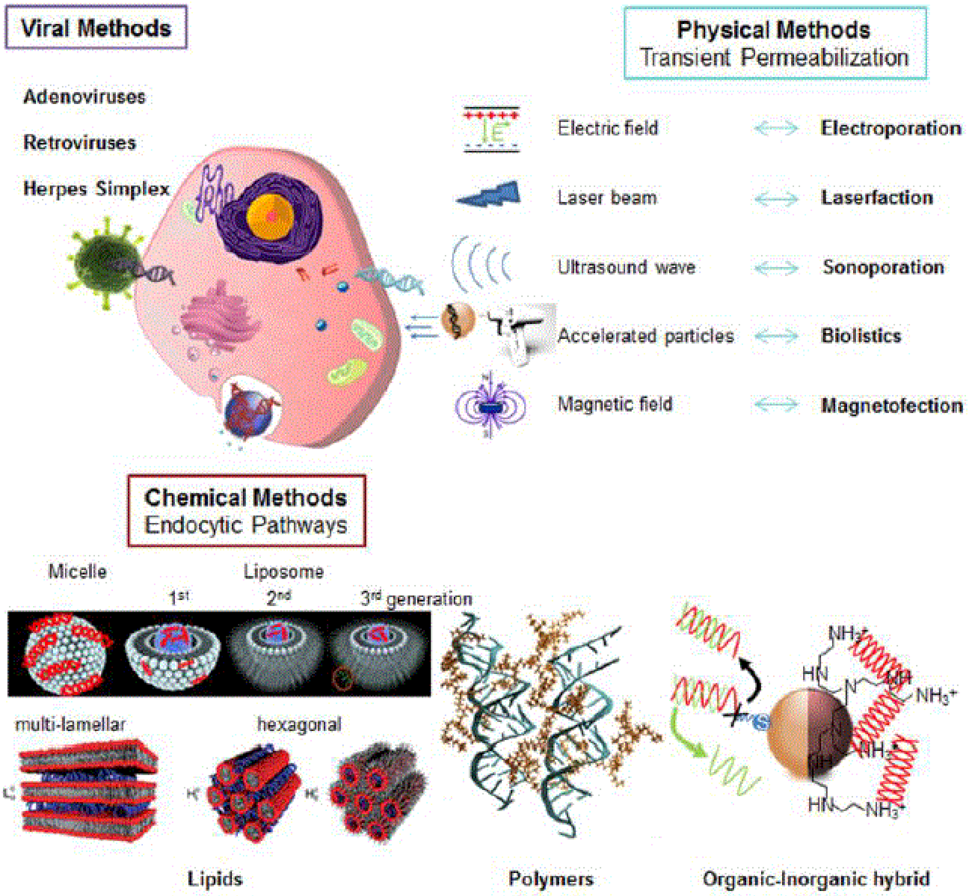

Fig. 3.15 Overview of the main strategies for DNA vectorizations. Adapted from [302].

3.2.1 History and principle of electropermeabilization

In 1958, Stampfli *et al.* was the first one to reveal the reversible breakdown of the cell membrane due to an external electric field [303]. Then, a series of three papers reported the non-thermal lethal effect of high electric fields on microorganisms, such as bacteria and yeasts [304–306]. In 1972, Neumann *et al.* demonstrated that transient electric fields (20 kV/cm exponential decay pulse with a decay time of 150 µs) induced transient permeability changes in the membrane of cells [307]. A few years later, this result was confirmed by a similar study performed by Kinosita and Tsong [308]. The experimental conditions were then optimized in order to introduce DNAs into cells [309, 310] allowing the perspective of medical applications of cell EPN. Nowadays, EPN has been extensively studied by many groups all around the world [311–314]. Many biomedical applications, such as electrochemotherapy (ECT) which combine EPN and chemotherapy, arose from this interaction between PEFs and biological cells.

3.2.2 Underlying mechanisms of cell electropermeabilization

The delivery of appropriate PEFs to cells induces the destabilization of the plasma membrane which is associated with a permeabilization of the plasma membrane. In the literature, this interaction between PEFs and cells is termed electroporation, EPN or electropulsation. The use of these three terms enhances the fact that the underlying mechanisms remain not yet fully understood. The next section will present the state of the art of the underlying mechanisms of the interaction between PEFs and live cells.

3.2.2.1 Transmembrane potential modulated by external pulsed electric fields

When an external electric field is applied to a cell, the associated electrophoretic force creates a movement of the charges present in the intra and extra cellular media. This charge displacement unbalances the electrical potential across the membrane naturally generated by the cell metabolism. Thus an additive transmembrane potential $\Delta\Psi_i$ superimposes to the resting transmembrane potential of the cell $\Delta\Psi_0$. This new transmembrane potential has been mathematically described by Schwan *et al.* [315]. By solving the Laplace equation, the additive transmembrane potential on a given position of the plasma membrane of a spherical cell can be modelled by the equation 3.1 [316].

$$\Delta\Psi_i = f \cdot R \cdot \cos(\theta) \cdot (1 - e^{\frac{-t}{\tau_m}}) \tag{3.1}$$

where $\Delta\Psi_i$ is the induced transmembrane potential, f is a function depending on physical and geometrical properties of the cell, R is the radius of the spherical cell, E is the magnitude of the electric field applied, θ is the angle between the electric field and the normal to the membrane at a given position on the cell membraneand τ_m is the time constant of the membrane.

f can be described by the equation 3.2 [317].

$$f = \frac{3 \cdot \sigma_0 \cdot \left[3 \cdot d \cdot R^2 \cdot \sigma_i + (3 \cdot d^2 \cdot R - d^3) \cdot (\sigma_m + \sigma_i)\right]}{2 \cdot R^3 \cdot (\sigma_m + 2 \cdot \sigma_0) \cdot (\sigma_m + \frac{1}{2}\sigma_i) - 2 \cdot (R - d)^3 \cdot (\sigma_0 + \sigma_m) \cdot (\sigma_i + \sigma_m)} \tag{3.2}$$

where d is the thickness of the cell membrane, R is the radius of the spherical cell, σ_i is the conductivity of the cytoplasm, σ_m is the conductivity of the cell membrane and σ_0 is the conductivity of the extracellular medium.

τ_m can be described by the equation 3.3 [315].

$$\tau_m = \frac{R \cdot C_m}{\frac{2 \cdot \sigma_0 \cdot \sigma_i}{2 \cdot \sigma_0 + \sigma_i} + \frac{R}{d} \cdot \sigma_m} \tag{3.3}$$

where τ_m is the charging time constant of the membrane, d is the thickness of the cell membrane, R is the radius of the spherical cell, σ_i is the conductivity of the cytoplasm, σ_m is the conductivity of the cell membrane, σ_0 is the conductivity of the extracellular medium and C_m is the capacitance of the membrane.

Under the assumptions that the membrane is perfectly insulating ($\sigma_m = 0$) and that the time constant of the cell membrane (in the range of hundreds of nanosecond) is significantly smaller than the duration of the PEF (in the range of millisecond to microsecond) ($\tau_m << T_{pulse}$), the equation 3.1 can be simplified by 3.4. This equation is commonly termed "Schwann equation" (equation 3.4).

$$\Delta\Psi_i = \frac{3}{2} \cdot R \cdot E \cos(\theta) \tag{3.4}$$

where $\Delta\Psi_i$ is the induced transmembrane potential, R is the radius of the spherical cell, σ_i is the conductivity of the cytoplasm, σ_m is the conductivity of the cell membrane, σ_0 is the conductivity of the extracellular medium and C_m is the capacitance of the membrane.

Fig. 3.16 presents a scheme of the additive transmembrane $\Delta\Psi_i$ along the cell surface. Based on the Schwann equation, the cathode side of the cell, meaning the side close to the cathode of the generator is depolarized by the fact that the induced transmembrane potential is in the opposite direction of the resting transmembrane potential. Thus, the total transmembrane potential has a higher value than the resting transmembrane potential. On the contrary, the anode side of the cell is hyperpolarized. The resting transmembrane potential is generally between -20 mV and -200 mV depending on the cell type [318]. For a cell of a radius of 10 µm and a magnitude of the external electric field of 1000 V/cm, the induced transmembrane potential equals to 1.5 V at the pole of the cell, meaning in the axis of the electric field. This value can be higher than the resting transmembrane potential. The effect of the induced transmembrane potential is magnified by the fact that the thickness of the lipid bilayer of the plasma membrane is around 6 nm. Thus, the local electric field is around $2.5*10^6$ V/cm, which is 2500 times higher than the initial external electric field.

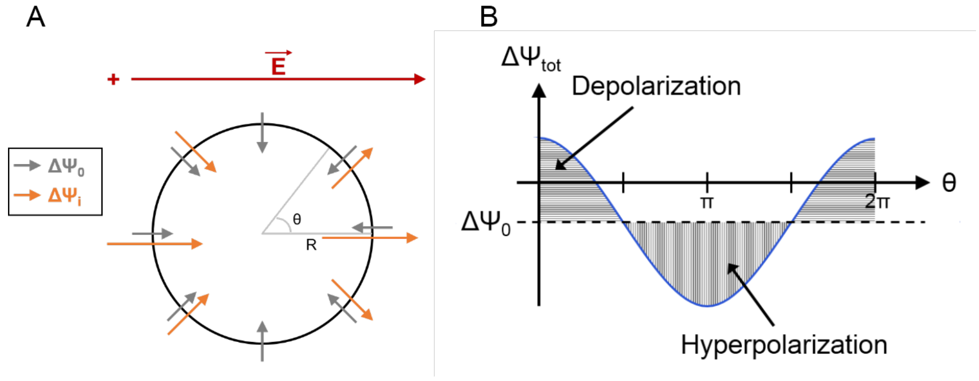

Fig. 3.16 Scheme of the different transmembrane voltages. A – Scheme of a cell under an external electric field and the induced and resting transmembrane potentials. B – Evolution of the total transmembrane potential along the cell membrane as a function of the angle between the electric field and a point on the cell membrane.

It has to be mentioned that the Schwann equation is valid only on a spherical cell. Kinosita et al. was the first to experimentally investigate the validity of the Schwann equation, on unfertilized eggs of sea urchins which are spherical shape cells [319]. Kotnik *et al.* also experimentally demonstrated the validity of the Schwann equation on living cells in suspension 3.17.

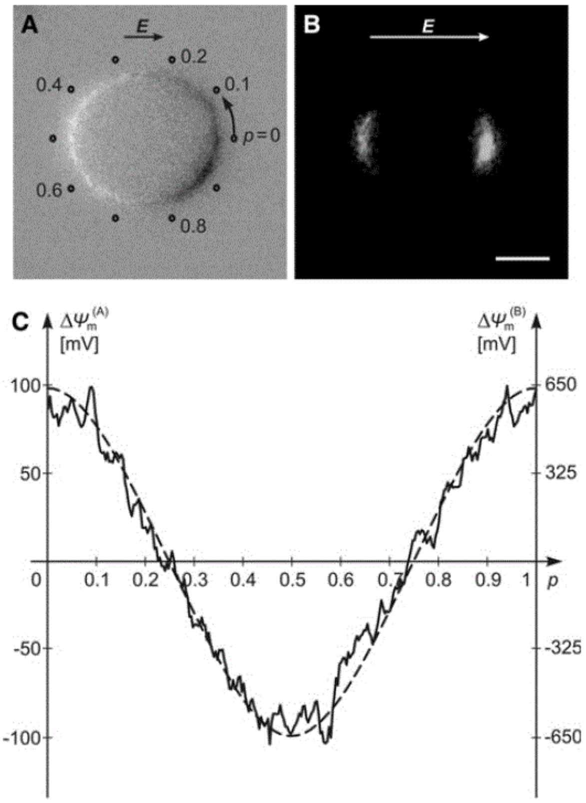

Fig. 3.17 Steady-state transmembrane potential $\Delta\Psi_m$ and electroporation of a spherical CHO cell. A - Changes in fluorescence of di-8-ANEPPS caused by a nonporating 50 ms, 100 V/cm pulse. B - Transport of PI into the same cell caused by a porating 1.5 ms, 650 V/cm pulse as visualized 200 ms after exposure. C – Steady-state transmembrane potential $\Delta\Psi_m$ measured along the path shown in A (full line) as predicted by the Schwann equation (dashed line). Adapted from [320].

In order to trigger the permeabilization of the membrane, it has been demonstrated that the total transmembrane potential has to exceed a threshold value [307]. This permeabilization threshold depends on many parameters such as the cell type, the resting transmembrane potential or the size of the cells. For instance, Teissie *et al.* demonstrated that the transmembrane potential has to reach 250 mV to permeabilize CHO cells [321]. But, in the case of erythrocytes, the permeabilization threshold is associated to a transmembrane potential of 1 V [308]. According to the literature, the permeabilization threshold of the transmembrane potential ranges from 200 to 1000 mV and depends on the biomarker used to detect permeabilization [322–324].

3.2.2.2 Electroporation: from numerical models to experimental proofs

As mentioned before, the underlying mechanisms of the interaction between PEFs and biological membranes are still under investigation. Purely theoretical models have been designed in order to get access to information that are not accessible through experiments [314, 325, 326]. According to the results obtained by numerical simulations, the intense electric field applied on a phospholipid membrane induces forces able to create pores into the membrane, also called electropores. The term electroporation is directly related to this pore creation hypothesis. Numerical simulations based on molecular dynamics (MD) contributed to a better understanding of the electroporation process (Fig. 3.18).

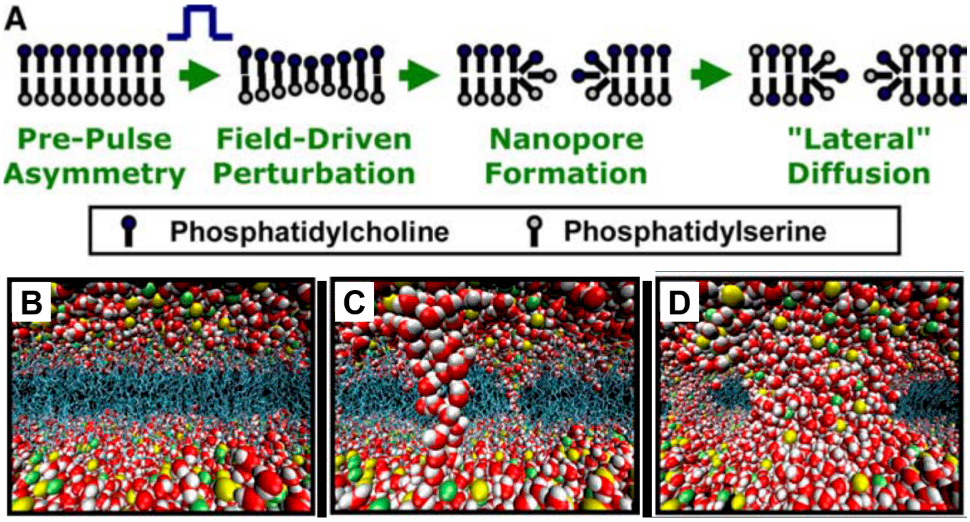

Fig. 3.18 Pore creation. A – Diagram showing electropulse induced pore formation and “lateral” diffusion of PS from the inner to the outer leaflet of the membrane lipid bilayer. B-D Snapshot of a MD simulation showing pore formation. In these three panels, water molecules (O, red; H, white), phosphatidylcholine (P, yellow, and N, green); acyl chains (cyan). Adapted from [327, 328].

The dynamics and the size of the pores have been studied by molecular dynamics simulations [329–332]. Basically, the pore is created in the range of nanoseconds after the beginning of the application of the external PEFs (Fig. 3.19). The pore closes within the same duration after the end of the PEFs delivery. It means that the pores would be present only during the presence of the electric pulses. The size of the pore is in the range of nanometres. The interfacial water, meaning the few layers of water in immediate proximity with the phospholipid head groups, seems to play a key role in the initiation and the stabilization of the pores [333, 334]

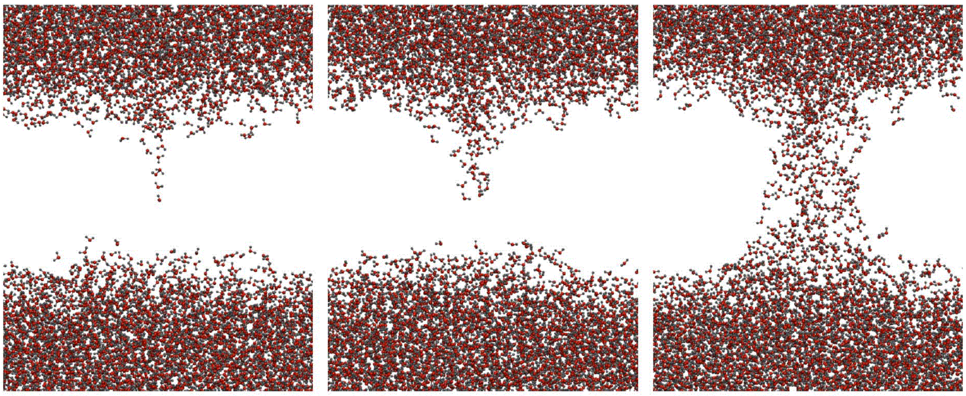

Fig. 3.19 Snapshots of the time evolution of water-lipid-water under an external electric field of 5 MV/cm. The snapshot are 5.8, 6.7 and 7.3 ns from the start of the simulation. Adapted from [333].

The molecular composition of the membrane is also critical to the pore formation. Casciola *et al.* demonstrated that an increase in the concentration of cholesterol in the membrane composition, induces an increase in the electroporation threshold [335]. This is consistent with the present knowledge stating that cholesterol is known to enhance membrane rigidity of fluid membranes [336, 337] and thus to increase the energy barrier that has to be overcome to create pores into the membrane.

Although MD simulations provide detailed information at time and space resolutions that no experimental system is able to reach at the moment, one of its limitations consists in the non-realistic biochemical composition of the plasma membrane especially with the absence of proteins in the bilayers. Thus, the MD results are difficult to be extrapolated to biological cells. In order to compare MD and experiments, a simplified model of membrane is commonly used. Giant unilamellar vesicles (GUVs) are constituted by a single lipid bilayer and they have a size similar to the cell (diamter ≈ 10 µm). GUVs are commonly used as cell membrane models [338, 339] and they have been exposed to PEFs [340, 341]. The forces induced by the electric fields can strongly modify the spherical shape of the GUV (Fig. 3.20). Moreover, phase contrast images indicate potential pores at the vesicles pole according to the electric field direction. GUVs can also shrink under electroporation. It has been demonstrated that membrane loss of GUVs can be the underlying mechanism of shrinkage [342]. By comparing MD simulation and experiments on GUVs under nanosecond electric pulses, Breton *et al.* demonstrated that the transport of siRNA through the lipid bilayer during the electric pulses is related to the creation of pores into the GUV membrane [343].

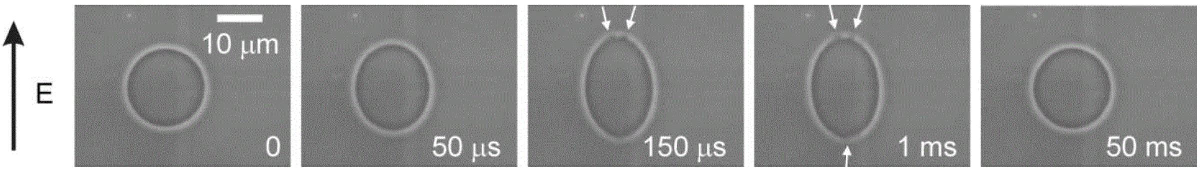

Fig. 3.20 Poration of a vesicle (phase-contrast microscopy). The DC pulse duration is 200 µs and the field strength if 1.4 kV/cm. From [338].

3.2.2.3 Biochemical effects of pulsed electric fields

The pores creation in the membrane is not sufficient to describe all the effects of pulsed electric fields on the plasma membrane. Although the MD simulations indicate that the pores collapse as soon as the electric field is turned off, the cells can remain permeable for tens of minutes after the delivery of the electric shock [344]. The origins of this long term electropermeabilized state are multiple and might be related to biochemical consequences of the delivery of external electric field.

In 1994, Gabriel *et al.* showed that millisecond PEFs create reactive oxygen species (ROS) such as hydrogen peroxide (H_2O_2) or hydroxyl radical ($\bullet OH$) in the surrounding of the electropermeabilized cell [345]. The ROS production has been also detected after the delivery of nanosecond PEFs [346]. ROS are known to be associated with oxidative stress for the cells [347, 348]. This oxidative stress is known to mediate lipid peroxidation through a chemical chain reaction (Fig. 3.21). This chemical reaction is specific to the unsaturated lipids which are present in the cell membrane [349]. Lipid peroxidation is known to affect the cellular metabolism and to induce tissue damages [350–352]

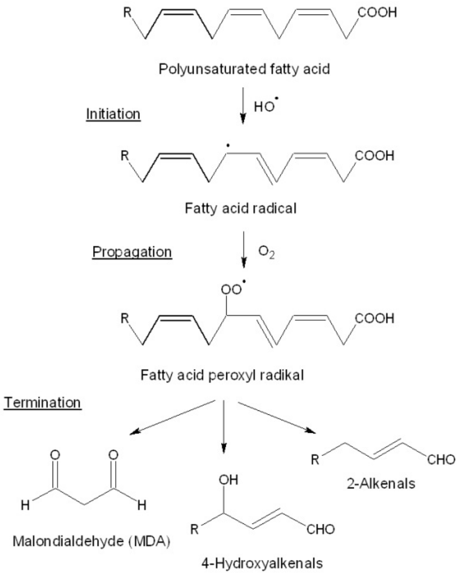

Fig. 3.21 Steps in lipid peroxidation process. From [353].

First of all, the lipid peroxidation hypothesis has been studied thanks to MD simulation. It has been demonstrated that a polyunsaturated lipid bilayer is susceptible to lipid peroxidation from an energetic point-of-view [354]. This is supported by the molecules dynamics simulations showing that various ROS, HO and H_2O_2 for instance, were able to penetrate deep into the lipid headgroups region and thus access to potential peroxidation sites along the lipid hydrocarbon chains [355]. Numerical models demonstrated that the presence of peroxidized lipids in the lipid bilayer reduces significantly its impermeability. The peroxidation reaction changes the conformation of the lipids. The area per lipid increases and thus the lipids spacing also (Fig. 3.22). These conformational modifications contribute to reduce the energetic barrier, to water for instance [356]. Moreover, a thickness reduction of the bilayer is noticed in membranes with peroxidized lipids. This also contributes to decrease the impermeability of the bilayer [357]. A simulation by quantum mechanics brings detailed information about this conformational modification of the phospholipids due to peroxidation. It reveals that hydroperoxides are more subject to conformational modifications than the peroxyl radicals because peroxyl radicals remain located quite deep inside the bilayer where as hydroperoxides have a tendency to float close to the lipid headgroup [358].

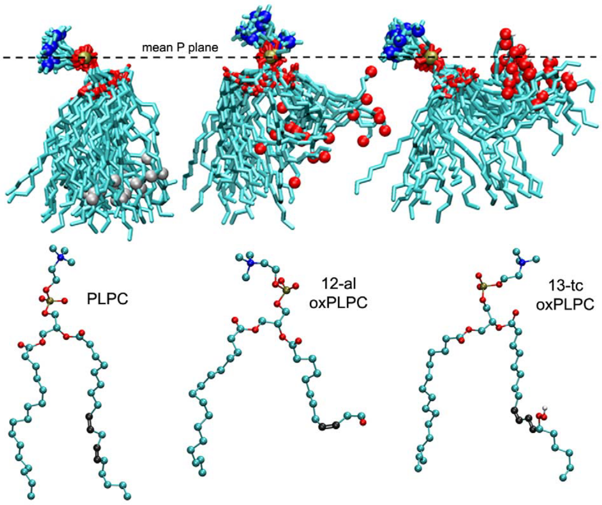

Fig. 3.22 Oxidized and unoxidized phospholipid conformations change over time. From [359].

A study combining MD simulations and experiments performed on Jurkat cells has demonstrated that an external oxidative stress enhances the susceptibility of the membrane to the electric field [359]. This study reports also that the pores formation is facilitated at location containing peroxidized lipids. Based on experiments performed with GUVs made of different phospholipids, mass spectrometry analysis showed that the level of oxidation is highly dependent on the degree of unsaturation of the phospholipid [360].

Previously, this oxidative stress has been associated to the long-lasting EPN state of the cells [361]. Recently, a new impermeability model has been suggested by combining the electroporation concept and the long-term permeabilization induced by the oxidative stress (Fig. 3.23). In this model, the lipid peroxidation is the direct consequence of the creation of pores into the lipid bilayer. Thus, the electroporation can be seen as the initiation step of EPN. In the rest of the manuscript, the term “electropermeabilization” will be used rather than “electroporation” in order to take into account the long-lasting permeabilization.

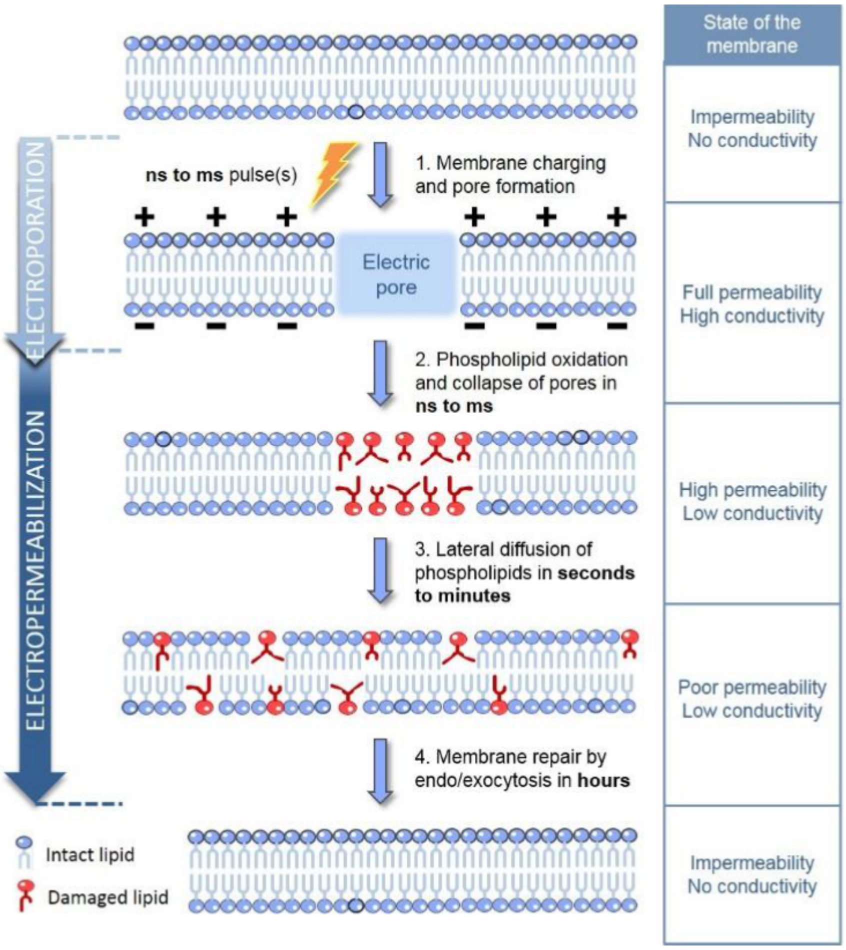

Fig. 3.23 Scheme representing the model of the membrane impermeability rupture caused by the interaction of electric pulses and cell membranes as well as the description of the state of the membrane in terms of permeability and conductivity. From [362].

3.2.2.4 Biological effects on the cells

As described by the Schwan's equation, the size of the cell will affect the additive transmembrane voltage and thus the sensitivity of the cell to the electric pulses. But many others parameters influence the coupling between the electric pulses and the cells. Depending on the cell type, when a cell is attached to a substrate, it can present different morphologies which will therefore impact the sensitivity of the cell to the electric pulses. Experiments and numerical models demonstrated that the sphere is the most sensitive cell shape to the electric field [363, 364]. Nowadays, microdosimetry allows to determine accurately the spatial distribution of the electric field into the cells and the different internal organelles [365, 366]. The cell density also impacts the efficiency of EPN. When the cell concentration increases, a shielding effect induces a reduction of the percentage of permeabilized cell (Fig. 3.24). Numerical studies confirmed the impact of cell-cell proximity on the EPN efficiency [367, 368]. The authors concluded that the EPN threshold is increased from 5 to 10 % when cells are in contact. Cells aligned parallel to the electric field required higher electric field to be permeabilized than cell aligned perpendicularly to the electric field. The EPN threshold depends also on the cell cycle. Cells in the G0/G1 cell cycle appear to be more resistant and to reseal faster than the cells in the S + G2/M phase [369].

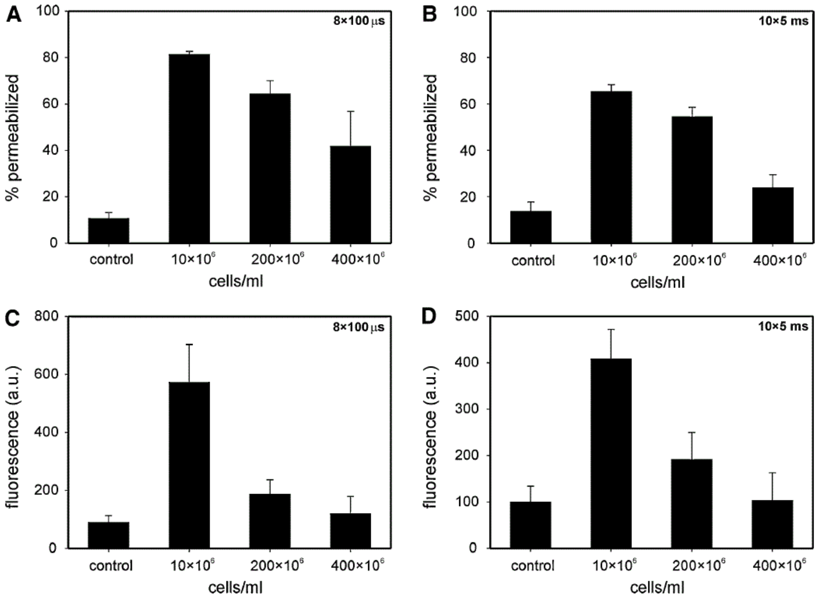

Fig. 3.24 Electropermeabilization percentage as function of CHO cell density for A 8 x 100 µs (700 V/cm) and B 10 x 5 ms (400 V/cm) pulse protocols. Fluorescence as a function of cell density for C: 8 x 100 µs (700 V/cm) and D: 10 x 5 ms (400 V/cm) pulses. From [370].

Swelling and blebbing are among the well-known consequences of the delivery of PEFs on attached cells 3.25. The permeabilization of the plasma membrane induced an osmotic imbalance due to a water influx. As water is a very small molecule (18 Da), cell swelling can be used as a very sensitive biomarker of the preliminary steps of EPN. The composition of the pulsing buffer is critical in this osmotic imbalance. It can impact the gene transfer efficiency [371]. Romeo *et al.* quantified the changes in cell volume (about 15 %) after the delivery of 100 kV/cm pulses of 5 ns duration on Jurkat T lymphoblasts in growth medium [372] and they showed that cell swelling remains visible 60 seconds after the delivery of the electric pulses. Not all cell types display swelling after EPN. For example, adrenal chromaffin cells do no swell after the exposition to nanosecond electric pulses [373].

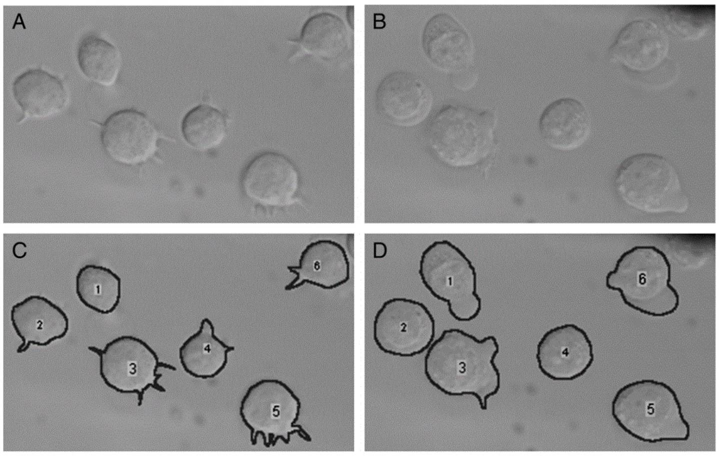

Fig. 3.25 Osmotic swelling after nanoelectropulse exposure. A - Jurkat cells before pulse exposure. B - Same cells 60 s after exposure to 30, 5 ns, 100 kV/cm pulses at 1 kHz. C and D - Cells in A and B are outlined for area extraction with ImageJ. Adapted from [372].

PEFs are also known to strongly alter the cytoskeleton. The disruption of the network of microfilaments and microtubules of cells exposed to electric pulses has been demonstrated [374–376]. As a consequence, several studies by atomic force licroscopy (AFM), an optical instrumentation sensitive to the mechanical properties of the surface of the sample demonstrated a decrease in the elasticity of the cell membrane after the exposition to PEFs (Fig. 3.26) [377, 378].

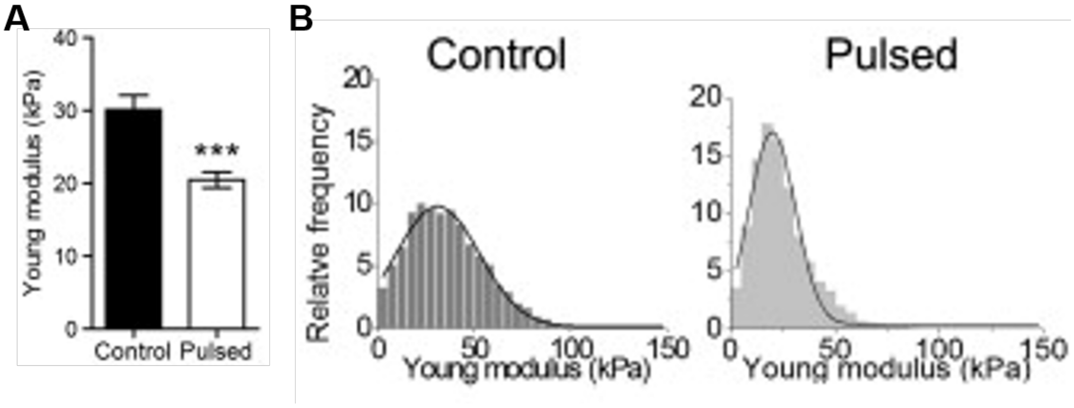

Fig. 3.26 Elasticity of the plasma membrane of fixed CHO cells. A – Young modulus values for control and fixed cells (mean +/- standard deviation to the mean). B – Frequency distribution of the Young modulus value of one control and one pulsed cell. Adapted from [379].

The cytoskeleton is known to take part in the cell membrane repair mechanisms [380]. Rols *et al.* showed that the cell cytoskeleton was disrupted after the delivery of PEFs on mammalian cells [374]. Although cell membrane repair has been studied for decades, the exact underlying mechanisms in the specific case of cell EPN are not yet fully understood [381–384].

Finally, adenosine triphosphate (ATP) release has been detected after the delivery of electric pulses [345]. In a next section, we will discuss the *in vivo* consequences of the ATP release induced by EPN.

3.2.2.5 Impact of the external parameters

The permeabilization of plasma membrane induced by electric pulses is not a binary process. Depending on the electric pulse parameters used, three different EPN states of the plasma membrane can be induced: no EPN, reversible EPN and irreversible EPN (IRE). Reversible permeabilization means that the cell is able to recover its membrane impermeability thanks to membrane resealing processes. In the case of irreversible permeabilization, the membrane resealing processes are not able to restore the membrane impermeability. Thus, the membrane remains permeabilized which finally leads to cell death. As shown in Fig. 3.27, these three permeabilization states depend on the electric pulse parameters.

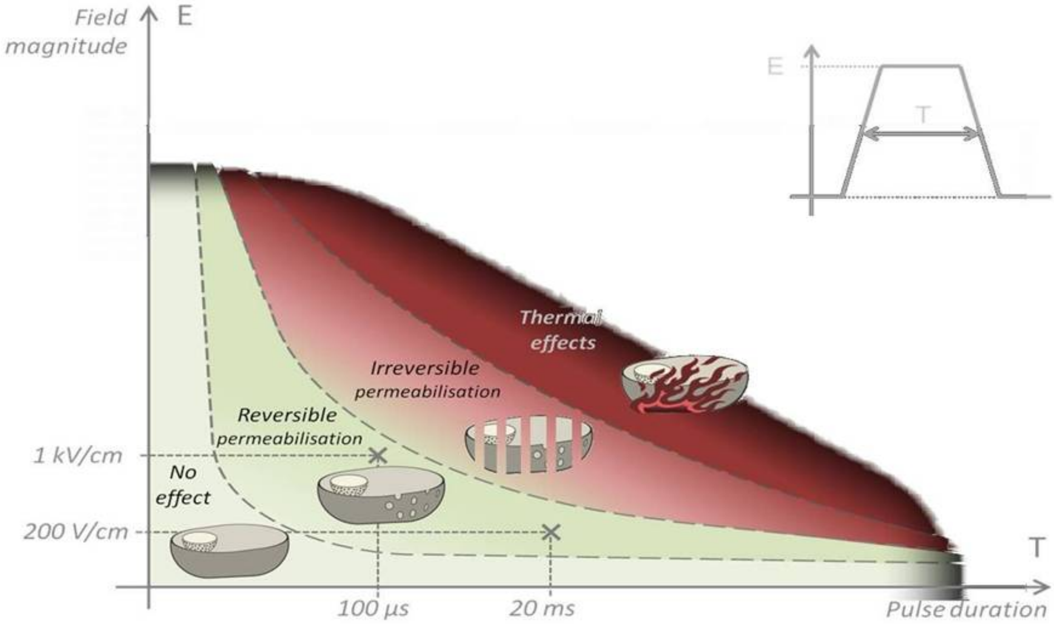

Fig. 3.27 Schema of the different effects of the delivery of PEF on cell. From [385].

The magnitude of the electric field applied to the cells has been the first electrical parameter studied to define the different membrane states and the thresholds associated to these three membrane permeabilization states [307, 309]. These thresholds are cell type dependent. Moreover, the determination of the reversible permeabilization threshold depends also on the biomarker used to monitor the permeabilization (Fig. 3.28-A). In the range of the electric field magnitude associated to a reversible permeabilization, a linear relation between the percentage of permeabilized cells and 1/E has been established with a regression coefficient of over 94 % (Fig. 3.28). Pucihar *et al.* demonstrated that the kinetics of the transport of PI was strongly affected by the pulse amplitude . The relationship between the kinetics of the transport of PI and the pulse amplitude was not a linear relationship and related to different mechanisms [386].

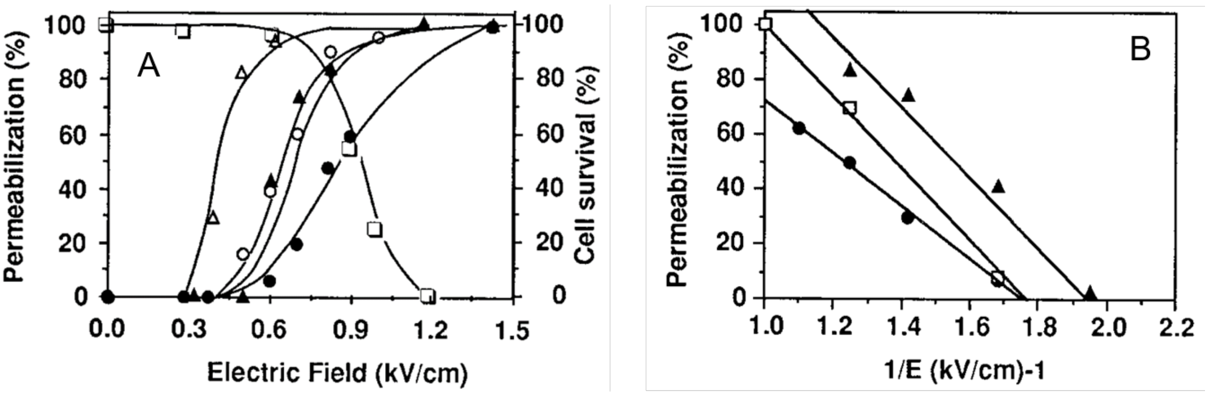

Fig. 3.28 A -Effect of the electric field magnitude on permeabilization efficiency and cell survival. CHO cell were pulsed 10 times at 1 Hz with a pulse duration of 5 ms at various electric field magnitudes in the presence of different molecules: propidium iodide (△), β-gal (▲), trypan blue (○) and FD-70 (●). The percentage of cell survival is plotted as a function of electric field magnitude (□). B – The percentage of permeable cells is plotted as a function of 1/E. □ is related to FD-40. Adapted from [387].

Number and duration are two other pulse parameters able to modulate the level of permeabilization [388–390]. Basically, if the number of pulses increases, the level of permeabilization increases. The same trend occurs for the pulse duration except for the electric pulses of submicrosecond duration that will be detailed in section 3.2.2.7. Hence, the level of cell permeabilization shows a dose-effect response as a function of the magnitude of the electric field, the number of electric pulses and the pulse duration. The effects of the frequency rate on the permeabilization have been studied for the first time in 1999 [391]. These effects are more complex and the underlying mechanisms are still under debate in the EPN community. It has been demonstrated that an increase in the frequency rate above a frequency rate threshold around 100 Hz is associated with a decrease in the permeabilization efficiency (Fig.3.29). Silve and colleagues associated this behaviour to a desensitization of the plasma membrane to the electric field [392]. The electro-desensitization phenomenon is associated with the generation of local defects in the plasma membrane due the electric field. Let's assume that each electric pulse creates membrane defects at the pole of the cell, which is the spatial localization of the higher effect based on the Schwann equation, and that these defect structures can laterally diffuse in the membrane. If the time between two consecutives pulses ($T_{betweenpulses}$) is lower than the time for lateral diffusion of the defects ($T_{defectsdiffusion}$), the ability of the second electric pulse to create new defects will be reduced. This concept can be associated to the chemical damages (lipid peroxidation) created by the electric field at the level of the membrane. On the contrary, Pakhomova *et al.* detailed the "electrosensitization" phenomenon [393, 394]. Basically, the authors exposed cells to a single shot dose (1 train of 8 electric pulses) and to a split dose (2 trains of 4 electric pulses delivered at 100 Hz with a delay time between the two trains of electric pulses of 5 minutes). Their results showed that a split dose is more efficient in terms of permeabilization level and drug uptake than a single shot dose. Moreover, the first train of 4 electric pulses caused less damage than the second train of 4 electric pulses, meaning that the cell membrane is getting more and more sensitive to the electric fields. The accurate comparison of these studies is complicated because the electric pulse parameters strongly differ. Moreover, it has to be mentioned that the electro-sensitization phenomenon is buffer dependent [395].

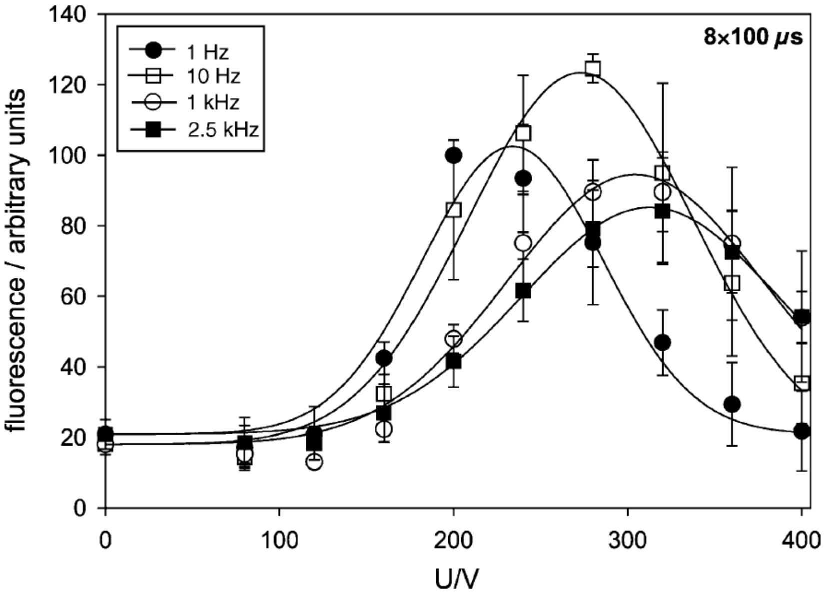

Fig. 3.29 The uptake of Lucifer Yellow as a function of pulse amplitude U at pulse repetition frequencies of 1 Hz (●), 10 Hz (□), 1 kHz (○) and 2.5 kHz (■) (8 pulses of 100 µs duration). The distance between the electrodes is 2 mm. Each point on the figure represents the mean of three values +/- standard deviation. Adapted from [396].

As the induced transmembrane potential is highly related to the direction of the electric field, the impact of the polarity of the electric pulses on the level of permeabilization has been studied. It has been demonstrated that bipolar pulses with a duration in the range of hundreds of microseconds are around 20 % more efficient in the uptake of Lucifer yellow than unipolar pulses [397]. The exposition to symmetrical bipolar pulses are known to reduce the electrolytic contamination due to ions released from aluminium cuvettes (Al^{3+}) and stainless steel electrodes (Fe^{2+}/Fe^{3+}) [398]. This point is crucial when the instrumentation used to monitor the EPN is sensitive to the external conductivity of the external medium such as bioimpedance system.

The conductivity of the external medium also contributes to modulate the efficiency of EPN. Many experimental studies demonstrated that an increase in the external medium conductivity is associated to an increase in the EPN efficiency [399–403]. Two studies have opposite results but the use of a capacitance-discharge pulse generator to deliver electric pulses induces a strong bias and these generators are known to deliver electric pulses with a pulse length depending on the external medium conductivity. A numerical model revealed that the induced transmembrane potential depends on the cell membrane conductivity which is driven by the medium conductivity [404]. A recent study demonstrated that cumulative effects, the number of pulse or frequency rate for instance, can hide the effect of medium conductivity on the permeabilization efficiency [405]. The impact of the external temperature on the EPN efficiency has been less investigated. Some studies revealed that an increase in temperature induced an increase in EPN efficiency in cells [406, 407] or tissues [408]. These results can be explained by the relationship between the membrane fluidity and the external temperature [409]. Rols *et al.* demonstrated that a post-incubation at 37 °C enhanced the efficiency of electrotransfer [410].

3.2.2.6 From an electrical point of view

From an electrical point of view, the plasma membrane is described as a dielectric. Cole suggested an electrical model of the cells [411]. In this model, the membrane is represented as a combination of a capacitance and a resistance in parallel (Fig. 3.30-A). In the literature, it is generally found that the permittivity is about $4.4 * 10^{-11}$ F/m and the conductivity around 5 S/m [412]. Based on these values, the frequency cut is estimated at around 800 kHz (Fig. 3.30-B and C).

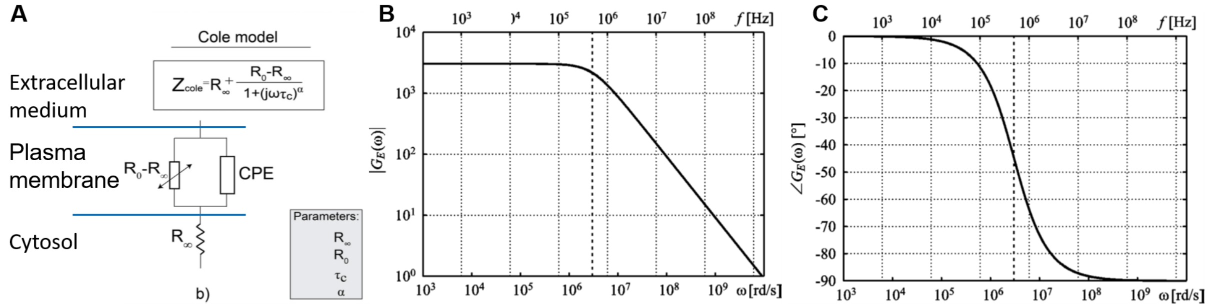

Fig. 3.30 Electrical model of the plasma membrane. A – Electrical representation of the Cole model. B - C Bode plot (magnitude and phase) of the amplification of an external AC electric field. The dotted line represents the cut off frequency. Adapted from [413, 414].

The electric pulses with a microsecond duration range are known to contain continuous frequency components up to 10 kHz [392]. Thus, bioimpedance measurements were performed in order to monitor EPN and to investigate the behaviour of the plasma membrane electrical model under PEFs. Garcia *et al.* measured major modifications of the electric properties of the membrane for two cell types. These modifications were associated with two different time constants related respectively to the short-term and long-term EPN dynamics [414]. *In vivo* bioimpedance measurements were also performed and they revealed that conductivity changes in electroporated tumors reflected the treatment outcome [415].

3.2.2.7 Specificity of nanosecond pulses

As mentioned before, the plasma membrane is considered as a dielectric barrier with a charging time of around 75 ns in the case of a spherical cell with a diameter of 10 µm [416]. Thus, the previous calculation of the induced transmembrane potential at the level of the plasma membrane cannot be used in the specific case of electric pulses with a pulse duration of around 100 nanoseconds. Theoretically, for this specific range of pulse durations, the plasma membrane should become electrically transparent. The opportunity to exert an electric field effect on cellular internal organelles is one of the major interest of nanosecond pulses. Recently, the design of new generators compatible with nanosecond pulse duration emphasized the growing interest towards nanosecond pulses [417–420]. In the rest of the manuscript, electric pulses with durations up to 600 ns will be termed nanosecond pulsed electric fields (nsPEFs).

The first experimental proof of intra-cellular permeabilization by nanopulses was published in 2001 by Schoenbach *et al.* [421]. Since 2001, many studies reported the effect of nanosecond pulses on cells and several reviews are now available [416, 422–425].

One of the first intracellular effects due to the cells exposition to nsPEFs that has been studied is the cytoplasmic calcium release [426, 427]. Calcium is known to be stored into inner organelles via the endoplasmic reticulum [428] and the mitochondria [429]. It has been demonstrated that the exposition of cells to nanoseconds electric pulses can permeabilize the endoplasmic reticulum [430] and the mitochondria [431, 432]. Another source of calcium influx is the activation of voltage-gated calcium channels present in the membrane induced by the delivery of nsPEFs [430, 433]. Membrane repair, based on exocytosis/endocytosis, is known to be calcium dependent [434–436]. Thompson *et al.* demonstrated that the resealing of the plasma membrane is affected by nanosecond electric pulses due to this calcium-dependent process [437]. Finally, some cell types, such as mesenchymal stem cells, display spontaneous calcium oscillations. De Menorval *et al.* demonstrated that nsPEFs are able to generate spontaneous-like calcium oscillations in this cell line [438].

As a consequence of this massive calcium influx into the cytoplasm, the triggering of apoptotic processes is enhanced after the exposition of cells to nsPEFs [439–441]. The triggering of apoptosis is not only related to the intracellular calcium. It has been demonstrated that nanosecond electric pulses can also trigger apoptosis through caspase and mitochondria involvements [442–444]. Moreover, the cytoskeleton is also affected by the nsPEFs. The disruption of the actin network contributed to reduce the viability of cells [437, 445]. Nanosecond electric pulses on the plasma membrane induced the translocation of phosphatidylserine [446, 447] and the the hydrolysis of the phosphatidylinositol-4,5-bisphophate (PIP_2) [448]. These two effects are involved in signalling pathway related to apoptosis. Finally, the effects on nucleus and DNA is another contribution to the induction of apoptosis [449–451]. Although the nanosecond electric pulses are known to affect the nucleus, contrary to the micro- or millisecond pulses, the efficiency of the electrotransfer of a plasmid coding for green fluorescent protein is not enhanced by the use of nanosecond pulses [379].

At the beginning of the 2000s, many studies reported that nanosecond pulses were not affecting the plasma membrane and its impermeability [421, 426, 452]. More recently, the effect of nanosecond pulses on the plasma membrane has been largely demonstrated by comparing the influx of intracellular calcium when the buffer contains calcium or not [453, 454] and by performing patch-clamp recordings [454, 455]. The size of the fluorescence markers that were used could be one of the explanations of the previous absence of detection of the plasma membrane permeabilization [456]. Finally, numerical models demonstrated the ability of nanosecond pulses to generate aqueous pores in the membrane [326, 327, 447, 452]. As mentioned previously, the experimental visualisation of these pores has not yet been done. As nanosecond pulses are compatible with the MD simulation duration, the comparisons between *in silico* MD simulations and *in vitro* experiments are now possible [343] and contribute to a better understanding of the underlying mechanisms of EPN.

It has been demonstrated that bipolar nanosecond electric pulses were less efficient in terms of permeabilization level than unipolar electric pulses [457]. This result is in contradiction with a microsecond electric pulses study from Kotnik *et al.* [398]. It can be explained by the fact that the Schwann equation is valid only if the plasma membrane has enough time to charge which is not the case when the cells are exposed to nanosecond electric pulses.

3.2.2.8 *In vivo* consequences

In the perspective of biomedical applications, the study of the interactions between PEFs and tissues is another hot topic. The delivery of PEFs to tissues involves specific mechanisms. In 1998, it has been reported that tissue electroporation induces a strong reduction of the blood flow in the area where the electric field is delivered [458]. This phenomenon, termed “vascular lock” has been noticed on many tissues submitted to pulsed electric fields [459–461]. The vascular lock is based on two mechanisms. First, the electrical stimulation causes a rapid vasoconstriction of the blood vessels. Then, the permeabilization of the endothelial cells induces a local increase in the interstitial pressure and a decrease in the intravascular pressure. Electric pulses can be used to temporary interrupt the blood flow [462, 463]. The vascular lock phenomenon contributes to a temporary increase of the concentration of the drugs around and inside the tumour submitted to PEFs [464].

EPN is also known to boost the immune system. It has been demonstrated that the effect on tumor regression of electrochemotherapy (ECT) on immunocompetent mice was dramatically increased in comparison with immonudeficient mice [465], demonstrating the involvement of the immune system after the delivery of PEFs on tumours. As a confirmation of this result, it has been observed that the oedema observed after the delivery of PEFs on tumours were more severe in immunocompetent than in immonudeficient mice. Calvet *et al.* demonstrated that ECT induces the hallmarks of immunogenic cell death [466]. These hallmarks consist in the liberation of ATP and high mobility group box 1 protein and the membrane externalization of calreticuline. Finally, some studies demonstrated the systemic effect of the combination of ECT and immunotherapy on distant non-treated tumours [467, 468].

3.2.3 Biomedical applications of electropermeabilization

As mentioned previously, the opportunity to overcome the plasma membrane barrier without any thermal effects has raised an interest for many biomedical applications. Fig. 3.31 presents the different EPN-based treatments developed up to now. Breton *et al.* reviewed the use of electric pulses in cancer treatments [343].

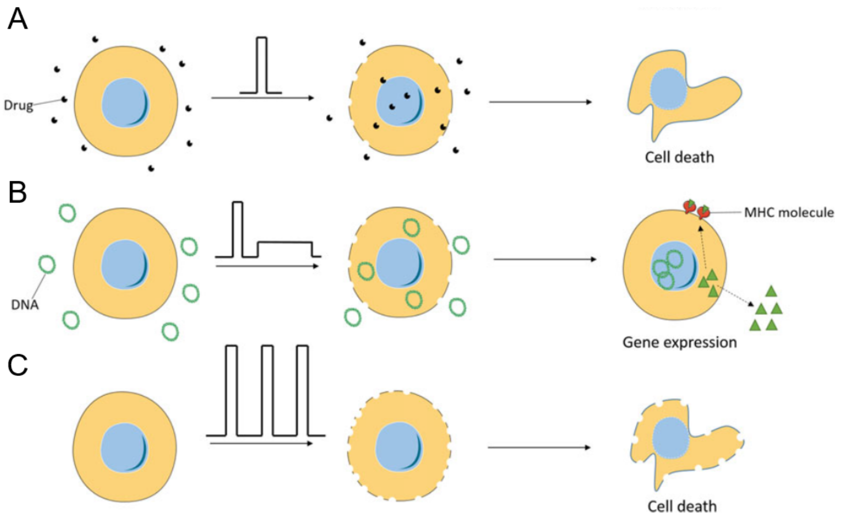

Fig. 3.31 Electropermeabilization-based treatments. A – Vectorization of non-permeant drugs into the cells via a single high and short electric pulse inducing reversible electropermeabilization. B – Vectorization of DNA into the cells via a high and short electric pulse inducing reversible electropermeabilization followed by a low and long electric pulse inducing driven-electrophoretic forces on DNA. C – Irreversible electropermeabilization of cells via a series of high and short electric pulses. Adapted from [469].

3.2.3.1 Electrochemotherapy

In 1991, Poddevin *et al.* demonstrated the opportunity to dramatically increase the cytotoxic effect of bleomycin, a low-permeant anti-tumor drug, in cells in culture [470]. The same year, the same team has reported a major tumour reduction in mice by combining bleomycin to a local treatment with electric pulses [471]. These two studies were the bases of the development of a new anticancer technique called electrochemotherapy (ECT). ECT consists in the combination of EPN with a non- or low-permeant chemotherapy in order to potentiate the cytotoxic effect of the drug into the tumour. In 2006, a multicentric clinical study (European Standard Operating Procedures of ECT: ESOPE) established the standard operating procedures of ECT that have been used in the clinics since then [472]. Now, ECT is routinely used in over 150 European cancer centers all over the world. By the end of 2015, about 13000 patients had been treated by ECT, particularly for cutaneous and subcutaneous tumours since these tumours are easily accessible with electrodes. ECT is reimbursed by the social insurance in 8 European countries including Spain, Denmark, Germany, Italy, and the UK [469].

Fig. 3.32 summarizes the protocol of ECT. The drug is administered systemically or intratumorally. After a few minutes, the electric pulses are delivered around the targeted tumours. The EPN of the tumour cells induces a highly efficient drug vectorization which eventually leads to the death of the tumour cells. The standard electrical parameters used in the clinics consist in 8 square-pulses of 100 µs and 1 to 1.3 kV/cm delivered at a frequency rate of 1 Hz or 5 kHz. Bleomycin is the most commonly drug used in ECT. Bleomycin is a non-permeant drug used in cancer treatments. Its mechanism of action is based on the generation of single and double DNA strand breaks. 500 hundred molecules of bleomycin entering the cell at the time of the pulses delivery are enough to kill the cell [473]. Cisplatin is also commonly used in ECT. Cisplatin acts in a different way as it is a more permeant drug and it interferes with DNA replication. The cytotoxicity of bleomycin and cisplatin is increased respectively by a factor of 700 and 10, respectively, when combined with electric pulses [474, 475]. This increase in the efficiency of the drug allows to reduce the administered drug amount and thus the associated secondary effects. Both bleomycin and cisplatin target selectively the dividing cells which is a well-known specificity of cancer cells [476]. Thus, the efficiency of ECT is enhanced on cancer cells in comparison with normal cells. The vascular lock associated with the delivery of PEFs on tissue induces the retention of the drug in the tissue surrounding the pulsed tumor and can increase the local concentration of the drug and therefore its efficiency. The side effects of ECT are minimum thanks to almost none damage on the surrounding pulsed tissue and a drug dose injected below the induced-toxicity threshold.

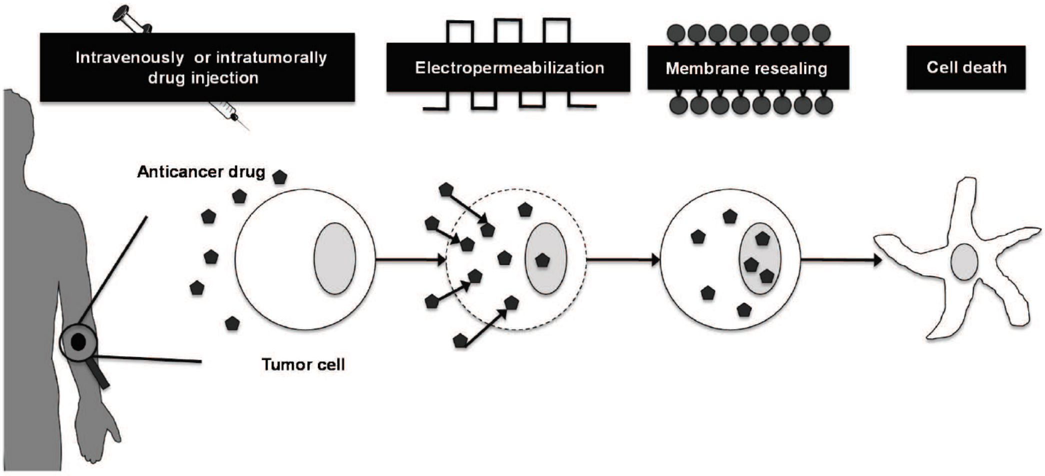

Fig. 3.32 Principle of electrochemotherapy. Non or poorly permeant antitumor drugs with intracellular target, injected either systemically or intratumorally, surround the tumor cells. Electric field application induces an increase in membrane permeability, which allows for the uptake of the antitumoral drug into the tumor cells. After membrane resealing, the drug exerts its highly cytotoxic action inducing tumor cell death. From [477].

During the ESOPE study, ECT treatment elicited an objective response rate of 85% of the treated tumour nodules with a complete response rate of 73.7% of the cases [472]. The antitumor effectiveness of ECT has been confirmed by a meta-analysis of over 44 studies involving 1894 tumours [478]. The ESOPE study restricted the treated tumours to nodules with a diameter lower than 3 cm. It has been demonstrated that ECT is more effective on small tumours than large tumours [479].

The current developments of ECT consist in the treatment of internal tumours such as liver [480], brain cancer [481], pancreatic adenocarcinoma [482](Bimonte et al. 2016), bone metastasis [483], colorectal metastasis [484]. Recently, the ECT efficiency for head and neck tumours has been proved by performing a treatment planning with navigation system [485]. Finally, the opportunity to combine ECT with immunotherapy is another hot topic in the biomedical applications of EPN [469, 486, 487].

3.2.3.2 Electrogenetherapy

Gene therapy and DNA vaccination are both based on the delivery of genetic material to the nucleus of cells in order to generate a therapeutic effect via the internal production of therapeutic proteins [488, 489]. In the treatment of cancer, the aim may be to silence or correct defective genes, to add genes encoding for therapeutic proteins or to initiate a targeted immune response. These promising treatment techniques have the major advantage to induce a therapeutic effect for a long time, from weeks to months, in comparison with treatments using classical drugs. Gene therapy and DNA vaccination in their initial protocols were of limited efficiency due to a low number of therapeutic DNA reaching the nucleus mainly because of the plasma membrane barrier. Thus, the vectorization of DNA or genes thanks to electric pulses has raised a big interest as it could increase the treatment efficiency while guaranteeing a safe procedure.

DNA has the specificity to be negatively charged. Hence, electrophoretic forces associated with electric field contribute to shift the gene towards its target by an electrophoretic movement. Thus, electric pulses for electrogenetransfer (EGT) are specific and combine electropermeabilizing pulses with electrophoretic pulses. The electropermeabilizing pulses, called high voltage (HVT), consist in high magnitude (around 1000 V/cm) and short duration (around 100 µs) electric pulses to induce EPN of the plasma membrane. The electrophoretic pulses, called low voltage (LVT), consist in low magnitude (around 10 V/cm) and long duration (around 100 ms) electric pulses in order to enhance the crossing through the previously electropermeabilized membrane. The combination of HVT and LVT pulses was carefully studied to optimise the efficiency of the EGT *in vitro* and *in vivo* [403, 490]. The mechanisms of gene electrotransfer are still not fully understood [491, 492]. However, the dual process, illustrated in Fig 3.33, is commonly accepted.

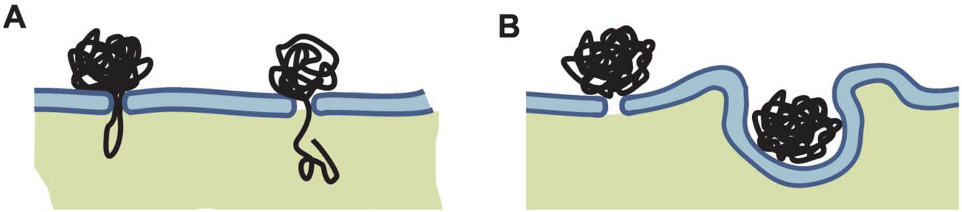

Fig. 3.33 Two possible hypothesis for DNA entry into the cytoplasm. (A) DNA is inserted into the permeabilized cell membrane during the electric pulses and is translocated inside the cell by a slow process after the pulse delivery. (B) DNA interacts with the permeabilized membrane and is consequently endocytosed. From [493].

Gene electrotransfer is not yet routinely integrated in the clinics. Only one Phase I clinical trial of gene electrotransfer in patients with metastatic melanoma is reported in the literature [494]. 8 over 19 patients (42%) showed partial responses and 2 over 19 patients (10%) showed complete regression of all metastases. There is still a lot of work in the improvement of obvious clinical outcome for gene electrotransfer. 4 other clinical trials on gene or DNA electrotransfer are currently running or are terminated, with no published study result yet (`https://clinicaltrials.gov`). Although the clinical perspectives are interesting, a lot of work is still necessary before EGT is commonly included in the clinics [495, 496].

3.2.3.3 Irreversible electropermeabilization

As mentioned before, IRE consists in the delivery of intense and short electric pulses that render the plasma membrane impossible to repair by the membrane resealing mechanisms. This inability to maintain homeostasis leads to cell death. No external agent (drug or gene) is involved in IRE. IRE has been considered as a tumour ablation modality [497, 498]. Although IRE is known to induce temperature increase in the pulsed tissue, it has been demonstrated that IRE is not only related to a thermal therapy mediated by PEFs [499, 500].

IRE has the major advantage to affect specifically the cell membrane, to spare tissue architecture and to minimize damages to blood vessels, nerves and the renal collecting system [501]. *In vivo* studies demonstrated that over 92% of treated subcutaneous tumours in a mice model were in complete regression after IRE protocol [502].

Some studies demonstrated the safety of IRE in humans [503, 504]. A phase I clinical trial on 6 patients reported that IRE was safe to treat patients with kidney tumours [505]. Fig. 3.34 shows a colorectal liver metastasis of a patient before and after IRE treatment. 43 clinical studies are currently running: 27 in Asia, 9 in Europe and 4 in North America. IRE is used in these clinical trials for the treatment of liver, pancreatic, kidney and prostate tumours [506].Finally, 7 clinical studies are completed but the results are not yet published (`https://clinicaltrial.gov`).

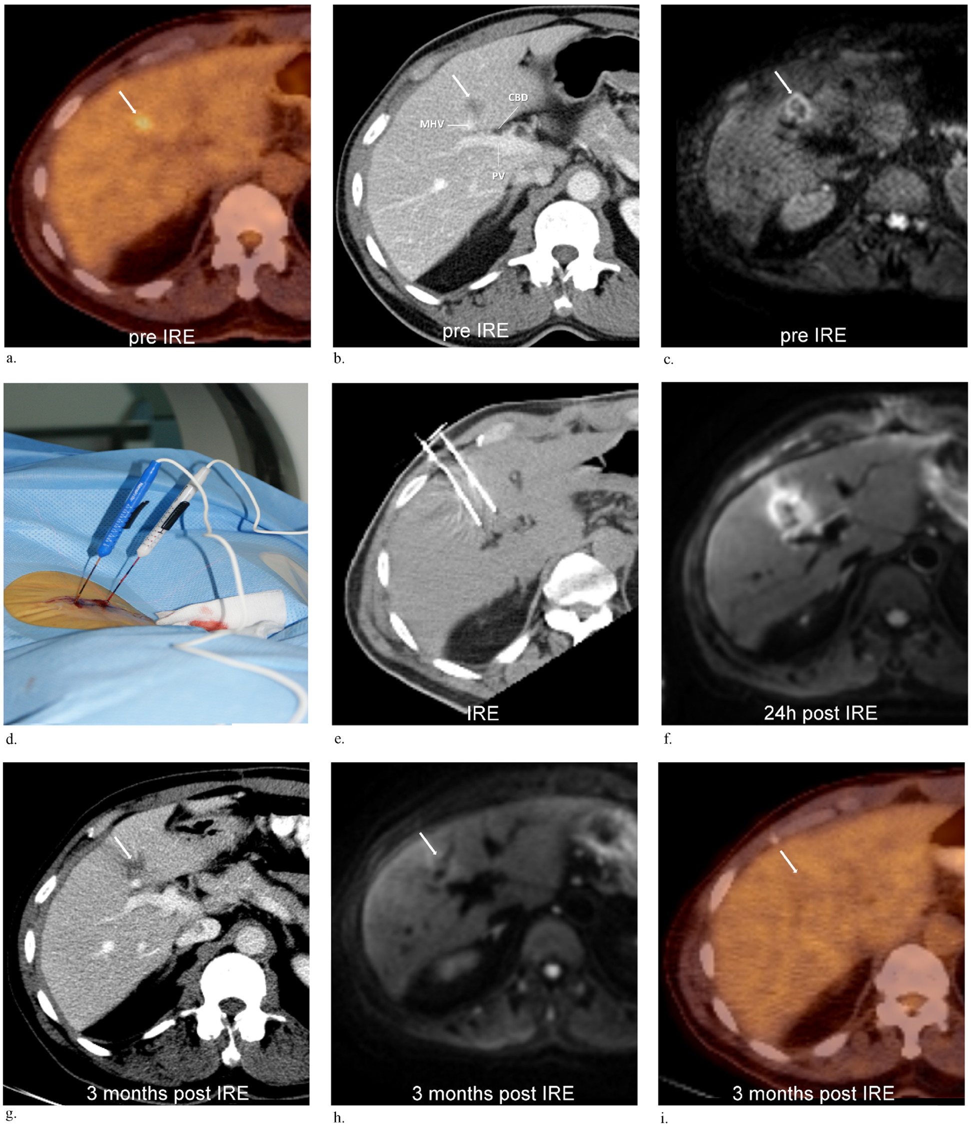

Fig. 3.34 IRE of a centrally located colorectal liver metastasis (arrow). (a–c) Fluorodeoxyglucose positron emission tomography/computed tomography, contrast-enhanced computed tomography, and magnetic resonance imaging diffusion-weighted imaging b800 images obtained before IRE show a small segment IV avid lesion abutting the middle hepatic vein and approximate to the common bile duct and portal vein. (d-e) picture and magnetic resonance image of Percutaneous computed tomography–guided IRE procedure with electrodes in situ. (f) Magnetic resonance imaging diffusion-weighted imaging b800 image obtained 24 hours after IRE shows a typical hypointense ablation zone surrounded by a hyperintense rim. (g–i) Images obtained 3 months after IRE show a vaguely demarcated hypodense scar lesion on contrast-enhanced computed tomography, which becomes isointense on magnetic resonance imaging diffusion-weighted imaging b800, and nonavid on fluorodeoxyglucose positron emission tomography/computed tomography. From [504].

4

Biophotonics to study electropermeabilization

In the perspective of potential improvements of EPN-based treatments, the underlying mechanisms of cell EPN have been extendedly studied for decades by many groups around the word. Photonic microscopy is one of the first instrumentation techniques used to investigate the interaction between PEFs and cell membranes. In 1986, the first optical images of a cell exposed to PEFs were published [507]. One year after, Ehrenberg et al. monitored the membrane potential of HeLa cells exposed to PEFs via fluorescence microscopy with the di-4-ANEPPS fluorescent dye [508]. Fig. 4.1 shows a typical example of fluorescence images of the transmembrane potential of cells exposed to PEFs.

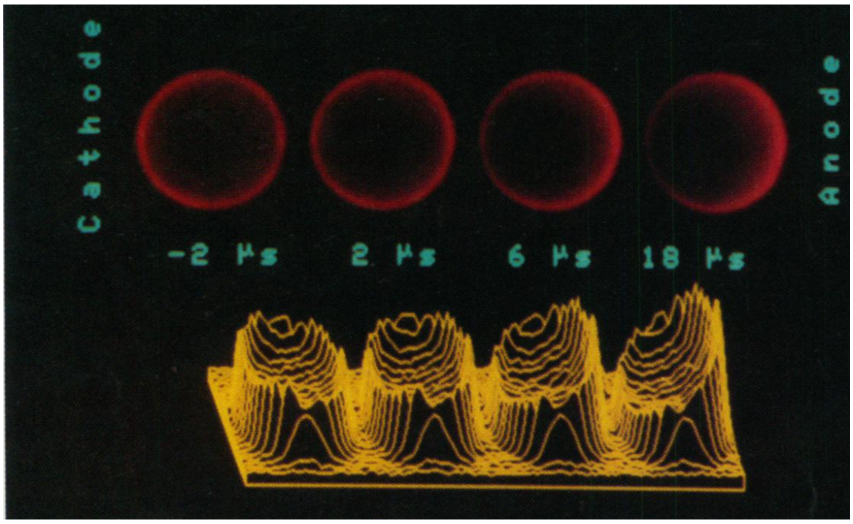

Fig. 4.1 Rise of the transmembrane potential of a cell membrane induced by a pulsed electric field. Images of red fluorescence (intensity profiles in yellow), from a sea urchin egg stained with the voltage-sensitive dye RH292, obtained at indicated times after the onset of a square-wave electric pulse (100 V/cm, duration 25 µs). Adapted from [319].

This section will focus on the contribution of biophotonics microscopy to the understanding of cell EPN mechanisms understanding.

4.1 Epifluorescence microscopy

Epifluorescence microscopy is the most commonly used biophotonics approach to investigate cell EPN. Many discoveries have been possible thanks to this technique.

4.1.1 Quantitative and qualitative anlysis of cell electropermeabilization

The level of permeabilization of cells exposed to PEFs is commonly assessed by fluorescence microscopy. The principle is based on the use of a non-permeant fluorescence dye which is in the extracellular medium. This dye can penetrate into the cell only if the cell plasma membrane is permeabilized. The fluorescence dyes generally used are molecules able to intercalate in DNA, such as PI or Yo-Pro-1, which have the property that their fluorescence quantum yield is significantly increased when they are bound to DNA [509]. By quantifying the fluorescence intensity into the cells, the level of permeabilization can be assessed by comparing the fluorescence intensity of pulsed cells to the fluorescence intensity of unpulsed cells. By sweeping the electric pulse parameters (i.e. electric field magnitude, number of pulses or pulse duration), the cell EPN threshold can be determined [387]. It has to be noticed that the determination of the EPN threshold based on fluorescence microscopy experiments is highly subjective. The results depend a lot on the experimental conditions, such as the fluorescent dye that is used, the extracellular concentration of the dye, or the exposure time of the fluorescence images that are acquired, the temperature, the conductivity of the extracellular medium, ... Vernier *et al.* demonstrated that CHO cells exposed to 10 electric pulses of 30 ns with a magnitude 25 kV/cm were permeabilized to calcium but not to PI

[426]. The molecular weight of calcium and PI is respectively 12 and 668.4 Da. Thus, it was assumed that the smaller is the biomarker, the more sensitive to EPN it is. But two studies demonstrated that Yo-Pro-1 is a more sensitive biomarker of EPN than PI (Fig. 4.2) [432, 452]. The molecular weights of Yo-Pro-1 and PI (629.3 vs 668.4 Da) are similar showing that the permeabilization threshold is not only related to the size of the biomarker. By monitoring the intracellular concentration of calcium via a calcium-green fluorescent dye, Vernier *et al.* showed a significant increase in the intracellular calcium concentration after the delivery of a single nanosecond electric pulse while no increase in Yo-Pro-1 intracellular fluorescence intensity was detected under the same exposure conditions [430].

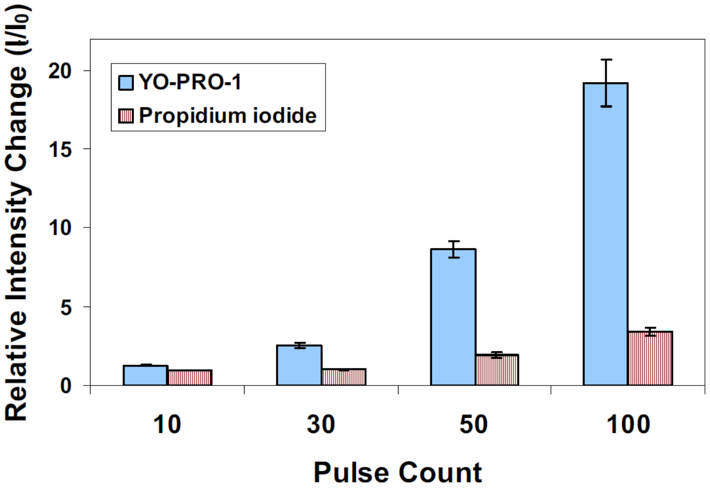

Fig. 4.2 Small molecule permeabilization by multiple, high-field amplitude, nanosecond pulses. Fluorescence microscopic images of individual Jurkat cells in growth medium containing Yo-Pro-1 (5.0 µM) or PI (7.5 µM) were captured immediately before and 5 min after the exposure of the cells to 4 ns, 8 MV/m pulses and the fluorescence intensity change for each cell was measured by photometric integration. Measurable influx of YO-PRO-1 occurs after 30 pulses delivered at 1 ms intervals (1 kHz repetition rate). At higher pulse counts, permeability of the cells to YO-PRO-1 increases and PI influx can be detected. Adapted from [452].

The fluorescent dyes specific to intracellular calcium are sensitive but not specific biomarkers of EPN. Actually, EPN of the plasma membrane is not the only mechanism involved in the increase in intracellular calcium concentration. It has been demonstrated that the voltage-gated Ca^{2+} channels can be activated by the delivery of electric pulses leading to the uptake of extracellular calcium by the cells [433]. The EPN of internal calcium stores such as the reticulum endoplasmic or mitochondria also contributes to an increase in the cytosolic concentration of calcium. In this framework, fluorescent dyes specific to calcium have been used to investigate the opportunity to also electropermeabilize the internal organelles. It has been demonstrated that the exposure of cells to nanosecond electric pulses can permeabilize both the endoplasmic reticulum [427, 430] and the mitochondria [431, 432]. De Menorval and colleagues demonstrated that both nanosecond and microsecond electric pulses can generate spontaneous-like calcium oscillations in mesenchymal stem cells [438].

4.1.2 Impact on the transmembrane potential

Many studies have been performed in order to prove the Schwann equation by measuring the transmembrane voltage of cells during the exposition to PEFs. Some fluorescence dyes are sensitive to the transmembrane potential and after a calibration step, they can provide quantitative information. The group of Kinosita was the first one to investigate this critical question by using the RH929 fluorescence dye (Fig. 4.1). Di-8-ANNEPS was also used and provided detailed information about the transmembrane potential and confirmed on spherical and attached cells (Fig. 4.3). More sensitive and stable fluorescence dye should be used, such as Annine-6 [510].

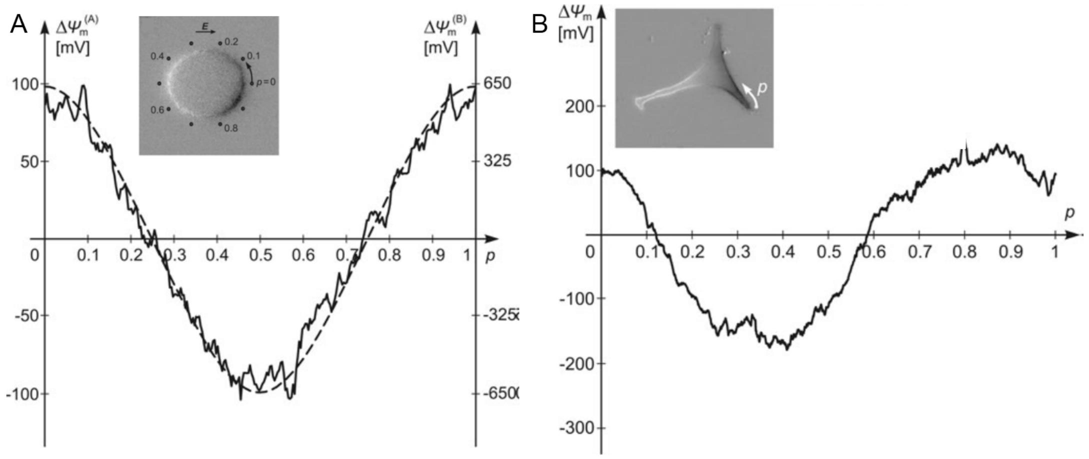

Fig. 4.3 Graph of the Induced transmembrane potential by pulsed electric fields on spherical CHO cells in suspension (A) and non-spherical attached CHO cells (B) measured with the probe Di-8-ANEPS. Adapted from [320].

4.1.3 Effect on the membrane phospholipid

Fluorescence dyes demonstrated the effect of PEFs on the lipids of the plasma membrane. Phosphatidylserine translocation induced by a single nanosecond pulse was shown on Jurkat T-lymphoblast cells [328, 447]. Translocation of phosphatidylserine is known to be a signal of apoptosis. Phospholipid scrambling and membrane disorder was also assessed by fluorescence microscopy. C6-NBD-PC is a fluorescent dye which can be incorporated into the outer leaflet of the plasma membrane cells [511]. Fig 4.4 shows that C6-NBD-PC was internalized after the delivery of millisecond pulses to CHO cells demonstrating that the lipids of the outer leaflet have moved to the inner leaflet. Finally, the delivery of 600 ns PEFs induced the depletion of phosphatidylinositol-4,5-biphosphate in the plasma membrane of CHO cells [448].

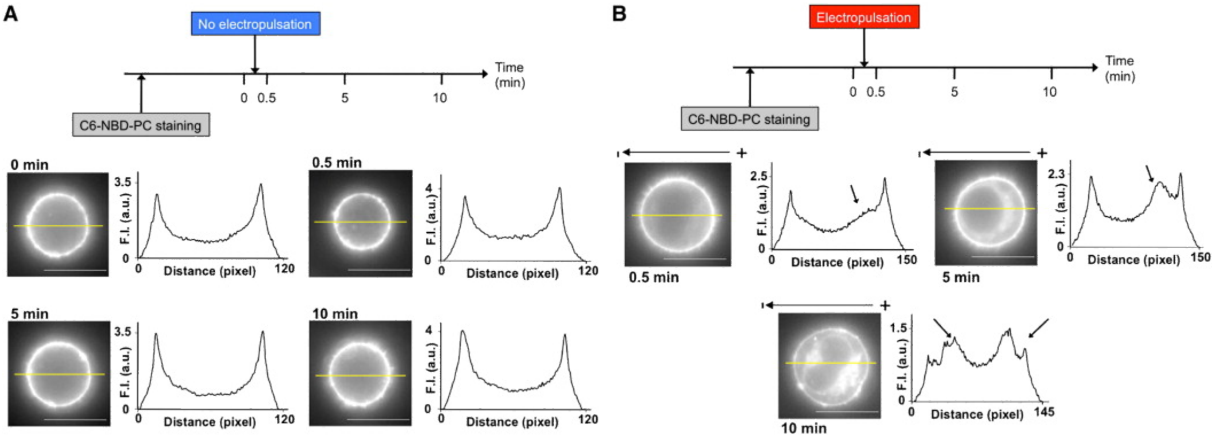

Fig. 4.4 Effect of msPEFs on the C6-NBD-PC internalization in CHO cells. A. C6-NBD-PC distribution in CHO cells before electropulsation. The outer leaflet of the plasma membrane was labeled with the C6-NBD-PC probe at 4 °C. The CHO cells were observed at the single-cell level over time. Fluorescent profile graphs represent fluorescence along the cell diameter (yellow line) (F.I., fluorescence intensity). (Scale bar, 15 µm). B. C6-NBD-PC distribution in CHO cells after electropulsation. The outer leaflet of the plasma membrane was labelled with the C6-NBD-PC probe at 4 °C. The CHO cells were observed at the single-cell level following the application of permeabilizing electric pulses (10 pulses of 5 ms and 0.7 kV/cm at a frequency of 1 Hz). Black arrows on the graphs show the C6-NBD-PC internalization. Graphs representing the fluorescence profile along the cell diameter (yellow line) are drawn parallel to electric field lines at the poles facing the electrodes (F.I., fluorescence intensity). (Scale bar, 15 µm). Adapted from [511].

4.1.4 Mechanism of gene electrotransfer

In the framework of gene electrotransfer, the mechanisms of intracellular trafficking of plasmid DNA were investigated. The contribution of endocytosis and endosomal trafficking of electrotransferred DNA was revealed by combining particle tracking of fluorescent plasmid DNA and colocalization with endocytic fluorescent markers [512]. This study showed that the internalization of aggregated DNA plasmids via endocytosis pathways was mediated for 50 % by the caveolin pathway, 25 % by the clathrin pathway and 25 % by micropinocytosis. A study reported that the microtubules were highly involved during the intracellular transport of plasmids to the nucleus [513]. The discrimination between active and passive transport of intracellular DNA was possible thanks to particle tracking of fluorescently labelled plasmid DNA (Fig. 4.5). Active transport of plasmid DNA along actin filaments and microtubules represents around 45 % of the DNA transport. For the active transport, the mean velocity is 256 nm/s with a mean duration of 6.5 s. For the passive transport, the mean diffusion coefficient is 6.2 x 10^{-3} µm^2/s.

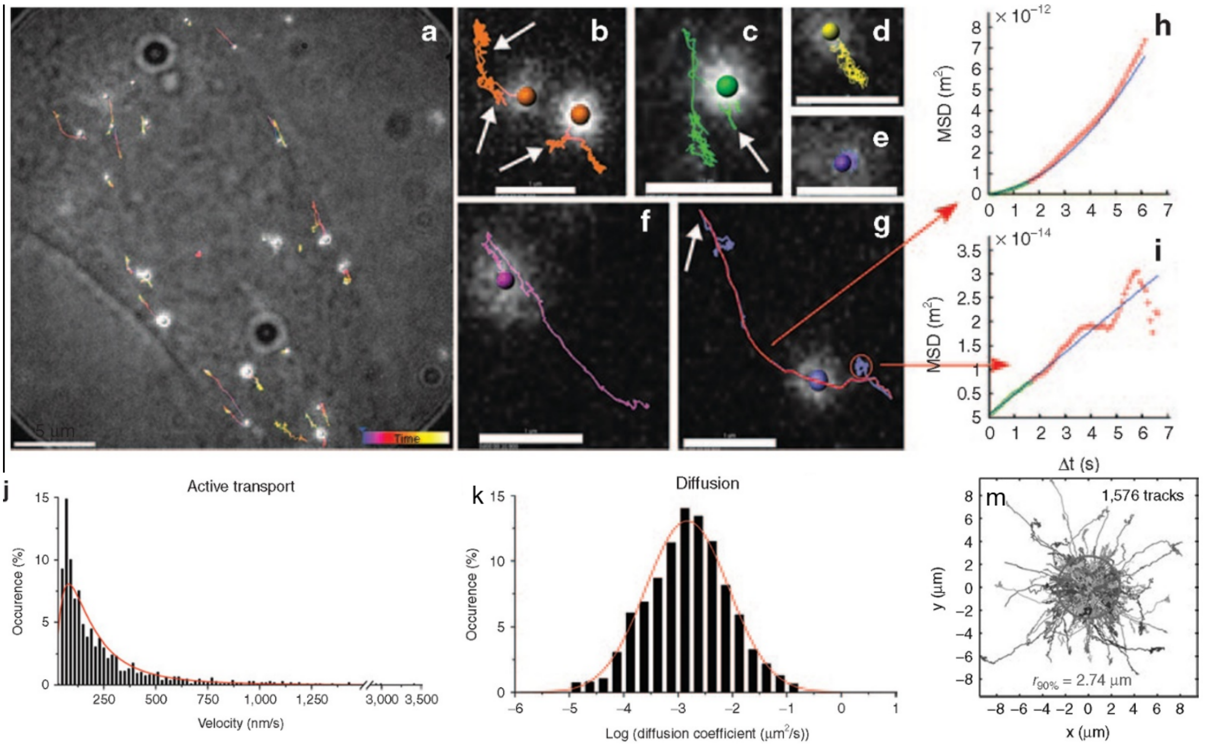

Fig. 4.5 Single-particle tracking of DNA aggregates in Chinese hamster ovary cells after electrotransfer and characterization of the modes of DNA motion. (a) Trajectories of fluorescent Cy5-labelled DNA aggregates inside a cell recorded 20 minutes after the application of the electric field (10 pulses at 0.35 kV/cm, 5 ms, and 1 Hz). Scale bars = 5µm. (b–g) Zoom of some trajectories of the time series presented in (a). Scale bar = 1µm. Trajectories show short (b–d) or long (f,g) distance excursions or almost immobile aggregates (e). Trajectories often had bidirectional movements (white arrows). Different modes of motion can be observed within one trajectory. Trajectories were automatically divided into segments exhibiting either only active transport or only diffusive motion. Totally, 1576 trajectories were analyzed, resulting in 3106 segments. The modes of motion were determined by mean squared displacement analysis: a quadratic fit corresponds to an active transport (h), a linear fit corresponds to a diffusive motion (i). Distributions for (j) velocities, and (k) diffusion coefficients for each mode of motion are calculated from the segments. The velocities distribution was fitted using a log-normal distribution (red line). Plot (k) represents the logarithm of the diffusion coefficients, therefore, it was fitted using a normal distribution (red line). (m) Graph presenting the track plots of all the DNA aggregates transport in the treated CHO cells. Adapted from [514].

4.1.5 ROS detection

PEFs are known to induce ROS formation in the cells and in their surroundings [345, 361] but the kinetics are not yet precisely established. The monitoring of ROS formation thanks to dihydroethidium (DHE), a fluorescence dye which become highly fluorescent under oxidative stress, has shown that the oxidation of dihydroethidium continued for minutes after the delivery of nanosecond electric pulses (Fig. 4.6).

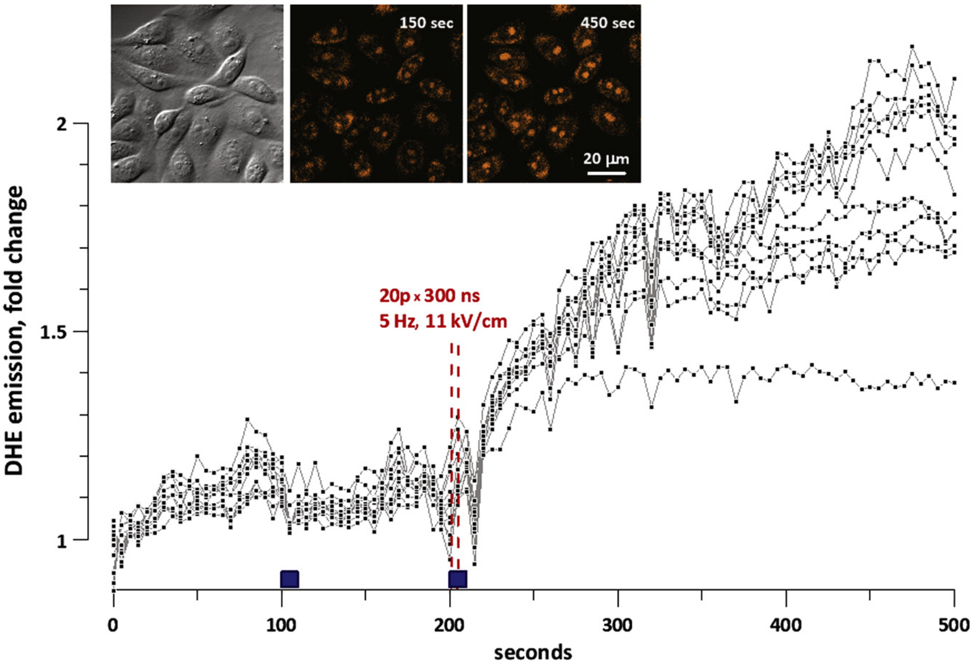

Fig. 4.6 ROS formation in nsPEF-exposed CHO cells as evidenced by the oxidation of dihydroethidium. The graph and insets show the data of one representative experiment (out of 8). Cells were bathed in physiological solution containing 30 µM of DHE. A group of cells located between the nsPEF-delivering electrodes was imaged every 5 s. Filled boxes above the abscissa show the time intervals when the solution flow in the bath was turned on. The first interval of perfusion was accompanied by a sham exposure (control). During the second interval of perfusion, cells were exposed to nsPEFs (vertical dashed lines). Plots show DHE emission in each individual cell. Inset: DIC and fluorescence images of the cells at selected time points. Adapted from [346].

4.1.6 Temperature increase detection

Under reasonable electrical pulse parameters, EPN was considered as a non-thermal technique. A recent study has demonstrated that the temperature can increases up to 2 °C for a few seconds by the delivery of the PEFs (Fig. 4.7). The authors of this study demonstrated that this transient increase in intracellular temperature did not impact the cell viability [515].

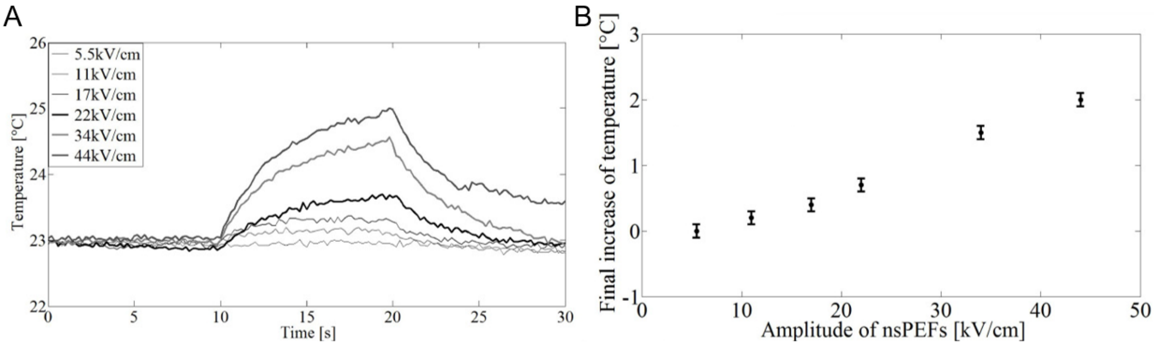

Fig. 4.7 The influence of pulse amplitude on temperature modifications induced by 100 nanoseconds PEFs of 10 ns at 10 Hz, measured by using Rhodamine B. A - Superposition of Rhodamine B measurements curves. B – Graph of the increase of temperature as a function of the amplitude of the nsPEFs. Adapted from [515].

4.1.7 *In vivo* consequences of electropermeabilization

The monitoring of blood vessels by fluorescence macroscopy has been allowed by the implantation of a dorsal window chamber in mice. The dorsal window chamber is biocompatible and is suitable for optical imaging (Fig. 4.8).

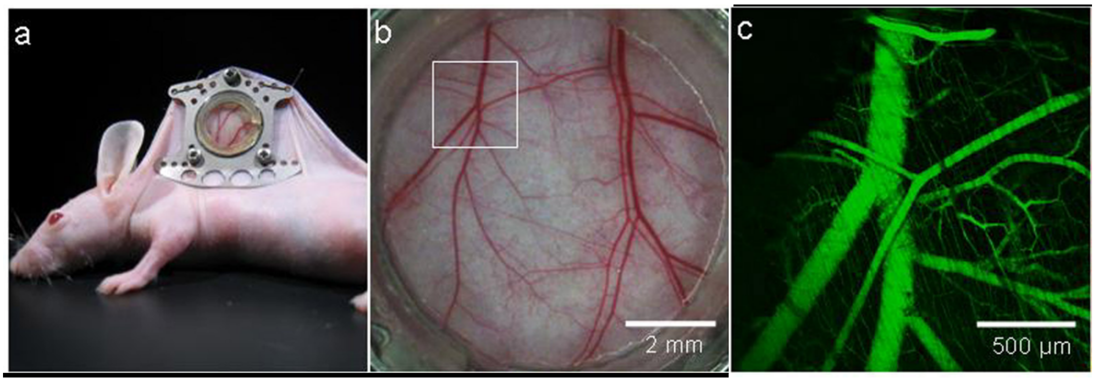

Fig. 4.8 (a) Dorsal window chamber allowing an easy visualization of the microvasculature in animals. (b) White light microscopy of an entire window. (c) Maximum intensity projection image of a fluorescence confocal z stack obtained using fluorescein Dextran (a fluorescent vascular contrast agent). Adapted from [516].

This set-up was used to investigate the vascular lock induced by the delivery of PEFs [517]. The vasoconstriction inducing the vascular lock phenomenon was more pronounced for arterioles than for venules, and occurred few seconds after the delivery of the electric pulses for both types of blood vessels. Deeper investigations of the interactions between PEFs and blood vessels revealed that the vasculature surrounding the tumor was disrupted by the EPN [464]. The dynamics of electropermeabilized subcutaneous blood vessels towards molecules of different sizes were assessed by *in vivo* fluorescence microscopy (Fig. 4.9). The authors demonstrated a transient vascular permeability to the fluorescent dyes with a recovery time depending on the molecular weight of the probed molecule.

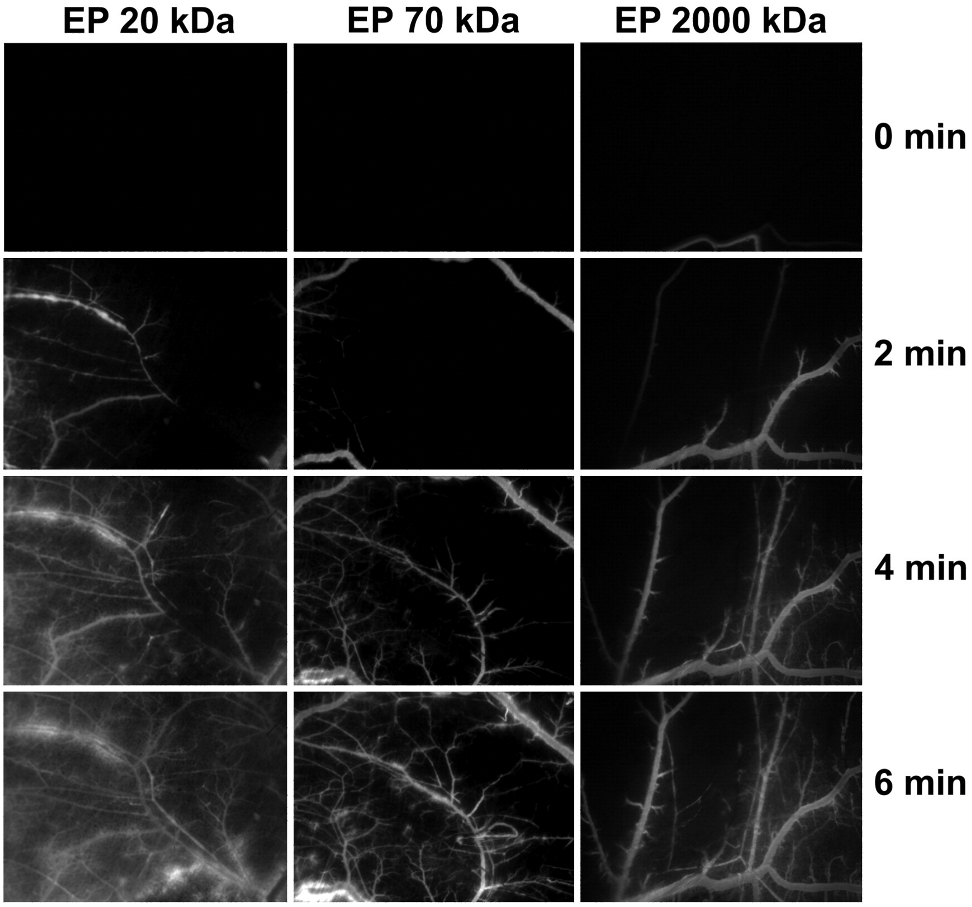

Fig. 4.9 Illustration of the EP-induced vascular lock. Eight square wave electric pulses, amplitude 1300 V/cm, pulse length 100 µs, repetition frequency 1 Hz were applied to mice. 20, 70 and 2000 kDa FITC-dextrans were intravenously injected 20 s after EP. Doral window chamber were observed by fluorescence macroscopy and images were acquired immediately (0 min), and 2, 4 and 6 min after fluorescent dextran injection. Adapted from [518].

4.2 Confocal microscopy

4.2.1 Investigation of the effect of pulsed electric fields on the cytoskeleton

The damages on the cytoskeleton induced by the delivery of nanosecond electric pulses was first demonstrated by epifluorescence microscopy [451]. The spatial resolution of epifluorescence microscopy was, however, not sufficient to clearly demonstrate the disruption of the actin network of cells exposed to nsPEFs (Fig. 4.10). The improvement of the spatial resolution thanks to confocal microscopy raised a non-negligible interest as it allows to monitor accurately the interactions between PEFs and small units of the cytoskeleton such as the actin filaments.

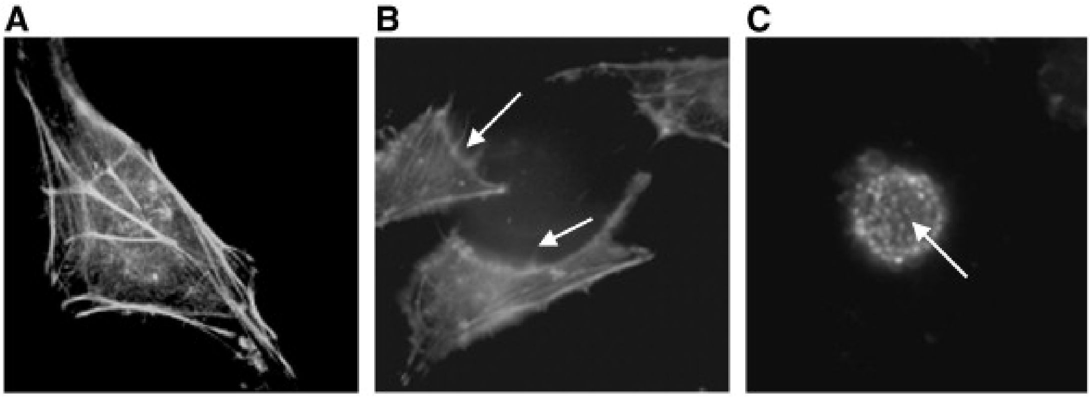

Fig. 4.10 Cytoskeleton damage induced by nsPEF application. (A) shows a representative image of a typical unexposed HeLa cell with an extensive actin network. (B) One minute post pulse cells still exhibit an extensive actin network but with evidence of a ruffled outer cell membrane (arrowed). (C) Four minutes post pulse cells have become rounded with the appearance of intensely stained actin spots (arrowed). Adapted from [451].

nsPEFs affect both the meshwork in the cell cortex close to the plasma membrane and the transvacuolar bundles of the nuclear envelope. As shown in Fig. 4.11, the meshwork cortex is disrupted and disappears after the delivery of nsPEFs and the actin bundles in the cell center detach. The detachment of actin bundles originates from a contraction of these bundles. The kinetics of these two events seems to be similar [519].

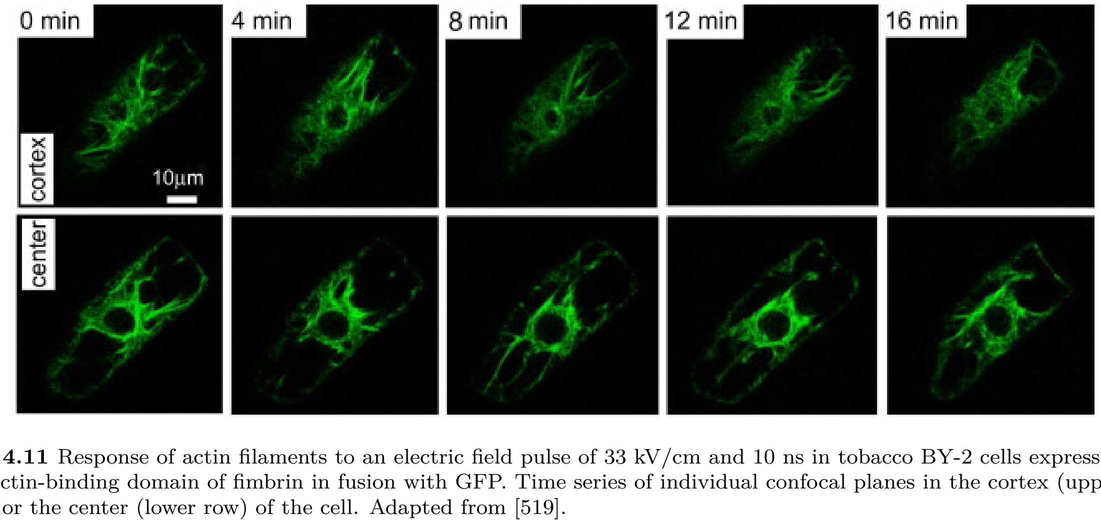

Fig. 4.11 Response of actin filaments to an electric field pulse of 33 kV/cm and 10 ns in tobacco BY-2 cells expressing the actin-binding domain of fimbrin in fusion with GFP. Time series of individual confocal planes in the cortex (upper row) or the center (lower row) of the cell. Adapted from [519].

The disruption of actin was also noticed in CHO cells exposed to different nsPEFs [437]. Actin disruption seems to be a damage of nsPEF on cells. Pakhomov *et al.* also noticed the disruption of the actin network after the delivery of nsPEFs. The authors related this damage to cell swelling [520]. Recently, it has been demonstrated that actin disruption induces PIP_2 depletion which is related to cell swelling and blebbing [521]. The visualization of cytoskeleton damage due to nsPEFs would not have been possible without the confocal microscopy and its improved spatial and temporal resolution. Finally, membrane repair of live cells is also affected by the delivery of nsPEFs. Microtubule depolymerization in combination with lysosome migrations are key events implicated in the membrane repair process [437].

4.2.2 Endocytosis and exocytosis

Confocal microscopy was used to demonstrate the involvement of the endocytic pathways in the electrotransfer of plasmid DNA into cells [522]. Cytoskeleton is a key contributor in the endocytosis process. Thanks to its high spatial resolution, confocal microscopy revealed the formation of actin patches at the plasma membrane around 5 minutes after the delivery of electric pulses. The patches of actin were colocalized with the aggregated DNA plasmids at the plasma membrane. This process fits with the internalization kinetics of DNA plasmids into the cell (Fig. 4.12).

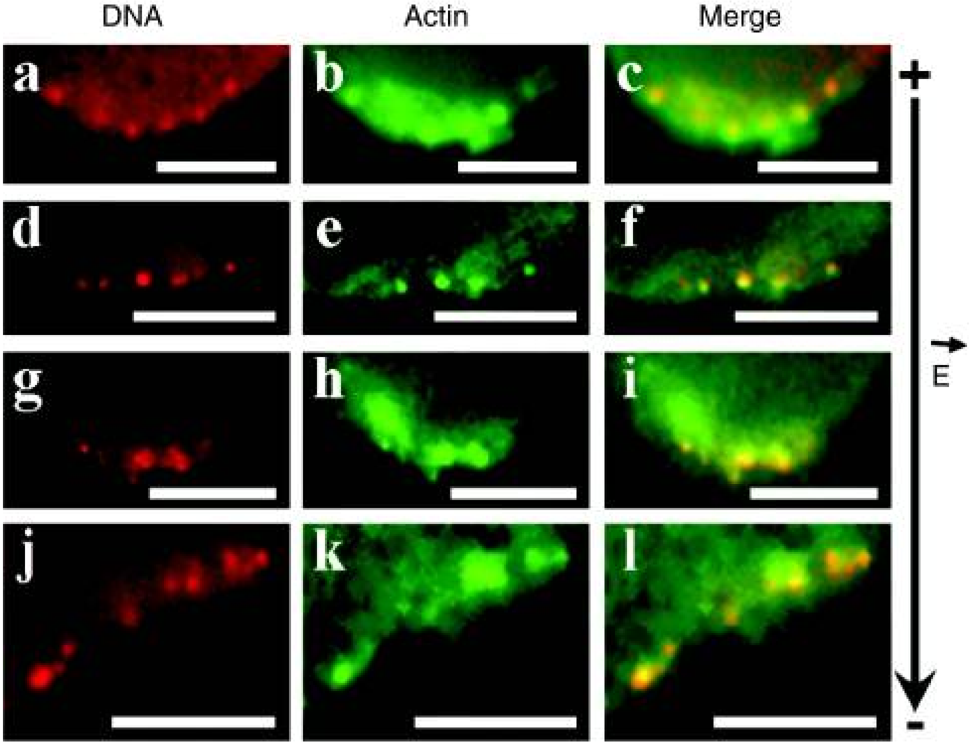

Fig. 4.12 Visualization of the DNA/membrane interaction and the actin cytoskeleton in CHO cells after application of an electric field. CHO cells transiently expressing the EGFP-actin protein were pulsed in the presence of POPO-3 labelled plasmid DNA with the following parameters: 10 pulses of 5 ms at 0.4 kV/cm and 1 Hz. The observations were performed using confocal microscopy between 5 and 30 minutes after application of the electric field. (a,d,g,j) POPO-3 labeled DNA, (b,e,h,k) EGFP-actin protein expression, (c,f,i,l) merge of the two channels. The black arrow on the right side indicates the direction of the electric field. Bar = 5 µm. CHO, Chinese hamster ovary; EGFP, enhanced green fluorescence protein. Adapted from [523].

4.2.3 Electroporation of giant unilamellar vesicles

The critical question of pores creation into the lipid bilayer submitted to electric pulses was indirectly answered by performing confocal fluorescence microscopy experiments on GUVs (Fig. 4.13). By applying a single nsPEF to GUVs in the presence of fluorescent small interefering RNA (siRNA) labelled with fluorescein (FITC) in the external medium, Breton *et al.* noticed not only the presence of the fluorescent siRNA inside the GUVs made of 1,2-Dioleoyl-sn-glycero-3-phosphocholine (DOPC)but also a dramatic increase in the siRNA-FITC fluorescence at the level of the lipid bilayer. This dramatic increase has been related to the trapping of the siRNA into the lipid bilayer which was associated with an increase in the fluorescence yield of the FITC moiety of the siRNA [343].

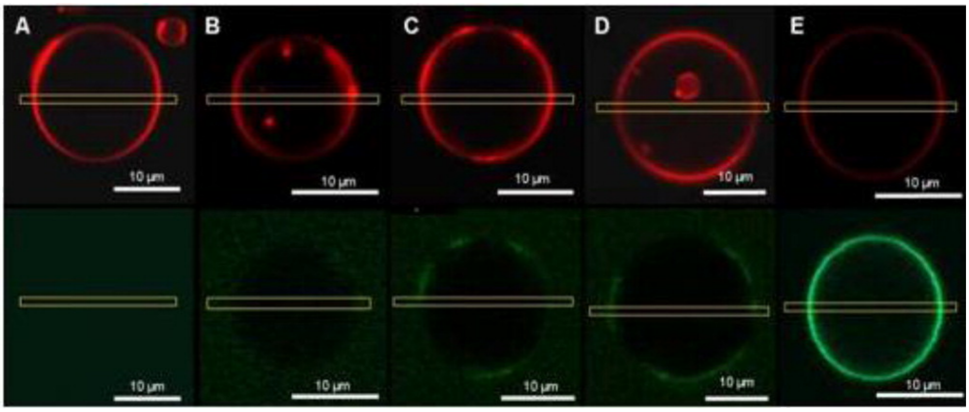

Fig. 4.13 Representative confocal microscopy images highlighting the effect of a 10 ns electric pulse on DOPC GUVs labeled with 1 % DOPE–rhodamine lipids (red fluorescence; upper row) in the presence of FITC-labeled siRNA (green fluorescence; bottom row). (A) DOPC vesicle in a glucose buffer. (B) DOPC vesicle in a glucose buffer with 500 nM siRNA. (C–E) DOPC vesicle in a glucose buffer with 500 nM siRNA after a 10 ns pulse with a magnitude of respectively 2, 3.2, or 5.8 kV/mm. Adapted from [343].

4.3 Multiphoton imaging

4.3.1 *In vitro* studies

The use of the multiphoton imaging technique for in vitro studies is based on a microscopy technique called Second Harmonic Generation (SHG) implemented with a fluorescent dye targeting the plasma membrane.

For instance, the SHG signal from SynaptoredTM C2 incorporated into plasma membrane of neuron cells, was significantly increased after EPN [524]. Fig. 4.14 shows that the SHG signal increase was higher close to the cathode of the generator than to the anode.

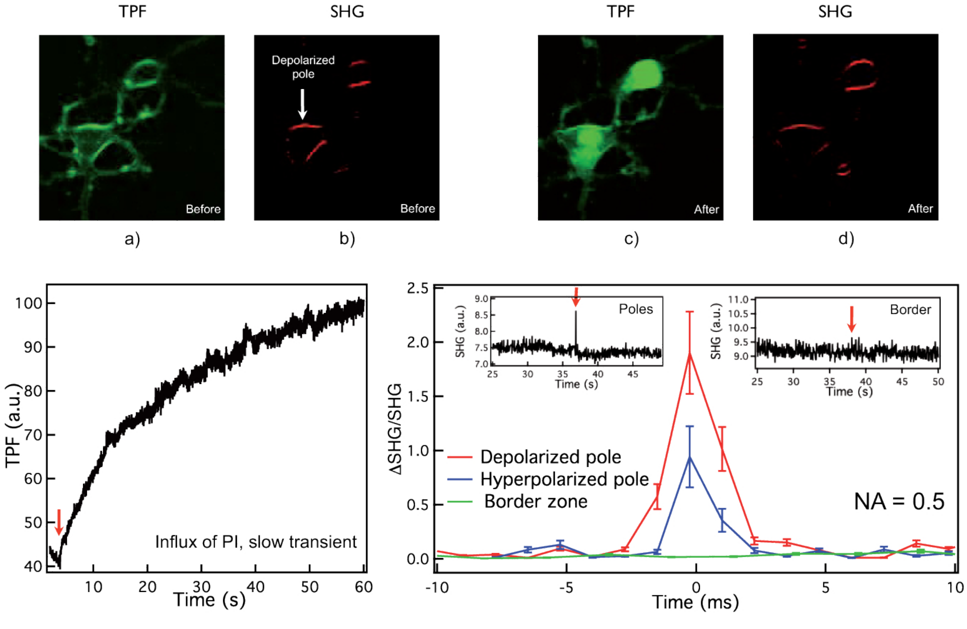

a) b) c) d)

e) f)

Fig. 4.14 Images of hippocampal neurons labelled with SynaptoredTM C2, (a) backward two photon fluorescence before electroporation, (b) forward SHG before electroporation showing localization of the depolarized (cathodic) pole; (c) backward TPF after electroporation of the same cells, (d) forward SHG after electroporation (same cells). (e) TPF signal after electroporation at the hyperpolarized pole. (f) Averaged SHG normalized to SHG when no pores are present, at depolarized poles (red), hyperpolarized poles (blue), and border region (green), collected with a NA = 0.5 condenser. Adapted from [524].

The group of Beier coupled SHG microscopy with Di-4-ANEPPDHQ, a fluorescent dye specifically reporting the transmembrane voltage, to monitor the impact of PEFs on Jurkat cells. The authors observed the modifications in the SHG after the delivery of PEFs but the modifications were different from the ones observed in previous studies. The SHG signal dropped by 50 % after the delivery of PEFs and the higher drop was noticed at the anodic pole of the cells [525]. This might be due to the mechanisms of SHG signal generation by the different fluorescent dyes used in the two studies. By changing the polarization of the beam from a linear polarization to a circular polarization, Moen *et al.* significantly improved the homogeneity of the SHG signal on unpulsed cells [526]. The dose effect relationship between the electric pulse parameters (i.e. electric field magnitude and pulse duration) and the modifications in the SHG signal were investigated [527]. Finally, the authors compared the impact on the SHG signal of bipolar or monopolar shape of the pulses (Fig. 4.15). As expected, the bipolar pulse induced less modifications in the SHG drop than the monopolar pulses. The time-delay between the positive and the negative pulse had to be around 10 µs in order to mimic SHG signal changes induced by an equivalent monopolar exposure [527].

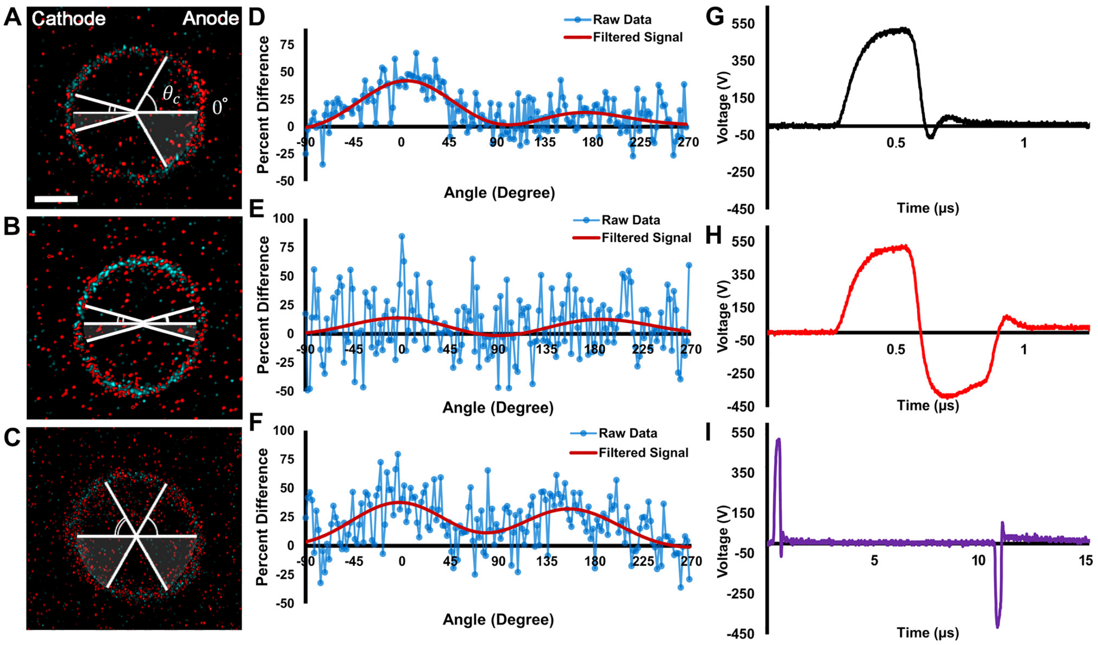

Fig. 4.15 Representative images of cell response. (A) – (C) Pseudocolor images illustrating the loss of SHG signal in live Jurkat cells as result of a pulse exposure. Red pixels denote signal loss. (A) 300 ns monopolar exposure, (B) 300 ns bipolar with a 10 ns refractory period exposure, and (C) 300 ns bipolar with a 10 µs refractory period exposure. Scale bar is 3 µm. (D) – (F) The loss in SHG signal around each cell shown at the left. (G) – (I) Corresponding traces for each nsPEF. From [527].

4.3.2 *In vivo* studies

The use of multiphoton imaging is rare in the case of *in vivo* studies on tissue electropermeabilized. One study reported the use of multiphoton fluorescence imaging to monitor the vascular perfusion in human glioblastoma xenografted on avian chorioallantoic membrane of quail eggs [528]. This study revealed the collapse of vascular vessels and thus of the microenvironment of glioblastoma caused by a single 10 ns electric pulse. The diameter of capillaries and large vessels was also altered by the nsPEF.

4.4 Total internal reflection fluorescence microscopy

TIRF microscopy allows to acquire detailed images with an in-depth resolution of only several nanometers. TIRF microscopy has been used to investigate the electropores created on droplet interface bilayers [529, 530]. The flux of potassium and calcium, which are non-permeant in the absence of electropores, were used as biomarkers of the presence of electropores in the droplet interface bilayers. Thanks to the geometry of the experimental setup, the signal acquired by the TIRF microscope originated specifically from the bilayer interface. Fig. 4.16 shows that the size of the electropores depends on the voltage across the bilayers. Sengel et al. observed fast (25 s^{-1}) and slow (2 s^{-1}) components in the dynamics of electropore creations [529]. These results would not have been obtained with classical epifluorescence microscopy because of the contribution of surrounding signals masking the useful signal.

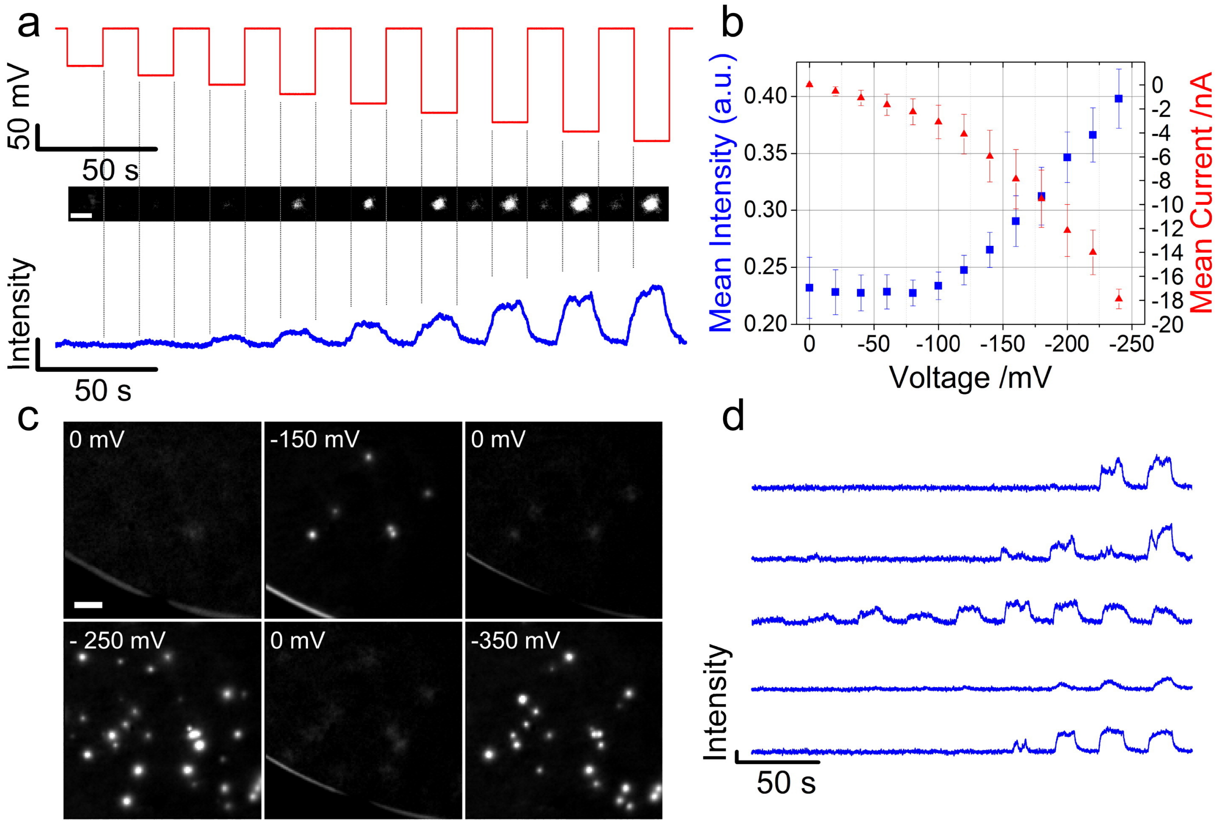

Fig. 4.16 Imaging multiple electropores. (a) Electropores increase in brightness (blue, and images) when applying the potential shown in the upper panel (red). Each image is the mean of 150 frames (20 Hz acquisition) from the selected region showing increasing size and brightness of the pore area as the applied potential becomes more negative. The corresponding intensity profile is depicted in the lower panel (blue). Scale bar 10 µm. (b) Fluorescence-voltage (squares) and current–voltage (triangles) response from electropores. Data is averaged over 13 measurements. (c) Image series from a different data set than that in panel (a) showing the appearance of multiple pores as the applied potential is decreased. Each image is an average of 100 frames (20 Hz acquisition). 30 pores are monitored simultaneously. Bilayers were essentially unstable below 250 mV. Scale bar 5 µm. (d) The fluorescence profile of individual pores while applying step potential shown in (a) shows pores appear at different times. From [530].

4.5 Super-resolution microscopy

Recently, the super resolution microscopy technique based on three dimensional structure illumination microscopy , allowed to demonstrate the dynamics of the disruption of microtubules due to the delivery of nsPEFs (Fig. 4.17). The authors demonstrated that nsPEFs induce the depolymerisation of microtubules which might be related to cell swelling.

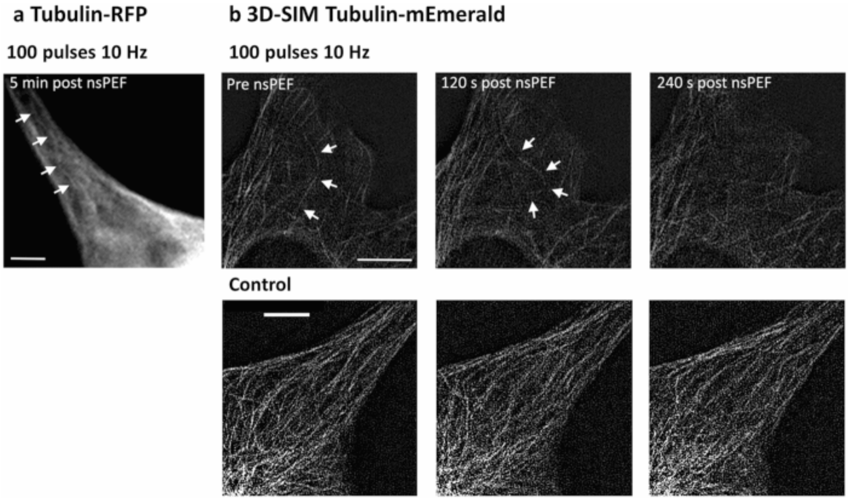

Fig. 4.17 nsPEF application can cause microtubule buckling and depolymerisation. (a) A U87-tubulin-RFP cell imaged with wide-field fluorescence microscopy showing post-pulse buckling of a microtubule bundle, as indicated by the arrows. Scale bar = 5µm (b) Top panel showing a U87 tubulin-mEmerald cell, imaged using 3D-SIM, demonstrating how individual microtubules can buckle following the pulse (120s post pulse image) resulting in loss of the microtubule by depolymerisation (240s post pulse image), with a time point matched non-nsPEF treated control in the bottom panel. Scale bars = 5µm. From [376].

4.6 Coherent Raman scattering microscopy

To our knowledge, there is only one publication using CARS microscopy to monitor the effects of electric field pulses on giant lipid vesicles [531]. By acquiring images at 2845 cm^{-1}, which corresponds to the vibrational resonance of the aliphatic C-H bounds of phospholipids, the authors demonstrated the loss of lipids from GUVs under an electric field (Fig. 4.18).

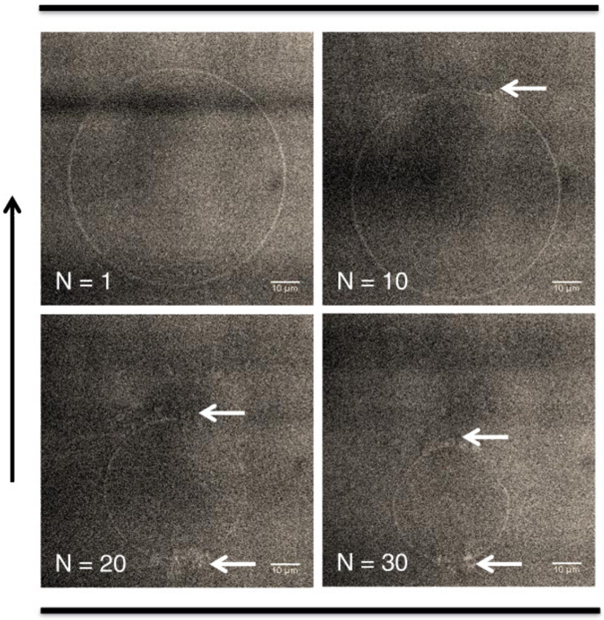

Fig. 4.18 Visualization by CARS microscopy of the EPN of a GUV. Images 1, 10, 20 and 30 of a time series acquired during electropermeabilization with an interval between each image of 310 ms. Image size: 151.17 x 151 x 17 µm with a resolution of 295 nm/pixel. White arrows indicate nanotubes shed from GUVs upon electropermeabilization. The black arrow indicates the electric field direction. From [531].

5

Research hypotheses and objectives

This research work was mainly focused on the investigation of the chemical damages induced by PEFs on live cells thanks to biophotonics techniques: confocal Raman microspectroscopy and THz microscopy. To our knowledge, these two optical techniques have never been used in the framework of the analysis of cell EPN. Thus, it was required to go step-by-step and to make all the controls necessary in order to avoid false positive results.

Although cell EPN has been studied for decades, the underlying mechanisms of the interaction between PEFs and the plasma membrane are not yet fully understood [532]. The creation of pores into the plasma membrane induced by the delivery of electric pulses is still under debate in the community. Although molecular dynamics studies have characterized the properties of these pores (size, lifetimes, creation and collapsing time), no direct experimental visualization has been obtained on live cells. It is commonly admitted that the long-lasting EPN is due to other mechanisms than only pore formation. A chemical modification of the plasma membrane is one of the recent hypothesis proposed to explain the long-lasting electropermeabilization. Numerical model studies demonstrated that the presence of peroxidized lipids into phospholipid bilayers decreases significantly the impermeability of the membrane [357]. Compared to non-oxidized lipid, Peroxidized lipids present conformational modifications which increase the area covered by each lipid and thus reduce the barrier capacity of the phospholipid bilayer, towards water for instance [356]. The combination of PEFs and oxidative stress has a synergistic effect on the level of permeabilization of Jurkat cells [359]. Using mass spectrometry, our group demonstrated the peroxidation of lipids caused by the delivery of electric pulses on a GUV model [360]. An unpublished work by our group suggests a new membrane impermeability rupture model suggesting that electroporation is the initiation step of the peroxidation of the membrane, which is related to EPN [362].

The chemical damages of PEFs on live cells have not been directly investigated. Mass spectrometry analysis of a whole cell is difficult due to the chemical complexity of the cell. Performing fluorescence microscopy experiments by labelling and individually monitoring the chemical compounds of the cells would be time-consuming and limited to a few chemical compounds. Thus, we sought to use confocal Raman microspectroscopy and THz microscopy to quantify the chemical composition of live cells exposed to PEFs. Confocal Raman microspectroscopy and THz microscopy can provide detailed information about the molecular composition of live cells in a non-invasive and label-free manner [106, 108, 118].

I specifically focuses on 100 µs electric pulses which are the most common type of electric pulses used in the clinics [472]. Confocal Raman microspectroscopy studies were foreseen to investigate step-by-step the interaction between PEFs and live cells. As confocal Raman microspectroscopy and THz microscopy are new biophotonics technique in the framework of cell EPN, it was also foreseen to compare these two biophotonics techniques with fluorescence microscopy which is considered as the reference optical technique for monitoring cell EPN.

Finally, a side project of the EPN topic has been part of this doctorate. The laboratory UMR 8203 is part of Gustave Roussy which is the first cancer centre in Europe. Based on the research and clinical work performed on ECT, the laboratory has a strong collaboration history with the Gustave Roussy clinicians. In this framework and following the work I have conducted on Raman microscopy, I have actively taken part in a clinical study on the monitoring of skin toxicity induced in patients by targeted cancer therapies by means of confocal Raman microspectroscopy.

6

Results

6.1 Demonstration of the Protein Involvement in Cell Electropermeabilization using Confocal Raman Microspectroscopy (article #1)

Previous works done by our group have demonstrated thanks to mass spectrometry that PEFs induce chemical damages on GUVs. In this framework, the potential chemical damages induced by the delivery of PEFs on live cells were investigated thanks to confocal Raman microspectroscopy. To our knowledge, this study is the first experimental investigation of the effect of permeabilizing electric pulses on the Raman signatures of live cells. Thus, the experiments have been designed in order to explore the evolution of the Raman signature without any background information. The Raman signatures of haMSC cells exposed or not to permeabilizing electric pulses were recorded at two different cell locations (i.e. cytoplasm and nucleus) and at two different vibrational frequency regions (FP: 600 – 1800 cm^{-1} and HWN: 2800 - 3100 cm^{-1}). In this study, 8 electric pulses of 100 µs duration at 1000 V/cm magnitude and 1 Hz repetition rate have been delivered in order to electropermeabilize haMSC cells. The electric pulse parameters were chosen in order to be similar to the electric pulse parameters used in the clinics.Our results revealed the modification of Raman bands related to proteins in living cells exposed to PEFs.

This work has been done in tight collaboration with the laboratory MEDyC (UMR 7369, CNRS, university of Reims Champagne-Ardenne) headed by Pr. Olivier Piot. The Raman and fluorescence experiments have been performed, respectively, at MEDyC and UMR 8203. The results of this work have been published in Scientific Reports in January 2017.

www.nature.com/scientificreports

SCIENTIFIC REPORTS

OPEN

Received: 03 June 2016
Accepted: 06 December 2016
Published: 19 January 2017

Demonstration of the Protein Involvement in Cell Electropermeabilization using Confocal Raman Microspectroscopy

Antoine Azan[1], Valérie Untereiner[2,3], Cyril Gobinet[2], Ganesh D. Sockalingum[2], Marie Breton[1], Olivier Piot[2,3] & Lluis M. Mir[1]

Confocal Raman microspectroscopy was used to study the interaction between pulsed electric fields and live cells from a molecular point of view in a non-invasive and label-free manner. Raman signatures of live human adipose-derived mesenchymal stem cells exposed or not to pulsed electric fields (8 pulses, 1 000 V/cm, 100 µs, 1 Hz) were acquired at two cellular locations (nucleus and cytoplasm) and two spectral bands (600–1 800 cm^{-1} and 2 800–3 100 cm^{-1}). Vibrational modes of proteins (phenylalanine and amide I) and lipids were found to be modified by the electropermeabilization process with a statistically significant difference. The relative magnitude of four phenylalanine peaks decreased in the spectra of the pulsed group. On the contrary, the relative magnitude of the amide I band at 1658 cm^{-1} increased by 40% when comparing pulsed and control group. No difference was found between the control and the pulsed group in the high wavenumber spectral band. Our results reveal the modification of proteins in living cells exposed to pulsed electric fields by means of confocal Raman microspectroscopy.

Electropermeabilization[1,2] (EPN), also known as electroporation, is the destabilisation of the plasma membrane of biological cells caused by intense pulsed electric fields. This destabilisation induces a strong increase in the permeability of the cell membrane, allowing an uptake of external non-permeant molecules by the treated cells. Electrochemotherapy[3] is one of the major medical applications of cell EPN. It consists in the combination of tumor cells EPN with a chemotherapy (bleomycin or cisplatin) in order to increase the anticancer drug efficiency by a factor ranging from 100 to 1000 depending on the drug. Gene electrotransfer[4,5] is another medical application of the EPN that allows the efficient delivery of plasmid DNA into the cells *in vitro* and *in vivo*.

Because of the complexity of the cell membrane, the underlying mechanisms of EPN are not yet fully understood[6]. It is well established that the electric field induces a transmembrane potential that adds to the resting transmembrane potential of the cell[7]. The membrane permeabilization is triggered as soon as this total transmembrane potential surpasses a certain threshold, which depends on the cell type[8]. Numerical modelling[9] has shown that the forces induced by the electric field are able to create aqueous pores in the phospholipid bilayer. Although the pores have not been directly visualized in cell membrane[10,11], a computational and experimental study[12] has demonstrated that siRNA can penetrate into a lipid membrane through the pores created by the intense electric field. Pulsed electric fields are also known to be able to permeabilize the cells for tens of minutes after the delivery of the electric shock[13] meaning that long term effects are also induced by the EPN process. Atomic Force Microscopy (AFM) performed after the delivery of pulsed electric fields revealed that the membrane elasticity decreased by 40% in live cells[14]. We have shown, by mass spectrometry analysis, that pulsed electric fields initiate chemical reactions at the level of the phospholipids in simple membrane models[15]. Moreover, it has been demonstrated that the presence of modified phospholipids affect the impermeability of the cell membrane[16,17]. Therefore, we investigated the potential chemical modifications of cells exposed to pulsed electric fields by confocal Raman microspectroscopy of live cells.

[1]Vectorology and Anticancer Therapies, UMR 8203, CNRS, Gustave Roussy, Univ. Paris-Sud, Université Paris-Saclay, 114 rue Edouard Vaillant, 94805 Villejuif, France. [2]MeDIAN, Biophotonics and Technologies for Health, MEDyC, UMR 7369, CNRS, University of Reims Champagne-Ardenne, 51 rue Cognacq-Jay, 51096 Reims, France. [3]Cellular and Tissular Imaging Platform PICT, Faculty of Pharmacy, University of Reims Champagne-Ardenne, 51 rue Cognacq-Jay, 51096 Reims, France. Correspondence and requests for materials should be addressed to L.M.M. (email: Luis.Mir@gustaveroussy.fr)

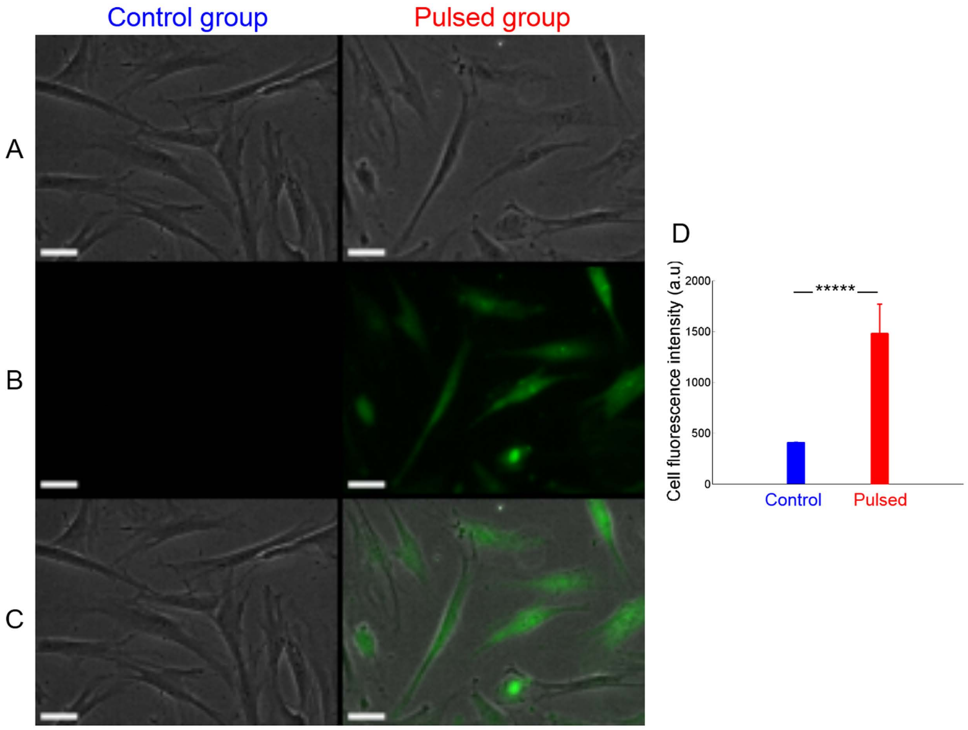

Figure 1. Bright-field and fluorescence microscopy images of control and pulsed haMSC cells. (**A**) – Bright-field images, (**B**) – Yo-Pro-1 fluorescence images, (**C**) – Combined images, (**D**) –Yo-Pro-1 fluorescence intensity into cells. Scale bar: 50 μm. The pulse conditions are 8 pulses, 100 μs, 1 000 V/cm and 1 Hz. The exposure time for fluorescence images was fixed to 200 ms. Images were taken 10 minutes after the delivery of pulsed electric fields. Student's *t*-test: ****p-value ≤ 0.01%.

Raman spectroscopy[18,19] is a non-invasive and label-free optical technique that provides detailed information on the molecular composition of the sample. Raman spectroscopy is based on the Raman effect[20] which consists in an inelastic scattering of light. When a laser beam interacts with a sample, the spectral composition of the scattered light is related to the molecular composition of the sample. This technique has been widely used on biological samples to characterize cells[21], stem cells differentiation[22,23], drug delivery systems[24] or to discriminate normal tissues from cancer tissues[25].

In this study, we have used confocal Raman microspectroscopy to investigate the effect of pulsed electric fields on living cells by comparing the Raman signatures of control and pulsed human adipose-derived Mesenchymal Stem Cells (haMSC). These multipotent adult stem cells are widely used as *in vitro* models[26,27]. Their large size and fibroblast-like aspect allows an easy access to the cytoplasmic area far away from the nucleus. Moreover, our laboratory has a strong background on the EPN of haMSC[28,29]. The acquisition of the Raman signature of living haMSC was performed for two different spectral ranges and in two different Regions Of Interest (ROI), namely the nucleus and a "cytosolic" nucleus-free area facing the cathode of the generator. The choice of the second ROI was based on fluorescence microscopy *in vitro* studies[8,30] that demonstrated that the strongest effect of pulsed electric fields on the plasma membrane occurred close to the cathode.

Results

Fluorescence microscopy of electropermeabilized cells.

Cells were exposed or not to electric pulses (8 pulses, 100 μs, 1 000 V/cm and 1 Hz) in the presence of Yo-Pro-1 fluorescent dye. Figure 1 shows that the fluorescence intensity of the Yo-Pro-1 into inside the cells increased by a factor around 3 between the control group and the pulsed group. This result confirms that haMSC cells have been permeabilized under the condition used for the Raman experiments.

Micro-Raman analysis of single live cells.

Spectra were acquired at about 12 adjacent positions either in the nucleus area, termed "Nucleus" ROI, or in the "cathodic" part of the cytoplasm, termed "Cathode" ROI (Supplemental Figure S1) for two classical spectral ranges, the FingerPrint (FP) band and the High Wave Number (HWN) band. Figure 2 shows the two mean spectra and the difference spectrum between the pulsed and the control groups for four conditions ("Cathode, FP", "Nucleus, FP", "Cathode, HWN" and "Nucleus, HWN").

As expected[31], the mean spectrum acquired in the nucleus ROI presents a strong contribution of the DNA/RNA vibrational modes. Among them, the peaks around 783–790 cm^{-1} attributed to the O-P-O backbone

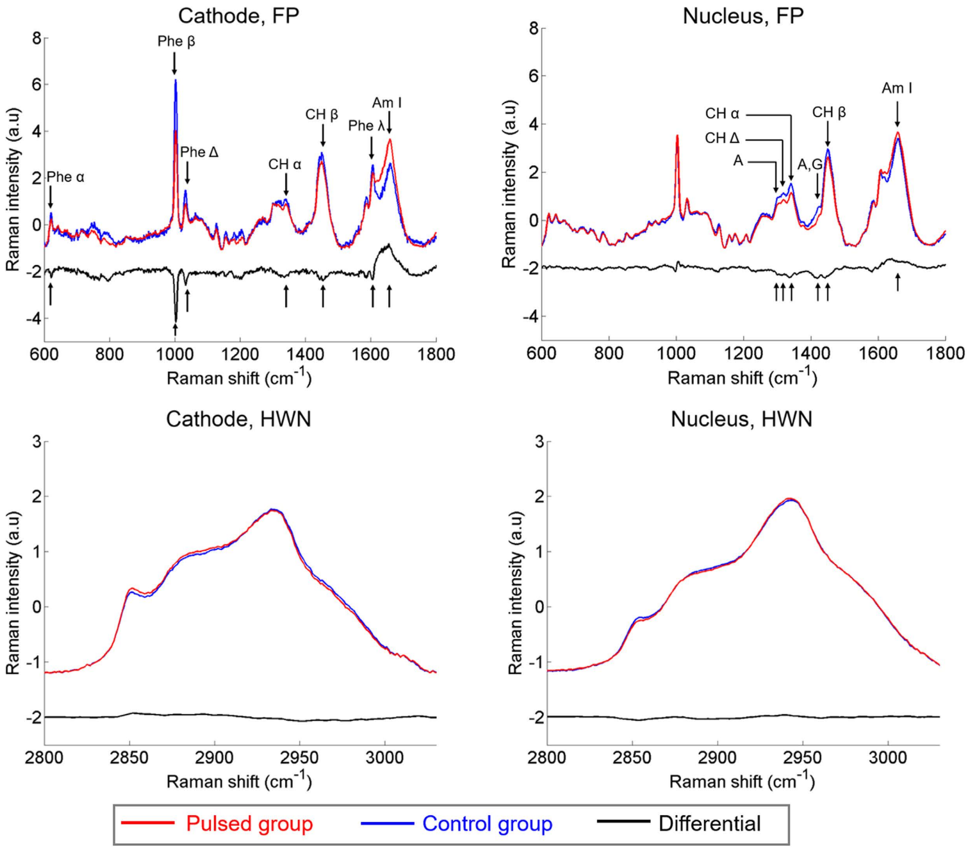

Figure 2. Mean normalized Raman signatures of pulsed and control haMSC cells. The differential spectrum (pulsed group minus control group) is also displayed. For more clarity, differential spectra are displayed with vertical offset. The black arrows indicate the discriminant peaks in the "Cathode, FP" and "Nucleus, FP" conditions. The pulse conditions are 8 pulses, 100 μs, 1 000 V/cm and 1 Hz.

stretching of DNA/RNA were observed. The contribution of adenine bands (A) was noteworthy at 1303 and 1425 cm^{-1}. The peak at 1425 cm^{-1} was also attributed to the nucleic acids guanine (G) contribution. Protein bands were also present with C-C and C-N stretching modes at 1128 cm^{-1}, the phenylalanine (Phe) ring breathing mode at 1003 cm^{-1}, and the amide I band (Am I) at 1658 cm^{-1}. The "Cathode spectra" were mainly composed of proteins and lipids signatures. In the amide I band, the maximum intensity at 1658 cm^{-1} suggests a predominant α-helix conformation of the proteins[32]. Relatively, the contribution of the phenylalanine peak at 1003 cm^{-1} was higher in the Cathode ROI than in the Nucleus ROI. A tentative band assignment for the haMSC cells spectra based on litterature[31,33–35] is summarized in the Supplementary Information (SI).

Figure 2 shows that the strongest differences between the mean normalized spectrum of the two groups (i.e., control and pulsed) were observed for the "Cathode, FP" condition. Based on the differential spectrum of the "Cathode, FP" condition, seven discriminant bands were identified: 621, 1003, 1033, 1342, 1448, 1607 and 1658 cm^{-1} respectively labelled "Phe α", "Phe β", "Phe Δ", "CH α", "CH β", "Phe λ" and "Am I". As reported in the SI, four discriminant peaks belong to the phenylalanine vibrational modes: 621, 1003, 1033, and 1607 cm^{-1}. The 1342 and 1448 cm^{-1} peaks are related to the CH deformation of proteins and lipids, while the 1658 cm^{-1} is assigned to the amide I vibrational mode (C=O stretch). Consistently, the relative magnitude of the four peaks attributed to phenylalanine are decreased when comparing the pulsed group to the control group. No wavenumber shift of the discriminant peaks of phenylalanine was noticed. Thus, we can conclude that the relative concentration of the phenylalanine molecules in the cell decreased or/and that the environment of the phenylalanine molecules was modified after the application of pulsed electric fields. The axial resolution of confocal Raman microspectroscopy did not allow to discriminate the signal contribution from the plasma membrane or from other cellular organelles. But because of its hydrophobic properties, phenylalanine is known to be present in the plasma membrane and to be part of many transmembrane domains[36]. Based on our experience concerning the chemical modifications of phospholipids in the plasma membrane after the delivery of pulsed electric fields, we cannot exclude that chemical modifications of the phenylalanine may be triggered by the EPN process. Our results in the "Cathode, FP" condition show that the relative magnitude of the amide I peak at 1658 cm^{-1} is increased of 40% in the pulsed group with respect to the control group. The amide I band is involved in the peptide bond between consecutive amino acids in the primary structure of proteins. Maiti *et al.* demonstrated that the 1658 cm^{-1} peak is related to the unfolded state of proteins[37]. Recent numerical models have shown that pulsed electric fields can alter the folding of membrane proteins[38]. The evolution of the amide I band may be directly related to the structural modifications of proteins and especially to their folding state. The magnitude of the two vibrational bands attributed to CH deformation (1342 and 1448 cm^{-1}) is decreased in the pulsed group compared to the control group. These two vibrational modes are both related to proteins and lipids. This confirms previous results indicating an alteration of lipids in membrane models[15]. Small differences were also noticed around 800 cm^{-1} but remained difficult to attribute to specific bands due to the complex number of vibrational frequencies overlapping in this region. Moreover, the relative differences in these bands were close to the standard deviation of the data set.

For the "Nucleus, FP" condition, the differences were smaller than for the "Cathode, FP" condition. Six discriminant peaks were identified: 1303, 1319, 1342, 1425, 1448 and 1658 cm^{-1} respectively labelled "A", "CH Δ", "CH α", "A, G", "CH β" and "Am I". The 1303 and 1425 cm^{-1} peaks belong to the vibrational modes of DNA/RNA. The relative magnitudes of these two vibrational modes attributed to DNA/RNA are decreased in the pulsed cells spectra with respect to the control cells spectra. It is well established that the EPN process induces the generation of Reactive-Oxygen Species (ROS)[39,40]. ROS are known to induce strong DNA damages[41]. Moreover, Poplineau *et al.* demonstrated that confocal Raman microspectroscopy is able to detect modifications of DNA in living cells[42]. The decrease of the DNA vibrational peaks observed in the pulsed is consistent with the present literature. The 1319, 1342 and 1448 cm^{-1} peaks are related to the CH deformation of proteins and lipids. Consistently, the magnitude of the three peaks related to CH vibrational modes are decreased when comparing the pulsed group to the control group. The amide I band relative magnitude is increased between the pulsed and control groups. As for the "Cathode, FP" condition, this may be associated to the structural modification of proteins induced by pulsed electric fields. Among these six discriminant peaks of the "Nucleus, FP" condition, three of them (1342, 1448 and 1658 cm^{-1}) shared the same evolution in the "Cathode, FP" condition and "Nucleus, FP" condition when comparing the control group and the pulsed group. The modification of the magnitude of CH and amide I bands confirms the strong impact of EPN on the structure of proteins in different cellular organelles.

Contrary to the data in the FP region, the results of HWN region results did not present any obvious difference between the two groups and no clear pattern was observed. Hence, the vibrational modes related to the HWN did not seem to be modified between the control and pulsed groups. The HWN region is mainly composed of CH_2 and CH_3 stretching vibrational modes of lipids[43]. The absence of modification in this region would indicate that the lipids were not affected by the pulsed electric fields. Unfortunately, the in-depth resolution of confocal Raman microspectroscopy does not allow to discriminate the signal contribution of the lipids of the plasma membrane from the contribution of the lipids of any cell organelle. Therefore, we cannot exclude that the lipids of the plasma membrane were affected by the pulsed electric fields. Performing the same experiments with a membrane model, Giant Unilamellar Vesicles (GUV), which is a lipid bilayer with a size similar to that of cells[44], would allow to focus only on the interaction between pulsed electric fields and a lipid bilayer. Acquiring the Raman signatures of GUVs has already been done with a similar confocal Raman microspectroscope[45]. The acquisition of the Raman spectra in the HWN region was also used to monitor the transmembrane potential of cells[46,47]. These previous studies have demonstrated that the intensity ratio of the 2930 cm^{-1} peak on the 2850 cm^{-1} peak is related to the transmembrane potential. By calculating this ratio for the "Cathode, HWN" data set, no statistically significant difference appeared between pulsed and control group (data not shown).

Based on this first results, we have investigated the variability and statistical difference of the discriminant peaks identified in the "Cathode, FP" and the "Nucleus, FP" conditions.

As shown in the "Cathode, FP" panel of Fig. 3 corresponding to the Cathode spectra, the relative magnitude of the four peaks attributed to the phenylalanine amino-acid (i.e., 621, 1003, 1033 and 1607 cm^{-1}) is decreased by 30% in the pulsed group versus the control group. Among these four peaks, three of them (621, 1003 and 1033 cm^{-1}) showed statistically significant differences between the two groups, supporting the hypothesis of an important effect of pulsed electric fields on the phenylalanine. The 1607 cm^{-1} peak does not show any statistical difference between the two groups. This might be explained by the fact that the 1607 cm^{-1} peak is also attributed to the tryptophan amino-acid which might not be affected by the pulsed electric fields as suggested by the other vibrational modes specific to the tryptophan (762 cm^{-1}). The relative magnitude of the amide I band at 1658 cm^{-1} is increased with a statistically significant difference in the pulsed group with respect to the control group. For the CH vibrational modes at 1342 and 1448 cm^{-1}, a decrease of 15% is observed when comparing the pulsed group to the control group. This difference is statistically significant for the 1342 cm^{-1} peak but not for the 1448 cm^{-1} peak because of the larger standard deviation due to the predominance of the CH_2 bending mode of lipids.

For the "Nucleus, FP" condition (Fig. 3), the differences between the two groups were smaller but more statistically significant, than for the "Cathode, FP" condition. All the bands related to CH and CH_2 bonds (1319, 1342 and 1448 cm^{-1}) are decreased by about 20% in the pulsed group with respect to the control group, with a p-value lower than 0.01%. The peaks attributed to DNA/RNA, labeled "A", and "A, G", both decreased in the pulsed group compared to the control group. Among the six discriminant peaks identified, the evolution of three of these peaks, 1342, 1448 and 1658 cm^{-1}, are similar to that of the "Cathode, FP" analysis but with different p-values. These three peaks are all related to proteins, thus demonstrating that pulsed electric fields strongly affect the proteins present in different cellular compartments.

Multivariable analysis. In order to confirm these quantitative results, an unsupervised multivariable analysis, Principal Component Analysis (PCA)[48], was performed for the four different conditions: "Cathode, FP", "Nucleus, FP", "Cathode, HWN" and "Nucleus, HWN" (Table 1).

Based on the two selective criteria described in the Materials and Methods section (p-value $< 5\%$ and at least 5% of the total variance supported by the selected Principal Components (PCs)), only one PC have been selected for the "Cathode, FP" condition and for the "Nucleus, FP" condition. In the HWN region, none of the PCs fulfills

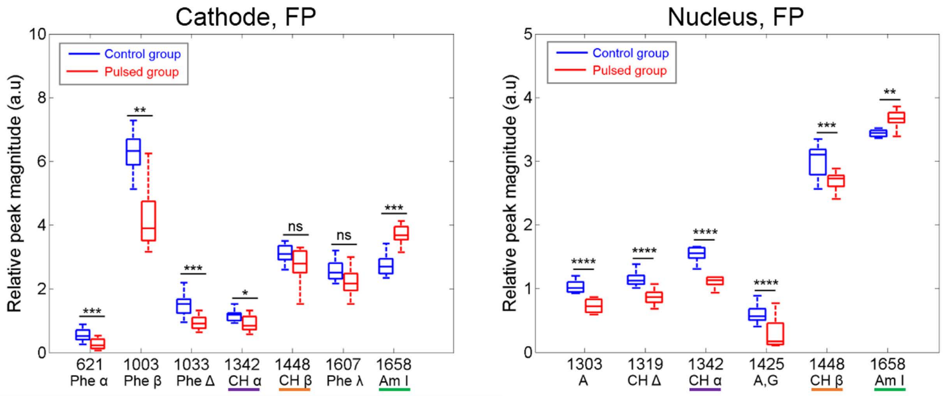

Figure 3. Relative peak magnitude of the discriminant peaks identified of "Cathode, FP" and "Nucleus, FP" conditions. The common bands in the two conditions are underlined with specific color. The p-values between the two groups are displayed. The pulse conditions are 8 pulses, 100 μs, 1 000 V/cm and 1 Hz. Student's *t*-test: ns (non-statically significant): p-value > 5%, p-value ≤ 5%, **p-value ≤ 1%, ***p-value ≤ 0.1%, ****p-value ≤ 0.01%.

PC	Cathode, FP		Nucleus, FP		Cathode, HWN		Nucleus, HWN	
	Variance (%)	p-value (%)	Variance (%)	p-value (%)	Variance (%)	p-value (%)	Variance (%)	p-value (%)
1	**52.7**	**<0.1**	61.6	6	84.1	40	82.2	22
2	24.5	49	**15.3**	**<0.01**	7.9	74	n/a	n/a
3	11.7	68	11.2	14	n/a	n/a	n/a	n/a
4	n/a	n/a	n/a	n/a	n/a	n/a	n/a	n/a
5	n/a	n/a	n/a	n/a	n/a	n/a	n/a	n/a

Table 1. Comparison of PCA results for the conditions: "Cathode, FP", "Nucleus, FP", "Cathode, HWN" and "Nucleus, HWN". The PCs supporting a total variance percentage lower than 5% are indicated as not applicable (n/a). The p-value is calculated based on the Student's *t*-test. The PCs fulfilling the two selective criteria (i.e., total variance >5% and p-value ≤ 5%) are indicated in bold.

the two criteria. This confirms our previous result demonstrating that the HWN region is not a suitable spectral band to detect any difference in the Raman signature between control cells and pulsed cells. In the case of the "Cathode, FP" condition, the PC1 was selected and accounts for 52.7% of the total variance. PC2 was selected in the "Nucleus, FP" analysis and accounts for 15.3% of the total variance (Fig. 4). This underlines that, for the FP region, the differences between the two groups are stronger in the Cathode ROI than in the Nucleus ROI.

Considering the "Cathode, FP" condition presented in Fig. 4, the selected PC (PC1) obviously shares similar patterns to those of the differential spectrum displayed in Fig. 3. The discriminant peaks identified in the differential spectrum of Fig. 2 are reported with the same labels in Fig. 4. The phenylalanine peaks at 621, 1003 1033 cm^{-1} and around 1200 cm^{-1} contribute to this PC1. The phenylalanine peak at 1003 cm^{-1} is again predominant. Others peaks such as 1658, 1607 1448, 1200 and 800 cm^{-1} are both part of PC1 and of the differential spectrum and share similar relative magnitudes. For this "Cathode, FP" analysis, the correlation coefficient between PC1 and the differential spectrum is equal to 98.6%. When considering the PC1 score (Fig. 4), the difference between the two groups is statistically significant with a p-value lower than 0.1% which means that PC1 seems to be an accurate biomarker of the differences in the Raman signature between pulsed and control haMSC cells.

For the "Nucleus, FP" analysis (Fig. 5), the selected PC (PC2) displays also a pattern similar to the differential spectrum of Fig. 3. The selected PC shows the typical pattern of the shift of the 1003 cm^{-1} peak. The bands at 1303, 1319, 1342, 1425, 1448 and 1658 cm^{-1} are part of both PC2 and the differential spectrum. The relative magnitude of these common bands differs between the two spectra. In PC2, the multiple peaks between 1150 and 1200 cm^{-1} remains difficult to attribute and do not fit with the band assignments reported in the literature. This might be due to the high number of vibrational modes overlapping in this region. The difference between the scores of PC2 of the two groups are statistically significant with a p-value lower than 0.01% (Fig. 5). This confirms our previous analysis showing that the differences in the "Nucleus, FP" condition between the two groups are smaller than in the "Cathode, FP analysis", but that these differences are statistically more significant.

Discussion

For the first time, the Raman signatures of living cells submitted to intense pulsed electric fields have been investigated. Our results show that the Raman signature of cells in the FP band is strongly modified by the EPN process. This modification depends on the ROI investigated. For the Cathode ROI, the vibrational modes of

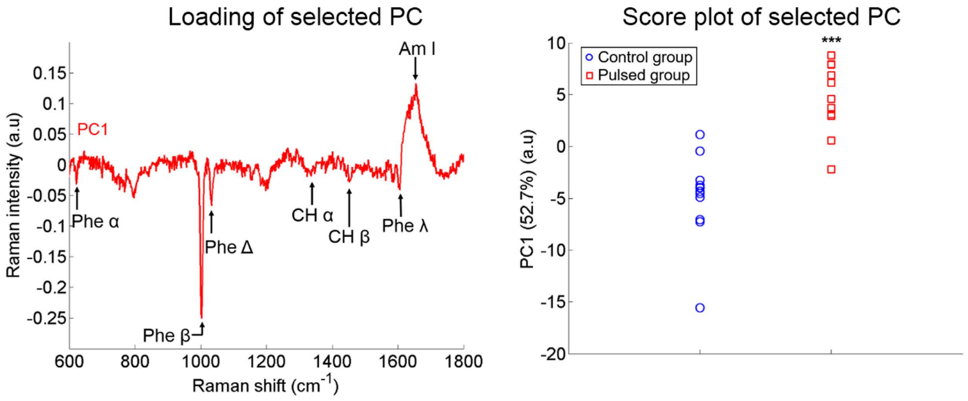

Figure 4. PCA results for the "Cathode, FP" condition. The percentage of variance supported by the selected PC is indicated in brackets. The discriminant peaks identified in Fig. 2 are reported with the same labels on the loading of the selected PC (left). In the score plot, the p-value between the two groups is lower than 0.1% (right). The pulse conditions are 8 pulses, 100 µs, 1 000 V/cm and 1 Hz.

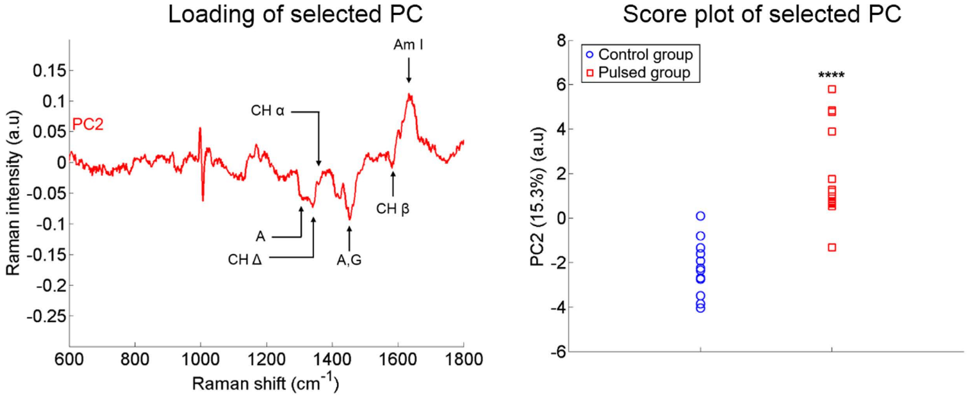

Figure 5. PCA results for the "Nucleus, FP" condition. The percentage of variance supported by the selected PC is indicated in brackets. The discriminant peaks identified in Fig. 2 are reported with the same labels on the loading of the selected PC (left). In the score plot, the p-value between the two groups is lower than 0.01% (right). The pulse conditions are 8 pulses, 100 µs, 1 000 V/cm and 1 Hz.

phenylalanine, CH chemical bonds of proteins and lipids, as well as amide I are affected by the pulsed electric fields. Peak magnitude analysis demonstrates that the differences between the two groups (control and pulsed) are statistically significant. In the Nucleus ROI, vibrational modes of DNA/RNA, amide I and CH/CH_2 bonds of proteins and lipids are impacted by the delivery of pulsed electric fields. Acquisition of Raman signature of control and pulsed cells in the HWN spectral band does not show any significant differences. A multivariable analysis by PCA confirmed these results.

This study provides new information at a molecular level on the effect of pulsed electric fields on living cells. This study has revealed significant modifications of phenylalanine and amide I which are directly involved in the protein composition and structure. After the demonstration of the effect of pulsed electric fields on phospholipids using a simple membrane model[15], our present results show, in a non-invasive and label-free way, that proteins of live cells are also affected by the pulsed electric fields. The axial resolution of confocal Raman microspectroscopy does not allow to discriminate the contribution to the signal coming from the plasma membrane or from other cellular organelles. Acquiring the Raman signature of GUVs and of various ROI of cells, such as the pseudopodia, will allow to investigate deeper the origin of the signal.

Methods

Experimental design. Cells were exposed or not to pulsed electric fields (8 pulses, 100 µs, 1 000 V/cm and 1 Hz). Control cells underwent sham exposures. The Raman signatures of cells were acquired just after the exposition to pulsed electric fields. Each recorded spectrum was labelled as "control" or "pulsed" based on the delivery or not of pulsed electric fields. In a first experiment, the Raman signature of cells was acquired at a specific ROI and

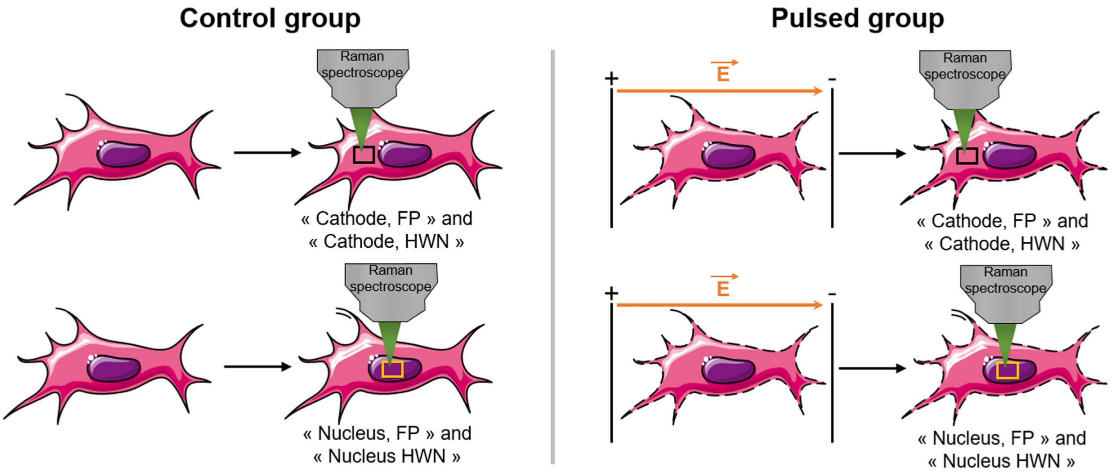

Figure 6. Experimental design for the characterization of control and pulsed haMSC cells by confocal Raman microspectroscopy. The pulse conditions are 8 pulses, 100 µs, 1 000 V/cm and 1 Hz. A 532 nm continuous wave laser of 20 mW is focused on the haMSC cells through a 100 X water immersion objective. In the FP spectral band, the exposure time is fixed to 2 accumulation of 30 seconds. In the HWN spectral band, the exposure time tis fixed to 2 accumulation of 10 seconds. This schematic is adapted from Servier Medical Art.

spectral band. The first ROI investigated was an area of the cell between the nucleus and the edge of the cell facing the cathode of the pulse generator (termed here "Cathode"). In another experiment, the Raman signatures at the nuclear compartment of the cells were acquired. Since at this ROI, the nucleus occupies most of the volume, the corresponding Raman spectra were termed "Nucleus". The differences in the Raman signature between control and pulsed cells were investigated in the FP region (600–1800 cm^{-1}) and the HWN region (2600–3100 cm^{-1}) for the two specific ROIs (Cathode and Nucleus). In order to limit as much as possible the membrane resealing process following the pulsed electric fields, every experiment was performed at 4 °C, which is known to block the endocytic membrane trafficking[49,50] and causes a "rigidification" of the membrane[51]. It has also been demonstrated that cells can be maintained permeabilized for hours at 4 °C without affecting the cell viability[52]. In total, the Raman signatures of cells were acquired in four different conditions (two ROIs: Cathode and Nucleus and two spectral regions: FP and HWN). Figure 6 summarizes the experimental design.

Cell culture. haMSC cells were grown in Dulbecco's Modified Eagle Medium – DMEM - (Life Technologies, Cergy-Pontoise, France) with 10% fetal bovine serum (Life Technologies) and 1% of penicillin-streptomycin (Life Technologies). The cells were maintained in a humidified atmosphere at 37 °C and 5% CO_2. For the experiment conducted under the confocal Raman microspectroscope, the cells were plated at 5 000 cells/cm^2 in a 35 mm Petri dish (Thermo Fisher Scientific, Illkirch, France) in which a CaF_2 window (Crystran, Poole, United Kingdom) was placed at the bottom of the Petri dish before adding the cells. CaF_2 was chosen because it has been recently proven that a CaF_2 substrate and a 532 nm laser source is the best combination to acquire Raman signatures of living cells with an optimal quality[53]. After the cells attached to the CaF_2 window, they were incubated overnight before performing the experiments. No morphological changes were noticed in the cells cultured on this specific substrate. It has been demonstrated previously that CaF_2 windows are compatible with live cell studies[54]. For this study, haMSC cells were from passage 8 to 11.

Pulse generator and pulses condition. A commercially available generator (Cliniporator, IGEA, Italy) was used to treat the cells. The pulse conditions were 8 pulses of 100 µs at a magnitude of 1 000 V/cm and a frequency rate of 1 Hz. To deliver the electric pulses on attached cells, a homemade system of electrodes was used. It consisted of two stainless steel plate electrodes and a specific cover that matched with the diameter of the Petri dish. The cover has two slots designed to space the two plate electrodes by 4 mm. When the cover was placed on the Petri dish, the plate electrodes were dropped on the CaF_2 window through the slots which fixed the distance between the two parallel plates. The plate electrodes were connected to the Cliniporator with alligator clips. Before delivering the pulsed electric fields, the cell culture medium was removed and replaced by a saline solution pre-cooled at 4 °C (B. Braun, Boulogne-Billancourt, France) after washing twice with phosphate-buffered saline. The saline solution, which is a solution of NaCl at 154 mM, was selected as a cell solution because of its low Raman signature and its compatibility with biological cells. No heating effect, pH change or bubble formation have been noticed after the delivery of pulsed electric fields.

Fluorescence Microscopy. The achievement of cell EPN under strictly the same experimental condition as Raman experiments (5 000 cells/cm^2 platted overnight on CaF_2 substrate in 35 mm Petri dish, saline solution maintained at 4 °C, 8 electric pulses of 100 µs duration at a frequency of 1 Hz, magnitude of the electric field of 1 000 V/cm) was checked by fluorescence microscopy[55]. Yo-Pro-1, with λexcitation = 491 nm and λemission = 509 nm, (Life technologies) is a non-permeant intercalating fluorescence dye commonly used to check cell

		Number of cells characterized	
		Control group	Pulsed group
FP	Cathode	13	12
	Nucleus	12	15
HWN	Cathode	17	22
	Nucleus	23	20

Table 2. Number of cells characterized by confocal Raman microspectroscopy per condition.

permeabilization[55,56]. The level of Yo-Pro-1 fluorescence strongly increases when the dye reaches the nucleus. haMSC cells were platted overnight on a CaF_2 substrate. Before delivering the pulsed electric field, Yo-Pro-1 was added to the saline solution at a final concentration of 1 μM. Images were acquired with an Observer Z1 inverted microscope (Zeiss, Marly-le-Roi, France) with a LED-based illumination system (Mightex, Toronto, Canada). The LEDs were supplied by a specific power supply system combining three devices (2651 A, 3706AS and 3721) from Keithley (Les Ulis France). Images were acquired with an exposure time fixed to 200 ms for the green channel and 40 ms for the bright-field channel. The lookup table was the same for all the images shown. For the pulsed group, images were acquired 10 minutes after the delivery of pulsed electric fields. In order to quantify the mean level of fluorescence, each cell was isolated on the bright field images. The mean fluorescence per cell was determined with the Zen Blue 2 Zeiss software. The statistical difference between the two groups (control and pulsed) was calculated by Student's *t*-test.

Raman Measurements. A confocal Raman microspectrometer LabRam ARAMIS (Horiba Jobin Yvon, Villeneuve d'Ascq, France) coupled with an upright Olympus microscope BX 41 (Olympus, Rungis, France) was used to acquire the Raman spectra of living cells. A 100 X water immersion objective (LUMPLFL 100X/W, Olympus, Rungis, France) was used to focus the laser on the sample and to collect the Raman scattered light. The power of the 532 nm continuous wave laser was around 20 mW at the sample. Similar lasers have been used to acquire the Raman signature of live cells without inducing any phototoxicity[57–59]. The illumination system provided a lateral resolution of 1 μm. The axial resolution was about 7 μm. A 1200 lines/mm diffraction grating was used. It provided a spectral resolution of 1.29 cm^{-1}. By rotating the diffraction grating, the FP region (600–1800 cm^{-1}) and the HWN region (2600–3100 cm^{-1}) were accessible. The sample was placed on an XY piezoelectric stage to investigate various locations.

Prior to any measurement, the confocal Raman microspectroscope was calibrated with a Silicon sample using the 519 cm^{-1} band and the laser power was checked. The acquisition time was fixed to two accumulations of 30 seconds (60 seconds in total) for the FP region and two accumulations of 10 seconds (20 seconds in total) for the HWN region. During each session, the Raman signatures of three to five cells were measured. The measurements were performed consecutively cell by cell with about 10 spots per cell. Due to the laser spot size of 1 μm, the minimum step size was fixed to 2.5 μm in order to avoid any overlapping. Figure S1 displays representative examples of acquisition spots in the living haMSC in the 2 ROIs. No specific cell orientation to the electric field was selected. During the Raman measurements, cells were maintained at 4 °C by the T95 temperature controller (Linkam Scientific Instrument Ltd, Tadworth, UK). Each measurement session lasted one hour maximum. The cells showed no morphological changes during that time period. At the end of the experiment, a Trypan blue test was performed and remained negative, showing that the cells were still alive after one hour under the confocal Raman microspectroscope. No time effect was noticed in the spectral data set, meaning that the first recorded Raman spectrum is similar to the last one, after one hour of Raman signal acquisition.

The confocal Raman microspectroscope was controlled by the LabSpec 5 software (Horiba, Villeneuve d'Ascq, France). Each experiment was independently repeated three times. The Raman signature of the saline solution was acquired in order to be able to remove this interference signal from the measured spectra. In total, 1 318 spectra were collected, attributed to 134 cells. Table 2 details the number of cells per condition. The exposure time in the HWN region is lower than for the FP region. Thus, more cells were investigated in the HWN region than in the FP region within the one-hour duration of the experiment.

Raman data pre-processing and processing. First of all, each spectrum with a Signal-to-Noise Ratio (SNR) lower than 10 was discarded from the dataset. SNR was calculated on the measured spectra using equation (1):

$$SNR = \frac{S * G}{\sqrt{N * G}} \tag{1}$$

where S is the magnitude of the peak at 1003 cm^{-1}, N is the total magnitude of the signal at 1003 cm^{-1} minus the CCD offset and G is the gain of the CCD detector. Less than 5% of the total data set was removed.

Data pre-processing consisted in four steps: Savitsky-Golay smoothing (12 points, 2nd order polynomial)[60], removing of the saline solution signal, baseline subtraction (8th order polynomial for the FP region, 2nd order polynomial for the HWN region) and normalization by Standard Normal Variance (SNV) method[61]. Each cell was represented by the mean of all its normalized spectra.

For the two groups (control and pulsed), the mean normalized spectrum was calculated. The difference spectrum between the two groups (pulsed group minus control group) was also determined. Based on the difference spectrum, discriminant peaks were identified. Student's *t*-tests were performed to evaluate the statistical differences between the two groups in the normalized Raman intensity of these discriminant peaks.

Multivariate analyses were performed to quantify the effect of pulsed electric fields on the Raman spectrum of the cells. After mean-centering the data set, PCA was performed on the control and pulsed groups. The PC selection was based on two quantitative criteria that had to be fulfilled. The variance supported by the PC had to be higher than 5% of the total variance of the data set. Otherwise, the risk to take into account a PC attributed to noise variance was non-negligible. Also, the scores of the PC for the two groups had to be statically significant (Student's *t*-test, p-value < 0.05) in order to consider that this PC was statistically linked to EPN. This data processing was applied for the four conditions (i.e., "Cathode, FP", "Nucleus, FP", "Cathode, HWN" and "Nucleus, HWN"). All data processing and data analysis were performed under MATLAB v2009b (MathWorks, Meudon, France).

References

1. Tsong, T. Y. Y. Electroporation of cell membranes. *Biophys. J.* **60,** 297–306 (1991).
2. Chen, C., Smye, S. W. W., Robinson, M. P. P. & Evans, J. A. A. Membrane electroporation theories: a review. *Med. Biol. Eng. Comput.* **44,** 5–14 (2006).
3. Mir, L. M., Orlowski, S., Belehradek, J. & Paoletti, C. Electrochemotherapy potentiation of antitumour effect of bleomycin by local electric pulses. *Eur. J. Cancer* **27,** 68–72 (1991).
4. Fei, Z. *et al.* Gene transfection of mammalian cells using membrane sandwich electroporation. *Anal. Chem.* **79,** 5719–22 (2007).
5. Mir, L. M. Nucleic acids electrotransfer-based gene therapy (electrogenetherapy): Past, current, and future. *Mol. Biotechnol.* **43,** 167–176 (2009).
6. Teissie, J., Golzio, M. & Rols, M. P. Mechanisms of cell membrane electropermeabilization: a minireview of our present (lack of ?) knowledge. *Biochim. Biophys. Acta* **1724,** 270–280 (2005).
7. Schwan, H. P. *Biological Effects and Dosimetry of Nonionizing Radiation*, doi: 10.1007/978-1-4684-4253-3 (Springer US, 1983).
8. Kotnik, T., Pucihar, G. & Miklavcic, D. Induced transmembrane voltage and its correlation with electroporation-mediated molecular transport. *J. Membr. Biol.* **236,** 3–13 (2010).
9. Tarek, M. Membrane electroporation: a molecular dynamics simulation. *Biophys. J.* **88,** 4045–4053 (2005).
10. Sengel, J. T. & Wallace, M. I. Imaging the dynamics of individual electropores. *Proc. Natl. Acad. Sci.* **113,** 5281–5286 (2016).
11. Szabo, M. & Wallace, M. I. Imaging potassium-flux through individual electropores in droplet interface bilayers. *Biochim. Biophys. Acta* **1858,** 613–7 (2016).
12. Breton, M., Delemotte, L., Silve, A., Mir, L. M. & Tarek, M. Transport of siRNA through lipid membranes driven by nanosecond electric pulses: an experimental and computational study. *J. Am. Chem. Soc.* **134,** 13938–41 (2012).
13. Gabriel, B. & Teissié, J. Control by electrical parameters of short- and long-term cell death resulting from electropermeabilization of Chinese hamster ovary cells. *Biochim. Biophys. Acta* **1266,** 171–8 (1995).
14. Chopinet, L., Roduit, C., Rols, M. P. & Dague, E. Destabilization induced by electropermeabilization analyzed by atomic force microscopy. *Biochim. Biophys. Acta - Biomembr.* **1828,** 2223–2229 (2013).
15. Breton, M. & Mir, L. M. A chemical study of the interaction of electric pulses with a cell model: giant unilamellar vesicles. In *1st World Congress on Electroporation and Pulsed Electric Fields in Biology, Medicine and Food & Environment Technologies* **4** (2015).
16. Vernier, P. T. *et al.* Electroporating fields target oxidatively damaged areas in the cell membrane. *PLoS One* **4** (2009).
17. Garrec, J., Monari, A., Assfeld, X., Mir, L. M. & Tarek, M. Lipid Peroxidation in Membranes: The Peroxyl Radical Does Not 'Float'. *J. Phys. Chem. Lett.* **5,** 1653–1658 (2014).
18. Downes, A. & Elfick, A. Raman spectroscopy and related techniques in biomedicine. *Sensors* (*Basel*). **10,** 1871–89 (2010).
19. Brauchle, E. & Schenke-Layland, K. Raman spectroscopy in biomedicine - non-invasive *in vitro* analysis of cells and extracellular matrix components in tissues. *Biotechnol. J.* **8,** 288–97 (2013).
20. Raman, C. V. V. A new radiation. *Indian J. Phys.* **2,** 387–398 (1928).
21. Puppels, G. J. *et al.* Studying single living cells and chromosomes by confocal Raman microspectroscopy. *Nature* **347,** 301–303 (1990).
22. Downes, A., Mouras, R., Bagnaninchi, P. & Elfick, A. Raman spectroscopy and CARS microscopy of stem cells and their derivatives. *J. Raman Spectrosc.* **42,** 1864–1870 (2011).
23. Sulé-Suso, J., Forsyth, N. R., Untereiner, V. & Sockalingum, G. D. Vibrational spectroscopy in stem cell characterisation: is there a niche? *Trends Biotechnol.* **32,** 254–62 (2014).
24. Smith, G. P. S., McGoverin, C. M., Fraser, S. J. & Gordon, K. C. Raman imaging of drug delivery systems. *Adv. Drug Deliv. Rev.* **89,** 21–41 (2015).
25. Barroso, E. M. *et al.* Discrimination between oral cancer and healthy tissue based on water content determined by Raman spectroscopy. *Anal. Chem.* **87,** 2419–26 (2015).
26. Caplan, A. I. Mesenchymal stem cells. *J. Orthop. Res.* **9,** 641–50 (1991).
27. Minguell, J. J., Erices, A. & Conget, P. Mesenchymal stem cells. *Exp. Biol. Med.* (*Maywood*). **226,** 507–20 (2001).
28. Ferreira, E. *et al.* Optimization of a gene electrotransfer method for mesenchymal stem cell transfection. *Gene Ther.* **15,** 537–44 (2008).
29. Liew, A. *et al.* Robust, efficient, and practical electrogene transfer method for human mesenchymal stem cells using square electric pulses. *Hum. Gene Ther. Methods* **24,** 289–97 (2013).
30. Silve, A., Poignard, C., Sack, M., Straessner, R. & Frey, W. Study of Transmembrane Voltage Kinetics During 100 us Pulse using Voltage Sensitive Dyes. In *1st World Congress on Electroporation and Pulsed Electric Fields in Biology, Medicine and Food & Environment Technologies* **74** (2015).
31. Notingher, I. *et al. In situ* characterisation of living cells by Raman spectroscopy. *Spectroscopy* **16,** 43–51 (2002).
32. Puppels, G. J., Garritsen, H. S., Segers-Nolten, G. M., de Mul, F. F. & Greve, J. Raman microspectroscopic approach to the study of human granulocytes. *Biophys. J.* **60,** 1046–56 (1991).
33. Chan, J. W., Lieu, D. K., Huser, T. & Li, R. A. Label-free separation of human embryonic stem cells and their cardiac derivatives using Raman spectroscopy. *Anal. Chem.* **81,** 1324–31 (2009).
34. Chen, P. *et al.* In *Stem Cells in Clinic and Research* (ed. Gholamrezanezhad, A.) 765–790, doi: 10.5772/740 (InTech, 2011).
35. Talari, a. C. S., Evans, C. a., Holen, I., Coleman, R. E. & Rehman, I. U. Raman spectroscopic analysis differentiates between breast cancer cell lines. *J. Raman Spectrosc.* n/a-n/a doi: 10.1002/jrs.4676 (2015)
36. Unterreitmeier, S. *et al.* Phenylalanine promotes interaction of transmembrane domains via GxxxG motifs. *J. Mol. Biol.* **374,** 705–18 (2007).
37. Maiti, N. C., Apetri, M. M., Zagorski, M. G., Carey, P. R. & Anderson, V. E. Raman spectroscopic characterization of secondary structure in natively unfolded proteins: alpha-synuclein. *J. Am. Chem. Soc.* **126,** 2399–408 (2004).
38. Cournia, Z. *et al.* Membrane Protein Structure, Function, and Dynamics: a Perspective from Experiments and Theory. *J. Membr. Biol.* **248,** 611–40 (2015).

39. Gabriel, B. & Teissié, J. Generation of reactive-oxygen species induced by electropermeabilization of Chinese hamster ovary cells and their consequence on cell viability. *Eur. J. Biochem.* **223,** 25–33 (1994).
40. Pakhomova, O. N. *et al.* Oxidative effects of nanosecond pulsed electric field exposure in cells and cell-free media. *Arch. Biochem. Biophys.* **527,** 55–64 (2012).
41. Wiseman, H. & Halliwell, B. Damage to DNA by reactive oxygen and nitrogen species: role in inflammatory disease and progression to cancer. *Biochem. J.* **313(Pt 1**), 17–29 (1996).
42. Poplineau, M. *et al.* Raman microspectroscopy detects epigenetic modifications in living Jurkat leukemic cells. *Epigenomics* **3,** 785–94 (2011).
43. García-Flores, A. F. *et al.* High-wavenumber FT-Raman spectroscopy for *in vivo* and *ex vivo* measurements of breast cancer. *Theor. Chem. Acc.* **130,** 1231–1238 (2011).
44. Riske, K. A. & Dimova, R. Electro-deformation and poration of giant vesicles viewed with high temporal resolution. *Biophys. J.* **88,** 1143–1155 (2005).
45. Kirchner, S. R. *et al.* Membrane composition of jetted lipid vesicles: A Raman spectroscopy study. *J. Biophotonics* **5,** 40–46 (2012).
46. Mikkelsen, R. B., Verma, S. P. & Wallach, D. F. Effect of transmembrane ion gradients on Raman spectra of sealed, hemoglobin-free erythrocyte membrane vesicles. *Proc. Natl. Acad. Sci. USA* **75,** 5478–82 (1978).
47. Liu, B. *et al.* Label-free spectroscopic detection of membrane potential using stimulated Raman scattering. *Appl. Phys. Lett.* **106,** 173704 (2015).
48. Wold, S., Esbensen, K. & Geladi, P. Principal component analysis. *Chemom. Intell. Lab. Syst.* **2,** 37–52 (1987).
49. Punnonen, E.-L., Ryhänen, K. & Marjomi, V. S. At reduced temperature, endocytic membrane traffic is blocked in multivesicular carrier endosomes in rat cardiac myocytes. *Eur. J. Cell Biol.* **75,** 344–352 (1998).
50. Haylett, T. & Thilo, L. Endosome-lysosome fusion at low temperature. *J. Biol. Chem.* **266,** 8322–7 (1991).
51. Los, D. A. & Murata, N. Membrane fluidity and its roles in the perception of environmental signals. *Biochim. Biophys. Acta - Biomembr.* **1666,** 142–157 (2004).
52. Lopez, A., Rols, M. P. & Teissie, J. Phosphorus-31 NMR analysis of membrane phospholipid organization in viable, reversibly electropermeabilized Chinese hamster ovary cells. *Biochemistry* **27,** 1222–1228 (1988).
53. Kerr, L. T., Byrne, H. J. & Hennelly, B. M. Optimal choice of sample substrate and laser wavelength for Raman spectroscopic analysis of biological specimen. *Anal. Methods* **7,** 5041–5052 (2015).
54. Draux, F. *et al.* Raman spectral imaging of single living cancer cells: a preliminary study. *Analyst* **134,** 542–548 (2009).
55. García-Sánchez, T. *et al.* Interpulse multifrequency electrical impedance measurements during electroporation of adherent differentiated myotubes. *Bioelectrochemistry* **105,** 123–35 (2015).
56. Vernier, P. T. *et al.* Nanoelectropulse-driven membrane perturbation and small molecule permeabilization. *BMC Cell Biol.* **7,** 37 (2006).
57. Klein, K. *et al.* Label-Free Live-Cell Imaging with Confocal Raman Microscopy. *Biophys. J.* **102,** 360–368 (2012).
58. Hamada, K. *et al.* Raman microscopy for dynamic molecular imaging of living cells. *J. Biomed. Opt.* **13,** 44027 (2008).
59. Oshima, Y., Shinzawa, H., Takenaka, T., Furihata, C. & Sato, H. Discrimination analysis of human lung cancer cells associated with histological type and malignancy using Raman spectroscopy. *J. Biomed. Opt.* **15,** 17009 (2010).
60. Savitzky, A. & Golay, M. J. E. Smoothing and Differentiation of Data by Simplified Least Squares Procedures. *Anal. Chem.* **36,** 1627–1639 (1964).
61. Notingher, I. *et al. In situ* spectral monitoring of mRNA translation in embryonic stem cells during differentiation *in vitro*. *Anal. Chem.* **76,** 3185–93 (2004).

Acknowledgements

The authors thank Ecole Normale Supérieure de Cachan, CNRS, Gustave Roussy, Univ. Paris-Sud, Université Paris-Saclay and Fondation EDF for financial support of this work. This study was also supported by the Université Reims Champagne-Ardenne and IBiSA Cellular and Tissular Imaging Platform PICT. Authors also thank Dr. Peter Caspers, Dr. Tom Bakker Schut and Dr. Gerwin Puppels from Erasmus MC for discussion on the statistical analysis employed here, Michaël Scherman and Brigitte Attal-Trétout from ONERA for introduction to the Raman technique and Pr. Michel Manfait from Université Reims Champagne-Ardenne for permitting the initiation of this collaboration between the two groups. This study was conducted in the scope of LEA EBAM (European Laboratory of Pulsed Electric Fields Applications in Biology and Medicine).

Author Contributions

A.A., V.U., O.P. and L.M.M. conceived the experiments. A.A. conducted the experiments. A.A. performed the data analysis under the supervision of C.G., A.A. wrote the manuscript. All authors discussed the results and commented on the paper.

Additional Information

Supplementary information accompanies this paper at http://www.nature.com/srep

Competing financial interests: The authors declare no competing financial interests.

How to cite this article: Azan, A. *et al.* Demonstration of the Protein Involvement in Cell Electropermeabilization using Confocal Raman Microspectroscopy. *Sci. Rep.* **7**, 40448; doi: 10.1038/srep40448 (2017).

Demonstration of the Protein Involvement in Cell Electropermeabilization using Confocal Raman Microspectroscopy

Antoine Azan[1], Valérie Untereiner[2,3], Cyril Gobinet[2], Ganesh D. Sockalingum[2], Marie Breton[1], Olivier Piot[2,3], and Lluis M. Mir[1,*]

[1]Vectorology and Anticancer Therapies, UMR 8203, CNRS, Gustave Roussy, Univ. Paris-Sud, Université Paris-Saclay, 114 rue Edouard Vaillant, 94805 Villejuif, France.

[2]MeDIAN, Biophotonics and Technologies for Health, MEDyC, UMR 7369, CNRS, University of Reims Champagne-Ardenne, 51 rue Cognacq-Jay, 51096 Reims, France.

[3]Cellular and Tissular Imaging Platform PICT, Faculty of Pharmacy, University of Reims Champagne-Ardenne, 51 rue Cognacq-Jay, 51096 Reims, France.

Correspondence and requests for materials should be addressed to Lluis. M. Mir (Luis.Mir@gustaveroussy.fr)

Supplementary Information

Figure S1: Representative example of acquisition spots in living haMSC in A – Cathode ROI, B – Nucleus ROI. The green dots represent the spots where the Raman signatures were acquired.

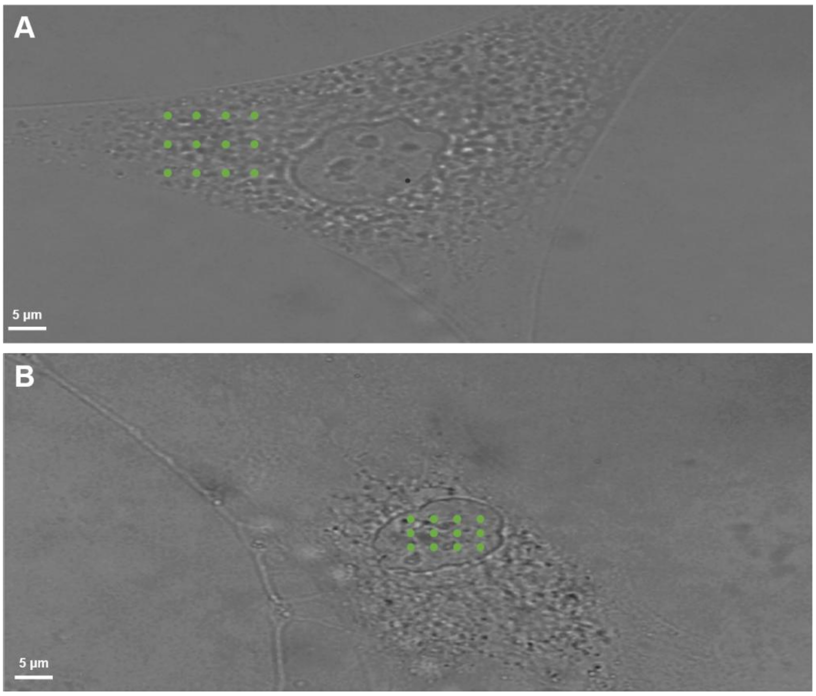

Table 1: Tentative Raman band assignment of haMSC cells. Abbreviations: A: Adenine, G: Guanine, T: Thymine, C: Cytosine, U: Uracil, Phe: Phenylalanine, Tyr: Tyrosine, Trp: Tryptophan, str: stretching; def: deformation, bend: bending, sym: symmetric, asym

	Raman Shift (cm^{-1})	Tentative Raman band assignment		
		DNA / RNA	Proteins	Lipids
FP band	623		Phe (skeletal)	
	643		Tyr (skeletal)	
	670	T ring angle bend		
	684	G ring breath		
	702			Cholesterol
	713			$CN^+(CH_3)_3$ str
	744	T C=O out of plane bend		
	762		Trp ring breath	
	783-790	O-P-O str U,C ring breath		
	828		Tyr out of plane ring breath	
	834	Ribose-phosphate		
	855		Tyr ring breath	
	877			C-C sym str
	900	Deoxyribose		
	936		C-C backbone str	
	980			=CH bend
	1003		Phe sym ring breath	
	1033		Phe C-H in-plane	
	1064			Chain C-C str
	1083	C-O str	C-N str	Chain C-C str
	1097	$O-P-O^-$ str		
	1127		C-N str	C-C str
	1157	Ribose Phosphatase	C-N str	
	1176		Tyr, Phe	
	1205		Phe $C-C_6H_5$ str	
	1231		Amide III random coil	
	1258		Amide III β-sheet	
	1284		Amide III α-helix	
	1303	A		CH_2 twist
	1319	G	CH def	
	1342		CH def	CH def
	1364			CH_3 sym str
	1380	T,A,G		
	1425	A,G		
	1448	CH def	CH def	CH def
	1585	A,G		
	1607		Try and Phe C=C	
	1660		Amide I α-helix	C=C str

6.2 Comprehensive Characterization of the Interaction between Pulsed Electric Fields and Live Cells by Confocal Raman Microspectroscopy (article #2)

In the first publication, we demonstrated that PEFs induce major biochemical modifications of live cells, especially on proteins. It is well known that the effects of PEFs are not homogeneously distributed on the cell. Thus, the Raman signatures of control and pulsed haMSC cells have been acquired at different cellular positions around the nucleus in order to monitor the spatial distribution of the electro-induced biochemical modifications. Since it was known that the permeabilization level is highly dependent on the electric pulse parameters, we have investigated the potential dose effect of the electric pulse parameters on the Raman signatures of live haMSC cells by sweeping the electric field magnitude, the number of pulses or the repetition rate. The resealing of the membrane was also assessed by tuning the temperature of the experiments in order to block or not the membrane repair mechanisms. Finally, the Raman signatures of live control and pulsed LPB cells were performed in order to investigate the potential cell line-dependency of our previous results.

This work is in the continuity of the published article #1 and has been conducted in collaboration with the laboratory MEDyC (UMR 7369, CNRS, university of Reims Champagne-Ardenne) headed by Pr. Olivier Piot. The Raman and fluorescence experiments have been performed, respectively, at MEDyC and UMR 8203. The results of this work are submitted for publication.

Comprehensive Characterization of the Interaction between Pulsed Electric Fields and Live Cells by Confocal Raman Microspectroscopy

Antoine Azan[†], Valérie Untereiner[§,#], Lucie Descamps[†], Caterina Merla[†], Cyril Gobinet[§], Olivier Piot[§,#], and Lluis M. Mir[†,*]

[†] Vectorology and Anticancer Therapies, UMR 8203, CNRS, Gustave Roussy, Univ. Paris-Sud, Université Paris-Saclay, 94805 Villejuif, France

[§] MeDIAN, Biophotonics and Technologies for Health, MEDyC, UMR 7369, CNRS, University of Reims Champagne-Ardenne, 51096 Reims, France

[#] Cellular and Tissular Imaging Platform (PICT), Faculty of Pharmacy, University of Reims Champagne-Ardenne, 51096 Reims, France

ABSTRACT (80-250 words): This study reports an extended analysis of the effect of 100 µs electric pulses on the biochemical composition of live cells using confocal Raman microspectroscopy. We investigated different regions of interest around the nucleus of the cells, the dose-effect relationship related to different electric pulse parameters and extended the study to another cell type. Our results confirmed a previous publication showing that proteins and lipids were highly impacted by the delivery of electric pulses. These chemical changes were similar in different locations around the cell nucleus. By sweeping the field magnitude, the number of electric pulses or the repetition rate, the Raman signatures of live cells appeared to be related to the electropermeabilization state, meaning electropermeabilized or not electropermeabilized, and not to the level of electropermeabilization. Membrane resealing was monitored by pulsing the cells in reversible or irreversible permeabilization condition at different temperatures. We also demonstrated that the chemical changes in the Raman signatures were cell-dependent even if common features were noticed between the two cell types.

Cell membrane electropermeabilization, also termed electroporation, results in the exposure of cells to short and intense pulsed electric fields (PEF)[1,2]. The possibility to destabilize the plasma membrane by the delivery of electric pulses was discovered by Stampfli in 1958[3]. Nowadays, electropermeabilization is commonly used in medicine[4] or industry[5] . For instance, electrochemotherapy consists in the combination of chemotherapy with electropermeabilization to treat tumor cells[6]. The interaction between PEF and biological cells has been widely studied but the underlying mechanisms remain still unclear. Recently, the effects of PEF on the biochemical composition of the cells has been under investigation as the major mechanism of electropermeabilization. Mass spectrometry analysis of simple membrane model, Giant Unilamellar Vesicles (GUV), experimentally demonstrated the phospholipid peroxidation induced by the delivery of electric pulses on lipid bilayer[7]. Other studies showed that oxidized phospholipids contributed to make the membrane more permeable[8,9], especially when exposed to electric pulses[10]. Using confocal Raman microspectroscopy (CRM), our groups have recently revealed major modifications of proteins and lipids in cells exposed to PEF[11]. This publication was not only the first one showing protein involvement in cell electropermeabilization using CRM, but was also a proof of concept that CRM can provide useful information of the biochemical composition of the electropermeabilized cells.

In this study, we report an extended characterization of cell electropermeabilization by monitoring the effect of electric pulses on the biochemical composition of live cells at different cell locations, for different cell types and electric pulses exposures.

EXPERIMENTAL SECTION

Cell culture

Primary human-adipose derived Mesenchymal Stem Cell (haMSC) and the established murine LPB cell line were used as cell models because they have strong differences: species origin, morphology, size, immortality, metabolism, etc. haMSC and LPB cells were both grown in a humidified atmosphere at 37°C and 5% CO2 in Dulbecco's Modified Eagle Medium (DMEM) supplemented with 10 % fetal bovine serum and 1 % of penicillin streptomycin (Life Technologies, Cergy-Pontoise, France). For the experiments, 5.10^3 cells/cm^2 were plated in a 35 mm Petri dish (Thermo Fisher Scientific, Illkirch, France) in which a CaF_2 window

(Crystran, Poole, United Kingdom) was placed at the bottom before adding the cells. The cells were incubated overnight and attached to the CaF_2 window before performing the experiments.

Pulse generator and pulses condition

A commercially available generator (Cliniporator, IGEA, Italy) was used to treat the cells. To deliver the electric pulses on attached cells, two stainless steel plate electrodes spaced by 4 mm were used. The Cliniporator was connected to the plate electrodes with alligator clips. Before delivering the electric pulses, the complete culture medium was removed and replaced by physiological water, NaCl 0.9%, (B. Braun, Boulogne-Billancourt, France) after washing twice with phosphate-buffered saline (PBS). Before addition to the Petri dish, the physiological water was stored at fixed temperatures (4, 20 or 37°C). The electric pulses parameters were depending on the experiments performed.

Raman measurements

The equipment and its configuration were previously detailed in Azan *et al.* (2017)[11]. Briefly, a confocal Raman microscope LabRam ARAMIS (Horiba Jobin Yvon, Villeneuve d'Ascq, France) was used to acquire the Raman spectra of live cells. The samples were excited with a 532 nm continuous wave laser through a 100 X water immersion objective (LUMPLFL 100X/W, Olympus, Rungis, France). The Raman signatures of the samples were acquired in the fingerprint region (600 – 1800 cm^{-1}) with an exposure time fixed to 60 s. The Raman signatures of live cells were acquired at 4 different Region Of Interests (ROIs) around the nucleus, termed: cathode, anode, antipole 1 and antipole 2. The cathode ROI was the area of the cell between the nucleus and the edge of the cell facing the cathode of the pulse generator. The anode ROI was the area between the nucleus and the edge of the cell facing the anode of the pulse generator. The antipole 1 and the antipole 2 ROIs were the area at 90° anti-clockwise and clockwise rotations, respectively, starting from the anode ROI. Representative examples of the different ROIs are displayed in figure S1. Each Raman experiment lasted one-hour maximum in order to preserve cells viability. During all the acquisitions, the samples were maintained at a fixed temperature (4, 20 or 37°C) by T95 system controller (Linkam Scientific Instrument Ltd, Tadworth, UK). The acquisition of the Raman signatures of cells were started less than 1 minute after the delivery of the electric pulses. In total, 1838 Raman signatures from 209 cells were measured.

Raman data pre-processing and processing

The pre-processing method was also detailed in Azan *et al.* (2017)[11]. Briefly, after removing the spectrum with a signal-to-noise ratio (SNR) lower than 10, data pre-processing consisted in Savitsky-Golay smoothing[12], removal of physiological water signal, baseline subtraction and normalization by the Standard Normal Variance method[13,14].

Multivariate analyses were performed to quantify the effect of PEF on the Raman spectra of the cells for the several experimental parameters investigated. After mean-centering the data set, Principal Component Analysis (PCA)[15] or Partial Least-Square regression (PLS)[16] were performed. In the case of the analysis of the different ROIs probed, a leave-one-out cross-validation (LOOCV) based on PCA was performed on the combined control and cathode data set, which corresponded to our original data set. At each iteration of the LOOCV, PC1 was selected in order to split the control and the cathode date sets. The mean of each PC1 was calculated and called "Model" in the rest of manuscript. This model was applied to a more extensive data set combining the control, cathode, antipole 1, anode and antipole 2 groups. In the case of the electric field magnitude dose-effect, PCA was applied to the data set. No external observation variable, meaning the electric field magnitude, was required to split the Raman signatures of haMSC cells from the different experimental conditions. In the case of the analysis of the number of electric pulses or the repetition rate, observable variable was required to investigate the dose-effect relationship. Thus, PLS was applied to the data set by using the number of electric pulses or the repetition rate respectively as the observation variable. In the case of the temperature effect and the use of LPB cells, PCA was applied to the data set. A One-way ANalysis Of VAriance (ANOVA) was performed to statistically compare the groups two by two.

All data processing and data analysis were performed under MATLAB v2009b (MathWorks, Meudon, France).

Fluorescence microscopy

The percentage of electropermeabilized cells was quantified by fluorescence microscopy using Yo-Pro-1 uptake (Life technologies). Two channels fluorescence images (blue for Hoechst 33342 $\lambda_{emission}$=450 nm, green for Yo-Pro-1 $\lambda_{emission}$=510 nm) were acquired. The blue channel image was used to define a mask specific to the nucleus of each cell present in the field of view. This mask was applied to the green channel image in order to assess specifically the Yo-Pro-1 fluorescence intensity into the nuclei. The extraction of the Yo-Pro-1 fluorescence intensity per cell nucleus was performed on FIJI software (ImageJ, version 1.50g). A cell was considered as permeabilized if its Yo-Pro-1 fluorescence intensity was higher than the maximal intensity of the Yo-Pro-1 fluorescence intensity of all the cells in the control group. Thus, the percentage of cells permeabilized to Yo-Pro-1 by the delivery of electric pulses could be precisely quantified.

Exactly like in the Raman experiments, $5\ 10^3$ cells/cm^2 were platted overnight on CaF_2 substrate. Cells were incubated with 370 nM of Hoechst 33342 in the culture medium for 30 minutes before the experiments. The culture medium containing the Hoechst 33342 was removed and replaced by fresh culture medium after washing two times with PBS. Less than one minute before the delivery of the electric pulses, the culture medium was removed and replaced by a buffer solution of Yo-Pro-1 at a final concentration of 1 µM in physiological water.

Images were acquired with an Observer Z1 inverted microscope (Zeiss, Marly-le-Roi, France). The exposure time was fixed to 50 ms (phase contrast images) or 300 ms (fluorescence images, either in the blue or green channel). The lookup table was the same for all the images shown. For each condition, at least 4 independent ROIs were acquired in order to get robust data set. Images were acquired 10 minutes after the delivery of PEF except in the specific case of irreversible permeabilization, where images were recorded 50 minutes after the delivery of PEF. In this case, cells were put back in culture after delivered the PEF and replaced the physiological water by fresh culture medium. After 40 minutes in the incubator, culture medium was replaced by physiological water with Yo-Pro-1. Then 10 minutes later (50 minutes in total after the delivery of PEF), images were acquired.

RESULTS AND DISCUSSION

Experimental design

In a first series of experiments, the Raman signatures of live cells exposed or not to electric pulses were acquired at 4 different ROIs around the nucleus (figure S1). The electric pulses parameters were fixed to 8 pulses, 100 µs duration, 1000 V/cm field magnitude and 1 Hz repetition rate.

In a second series of experiments, the dose effect relationship was investigated by sweeping one of the electric pulse parameters (i.e. the electric field magnitude, the number of pulses or the repetition rate) while the other pulse parameters were maintained equals to the initial electric pulse parameters used in our previous publication: 8 pulses, 100 µs duration, 1000 V/cm magnitude field and 1 Hz repetition rate[11].

In a third series of experiments, the effect of the temperature on the Raman signatures of cells exposed or not to PEF was assessed. The experiments were performed at 4°C, 20°C or 37 °C in order to modulate the cellular metabolism such as membrane resealing. The pulsed cells were permeabilized in a reversible or irreversible conditions.

Finally, LPB, another cell type, was used to compare the results obtained with haMSC, the initial cell type.

In parallel, the percentage of permeabilized cells under exactly the same experimental condition used in the Raman measurements was quantified by fluorescence microscopy.

Spatial characterization of the effect of PEF on the Raman signatures of haMSC

In this experiment, the electric pulses parameters were fixed to 8 pulses of 100 µs duration with a magnitude of 1000 V/cm and a repetition rate of 1 Hz. The Raman signatures of live haMSC cells were acquired at different cell location around the nucleus. As expected, the Raman signatures of unexposed cells acquired at the 4 different ROIs were similar (data not shown) and were combined in the control group. PCA coupled with LOOCV was performed on the combined control and cathode data set in order to determine a model further applied to the other ROI (i.e. anode, antipole 1, antipole 2) spectrum data sets. The control and cathode data set were selected as our reference data set from a previous publication[11]. Figure 1.A shows the loading of the model. Two Raman peaks were predominant: 1658 and 1003 cm^{-1}, respectively attributed to the amide I and to the ring breathing mode of phenylalanine according to classical band assignments[17,18]. Phenylalanine is an amino-acids present in the transmembrane domains of many proteins[19]. Amide I Raman band is known to be related to the secondary structure of proteins[20]. Thus these findings confirmed our previous results that PEF has a strong effect on the proteins (structure, composition and environment) of the cells[11]. Figure 1.B shows the score of the spectra from the different locations projected on the model determined by LOOCV. The model score of the control and the combined pulsed groups was respectively -4.04 ±3.30 and 5.01 ±4.43. After performing a statistical analysis on the model score, strong significant differences (p-value < 0.1%) were found between the pulsed groups and the control group. On the contrary, there was no statistically significant difference within the groups at the different ROIs. We can conclude that the electric pulses have an effect on the biochemical composition of pulsed cells in comparison with the unpulsed cells. These biochemical effects were similar at the different spatial locations probed around the nucleus. A complete Raman mapping of pulsed cell *versus* control cells would reinforce this first result showing that the effect of PEF on the Raman signatures of cells is global. Unfortunately, the Raman signal is a low signal and thus long acquisition time is necessary (60 s in our case). A full cartography of one 70 µm diameter haMSC cell would take 81 hours considering that the haMSC cell extends over 70 x 70 pixels with a pixel size of 1 µm. Using fixed cells is possible[21], but it has been demonstrating that the chemical fixation protocol has an impact on the Raman signature of cells[22]. As noticed before, the model displayed two critical bands at 1003 and 1658 cm^{-1}, both related to proteins (composition and structure). By monitoring the magnitude of these two Raman peaks, the 4 pulsed groups (cathode, anode, antipole 1 and antipole 2) were significantly separated from the control group (figure 1.C). No difference has been found within pulsed groups based on the statistical analysis of the magnitude of the two critical peaks identified. This would confirm that the biochemical modifications of cells exposed to PEF are uniform around the nucleus. This conclusion is in contradiction with fluorescence microscopy study showing that the uptake of non-permeant dye starts at the pole positions (i.e. anode and cathode) hundreds of milliseconds after the delivery of electric pulses[24]. Raman microspectroscopy has the limitation to have low signal and thus low time-resolution (60 s in our case). Fluorescence Recovery After Photobleaching measurements have demonstrated that the lateral diffusion coefficient of lipids and proteins into the plasma membrane was 1 µm^2/s at maximum[25]. Considering the approximately 600 s necessary to characterize one cell (around 10 spectra / cell with 60 s / spectrum), the defaults generated at the poles of the cell by the PEF have time to laterally diffuse along 600 µm^2 which represents most of the haMSC cell surface and thus are uniformly distributed at the cell surface. Leguèbe *et al.* have designed a new numerical model which takes into account the lateral diffusion of the created defaults[26]. This new model has been validated by experiments and has revealed the effect of lateral diffusion on the electropermeabilization level. Thus, the time-resolution of Raman microspectroscopy does not allow to have access to such dynamic process. In order to investigate deeper the spatial effect of electric pulses on the vibrational footprint of cells, coherent Raman microscopy, such as Coherent Anti-stokes Raman Scattering (CARS) or Stimulated Raman Scattering (SRS), would be necessary to monitor these specific vibrational peaks in cells with a video-rate time resolution[27,28].

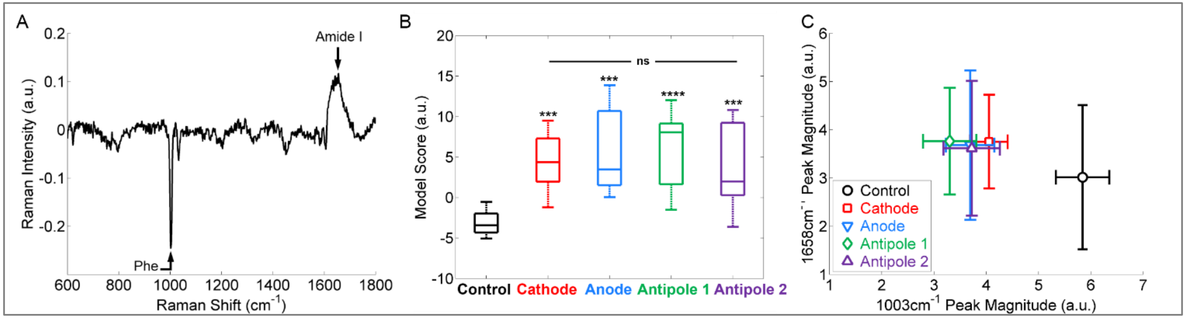

Figure 1: Spatial monitoring of the effect of PEF on the Raman signatures of haMSC cells. The Raman signatures of cells were acquired at different locations around the nucleus (cathode, anode, antipole 1, antipole 2). A – Model from the LOOCV performed on the control and cathode data sets. B – Model score per group. C – Magnitude of the 2 critical peaks identified (1003 and 1658 cm^{-1}) per group. The symbol and the error bars represent respectively the mean value and the standard deviation of the data set. The pulsed electric fields parameters were fixed to 8 pulses of 100 µs with an electric field magnitude of 1000 V/cm and a repetition rate of 1 Hz; The control group underwent sham exposure. The Raman signatures of cells not exposed to PEF were similar at the 4 different ROIs around the nucleus. The arrows indicate the position of phenylalanine (Phe) and amide I Raman peaks. Student's *t*-test: ns (non-statistically significant): p-value > 5%, ***: p-value ≤ 0.1%, ****: p-value ≤ 0.01%.

Effect of the electric field magnitude on the Raman signatures of haMSC

The dose-response relationship due to different electric field magnitudes on the Raman signatures of live haMSC cells was investigated. The electric field magnitude applied was 0, 500, 750, 1000, 1250 or 1500 V/cm. The others electric pulses parameters remained fixed to 8 pulses of 100 µs duration delivered at a repetition rate of 1 Hz. PCA was performed on the complete data set. Figure 2.A shows the loading of the Principal Component 1 (PC1). Based on the predominant peaks at 1003 and 1658 cm^{-1}, the effect of PEF on the proteins was confirmed again. Like the 1003 cm^{-1} peak, Raman bands at 620, 1033 and 1607 cm^{-1} also displayed negative contribution to the PC1. These Raman bands are known to be associated to the phenylalanine amino acid like the 1003 cm^{-1} Raman peak[17]. The large band around 1440 cm^{-1} of PC1 is related to the CH stretching modes of lipids[18]. This results confirm the well-established knowledge that PEF affect the lipids[29,30]. The PC1 score for the 0 and the 500 V/cm group were -5.28 ± 7.35 and -4.62 ± 5.3 (Figure 2.B). No significant difference was found between these two groups (p-value > 5 %). For an electric field higher or equal to 750 V/cm (i.e. 750 ,1000, 1250 and 1500 V/cm), the PC1 score per group shows statistically significant differences (p-value < 1%) between the control and the pulsed groups. It would indicate that under these experimental conditions, the biochemical composition of cells was significantly modified for an electric field magnitude higher than 500 V/cm. The PC1 scores for the 750, 1000, 1250 and 1500 V/cm did not show any statistical difference, meaning that the biochemical composition of cells was affected in a similar way.

In order to check the electropermeabilization level of haMSCs, fluorescence experiments with Yo-Pro-1 were performed under strictly the same experimental conditions (Figure 2.C). For the control condition and an electric field magnitude of 500 V/cm, none cell was permeabilized to Yo-Pro-1. For an electric field magnitude higher or equal to 750 V/cm, the percentage of permeabilized cells to Yo-Pro-1 was 94.89 ± 6.23 %. Thus, cell electropermeabilization threshold can be estimated between 500 and 750 V/cm under these experimental conditions. Raman microspectroscopy results were also providing a threshold value between 500 and 750 V/cm. We may speculate that the PC1 score is a biomarker of the permeabilization state, meaning not permeabilized or permeabilized, of the haMSC cells exposed to PEF. The criteria of permeabilization state has been established based on the uptake of Yo-Pro-1 which has a specific size of 630 Da. The permeabilization threshold is highly depending on the biomarker used. Performing similar experiments with a smaller biomarker such as calcium ion thanks to calcium-green[31] or fluo-4[32] fluorescence dyes would give rise to different permeabilization threshold. Thus, more experiments are needed to confirm this speculative conclusion.

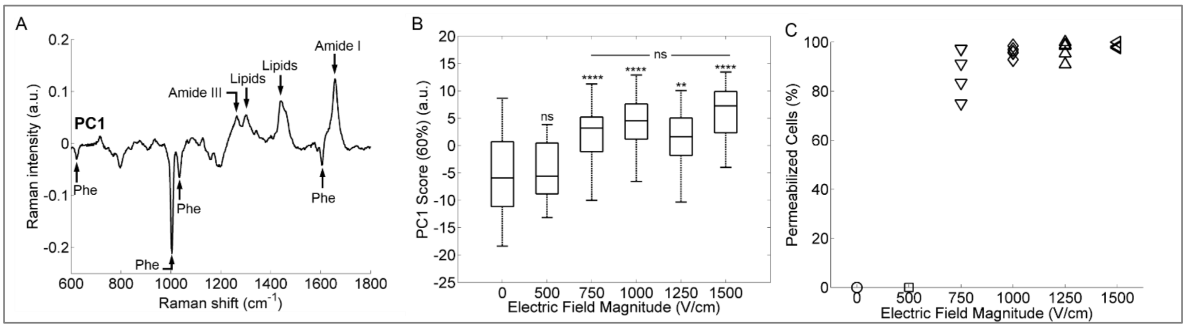

Figure 2: Effect of the electric field magnitude (0, 500, 750 1000, 1250 and 1500 V/cm) on the Raman signatures of haMSC cells. A – Loading of the PC1 from the PCA. B – PC1 score per group. The percentage of variance supported by the PC1 is indicated in brackets. C – Percentage of permeabilized haMSC cells per group based on Yo-Pro-1 uptake. The other pulsed electric fields parameters were fixed to 8 pulses with a duration of 100 µs at a repetition rate of 1 Hz. The control group underwent sham exposure. The Raman signatures of haMSC cells were acquired at the cathode ROI. The arrows indicate the position of phenylalanine (Phe), lipids, amide I and amide III Raman peaks. Student's *t*-test: ns (non-statistically significant): p-value > 5%, **: p-value ≤ 1%, ****: p-value ≤ 0.01%.Abreviation: Phe - phenylalanine

Effect of the number of electric pulses on the Raman signatures of haMSC

The dose effect relationship between the number of electric pulses applied and the Raman signatures of haMSC cells was also investigated. The number of electric pulses delivered to the cells was 0, 1, 2, 4 or 8. The others PEF parameters remained fixed to 100 µs pulse duration with 1000 V/cm electric field magnitude and 1 Hz repetition rate. PLS was performed on the complete data set using the number of electric pulses as the observation variable. Figure 3.A shows the Latent Variable 1 (LV1) score per group. For the groups 0, 1 or 2 electric pulses delivered, the LV1 scores were respectively -3.32 ± 2.66, -4.61 ± 2.10, -1.82 ± 2.24. No difference was noticed in the Raman signatures of haMSC cells between these groups. As a confirmation, the percentage of permeabilized cells exposed to the same electric pulses was around 0% showing that the plasma membrane was not permeabilized to Yo-Pro-1 by the small number of PEF (figure 3.B). For a number of electric pulses higher than 2, the LV1 scores of cells exposed to PEF were significantly different (p-value < 0.01%) of those of the control group. No difference in the LV1 score was noticed between the groups with 4 or 8 electric pulses. The loading of LV1 (data not shown) did not display any obvious pattern or critical Raman peaks. This might be explained by a data set with a lower level of electropermeabilization and thus a lower effect on the Raman signatures of cells exposed to such electric pulses. The relative variance supported by the LV1 was lower than in the electric magnitude field study (29% vs 60%) which confirms the low level of permeabilization.

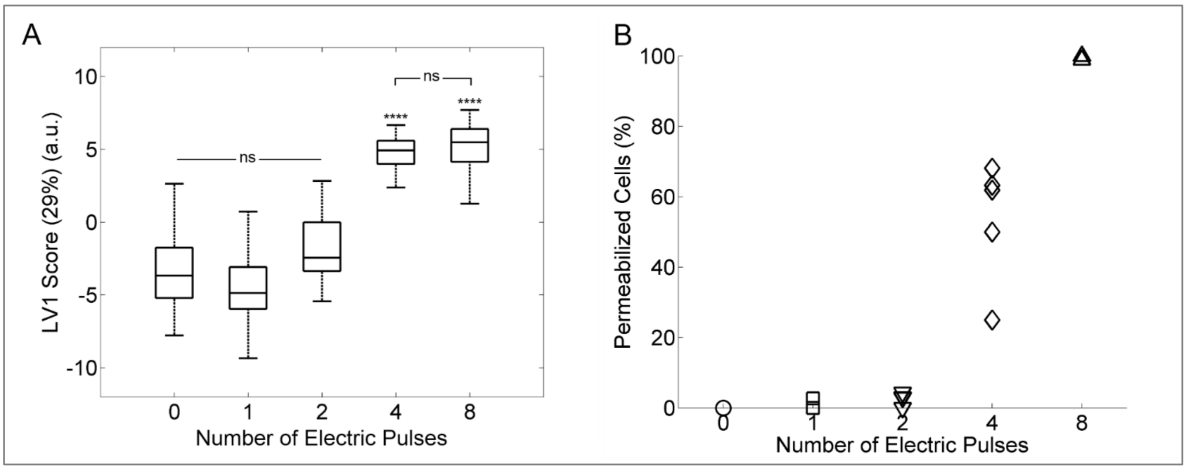

Figure 3: Effect of the number of electric pulses (0,1, 2, 4 and 8) on the Raman signatures of haMSC cells. A – LV1 score per group. The percentage of variance supported by the LV1 is indicated in brackets. B – Percentage of permeabilized haMSC cells per group based on the Yo-Pro-1 uptake. The other pulsed electric fields parameters were fixed to a pulse duration of 100 µs with a magnitude of 1000 V/cm and a repetition rate of 1 Hz. The control group underwent sham exposure. The Raman signatures of haMSC cells were acquired at the cathode ROI. Student's *t*-test: ns (non-statistically significant): p-value > 5%, ****: p-value ≤ 0.01%.

Effect of the repetition rate on the Raman signatures of haMSC

It is well known that the repetition rate affects the effectiveness of cell electropermeabilization: for a repetition above 1 Hz, the level of permeabilized decreases with the repetition rate[33,34]. This dose-response relationship has been explained by an electro-desensitization phenomenon[26,35]. Figure 4.A shows the LV1 loading from the PLS analysis performed on the Raman signatures of haMSC exposed or not to PEF with different repetition rates. The LV1 loading was similar to the PC1 loading when monitoring the effect of the electric field magnitude on the Raman signature of haMSC. The decrease of the Raman peak at 623, 1003 and 1033 cm^{-1} confirmed the effect of PEF on the phenylalanine molecules. The peaks at 1264 and 1658 cm^{-1} were related respectively to the amide III and amide I band which are biomarkers of the secondary structure of proteins. Finally, the Raman peaks at 1303 and 1450 cm^{-1} were related to the lipids. By plotting the LV1 scores per group and performing statistical analysis, we demonstrated that all the pulsed groups were statistically significantly different from the control group (figure 4.B). No statistical difference was noticed within pulsed groups. The Raman peaks at 1003 and 1658 cm^{-1} were the major contributors of LV1. The peak magnitude of the 1003 and 1658 cm^{-1} Raman peak, which were the major contributors of the LV1, were monitored for each group (Figure 4.C). As in the case of the LV1 score, all the pulsed groups were splitted from the control group. The data from a pulsed condition could not be separated from the data of another pulsed condition. Figure 4.D shows the percentage of haMSC permeabilized cells exposed to electric pulses with different repetition rates. All the pulsed groups were different from the control group demonstrating that the cells were permeabilized to Yo-Pro-1 by the electric pulses delivered. Our result fit with the literature with a decrease of the effectiveness of the permeabilization of cells exposed to PEF at repetition rates above 1 Hz[33,34]. This decrease of effectiveness of permeabilization was not noticed in the Raman results demonstrating that CRM might be related to the permeabilization state and not the permeabilization level achieved.

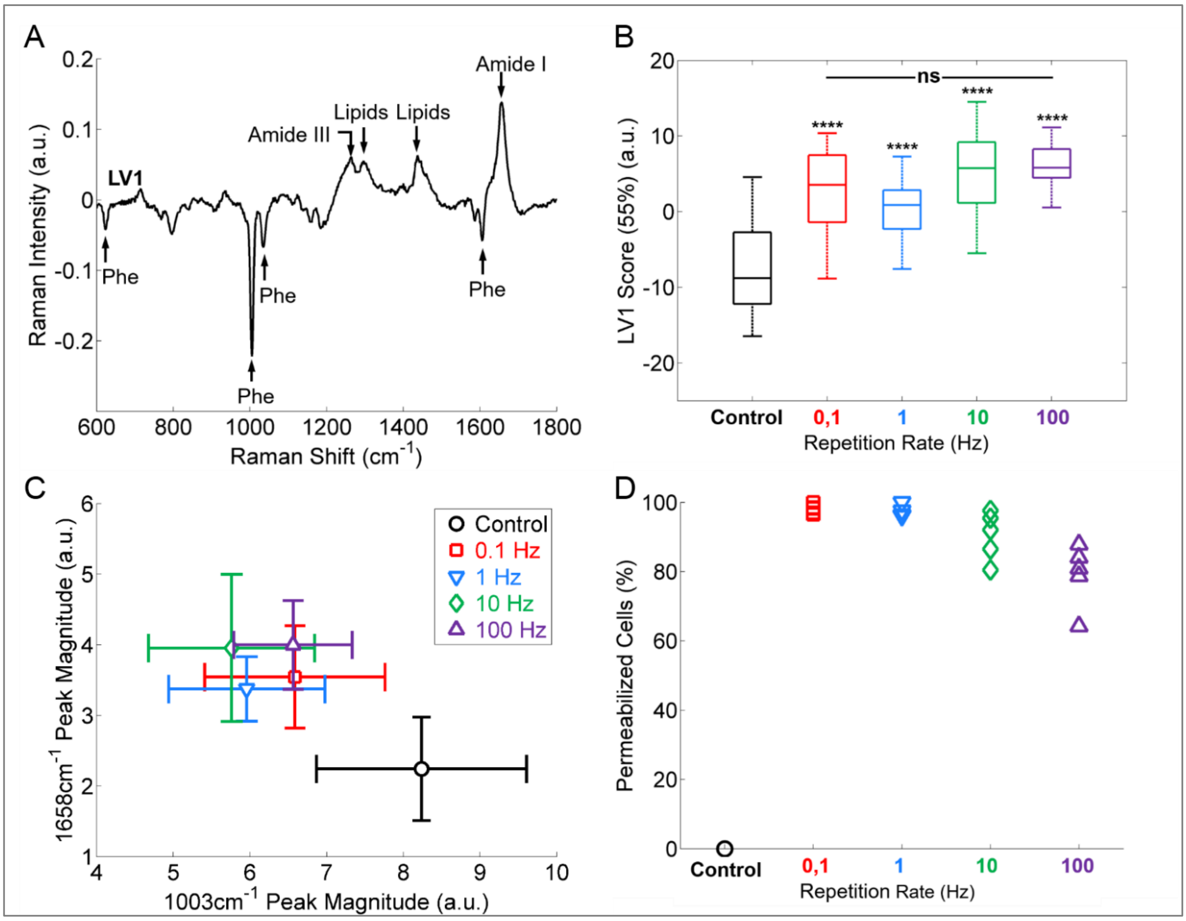

Figure 4: Effect of the repetition rate (0.1, 1, 10 and 100 Hz) on the Raman signatures of haMSC cells. A - Loading of the LV1 from the PLS analysis. B – LV1 score per group. The percentage of the variance supported by the LV1 is indicated in brackets. C – Peak magnitude of the 2 critical bands identified in LV1 per group. The symbol and the error bars represent respectively the mean value

and the standard deviation of the data set. D – Percentage of permeabilized haMSC cells per group based on the Yo-Pro-1 uptake. The other pulsed electric fields parameters were fixed to 8 pulses with a duration of 100 µs and a field magnitude of 1000 V/cm. The control group underwent sham exposure. The Raman signatures of haMSC cells were acquired at the cathode ROI. The arrows indicate the position of phenylalanine (Phe), lipids, amide I and amide III Raman peaks. Student's *t*-test: ns (non-statistically significant): p-value > 5%, ****: p-value ≤ 0.01%.

Effect of the temperature on the Raman signatures of haMSC

Temperature is known to have a strong effect on the duration of permeabilization via changes in the cell metabolism such as endocytosis, or membrane fluidity[36,37]. The dynamics of membrane resealing after the delivery of electric pulses on cells was temperature dependent. Thus, the recovery time of the reversibly permeabilized plasma membrane was also affected by the temperature[38]. In order to investigate the effect of the temperature on the biochemical composition of cells, the Raman signatures of pulsed and control haMSC cells were acquired at different temperatures: 4, 20 and 37°C associated to different kinetics of membrane resealing. It has been demonstrating that exposing the cells to 100 µs electric pulses at 4°C maintained the permeabilization for several hours without affecting cell viability[38]. Thus, the 4°C condition aimed to mimic a "static" cell model without any membrane resealing process. At 37°C, the cells are metabolically actives and so is the membrane resealing. An intermediate temperature value of 20°C was also selected. Cells were pulsed under reversible or irreversible permeabilization conditions meaning an electric field magnitude fixed to 1000 or 1500 V/cm, respectively. The others electric pulses parameters were fixed to 8 pulses of 100 µs at a repetition rate of 1Hz. These reversible and irreversible pulse conditions were checked by Yo-Pro-1 uptake (figure S2). Figure 5.A displays the distribution of the PC1 scores of the control and pulsed groups in the case of a reversible permeabilization induced at the 3 temperatures used. At 4°C, the PC1 scores of the control and the pulsed groups were respectively -6.15 ± 7.10 and 11.30 ± 3.26 and were significantly statistically different with a p-value lower than 0.01%. At 20°C, the p-value between the PC1 scores of the control and the pulsed group were lower than 5%. At 37°C, the PC1 scores of the control and the pulsed group were respectively -3.13 ± 8.36 and -5.16 ± 7.04 and were not different based on the Student's *t*-test (p-value > 5%). The p-value of the PC1 scores between the control and the pulsed group was increasing with the temperature, meaning that the difference in the PC1 scores was highly statistically significant at 4°C and not-statistically significant at 37°C. This result could be related to the membrane resealing process which is not active at 4°C and is active at 37°C allowing the cell to repair its plasma membrane. The acquisition time per cells (10 minutes= acquisition time / spectrum x number of spectrum / cells = 60 s x 10) fits with the known kinetics of the membrane resealing which is in the range of minutes[39,40]. It can be noticed that the variability of the PC1 scores of the control group is higher at 37°C than at 4°C. At 37°C, the cellular metabolism is active and thus it induces additional sources of variability in the Raman signatures that is not present at 4°C. When the cells were pulsed under irreversible permeabilization conditions, the control and the pulsed were always statistically significant for the different temperature conditions (p-value < 0.01%) (figure 5.B). Our results fit with the literature because irreversible permeabilization corresponds to the impossibility to the cells to reseal the membrane after the delivery of PEF[41].

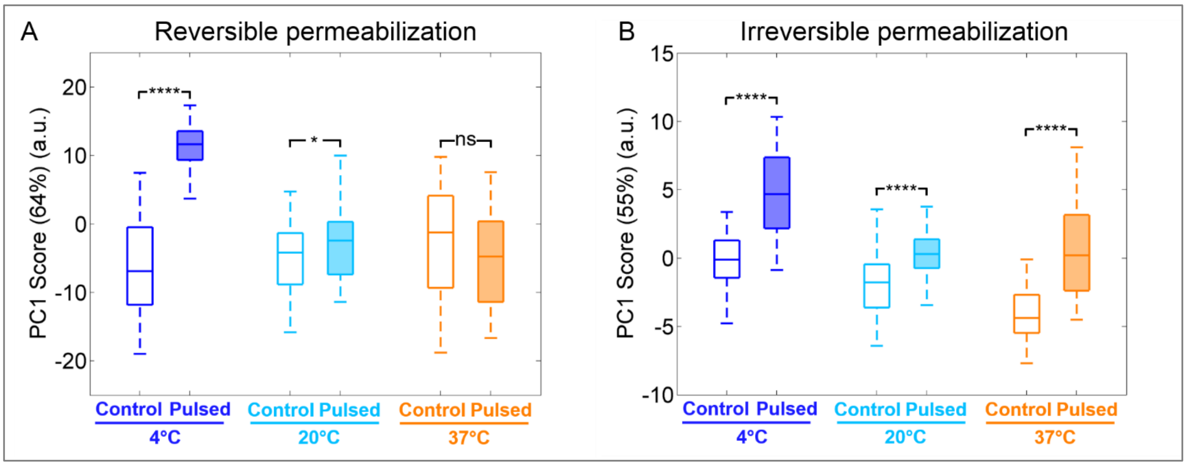

Figure 5: PCA results of the effect of temperature (4, 20 and 37°C) on the Raman signatures of live haMSC cells exposed to PEF in a reversible (A) and irreversible (B) condition. The reversible and irreversible permeabilization states were identified based on the Yo-Pro-1 fluorescence dye uptake after 10 minutes and 50 minutes, respectively, after the delivery of the electric pulses. The PEF parameters were fixed to 8 pulses with a duration of 100 µs at a repetition rate of 1 Hz. The electric field magnitudes were 1000 V/cm and 1500 V/cm in the case of the reversible and the irreversible permeabilization, respectively. The control group underwent sham exposure. The Raman signatures of haMSC cells were acquired at the cathode ROI. The sample temperature was fixed during all the experiments. Student's *t*-test: ns (non-statistically significant): p-value > 5%, *: p-value ≤ 1%, ****: p-value ≤ 0.01%.

Investigations on another cell type

In order to investigate the potential cell-dependency of the effect of PEF on the Raman signatures of cells, we acquired the Raman signatures of live LPB cells exposed or not to PEF. Figure 6.A shows the mean Raman signatures of LPB exposed or not to electric pulses. The differential spectrum (pulsed minus control) demonstrated the effect of PEF on the Raman signatures of LPB cells. Vibrational peaks at 1003, 1033, 1449, 1605 and 1650 cm^{-1} were modified by the delivery of electric pulses. It can be noted that the general magnitude of the differential LPB Raman spectrum was lower than the general magnitude of the differential haMSC Raman spectra. It would indicate that the effects of PEF on the biochemical composition were smaller in the case of LPB cell line. This might be due to different permeabilization level in the case of LPB and haMSC under our experimental conditions. Baseline differences between the control and the pulsed mean spectra were noticed and attributed to imperfection in the baseline removal data preprocessing. Even if the differences were smaller in the LPB cell line that in haMSC, it can be noticed that 1003, 1033, 1449 and 1650 cm^{-1} Raman peaks were modified by the delivery of PEF in both cell lines. The evolution of these peaks was not similar in haMSC and LPB cells. For instance, the magnitude of 1003 cm^{-1} Raman peak increased when comparing the Raman signatures of pulsed LPB *versus* unpulsed LPB; while it decreased when comparing the Raman signatures of pulsed haMSC *versus* unpulsed haMSC. These results demonstrate that the differences in the Raman signatures of live cells exposed or not to PEF were cell-dependent. Figure 6.B and 6.C shows the PCA results. PC2 was selected instead of PC1, which did not support any variance related to the effect of the PEF on LPB cells. PC2 loading displayed a peak at 1003 and 1660 cm^{-1}. The other patterns were attributed to imperfect baseline removal. By plotting PC2 score per group, strong significantly statistically differences were found between the pulsed and the control group. Although the p-value was smaller than 0.01%, the effect of PEF on the Raman signatures of LPB cells seems to be lower than on the Raman signatures of haMSC cells. LPB cells are smaller than haMSC cells and cell size is known to affect the permeabilization level[42]. The smaller cells are less sensitive to electric fields. Thus, our results fit with the literature.

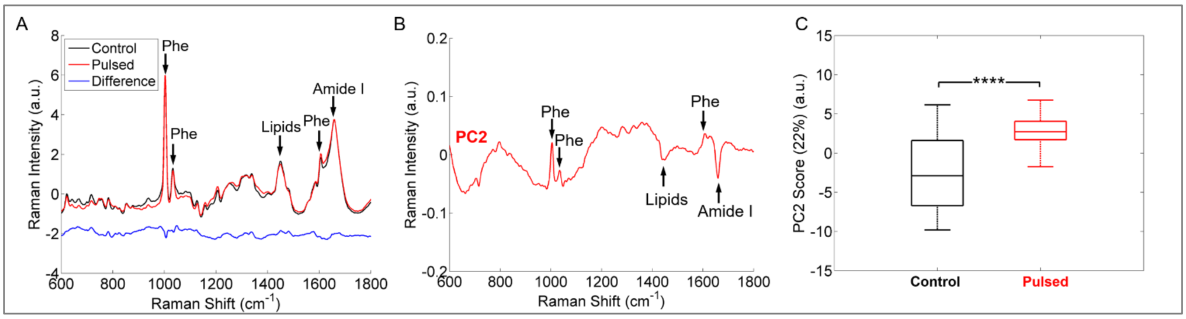

Figure 6: Analysis of the Raman signatures of LPB cells exposed or not to pulsed electric fields. A – Mean normalized Raman signatures of pulsed and control LPB cells. The differential spectrum (pulsed minus control) is also displayed. For more clarity, differential spectrum is displayed with vertical offset. B – Loading of PC2 from the PCA analysis performed on the control and the pulsed data set. C – Score of PC2 for the control and the pulsed groups. The percentage of variance supported by the PC2 is indicated in brackets. The pulsed electric fields parameters were fixed to 8 pulses with a duration of 100 µs, an electric field magnitude of 1000 V/cm and a repetition rate of 1 Hz. The control group underwent sham exposure. The Raman signatures of LPB cells were acquired at the cathode ROI. The arrows indicate the position of phenylalanine (Phe), lipids and amide I Raman peaks. Student's *t*-test: ****: p-value ≤ 0.01%.

CONCLUSION

In this study, we report an extended characterization of the effect of PEF on the Raman signatures of live cells. Our results show that the biochemical composition of cells exposed to PEF was modified uniformly at the different localization around the nucleus probed. Although the impact of PEF on proteins and lipids were proved for different electric pulses parameters, no obvious dose-effect response was detected in contrary to fluorescence microscopy results. We might speculate that Raman microspectroscopy is sensitive to the permeabilization state of cells and not the permeabilization level. The resealing of the membrane was indirectly assessed by tuning the cellular metabolism via the temperature. Finally, the effect of PEF on the biochemical of cells appears to be cell-dependent even if common features were noticed between the two cell types used. This study reports an extension of our first proof of concept publication[11] and provide new critical information at the molecular level of the interaction between PEF and live cells.

AUTHOR INFORMATION

Corresponding Author

* Lluis M. Mir. e-mail; luismir@cnrs.fr. tel: (0033) 142114792

Author Contributions

A.A, C.M and V.U performed the Raman experiments. A.A and L.D performed the fluorescence experiments. A.A performed the multivariable analyses under the supervision of C.G. A.A and L.D performed the fluorescence data analyses. This study was supervised by O.P and L.M.M. The manuscript was written by A.A through contributions of all authors. All authors have given approval to the final version of the manuscript.

Notes

The authors declare no competing financial interest.

ACKNOWLEDGMENT

The authors would like to thank Ecole Normale Supérieure de Cachan, CNRS, Gustave Roussy, Univ. Paris-Sud, Université Paris-Saclay and Fondation EDF for financial support of this work. This study was also supported by the IBiSA Cellular and Tissular Imaging Platform (PICT). This study was conducted in the scope of LEA EBAM (European Laboratory of Pulsed Electric Fields Applications in Biology and Medicine)

REFERENCES

((1) Tsong, T. Y. Y. *Biophys. J.* **1991**, *60* (2), 297–306.

(2) Chen, C.; Smye, S. W. W.; Robinson, M. P. P.; Evans, J. A. A. *Med. Biol. Eng. Comput.* **2006**, *44* (1–2), 5–14.

(3) Stampfli, R. *Ann. Acad. Bras. Cien.* **1958**, *30*, 57–63.

(4) Yarmush, M. L.; Golberg, A.; Serša, G.; Kotnik, T.; Miklavčič, D. **2014**.

(5) Raso, J.; Heinz, V. *Pulsed electric fields technology for the food industry : fundamentals and applications*; Springer, 2006.

(6) Breton, M.; Mir, L. M. *Bioelectromagnetics* **2012**, *33* (2), 106–123.

(7) Breton, M.; Mir, L. M. In *1st World Congress on Electroporation and Pulsed Electric Fields in Biology, Medicine and Food & Environment Technologies*; 2015; p 4.

(8) Wong-Ekkabut, J.; Xu, Z.; Triampo, W.; Tang, I.-M.; Tieleman, D. P.; Monticelli, L. *Biophys. J.* **2007**, *93* (12), 4225–4236.

(9) Volinsky, R.; Kinnunen, P. K. J.; Kinnunen, P. K. J. *FEBS J.* **2013**, *280* (12), 2806–2816.

(10) Vernier, P. T.; Levine, Z. a.; Wu, Y. H.; Joubert, V.; Ziegler, M. J.; Mir, L. M.; Tieleman, D. P. *PLoS One* **2009**, *4* (11).

(11) Azan, A.; Untereiner, V.; Gobinet, C.; Sockalingum, G. D.; Breton, M.; Piot, O.; Mir, L. M. *Sci. Rep.* **2017**, *7*, 297–306.

(12) Savitzky, A.; Golay, M. J. E. *Anal. Chem.* **1964**, *36* (8), 1627–1639.

(13) Notingher, I.; Bisson, I.; Bishop, A. E.; Randle, W. L.; Polak, J. M. P.; Hench, L. L. *Anal. Chem.* **2004**, *76* (11), 3185–3193.

(14) Barnes, R. J.; Dhanoa, M. S.; Lister, S. J. *Appl. Spectrosc. Vol. 43, Issue 5, pp. 772-777* **1989**, *43* (5), 772–777.

(15) Wold, S.; Esbensen, K.; Geladi, P. *Chemom. Intell. Lab. Syst.* **1987**, *2* (1–3), 37–52.

(16) Wold, S.; Sjöström, M.; Eriksson, L. *Chemom. Intell. Lab. Syst.* **2001**, *58* (2), 109–130.

(17) Chan, J. W.; Lieu, D. K.; Huser, T.; Li, R. A. *Anal. Chem.* **2009**, *81* (4), 1324–1331.

(18) Gao, Y.; Xu, C.; Wang, L. *RSC Adv.* **2016**, *6* (66), 61771–61776.

(19) Unterreitmeier, S.; Fuchs, A.; Schäffler, T.; Heym, R. G.; Frishman, D.; Langosch, D. *J. Mol. Biol.* **2007**, *374* (3), 705–718.

(20) Maiti, N. C.; Apetri, M. M.; Zagorski, M. G.; Carey, P. R.; Anderson, V. E. *J. Am. Chem. Soc.* **2004**, *126* (8), 2399–2408.

(21) Farhane, Z.; Bonnier, F.; Maher, M. A.; Bryant, J.; Casey, A.; Byrne, H. J. *J. Biophotonics* **2016**.

(22) Meade, A. D.; Clarke, C.; Draux, F.; Sockalingum, G. D.; Manfait, M.; Lyng, F. M.; Byrne, H. J. *Anal. Bioanal. Chem.* **2010**, *396* (5), 1781–1791.

(23) Schwan, H. P. *Biological Effects and Dosimetry of Nonionizing Radiation*; Grandolfo, M., Michaelson, S. M., Rindi, A., Eds.; Springer US: Boston, MA, 1983.

(24) Kotnik, T.; Pucihar, G.; Miklavcic, D. *J. Membr. Biol.* **2010**, *236* (1), 3–13.

(25) Berg, J. M.; Tymoczko, J. L.; Stryer, L. In *Biochemistry, Fifth Edition*; Berg, J. M., Tymoczko, J. L., Stryer, L., Eds.; W. H. Freeman: New-york, 2002.

(26) Leguèbe, M.; Silve, A.; Mir, L. M.; Poignard, C. *J. Theor. Biol.* **2014**, *360*, 83–94.

(27) Freudiger, C. W.; Min, W.; Saar, B. G.; Lu, S.; Holtom, G. R.; He, C.; Tsai, J. C.; Kang, J. X.; Xie, X. S. *Science* **2008**, *322* (5909), 1857–1861.

(28) Camp Jr, C. H.; Lee, Y. J.; Heddleston, J. M.; Hartshorn, C. M.; Walker, A. R. H.; Rich, J. N.; Lathia, J. D.; Cicerone, M. T. *Nat. Photonics* **2014**, *8* (8), 627–634.

(29) Escoffre, J. M.; Bellard, E.; Faurie, C.; Sébaï, S. C.; Golzio, M.; Teissié, J.; Rols, M. P. *Biochim. Biophys. Acta - Biomembr.* **2014**, *1838* (7), 1701–1709.

(30) Vernier, P. T.; Sun, Y.; Marcu, L.; Craft, C. M.; Gundersen, M. A. *Biophys. J.* **2004**, *86* (6), 4040–4048.

(31) Tolstykh, G. P.; Beier, H. T.; Roth, C. C.; Thompson, G. L.; Ibey, B. L. *Bioelectrochemistry* **2014**, *100*, 80–87.

(32) Hanna, H.; André, F. M.; Mir, L. M. In *1st World Congress on Electroporation and Pulsed Electric Fields in Biology, Medicine and Food & Environment Technologies*; 2015; p 82.

(33) Rols, M.-P.; Teissié, J. *Biophys. J.* **1998**, *75* (3), 1415–1423.

(34) Pucihar, G.; Mir, L. .; Miklavčič, D. *Bioelectrochemistry* **2002**, *57* (2), 167–172.

(35) Silve, A.; Guimerà Brunet, A.; Al-Sakere, B.; Ivorra, A.; Mir, L. M. *Biochim. Biophys. Acta - Gen. Subj.* **2014**, *1840* (7), 2139–2151.

(36) Knaduser, M.; Sentjurc, M.; Miklavcic, D. In *11th Mediterranean Conference on Medical and Biomedical Engineering and Computing 2007*; Springer Berlin Heidelberg: Berlin, Heidelberg, 2007; pp 570–573.

(37) Teissié, J.; Rols, M. P. *Biophys. J.* **1993**, *65* (1), 409–413.

(38) Lopez, A.; Rols, M. P.; Teissie, J. *Biochemistry* **1988**, *27* (4), 1222–1228.

(39) Bier, M.; Hammer, S. M.; Canaday, D. J.; Lee, R. C. *Bioelectromagnetics* **1999**, *20* (3), 194–201.

(40) Saulis, G.; Venslauskas, M. S.; Naktinis, J. *J. Electroanal. Chem. Interfacial Electrochem.* **1991**, *321* (1), 1–13.

(41) Wagstaff, P.; Buijs, M.; van den Bos, W.; de Bruin, D.; Zondervan, P.; de la Rosette, J.; Laguna, P. *Onco. Targets. Ther.* **2016**, *9*, 2437.

(42) Agarwal, A.; Zudans, I.; Weber, E. A.; Olofsson, J.; Orwar, O.; Weber, S. G. *Anal. Chem.* **2007**, *79* (10), 3589–3596.

Comprehensive Characterization of the Interaction between Pulsed Electric Fields and Live Cells by Confocal Raman Microspectroscopy

Antoine Azan[†], Valérie Untereiner[§,#], Lucie Descamps[†], Caterina Merla[†], Cyril Gobinet[§], Olivier Piot[§,#], and Lluis M. Mir[†,*]

[†] Vectorology and Anticancer Therapies, UMR 8203, CNRS, Gustave Roussy, Univ. Paris-Sud, Université Paris-Saclay, 94805 Villejuif, France

[§] MeDIAN, Biophotonics and Technologies for Health, MEDyC, UMR 7369, CNRS, University of Reims Champagne-Ardenne, 51096 Reims, France

[#] Cellular and Tissular Imaging Platform (PICT), Faculty of Pharmacy, University of Reims Champagne-Ardenne, 51096 Reims, France

SUPPLEMENTARY INFORMATION

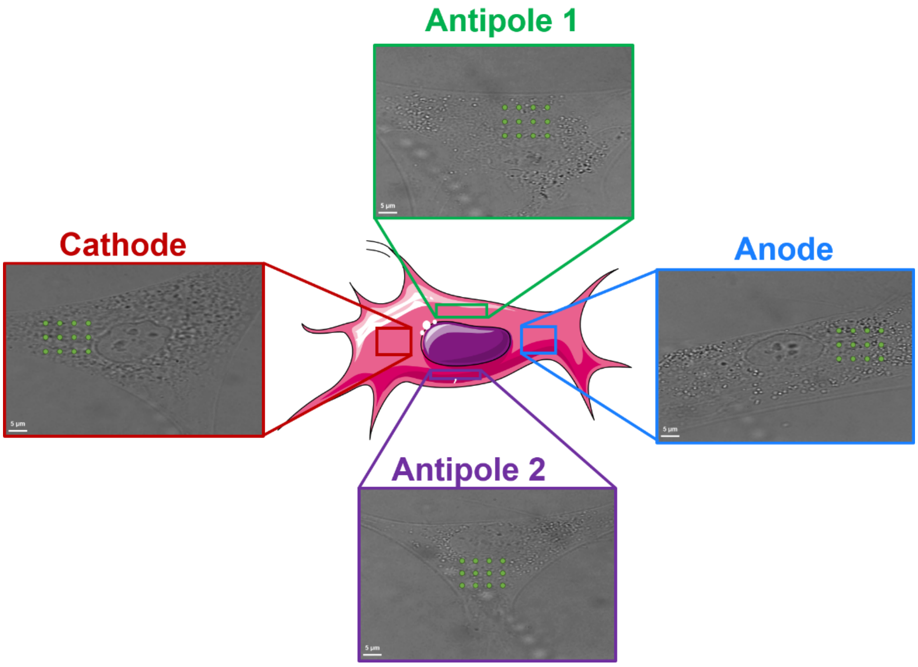

Figure S1: Illustration of the different ROIs analyzed by confocal Raman microspectroscopy. The green dots represent the spots where the Raman signatures were acquired. This schematic is adapted from Servier Medical Art.

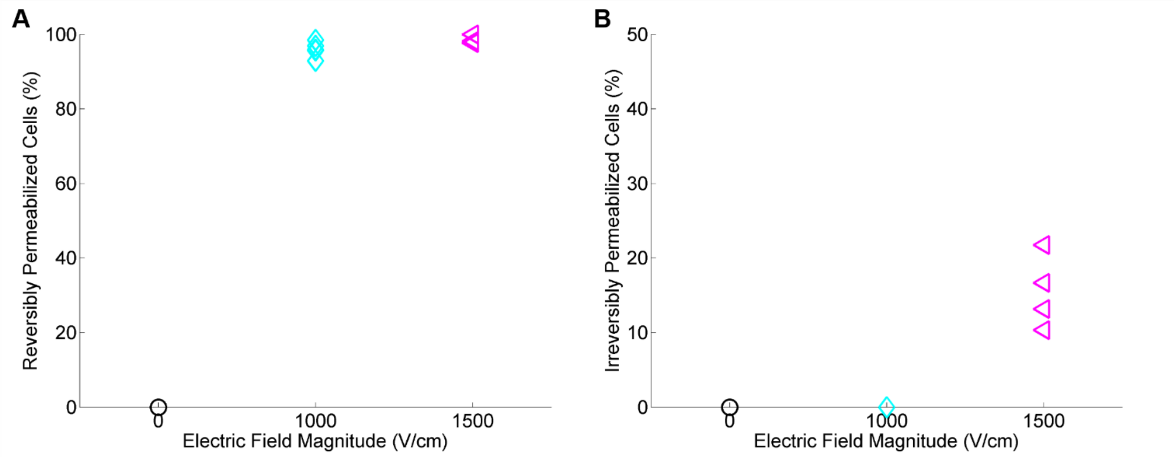

Figure S2: Determination of the reversible and irreversible permeabilization conditions via Yo-Pro-1 uptake in fluorescence microscopy. A - Percentage of cells reversibly permeabilized. B -Percentage of cell irreversibly permeabilized. The control group underwent sham exposure. The reversible and irreversible permeabilization states were identified based on the Yo-Pro-1 fluorescence dye uptake after 10 minutes and 50 minutes, respectively, after the delivery of the electric pulses. The electric field magnitude was fixed to 0, 1000 or 1500 V/cm. The others The other pulsed electric fields parameters were fixed to 8 pulses with a duration of 100 µs at a repetition rate of 1 Hz.

6.3 Discrimination between the Different Electropermeabilization States based on the Raman Signatures of Live Cells (article #3)

Electropermeabilization is not a linear process. Depending on the electric pulse parameters, the plasma membrane can reach three different states: not detectable permeabilization, reversible permeabilization or irreversible permeabilization. It has be noted that the determination of permeabilizing threshold is dependent on the membrane permeabilization marker properties and concentration. In the case of reversible permeabilization, the membrane repair cell mechanisms are able to reseal the plasma membrane to its basal state. In the case of irreversible permeabilization state, the membrane repair mechanisms are not sufficient to reseal the plasma membrane and the cell will dye. The underlying mechanisms of the transition from the reversible to the irreversible electropermeabilization states are poorly studied. In previous works, we have demonstrated that the Raman signatures of live cells could be used as a biomarker of EPN and we have confirmed that the delivery of PEFs on cells triggers chemical reactions. This study aims to compare the Raman signatures of live haMSC cells belonging to the different states listed abobe. A discriminative algorithm based on RF was designed on the Raman signatures acquired at two different vibrational frequency regions (FP: 600 – 1800 cm^{-1} and HWN: 2800 - 3100 cm^{-1}) of live haMSC cells in the three states. The discriminative powers were quantitatively and qualitatively compared.

This work is in the continuity of the articles #1 and #2. It has been conducted in collaboration with the laboratory MEDyC (UMR 7369, CNRS, university of Reims Champagne-Ardenne) headed by Pr. Olivier Piot. The Raman and fluorescence experiments have been performed, respectively, at MEDyC and UMR 8203. The publication related to this work is currently under careful internal reading before being submitted for publication as soon as possible.

Discrimination between the Different Electropermeabilization States based on the Raman Signatures of Live Cells

Antoine Azan[†], Louis H. Liu[§], Lucie Descamps[†], Valérie Untereiner[§,#], Cyril Gobinet[§], Olivier Piot[§,#], and Lluis M. Mir[†,*]

[†] Vectorology and Anticancer Therapies, UMR 8203, CNRS, Gustave Roussy, Univ. Paris-Sud, Université Paris-Saclay, 94805 Villejuif, France

[§] MeDIAN, Biophotonics and Technologies for Health, MEDyC, UMR 7369, CNRS, University of Reims Champagne-Ardenne, 51096 Reims, France

[#] Cellular and Tissular Imaging Platform PICT, Faculty of Pharmacy, University of Reims Champagne-Ardenne, 51096 Reims, France

ABSTRACT: Electropermeabilization consists in the destabilization of the plasma membrane based on the delivery of pulsed electric fields. Based on the electric pulse parameters, electropermeabilization can be reversible or irreversible. In this study, we sought at investigating the different electropermeabilization based on the Raman signatures of live cells. A multivariable analysis succeeded to discriminate the Raman signatures of cells under the different electropermeabilization states. The analysis of the discriminant models revealed that lipids were highly involved in the discrimination between the reversible and the irreversible electropermeabilization states. For the first time, we report that the pulsed electric fields induced different biochemical modifications on live cells based on the electropermeabilization state induced.

INTRODUCTION

The permeabilization of the plasma membrane by the delivery of pulsed electric fields (PEFs) is an elegant physical method to deliver non-permeant molecules into the cells (Poddevin et al. 1991). Many biomedical applications have developed based on the electropermeabilization (EPN) phenomenon. For instance, electrochemotherapy (ECT) consists in the combination of EPN of tumor cells and chemotherapy (Marty et al. 2006). ECT allows to significantly increase the efficiency of the drugs. Based on the electric pulses parameters, different EPN states can be induced: reversible or irreversible EPN. Reversible EPN is associated with a transient permeabilization state, meaning that membrane repair mechanism allows to reseal the plasma membrane impermeability. In the case of irreversible EPN, cell metabolisms are not able to overcome the damages induced by the delivery of electric pulses (Wagstaff et al. 2016). Irreversible EPN has also been used in clinics to treat tumors cells (Ivorra and Rubinsky 2010; Rubinsky 2007). Although reversible EPN has been extensively studied for decades (Chen et al. 2006), the underlying mechanisms of irreversible EPN has been poorly understood. Long-lasting pores creation has been suggested (Weaver et al. 1996) but does not seem to be the main mechanisms involved in irreversible EPN.

Recently the hypothesis of chemical modifications of the plasma membrane due to the exposure to electric pulses has been investigated as the major mechanism of cell EPN. Numerical model demonstrated that the presence of peroxidized lipids reduces significantly the impermeability to a lipid bilayer (Van der Paal et al. 2016). This might be related to the 20% decrease in the thickness of a lipid bilayer including peroxidized lipids in comparison to a lipid bilayer without peroxidized lipids (Wong-Ekkabut et al. 2007). Vernier *et al.* demonstrated that PEFs and oxidative stress have synergetic effect in the level of EPN (Vernier et al. 2009). An experimental study performed on a simple membrane model, Giant Unilamellar Vesicles (GUVs), demonstrated a significant increase in the percentage of peroxidized lipids in GUVs exposed to PEFs (Breton and Mir 2015). Finally, a previous publication by our groups emphasized the chemical damages induced by the delivery of electric pulses on live cells thanks to the modifications of Raman signatures of live cells (Azan et al. 2017).

This publication reports the opportunity to use the Raman signature of cell as a non-invasive and label-free biomarker of EPN. Confocal Raman microspectroscopy is a widely optical methods allowing to have to detailed information about the biomolecular of the sample (Downes and Elfick 2010). The Raman signatures of cells were already used to investigate the biochemical consequences of external stress, such as drugs , on live cells (Farhane et al. 2016).

Thus, we sought at investigating the opportunity to use confocal Raman microspectroscopy to discriminate the different EPN states.

MATERIALS AND METHODS

Cell culture

Primary human-adipose derived Mesenchymal Stem Cell (haMSC) were grown in a humidified atmosphere at 37°C and 5% CO2 in Dulbecco's Modified Eagle Medium (DMEM) supplemented with 10 % fetal bovine serum and 1 % of penicillin streptomycin (Life Technologies, Cergy-Pontoise, France). For the experiments, 5 000 cells/cm^2 were plated in a 35 mm Petri dish (Thermo Fisher Scientific, Illkirch, France) in which a CaF_2 window (Crystran, Poole, United Kingdom) was placed at the bottom. The cells were incubated overnight and attached to the CaF_2 window before performing the Raman or fluorescence experiments.

Pulse generator and pulses condition

A commercially available generator (Cliniporator, IGEA, Italy) was used to treat the cells. To deliver the electric pulses on attached cells, two stainless steel plate electrodes spaced by 4 mm were used. The Cliniporator was connected to the plate electrodes with alligator clips. Before delivering the electric pulses, the complete culture medium was removed and replaced by physiological water, NaCl 0.9%, (B. Braun, Boulogne-Billancourt, France) after washing twice with phosphate-buffered saline (PBS). Before addition to the Petri dish, the physiological water was stored at 4 °C. The electric pulses parameters were depending on the experiments performed.

Raman Measurements

The equipment and its configuration was previously detailed in Azan *et al.* (2017)[1]. Briefly, a confocal Raman microscope LabRam ARAMIS (Horiba Jobin Yvon, Villeneuve d'Ascq, France) was used to acquire the Raman spectra of live cells. The samples were excited with a 532 nm continuous wave laser through a 100 X water immersion objective (LUMPLFL 100X/W, Olympus, Rungis, France). The Raman signatures of the samples were acquired in the fingerprint region (FP) (600 – 1800 cm^{-1}) and high wavenumber region (HWN) (2800 – 3030 cm^{-1}) with an exposure time fixed to 60 and 20 seconds, respectively. The Raman signatures of live cells were acquired at a specific Regions Of Interest (ROI), termed: cathode. The cathode ROI was the area of the cell between the nucleus and the edge of the cell facing the cathode of the pulse generator. Each Raman experiment lasted one-hour maximum in order to preserve cells viability. During all the acquisitions, the samples were maintained at a 4°C by T95 system controller (Linkam Scientific Instrument Ltd, Tadworth, UK). The acquisition of the Raman signatures of cells were started less than 1 minute after the delivery of the electric pulses.

Raman data pre-processing and processing

The pre-processing method is detailed in Azan *et al.* (2017)[1]. Briefly, after removing the spectrum with a signal-to-noise ratio lower than 10, data pre-processing consisted in Savitsky-Golay smoothing[2], removal of physiological water signal, baseline subtraction and normalization by the standard normal variance method[3,4].

An univariate analysis was first performed to investigate the spectral differences between the reversible EPN and control groups and between the irreversible and reversible EPN states. Thus, the Raman data set were splitted into three groups, termed control, reversible and irreversible. The control group consisted in the Raman spectra of haMSC cells underwent sham exposure condition. The reversible group was the Raman spectra of haMSC cells exposed to 750 and 1000 V/cm. The irreversible group was combining the Raman spectra of haMSC cells exposed to 1500 V/cm. For these three groups, an average Raman spectrum was calculated based on the pre-processed spectra. Spectral differences between the reversible and control groups and between the irreversible and reversible groups were assessed by creating difference spectra. Difference spectra were calculated by subtracting the Raman spectra of one group to the average Raman spectrum of the to be compared group. For instance, the reversible Raman spectra were subtracted to the average control Raman spectrum in the case of reversible versus control comparison. Same procedure was performed in the framework of the comparison between the irreversible and reversible group. The mean differential spectrum was calculated based on the difference spectra. This univariate analysis was performed for the two spectral bands: FP and HWN.

Then, a multivariable discriminative analysis was performed based on Random Forest (RF) in order to discriminate the control to the EPN states of cells and the reversible EPN to the irreversible EPN states. For these two discriminations, the Raman data set was splitted in four groups. The control, the reversible and the irreversible groups are the same as for the univariate analysis. The last group combined the reversible and irreversible groups. RF was used as a classifier to split the Raman signatures of cells into groups related to the different EPN states. RF is a well-known machine learning method widely used in classification. RF consists in an ensemble of decision trees, each decision tree can be considered as a classifier. Like most of supervised machine learning methods, RF needs to be trained on a labelled data set before being used in classification on an unlabelled data set. During training, the data were randomly sampled in order to construct a decision tree. For each decision tree, the training data was progressively split into smaller subsets, aka node in the structure, with higher homogeneity in class label. The variable used at each split was chosen based on certain criteria. One of these criteria was the Gini impurity, measuring the impurity of the output subsets after split. A zero Gini impurity implies a perfectly pure subset. As decision tree aims at dividing the data into more and more homogeneous subset, the variable with the smallest Gini impurity index at each stage was selected for the splitting. The splitting process continued until the subset was entirely homogenous, or the maximal number of split was attained. The final nodes at the extremities of a tree were called leaves. They were labeled by the major class in the final subsets of splits. For classifying a new data, the data was input into the trees with different structures. Then, each structure led the data to one of the leaves in that tree, according to comparison results at each splitting node. The label of the leaf the data arrived at is the class output produced by that tree. RF aggregated the results of all the decision trees, and took the mode as the final result for classification. In order to examine the discriminate power of RF in our classification problem, we carried out a 100-iteration repeated randomly sampling cross-validation, with training test set split ratio at 70:30.

In addition, it is worth noting that RF can rank the importance of the variables used for classification problem in a natural way. Every time a subset was split on a variable (wavenumber), the Gini impurity for the two child subsets was less than the parent one. This was because the dataset was gradually being sorted into predicted classes, and becoming more homogeneous with respect to the precedent subsets. Thus, the Gini impurity continued to decrease with the split. When a parent subset α was split into two child subsets β and γ, the change in Gini (Δg) was calculated by the equation below:

$$\Delta \boldsymbol{g} = \boldsymbol{g}(\boldsymbol{\alpha}) - \left(\frac{\boldsymbol{n_\beta}}{\boldsymbol{n}}\right) \boldsymbol{g}(\boldsymbol{\beta}) - \left(\frac{\boldsymbol{n_\gamma}}{\boldsymbol{n}}\right) \boldsymbol{g}(\boldsymbol{\gamma})$$

where the n, n_β and n_γ were the numbers of spectra in the subsets α, β and γ, respectively. The value of Δg was larger when a greater change in impurity occurred after the split, thus allowing for the decrease in Gini to be used as a measure of importance of a certain wavenumber in classification using one decision tree. Thus, the overall Gini importance (G) of one particular spectral variable θ in a Random Forest was estimated by the sum of its Gini impurity decrease across all the splits among all the decision trees in the forest.

$$\boldsymbol{G}(\boldsymbol{\theta}) = \sum_{i=1}^{N} \sum_{j=1}^{K} \Delta \boldsymbol{g}_{i,j}$$

where K was the number of splits using the variable θ in one decision tree, N was the number of trees in the forest.

Finally, the general discriminant power of one spectral variable was estimated by the mean Gini importance averaged over 100 iterations of cross-validation, as shown in the figures in the further section.

All data-processing and data-analysis were performed under MATLAB (MathWorks, Meudon, France).

Fluorescence Microscopy

Fluorescence microscopy was used to quantify the level of reversible and irreversible electropermeabilization based on the uptake of Yo-Pro-1 (Life technologies) at different times after the delivery of the electric pulses.

To do so, 2 channels fluorescence images (blue for Hoechst 33342 $\lambda_{emission}$=450 nm, green for Yo-Pro-1 $\lambda_{emission}$=510 nm) were acquired. The blue channel image was used to define a mask specific to the nucleus of each cell in the field of view. This mask was applied to the green channel image in order to assess specifically the Yo-Pro-1 fluorescence intensity into the nuclei. The extraction of the Yo-Pro-1 fluorescence intensity per cell nucleus was performed on FIJI software (ImageJ, version 1.50g). A cell was considered as permeabilized if its Yo-Pro-1 fluorescence intensity was higher than the maximum of the Yo-pro-1 fluorescence intensity of all the cells in the control group. Thus, the percentage of cells permeabilized to Yo-Pro-1 by the delivery of electric pulses have been quantified.

Cells were incubated with 370nM of Hoechst 33342 in the culture medium for 30 minutes before the experiments. The culture medium containing the Hoechst 33342 was removed. The cells were washed two times with PBS before adding fresh culture medium. Less than one minute before the delivery of the electric pulses, the culture medium was removed and replaced by physiological water with or without 1 µM of Yo-Pro-1 in the case of respectively reversible or irreversible electropermeabilization experiments.

In the case of reversible permeabilization experiments, images were acquired 10 minutes after the delivery of the electric pulses. In the case of irreversible permeabilization experiments, the cells were put back in culture after the delivery of the PEFs and the replacement of the physiological water by fresh culture medium. After 40 minutes in the incubator, culture medium was replaced by physiological water with 1 µM of Yo-Pro-1. Then 10 minutes later, images were acquired. In final, images were acquired 50 minutes after the delivery of the electric pulses.

Images were acquired with an Observer Z1 inverted microscope (Zeiss, Marly-le-Roi, France). The exposure time was fixed to 50 ms (phase contrast images) or 300 ms (fluorescence images, either in the blue or green channel). For each condition, at least 4 independent ROIs were acquired in order to get robust data set.

RESULTS AND DISCUSSION

Determination of the reversible and irreversible permeabilization thresholds

Figure 1 shows the results of the reversible (A) and irreversible (B) electropermeabilization fluorescence experiments for the different electric field magnitudes. The haMSC cell fluorescence intensity of the control and the 500 V/cm groups were respectively 165.6 +/- 3.2 and 161.5 +/-5.5. There was no statistically significant difference between the two groups, showing that the cells were not permeabilized to Yo-Pro-1 under the 500 V/cm electric field exposure. For an electric field magnitude above 750 V/cm, the cell fluorescence intensity was statistically significantly different than the cell fluorescence intensity of the control group (p-value < 0.01%). At 750 V/cm, the percentage of permeabilized cells was 91.6 +/- 5.1 %. Hence, the reversible electropermeabilization threshold of Yo-Pro-1 can be estimated between 500 V/cm and 750 V/cm under our experimental conditions. Above this reversible electropermeabilization threshold, the cell fluorescence intensity increased with the electric field magnitude as reported in the literature (Rols and Teissié 1998; Pucihar et al. 2008). For the experimental conditions above the reversible electropermeabilization threshold, the coefficient of linear regression between the electric field magnitude and the cell fluorescence intensity was 21.2% emphasizing that the dose-effect relationship between the level of electropermeabilization and the electric field magnitude is a complex process. By quantifying the uptake of Yo-Pro-1 50 minutes after the delivery of the electric pulses, the irreversible electropermeabilization threshold was determined between 1250 V/cm and 1500 V/cm (Figure 1-B). None cell was found irreversibly permeabilized for an electric field magnitude below 1000 V/cm. At 1500 V/cm, 15.0 +/- 5.1 % of the cells was irreversibly electropermeabilized under our experimental conditions. The 1250 V/cm experimental condition was at the border to the irreversible electropermeabilization threshold. The reversible and irreversible electropermeabilization thresholds were indicated respectively by grey dashed and dotted lines in the Figure 1.

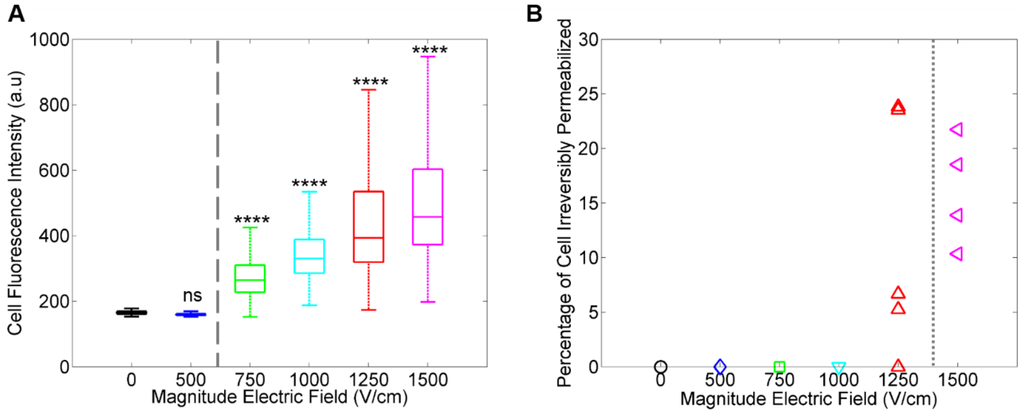

*Figure 1: **Determination of the reversible and irreversible permeabilization threshold based on fluorescence microscopy**. A – Yo-Pro-1 fluorescence intensity per group. The grey dashed line indicates the reversible electropermeabilization threshold. B – Percentage of electropermeabilized haMSC cells per group based on the Yo-Pro-1 uptake. The grey dotted line indicates the irreversible electropermeabilization threshold. The electric field magnitude applied was 0, 500, 750, 1000, 1250 or 1500 V/cm. The other pulsed electric fields parameters were fixed to 8 pulses with a duration of 100 µs at a repetition rate of 1 Hz. The control group underwent sham exposure. Student's t-test: ns (non-statistically significant): p-value > 5%, **: p-value ≤ 1%, ****: p-value ≤ 0.01%.*

Univariate analysis of the differences between the Raman signatures of control, reversible permeabilization and irreversible permeabilization

The Raman signatures of live haMSC cells were acquired at the different electric field magnitudes. Based on the reversible and irreversible electropermeabilization thresholds determined by fluorescence microscopy, three groups have been created: control, reversible and irreversible. The control group consisted in the Raman data set of the sham exposure. The reversible group consisted in the combination of the 750 and 1000 V/cm Raman spectra. Finally, the irreversible group was the 1500 V/cm Raman data set. The 1250 V/cm Raman data set was not included in any group due to its intermediate status between reversible and irreversible EPN state.

Figure 2 shows the mean Raman spectrum for the three groups and the two mean differential spectra associated. The standard deviation of the different data sets was also displayed. The Raman signatures of haMSC cells provided detailed information about proteins, lipids and amino-acids (Notingher et al. 2002). Information about the lipids and their environment are provided via the large Raman band between 2800 and 3000 cm^{-1} related to CH stretching vibrational modes (Larsson and Rand 1973). In a previous publication, we performed a tentative based assignment specific for the haMSC cells (Azan et al. 2017).

Major spectral differences were noticed between the reversible and the control groups in the FP spectral band (Figure 2-B). As a confirmation to our previous publication, Raman peaks related to proteins were significantly modified by the induced-reversible EPN (Azan et al. 2017). The magnitude of the vibrational peaks of phenylalanine at 623, 1003, 1033, 1205 and 1607 cm^{-1} is decreased in the reversible group compared to the control group. For instance, the magnitude of the 1003 cm^{-1} vibrational peaks of phenylalanine is about 16% lower in the reversible group than in the control group. Another vibrational study interpreted the decrease in the magnitude of the 1003 cm^{-1} Raman peak to protein leakage (Okuno et al. 2014). An increase in the magnitude amide I band around 1660 cm^{-1} by 33% was noticed when comparing the reversible group to the control group. An increase in amide I band is known to be related to a predominant unfolded state of proteins (Maiti et al. 2004). This experimental result confirms a recent numerical model study demonstrating that PEFs can induce the unfolding of membrane proteins (Cournia et al. 2015). A similar increase was also noticed in the amide III band around 1260 cm^{-1} also related to the secondary structure of proteins (Pelton and McLean 2000). Vibrational modes of lipids are also affected by the reversible-induced electropermeabilization. The lipids Raman peaks at 1308 cm^{-1} and around 1450 cm^{-1} are increased in the reversible group compare to the control group.

Figure 2-B shows also major spectral differences between the irreversible and the reversible group in the FP spectral band. On the one hands, some Raman bands share similar evolution between the two differential spectra, meaning irreversible minus reversible and reversible minus control. For instance, the magnitude of the vibrational peaks of phenylalanine at 623, 1003, 1033, 1205 and 1607 cm^{-1} is also decreased in the irreversible group compared to the reversible group. The magnitude of the amide I band at 1660 cm^{-1} is increased by 22% when comparing the irreversible group and the reversible group, like in the reversible versus control comparison. The evolution of these bands emphasized the major effect of PEFs on proteins at the different EPN states. On the other hand, the vibrational bands of lipids have opposite evolutions between the irreversible and reversible groups than between the reversible and control groups. The magnitude of the 1308 and 1450 cm^{-1} Raman bands is decreased when comparing the irreversible group to the reversible group; whereas the magnitude of these bands is increased in the reversible group compared to the control group. Thus, we might speculate that the effect of PEFs differs the lipids in the case of reversible-induced EPN and irreversible-induced EPN.

In order to investigate deeper this hypothesis, we performed similar experiments but in the HWN spectral band which is known to be highly related to the lipids (Zumbusch, Langbein, and Borri 2013). Figure 2-C shows the mean spectrum for the three groups. According to the literature, the 2850 cm^{-1} Raman peak is attributed to the symmetric stretching vibration of CH_2 of lipids, the 2875 cm^{-1} Raman peak is attributed to the asymmetric stretching vibration of CH_2 of lipids, the 2930 cm^{-1} Raman peak is attributed to the symmetric stretching vibration of CH_3 proteins, the 2970 cm^{-1} Raman peak is attributed to the asymmetric stretching vibration of CH_3 of proteins (Orendorff, Ducey, and Pemberton 2002; Wurpel, Schins, and Müller 2004; Larsson and Rand 1973; Santos et al. 2016). The differential spectrum between the reversible and the control groups does not show any obvious spectral modification between the two groups. The differential spectrum between the irreversible and the reversible groups presents obvious spectral modifications. First, the magnitude of the Raman peak at 2845 cm^{-1} is increased in the irreversible group compare to the reversible group. As a confirmation, the magnitude of the Raman peak at 1875 is also increased between these two groups but with a lower difference. Vibrational band of proteins are also modified when comparing the irreversible versus the reversible group. The magnitude of a large Raman band between 2945 and 2985 cm^{-1} is lower in the irreversible group compare to the reversible group. This might be due to the decrease of the 2970 cm^{-1} Raman peak which impact the global magnitude of this large band.

This univariate analysis demonstrates that specific Raman signatures are related to the three EPN states. The spectral modifications depend on the nature of the transition between the three states. Thus, we might conclude that the Raman signature of live cells is a biomarker of the EPN states. In order to investigate deeper this hypothesis, multivariable analysis was performed to discriminate first the control versus the permeabilization state, which combines the reversible and irreversible state and then to discriminate the reversible versus irreversible EPN state.

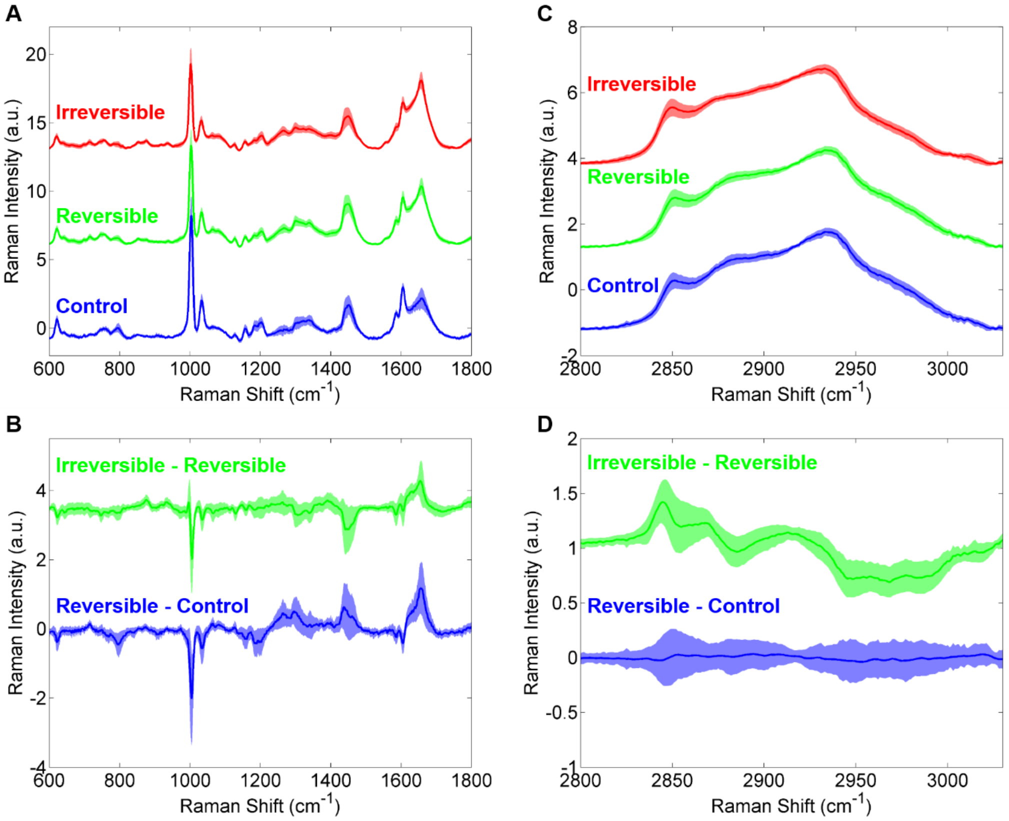

Figure 2: ***Univariate analysis of the Raman spectrum of the control (blue), reversible (green) and irreversible (red) groups****. Mean Raman spectrum in the FP (A) and HWN (C) regions for the three groups. Mean differential spectrum in the FP (B) and HWN (D) regions for the reversible versus the control groups (blue) and the irreversible versus the reversible groups (green). The standard deviation was plotted in shadow around the mean spectrum. The control group consisted in the Raman spectra of cells underwent sham exposure. The reversible group combined the Raman spectra of cells exposed to 8 pulses of 100 µs with a repetition rate of 1 Hz and an electric field magnitude of 750 or 1000 V/cm. The irreversible group was the Raman spectra of cells exposed to 8 pulses of 100 µs with a repetition rate of 1 Hz and an electric field magnitude of 1500 V/cm.*

Multivariate discriminative analysis

Table 1 shows the percentage of correct classification in each group for the two discriminations performed in the two spectral bands. The percentage of correct classification is higher in the discrimination reversible versus irreversible than in the discrimination no permeabilization versus permeabilization (95.5% versus 82.9%). This would indicate that the differences in the Raman signatures of the reversible group versus the Raman signatures of the irreversible group are statistically more significant than the differences in the Raman signatures of the no permeabilization group versus the Raman signatures of the permeabilization group. In the case of the no permeabilization versus permeabilization discrimination, the difference in the percentage of correct classification of the permeabilization group is 19.6% when comparing the results of the FP spectral band and the HWN spectral band (91.1 +/- 3.7 % versus 71.4 +/- 3.2%). This confirms our previous published results demonstrating that HWN spectral band is not suitable to investigate the effect of permeabilizing PEFs on live haMSC cells (Azan et al. 2017). In the reversible versus irreversible discrimination, the HWN spectral band allows a higher percentage of correct classification compare to the FP spectral band (98.3% versus 92.8%). As the HWN spectral band is highly related to the lipid composition, we might speculate that lipids play a key role in the discrimination between the reversible and the irreversible EPN state. Figure 4 displays the RF discriminant models of the two discriminations in the two spectral bands. The RF discriminant models confirm the results of the percentage of correct classification presented above. In the HWN spectral band, the percentage of correct classification is significantly higher in the reversible versus irreversible discrimination than in the no permeabilization versus permeabilization discrimination (98.3% versus 77.3%).

Correct classification (%)

	No Permeabilization vs Permeabilization		Reversible vs Irreversible	
	Control	Permeabilization	Reversible	Irreversible
FP	86 +/- 7,1	91,1 +/- 3,7	**94,8 +/- 4,4**	**90,8 +/-8,2**
HWN	83,1 +/- 4,4	71,4 +/- 3,2	**97,3 +/- 2**	**99,2 +/- 1**

Table 1: Discrimination results obtained on the testing data set for the different classifications performed on the FP and HWN spectral bands.

The RF discriminant model in the reversible versus irreversible discrimination displays obvious pattern with contribution of Raman peaks around 2840, 2920 and 2970 cm^{-1} (Figure 4-D); whereas the RF discriminant model in the no permeabilization versus permeabilization discrimination contains a large number of Raman peaks without any obvious contribution of one or several bands. The major Raman peak contributors of the reversible versus irreversible discrimination are related to lipid vibrational bands. For the same discrimination performed in the FP spectral band, the major Raman peal contributors are related to proteins and lipids. The protein contributions are related to the phenylalanine Raman peak at 622, 1003 and 1033 cm^{-1} and the proteins backbone at 938 cm^{-1}. The lipid contributions are based on the CH deformation at 1640 cm^{-1}. Figure 4-A shows the RF discriminant model of the no permeabilization versus permeabilization discrimination in the FP spectral band, which is mainly composed of proteins vibrational modes with the amide I band at 1650 cm^{-1} and phenylalanine band at 620 cm^{-1}. The Raman band around 800 cm^{-1} seems to be related to RNA contributions.

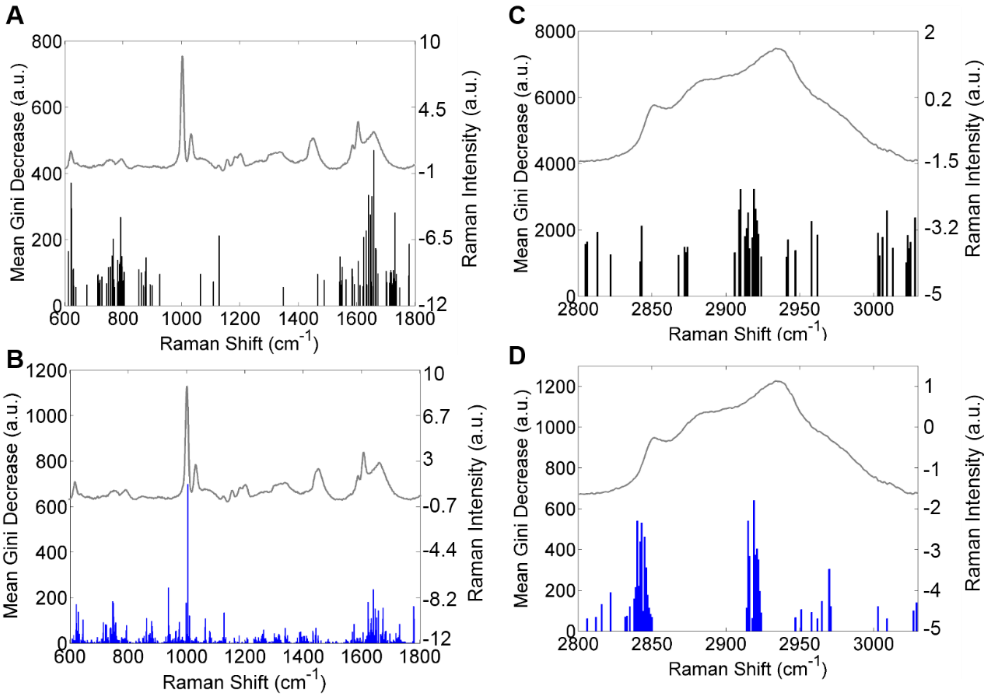

*Figure 3: **RF discrimination models**. The no-permeabilization versus permeabilization RF discrimination models are displayed in black bar in the FP (A) and HWN (C) vibrational bands. The reversible permeabilization versus irreversible permeabilization RF discrimination models are displayed in blue bar in the FP (B) and HWN (D) vibrational bands. To facilitate the interpretation of the discriminant models, a representative normalized Raman spectrum of haMSC cells is displayed (grey line) (A-D). The haMSC cell Raman spectrum is vertically offsetted for more clarity. The left y-axis is related to the RF discriminant model and the right y-axis to the Raman spectrum.*

CONCLUSION

For the first, we investigated the differences in the Raman signatures of live cells under different EPN states. Our results showed that high discriminative performance can be done between different EPN states. Surprisingly, the differences in the

Raman signatures of live cells were found statistically more significant when comparing the reversible and the irreversible EPN states than when comparing the no permeabilization and the permeabilization EPN sates. We demonstrated that the chemical damages induced by the PEFs were different between the three EPN states and that lipids were highly modified when comparing the irreversible and reversible EPN state. We might speculate that the irreversible EPN state is mostly related to chemical damages of the lipids that cannot be overcome by the cell metabolisms.

AUTHOR INFORMATION

Corresponding Author

* Lluis M. Mir. e-mail; luismir@cnrs.fr. tel: (0033) 142114792

Author Contributions

A.A performed the Raman experiments under the supervision of V.U. A.A and L.D performed the fluorescence experiments. A.A and L.H.L performed respectively the univariate and the multivariate analysis under the supervision of C.G. A.A and L.D performed the fluorescence data analyses. This study was supervised by O.P and L.M.M. The manuscript was written by A.A through contributions of all authors. All authors have given approval to the final version of the manuscript.

Notes

The authors declare no competing financial interest.

ACKNOWLEDGMENT

REFERENCES

Azan, Antoine, Valérie Untereiner, Cyril Gobinet, Ganesh D. Sockalingum, Marie Breton, Olivier Piot, and Lluis M. Mir. 2017. "Demonstration of the Protein Involvement in Cell Electropermeabilization Using Confocal Raman Microspectroscopy." *Scientific Reports* 7. Nature Publishing Group: 297–306. doi:10.1038/srep40448.

Breton, Marie, and Lluis M. Mir. 2015. "A Chemical Study of the Interaction of Electric Pulses with a Cell Model : Giant Unilamellar Vesicles." In *1st World Congress on Electroporation and Pulsed Electric Fields in Biology, Medicine and Food & Environment Technologies*, 4.

Chen, C., S.W. W Smye, M.P. P Robinson, and J.A. A Evans. 2006. "Membrane Electroporation Theories: A Review." *Medical & Biological Engineering & Computing* 44 (1–2). Springer-Verlag: 5–14. doi:10.1007/s11517-005-0020-2.

Cournia, Zoe, Toby W Allen, Ioan Andricioaei, Bruno Antonny, Daniel Baum, Grace Brannigan, Nicolae-Viorel Buchete, et al. 2015. "Membrane Protein Structure, Function, and Dynamics: A Perspective from Experiments and Theory." *The Journal of Membrane Biology* 248 (4): 611–40. doi:10.1007/s00232-015-9802-0.

Downes, Andrew, and Alistair Elfick. 2010. "Raman Spectroscopy and Related Techniques in Biomedicine." *Sensors (Basel, Switzerland)* 10 (3). Molecular Diversity Preservation International: 1871–89. doi:10.3390/s100301871.

Farhane, Zeineb, Franck Bonnier, Marcus Alexander Maher, Jane Bryant, Alan Casey, and Hugh James Byrne. 2016. "Differentiating Responses of Lung Cancer Cell Lines to Doxorubicin Exposure: In Vitro Raman Micro Spectroscopy, Oxidative Stress and bcl-2 Protein Expression." *Journal of Biophotonics*. WILEY-VCH Verlag. doi:10.1002/JBIO.201600019.

Ivorra, Antoni, and Boris Rubinsky. 2010. "Historical Review of Irreversible Electroporation in Medicine." In , 1–21. Springer Berlin Heidelberg. doi:10.1007/978-3-642-05420-4_1.

Larsson, Kare, and R.P. Rand. 1973. "Detection of Changes in the Environment of Hydrocarbon Chains by Raman Spectroscopy and Its Application to Lipid-Protein Systems." *Biochimica et Biophysica Acta (BBA) - Lipids and Lipid Metabolism* 326 (2): 245–55. doi:10.1016/0005-2760(73)90250-6.

Maiti, Nakul C, Mihaela M Apetri, Michael G Zagorski, Paul R Carey, and Vernon E Anderson. 2004. "Raman Spectroscopic Characterization of Secondary Structure in Natively Unfolded Proteins: Alpha-Synuclein." *Journal of the American Chemical Society* 126 (8): 2399–2408. doi:10.1021/ja0356176.

Marty, Michel, Gregor Sersa, Jean Rémi Garbay, Julie Gehl, Christopher G. Collins, Marko Snoj, Valérie Billard, et al. 2006. "Electrochemotherapy – An Easy, Highly Effective and Safe Treatment of Cutaneous and Subcutaneous Metastases: Results of ESOPE (European Standard Operating Procedures of Electrochemotherapy) Study." *European Journal of Cancer Supplements* 4 (11): 3–13. doi:10.1016/j.ejcsup.2006.08.002.

Notingher, I., S. Verrier, H. Romanska, a. E. Bishop, J. M. Polak, and L. L. Hench. 2002. "In Situ Characterisation of Living Cells by Raman Spectroscopy." *Spectroscopy* 16 (2): 43–51. doi:10.1155/2002/408381.

Okuno, Masanari, Hideaki Kano, Kenkichi Fujii, Kotatsu Bito, Satoru Naito, Philippe Leproux, Vincent Couderc, and Hiro O. Hamaguchi. 2014. "Surfactant Uptake Dynamics in Mammalian Cells Elucidated with Quantitative Coherent Anti-Stokes Raman Scattering Microspectroscopy." *PLoS ONE* 9 (4): 2–8. doi:10.1371/journal.pone.0093401.

Orendorff, Christopher J., Michael Ducey, and Jeanne E. Pemberton. 2002. “Quantitative Correlation of Raman Spectral Indicators in Determining Conformational Order in Alkyl Chains.” American Chemical Society. doi:10.1021/JP014311N.

Pelton, John T., and Larry R. McLean. 2000. “Spectroscopic Methods for Analysis of Protein Secondary Structure.” *Analytical Biochemistry* 277 (2): 167–76. doi:10.1006/abio.1999.4320.

Poddevin, B., S. Orlowski, J. Belehradek, and L.M. Mir. 1991. “Very High Cytotoxicity of Bleomycin Introduced into the Cytosol of Cells in Culture.” *Biochemical Pharmacology* 42 (December): S67–75. doi:10.1016/0006-2952(91)90394-K.

Pucihar, Gorazd, Tadej Kotnik, Damijan Miklavčič, and Justin Teissié. 2008. “Kinetics of Transmembrane Transport of Small Molecules into Electropermeabilized Cells.” *Biophysical Journal* 95 (6): 2837–48. doi:10.1529/biophysj.108.135541.

Rols, Marie-Pierre, and Justin Teissié. 1998. “Electropermeabilization of Mammalian Cells to Macromolecules: Control by Pulse Duration.” *Biophysical Journal* 75 (3): 1415–23. doi:10.1016/S0006-3495(98)74060-3.

Rubinsky, B. 2007. “Irreversible Electroporation in Medicine.” *Technology in Cancer Research & Treatment* 6 (4). SAGE Publications: 255–59. doi:10.1177/153303460700600401.

Santos, Inês P., Peter J. Caspers, Tom C. Bakker Schut, Remco van Doorn, Vincent Noordhoek Hegt, Senada Koljenović, and Gerwin J. Puppels. 2016. “Raman Spectroscopic Characterization of Melanoma and Benign Melanocytic Lesions Suspected of Melanoma Using High-Wavenumber Raman Spectroscopy.” *Analytical Chemistry* 88 (15). American Chemical Society: 7683–88. doi:10.1021/acs.analchem.6b01592.

Van der Paal, Jonas, Erik C. Neyts, Christof C. W. Verlackt, and Annemie Bogaerts. 2016. “Effect of Lipid Peroxidation on Membrane Permeability of Cancer and Normal Cells Subjected to Oxidative Stress.” *Chem. Sci.* 7 (1). Royal Society of Chemistry: 489–98. doi:10.1039/C5SC02311D.

Vernier, P. T., Zachary a. Levine, Yu Hsuan Wu, Vanessa Joubert, Matthew J. Ziegler, Lluis M. Mir, and D. Peter Tieleman. 2009. “Electroporating Fields Target Oxidatively Damaged Areas in the Cell Membrane.” *PLoS ONE* 4 (11). doi:10.1371/journal.pone.0007966.

Wagstaff, Peter, Mara Buijs, Willemien van den Bos, Daniel de Bruin, Patricia Zondervan, Jean de la Rosette, and Pilar Laguna. 2016. “Irreversible Electroporation: State of the Art.” *OncoTargets and Therapy* 9 (April): 2437. doi:10.2147/OTT.S88086.

Weaver, James C. JC, Yu.A. YA Yu.A. Chizmadzhev, Yu.A. YA Yu.A. Chizmadzhev, MR Prausnitz, VG Bose, R Langer, James C. JC Weaver, et al. 1996. “Theory of Electroporation: A Review.” *Bioelectrochemistry and Bioenergetics* 41 (2). Elsevier: 135–60. doi:10.1016/S0302-4598(96)05062-3.

Wong-Ekkabut, J, Z Xu, W Triampo, I-M Tang, D P Tieleman, and L Monticelli. 2007. “Effect of Lipid Peroxidation on the Properties of Lipid Bilayers: A Molecular Dynamics Study.” *Biophysical Journal* 93 (12). Elsevier: 4225–36. doi:10.1529/biophysj.107.112565.

Wurpel, George W. H., Juleon M. Schins, and Michiel Müller. 2004. “Direct Measurement of Chain Order in Single Phospholipid Mono- and Bilayers with Multiplex CARS.” American Chemical Society. doi:10.1021/JP037629J.

Zumbusch, Andreas, Wolfgang Langbein, and Paola Borri. 2013. “Nonlinear Vibrational Microscopy Applied to Lipid Biology.” *Progress in Lipid Research* 52 (4): 615–32. doi:10.1016/j.plipres.2013.07.003.

6.4 Monitoring the Molecular Composition of Live Cells Exposed to Pulsed Electric Fields via Label-free Optical Methods (article #4)

Our previous works have demonstrated major chemical modifications of live cells under EPN thanks to confocal Raman microspectroscopy. In this study, the chemical composition of live cells exposed to electric pulses was assessed via confocal Raman microspectroscopy and THz microscopy. Confocal Raman microspectroscopy and THz microscopy are both non-invasive and label free optical techniques that provided detailed information about the molecular composition of the cells. The Raman signatures of live haMSC cells exposed to different electric field magnitudes were acquired. MDCK cells were pulsed under THz microscopy. haMSC and MDCK were selected as cell models based on the background and knowledge of the authors : haMSC for Raman microspectroscopy and MDCK for THz microscopy. The monitoring of the THz signal of MDCK cells pulsed at different electric field magnitudes was performed. As the use of confocal Raman microspectroscopy and THz microscopy are both new concerning the investigation of the electropermeabilization process, we have performed an quantitative and qualitative comparison between these two biophotonics and fluorescence microscopy which is considered as the reference optical technique in the framework of electropermeabilization. To do so, fluorescence microscopy experiment have been performed under strictly identical conditions.

This work has been conducted in collaboration with the laboratory MEDyC – UMR 7369, CNRS, university of Reims Champagne-Ardenne - headed by Pr. Olivier Piot for the confocal Raman microspectroscopy experiments and the Laboratory for Optics & Biosciences (LOB) - Ecole Polytechnique - through the team headed by Dr. Guilhem Gallot for the THz microscopy experiments. The Raman, fluorescence and THz experiments have been performed, respectively, at MEDyC, UMR 8203 and LOB. Although, this work has provided many critical new informations about the molecular composition of pulsed cells, it is not yet perfectly finalized, especially concerning the time-evolution of the fluorescence signal. The last fluorescence experiments are currently running and the last results will be hopefully included in the PhD defence. The article related to this work is currently under careful internal reading before the inclusion of the last results and will be submitted for publication as soon as possible.

Monitoring the Molecular Composition of Live Cells Exposed to Pulsed Electric Fields via Label-free Optical Methods

Antoine Azan[1], Marianne Grognot[2], Lucie Descamps[1], Valérie Untereiner[3,4], Olivier Piot[3,4], Guilhem Gallot[2], and Lluis M. Mir[1*]

[1]Vectorology and Anticancer Therapies, UMR 8203, CNRS, Gustave Roussy, Univ. Paris-Sud, Université Paris-Saclay, 114 rue Edouard Vaillant, 94805 Villejuif, France.

[2]Laboratoire d'Optique et Biosciences, Ecole Polytechnique, UMR7645, CNRS, Route de Saclay, 91128 Palaiseau, France.

[3]MeDIAN, Biophotonics and Technologies for Health, MEDyC, UMR 7369, CNRS, University of Reims Champagne-Ardenne, 51 rue Cognacq-Jay, 51096 Reims, France.

[4]Cellular and Tissular Imaging Platform PICT, Faculty of Pharmacy, University of Reims Champagne-Ardenne, 51 rue Cognacq-Jay, 51096 Reims, France.

Correspondence and requests for materials should be addressed to Lluis. M. Mir (Luis.Mir@gustaveroussy.fr)

ABSTRACT (150 words)

This study focuses on the impact of pulsed electric fields on the biochemical composition of live cells thanks to label-free optical methods: confocal Raman microspectroscopy and Terahertz microscopy. The dose effect was investigating by exposing the cells to different electric field magnitudes (0, 500, 750, 1000, 1250 or 1500 V/cm). The other electric pulses parameters were fixed to 8 pulses, 100 µs pulse duration and 1 Hz repetition rate. Our results demonstrated a major impact of electric pulses on the proteins of the cells. Raman measurements revealed that the secondary structure was highly modified by the pulsed electric field and THz measurements showed a leakage of proteins after the delivery of pulsed electric pulses. Raman and Terahertz modalities were compared to fluorescence microscopy which is the reference optical technique in the case of electropermeabilization of cells. We showed that these two label-free techniques were more sensitive than fluorescence microscopy.

The main non-thermal consequence of the delivery of pulsed electric fields (PEF) on biological samples is the permeabilization of the plasma membrane[1]. This interaction, recently termed electropulsation to reconcile the previous terms electropermeabilization or electroporation that were reflecting different concepts. The application of electric pulses to biological samples has led to many applications in medicine or industry. For instance, electrochemotherapy, which consists in the combination of electropermeabilization of tumor cells with a chemotherapy based on bleomycin or cisplatin[2,3] is now routinely used to treat many cancer types: skin cancer[4], breast cancer[5,6], head and neck carcinomas[7], pancreatic tumors[8], … Although electropulsation has been studied for decades, the underlying mechanisms are still not fully understood[9]. It is well established that the electric field induces an additive transmembrane potential to the resting transmembrane potential of cells[10]. Numerical and experimental studies have demonstrated the creation of pores into the membrane related to this new transmembrane potential[11–13]. The destabilization of the cell membrane is also associated with long-term effect on the membrane, such as membrane disorder and a decrease of membrane elasticity[14,15], that last for minutes after the delivery of the PEF. Recently, our group has considered biochemical modifications of the membrane as the major contributor to the electropermeabilization process. Mass spectrometry analysis of the chemical composition of simple membrane model, Giant Unilamellar Vesicles (GUV), exposed to PEF revealed the peroxidation of phospholipids induced by the delivery of electric pulses [16]

This chemical damage hypothesis is supported by numerical models[17,18] and experiments[19,20]. Probing the molecular composition of live cells seems to be a critical point in order to better understand the interaction between PEF and biological cells. In this study, we used confocal Raman microspectroscopy (CRMS) and Terahertz (THz) microscopy to monitor biochemical consequences of the interaction between PEF and live cells. These two label-free and non-invasive optical techniques have the major advantage to provide detailed information about the intrinsic molecular composition of the sample.

CRMS gives access to biological sample vibrational footprint which is related with its biochemical composition. CRMS allows to extract information about lipids, proteins and DNA content and environment in biological samples[21]. CRMS is now commonly used to characterize cells[22,23] and tissues[24,25]. In a first published study, our group demonstrated the opportunity to use CRMS to investigate the electropermeabilization process[26]. The THz domain (1 THz = 1×10^{12} Hz) lies between the infrared and microwave domains. THz waves do not suffer from a high absorption in the biological medium, as the infrared ones, and they offer better resolution than the hyper-frequency domain (due to their lower wavelength). Despite a technology gap that has long kept the study of biological objects down to the single purified molecule, simplified and/or pretreated biological structures[27,28], the THz region has been shown to have potential in biomedical applications [29]. In this field, the most important feature of THz is its direct sensitivity to liquid water state, amount and content. [..]. Up to date, even if the question is still open for mid-long term effects, the THz waves are believed to be totally non-invasive for biological specimens at the power levels (sub-milliwatt, centered at the microwatt level) we use[30]. Recent work have demonstrated the possibility to detect and spectroscopically investigate complex system as living cells[31,32] and even *in vivo* accessible tissues[33,34]. In a first publication, our groups have demonstrated the ability to monitor the chemical permeabilization of live cells via THz microscopy[35].

Based on two previous publications using CRMS or THz to monitor permeabilization[26,35], we investigated the biochemical composition of live cells exposed to PEF of different electric field magnitudes. The study was conducted on human adipose-derived Mesenchymal Stem Cells (haMSC) and Madin-Darby Canine Kidney (MDCK) cells for the Raman and the THz experiments respectively. haMSC are very large cells (~ 70 μm diameter for attached cells) and allow easy access to cytoplasm area to acquire distinct "nucleus" and “cytoplasmic” Raman signatures. MDCK cells have the major advantage to easily grow at high cell densities on the specific substrate requested for the THz signals acquisition.

Raman and THz microscopies are new and innovative modalities that can provide detailed information of the molecular impact of PEF on live cells, while fluorescence microscopy is considered as the reference optical method to characterize cell electropermeabilization, for example using non-permeant fluorescent dyes such as Yo-Pro or Propidium Iodide (PI) [36,37]. Therefore, a quantitative and qualitative comparison between the Raman/THz modalities and the fluorescence microscopy was also performed. To this end, the experimental conditions used with CRMS or THz microscopy were exactly reproduced for the fluorescence microscopy acquisitions.

RESULTS

Raman signature of live cells exposed to PEF

The Raman signatures of live haMSC cells exposed to PEF of different field magnitude were acquired using a confocal Raman microscope (fig 1.a). The difference between the mean normalized Raman spectrum of each experimental condition and the mean normalized Raman spectrum of the control group (i.e. 0 V/cm) is reported in fig 1.b. Confirming a recent study[26], several Raman peaks were affected by the delivery of the electric pulses. The phenylalanine ring breathing vibrational mode at 1003 cm^{-1} and the Amide I band at 1658 cm^{-1} were the predominantly affected bands. A dose effect was noticed when monitoring the magnitude of these two peaks. The Raman peak at 1033 and 1605 cm^{-1} decreased when comparing the control group to the groups pulsed at increasing field magnitudes, confirming the strong effect of PEF on the phenylalanine residues. A multivariable analysis by Partial Least Square regression (PLS)[38] confirmed the existence of this dose effect. The major Raman peak contributors to the Latent Variable 1 (LV1) were also at 1003 and 1658 cm^{-1} (fig 1.c) which are attributed to proteins. Stretching mode of CH in lipids around 1448 cm^{-1} was also part of LV1 which is consistent with the known effect of PEF on the lipid bilayer[14]. Statistical analysis of the LV1 score per group (fig 1.d) revealed three groups with strong statistically significant intergroup differences and no statistically significant intragroup difference: {0, 500 V/cm}, {750, 1000 and 1250 V/cm} and 1500 V/cm.

The uptake of the non-permeant fluorescence dye Yo-Pro-1 was used to quantify the permeabilization of haMSC cells exposed to the same electric pulses as in the Raman experiments using, moreover, exactly the same experimental conditions (CaF_2 windows for the cells culture and exposure substrate, electrodes, medium, volume of medium, temperature …). Figure 1.e shows representative examples of fluorescence images acquired for the different electric field magnitudes delivered to the cells. The quantification of Yo-Pro-1 fluorescence intensity into the cells as a function of the field magnitudes displayed a dose-effect response combined with a threshold behavior (fig.1.f). At 500 V/cm, no cell permeabilized to Yo-Pro-1 was detected. For the field magnitudes above 500 V/cm, the Yo-Pro-1 cell fluorescence intensity was statistically significantly higher than in the control group. For an electric field magnitude from 500 V/cm to 1500 V/cm, the cell fluorescence intensity increased with the magnitude of the electric field applied. The high standard deviation in the fluorescence intensity might be associated to the cell shape, the cell orientation or any shielding effect[39,40], noting that we cannot exclude any inhomogeneity of the local electric field.

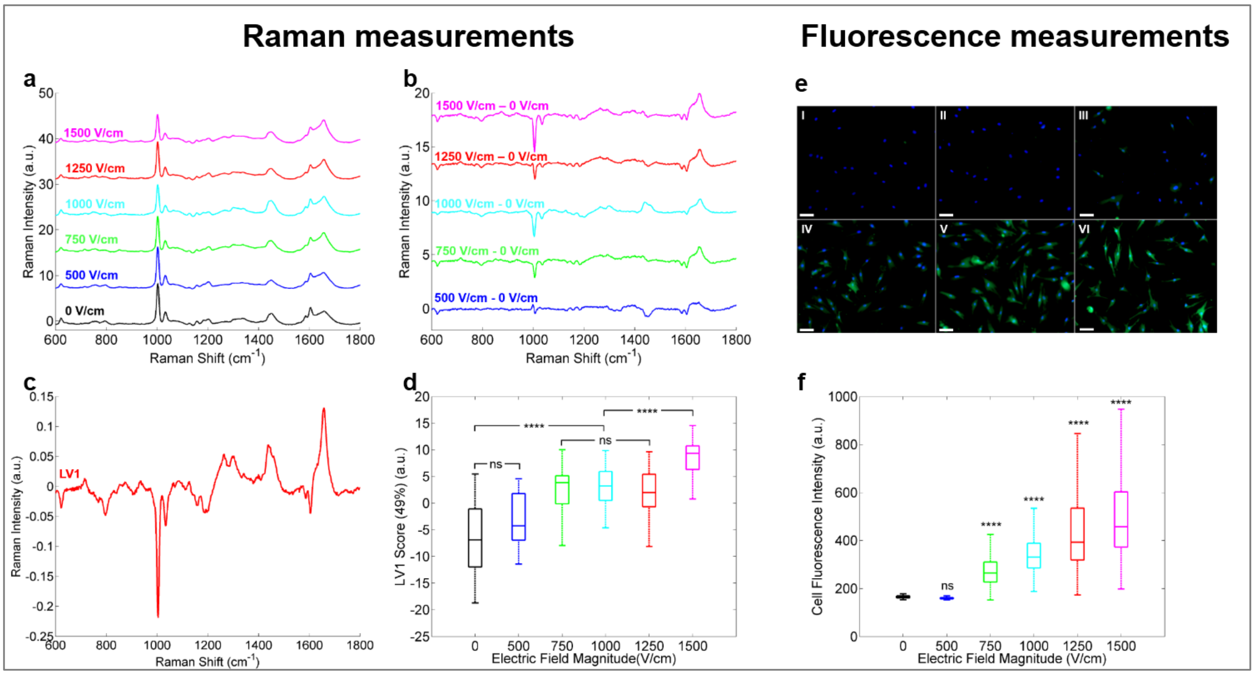

*Figure 1: Raman (a-d) and fluorescence (e-f) measurements of live haMSC cells exposed to pulsed electric fields. The magnitude of the electric fields was 0 V/cm (black), 500 V/cm (dark blue), 750 V/cm (green), 1000 V/cm (light blue), 1250 V/cm (red) or 1500 V/cm (magenta) The other pulse parameters are fixed to 8 pulses, 100 µs and 1 Hz. a – Mean normalized Raman signature of cells per group. b – Mean normalized Raman signature of cells minus the mean normalized Raman signature of cells under sham exposure (0 V/cm). c – Loading of LV1 from PLS analysis. d – LV1 score per group. The percentage of variance supported by the LV1 is indicated in brackets. e – Representative examples of Hoechst 3342 (blue) and Yo-Pro-1 (green) fluorescence images of haMSC cells exposed to pulsed electric field of 0 V/cm (I), 500 V/cm (II), 750 V/cm (III), 1000 V/cm (IV), 1250 V/cm (V) and 1500 V/cm (VI) magnitude. Scale bar = 100 µm. f - Quantitative analysis of the Yo-Pro-1 fluorescence intensity of haMSC cells exposed to pulsed electric fields. Student's t-test: ns (non-statistically significant): p-value >5%, ****: p-value≤0.01%.*

In order to compare the Raman modality with the fluorescence modality, the normalized relative Raman and fluorescence signal, respectively symbolized by Δ_{Raman} and Δ_{Fluo}, were calculated for the different magnitudes of the delivered electric field (fig.2). At 500 and 750 V/cm, CRMS provides higher difference with respect to the control group than the fluorescence. In particular, no difference in the fluorescence signal was noticed between the 500 V/cm group and the control group, whereas a significant 68% relative increase of the Raman signal was already recorded at 500 V/cm. When the cells were exposed to 1000 V/cm, the relative evolution of the signal was basically the same for the two modalities. At 1250 and 1500 V/cm, the fluorescence modality displayed a higher difference in the signal magnitude than the Raman modality. Raman and fluorescence signal were increased by 200% in comparison to the signal of the respective control groups. It is important to remind that the fluorescence results were highly dependent on the fluorescent dye used in the experiments, namely the 630 Da Yo-Pro-1. The fluorescent results are dependent on the fluorescent dye, its size, its charge, and its external concentration. On the contrary, CMRS is a label-free optical technique and thus the results are related to the intrinsic chemical composition of cells.

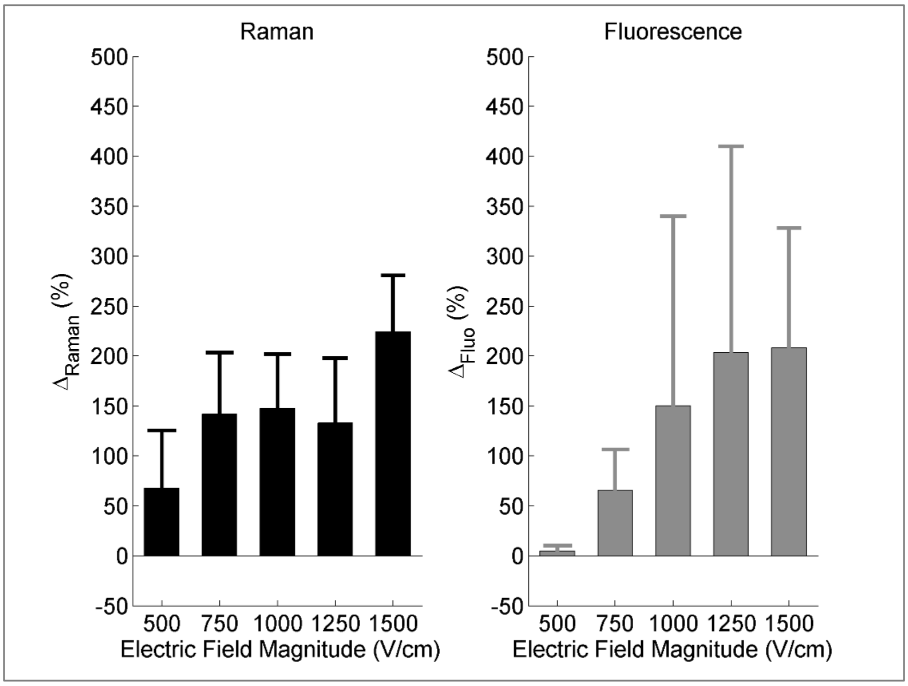

Figure 2: Quantitative comparison of Raman and fluorescence modalities in the case of live haMSC cells exposed to different electric field magnitude under exactly the same experimental conditions. Δ_{Raman} and Δ_{Fluo} respectively represent the normalized relative Raman (left) and fluorescence (right) signal with respect to the corresponding control group. The electric field magnitude varied from 500 to 1500 V/cm. The other pulse parameters were fixed to 8 pulses, 100 µs and 1 Hz for all the experiments. The bar and the error bar represent the mean and the standard deviation of the distribution, respectively, per experimental condition

THz modality to monitor the proteins leakage of live cells exposed to PEF

For the first time, a Terahertz time-domain spectroscopy (THz-TDS) experimental setup was used to investigate the interaction between PEF and live cells. The THz and fluorescence signals of MDCK cells were recorded before and after the delivery of the electric pulses. As illustrated in figure 3.a, the THz signal was sensitive to the presence of cells. In the supplementary information, we bring the demonstration that the THz signal can be used as a label-free biomarker of the amount of proteins into cells. The relative THz signal decreased after the delivery of the electric pulses (figure 3.b). This relative signal decrease was associated to proteins leakage due to the electropermeabilization of MDCK cells. Figure 3.c displays the evolution of the normalized THz signal after the delivery of the electric pulses and the mathematical model used to fit the measurements. In order to compare the THz and the fluorescence modalities, figure 3.d shows an example of the time-lapse Yo-Pro-1 images of MDCK cells exposed to the same electric pulses. The uptake of Yo-Pro-1 into cells was assessed in order to quantify the dynamics of the electropermeabilization process. A representative example of the evolution of the normalized relative fluorescence signal and its mathematical model are shown in figure 3.e. The signal-to-noise ratio (SNR) was higher in the case of the fluorescence experiments than in the THz acquisitions. This might be associated to the technology maturity. Indeed, fluorescence microscopy is a well-established technology; whereas THz-TDS technology is still under development.

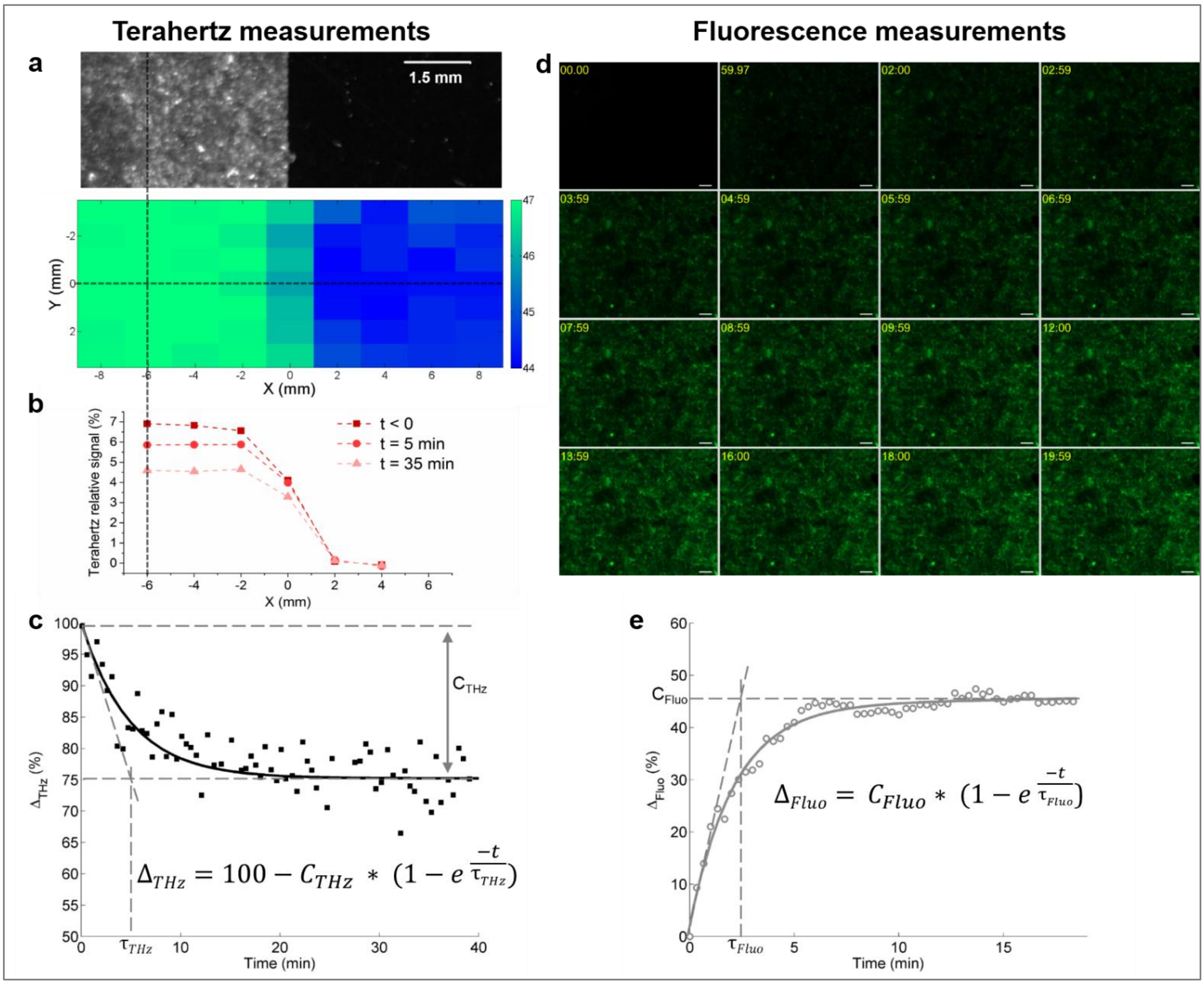

Figure 3: Illustration of the THz (a – c) and fluorescence (d – e) measurements. a – Bright-field (top) and THz-ATR (bottom) images with MDCK epithelial cell monolayer (left) compared without cells (right). b – Representative examples of THz relative signal of sample along the X axis at three times: before, 5 minutes and 35 minutes after the delivery of the electric pulses. c - Example of the time-evolution of the normalized THz relative signal of live MDCK cells exposed to pulsed electric fields. ■ corresponds to the measurements and the black line to the fitted mathematical model. d - Representative example of Yo-Pro-1 fluorescence time-lapse images of live MDCK cells exposed to pulsed electric fields. The delivery of the electric pulses was at time 00:00. For each image, the relative acquisition time was reported. Scale bar = 100 µm. e - Example of the time-evolution of the normalized Yo-Pro-1 fluorescence relative signal of live MDCK cells exposed to pulsed electric fields. ○ corresponds to the measurements and the grey line to the fitted mathematical model fitted. The delivery of the electric pulses was at time 00:00. For all these graphs, the parameters of the pulsed electric fields were 8 pulses, 1250 V/cm, 100 µs and 1 Hz. The mathematical models used to fit the measurements were reported in c and e.

In both modalities, the mathematical models used to fit the measurements were based on an exponential function. Thus, two quantitative parameters can be extracted from these models, a plateau value and a time constant (figure 4). First, the THz plateau value was much lower than the plateau value of the fluorescence results under the electric pulses parameters used. At 500 V/cm, the fluorescence plateau value was close to 0; whereas the THz plateau value was around 9.3 (+/-4) %. This would indicate that the detection threshold of THz setup was lower than the detection threshold of fluorescence. When increasing the electric field magnitude, a dose effect on the THz and fluorescence plateau values was noticed. The maximum of the plateau value was higher in the case of the fluorescence than in THz. Figure 4.c shows that the THz time constant decreased with the field magnitude. On the contrary, the fluorescence time constant increased with the field magnitude.

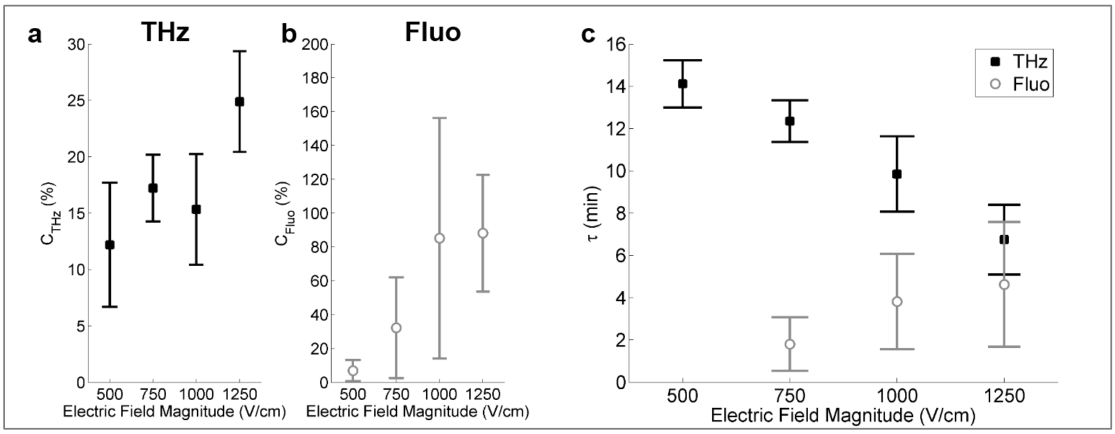

Figure 4: Evolution of the model fitted to the THz and fluorescence measurements of live MDCK cells exposed to pulsed electric fields with different electric field magnitudes. Plateau value for the THz (a) and Yo-Pro-1 fluorescence normalized signals (b) per experimental condition. c - Time constant for the THz (black) and Yo-Pro-1 fluorescence (grey) normalized signals per experimental condition. ■ corresponds to the mean of plateau value for the THz experiments per experimental condition. ○ corresponds to the mean of plateau value for the Yo-Pro-1 fluorescence experiments pear experimental condition. The error bar represents the standard deviation of the data set per experimental condition. τ was not determined if the coefficient of determination (R^2) between the model and the measurement was below 90%. The magnitude of electric field applied to the cells was 500, 750, 1000 or 1250 V/cm. The other electric pulse parameters were fixed to 8 pulses, 100 µs and 1 Hz.

DISCUSSION

In this study, we report a quantitative and qualitative comparison between fluorescence microscopy and label-free optical methods, CRMS and THz microscopy, to investigate the interaction between PEF and live cells. Our CRMS results demonstrated the effect of electric pulses on proteins into live cells via the modification of phenylalanine and Amide I vibrational modes. Phenylalanine is known to be present in many transmembrane domains[41]. Maiti *et al.* have demonstrated that the Amide I band at 1658 cm^{-1} is related to the secondary structure of unfolded proteins[42]. Numerical model confirmed our results by demonstrating the effect of electric pulses on the folding state of membrane proteins[43]. A dose effect was noticed in the Raman signature of live cells when increasing the field magnitude. The statistical analysis reveals three groups with high intergroup statistical differences and no intragroup statistical differences. We may speculate that these three groups are associated with three different states of the plasma membrane, meaning no permeabilization, reversible permeabilization and irreversible permeabilization. If so, the Raman signature of cells would be a biomarker of the permeabilized state of the plasma membrane. But further investigations are necessary. A fluorescence intensity increase relatively to the control group was also noticed when increasing the field magnitude above 750 V/cm. As a comparison with the CRMS results, a relative increase over 53% in the Raman signal was noticed when comparing the 500 V/cm field magnitude experiment condition and the control group. This would indicate that CRMS is a more sensitive technique than the fluorescence modality. It has to be noticed that fluorescence microscopy results depend on the properties of the fluorescence dye used. The results would be different with another fluorescent permeabilization marker such as calcium green or Fluo-4[44].

Thanks to THz measurements, the leakage of amino-acids residues of cells exposed to PEF was demonstrated. Even though amino acids and proteins leakage was extensively studied more than 50 years ago (when the process was termed “membrane dielectric breakdown”)[45]. This amino acids leakage is not usually evoked when the consequences of the cell membrane permeabilization are listed. However, like all the other non-permeant molecules, amino acids and proteins crossing of the cell membrane will occur, as the well-known leaks of other internal substances like the ATP [46]. As expected for a dose effect behavior, an increase in the field magnitude delivered was associated with an increase in the normalized THz relative signal. The time constant of the THz signal decreased with an increase of the field magnitude revealing a faster leakage across a more permeabilized membrane. On the contrary, the evolution of the fluorescence time constant increased with the field magnitude. This dose effect behavior is well known in the literature and is related with the membrane resealing which takes longer at high electric field magnitude than at low field magnitude[47]. The THz results is unusual and might be due to the origin of the THz signal. As demonstrated in supplementary information, the THz signal originates from the presence of small (~ 100 Da) to large (~ 200 kDa) molecules, mainly from amino acids to proteins, in large concentrations close to the CaF window, that is inside the cells attached to this substrate. Some studies performed with fluorescence microscopy have demonstrated that the permeabilization threshold is depending on the fluorescence dye size[36,48]. Thus low electric field allows small non-permeant molecules to cross the plasma membrane. High electric field allows small and larger non-permeant molecules to cross the plasma membrane. In the case of the THz microscopy, depending on the molecular weight, molecules contribute in a different manner to the THz signal (supplementary figure). Thus THz signal is a global response of the leakage of amino-acids residues and it is difficult to attribute the THz time evolution to a specific molecule.

For the first time, label-free optical methods (CRMS and THz microscopy) demonstrates the strong impact on the chemical composition, especially the proteins, of live cells exposed to PEF. The Raman and THz modalities were quantitative and qualitatively compare to fluorescence microscopy. Table 1 summarizes the THz, the Raman and the fluorescence modalities in the framework of the interaction between PEF and live cells.

	Raman	Fluorescence	Terahertz
Origin of the signal	Intrinsic chemical composition of the cell	Amount of fluorescence dye inside the cell	Amount of the amino acids residue inside the cell
Signal acquired	Vibrational spectrum	Fluorescence intensity	THz peak magnitude
Origin of the signal evolution after the delivery of PEF	Changes in the molecular composition of the cell	Internalization of non-permeant fluorescence dye into the cell	Leakage of amino acids residue across the membrane
Detection threshold (V/cm) in comparison with control group	≤ 500	> 500 and ≤ 750	≤ 500
Dose effect	Signal maybe related to the permeabilization state of the plasma membrane	Signal increase with the electric field magnitude for electric field magnitude above the detection threshold	Signal increase with the electric field magnitude
Label	No	Yes	No
Time resolution	Very low (~ 60 s)	Good (~0.3s)	Low (~10s)
Spatial resolution	Very good (~1 µm)	Very good (~1 µm)	Very low (~2500 µm)

Quantitative signal	Normalization of the spectrum	Internal references necessary	Internal reference necessary
Signal stability	Excellent (~ hours)	Low (~ 10 seconds) (photobleaching)	Moderate (~ 10 minutes) (laser damage)
Data process	Multivariate analysis	Univariate analysis	Univariate analysis
Sample preparation	Specific substrate and solution	Labeling protocol	Specific substrate and solution
Technology maturity	Research set-up	Commercialized equipment	Commercialized equipment

REFERENCES

1. Chen, C., Smye, S. W. W., Robinson, M. P. P. & Evans, J. A. A. Membrane electroporation theories: a review. *Med. Biol. Eng. Comput.* **44,** 5–14 (2006).
2. Mir, L. M., Orlowski, S., Belehradek, J. & Paoletti, C. Electrochemotherapy potentiation of antitumour effect of bleomycin by local electric pulses. *Eur. J. Cancer* **27,** 68–72 (1991).
3. Yarmush, M. L., Golberg, A., Serša, G., Kotnik, T. & Miklavčič, D. Electroporation-Based Technologies for Medicine: Principles, Applications, and Challenges. (2014). doi:10.1146/annurev-bioeng-071813-104622
4. Kunte, C. *et al.* Electrochemotherapy in the treatment of metastatic malignant melanoma: A prospective cohort study by InspECT. *Br. J. Dermatol.* (2017). doi:10.1111/bjd.15340
5. Schmidt, G., Juhasz-Böss, I., Solomayer, E.-F. & Herr, D. Electrochemotherapy in Breast Cancer: A Review of References. *Geburtshilfe Frauenheilkd.* **74,** 557–562 (2014).
6. Matthiessen, L. W. *et al.* Electrochemotherapy for breast cancer - results from the INSPECT database. *Ann. Oncol.* **27,** (2016).
7. Bertino, G. *et al.* European Research on Electrochemotherapy in Head and Neck Cancer (EURECA) project: Results of the treatment of skin cancer. *Eur. J. Cancer* **63,** 41–52 (2016).
8. Granata, V. *et al.* Electrochemotherapy in locally advanced pancreatic cancer: Preliminary results. *Int. J. Surg.* **18,** 230–236 (2015).
9. Teissie, J., Golzio, M. & Rols, M. P. Mechanisms of cell membrane electropermeabilization: a minireview of our present (lack of ?) knowledge. *Biochim. Biophys. Acta* **1724,** 270–280 (2005).
10. Kotnik, T., Bobanović, F. & Miklavcic, D. Sensitivity of transmembrane voltage induced by applied electric fields—A theoretical analysis. *Bioelectrochemistry Bioenerg.* **43,** 285–291 (1997).
11. Tarek, M. Membrane electroporation: a molecular dynamics simulation. *Biophys. J.* **88,** 4045–4053 (2005).
12. Tieleman, D. P. The molecular basis of electroporation. *BMC Biochem.* **5,** (2004).
13. Breton, M., Delemotte, L., Silve, A., Mir, L. M. & Tarek, M. Transport of siRNA through lipid

membranes driven by nanosecond electric pulses: an experimental and computational study. *J. Am. Chem. Soc.* **134,** 13938–41 (2012).

14. Escoffre, J. M. *et al.* Membrane disorder and phospholipid scrambling in electropermeabilized and viable cells. *Biochim. Biophys. Acta - Biomembr.* **1838,** 1701–1709 (2014).
15. Chopinet, L., Roduit, C., Rols, M. P. & Dague, E. Destabilization induced by electropermeabilization analyzed by atomic force microscopy. *Biochim. Biophys. Acta - Biomembr.* **1828,** 2223–2229 (2013).
16. Breton, M. & Mir, L. M. A chemical study of the interaction of electric pulses with a cell model : giant unilamellar vesicles. in *1st World Congress on Electroporation and Pulsed Electric Fields in Biology, Medicine and Food & Environment Technologies* 4 (2015).
17. Vernier, P. T. *et al.* Electroporating fields target oxidatively damaged areas in the cell membrane. *PLoS One* **4,** (2009).
18. Garrec, J., Monari, A., Assfeld, X., Mir, L. M. & Tarek, M. Lipid Peroxidation in Membranes: The Peroxyl Radical Does Not 'Float'. *J. Phys. Chem. Lett.* **5,** 1653–1658 (2014).
19. Pakhomova, O. N. *et al.* Oxidative effects of nanosecond pulsed electric field exposure in cells and cell-free media. *Arch. Biochem. Biophys.* **527,** 55–64 (2012).
20. Benov, L. C., Antonov, P. a. & Ribarov, S. R. Oxidative damage of the membrane lipids after electroporation. *Gen. Physiol. Biophys.* **13,** 85–97 (1994).
21. Kann, B., Offerhaus, H. L., Windbergs, M. & Otto, C. Raman microscopy for cellular investigations--From single cell imaging to drug carrier uptake visualization. *Adv. Drug Deliv. Rev.* **89,** 71–90 (2015).
22. Pascut, F. C. *et al.* Non-invasive label-free monitoring the cardiac differentiation of human embryonic stem cells in-vitro by Raman spectroscopy. *Biochim. Biophys. Acta* **1830,** 3517–24 (2013).
23. Sulé-Suso, J., Forsyth, N. R., Untereiner, V. & Sockalingum, G. D. Vibrational spectroscopy in stem cell characterisation: is there a niche? *Trends Biotechnol.* **32,** 254–62 (2014).
24. Byrne, H. J. *et al.* Spectropathology for the next generation: Quo vadis? *Analyst* **140,** 2066–2073 (2015).
25. Butler, H. J. *et al.* Using Raman spectroscopy to characterize biological materials. *Nat. Protoc.* **11,** 664–687 (2016).
26. Azan, A. *et al.* Demonstration of the Protein Involvement in Cell Electropermeabilization using Confocal Raman Microspectroscopy. *Sci. Rep.* **7,** 297–306 (2017).
27. Plusquellic, D. F., Siegrist, K., Heilweil, E. J. & Esenturk, O. Applications of Terahertz Spectroscopy in Biosystems. *ChemPhysChem* **8,** 2412–2431 (2007).
28. Jepsen, P. U., Cooke, D. G. & Koch, M. Terahertz spectroscopy and imaging - Modern techniques and applications. *Laser Photon. Rev.* **5,** 124–166 (2011).
29. Yang, X. *et al.* Biomedical Applications of Terahertz Spectroscopy and Imaging. *Trends Biotechnol.* **34,** 810–824 (2016).

30. Wilmink, G. J. & Grundt, J. E. Invited Review Article: Current State of Research on Biological Effects of Terahertz Radiation. *J. Infrared, Millimeter, Terahertz Waves* **32,** 1074–1122 (2011).

31. Yang, X., Yang, K., Luo, Y. & Fu, W. Terahertz spectroscopy for bacterial detection: opportunities and challenges. *Appl. Microbiol. Biotechnol.* **100,** 5289–5299 (2016).

32. Shiraga, K. *et al.* Characterization of Dielectric Responses of Human Cancer Cells in the Terahertz Region. *J. Infrared, Millimeter, Terahertz Waves* **35,** 493–502 (2014).

33. Tewari, P. *et al.* In vivo terahertz imaging of rat skin burns. *J. Biomed. Opt.* **17,** 40503 (2012).

34. Fan, S., Ung, B. S. Y., Parrott, E. P. J., Wallace, V. P. & Pickwell-MacPherson, E. *In vivo* terahertz reflection imaging of human scars during and after the healing process. *J. Biophotonics* (2016). doi:10.1002/jbio.201600171

35. Grognot, M. & Gallot, G. Quantitative measurement of permeabilization of living cells by terahertz attenuated total reflection. *Appl. Phys. Lett.* **107,** 103702 (2015).

36. Vernier, P. T., Sun, Y. & Gundersen, M. A. Nanoelectropulse-driven membrane perturbation and small molecule permeabilization. *BMC Cell Biol.* **7,** 37–53 (2006).

37. Müller, K. J., Sukhorukov, V. L. & Zimmermann, U. Reversible electropermeabilization of mammalian cells by high-intensity, ultra-short pulses of submicrosecond duration. *J. Membr. Biol.* **184,** 161–70 (2001).

38. Haaland, D. M. & Thomas, E. V. Partial least-squares methods for spectral analyses. 1. Relation to other quantitative calibration methods and the extraction of qualitative information. *Anal. Chem.* **60,** 1193–1202 (1988).

39. Pucihar, G., Kotnik, T., Teissié, J. & Miklavčič, D. Electropermeabilization of dense cell suspensions. *Eur. Biophys. J.* **36,** 173–185 (2007).

40. Henslee, B. E., Morss, A., Hu, X., Lafyatis, G. P. & James Lee, L. Cell-cell proximity effects in multi-cell electroporation. *Biomicrofluidics* **8,** 52002 (2014).

41. Unterreitmeier, S. *et al.* Phenylalanine promotes interaction of transmembrane domains via GxxxG motifs. *J. Mol. Biol.* **374,** 705–18 (2007).

42. Maiti, N. C., Apetri, M. M., Zagorski, M. G., Carey, P. R. & Anderson, V. E. Raman spectroscopic characterization of secondary structure in natively unfolded proteins: alpha-synuclein. *J. Am. Chem. Soc.* **126,** 2399–408 (2004).

43. Cournia, Z. *et al.* Membrane Protein Structure, Function, and Dynamics: a Perspective from Experiments and Theory. *J. Membr. Biol.* **248,** 611–40 (2015).

44. de Menorval, M.-A. *et al.* Electric pulses: a flexible tool to manipulate cytosolic calcium concentrations and generate spontaneous-like calcium oscillations in mesenchymal stem cells. *Sci. Rep.* **6,** 32331 (2016).

45. Zimmermann, U., Pilwat, G. & Riemann, F. Preparation of erythrocyte ghosts by dielectric breakdown of the cell membrane. *Biochim. Biophys. Acta - Biomembr.* **375,** 209–219 (1975).

46. Calvet, C. Y., Famin, D., André, F. M. & Mir, L. M. Electrochemotherapy with bleomycin induces

hallmarks of immunogenic cell death in murine colon cancer cells. *Oncoimmunology* **3,** e28131 (2014).

47. He, H., Chang, D. C. & Lee, Y.-K. Nonlinear current response of micro electroporation and resealing dynamics for human cancer cells. *Bioelectrochemistry* **72,** 161–8 (2008).
48. Vernier, P. T. *et al.* Calcium bursts induced by nanosecond electric pulses. *Biochem. Biophys. Res. Commun.* **310,** 286–295 (2003).
49. Wojdyla, A. & Gallot, G. Attenuated internal reflection terahertz imaging. *Opt. Lett.* **38,** 112–4 (2013).
50. Poplineau, M. *et al.* Raman microspectroscopy detects epigenetic modifications in living Jurkat leukemic cells. *Epigenomics* **3,** 785–94 (2011).
51. Klein, K. *et al.* Label-Free Live-Cell Imaging with Confocal Raman Microscopy. *Biophys. J.* **102,** 360–368 (2012).
52. Hamada, K. *et al.* Raman microscopy for dynamic molecular imaging of living cells. *J. Biomed. Opt.* **13,** 44027 (2008).
53. Oshima, Y., Shinzawa, H., Takenaka, T., Furihata, C. & Sato, H. Discrimination analysis of human lung cancer cells associated with histological type and malignancy using Raman spectroscopy. *J. Biomed. Opt.* **15,** 17009 (2010).

METHODS

Cell culture

For this study, two different cell types were used. MDCK cells were used in the case of THz and fluorescence time-lapse experiments, whereas haMSC cells were used in the case of Raman and fluorescence experiments. The selection of the cell lines was based on our previous published work with MDCK cells for the THz experiments[35] and haMSC for the Raman experiments[26].

Both cell types were grown in a humidified atmosphere at 37°C and 5 % CO_2 in Dulbecco's Modified Eagle Medium (DMEM) supplemented with 10% serum (fetal calf serum for MDCK and fetal bovine serum for haMSC) and 1% penicillin-streptomycin (Life Technologies).

For the THz experiments, the MDCKs were plated at a density of 30000 cells/cm^2 on a 3-mm thick 37-mm diameter high-resistivity silicon (HR-Si) window, which is the optimal substrate for THz experiments in attenuated total internal reflection geometry[35,49], and placed in a 60-mm Petri dish. Cells were grown for three to five days until confluence. Then part of the cells was removed by scratching from half of the HR-SI window. This are served as the reference. Before the THz experiments, the culture medium was replaced by 2 mL of a buffered minimal medium (HBSS with10 mM HEPES buffer, without Ca^{2+}) at room temperature. Due to the opacity of the HR-Si supports which is not compatible with light microscopy, the cells were prepared exactly under the same conditions in a 35-mm Petri dish with no HR-Si window for the fluorescence experiments to be compared to the THz experiments. No cell morphology or proliferation difference was noticed between the culture on the HR-Si windows and the Petri dishes.

For the Raman experiments, the haMSCs were plated at a density of 5000 cells/cm^2 on a CaF_2 window (Crystran, Poole) placed at the bottom of a 35-mm Petri dish. Cells were grown overnight. Before the

Raman experiments, the medium was replaced by 2 mL of a saline solution, NaCl 154 mM (B. Braun) at 4 °C. This saline solution is commonly used for CRMS acquisitions on living cells[50]. The cells were prepared exactly under the same conditions for the fluorescence experiments to be compared to the Raman experiments.

Pulse generator and pulses condition.

A commercially available electric pulses generator (Cliniporator™) was used to treat the cells with 8 pulses of 100 µs delivered at a repetition frequency of 1 Hz. The magnitude of the electric field was 0, 500, 750, 1000, 1250 or 1500 V/cm depending on the experiments. To deliver the electric pulses on attached cells, a homemade system of electrodes was used based on two stainless steel parallel plate electrodes separated by a fixed distance of 4 mm or 8 mm in the case of the Raman experiments and THz experiments respectively. The 8 mm distance between the electrodes was chosen in order to prevent any perturbation of the 2.5mm-diamter THz evanescent field. Because the maximum output voltage of the pulse generator was 1000 V, the distance of 8 mm between the plate electrodes restricted the maximum electric field magnitude delivered to 1250 V/cm. Therefore, the electric field magnitude of 1500 V/cm was only used for the Raman experiments. The Cliniporator was connected to the plate electrodes with alligator clips. The delivery of the electric pulses was performed at 4°C or room temperature for the Raman or THz experiments, respectively. As mentioned in our previous work, no heating effect, pH change or bubble formation were noticed after the delivery of the PEF[26].

CRMS and spectra processing

The Raman experiments were performed under similar experimental conditions detailed in Azan *et al.*[26]. Briefly, a confocal Raman microspectrometer LabRam ARAMIS (Horiba Jobin Yvon) with a 532 nm continuous wave laser was used to acquire the Raman spectra of living haMSC cells. The power at the sample was around 20 mW which is known to be non-toxic for the cells[51–53]. Prior to any measurement, the confocal Raman microspectroscope was calibrated with a Silicon sample using the 519 cm^{-1} band and the laser power was checked. The Raman signatures were acquired in the FP region (600 – 1800 cm^{-1}). The acquisition time was fixed to two accumulations of 30 seconds (60 seconds in total). The sample was placed on an XY piezoelectric stage to investigate multiple locations. During the Raman measurements, cells were maintained at 4 °C by the T95 temperature controller (Linkam Scientific Instrument Ltd). The Raman signature of the saline solution was acquired in order to be able to remove this background signal from the measured spectra. In total, 264 Raman spectra were collected.

The measured Raman spectra were pre-processed as detailed in Azan *et al.*[26]. Briefly, a quality check was performed on each individual Raman spectrum collected, meaning that the measured spectra with a SNR lower that 10 were discarded from the data set. Then the spectra were smoothed using the Savistky-Golay filter (12 points, 2nd order polynomial). Then the baseline and the saline solution background signal were removed. Finally, the spectra were normalized using the standard normal variance (SNV) method. The mean normalized spectra for each electric pulse condition were calculated. The difference between the mean normalized spectra at a specific electric pulses condition and the mean normalized spectra of control (sham exposure, 0 V/cm) was also calculated. Multivariate analysis, based on PLS was performed on the mean-centered combined data set. The magnitude of the electric field was used as the observable variable for PLS analysis.

Terahertz-attenuated total reflection and specific data processing

The Terahertz-Attenuated Total Reflection (THz-ATR) device is a completely transparent HR-Si isosceles prism (R > 10 Ω.cm, n=3.42) with a base angle of 42°. This incident angle provides total internal reflection conditions. For imaging purpose, the silicon prism was topped with a 3 mm thick HR-Si window on which cells and their buffered medium were placed and which could be mechanically moved very precisely. The THz signal was generated and detected by a classical Terahertz time-domain spectroscopy (THz-TDS) setup [49]. Under such conditions, the cell layer was probed by an evanescent wave of a thickness of about 20 µm generated at the surface of the HR-Si window. Support displacement allowed the acquisition of images, pixel by pixel, with a lateral resolution of 2.5 mm. An example of such image is given in figure 3.a. Three pixels in the cell layer region and two in the reference region were taken along the cross-section (dotted black line) in approximately 15 seconds to obtain one THz relative signal value. These images show an approximate 6 to 8 % peak amplitude signal difference between cells and their outer medium, further called THz relative signal.

In supplementary information, we demonstrate that THz signal variations originated from changes in the intracellular proteins concentration, with an equal sensitivity to protein of all size above 2 kDa. Thus, the THz signal variations could be used to quantitatively follow protein leakage during cell permeabilization[35]. The THz relative signal was normalized by its value before the delivery of electric pulses to obtain the normalized THz relative signal, Δ_{THz}. Hence, Δ_{THz} was ranging from 100 % (no protein leakage) to 0 % (total protein leakage, but cells would detach beforehand). A Δ_{THz} measure reflected the mean internal protein mass concentration changes of a roughly estimated forty thousand cells. Without any perturbation, the THz signal was stable for hours at room temperature (21°C).

Fluorescence microscopy (including data pre-processing and processing)

In all the fluorescence experiments, Hoechst 33342 was used to stain the cell nucleus and to localize all the cells, permeabilized or not. Yo-Pro-1 was used as a classical fluorescence biomarker of cell electropermeabilization[36]. Prior to the fluorescence experiments, cells were incubated in the presence of 370 nM of Hoechst 33342 for 30 minutes at 37 °C and 5 % CO_2. After two washes with phosphate-buffered saline (PBS), 1 µM of Yo-Pro-1 was added to the cell solution. In the case of the comparison between fluorescence experiments and THz experiments or Raman experiments, the cell solution was HBSS with 10 mM HEPES buffer or saline solution, respectively. Fluorescence and bright-field images were acquired with an Observer Z1 inverted microscope (Zeiss). Images were acquired with an exposure time fixed to 300 ms for the green (Yo-Pro-1) and blue (Hoechst 33342) channel and 40 ms for the bright-field channel. The microscope was controlled by the Zen Blue 2 Zeiss software.

In the case of the comparison between fluorescence and Raman modalities, bright-field and 2 channel fluorescence images were acquired 10 minutes after the electric pulses delivery. In order to focus only on the Yo-Pro-1 fluorescence, the Yo-Pro-1 fluorescence intensity was extracted from cell nuclear location labeled by the Hoechst 33342 dye. Thus, the Yo-Pro-1 fluorescence intensity specific to cells, coined I_{Fluo}, was accessible. The sample preparation was strictly the same for the Raman and the fluorescence experiments.

In the case of the comparison between fluorescence and THz methods, the 2 channel fluorescence images were acquired every 20 seconds for at least 20 minutes. 4 images were acquired before delivering the electric pulses. The only difference between the THz experiments and the time-lapse fluorescence experiments was the substrate: the HR-Si for THz experiments and the Petri dish for fluorescence experiments. All the other experimental parameters or sample preparation processes remained strictly the same. At the end of the fluorescence experiments, no cell morphology modification was noticed and cells grew normally if they were put in culture, showing absence of phototoxicity. Under these experimental conditions used, we also checked the absence of Yo-Pro-1 and Hoechst 33342 photobleaching. In each image, 5 regions of interests (ROI) with cells and 1 ROI without cell were selected. The ROI without cells was used to quantify the light power during the acquisition in order to be immune from any light fluctuation when analyzing the fluorescence in the ROIs with cells. For each ROIs with cells, the normalized fluorescence was calculated by dividing the Yo-Pro-1 mean fluorescence in each ROI with cells by the Yo-Pro-1 mean fluorescence in the ROI without cells. This normalized fluorescence aims to limit the impact of the light power fluctuation in the quantification of the fluorescence intensity. The fluorescence relative signal, Δ_{Fluo}, was calculated by the relative variation between the normalized fluorescence after the delivery of the electric pulses and the normalized fluorescence before the delivery of the electric pulses.

Data process to compare the different instrumentations

In order to perform quantitative and qualitative comparison between the different modalities (Raman vs fluorescence and THz vs fluorescence), specific parameters were defined. Δ_{Raman} and Δ_{Fluo}, respectively termed normalized relative Raman signal and normalized fluorescence signal, were used to compare Raman to fluorescence modality. $\Delta_{THz}(t)$ and $\Delta_{Fluo}(t)$, respectively termed time-evolution of the normalized relative THz signal and time-evolution of the normalized relative fluorescence signal, were used to compare THz to fluorescence modality. These parameters were defined by the following equation:

$$\Delta_{Raman} = \frac{I_{Raman} - < I_{Raman\ Control} >}{< I_{Raman\ Control} >}$$

where I_{Raman} was the LV1 score and $<I_{Raman\ Control}>$ was the mean LV1 score of the control group (0 V/cm)

$$\Delta_{Fluo} = \frac{I_{Fluo} - < I_{Fluo\ Control} >}{< I_{Fluo\ Control} >}$$

where I_{Fluo} was the Yo-Pro-1 fluorescence intensity per cell and $<I_{Fluo\ Control}>$ was the mean Yo-Pro-1 fluorescence intensity of the control group (0 V/cm)

$\Delta_{Fluo}(t)$ and $\Delta_{THz}(t)$ were fitted with a mathematical model based on exponential functions:

$$\Delta_{Fluo}\,(\mathrm{t}) = C_{Fluo} * (1 - e^{\frac{-t}{\tau_{Fluo}}})$$

where C_{Fluo} and τ_{Fluo} were respectively related to the fluorescence plateau value and to the fluorescence time constant.

$$\Delta_{THz}\,(\mathrm{t}) = 100 - C_{THz} * (1 - e^{\frac{-t}{\tau_{THz}}})$$

where C_{THz} and τ_{THz} were related to the THz plateau value and to the THz time constant, respectively.

C_{Fluo} and τ_{Fluo} were compare respectively to C_{THz} and τ_{THz} in order to perform quantitative and qualitative comparison between the fluorescence and the THz modalities.

Monitoring the Molecular Composition of Live Cells Exposed to Pulsed Electric Fields via Label-free Optical Methods

Antoine Azan[1], Marianne Grognot[2], Lucie Descamps[1], Valérie Untereiner[3,4], Olivier Piot[3,4], Guilhem Gallot[2], and Lluis M. Mir[1*]

[1]Vectorology and Anticancer Therapies, UMR 8203, CNRS, Gustave Roussy, Univ. Paris-Sud, Université Paris-Saclay, 114 rue Edouard Vaillant, 94805 Villejuif, France.

[2]Laboratoire d'Optique et Biosciences, Ecole Polytechnique, UMR7645, CNRS, Route de Saclay, 91128 Palaiseau, France.

[3]MeDIAN, Biophotonics and Technologies for Health, MEDyC, UMR 7369, CNRS, University of Reims Champagne-Ardenne, 51 rue Cognacq-Jay, 51096 Reims, France.

[4]Cellular and Tissular Imaging Platform PICT, Faculty of Pharmacy, University of Reims Champagne-Ardenne, 51 rue Cognacq-Jay, 51096 Reims, France.

Correspondence and requests for materials should be addressed to Lluis. M. Mir (Luis.Mir@gustaveroussy.fr)

SUPPLEMENTARY INFORMATION

In supplementary information, we demonstrated that THz signal variations originated from changes of the intracellular proteins concentration. More precisely, the THz relative signal difference between the cells and their outer medium is proportional to the mass concentration of all intracellular proteins. To demonstrate this, we measured the THz relative signal obtained between simple solutions of molecules compared to pure water. Acquisitions of the THz relative signal was made on amino-acids, peptides and proteins up to 250 kDa. As shown in figure S1.a for a few examples, there was a linear relationship between a molecule mass concentration (in the biological range) and the THz relative signal generated. These slopes values are the THz relative signal sensitivity to mass concentration for each molecule. Values of all THz relative signal sensitivity given the size of the molecules tested are given in (Figure S1.b). The observed evolution of THz sensitivity with molecular weight can be understood and fitted by a simple volume model, as detailed in (X). One can see that for species above 2 kDa, the ratio of THz relative signal per gram per liter of protein is a constant (within a 12 % margin). Given the very small amount (in terms of mass) of amino-acids and peptides in the cells, compared to proteins, we can safely ignore their participation.

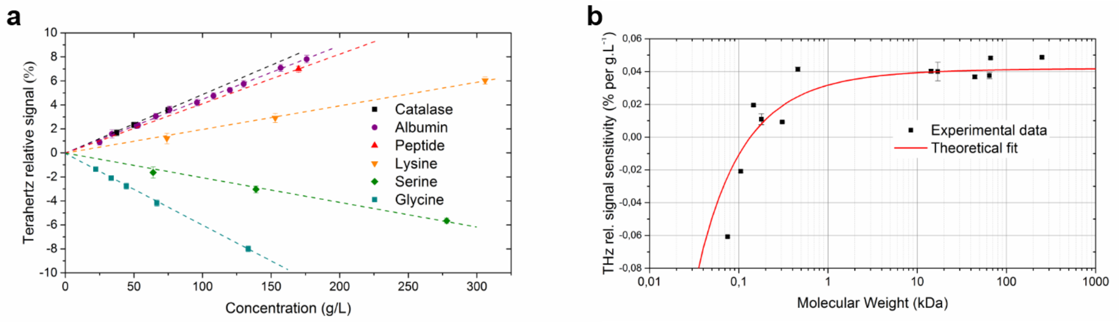

Figure S1: THz relative signal for amino-acid, peptide or protein solutions shows a linear relationship with mass concentration, with a slope depending on the tested molecule (a). Each slope illustrates the THz relative signal sensitivity to mass concentration of a given molecule. When plotted with respect to the molecular weight (b, black squares), sensitivity shows a global tendency that can be well fitted by a theoretical *model (b, red line) such as described in Grognot* et al.. *Above 2 kDa, sensitivity reach a constant value (within a 12% margin), meaning that a THz measure will only probe the protein mass concentration regardless of their molecular weight.*

6.5 A Novel Spectroscopically Determined Pharmacodynamic Biomarker for Skin Toxicity in Cancer Patients Treated with Targeted Agents (article #5)

Targeted therapies have significantly improved the treatment efficiency of various types of cancer such as melanoma, lung cancer or breast cancer. Based on tyrosine kinase inhibitors (TKIs), targeted anticaner therapies has become a standard treatment in various types of cancer. Although, the efficiency of TKI-based treatments against cancer is established, most patients are suffering from severe cutaneous side effects. In this study, we have investigated the opportunity to use confocal Raman microspectroscopy to detect skin toxicity in a non-invasive and label free manner. The Raman signatures of the skin of patients have been acquired before and during the first month of their TKI-based treatments. An algorithm has been designed to determine a new pharmacodynamic biomarker for skin toxicity in cancer patients treated with targeted agents.

This work has been conducted in collaboration with:

- the dermatology and the pulmonology departments of Gustave Roussy respectively headed by respectively Pr. Caroline Robert and Dr. Benjamin Besse who recruited the patients
- the Center for Optical Diagnostics & Therapy - Erasmuc MC, Rotterdam, The Netherlands - and RiverD international BV - Rotterdam, the Netherlands - headed by Dr. Gerwin Puppels who provided the confocal Raman microscope optimized for skin measurements
- the department of pharmacology and drugs analysis of Gustave Rousy headed by Pr. Angelo Paci who performed the drug titration into the patients' bloods
- the department of pathology of Gustave Roussy and Erasmus MC who performed the anatopathological analyses of the skin biopsies.

The Raman acquisitions of the skin of the patients have been performed at the dermatology department of Gustave Roussy. The results of this work have been published in Cancer Research in November 2016.

Therapeutics, Targets, and Chemical Biology

Cancer Research

A Novel Spectroscopically Determined Pharmacodynamic Biomarker for Skin Toxicity in Cancer Patients Treated with Targeted Agents

Antoine Azan[1], Peter J. Caspers[2,3], Tom C. Bakker Schut[2,3], Séverine Roy[4], Céline Boutros[4], Christine Mateus[4], Emilie Routier[4], Benjamin Besse[4], David Planchard[4], Atmane Seck[5], Nyam Kamsu Kom[6], Gorana Tomasic[7], Senada Koljenović[8], Vincent Noordhoek Hegt[8], Matthieu Texier[9], Emilie Lanoy[9], Alexander M.M. Eggermont[4,10], Angelo Paci[1,5], Caroline Robert[4,6,10], Gerwin J. Puppels[2,3], and Lluis M. Mir[1]

Abstract

Raman spectroscopy is a noninvasive and label-free optical technique that provides detailed information about the molecular composition of a sample. In this study, we evaluated the potential of Raman spectroscopy to predict skin toxicity due to tyrosine kinase inhibitors treatment. We acquired Raman spectra of skin of patients undergoing treatment with MEK, EGFR, or BRAF inhibitors, which are known to induce severe skin toxicity; for this pilot study, three patients were included for each inhibitor. Our algorithm, based on partial least squares-discriminant analysis (PLS-DA) and cross-validation by bootstrapping, discriminated to variable degrees spectra from patient suffering and not suffering cutaneous adverse events. For MEK and EGFR inhibitors, discriminative power was more than 90% in the viable epidermis skin layer; whereas for BRAF inhibitors, discriminative power was 71%. There was a 81.5% correlation between blood drug concentration and Raman signature of skin in the case of EGFR inhibitors and viable epidermis skin layer. Our results demonstrate the power of Raman spectroscopy to detect apparition of skin toxicity in patients treated with tyrosine kinase inhibitors at levels not detectable via dermatological inspection and histological evaluation. *Cancer Res; 77(2); 1–9. ©2016 AACR.*

Introduction

In recent years, targeted therapy has become a standard treatment against various types of cancer such as melanoma, lung cancer, and breast cancer. Many of these therapies target the intracellular MAPK pathway, also known as the "RAS–RAF–MEK–ERK pathway," which is abnormally activated in more than 7% of all human cancers (1). In particular, the *BRAF* gene coding for the serine/threonine-protein kinase BRAF is mutated in 60% to 70% of the melanomas (2). The MAPK pathway is involved in many cellular processes such as proliferation, differentiation, migration, and apoptosis (3). The use of tyrosine kinase inhibitors (TKI), for example, the inhibitors of the MEK, the EGFR, and the BRAF gene, are privileged strategies to regulate this pathway. Many TKI (4, 5) have recently received regulatory agency approval for the treatment of patients. Vemurafenib (GSK2118436), a BRAF inhibitor commercially available since 2011, has significantly improved the overall and progression-free survival of $BRAF^{V600E}$ mutation-positive melanoma patients (6–8). In the case of EGFR mutation-positive non–small cell lung cancer, studies have demonstrated a significant progression-free survival benefit in patients treated with erlotinib (EGFR inhibitor), in comparison with platinum-based chemotherapy when given as first line treatment to European and Asian patients (9, 10). Combination of these treatments is possible and contributes to improve the overall survival in patients with melanoma (11).

Although the efficiency of TKI against cancer is established, it is well-known that it induces strong cutaneous side effects. Lacouture and colleagues have shown that 92% to 95% of patients treated with vemurafenib showed dermatologic adverse events (12). Eighty-seven percent of patients treated

---

[1]UMR 8203, CNRS, Gustave Roussy, Univ. Paris-Sud, Université Paris-Saclay, Villejuif, France. [2]Center for Optical Diagnostics & Therapy, Department of Dermatology, Cancer Institute, Erasmus MC, Rotterdam, the Netherlands. [3]RiverD International B.V. Rotterdam, the Netherlands. [4]Department of Medical Oncology, Gustave Roussy, Villejuif, France. [5]Department of Pharmacology and Drug Analysis, Gustave Roussy, Villejuif, France. [6]UMR 981, INSERM, Gustave Roussy, Univ. Paris-Sud, Université Paris-Saclay, Villejuif, France. [7]Department of Pathology, Gustave Roussy, Villejuif, France. [8]Department of Pathology, Cancer Institute, Erasmus MC, Rotterdam, the Netherlands. [9]UMR 1018, INSERM, Gustave Roussy, Univ. Paris-Sud, Université Paris-Saclay, Villejuif, France. [10]Faculty of Medicine, Univ. Paris-Sud, Université Paris-Saclay, Le Kremlin Bicêtre, France.

Note: Supplementary data for this article are available at Cancer Research Online (http://cancerres.aacrjournals.org/).

Corresponding Author: Antoine Azan, CNRS, Gustave Roussy, Univ. Paris-Sud, Université Paris-Saclay, Gustave Roussy, PR2, rue Edoudard Vaillant 114, Villejuif 94805, France. Phone: 331-4211-4266; Fax: 331-4211-5245; E-mail: antoine.azan@gustaveroussy.fr.

doi: 10.1158/0008-5472.CAN-16-1733

with trametinib (a MEK inhibitor) experienced cutaneous toxicity (13). The underlying mechanisms of these adverse effects on the skin have been studied by many groups (14–16) but remains not completely understood.

Raman spectroscopy is a noninvasive technique that can provide information about the molecular composition of cells and tissues (17, 18). This nondestructive vibrational spectroscopy instrumentation is based on inelastic scattering of light caused by the interaction of light and molecular vibrations. It does not require reagents or the use of contrast enhancing agents. This technique is under investigation for many applications in biology. One of the main topics is the diagnosis of cancer through the identification of the biochemical differences between healthy and cancer tissue (19–22). Thanks to easy access, the skin is one of the major targeted tissues for *in vivo* Raman-based studies (23, 24).

In this study, we have evaluated the ability of Raman spectroscopy to detect cutaneous toxicity in patients under TKI treatment, namely with MEK, EGFR, or BRAF inhibitors, and so to use Raman signature of the skin as a new pharmacodynamic biomarker. We also report the specific methodology that we have developed to perform and analyze this dermatological application of Raman spectroscopy.

Patients and Methods

Patient population

This study was approved by the French Agency for the Safety of Health Products under ID RCB number 2010-A01051-37 and reference B101285-30. Patients were recruited from the dermatology unit and the pulmonology unit of the Department of Medical Oncology of Gustave Roussy (Villejuif, France). From January 2015 to March 2015, all patients, older than 18 years old, who were going to be treated with trametinib (MEK inhibitors), erlotinib, afatinib (EGFR inhibitors) dabrafenib, or vemurafenib (BRAF inhibitors) were invited to volunteer to this study. The volunteers signed an informed consent (SkinTarget Protocol CSET no. 2010/1664) permitting the research team to acquire *in vivo* skin Raman spectra, to perform skin biopsies, to have a dermatologist consultation, to take blood samples, and to take standardized pictures of the affected skin. Nine patients were included in this study, three undergoing treatment with a MEK inhibitor, three patients treated with an EGFR inhibitor, and three patients treated with a BRAF inhibitor. Patients were between 49 and 68 years old.

Data collection

For each patient, data acquisition was performed at three time points, apart from one patient due to a no-show. During each session, a complete dataset was collected the same day, comprising *in vivo* Raman measurements of the skin, a dermatologic report, a skin biopsy, a blood sample, and standardized pictures of the face, the hands, the nails, and the feet. The Raman measurements and the skin biopsies were done at a skin location that appeared healthy from a dermatologic point of view. This location was chosen in order to avoid potential interference of the Raman measurement by a local inflammatory reaction. The first data collection session was performed before the start of the treatment. The second and the last session were planned about 2 and 4 weeks after initiation of the treatment. This measurements schedule was based on the expected time to occurrence of skin toxicity observed with these agents and coincided with scheduled routine visits of the patients to the hospital.

Raman skin measurements

For this study, a commercially available gen2-SCA (Skin Composition Analyzer) from RiverD International B.V. was used (Fig. 1). This confocal Raman spectroscopy instrument has been optimized for *in vivo* skin measurements. It can measure the Raman spectrum in the Fingerprint (FP) region (400–1,800 cm^{-1}) using a 30 mW 785 nm continuous wave laser and the Raman spectrum in the high wavenumber (HWN) region (2,600–4,000 cm^{-1}) using a 20 mW 671 nm continuous wave laser. The laser light intensities comply with international laser safety standards (25). The laser is focused into the skin by a custom designed immersion microscope objective (100×, 1.2 numerical aperture). The depth resolution is better than 5 µm. Raman signal is collected using the same objective. An XY piezoelectric stage can translate the measurement window so as to access multiple skin locations. The objective can be Z-translated to focus the beam at different depths in the skin. The measurements were performed using the RiverICon software (RiverD International B.V.).

Before each Raman measurement session, the equipment was auto-calibrated and the power of the laser beams was checked.

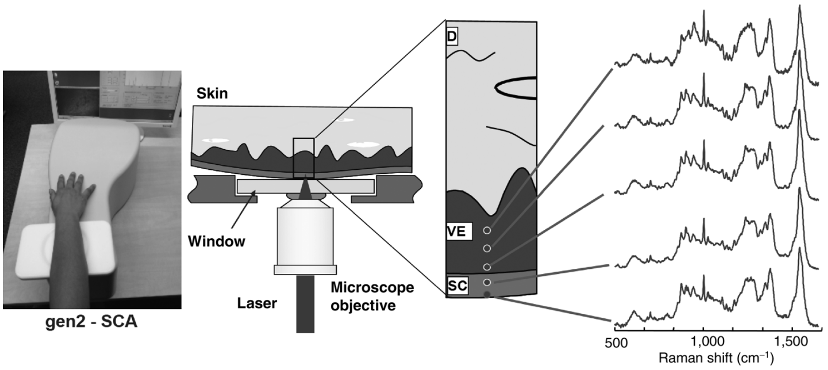

Figure 1.
Gen2SCA Skin Analyzer general operating scheme: the patient places his/her upper forearm on the window; the laser beam is focused into the skin through the microscope objective. The objective can be Z-translated to have access to different skin layers (SC and VE).

The measurements were performed on the lower forearm of the patients, far away from any skin lesion. Patients put their right arm on a fused silica measurement window through which the microscope objective focuses laser light in the skin. During each session, between five and nine different locations were acquired for both spectral regions (FP and HWN). At each location, Raman measurements with specific in-depth profile were performed to acquire several spectra from two skin layers: the stratum corneum (SC) and the viable epidermis (VE; ref. 26). For the FP spectral band, the Raman acquisitions were performed until 24-µm depth with a step size of 4 µm and two additional points at 32- and 40-µm of depths, which gives a total of nine spectra per in-depth profile. For the HWN spectral band, the Raman acquisitions were performed until 48 µm with a step size of 4 µm, which gives a total of 13 spectra per in-depth profile. To ensure spectra with high signal-to-noise ratio (SNR), the acquisition time was chosen in the range from 5 to 30 seconds in FP band and fixed to 1 second in HWN band. The maximum duration of the Raman data collection was 40 minutes. In total, 4,532 spectra were collected (1,854 in the FP region and 2,678 in the HWN region).

Raman data preprocessing

First of all, an analysis of the spectra quality on the FP dataset was performed. To do so, the signal-to-noise ratio (SNR) was calculated, with the Eq. 1, for each measured spectra in the FP band.

$$\mathrm{SNR} = \frac{S*G}{\sqrt{N*G}} \tag{1}$$

where S is the magnitude of the peak at 1,003 cm^{-1}, N is the total magnitude of the signal at 1,003 cm^{-1} minus the charge-coupled device (CCD) offset, and G is the gain of the CCD detector. All the spectra with SNR < 10 were removed from the dataset (representing less than 10%). Moreover, a few outlier spectra were also removed from the dataset.

Caspers and colleagues (27) demonstrated that the water mass concentration profile and the natural moisturizing factor (NMF) profile are good indicators of the SC/VE interface. Water mass in-depth profile can also be used to determine the SC apparent thickness (28). The SkinTools software v2.0 (RiverD International B.V.) was used to extract water mass profile from the HWN Raman measurements and so to determine the SC/VE interface (29). Thus, each spectrum acquired in the FP spectral band could be attributed to the appropriate skin layer, meaning SC or VE. Then, the FP spectra were preprocessed by extended multiplicative signal correction (EMSC; ref. 30) to normalize each spectrum to a unique reference spectrum while removing the spectral variance due to fused silica and room light. Based on the dermatologic exam performed on the same day as the Raman acquisition, each recorded Raman spectrum was labeled as: "toxicity" meaning spectrum from patient suffering of skin toxicity or "no toxicity" meaning spectrum from patient not suffering of skin toxicity. For the two groups (i.e., "toxicity" and "no toxicity"), the mean spectrum for each skin layer investigated and each inhibitor was calculated.

Statistical analysis

Multivariable analysis was performed to classify the Raman signature of patient in the two groups. Multivariable analysis was based on partial least-square regression (PLS; ref. 31) coupled with linear discriminant analysis (LDA; ref. 32) in cross-validation by bootstrapping (33), coined her "PLS-DA."

Randomly 90% of the complete dataset was selected to establish a model (training dataset), and the remaining 10% of the dataset (validation dataset) was used to test the model. To avoid any bias, the ratio in the number of spectra belonging to the two groups (i.e., "toxicity" and "no toxicity") was preserved when splitting the dataset. PLS was performed on the mean-centered training dataset. The drug concentrations into patients' blood were used as the observable variable for the PLS analysis. The titration of the drugs is detailed in a specific paragraph and the results are reported in Supplementary Table S1. In the case of blood samples were missing, the corresponding spectra were removed from the PLS and subsequent LDA analysis. From the 10 first latent variables (LV) determined by PLS, LV selection was based on quantitative criterion. To be selected, the scores of the LV for the two groups (i.e., "toxicity" and "no toxicity") had to be statistically significant (Student *t* test, Bonferroni adjusted *P*-value <0.05; ref. 34). To prevent any overfitting in the model, the maximum number of LVs selected was equal to 6. The scores on the selected LVs were used as input for the LDA analysis to determine the linear discriminant (LD). The LD established on the training dataset was applied to the mean-centered validation dataset. So LD score was calculated for each spectrum of the validation dataset. On the basis of the LD scores of the validation dataset, the discriminative power between the two groups (i.e., "toxicity" and "no toxicity") was analyzed using receiver operating characteristic (ROC) curves (35). The area under the curve (AUC) of the ROC curve was calculated. Accuracy, sensitivity, and specificity were determined on the basis of the Youden index (36). Student *t* test was also performed to assess the statistical difference between the LD scores of the two groups in the validation dataset. At each iteration, ROC curve, AUC, accuracy, sensitivity, specificity, and *P* value were determined for the validation dataset. Moreover, LD scores of the validation were recorded. This individual cross-validation was repeated 5,000 times with different training and validation datasets. The number of iterations of bootstrapping was determined to include each spectrum of the complete dataset in the two sub-datasets (i.e., training and validation). The mean ROC curve, AUC, accuracy, sensitivity, and specificity were calculated. For each spectrum of the complete dataset, the mean LD score was calculated. The correlation between the Raman signature and the drug concentration was performed by calculating the coefficient of determination (R^2) between the mean LD scores and the drug concentration.

This data process was applied to the two skin layers (SC and VE) and the three groups of patients (MEK, EGFR, and BRAF inhibitors). All data processing and data analysis were performed under MATLAB v2009b (MathWorks).

Preparation of skin biopsy

Four millimeters diameter punch biopsies were performed on clinically unaffected skin. The skin biopsies were formalin fixed and paraffin embedded. Microscopic slides with 3-µm-thick tissue sections were stained with hematoxylin, eosin, and Safran (HES) and periodic acid-Schiff (PAS). The slides were analyzed by three pathologists from two different hospitals (Erasmus MC and Gustave Roussy) in an independent way.

Determination of the drugs concentration into the patient blood

Blood samples were centrifuged (3,000 rpm, 2,200 × *g* for 10 minutes) and plasma was separated in aliquots and stored at −20°C prior to analysis.

Plasma samples of patients treated with dabrafenib (BRAF inhibitor), trametinib (MEK inhibitor), and erlotinib (EGFR inhibitor) were analyzed by ultra-performance liquid chromatography combined to tandem mass spectrometry (UPLC-MS/MS) on Acquity-Xevo TQ system with MassLynx 4.1 software (Waters). Dabrafenib, trametinib, and erlotinib were analyzed using respectively [$^2H_9$]-dabrafenib, [$^{13}C_6$]-trametinib, and bosutinib as internal standards (IS). Dabrafenib, trametinib, and erlotinib and their IS were separated on a Acquity UPLC BEH C18 chromatography column (2.1 mm × 50 mm I.D., 1.7 μm; Waters) using gradient elution with mobile phases of acetonitrile ± methanol, ammonium formiate, and ultrapure water at a flow rate of 0.7 mL/minute.

Vemurafenib (BRAF inhibitor) was analyzed by high-performance liquid chromatography combined to UltraViolet detection (HPLC-UV) on a HPLC-UV 1200-1290 system (Agilent) using sorafenib as IS. Vemurafenib and the IS were separated on a Kinetex PFP 4.6 × 100 mm, 2.6 μm (Phenomenex) using gradient elution with mobile phases of acetonitrile, KH_2PO_4 20 mmol/L and ultrapure water at a flow rate of 1.0 mL/minute.

All analytic methods were validated in terms of specificity, linearity range, precision, and accuracy according to EMA guidelines. Dabrafenib and trametinib concentrations were determined between 1 and 2,000 ng/mL with intraday and interday precision coefficients of variation (CV) below 2.4%. Vemurafenib concentration was determined between 1 and 50 μg/mL with intraday and interday precision CVs below 6.9%. Erlotinib concentration was measured between 1 and 1,000 ng/mL with an intraday and interday precision CVs below 8.3%.

The results are reported in Supplementary Table S1.

Results

General

In this study, none of the nine patients included suffered from skin toxicity before the beginning of the treatment. After 1 month of treatment, all of them presented skin adverse events. The Supplementary Table S2 reports the various cutaneous adverse events for each patient at the two time points.

As expected (37, 38), patients of MEK and EGFR inhibitors groups were suffering from similar cutaneous adverse events. Five of 6 patients displayed folliculitis after 1 month of treatment. Figure 2 shows example of folliculitis on the face of patient treated with MEK inhibitors. Prurituses were detected in half of them. In the BRAF group, no folliculitis or pruritus was noticed contrary to patients treated by MEK or EGFR inhibitors. As expected (39, 40), two out of three patients of BRAF inhibitors groups were suffering from grade I keratosis. Two of 3 patients of BRAF inhibitors group were suffering from grade I xerosys. It has to be noticed that 6 of 9 patients of the cohort were displaying skin toxicity after 2 weeks of treatment.

Spectral analysis

The mean normalized Raman spectra of the two groups (i.e., toxicity and no toxicity) were calculated for the three inhibitors and the two skin layers investigated (Fig. 3). Because of the thickness of the SC compared with the VE, the number of spectra acquired in the SC for the FP band was 33% lower than in the VE (439 vs. 656). As expected, the shape of the Raman spectra in the SC and the VE was different. The SC spectra showed a peak at 880 cm^{-1}, which was not present in the VE spectra. This peak is attributed to the NMF, which is only present in the SC skin layer (27).

Figure 2.
Face picture of patient under MEK inhibitors before and after one month of treatment. This patient is suffering from grade I folliculitis.

The differential spectra (toxicity minus no toxicity) did not show clear and consistent differences. In the case of MEK and EGFR inhibitors in the SC, the differential spectral displayed a small decrease in the peak at 1,650 cm^{-1} attributed to keratin. For the same conditions, the peak at 1,442 cm^{-1} related to NMF displayed a small increase. The Raman signature of the drug itself could not be observed in the Raman spectra of the skin patients even after 1 month of treatment. This might be due to the residual amount of drugs in cutaneous tissue, which was below the detection limit of the equipment and/or to the metabolization of the drug ending to different chemical products with different Raman signatures. Therefore, for each skin layer and inhibitor, multivariable analysis was used to investigate the presence of systematic differences between the two groups (i.e., toxicity vs. no toxicity).

Multivariable statistical discrimination models

Figure 4 shows the ROC curves to quantify the discriminative power between the two groups (i.e., toxicity vs. no toxicity) for the different analysis performed. Table 1 summarizes the discrimination performances for each ROC curve by indicating the AUC, the accuracy, the specificity, and the sensitivity.

For patients treated with MEK inhibitors, the AUC of the ROC curve was 90% when investigating the VE skin layer (Fig. 4A). Accuracy, sensitivity, and specificity were around 90% (Table 1), indicating a good discriminative power between the two groups. In comparison, the AUC of the ROC curve for the SC was much lower (70% vs. 90%). Although the discriminative power was lower in the SC than in the VE, the LD scores between the two groups (i.e., toxicity vs. no toxicity) were significantly statistically different with a *P* value lower than 0.01% (Supplementary Fig. S1A and S1D).

For patients treated with EGFR inhibitors, the AUCs of the ROC curve in both skin layers were higher than 95%. The AUC of the ROC curve was slightly lower in the SC than in the VE (96% vs. 97%). Accuracy, sensitivity, and specificity in the two skin layers were more than 95%. The differences in the LD scores between the

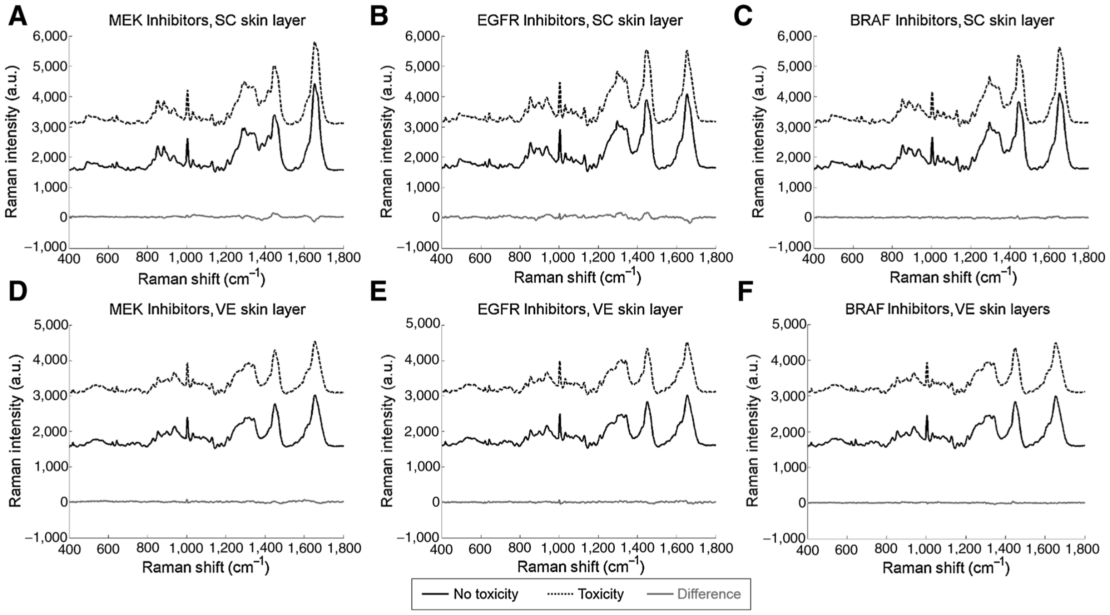

Figure 3.

Mean normalized Raman spectra from skin patients of the two groups. The differential spectrum (toxicity minus no toxicity) is also displayed. **A,** MEK inhibitors in the SC skin layer (no toxicity, $n = 114$; toxicity, $n = 85$). **B,** EGFR inhibitors in the SC skin layer (no toxicity, $n = 43$; toxicity, $n = 57$). **C,** BRAF inhibitors in the SC skin layer (no toxicity, $n = 44$; toxicity, $n = 96$). **D,** MEK inhibitors in the VE skin layer (no toxicity, $n = 88$; toxicity, $n = 111$). **E,** EGFR inhibitors in VE skin layer (no toxicity, $n = 67$; toxicity, $n = 129$). **F,** BRAF inhibitors in the VE skin layer (no toxicity, $n = 84$; toxicity, $n = 177$). The spectra are shown with vertical offset for more clarity.

two groups were statistically different with a P value lower than 0.01% (Supplementary Fig. S1B and S1E). It can be noticed that P value was lower in the VE than in the SC (1.51×10^{-31} vs. 4.3×10^{-17}). It confirms that the discriminative power was slightly better in the VE than in the SC for patients treated with EGFR inhibitors.

For patients treated with BRAF inhibitors, the AUC of the ROC curve in the VE was 71%. In comparison, the AUC of the ROC curve in the SC was lower (65% vs. 71%). Although the discriminative powers remained low, the LD scores between the two groups were statistically significantly different with a P value lower than 0.01% (Supplementary Fig. S1C and S1F). PLS data analysis implies that the variance of the dataset might be linearly related to a variable, in our case the drug concentration into patient's blood. Because of the low discriminative power of the PLS data analysis in the case of the BRAF inhibitors group (AUC = 65%), it was reasonable to consider that the previous hypothesis was not correct and was limiting the discri

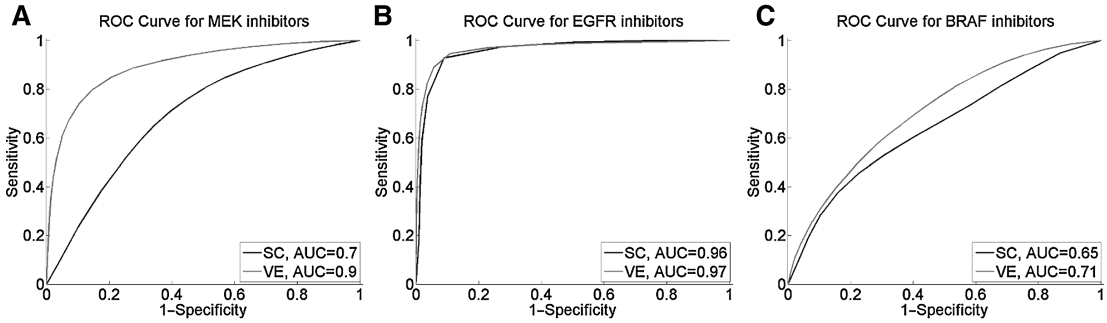

Figure 4.

ROC curves for the discrimination based on PLS-DA data analysis technique in the SC skin layer and VE for patient treated with MEK inhibitors (**A**), EGFR inhibitors (**B**), or BRAF inhibitors (**C**). In the inset, the value of the AUC is indicated for each ROC curve.

Table 1. Summary of the discrimination performance by PLS-DA between skin spectra from patients with or without skin toxicity for the three groups (MEK, EGFR, and BRAF inhibitors) and for the two skin layers (SC and VE)

	Discriminative performance			
	PLS-DA			
	AUC (%)	Accuracy (%)	Sensitivity (%)	Specificity (%)
SC				
MEK	70	74	66	80
EGFR	96	96	95	96
BRAF	65	75	89	49
VE				
MEK	90	88	87	90
EGFR	97	96	96	95
BRAF	71	77	90	51

minative performance. To try to improve the discriminative power of our model, we have performed the same data process but PLS was replaced by principal component analysis (PCA), which is an unsupervised multivariable data analysis technique. In this case, the discriminative result was 12% better in the SC in comparison with the PLS-DA data process (77% vs. 65%).

We correlated the Raman signature of patients' skin with the titration of the drug into patients' blood (Fig. 5). As a confirmation of the previous results, the best correlations were obtained for the EGFR inhibitors. In this case, the coefficients of determination were around 80% for the two skin layers investigated. The coefficient of determination was slightly higher in the VE than in the SC (81.5% vs. 79.6%), confirming the previous discriminative performance results. For MEK inhibitors in the VE, the coefficient of determination was 72.7%. In the case of BRAF inhibitors, the coefficients of determination were below 55% in the two skin layers investigated (Fig. 5C and F).

Histologic evaluation of skin biopsies

Histopathologic analysis of the microscopic slides of skin biopsies did not reveal any significant tissue disarray after 1 month of treatment (Fig. 6). In some cases, small variations in the SC with hyperkeratosis were noticed. In two biopsies, focal slight epidermal hyperplasia and slight dysplasia were present without any correlation with the treatment. No inflammation was noticed.

Discussion

The aim of this pilot study was to investigate the ability of Raman spectroscopy to detect skin toxicity in patients under treatment by TKI. Multivariable statistical analysis technique (PLS-DA) was tested to discriminate Raman signatures of skin from patient suffering of cutaneous toxicity and Raman signatures of skin from patient not suffering of cutaneous toxicity. The discriminative performances, evaluated by PLS-DA and cross-validation by bootstrapping, were found to be dependent on the treatment and the skin layers investigated. In general, the algorithm allowed better discriminative results for MEK and EGFR inhibitors than for patients treated with BRAF inhibitors. This

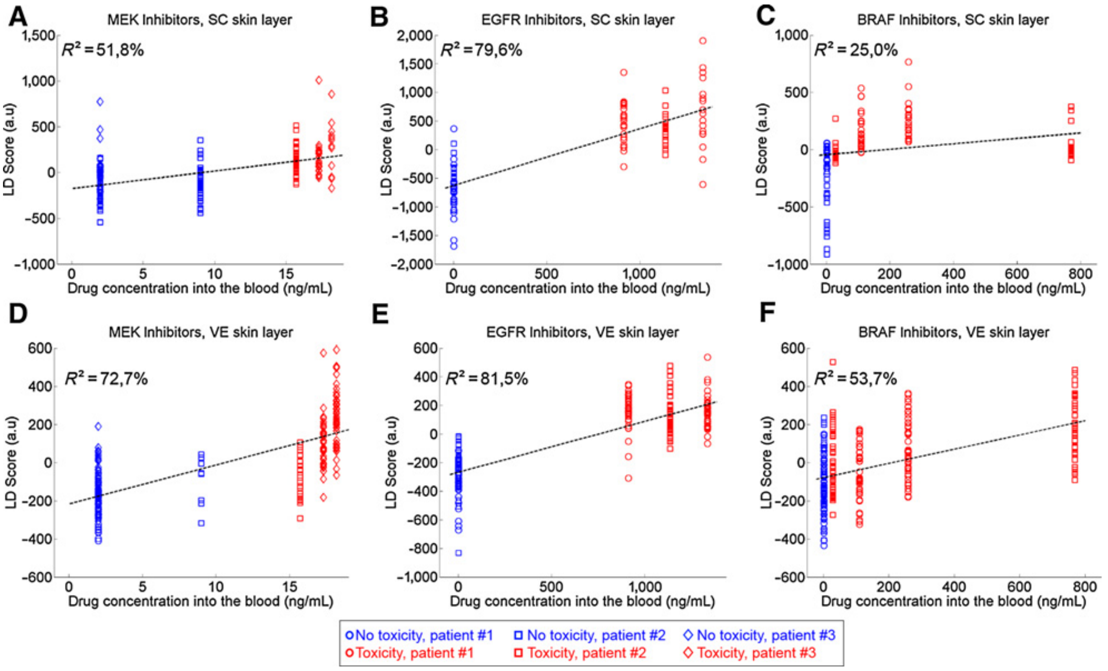

Figure 5.

Correlation plot between the drug concentration into blood sample and Raman signature of patient skin. The LD score refers to the mean LD score calculated in the validation dataset for each spectrum. The linear curve fitting the data is plotted in dash line. The coefficient of determination between LD score and drug concentration is indicated. Each patient is indicated with a specific marker type. In the case of drug concentration missing, the data are not represented.

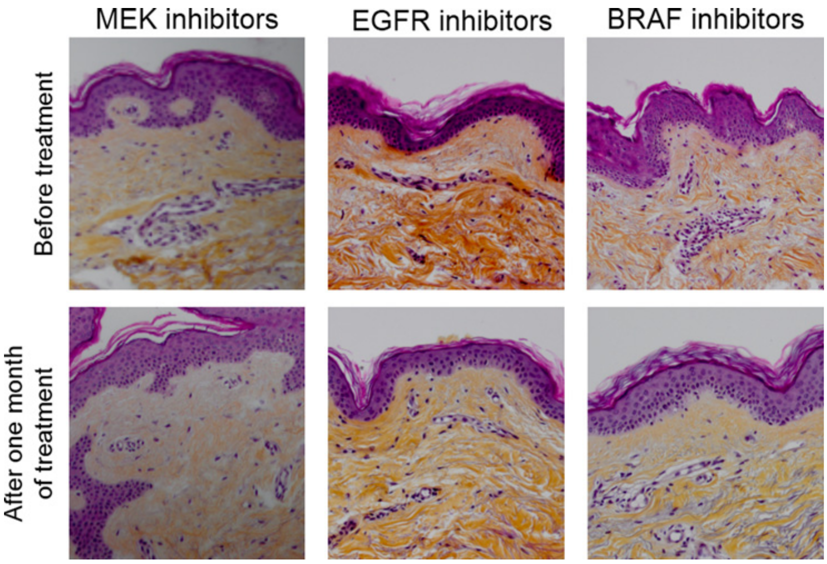

Figure 6.
HES staining of microscopic tissue sections from skin biopsies of the patients before (top row) and after one month of treatment (bottom row) with MEK inhibitors, EGFR inhibitors, and BRAF inhibitors.

might be related to the different mechanisms of these drugs on healthy tissue. It is well established that BRAF inhibitors activate the MAPK pathway in normal (wild-type *BRAF*) cells (41). This activation induces a dimerization of the RAF kinase inducing a phosphorylation of MEK and ERK kinase (42). In contrary, MEK and EGFR inhibitors inhibit the MAPK pathway in the wild-type cells (13, 38). Although, patients under MEK and EGFR inhibitors exhibit similar spectrum of skin adverse events with papulopustular rash, dry skin, perionyxis, and hair changes. Patients treated with BRAF inhibitors were suffering from follicular keratosis, palm and sole hyperkeratosis, eruptive papillomas, squamous cell carcinomas, or melanomas. We might speculate that Raman spectroscopy is more sensitive to chemical modifications of the skin induced by the inhibition of the MAPK pathway than its activation. It has to be noticed that even with a small number of patients, the discrimination results reached high level of accuracy, sensitivity, and specificity. A larger number of patients would contribute to enhance those differences. Moreover, Raman signatures were acquired at skin locations that were not-affected from a dermatologic point-of-view. Skin biopsies were also performed on healthy looking tissue and did not show modifications of the skin related to the treatment. Thus, Raman spectroscopy has access to information that is not detectable at the dermatologic and histologic levels. Similar results have been obtained by Le Naour and colleagues (43) when targeting liver steatosis by vibrational spectroscopy on tissue sections from histologically normal areas from an otherwise steatotic liver. Many studies have demonstrated the possibility of Raman spectroscopy to accurately discriminate cutaneous cancer tissue from normal tissue (44, 45).

For EGFR and MEK inhibitors, the best discriminative results were obtained in VE skin layer. In both groups, the AUC of the ROC curves for VE skin layer were more than 90%. These results are supported by dermatologic knowledge indicating that EGFR is mainly expressed in undifferentiated keratinocytes in the basal and suprabasal layers of the epidermis (46). Moreover, constitutive activation of upstream kinase MEK1 perturbed the differentiation of human keratinocytes located in the basal and suprabasal layers of the epidermis (47). This study points out that VE is the skin layer primarily impacted biochemically by MEK and EGFR inhibitors. The best discriminative result was obtained for the EGFR inhibitors in the VE skin layer with an accuracy of 96%, a sensitivity of 96% and a specificity of 95%. Even with a small number of patients, the correlation of the skin Raman signature and the drugs concentration was over 81%.

Our results show that Raman signature of patients dermatologically and histologically normal patients' skin can be used as a pharmacodynamic biomarker for cutaneous adverse events toxicity due to TKI treatment. The opportunity to predict skin toxicity via Raman spectroscopy, a noninvasive and label-free optical instrumentation, would be a great contribution to improve the life quality of patients under TKI treatment. Indeed, it could open the possibility to modify the treatment before the detection of visible and quality-of-life impairing skin toxicity. Moreover, because meta-analysis studies have demonstrated that skin toxicity is correlated with the response to the anti-EGFR treatment in non–small lung cancer (48, 49), investigating the correlation between Raman spectroscopy of the skin and anti-EGFR treatment efficacy would be interesting in the perspective of monitoring the treatment efficacy in a noninvasive way. Further investigations are thus necessary.

Conclusion

This pilot study is the first one to investigate the skin toxicity induced by new anticancer-targeted therapies by the means of Raman spectroscopy. Our results show that Raman spectroscopy is able to discriminate spectra from patients suffering of skin toxicity and patients not suffering of skin toxicity. By correlating the skin patients Raman signature and the drugs concentration into patient's blood, we can conclude that Raman spectroscopy can be used as a pharmacodynamic biomarker for skin toxicity induced by TKI treatment.

Disclosure of Potential Conflicts of Interest

D. Planchard is a consultant/advisory board member for Astrazeneca, Boehringer, Roche, BMS, MSD, Pfizer, and Novartis. S. Koljenović, V.N. Hegt, and G.J. Puppels have ownership interest (including patents) in RiverD International B.V. C. Robert is a consultant/advisory board member for Roche, BMS, MSD, Novartis, and Amgen. No potential conflicts of interest were disclosed by the other authors.

Authors' Contributions

Conception and design: A. Azan, P.J. Caspers, S. Koljenović, V. Noordhoek Hegt, A.M.M. Eggermont, C. Robert, G.J. Puppels, L.M. Mir
Development of methodology: A. Azan, P.J. Caspers, T.C. Bakker Schut, B. Besse, A. Seck, S. Koljenović, A. Paci, G.J. Puppels, L.M. Mir
Acquisition of data (provided animals, acquired and managed patients, provided facilities, etc.): A. Azan, C. Boutros, C. Mateus, E. Routier, B. Besse, D. Planchard, A. Seck, N. Kamsu Kom, G. Tomasic, S. Koljenović, V. Noordhoek Hegt, M. Texier, A. Paci
Analysis and interpretation of data (e.g., statistical analysis, biostatistics, computational analysis): A. Azan, P.J. Caspers, T.C. Bakker Schut, D. Planchard, S. Koljenović, V. Noordhoek Hegt, E. Lanoy, A. Paci, C. Robert, G.J. Puppels, L.M. Mir
Writing, review, and/or revision of the manuscript: A. Azan, P.J. Caspers, T.C. Bakker Schut, C. Boutros, D. Planchard, S. Koljenović, V. Noordhoek Hegt, E. Lanoy, A.M.M. Eggermont, C. Robert, G.J. Puppels
Administrative, technical, or material support (i.e., reporting or organizing data, constructing databases): A. Azan, A. Seck, G. Tomasic, S. Koljenović
Study supervision: C. Robert, G.J. Puppels, L.M. Mir

Acknowledgments

The authors thank the patients involved in this study, Cathy Philippe, Arthur Tenenhaus and Jane Merlevede for fruitful advice on the data process, Martin Van der Wolf and Kevin Stouten from River D International for technical support on the equipment, Bruno Thuillier from the dermatology unit of Gustave Roussy for logistic support, and Marie Breton from UMR8203 and Aliette Ventéjoux from EA 4398–PRISMES for carefully reading this article.

Grant Support

This study was financially supported by Gustave Roussy.

The costs of publication of this article were defrayed in part by the payment of page charges. This article must therefore be hereby marked *advertisement* in accordance with 18 U.S.C. Section 1734 solely to indicate this fact.

Received July 6, 2016; revised September 14, 2016; accepted October 2, 2016; published OnlineFirst November 11, 2016.

References

1. Platz A, Egyhazi S, Ringborg U, Hansson J. Human cutaneous melanoma; a review of NRAS and BRAF mutation frequencies in relation to histogenetic subclass and body site. Mol Oncol 2008;1:395–405.
2. Davies H, Bignell GR, Cox C, Stephens P, Edkins S, Clegg S, et al. Mutations of the BRAF gene in human cancer. Nature 2002;417:949–54.
3. Hilger RA, Scheulen ME, Strumberg D. The Ras-Raf-MEK-ERK pathway in the treatment of cancer. Onkologie 2002;25:511–8.
4. Ballantyne AD, Garnock-Jones KP. Dabrafenib: first global approval. Drugs 2013;73:1367–76.
5. Wright CJM, McCormack PL. Trametinib: first global approval. Drugs 2013;73:1245–54.
6. Chapman PB, Hauschild A, Robert C, Haanen JB, Ascierto P, Larkin J, et al. Improved survival with vemurafenib in melanoma with BRAF V600E mutation. N Engl J Med 2011;364:2507–16.
7. Ribas A, Flaherty KT. BRAF targeted therapy changes the treatment paradigm in melanoma. Nat Rev Clin Oncol 2011;8:426–33.
8. Kim G, McKee AE, Ning Y-M, Hazarika M, Theoret M, Johnson JR, et al. FDA approval summary: vemurafenib for treatment of unresectable or metastatic melanoma with the BRAFV600E mutation. Clin Cancer Res 2014; 20:4994–5000.
9. Zhou C, Wu Y-L, Chen G, Feng J, Liu X-Q, Wang C, et al. Erlotinib versus chemotherapy as first-line treatment for patients with advanced EGFR mutation-positive non-small-cell lung cancer (OPTIMAL, CTONG-0802): a multicentre, open-label, randomised, phase 3 study. Lancet Oncol 2011;12:735–42.
10. Rosell R, Carcereny E, Gervais R, Vergnenegre A, Massuti B, Felip E, et al. Erlotinib versus standard chemotherapy as first-line treatment for European patients with advanced EGFR mutation-positive non-small-cell lung cancer (EURTAC): a multicentre, open-label, randomised phase 3 trial. Lancet Oncol 2012;13:239–46.
11. Robert C, Karaszewska B, Schachter J, Rutkowski P, Mackiewicz A, Stroiakovski D, et al. Improved overall survival in melanoma with combined dabrafenib and trametinib. N Engl J Med 2014;372: 141116004513004.
12. Lacouture ME, Duvic M, Hauschild A, Prieto VG, Robert C, Schadendorf D, et al. Analysis of dermatologic events in vemurafenib-treated patients with melanoma. Oncologist 2013;18:314–22.
13. Livingstone E, Zimmer L, Vaubel J, Schadendorf D. BRAF, MEK and KIT inhibitors for melanoma: adverse events and their management. Chin Clin Oncol 2014;3:29.
14. Manousaridis I, Mavridou S, Goerdt S, Leverkus M, Utikal J. Cutaneous side effects of inhibitors of the RAS/RAF/MEK/ERK signalling pathway and their management. J Eur Acad Dermatology Venereol 2013;27:11–8.
15. Robert C, Thomas M, Mateus C. MAP-kinase pathway up or down? Just look at the skin of your patients! Melanoma Res 2014;24:421–3.
16. Boussemart L, Routier E, Mateus C, Opletalova K, Sebille G, Kamsu-Kom N, et al. Prospective study of cutaneous side-effects associated with the BRAF inhibitor vemurafenib: a study of 42 patients. Ann Oncol 2013;24:1691–7.
17. Notingher I.Raman spectroscopy cell-based biosensors. Sensors 2007; 7:1343–58.
18. Downes A, Elfick A. Raman spectroscopy and related techniques in biomedicine. Sensors 2010;10:1871–89.
19. Haka AS, Volynskaya Z, Gardecki JA, Nazemi J, Lyons J, Hicks D, et al. In vivo margin assessment during partial mastectomy breast surgery using Raman spectroscopy. Cancer Res 2006;66:3317–22.
20. Barman I, Dingari NC, Saha A, McGee S, Galindo LH, Liu W, et al. Application of Raman spectroscopy to identify microcalcifications and underlying breast lesions at stereotactic core needle biopsy. Cancer Res 2013;73:3206–15.
21. Barroso EM, Smits RWH, Bakker Schut TC, ten Hove I, Hardillo JA, Wolvius EB, et al. Discrimination between oral cancer and healthy tissue based on water content determined by Raman spectroscopy. Anal Chem 2015;87: 2419–26.
22. Downes A. Raman microscopy and associated techniques for label-free imaging of cancer tissue. Appl Spectrosc Rev 2015;50:641–53.
23. Ali SM, Bonnier F, Tfayli A, Lambkin H, Flynn K, McDonagh V, et al. Raman spectroscopic analysis of human skin tissue sections *ex vivo*: evaluation of the effects of tissue processing and dewaxing. J Biomed Opt 2013;18: 61202.
24. Vyumvuhore R, Tfayli A, Piot O, Le Guillou M, Guichard N, Manfait M, et al. Raman spectroscopy: *in vivo* quick response code of skin physiological status. J Biomed Opt 2014;19:111603.
25. Puppels GJ, Sterrenborg HJC. Laser safety aspects of the use of the Model 3510 Skin Composition Analyzer (SCA) in *in vivo* studies of human subjects; 2007.
26. Sandby-Møller J, Poulsen T, Wulf HC. Epidermal thickness at different body sites: relationship to age, gender, pigmentation, blood content, skin type and smoking habits. Acta Derm Venereol 2003;83:410–3.
27. Caspers PJ, Lucassen GW, Puppels GJ. Combined *invivo* confocal Raman spectroscopy and confocal microscopy of human skin. Biophys J 2003; 85:572–80.
28. Egawa M, Hirao T, Takahashi M. *In vivo* estimation of stratum corneum thickness from water concentration profiles obtained with Raman spectroscopy. Acta Derm Venereol 2007;87:4–8.
29. Caspers PJ, Lucassen GW, Carter EA, Bruining HA, Puppels GJ. In vivo confocal Raman microspectroscopy of the skin: noninvasive

determination of molecular concentration profiles. J Invest Dermatol 2001;116:434–42.

30. Martens H, Stark E. Extended multiplicative signal correction and spectral interference subtraction: new preprocessing methods for near infrared spectroscopy. J Pharm Biomed Anal 1991;9:625–35.
31. Wold S, Sjöström M, Eriksson L. PLS-regression: a basic tool of chemometrics. Chemom Intell Lab Syst 2001;58:109–30.
32. Altman EI. Financial ratios, discriminant analysis and the prediction of corporate bankruptcy. J Finance 1968;23:589–609.
33. Kohavi R. A study of cross-validation and bootstrap for accuracy estimation and model selection. Int Jt Conf Artif Intell 1995;2:1137–43.
34. Dunn OJ. Multiple comparisons among means. J Am Stat Assoc 1961;56:52–64.
35. Hanley JA, McNeil BJ. The meaning and use of the area under a receiver operating characteristic (ROC) curve. Radiology 1982;143: 29–36.
36. Youden WJ.Index for rating diagnostic tests. Cancer 1950;3:32–5.
37. Lacouture ME, Anadkat MJ, Bensadoun R-J, Bryce J, Chan A, Epstein JB, et al. Clinical practice guidelines for the prevention and treatment of EGFR inhibitor-associated dermatologic toxicities. Support Care Cancer 2011; 19:1079–95.
38. Balagula Y, Huston KB, Busam KJ, Lacouture ME, Chapman PB, Myskowski PL. Dermatologic side effects associated with the MEK 1/2 inhibitor selumetinib (AZD6244, ARRY-142886). Invest New Drugs 2011;29:1114–21.
39. Mandalà M, Massi D, De Giorgi V. Cutaneous toxicities of BRAF inhibitors: clinical and pathological challenges and call to action. Crit Rev Oncol Hematol 2013;88:318–37.
40. Anforth R, Fernandez-Peñas P, Long GV. Cutaneous toxicities of RAF inhibitors. Lancet Oncol 2013;14:e11–8.
41. Zhang C, Spevak W, Zhang Y, Burton EA, Ma Y, Habets G, et al. RAF inhibitors that evade paradoxical MAPK pathway activation. Nature 2015;526:583–6.
42. Belum VR, Fischer A, Choi JN, Lacouture ME. Dermatological adverse events from BRAF inhibitors: a growing problem. Curr Oncol Rep 2013;15:249–59.
43. Petit VW, Réfrégiers M, Guettier C, Jamme F, Sebanayakam K, Brunelle A, et al. Multimodal spectroscopy combining time-of-flight-secondary ion mass spectrometry, synchrotron-FT-IR, and synchrotron-UV microspectroscopies on the same tissue section. Anal Chem 2010;82:3963–8.
44. Santos IP, Caspers PJ, Schut TCB, van Doorn R, Hegt VN, Koljenovic S, et al. Raman spectroscopic characterization of melanoma and benign melanocytic lesions suspected of melanoma using High-wavenumber Raman Spectroscopy. Anal Chem 2016;88:7683–8.
45. Lui H, Zhao J, McLean D, Zeng H. Real-time Raman spectroscopy for in vivo skin cancer diagnosis. Cancer Res 2012;72:2491–500.
46. Lacouture ME.Mechanisms of cutaneous toxicities to EGFR inhibitors. Nat Rev Cancer 2006;6:803–12.
47. Hobbs RM, Silva-Vargas V, Groves R, Watt FM. Expression of activated MEK1 in differentiating epidermal cells is sufficient to generate hyperproliferative and inflammatory skin lesions. J Invest Dermatol 2004;123:503–15.
48. Liu H, Wu Y, Lv T, Yao Y, Xiao Y, Yuan D, et al. Skin rash could predict the response to EGFR tyrosine kinase inhibitor and the prognosis for patients with non-small cell lung cancer: a systematic review and meta-analysis. PLoS One 2013;8:e55128.
49. Petrelli F, Borgonovo K, Cabiddu M, Lonati V, Barni S. Relationship between skin rash and outcome in non-small-cell lung cancer patients treated with anti-EGFR tyrosine kinase inhibitors: a literature-based meta-analysis of 24 trials. Lung Cancer 2012;78:8–15.

A Novel Spectroscopically Determined Pharmacodynamic Biomarker for Skin Toxicity in Cancer Patients Treated with Targeted Agents

Antoine Azan[1], Peter J. Caspers[2,3], Tom C. Bakker Schut[2,3], Séverine Roy[4], Céline Boutros[4], Christine Mateus[4], Emilie Routier[4], Benjamin Besse[4], David Planchard[4], Atmane Seck[5], Nyam Kamsu Kom[6], Gorana Tomasic[7], Senada Koljenović[8], Vincent Noordhoek Hegt[8], Matthieu Texier[9], Emilie Lanoy[9], Alexander M.M. Eggermont[4,10], Angelo Paci[1,5], Caroline Robert[4,6,10], Gerwin J. Puppels[2,3], Lluis M. Mir[1]

[1]UMR 8203, CNRS, Gustave Roussy, Univ. Paris-Sud, Université Paris-Saclay, Villejuif, France.
[2]Center for Optical Diagnostics & Therapy, Department of Dermatology, Cancer Institute, Erasmus MC, Rotterdam, the Netherlands.
[3]RiverD International B.V. Rotterdam, the Netherlands
[4]Department of Medical Oncology, Gustave Roussy, Villejuif, France.
[5]Department of Pharmacology and Drug Analysis, Gustave Roussy, Villejuif, France.
[6]UMR 981, INSERM, Gustave Roussy, Univ. Paris-Sud, Université Paris-Saclay, Villejuif, France.
[7]Department of Pathology, Gustave Roussy, Villejuif, France.
[8]Department of Pathology, Cancer Institute, Erasmus MC, Rotterdam, the Netherlands.
[9]UMR 1018, INSERM, Gustave Roussy, Univ. Paris-Sud, Université Paris-Saclay, Villejuif, France.
[10]Faculty of Medicine, Univ. Paris-Sud, Université Paris-Saclay, Le Kremlin Bicêtre, France.

Supplementary Information

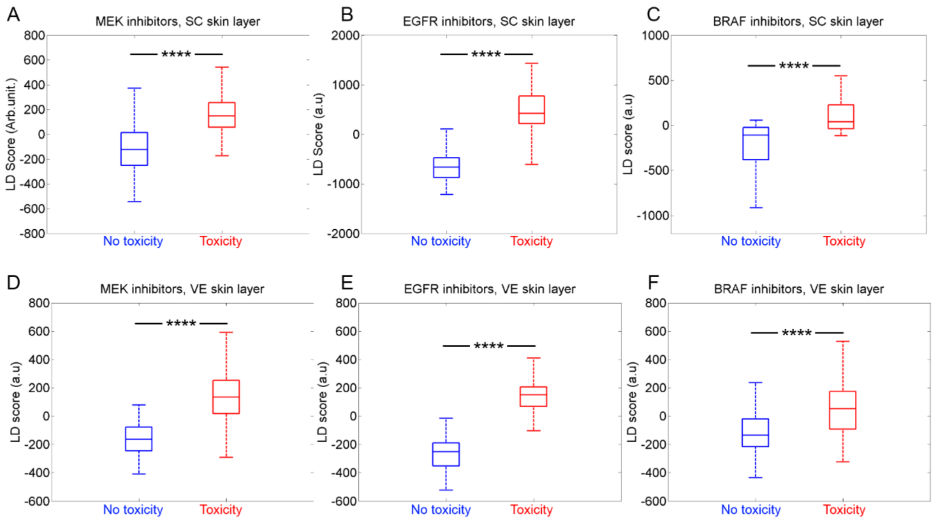

Figure S1: Mean LD score for the validation data set for Stratum Corneum skin layer for MEK inhibitors (A), EGFR inhibitors (B) and BRAF inhibitors (C) and for Viable Epidermis skin layer for MEK inhibitors (D), EGFR inhibitors (E) and BRAF inhibitors (F). The p-value between the two groups is reported. In the 6 conditions, the p-value is lower than 0.001%.

	Drug concentration (ng/mL)								
	MEK inhibitors			EGFR inhibitors			BRAF inhibitors		
	Patient #1	Patient #2	Patient #3	Patient #1	Patient #2	Patient #3	Patient #1	Patient #2	Patient #3
Drug	Trametinib	Trametinib	Trametinib	Erlotinib	Erlotinib	Afatinib	Dabrafenib	Dabrafenib	Vemurafenib
Daily Dose (mg)	2	2	2	150	150	40	300	300	1920
Measurement #1	<LOQ	<LOQ	<LOQ	<LOQ	<LOQ	n/a	<LOQ	<LOQ	<LOQ
Measurement #2	n/a	9	17,3	940,4	n/a	n/a	259,3	29,2	35 200
Measurement #3	n/a	15,7	18,2	1330,6	1121	n/a	110,6	769,3	72 800

LOQ: Limit Of Quantification = 2
n/a: not available

Table S1: Summary of the measurements of the drug concentration into patients' blood.

		Cutaneous adverse events due to the treatment		
Inhibitors		Type of toxicity	Grade at D15	Grade at D28
MEK	Patient #1	Folliculitus	0	1
	Patient #2	Vitiligo	0	1
	Patient #3	Folliculitus	1	1
		Pruritus	1	1
EGFR	Patient #1	Folliculitus	1	2
	Patient #2	Folliculitus	n/a	1
		Pruritus	n/a	1
	Patient #3	Dryness	1	1
		Folliculitus	1	1
BRAF	Patient #1	Keratosys	1	1
		Papillomatosis	1	1
		Xerosys	1	1
	Patient #2	Hand and feet desease	1	1
		Xerosys	1	1
	Patient #3	Dryness	0	1
		Keratosys	0	1

n/a: not available
D15: about 15 days after the beginning of the treatment
D28: about 28 days after the beginning of the treatment

Table S2: Summary of cutaneous adverse events at the different time point for each patient included in this study.

7

Discussion, perspectives and conclusion

The aim of this doctoral research was mainly to investigate the chemical modifications occurring in cells exposed to PEFs by means of confocal Raman microspectroscopy and THz microscopy, which are non-invasive and label-free optical techniques. To our knowledge, these two biophotonics techniques have never been used before to investigate the underlying mechanisms of cell EPN.

In this section, the results obtained will be discussed article by article and the associated perspectives will be established.

7.1 Demonstration of the Protein Involvement in Cell Electropermeabilization using Confocal Raman Microspectroscopy (article #1)

In the first study, the Raman signatures of live haMSC cells exposed or not to PEFs were acquired at different cellular locations (cytoplasm and nucleus) and vibrational frequency ranges (FGP and HWN) . Cells were exposed or not to 8 pulses of 100 µs duration with 1000 V/cm field magnitude and 1 Hz repetition rate, which are classical electric pulses parameters used in clinic [472]. By comparing the Raman signatures of the control and the pulsed groups, major modifications of the biochemical composition were revealed and several critical vibrational frequencies that characterize cell EPN were identified.

The main result of this study is the demonstration of protein involvement in cell EPN. First, the magnitude of several Raman peaks attributed to phenylalanine, an amino-acid present in many transmembrane domains [533], was decreased by 30 to 40 % in the pulsed group versus the control group. Another vibrational spectroscopy study on cells exposed to surfactant stress has associated the decrease in the magnitude of phenylalanine Raman peaks to protein leakage [176]. Moreover, the effect of PEFs on proteins was confirmed by the significant modification of the amide I Raman band. Amide I Raman band is known to be related to the secondary structure of proteins into the cells [534]. Numerical models have confirmed the unfolding of proteins exposed to intense electric pulses [535]. Further biomolecular investigations are required to emphasize the effect of PEFs on the proteins. For instance, we plan to incorporate transmembrane proteins into GUVs in order to monitor the potential electro-induced chemical modifications of these incorporated proteins by means of mass spectrometry. The incorporation of transmembrane proteins into GUVs has already been performed by other groups [536].

Electric pulses are known to affect also the lipids of the membrane in a different manner, through peroxidation [360] or phospholipid scrambling [511]. The modification of Raman peaks attributed to the lipids confirmed the previous results.

The acquisition of the Raman signatures of control and pulsed cells in the HWN region did not show any difference. This might be due to the in-depth resolution of our experimental system (over 1 µm) which does not allow to discriminate the signal contribution of the plasma membrane from the contribution of other internal organelles. Performing similar experiments on GUVs, meaning analysing the Raman signatures of control and pulsed GUVs, would allow to focus only on the interaction between PEFs and the phospholipid bilayer. The acquisition of the Raman signature of GUVs has already been done with a similar confocal Raman microscope [537].

Surprisingly, the modification of DNA Raman peaks was noticed in the Raman signatures acquired at the nucleus location. According to the literature, 100 µs PEFs are not able to reach the nucleus due to the plasma membrane acting like an isolator. DNA damages are known to be induced by nsPEFs [449, 538, 539]. Our group has recently investigated the opportunity to induce EPN of the endoplasmic reticulum via the delivery of a single 100 µs electric pulse. This study demonstrated that a 100 µs electric pulse is able to induce permeabilization of internal organelles. The modification of DNA Raman peaks observed in our study also emphasized the possibility of a 100 µs electric pulse to induce damage on internal organelles.

This first investigation of the effect of PEFs on the Raman signatures of live cells has revealed new underlying mechanisms. Raman microspectroscopy has a low time resolution due to the weak Raman signal. A complete Raman mapping of control and pulsed cells would allow to investigate any spatial heterogeneity of the effect of PEFs. In this framework, fixing the cells would be required but it has been noticed that the chemical fixation affects the Raman signatures of cells [138]. Moreover, chemical fixation protocols lasts about 30 minutes [379], so it would be necessary to experimentally limit the dynamics of any electro-induced cell metabolism, such as membrane resealing. Working at low temperature as we did in this study could be an effective experimental solution.

7.2 Comprehensive Characterization of the Interaction between Pulsed Electric Fields and Live Cells by Confocal Raman Microspectroscopy (article #2)

Our first published study demonstrated that confocal Raman microspectroscopy can provide useful biomolecular information on the interaction between PEFs and live cells. In a second step, we investigated deeper the interaction between electric pulses and living cells.

Fluorescence microscopy studies showed that the uptake of a non-permeant fluorescence dye after cell exposure to PEFs occurs first at the poles of the membrane [320]. After tens of seconds, the uptake of the non-permeant fluorescent dye is homogeneous in the whole cell membrane. Hence, we investigated the potential EPN spatial heterogeneity by acquiring Raman signatures of pulsed cells at different locations around the nucleus. Our results demonstrate that the Raman signatures of pulsed cells were similar at the different locations probed. The Raman signatures of pulsed cells at the different positions tested were different from the Raman signatures of control cells. The spatial homogeneity of the biochemical modifications of pulsed cells may be explained by the time resolution of confocal Raman microscopy which is lower than the time constant of the lateral diffusion of permeable electro-induced structures into the membrane [264]. Coherent Raman scattering microscopy techniques, such as CARS or SRS, have a time resolution around tens of milliseconds per frame, which is more compatible to monitor such dynamic processes. Thus, the close to real-time monitoring of the different critical vibrational frequencies previously identified would allow to have an access to spatial and temporal information on the chemical damages induced by PEFS on live cells.

Thanks to the different collaborations of the UMR 8203 laboratory and the equipment available at the UMR 8203 laboratory, this exciting perspective can be achieved. Few years ago, our laboratory designed a homemade wide-field CARS microscope in order to monitor the biochemical consequences of the delivery of electric pulses on cells with a time resolution of 3 ns [385]. This CARS microscope has the possibility to be synchronized with an electric pulse generator. MEDyC laboratory owns a confocal SRS microscope with a spatial resolution around hundreds of nanometers. Finally, the team headed by Vincent Couderc at XLIM institute CNRS 6172, has designed a CARS microspectroscope able to acquire CARS hyperspectral images with a time resolution of 3 minutes for a whole cell [176]. By combining these different coherent Raman scattering systems, quantitative and qualitative analysis of the kinetics and the spatial distribution of the electro-induced chemical damages might be conducted.

To perform such experiments, it is necessary to pulse the cells under a CARS or SRS microscope. In this framework, the OPTIC BIOEM project started in october 2015. OPTIC BIOEM is a Marie Sklodowska Curie Action leaded by Caterina Merla and Lluis M. Mir. The aim of the OPTIC BIOEM project is to design a system to expose the cells to electric and electromagntetic fields, compatible with the optical specificities related to coherent Raman scattering microscopy. This project is on-going. The first exposure system prototypes have been designed and experimentally characterized. They are currently used under the wide-field CARS microscope at UMR 8203. More information about the OPTIC BIOEM project is available here: `https://sites.google.com/site/opticbioemmsca/`.

The dose-effect relation between electric pulse parameters and the Raman signatures of the cells were investigated by sweeping respectively the electric field magnitude, the number of electric pulses or the frequency rate. The results obtained with different electric pulse parameters confirm the major modifications of proteins and lipids in the biochemical composition of pulsed cells reported in article #1. No statistically significant modification of specific Raman bands was noticed according to specific electric pulses parameters. The Raman signature modifications were similar for all the electric pulses parameters applied. Fluorescence microscopy studies has shown that above the EPN threshold, the level of permeabilization increases with the electric field magnitude or the number of electric pulses [387, 390]. No such behaviour was noticed in the evolution of the Raman signature of cells. A statistical analysis demonstrated no differences between the Raman signatures of cells exposed above the EPN threshold but with different electro-doses, for instance from 750 to 1500 V/cm. Similar results were obtained for the Raman signatures of cells exposed under the electropermeabilization threshold but with different electro-doses, for instance from 0 to 2 electric pulses. Although no intragroup statistical difference was noticed, strong intergroup significant differences, meaning no EPN detectable by fluorescence microscopy versus EPN, were revealed. It would indicate that the Raman signature of the cell is a biomarker of the EPN state and not of the level of permeabilization. It has to be noticed that the EPN threshold was subjectively determined by the uptake of the fluorescent dye Yo-Pro-1 into pulsed cells. Electroermeabilization state and level are known to be highly dependent on the fluorescent probe used [452].

The acquisition of Raman signature of control and pulsed cells was also performed on another cell type: the LPB cell line. LPB cells were selected because they have strong differences: species origin, morphology, size, immortality, metabolism... in comparison with haMSC cells. First, the Raman signatures of pulsed LPB was significantly different from the Raman signature of control LPB. The nature of the electro-induced chemical damages in LPB was different from the ones revealed in haMSC cells. Further investigations are necessary to better understand the reason of this cell dependency of the results.

7.3 Discrimination between the Different Cell Electropermeabilization States based on the Raman Signatures (article #3)

In the previous research work, the Raman signature of cells could be identified as a biomarker of the EPN state and not of the level of EPN. Until now, the underlying mechanisms of the differences between reversible and irreversible EPN have been poorly studied. Numerical models and electronic microscopy studies suggest the creation of long-lasting pores into the membrane as the main consequence of irreversible EPN [325, 540, 541]. This hypothesis of long-lasting electropores is strongly under debate in the EPN community.

In this study, we investigated the opportunity to discriminate the three different EPN states of the plasma membrane - meaning no detectable EPN (using classical fluorescent markers), reversible EPN and irreversible EPN - based on the biochemical composition of the cells determined thanks to confocal Raman microspectroscopy. The electric pulse parameters able to induce the three different EPN states were determined by fluorescence microscopy and cellular uptake of Yo-Pro-1. The Raman signatures of live haMSC cells associated to the three different EPN states were acquired at two spectral regions: FGP and HWN. A discriminative algorithm was designed to discriminate the different EPN states in the two vibrational frequency ranges. The discrimination was performed in two steps. First, a discriminative model was designed to investigate the differences in the Raman signatures between the no EPN and the EPN groups. The EPN group combines the Raman data set of the reversible and irreversible EPN groups. Then, another model was designed to specifically discriminate the reversible and irreversible EPN groups.

Our results show that the discriminative power of the model was higher in the cs of the comparison between the reversible and the irreversible groups than for the comparison between the no detectable EPN and the EPN groups, 95,5 % versus 82,9 %. This would indicate that the biochemical modifications are statistically more significant between the reversible and the irreversible EPN state than between the no detectable EPN and the EPN group. The mean percentage of correct classification in the reversible and the irreversible groups was higher in the discriminative analysis performed based on the HWN Raman data set than on the FGP Raman data set, 98.3 % versus 92.8 %. The discriminative models designed for the two discriminations did not display the same pattern. Vibrational frequencies of proteins are the major contributors of the discriminative model for the discrimination between no detectable EPN and EPN groups; whereas vibrational frequencies of lipids are the major contributors to the discriminative model for the discrimination between reversible and irreversible EPN groups.

For the first time, the biochemical consequences of the delivery of electric pulses on live cells between the different EPN states were investigated and revealed major differences between the three groups. Further investigations by mass spectrometry would emphasize this dose effect relationship.

However, hypothesis, by the time being rather speculative, can be formulated under the light of these new data: irreversibility could be linked to major lipid modifications. The cells can recover their impermeabilitiy (reversible EPN) only if lipids changes remain moderate. In this later case, because lipids changes do not dominate the modification in the Raman signatures, changes in proteins remain detectable, either due to the lipid environment modification or to direct effects on proteins.

7.4 Monitoring the Molecular Composition of Live Cells Exposed to Pulsed Electric Fields via Label-free Optical Methods (article #4)

THz microscopy is another non-invasive and label-free biophotonics technique sensitive to the molecular composition of the cells [206]. In this study, the molecular composition of live cells exposed to different electric field magnitudes was monitored by confocal Raman microspectroscopy and THz microscopy. Until now, these two biophotonics techniques have never been used to investigate cell EPN. Thus, we have compared the experimental results obtained by these two new techniques with the results obtained by fluorescence microscopy which is the biophotonics reference technique under the same experimental conditions. THz microscopy has a time resolution of about seconds [221]. Thus the real-time recording of the THz signal of cells exposed to PEFs was performed in order to have access to the cell EPN dynamics, which is not possible with confocal Raman microspectroscopy.

The evolution of the THz signal of pulsed cells revealed a leakage of proteins. This result emphasized the results obtained by confocal Raman microspectroscopy in the first article. The kinetics of this proteins leakage was faster when the cells were exposed to higher electric field magnitude. The kinetics of the evolution of the fluorescence signal was slower but the complete interpretation of these results is still on-going.

7.5 A Novel Spectroscopically Determined Pharmacodynamic Biomarker for Skin Toxicity in Cancer Patients Treated with Targeted Agents (article #5)

In this clinical study, we investigated the opportunity to monitor the skin toxicity of patients under targeted therapy treatments by means of confocal Raman microspectroscopy. We followed 9 cancer patients during the first month of the treatment. Before the beginning of the treatment and each two weeks after the beginning of the treatment, the Raman signatures of the patients' skin were acquired at different skin depth in order to access the two first upper layers of the skin: the SC and the VE. Three different inhibitors, namely MEK, EGFR and BRAF inhibitors, were selected because tehse targeted therapies are known to induce severe cutaneous side effects. Based on the dermatology investigation performed the same day as the Raman acquisition, the acquired Raman spectra were distributed into two groups, corresponding to the Raman spectra from patients suffering, or not, from skin toxicity. The goal of this study was to determine a model able to discriminate the Raman spectra from these two groups. A discriminative algorithm using the drug concentration into the patients' blood as supplementary input parameter was designed and applied to six different Raman data sets in order to cover the two skin layers and the three inhibitors.

The discriminative powers obtained depended on the drugs and the skin layers investigated. The discriminative power was over 90 % in the case of EGFR and MEK inhibitors; whereas the higher discriminative power was only 71 % for BRAF inhibitors. It is well established that EGFR and MEK inhibitors induce skin toxicity with similar patterns: papulopustular rash, perionyxis, abnormality in hair growth [542, 543]. The cutaneous adverse events related to BRAF inhibitors are really different: hyperkeratosis, folliculitis [544, 545]. The biological origin of these two patterns of skin toxicity was analysed in normal cells in culture. These studies demonstrated that EGFR and MEK inhibitors induce the inhibition of the MAPK pathway on normal cells [546]; whereas BRAF inhibitors induce a paradoxical activation of the MAPK pathway [547, 548]. Thus, we might speculate that Raman microspectroscopy of the skin is more sensitive to the biochemical consequences of the EGFR and MEK inhibitors than the ones induced by BRAF inhibitors.

In the case of the EGFR inhibitors, the correlation between the Raman signature of patient's skin and the drug concentration into the patient's blood was around 80 %. Thus, Raman spectroscopy has allowed to determine a non-invasive and label-free pharmacodynamic biomarker to detect skin toxicity induced by targeted therapy. Meta-analyses have demonstrated that the treatment efficacy is correlated to skin toxicity in the case of EGFR inhibitors [549, 550]. Further investigations are required to determine if Raman microspectroscopy of the skin could be used as a biomarker to predict treatment efficacy.

7.6 Final conclusion

This research work reports the use of various biophotonics techniques to investigate biomedical questions, from basic research (interaction between PEFs and cells) to clinical studies (skin toxicity induced in patients treated with targeted anticancer therapies).

This manuscript reports, for the first time, the use of confocal Raman microspectroscopy and THz microscopy to investigate the cell EPN process from a molecular point of view. The evolution of the Raman signatures of cells exposed to PEFs has been comprehensively studied and our results demonstrate the involvement of the proteins in cell EPN. The modifications of the Raman signatures of pulsed cells versus control cells were homogeneously distributed around the nucleus of the cells. Moreover, we have shown that the Raman signatures of the cells could be used as an accurate biomarker of the different states of the cells exposed to PEFs, corresponding to no detectable EPN, reversible EPN and irreversible EPN. By analysing the vibrational bands modified between the different states, we reveal that proteins were mainly modified by the reversible EPN process and that lipids were mainly affected by the irreversible EPN process. This would indicate that the nature of the chemical damages depends on the EPN-induced states. This conclusion provides new information about the underlying mechanisms between PEFs and live cells at a molecular level.

For the first time, the effect of PEFs on proteins has also been demonstrated by THz microscopy experiments. The evolution of the THz signal of pulsed cells revealed a leakage of proteins. The higher the electric field magnitude was, the faster the kinetics of the protein leakage was.

Finally, this doctorate research demonstrates the opportunity to predict skin toxicity induced by targeted anticancer therapies by means of confocal Raman microspectroscopy. A pharmacodynamic biomarker was determined based on the Raman signatures of patients' skin. The accuracy of the biomarker depended on the cancer treatment and the skin layer investigated. In the case of the EGFR inhibitors, the correlation between the Raman signatures of patient's skin and the drug concentrations into the blood was around 80 %. Skin toxicity induced by EGFR inhibitors is known to be correlated with the treatment efficiency. Further investigations of the correlation between the treatment efficiency and the Raman signature of patients' skin would allow to determine a potential non-invasive and label-free biomarker of treatment efficiency.

8

Discussion, perspectives et conclusion en langue française

L'objectif principal de ce doctorat est l'étude des modifications chimiques se produisant dans des cellules biologiques exposées à des champs électriques impulsionnels, au moyen de la microspectroscopie Raman confocale et de la microscope THz. À notre connaissance, ces deux techniques biophotoniques n'ont jusqu'à présent jamais été utilisées pour étudier les mécanismes sous-jacents de l'électroperméabilisation cellulaire.

Dans cette partie, les résultats obtenus seront discutés article par article et les perspectives associées seront établies.

8.1 Démontration de l'implication des protéines dans le phénomène d'électroperméabilisation des cellules par microspectroscopie Raman confocale (article #1)

Dans cette première étude, les signatures Raman de cellules haMSC vivantes exposées ou non à des champs électriques impulsionnels ont été mesurées à différents endroits de la cellule (cytoplasme et noyau) et sur deux plages spectrales (FGP et HWN). Les cellules ont été exposées ou non à 8 impulsions de 100 µs de durée avec une amplitude de champs électrique de 1000 V/cm et un taux de répétition de 1 Hz. Ces paramètres d'impulsions électriques sont ceux classiquement utilisés en clinique [472]. En comparant les signatures Raman des cellules du groupe contrôle et les signatures Raman des cellules du groupe pulsé, des modifications majeures de la composition biochimique des cellules ont été révélées. Plusieurs fréquences vibrationnelles critiques caractérisant spécifiquement l'électroperméabilisation des cellules ont été identifiées.

Le résultat principal de cette étude est la démonstration de l'implication des protéines dans le phénomène d'électroperméabilisation des cellules. Tout d'abord, l'amplitude de plusieurs bandes Raman attribuées à la phénylalanine, un acide aminé présent dans de nombreuses protéines transmembranaires [533], a été diminué de 30 à 40 % dans le groupe pulsé par rapport au groupe contrôle. Une autre étude de spectroscopie vibrationnelle sur des cellules exposées à des tensioactifs a associé la diminution de l'amplitude des bandes Raman de la phénylalanine à la fuite des protéines [176]. En outre, l'effet des champs électriques impulsionnels sur les protéines a été confirmé par la modification significative de la bande Raman amide I. La bande Raman amide I est connue pour être liée à la structure secondaire des protéines dans les cellules [534]). Les modèles numériques ont confirmé le déploiement de protéines exposées à des impulsions électriques intenses [535]. Des études complémentaires sont nécessaires pour mettre en valeur l'effet des champs électriques impulsionnels sur les protéines cellulaires. Par exemple, nous prévoyons d'incorporer des protéines transmembranaires dans des GUVs afin de surveiller les potentielles modifications chimiques de ces protéines par des analyses en spectrométrie de masse. L'incorporation de protéines transmembranaires dans les GUVs a déjà été réalisée par d'autres groupes [536].

Les impulsions électriques sont connues pour affecter également les lipides membranaires via une peroxydation [360] ou un trouble de l'organisation lipidique [511] par exemple. La modification de bandes Raman attribuées aux lipides a confirmé ces précédents résultats.

L'acquisition des signatures Raman des cellules non pulsées et pulsées dans la région spectrale HWN n'a montré aucune différence entre les deux groupes. Cela peut s'expliquer par la faible résolution spatiale axiale de notre système expérimental (plus de 1 µm) qui ne permet pas de discriminer la contribution du signal de la membrane plasmique de la contribution du signal d'autres organites internes. L'analyse des signatures Raman de GUV pulsés ou non permettrait de se concentrer uniquement sur l'intéraction entre les champs électriques impulsionnels et la bicouche de phospholipides. La mesure de signature Raman des GUVs a déjà été réalisée avec un microscope Raman confocal similaire à celui utilisé dans notre étude [537].

De manière surprenante, des modifications des bandes Raman de l'ADN ont été détectées dans les signatures Raman acquises au niveau du noyau cellulaire. Selon la littérature, les impulsions électriques de 100 µs ne sont pas en mesure d'affecter le noyau en raison de la membrane plasmique agissant comme un isolant. D'après la littérature, les modifications de l'ADN et/ou des organites internes ne seraient possibles uniquement que par des impulsions électriques nanosecondes [449, 538, 539]. Notre groupe a pourtant récemment démontré la possibilité d'induire l'électroperméabilisation du réticulum endoplasmique via l'exposition des cellules à une seule impulsion électrique de 100 µs (étude soumise à publication). La modification des bandes Raman de l'ADN confirme la possibilité qu'une impulsion électrique de 100 µs puisse induire des effets sur les organites internes également.

Cette première étude sur l'effet des champs électrique impulsionnels sur les signatures Raman des cellules vivantes a révélé de nouveaux mécanismes sous-jacents. La microspectroscopie Raman confocale a une faible résolution temporelle (60 secondes) en raison du faible signal Raman. Une cartographie Raman complète des cellules contrôles et pulsées permettrait d'étudier la distribution spatiale de l'effet des champs électriques impulsionnels sur la composition chimique de la cellule. Dans ce contexte, fixer les cellules est nécessaire car l'acquisition Raman d'une cellule complète prendrait quelques heures. Cependant, il a été remarqué que le protocole de fixation chimique modifie les signatures Raman des cellules [138]. De plus, les protocoles de fixation chimique durent environ 30 minutes [379], il apparaît donc nécessaire de limiter expérimentalement la dynamique de tout métabolisme cellulaire électro-induit, comme la réparation de la membrane plasmique. Travailler à basse température comme nous l'avons fait, est une solution opérationnelle.

8.2 Caractérisation complète de l'intéraction entre les champs électriques impulsionnels et les cellules vivantes par microspectroscopie Raman confocale (article #2)

Notre première étude publiée a démontré que la microspectroscopie Raman confocale peut fournir des informations précieuses concernant les effets des champs électriques impulsionnels sur les cellules vivantes au niveau moléculaire. Dans une deuxième étape, nous avons étudié plus précisément l'interaction entre les impulsions électriques et les cellules vivantes en modifiant les conditions expérimentales initiales.

Les études de microscopie de fluorescence ont montré que l'internalisation d'un fluorochrome non-perméant grâce à l'électroperméabilisation se produit d'abord aux pôles de la membrane [320]. Après quelques dizaines de secondes, l'internalisation de ce fluorochrome s'homogénéise à l'ensemble de la membrane cellulaire. Par conséquent, nous avons étudié l'éventuelle hétérogénéité spatiale du phénomène d'électroperméabilisation en faisant la mesure des signatures Raman de cellules pulsées à différents endroits autour du noyau. Nos résultats ont démontré que les signatures Raman des cellules pulsées étaient similaires aux différents endroits sondés. En revanche, ces signatures Raman des cellules pulsées aux différentes positions étaient toutes différentes des signatures Raman des cellules témoins. L'homogénéité spatiale des modifications biochimiques des cellules pulsées peut s'expliquer par la grande résolution temporelle de la microspectroscopie Raman confocale (60 secondes) qui est supérieure à la constante de temps de la diffusion latérale des structures perméables électro-induites dans la membrane (quelques secondes) [264]. Les techniques de microscopie Raman cohérente, telles que la microscopie diffusion Raman anti-Stokes cohérente (CARS en anglais) ou diffusion Raman stimulée (SRS en anglais), ont une résolution temporelles de l'ordre de la centaine de millisecondes par image, ce qui est compatible la cinétique de ces processus dynamiques. Ainsi, le suivi des différentes fréquences vibrationnelles critiques précédemment identifiées permettrait d'avoir accès à des informations spatiales et temporelles concernant les modifications chimiques induites par les champs électriques impulsionnels sur les cellules vivantes.

Grâce aux différentes collaborations du laboratoire UMR 8203 et aux équipements disponibles au sein de ce laboratoire, cette excitante perspective est possible. Il y a quelques années, notre laboratoire a conçu un microscope CARS champs large pour suivre les modifications biochimiques de l'application des impulsions électriques sur les cellules avec une résolution temporelle de 3 ns [385]. Le microscope CARS peut se synchroniser avec un générateur d'impulsions électriques afin de faire l'acquisition d'image CARS à différent instant pendant l'impulsion électrique. Le laboratoire MEDyC possède un microscope confocal SRS avec une résolution spatiale de l'ordre de la centaine de nanomètres. Enfin, l'équipe dirigée par Vincent Couderc à l'institut XLIM CNRS 6172 a conçu un microspectroscope CARS capable d'acquérir des images hyperspectrales CARS avec une résolution temporelle de 3 minutes pour une cellule entière [176]. En combinant ces différents systèmes Raman cohérents, l'analyse quantitative et qualitative de la cinétique et la répartition spatiale des dommages chimiques électro-induits pourraient être menées.

Pour effectuer de telles expériences, il faut pouvoir exposé les cellules directement sous le microscope CARS ou SRS. Dans ce contexte, le projet OPTIC BIOEM a débuté en octobre 2015 au laboratoire CNRS UMR 8203. OPTIC BIOEM est une action Marie Sklodowska Curie dirigée par Caterina Merla et Lluis M. Mir. L'objectif de ce projet est de concevoir un système d'exposition compatible avec les spécificités optiques liées à la microscopie Raman. Ce projet est actuellement en cours. Les premiers prototypes ont été réalisés et caractérisés expérimentalement. Ils sont actuellement utilisés dans le microscope CARS champs large de l'UMR 8203. Plus d'informations sur le projet OPTIC BIOEM sont disponibles ici: `https://sites.google.com/site/opticbioemmsca/`.

Dans cette étude, la relation dose-effet entre les différents paramètres des impulsions électriques et les signatures Raman des cellules a également été investiguée en faisant varier respectivement l'amplitude du champ électrique, le nombre d'impulsions électriques ou la fréquence de répétition. Les résultats obtenus avec différents paramètres d'impulsions électriques confirment les modifications majeures des protéines des cellules pulsées par rapport aux cellules contrôles. Les études en microscopie de fluorescence ont montré que, au-dessus du seuil d'électroperméabilisation, le niveau de perméabilisation des cellules augmente avec l'amplitude du champ électrique ou avec le nombre d'impulsions électriques [387, 390]. Un tel comportement n'a pas été observé dans l'évolution de la signature Raman des cellules en fonction de l'amplitude du champs électrique ou le nombre d'impulsions électriques. Une analyse statistique n'a démontré aucune différence entre les signatures Raman des cellules exposées au-dessus du seuil d'électroperméabilisation mais à différentes expositions électriques, par exemple de 750 à 1500 V/cm. Des résultats similaires ont été obtenus pour les signatures Raman des cellules exposées sous le seuil d'électroperméabilisation mais à différents expositions électriques, par exemple de 0 à 2 impulsions électriques. Bien qu'aucune différence statistique intragroupe n'ait été observée, de différences significatives intergroupes ont été révélées, électroperméabilisation non-détectable versus électroperméabilisation. Cela indiquerait que la signature Raman de la cellule est un biomarqueur de l'état d'électroperméabilisation et non du niveau d'électroperméabilisation. Il faut noter que le seuil de perméabilisation a été déterminé subjectivement par l'internalisation du fluorochrome Yo-Pro-1 dans des cellules pulsées. L'état et le niveau d'électroperméabilisation sont très fortement dépendants de la sonde fluorescente utilisée [452].

8.3 Investigation des différences de modifications biochimiques induites par l'électroperméabilisation réversible et irréversible des cellules vivantes par microspectroscopie Raman confocale (article #3)

Dans le travail de recherche précédent, la signature Raman des cellules a été identifiée comme un biomarqueur de l'état d'électroperméabilisation et non du niveau d'électroperméabilisation. Les mécanismes sous-jacents des différences entre l'électroperméabilisation réversible et l'électroperméabilisation irréversible ont été très peu étudiés. Les modèles numériques et les études en microscopie électronique suggèrent la création de pores durables dans la membrane comme conséquence principale de l'électroperméabilisation irréversible [325, 540, 541]. Cependant, cette hypothèse d'électropores durables est fortement débattue dans la communauté de l'électroperméabilisation.

Dans cette étude, nous avons étudié l'opportunité de discriminer trois états différents cellulaires - c'est-à-dire pas d'électroperméabilisation, électroperméabilisation réversible et électroperméabilisation irréversible - en se basant sur la signature Raman des cellules et donc leur composition biochimique. Les paramètres des impulsions électriques permettant d'induire les différents états cellulaire ont été déterminés par microscopie de fluorescence et par l'internalisation de Yo-Pro-1 dans les cellules. Les signatures Raman des cellules haMSC vivantes dans chacun des trois états ont été acquises dans deux régions spectrales: FGP et HWN. Un algorithme a été conçu pour discriminer les différents états cellulaires sur les deux plages de fréquence vibrationnelles. La discrimination a été effectuée en deux étapes. Tout d'abord, un modèle discriminatoire a été conçu pour étudier les différences dans les signatures Raman du groupe électropermeabilisation versus pas d'électroperméabilisation. Le groupe électroperméabilisation combine l'ensemble de données Raman des groupes électroperméabilisation réversible et électroperméabilisation irréversible. Ensuite, un autre modèle a été conçu pour discriminer spécifiquement les groupes électroperméabilisation réversible et électroperméabilisation irréversible.

Nos résultats ont montré que le pouvoir de discrimination du modèle était plus élevé lors de la discrimination des groupes réversible versus irréversible que lors de la discrimination des groupes de non perméabilisation versus perméabilisation (95,5 % contre 82,9 %). Cela indiquerait que les modifications biochimiques sont statistiquement plus significatives entre l'état d'électroperméabilisation réversible et irréversible que entre l'état sans électropermeabilisation et le groupe avec électroperméabilisation. Le pourcentage moyen de classification correcte dans les groupes réversible et irréversible sont plus élevés sur la plage spectrale HWN que sur la plage spectrale FGP, 98,3 % contre 92,8 %. Les modèles discriminants conçus pour les deux discriminations présentent des différences spectrales. Les fréquences vibrationelles des protéines sont les principales contributrices du modèle discriminant pour la discrimination entre les groupes sans électroperméabilisation et avec électroperméabilisation; Tandis que les fréquences vibrationelles des lipides sont les principales contributrices du modèle discriminant pour la discrimination entre les groupes électroperméabilisation réversibles et électroperméabilisation irréversible.

Pour la première fois, les conséquences biochimiques de l'exposition des impulsions électriques sur les cellules vivantes entre les différents états cellulaires ont été étudiées et ont révélé des différences majeures. D'autres recherches effectuées en spectrométrie de masse pourraient mettre l'accent cette relation dose-effet.

8.4 Suivi de la composition moléculaire de cellules vivantes exposés à des champs électriques impulsionnels par des méthodes optiques sans marquage (article #4)

La microscopie THz est une autre technique biophotonique non-invasive et sans marquage sensible à la composition chimique des cellules [206]. Dans cette étude, la composition chimique des cellules vivantes exposées à différentes amplitudes de champ électrique a été mesurée par microspectroscopie Raman confocale et microscopie THz. En dehors de ce doctorat, ces deux techniques biophotoniques n'ont jamais été utilisées dans le cadre de l'électroperméabilisation cellulaire. Ainsi, nous avons comparé les résultats expérimentaux obtenus par ces deux nouvelles techniques avec les résultats obtenus par microscopie à fluorescence, qui est la technique de référence biophotonique. La microscopie THz a une résolution de temps d'environ quelques secondes [221]. Ainsi, le suivi du signal THz de cellules exposées aux champs électriques impulsionnels a été effectué afin d'avoir accès à la dynamique d'électroperméabilisation des cellules, ce qui n'est pas possible avec la microspectroscopie Raman confocale.

L'évolution du signal de THz des cellules pulsées a révélé une fuite de protéines. Ce résultat confirme les résultats obtenus par la microspectroscopie Ramana confocale (cf article #1). La cinétique de cette fuite de protéines est plus rapide lorsque les cellules sont exposées à une grande amplitude de champ électrique. La cinétique de l'évolution du signal de fluorescence est plus lente, mais l'interprétation complète de ces résultats est encore en cours.

8.5 Un nouveau biomarqueur pharmacodynamique déterminé par spectroscopie pour la toxicité cutanée chez les patients cancéreux traités par des agents ciblés (article #5)

Dans cette étude clinique, nous avons étudié l'opportunité de détecter la toxicité cutanée de patients sous traitement à base de thérapies ciblées au moyen de la microspectroscopie Raman confocale. Nous avons suivi 9 patients atteints de cancer pendant le premier mois du traitement. Avant le début du traitement puis toutes les deux semaines après le début du traitement, les signatures Raman de la peau des patients ont été acquises à différentes profondeurs de la peau afin d'accéder aux deux premières couches supérieures de la peau: le Stratuem Corneum (SC) et l'épiderme viable (VE). Trois inhibiteurs différents, appelés inhibiteurs de MEK, EGFR et BRAF, ont été sélectionnés comme thérapies ciblées parce qu'ils sont connus pour induire de sévères effets secondaires cutanés. En se basant sur l'examen dermatologique réalisé le même jour que l'acquisition de Raman, les spectres Raman ont été classés selon deux groupes, spectre Raman de patient souffrant ou non de toxicité cutanée. L'objectif de cette étude était de déterminer un modèle capable de discriminer les spectres Raman de ces deux groupes. Un algorithme discriminant utilisant la concentration de médicament dans le sang des patients comme variables d'entrée a été conçu et appliqué à chacun des six jeux de données Raman: trois inhibitors et deux couches de la peau.

Les pouvoirs discriminatoires obtenus dépendaient des médicaments et des couches cutanées étudiées. Le pouvoir discriminatoire était supérieur à 90 % dans le cas des inhibiteurs EGFR et MEK; Alors que la pouvoir discriminatoire n'était au maximum que de 71 % pour les inhibiteurs BRAF. Il est bien établi que les inhibiteurs de EGFR et MEK induisent une toxicité cutanée de même nature: éruption cutanée papulopustulaire, perionyxis, peau sèche, anomalie de la croissance des cheveux [542, 543]. Les effets indésirables cutanés liés aux inhibiteurs BRAF sont extrèmements différents: hyperkératose, folliculite [544, 545]. L'origine biologique de ces deux types de toxicité de la peau a été analysée dans des cellules normales en culture. Ces études ont démontré que les inhibiteurs de EGFR et MEK induisent l'inhibition de la voie MAPK sur les cellules normales [546]; tandis que les inhibiteurs BRAF induisent une activation paradoxale de cette voie de signalisation [547, 548]. Ainsi, nous pouvons spéculer que la microspectroscopie Raman est plus sensible aux conséquences biochimiques des inhibiteurs EGFR et MEK sur la peau que ceux induits par les inhibiteurs de BRAF.

8.6 Conclusion finale

Ce travail de recherche rapporte l'utilisation de diverses techniques biophotoniques pour investiguer des questions biomédicales, de la recherche fondamentale (interaction entre les champs électriques impulsionnels et les cellules) aux études cliniques (toxicité cutanée induite chez les patients traités par des thérapies anticancéreuses ciblées).

Ce manuscrit rapporte, pour la première fois, l'utilisation de la microspectroscopie Raman confocale et de la microscope THz pour étudier le processus d'électroperméabilisation cellulaire d'un point de vue moléculaire. L'évolution des signatures Raman des cellules exposées aux champs électriques impulsionnels a été largement étudiée et nos résultats démontrent l'implication des protéines dans l'électroperméabilisation cellulaire. Les modifications des signatures Raman des cellules pulsées par rapport aux cellules témoins ont été réparties de manière homogène autour du noyau des cellules. De plus, nous avons montré que les signatures Raman des cellules pourraient être utilisées comme un biomarqueur précis des différents états des cellules exposées aux champs électriques impulsionnels, correspondant à pas d'électroperméabilisation détectable, électroperméabilisation réversible et électroperméabilisation irréversible. En analysant les bandes vibrationnelles modifiées entre les différents états, nous révélons que les protéines ont été principalement modifiées par le processus électroperméabilisation réversible et que les lipides ont été principalement affectés par le processus irréversible d'électroperméabilisation. Cela indiquerait que la nature des dommages chimiques dépend des états induits par d'électroperméabilisation. Cette conclusion fournit de nouvelles informations sur les mécanismes sous-jacents entre les champs électriques impulsionnels et les cellules vivantes au niveau moléculaire.

Pour la première fois, l'effet des champs électriques impulsionnels sur les protéines a également été démontré par des expériences de microscopie THz. L'évolution du signal de THz des cellules pulsées a révélé une fuite de protéines. Plus l'amplitude du champs électrique était élevée, plus la cinétique de la fuite de protéines était rapide.

Enfin, ce doctorat a démontré l'opportunité de prédire la toxicité cutanée induite par des thérapies anticancéreuses ciblées au moyen de la microspectroscopie Raman confocale. Un biomarqueur pharmacodynamique a été déterminé en fonction des signatures Raman de la peau des patients. La précision du biomarqueur dépend du traitement et de la couche de peau étudiée. Dans le cas des inhibiteurs EGFR, la corrélation entre les signatures Raman de la peau des patients et les concentrations de médicament dans le sang était d'environ 80 %. La toxicité cutanée induite par les inhibiteurs EGFR est connue pour être corrélée avec l'efficacité du traitement. Des recherches plus poussées sur la corrélation entre l'efficacité du traitement et la signature Raman de la peau des patients permettraient de déterminer un potentiel biomarqueur non-invasif et sans d'étiquette de l'efficacité du traitement.

References

[1] M. Jürgens, T. Mayerhöfer, J. Popp, G. Lee, D. L. Matthews, B. C. Wilson, M. Jürgens, T. Mayerhöfer, J. Popp, G. Lee, D. L. Matthews, and B. C. Wilson. Introduction to Biophotonics. In *Handbook of Biophotonics*. Wiley-VCH Verlag GmbH & Co. KGaA, Weinheim, Germany, jan 2013.

[2] C. V. Raman. A new radiation. *Indian Journal of Physics*, 2:387–398, 1928.

[3] A. T. Young. Rayleigh scattering. *Applied Optics*, 20(4):533, feb 1981.

[4] P. Gans. *Vibrating molecules : an introduction to the interpretation of infrared and Raman spectra*. Chapman and Hall, 1975. ISBN 0412102900.

[5] B. Ratajska-Gadomska and W. Gadomski. Water structure in nanopores of agarose gel by Raman spectroscopy. *The Journal of chemical physics*, 121(24):12583–8, dec 2004.

[6] L. Woodward. *Introduction to the Theory of Molecular Vibrations and Vibrational Spectroscopy*. Oxford University Press, 1972.

[7] N. B. Colthup, L. H. Daly, S. E. Wiberley, N. B. Colthup, L. H. Daly, and S. E. Wiberley. THE THEORETICAL ANALYSIS OF MOLECULAR VIBRATIONS. In *Introduction to Infrared and Raman Spectroscopy*, pages 483–542. 1990. ISBN 9780121825546.

[8] M. Diem. *Introduction to modern vibrational spectroscopy*. Wiley, 1993. ISBN 9780471595847.

[9] L. Barron and A. Buckingham. Rayleigh and Raman scattering from optically active molecules. *Molecular Physics*, 20(6):1111–1119, jan 1971.

[10] J.-X. Cheng and X. S. Xie. *Coherent Raman Scattering Microscopy*. CRC Press, 2012. ISBN 9781439867662.

[11] K. Huang. Maxwell-Boltzmann Distribution. In *Lectures on Statistical Physics and Protein Folding*, pages 11–16. WORLD SCIENTIFIC, may 2005.

[12] M. E. Starzak. Maxwell-Boltzmann Distributions. In *Energy and Entropy*, pages 197–216. Springer New York, New York, NY, 2010.

[13] D. Moore and S. McGrane. Raman temperature measurement. *Journal of Physics: Conference Series*, 500(19): 192011, may 2014.

[14] I. Notingher, S. Verrier, H. Romanska, a. E. Bishop, J. M. Polak, and L. L. Hench. In situ characterisation of living cells by Raman spectroscopy. *Spectroscopy*, 16(2):43–51, 2002.

[15] Q. Li, X. He, Y. Wang, H. Liu, D. Xu, and F. Guo. Review of spectral imaging technology in biomedical engineering: achievements and challenges. *Journal of Biomedical Optics*, 18(10):100901, oct 2013.

[16] I. W. Schie and T. Huser. Methods and applications of Raman microspectroscopy to single-cell analysis. *Applied spectroscopy*, 67(8):813–28, aug 2013.

[17] I. P. Santos, P. J. Caspers, T. Bakker Schut, R. van Doorn, S. Koljenović, and G. J. Puppels. Implementation of a novel low-noise InGaAs detector enabling rapid near-infrared multichannel Raman spectroscopy of pigmented biological samples. *Journal of Raman Spectroscopy*, 46(7):652–660, jul 2015.

[18] G. S. Duesberg, I. Loa, M. Burghard, K. Syassen, and S. Roth. Polarized Raman Spectroscopy on Isolated Single-Wall Carbon Nanotubes. *Physical Review Letters*, 85(25):5436–5439, dec 2000.

[19] K. Hamada, K. Fujita, N. I. Smith, M. Kobayashi, Y. Inouye, and S. Kawata. Raman microscopy for dynamic molecular imaging of living cells. *Journal of Biomedical Optics*, 13(4):044027, 2008.

[20] J. T. Motz, M. Hunter, L. H. Galindo, J. A. Gardecki, J. R. Kramer, R. R. Dasari, and M. S. Feld. Optical Fiber Probe for Biomedical Raman Spectroscopy. *Applied Optics*, 43(3):542, jan 2004.

[21] H. Sato, H. Shinzawa, and Y. Komachi. Fiber-Optic Raman Probes for Biomedical and Pharmaceutical Applications. pages 25–45. Springer Berlin Heidelberg, 2010.

[22] I. Latka, S. Dochow, C. Krafft, B. Dietzek, and J. Popp. Fiber optic probes for linear and nonlinear Raman applications - Current trends and future development. *Laser & Photonics Reviews*, 7(5):698–731, sep 2013.

[23] T. Dörfer, T. Bocklitz, N. Tarcea, M. Schmitt, and J. Popp. Checking and Improving Calibration of Raman Spectra using Chemometric Approaches. *Zeitschrift für Physikalische Chemie*, 225(6-7):753–764, jul 2011.

[24] J. D. Rodriguez, B. J. Westenberger, L. F. Buhse, and J. F. Kauffman. Standardization of Raman spectra for transfer of spectral libraries across different instruments. *The Analyst*, 136(20):4232–40, oct 2011.

[25] D. Hutsebaut, P. Vandenabeele, and L. Moens. Evaluation of an accurate calibration and spectral standardization procedure for Raman spectroscopy. *The Analyst*, 130(8):1204, 2005.

[26] T. Bocklitz, T. Dörfer, R. Heinke, M. Schmitt, and J. Popp. Spectrometer calibration protocol for Raman spectra recorded with different excitation wavelengths. *Spectrochimica Acta Part A: Molecular and Biomolecular Spectroscopy*, 149:544–549, 2015.

[27] L. T. Kerr, H. J. Byrne, and B. M. Hennelly. Optimal choice of sample substrate and laser wavelength for Raman spectroscopic analysis of biological specimen. *Anal. Methods*, 7(12):5041–5052, 2015.

[28] P. Lasch. Spectral pre-processing for biomedical vibrational spectroscopy and microspectroscopic imaging. *Chemometrics and Intelligent Laboratory Systems*, 117:100–114, 2012.

[29] R. Gautam, S. Vanga, F. Ariese, and S. Umapathy. Review of multidimensional data processing approaches for Raman and infrared spectroscopy. *EPJ Techniques and Instrumentation*, 2(1):8, dec 2015.

[30] U. B. Cappel, I. M. Bell, and L. K. Pickard. Removing Cosmic Ray Features from Raman Map Data by a Refined Nearest Neighbor Comparison Method as a Precursor for Chemometric Analysis. *Applied Spectroscopy*, 64(2):195–200, feb 2010.

[31] C. J. Behrend, C. P. Tarnowski, and M. D. Morris. Identification of Outliers in Hyperspectral Raman Image Data by Nearest Neighbor Comparison. *Applied Spectroscopy, Vol. 56, Issue 11, pp. 1458-1461*, 56(11):1458–1461, 2002.

[32] P. Marchand and L. Marmet. Binomial smoothing filter: A way to avoid some pitfalls of least-squares polynomial smoothing. *Review of Scientific Instruments*, 54(8):1034, 1983.

[33] F. Holler, D. H. Burns, and J. B. Callis. Direct Use of Second Derivatives in Curve-Fitting Procedures. *Applied Spectroscopy, Vol. 43, Issue 5, pp. 877-882*, 43(5):877–882, 1989.

[34] A. Savitzky and M. J. E. Golay. Smoothing and Differentiation of Data by Simplified Least Squares Procedures. *Analytical Chemistry*, 36(8):1627–1639, jul 1964.

[35] J. Zhao, H. Lui, D. I. McLean, and H. Zeng. Automated autofluorescence background subtraction algorithm for biomedical Raman spectroscopy. *Applied spectroscopy*, 61(11):1225–32, nov 2007.

[36] Z.-M. Zhang, S. Chen, Y.-Z. Liang, Z.-X. Liu, Q.-M. Zhang, L.-X. Ding, F. Ye, and H. Zhou. An intelligent background-correction algorithm for highly fluorescent samples in Raman spectroscopy. *Journal of Raman Spectroscopy*, 41(6): 659–669, oct 2009.

[37] B. D. Beier and A. J. Berger. Method for automated background subtraction from Raman spectra containing known contaminants. *The Analyst*, 134(6):1198, 2009.

[38] A. Tfayli, C. Gobinet, V. Vrabie, R. Huez, M. Manfait, and O. Piot. Digital dewaxing of Raman signals: discrimination between nevi and melanoma spectra obtained from paraffin-embedded skin biopsies. *Applied spectroscopy*, 63(5):564–70, may 2009.

[39] S. Rangan. Assessment of the onset and progress of apoptosis via Raman spectroscopy, 2016.

[40] S. K. Teh, W. Zheng, K. Y. Ho, M. Teh, K. G. Yeoh, and Z. Huang. Diagnostic potential of near-infrared Raman spectroscopy in the stomach: differentiating dysplasia from normal tissue. *British Journal of Cancer*, 98(2):457–465, jan 2008.

[41] R. J. Barnes, M. S. Dhanoa, and S. J. Lister. Standard Normal Variate Transformation and De-trending of Near-Infrared Diffuse Reflectance Spectra. *Applied Spectroscopy, Vol. 43, Issue 5, pp. 772-777*, 43(5):772–777, 1989.

[42] N. K. Afseth and A. Kohler. Extended multiplicative signal correction in vibrational spectroscopy, a tutorial. *Chemometrics and Intelligent Laboratory Systems*, 117:92–99, 2012.

[43] H. Martens, S. Jensen, and P. Geladi. Multivariate linearity transformations for near infrared reflectance spectroscopy. In O. Christie, editor, *Nordic Symposium on Applied Spectroscopy*, pages 625–635, 1983.

[44] P. Geladi, D. MacDougall, and H. Martens. Linearization and Scatter-Correction for Near-Infrared Reflectance Spectra of Meat. *Applied Spectroscopy, Vol. 39, Issue 3, pp. 491-500*, 39(3):491–500, 1985.

[45] H. Martens and E. Stark. Extended multiplicative signal correction and spectral interference subtraction: New preprocessing methods for near infrared spectroscopy. *Journal of Pharmaceutical and Biomedical Analysis*, 9(8): 625–635, jan 1991.

[46] H. Martens, J. P. Nielsen, and S. B. Engelsen. Light Scattering and Light Absorbance Separated by Extended Multiplicative Signal Correction. Application to Near-Infrared Transmission Analysis of Powder Mixtures. *Analytical Chemistry*, 75(3):394–404, feb 2003.

[47] N. K. Afseth, V. H. Segtnan, and J. P. Wold. Raman spectra of biological samples: A study of preprocessing methods. *Applied Spectroscopy*, 60(12):1358–1367, 2006.

[48] P. Heraud, B. R. Wood, J. Beardall, and D. McNaughton. Effects of pre-processing of Raman spectra onin vivo classification of nutrient status of microalgal cells. *Journal of Chemometrics*, 20(5):193–197, may 2006.

[49] C. Camerlingo, I. Delfino, G. Perna, V. Capozzi, and M. Lepore. Micro-Raman spectroscopy and univariate analysis for monitoring disease follow-up. *Sensors (Basel, Switzerland)*, 11(9):8309–22, 2011.

[50] H. Shinzawa, K. Awa, W. Kanematsu, and Y. Ozaki. Multivariate data analysis for Raman spectroscopic imaging. *Journal of Raman Spectroscopy*, 40(12):1720–1725, dec 2009.

[51] P. Geladi. Chemometrics in spectroscopy. Part 1. Classical chemometrics. *Spectrochimica Acta Part B: Atomic Spectroscopy*, 58(5):767–782, 2003.

[52] S. N. Deming. Chemometrics: an overview. *Clinical chemistry*, 32(9):1702–6, sep 1986.

[53] M. Sharaf, D. Illman, and B. Kowalski. *Chemometrics*. New-York, 1986.

[54] R. Baigorri, A. M. Zamarreño, M. Fuentes, G. González-Gaitano, J. M. García-Mina, G. Almendros, and F. J. González-Vila. Multivariate statistical analysis of mass spectra as a tool for the classification of the main humic substances according to their structural and conformational features. *Journal of agricultural and food chemistry*, 56 (14):5480–7, jul 2008.

[55] T. Zagar and D. Krizaj. Multivariate analysis of electrical impedance spectra for relaxed and contracted skeletal muscle. *Physiological measurement*, 29(6):S365–72, jun 2008.

[56] B. Lindholm-Sethson, J. Nyström, M. Malmsten, L. Ringstad, A. Nelson, and P. Geladi. Electrochemical impedance spectroscopy in label-free biosensor applications: multivariate data analysis for an objective interpretation. *Analytical and bioanalytical chemistry*, 398(6):2341–9, nov 2010.

[57] P. L. Cooley and R. L. Roenfeldt. A Comparative Multivariate Analysis of Factors Affecting Stock Returns. *The Financial Review*, 10(1):31–41, feb 1975.

[58] S. Wold, K. Esbensen, and P. Geladi. Principal component analysis. *Chemometrics and Intelligent Laboratory Systems*, 2(1-3):37–52, aug 1987.

[59] G. Dunteman. *Principal components analysis*. Sage Publications, 1989. ISBN 0803931042.

[60] I. Jolliffe and I. Jolliffe. Principal Component Analysis. In *Wiley StatsRef: Statistics Reference Online*. John Wiley & Sons, Ltd, Chichester, UK, sep 2014.

[61] G. H. Golub and C. Reinsch. Singular value decomposition and least squares solutions. *Numerische Mathematik*, 14 (5):403–420, apr 1970.

[62] D. Tsikritsis, S. Richmond, P. Stewart, A. Elfick, and A. Downes. Label-free identification and characterization of living human primary and secondary tumour cells. *The Analyst*, 140(15):5162–5168, 2015.

[63] R. Dubes and A. K. Jain. Clustering techniques: The user's dilemma. *Pattern Recognition*, 8(4):247–260, 1976.

[64] A. K. Jain and R. C. Dubes. *Algorithms for clustering data*. Prentice Hall, 1988. ISBN 013022278X.

[65] A. Nijssen, T. C. B. Schut, F. Heule, P. J. Caspers, D. P. Hayes, M. H. A. Neumann, and G. J. Puppels. Discriminating Basal Cell Carcinoma from its Surrounding Tissue by Raman Spectroscopy. *Journal of Investigative Dermatology*, 119:64–69, 2002.

[66] A. Ahmad and L. Dey. A k-mean clustering algorithm for mixed numeric and categorical data. 2007.

[67] P. Rösch, M. Harz, M. Schmitt, and J. Popp. Raman spectroscopic identification of single yeast cells. *Journal of Raman Spectroscopy*, 36(5):377–379, may 2005.

[68] A. Bonifacio, C. Beleites, F. Vittur, E. Marsich, S. Semeraro, S. Paoletti, and V. Sergo. Chemical imaging of articular cartilage sections with Raman mapping, employing uni- and multi-variate methods for data analysis. *The Analyst*, 135(12):3193, 2010.

[69] S. Wold, M. Sjöström, and L. Eriksson. PLS-regression: a basic tool of chemometrics. *Chemometrics and Intelligent Laboratory Systems*, 58(2):109–130, oct 2001.

[70] A. J. Berger, T.-W. Koo, I. Itzkan, G. Horowitz, and M. S. Feld. Multicomponent blood analysis by near-infrared Raman spectroscopy. *Applied Optics*, 38(13):2916, may 1999.

[71] E. I. Altman. Financial Ratios, Discriminant Analysis and the Prediction of Corporate Bankruptcy. *The Journal of Finance*, 23(4):589–609, sep 1968.

[72] P. Crow, A. Molckovsky, N. Stone, J. Uff, B. Wilson, and L.-M. WongKeeSong. Assessment of fiberoptic near-infrared raman spectroscopy for diagnosis of bladder and prostate cancer. *Urology*, 65(6):1126–1130, 2005.

[73] K. Christian, M. Johanna, A. Werner, B. Kathrin, G. M. Tesfay, H. Robert, A. Abbas, W. Stefan, B. Andreas, N. F. Wilhelm, and S. Florian. Raman difference spectroscopy: a non-invasive method for identification of oral squamous cell carcinoma. *Biomedical optics express*, 5(9):3252–65, 2014.

[74] S. Duraipandian, W. Zheng, J. Ng, J. J. H. Low, A. Ilancheran, and Z. Huang. In vivo diagnosis of cervical precancer using Raman spectroscopy and genetic algorithm techniques. *The Analyst*, 136(20):4328, 2011.

[75] M. R. de Almeida, D. N. Correa, W. F. Rocha, F. J. Scafi, and R. J. Poppi. Discrimination between authentic and counterfeit banknotes using Raman spectroscopy and PLS-DA with uncertainty estimation. *Microchemical Journal*, 109:170–177, 2013.

[76] E. M. Kanter, S. Majumder, E. Vargis, A. Robichaux-Viehoever, G. J. Kanter, H. Shappell, H. W. Jones III, and A. Mahadevan-Jansen. Multiclass discrimination of cervical precancers using Raman spectroscopy. *Journal of Raman Spectroscopy*, 40(2):205–211, feb 2009.

[77] M. Hearst, S. Dumais, E. Osman, J. Platt, and B. Scholkopf. Support vector machines. *IEEE Intelligent Systems*, 13(4):18–28, jul 1998.

[78] I. Steinwart and A. Christmann. *Support Vector Machines*. Information Science and Statistics. Springer New York, New York, NY, 2008. ISBN 978-0-387-77241-7.

[79] b. F. David Meyer Technikum Wien and A. DavidMeyer. Support Vector Machines * The Interface to libsvm in package e1071. 2015.

[80] E. Widjaja, W. Zheng, and Z. Huang. Classification of colonic tissues using near-infrared Raman spectroscopy and support vector machines. *International journal of oncology*, 32(3):653–62, mar 2008.

[81] M. Sattlecker, C. Bessant, J. Smith, and N. Stone. Investigation of support vector machines and Raman spectroscopy for lymph node diagnostics. *The Analyst*, 135(5):895–901, 2010.

[82] U. Thissen, M. Pepers, B. Üstün, W. Melssen, and L. Buydens. Comparing support vector machines to PLS for spectral regression applications. *Chemometrics and Intelligent Laboratory Systems*, 73(2):169–179, 2004.

[83] C. Hu, J. Wang, C. Zheng, S. Xu, H. Zhang, Y. Liang, L. Bi, Z. Fan, B. Han, and W. Xu. Raman spectra exploring breast tissues: comparison of principal component analysis and support vector machine-recursive feature elimination. *Medical physics*, 40(6):063501, jun 2013.

[84] J. Shawee-Taylor and N. Cristianini. *Kernel Methods for Pattern Analysis.* Cambridge University Press, New York, NY, 2004. ISBN 9780521813976.

[85] L. Breiman. Random Forests. *Machine Learning*, 45(1):5–32, 2001.

[86] A. Liaw and M. Wiener. Classification and Regression by randomForest. 23, 2002.

[87] S. K. Teh, W. Zheng, D. P. Lau, and Z. Huang. Spectroscopic diagnosis of laryngeal carcinoma using near-infrared Raman spectroscopy and random recursive partitioning ensemble techniques. 2009.

[88] B. R. Smith, K. M. Ashton, A. Brodbelt, T. Dawson, M. D. Jenkinson, N. T. Hunt, D. S. Palmer, and M. J. Baker. Combining random forest and 2D correlation analysis to identify serum spectral signatures for neuro-oncology. *The Analyst*, 141(12):3668–3678, 2016.

[89] M. Kinalwa, E. W. Blanch, and A. J. Doig. Determination of protein fold class from Raman or Raman optical activity spectra using random forests. 2011.

[90] J. A. Hanley and B. J. McNeil. The meaning and use of the area under a receiver operating characteristic (ROC) curve. *Radiology*, 143(1):29–36, apr 1982.

[91] A. P. Bradley. The use of the area under the ROC curve in the evaluation of machine learning algorithms. *Pattern Recognition*, 30(7):1145–1159, jul 1997.

[92] W. J. Youden. Index for rating diagnostic tests. *Cancer*, 3(1):32–35, 1950.

[93] R. Kohavi. A Study of Cross-Validation and Bootstrap for Accuracy Estimation and Model Selection. In *International Joint Conference of Artificial Intelligence*, pages 1137–1143, 1995.

[94] M. W. Browne. Cross-Validation Methods. *Journal of Mathematical Psychology*, 44(1):108–132, 2000.

[95] J. Rodriguez, A. Perez, and J. Lozano. Sensitivity Analysis of k-Fold Cross Validation in Prediction Error Estimation. *IEEE Transactions on Pattern Analysis and Machine Intelligence*, 32(3):569–575, mar 2010.

[96] A. Molckovsky, L.-M. W. K. Song, M. G. Shim, N. E. Marcon, and B. C. Wilson. Diagnostic potential of near-infrared Raman spectroscopy in the colon: Differentiating adenomatous from hyperplastic polyps. *Gastrointestinal Endoscopy*, 57(3):396–402, 2003.

[97] N. Stone, C. Kendall, J. Smith, P. Crow, and H. Barr. Raman spectroscopy for identification of epithelial cancers. *Faraday Discussions*, 126(0):141, 2004.

[98] Y. Wang, D. C. Alsmeyer, and R. L. McCreery. Raman spectroscopy of carbon materials: structural basis of observed spectra. *Chemistry of Materials*, 2(5):557–563, sep 1990.

[99] X. Zhang, Q.-H. Tan, J.-B. Wu, W. Shi, and P.-H. Tan. Review on the Raman spectroscopy of different types of layered materials. *Nanoscale*, 8(12):6435–50, mar 2016.

[100] K. Mizoguchi, Y. Hori, and Y. Tominaga. Study on dynamical structure in water and heavy water by low-frequency Raman spectroscopy. *The Journal of Chemical Physics*, 97(3):1961, 1992.

[101] D. M. Carey and G. M. Korenowski. Measurement of the Raman spectrum of liquid water. *The Journal of Chemical Physics*, 108(7):2669, 1998.

[102] R. S. Das and Y. Agrawal. Raman spectroscopy: Recent advancements, techniques and applications. *Vibrational Spectroscopy*, 57(2):163–176, 2011.

[103] M. E. Keating and H. J. Byrne. Raman spectroscopy in nanomedicine: current status and future perspective. *Nanomedicine (London, England)*, 8(8):1335–51, 2013.

[104] A. Downes. Raman Microscopy and Associated Techniques for Label-Free Imaging of Cancer Tissue. *Applied Spectroscopy Reviews*, 50(8):641–653, jul 2015.

[105] K. Kong, C. Kendall, N. Stone, and I. Notingher. Raman spectroscopy for medical diagnostics - From in-vitro biofluid assays to in-vivo cancer detection. *Advanced Drug Delivery Reviews*, 89:121–134, 2015.

[106] T. Huser and J. Chan. Raman spectroscopy for physiological investigations of tissues and cells. *Advanced Drug Delivery Reviews*, 89:57–70, 2015.

[107] G. J. Puppels, H. S. Garritsen, G. M. Segers-Nolten, F. F. de Mul, and J. Greve. Raman microspectroscopic approach to the study of human granulocytes. *Biophysical journal*, 60(5):1046–56, nov 1991.

[108] I. Notingher. Raman spectroscopy cell-based biosensors. *Sensors*, 7(8):1343–1358, 2007.

[109] R. Tuma. Raman spectroscopy of proteins: from peptides to large assemblies. *Journal of Raman Spectroscopy*, 36 (4):307–319, apr 2005.

[110] S. U. Sane, S. M. Cramer, and T. M. Przybycien. A Holistic Approach to Protein Secondary Structure Characterization Using Amide I Band Raman Spectroscopy. *Analytical Biochemistry*, 269(2):255–272, may 1999.

[111] G. J. Thomas. Raman Spectroscopy of Protein and Nucleic Assemblies. *Annual Review of Biophysics and Biomolecular Structure*, 28(1):1–27, jun 1999.

[112] A. Rygula, K. Majzner, K. M. Marzec, A. Kaczor, M. Pilarczyk, and M. Baranska. Raman spectroscopy of proteins: a review. *Journal of Raman Spectroscopy*, 44(8):1061–1076, aug 2013.

[113] J. T. Pelton and L. R. Mclean. Spectroscopic Methods for Analysis of Protein Secondary Structure. *Analytical Biochemistry*, 277:167–176, 2000.

[114] K. A. Okotrub, N. V. Surovtsev, V. F. Semeshin, and L. V. Omelyanchuk. Raman spectroscopy for DNA quantification in cell nucleus. *Cytometry Part A*, 87(1):68–73, jan 2015.

[115] K. Czamara, K. Majzner, M. Z. Pacia, K. Kochan, a. Kaczor, and M. Baranska. Raman spectroscopy of lipids: a review. *Journal of Raman Spectroscopy*, 46(1):4–20, jan 2015.

[116] J. De Gelder, K. De Gussem, P. Vandenabeele, and L. Moens. Reference database of Raman spectra of biological molecules. *Journal of Raman Spectroscopy*, 38(9):1133–1147, sep 2007.

[117] J. W. Chan and D. K. Lieu. Label-free biochemical characterization of stem cells using vibrational spectroscopy. *Journal of Biophotonics*, 2(11):656–668, 2009.

[118] A. Downes and A. Elfick. Raman spectroscopy and related techniques in biomedicine. *Sensors (Basel, Switzerland)*, 10(3):1871–89, jan 2010.

[119] R. J. Swain, G. Jell, and M. M. Stevens. Non-invasive analysis of cell cycle dynamics in single living cells with Raman micro-spectroscopy. *Journal of Cellular Biochemistry*, 104(4):1427–1438, jul 2008.

[120] I. Notingher, S. Verrier, S. Haque, J. M. Polak, and L. L. Hench. Spectroscopic study of human lung epithelial cells (A549) in culture: Living cells versus dead cells. *Biopolymers*, 72(4):230–240, 2003.

[121] G. P. S. Smith, C. M. McGoverin, S. J. Fraser, and K. C. Gordon. Raman imaging of drug delivery systems. *Advanced Drug Delivery Reviews*, 89:21–41, 2015.

[122] C. Zhou, Y.-L. Wu, G. Chen, J. Feng, X.-Q. Liu, C. Wang, S. Zhang, J. Wang, S. Zhou, S. Ren, S. Lu, L. Zhang, C. Hu, C. Hu, Y. Luo, L. Chen, M. Ye, J. Huang, X. Zhi, Y. Zhang, Q. Xiu, J. Ma, and C. You. Erlotinib versus chemotherapy as first-line treatment for patients with advanced EGFR mutation-positive non-small-cell lung cancer (OPTIMAL, CTONG-0802): a multicentre, open-label, randomised, phase 3 study. *The Lancet. Oncology*, 12(8): 735–42, aug 2011.

[123] R. Rosell, E. Carcereny, R. Gervais, A. Vergnenegre, B. Massuti, E. Felip, R. Palmero, R. Garcia-Gomez, C. Pallares, J. M. Sanchez, R. Porta, M. Cobo, P. Garrido, F. Longo, T. Moran, A. Insa, F. De Marinis, R. Corre, I. Bover, A. Illiano, E. Dansin, J. de Castro, M. Milella, N. Reguart, G. Altavilla, U. Jimenez, M. Provencio, M. A. Moreno, J. Terrasa, J. Muñoz-Langa, J. Valdivia, D. Isla, M. Domine, O. Molinier, J. Mazieres, N. Baize, R. Garcia-Campelo, G. Robinet, D. Rodriguez-Abreu, G. Lopez-Vivanco, V. Gebbia, L. Ferrera-Delgado, P. Bombaron, R. Bernabe, A. Bearz, A. Artal, E. Cortesi, C. Rolfo, M. Sanchez-Ronco, A. Drozdowskyj, C. Queralt, I. de Aguirre, J. L. Ramirez, J. J. Sanchez, M. A. Molina, M. Taron, and L. Paz-Ares. Erlotinib versus standard chemotherapy as first-line treatment for European patients with advanced EGFR mutation-positive non-small-cell lung cancer (EURTAC): a multicentre, open-label, randomised phase 3 trial. *The lancet oncology*, 13(3):239–46, mar 2012.

[124] S. F. El-Mashtoly, D. Niedieker, D. Petersen, S. D. Krauss, E. Freier, A. Maghnouj, A. Mosig, S. Hahn, C. K??tting, and K. Gerwert. Automated identification of subcellular organelles by coherent anti-stokes raman scattering. *Biophysical Journal*, 106(9):1910–1920, 2014.

[125] M. F. Pittenger, A. M. Mackay, S. C. Beck, R. K. Jaiswal, R. Douglas, J. D. Mosca, M. A. Moorman, D. W. Simonetti, S. Craig, and D. R. Marshak. Multilineage potential of adult human mesenchymal stem cells. *Science (New York, N.Y.)*, 284(5411):143–7, apr 1999.

[126] T. Reya, S. J. Morrison, M. F. Clarke, and I. L. Weissman. Stem cells, cancer, and cancer stem cells. *Nature*, 414 (6859):105–111, nov 2001.

[127] G. Chamberlain, J. Fox, B. Ashton, and J. Middleton. Concise Review: Mesenchymal Stem Cells: Their Phenotype, Differentiation Capacity, Immunological Features, and Potential for Homing. *Stem Cells*, 25(11):2739–2749, nov 2007.

[128] J. M. Gimble, A. J. Katz, and B. A. Bunnell. Adipose-Derived Stem Cells for Regenerative Medicine. *Circulation Research*, 100(9):1249–1260, apr 2007.

[129] A. Downes, R. Mouras, P. Bagnaninchi, and A. Elfick. Raman spectroscopy and CARS microscopy of stem cells and their derivatives. *Journal of Raman Spectroscopy*, 42(10):1864–1870, 2011.

[130] J. Sulé-Suso, N. R. Forsyth, V. Untereiner, and G. D. Sockalingum. Vibrational spectroscopy in stem cell characterisation: is there a niche? *Trends in biotechnology*, 32(5):254–62, may 2014.

[131] F. C. Pascut, S. Kalra, V. George, N. Welch, C. Denning, and I. Notingher. Non-invasive label-free monitoring the cardiac differentiation of human embryonic stem cells in-vitro by Raman spectroscopy. *Biochimica et biophysica acta*, 1830(6):3517–24, jun 2013.

[132] L. L. McManus, G. A. Burke, M. M. McCafferty, P. O'Hare, M. Modreanu, A. R. Boyd, and B. J. Meenan. Raman spectroscopic monitoring of the osteogenic differentiation of human mesenchymal stem cells. *The Analyst*, 136(12): 2471–81, jun 2011.

[133] P.Chen, F.Zhang, L.Lin, H.Bai, L.Zhang, G.Q.Tang, H.Fang, G.G.Mu, W. Gong, Z. P. Liu, Z. B. Han, H. Zhao, and Z. C. Han. Raman Spectroscopy for Noninvasive Monitoring of Umbilical Cord Mesenchymal Stem Cells Viability Transitions. In A. Gholamrezanezhad, editor, *Stem Cells in Clinic and Research*, chapter 32, pages 765 – 790. InTech, aug 2011. ISBN 978-953-307-797-0.

[134] D. Tsikritsis, H. Shi, Y. Wang, S. Velugotla, V. Srsen, A. Elfick, and A. Downes. Label-free biomarkers of human embryonic stem cell differentiation to hepatocytes. *Cytometry. Part A : the journal of the International Society for Analytical Cytology*, may 2016.

[135] T. Tolstik, C. Marquardt, C. Matthäus, N. Bergner, C. Bielecki, C. Krafft, A. Stallmach, and J. Popp. Discrimination and classification of liver cancer cells and proliferation states by Raman spectroscopic imaging. *The Analyst*, 139(22): 6036–43, nov 2014.

[136] A. T. Harris, M. Garg, X. B. Yang, S. E. Fisher, J. Kirkham, D. A. Smith, D. P. Martin-Hirsch, and A. S. High. Raman spectroscopy and advanced mathematical modelling in the discrimination of human thyroid cell lines. *Head & Neck Oncology*, 1(1):38, 2009.

[137] C. M. Krishna, G. D. Sockalingum, G. Kegelaer, S. Rubin, V. B. Kartha, and M. Manfait. Micro-Raman spectroscopy of mixed cancer cell populations. *Vibrational Spectroscopy*, 38(1):95–100, 2005.

[138] F. Draux, C. Gobinet, J. Sulé-Suso, A. Trussardi, M. Manfait, P. Jeannesson, and G. D. Sockalingum. Raman spectral imaging of single cancer cells: Probing the impact of sample fixation methods. *Analytical and Bioanalytical Chemistry*, 397(7):2727–2737, 2010.

[139] P. Matousek and M. D. Morris, editors. *Emerging Raman Applications and Techniques in Biomedical and Pharmaceutical Fields*. Biological and Medical Physics, Biomedical Engineering. Springer Berlin Heidelberg, Berlin, Heidelberg, 2010. ISBN 978-3-642-02648-5.

[140] C. Krafft and J. Popp. 4.13 - Raman-Based Technologies for Biomedical Diagnostics. In *Comprehensive Biomedical Physics*, pages 189–208. 2014. ISBN 9780444536334.

[141] R. Goodacre, V. Sergo, H. Barr, C. Sammon, Z. D. Schultz, M. J. Baker, D. Graham, M. P. Marques, J. Sulé-Suso, J. Livermore, K. Faulds, F. Sinjab, P. Matousek, C. J. Campbell, R. Dluhy, P. Gardner, C. Phillips, M. Diem, B. Wood, A. Apolonskiy, S. Kazarian, L. Fullwood, K. Gough, W. Petrich, G. Lloyd, O. Ibrahim, G. Cinque, G. D. Sockalingum, N. Stone, C. Kendall, S. McAughtrie, D. Perez-Guaita, L. Clark, K. Gerwert, A. Bonifacio, I. Notingher, P. Lasch, R. Bhargava, G. Lepert, K. Mader, and C. Paterson. Clinical Spectroscopy: general discussion. *Faraday Discuss.*, 187(0):429–460, 2016.

[142] H. J. Byrne, M. Baranska, G. J. Puppels, N. Stone, B. Wood, K. M. Gough, P. Lasch, P. Heraud, J. Sulé-Suso, and G. D. Sockalingum. Spectropathology for the next generation: Quo vadis? *The Analyst*, 140(7):2066–2073, 2015.

[143] C. Kendall, M. Isabelle, F. Bazant-Hegemark, J. Hutchings, L. Orr, J. Babrah, R. Baker, and N. Stone. Vibrational spectroscopy: a clinical tool for cancer diagnostics. *The Analyst*, 134(6):1029, 2009.

[144] P. Matousek and N. Stone. Recent advances in the development of Raman spectroscopy for deep non-invasive medical diagnosis. *Journal of Biophotonics*, 6(1):7–19, jan 2013.

[145] P. J. Caspers, G. W. Lucassen, E. A. Carter, H. A. Bruining, and G. J. Puppels. In vivo confocal Raman microspectroscopy of the skin: noninvasive determination of molecular concentration profiles. *The Journal of investigative dermatology*, 116(3):434–442, mar 2001.

[146] E. M. Barroso, R. W. H. Smits, T. C. Bakker Schut, I. ten Hove, J. A. Hardillo, E. B. Wolvius, R. J. Baatenburg de Jong, S. Koljenović, and G. J. Puppels. Discrimination between oral cancer and healthy tissue based on water content determined by Raman spectroscopy. *Analytical chemistry*, 87(4):2419–26, feb 2015.

[147] E. M. Barroso, R. W. H. Smits, C. G. F. Van Lanschot, P. J. Caspers, I. Ten Hove, H. Mast, A. Sewnaik, J. A. Hardillo, C. A. Meeuwis, R. Verdijk, V. N. Hegt, R. J. Baatenburg De Jong, E. B. Wolvius, T. C. Bakker Schut, S. Koljenović, and G. J. Puppels. Water concentration analysis by Raman spectroscopy to determine the location of the tumor border in oral cancer surgery Disclosure of Potential Conflicts of Interest. *Cancer research*, 2016.

[148] A. S. Haka, K. E. Shafer-Peltier, M. Fitzmaurice, J. Crowe, R. R. Dasari, and M. S. Feld. Diagnosing breast cancer by using Raman spectroscopy. *Proceedings of the National Academy of Sciences of the United States of America*, 102 (35):12371–6, aug 2005.

[149] A. S. Haka, Z. Volynskaya, J. A. Gardecki, J. Nazemi, J. Lyons, D. Hicks, M. Fitzmaurice, R. R. Dasari, J. P. Crowe, and M. S. Feld. In vivo margin assessment during partial mastectomy breast surgery using raman spectroscopy. *Cancer research*, 66(6):3317–22, mar 2006.

[150] A. T. Harris, A. Rennie, H. Waqar-Uddin, S. R. Wheatley, S. K. Ghosh, D. P. Martin-Hirsch, S. E. Fisher, A. S. High, J. Kirkham, and T. Upile. Raman spectroscopy in head and neck cancer. *Head & Neck Oncology*, 2(1):26, 2010.

[151] N. Stone, P. Stavroulaki, C. Kendall, M. Birchall, and H. Barr. Raman Spectroscopy for Early Detection of Laryngeal Malignancy: Preliminary Results. *The Laryngoscope*, 110(10):1756–1763, oct 2000.

[152] D. P. Lau, Z. Huang, H. Lui, D. W. Anderson, K. Berean, M. D. Morrison, L. Shen, and H. Zeng. Raman spectroscopy for optical diagnosis in the larynx: Preliminary findings. *Lasers in Surgery and Medicine*, 37(3):192–200, sep 2005.

[153] S. P. Singh, A. Deshmukh, P. Chaturvedi, and C. M. Krishna. In vivo Raman spectroscopy for oral cancers diagnosis. page 82190K, feb 2012.

[154] I. P. Santos, P. J. Caspers, T. C. Bakker Schut, R. van Doorn, V. Noordhoek Hegt, S. Koljenović, and G. J. Puppels. Raman Spectroscopic Characterization of Melanoma and Benign Melanocytic Lesions Suspected of Melanoma Using High-Wavenumber Raman Spectroscopy. *Analytical Chemistry*, 88(15):7683–7688, aug 2016.

[155] J. Schleusener, P. Gluszczynska, C. Reble, I. Gersonde, J. Helfmann, J. W. Fluhr, J. Lademann, J. Röwert-Huber, A. Patzelt, and M. C. Meinke. <i>In vivo</i> study for the discrimination of cancerous and normal skin using fibre probe-based Raman spectroscopy. *Experimental Dermatology*, 24(10):767–772, oct 2015.

[156] R. Kast, G. Auner, S. Yurgelevic, B. Broadbent, A. Raghunathan, L. M. Poisson, T. Mikkelsen, M. L. Rosenblum, and S. N. Kalkanis. Identification of regions of normal grey matter and white matter from pathologic glioblastoma and necrosis in frozen sections using Raman imaging. *Journal of neuro-oncology*, 125(2):287–95, nov 2015.

[157] M. Jermyn, K. Mok, J. Mercier, J. Desroches, J. Pichette, K. Saint-Arnaud, L. Bernstein, M.-C. Guiot, K. Petrecca, and F. Leblond. Intraoperative brain cancer detection with Raman spectroscopy in humans. *Science Translational Medicine*, 7(274):274ra19–274ra19, feb 2015.

[158] R. O. P. Draga, M. C. M. Grimbergen, P. L. M. Vijverberg, C. F. P. van Swol, T. G. N. Jonges, J. A. Kummer, and J. L. H. Ruud Bosch. In Vivo Bladder Cancer Diagnosis by High-Volume Raman Spectroscopy. *Analytical Chemistry*, 82(14):5993–5999, jul 2010.

[159] C. Krafft, S. Dochow, I. Latka, B. Dietzek, and J. Popp. Diagnosis and screening of cancer tissues by fiber-optic probe Raman spectroscopy. *Biomedical Spectroscopy and Imaging*, 1(1):39–55, 2012.

[160] J.-x. Cheng and X. S. Xie. Coherent Anti-Stokes Raman Scattering Microscopy: Instrumentation, Theory, and Applications. *Journal of physics Chemical B*, 108(1):827–840, jan 2004.

[161] F. El-Diasty. Coherent anti-Stokes Raman scattering: Spectroscopy and microscopy. *Vibrational Spectroscopy*, 55(1): 1–37, 2011.

[162] C. L. Evans and X. S. Xie. Coherent Anti-Stokes Raman Scattering Microscopy: Chemical Imaging for Biology and Medicine. *Annual Review of Analytical Chemistry*, 1(1):883–909, jul 2008.

[163] C. H. Camp Jr and M. T. Cicerone. Chemically sensitive bioimaging with coherent Raman scattering. *Nature Photonics*, 9(5):295–305, apr 2015.

[164] I. Pope, L. Payne, G. Zoriniants, E. Thomas, O. Williams, P. Watson, W. Langbein, and P. Borri. Coherent anti-Stokes Raman scattering microscopy of single nanodiamonds. *Nature Nanotechnology*, 9(11):940–946, 2014.

[165] B. G. Saar, C. W. Freudiger, J. Reichman, C. M. Stanley, G. R. Holtom, and X. S. Xie. Video-rate molecular imaging in vivo with stimulated Raman scattering. *Science (New York, N.Y.)*, 330(6009):1368–70, dec 2010.

[166] C. L. Evans, E. O. Potma, M. Puoris'haag, D. Côté, C. P. Lin, and X. S. Xie. Chemical imaging of tissue in vivo with video-rate coherent anti-Stokes Raman scattering microscopy. *Proceedings of the National Academy of Sciences of the United States of America*, 102(46):16807–12, nov 2005.

[167] X. Zhang, M. B. J. Roeffaers, S. Basu, J. R. Daniele, D. Fu, C. W. Freudiger, G. R. Holtom, and X. S. Xie. Label-Free Live-Cell Imaging of Nucleic Acids Using Stimulated Raman Scattering Microscopy. *ChemPhysChem*, 13(4): 1054–1059, mar 2012.

[168] H. Kano, H. Segawa, M. Okuno, P. Leproux, and V. Couderc. Hyperspectral coherent Raman imaging - principle, theory, instrumentation, and applications to life sciences. *Journal of Raman Spectroscopy*, 47(1):116–123, jan 2016.

[169] E. M. Vartiainen. Phase retrieval approach for coherent anti-Stokes Raman scattering spectrum analysis. *Journal of the Optical Society of America B*, 9(8):1209, aug 1992.

[170] F. Masia, A. Karuna, P. Borri, and W. Langbein. Hyperspectral image analysis for CARS, SRS, and Raman data. *Journal of Raman Spectroscopy*, pages n/a–n/a, jun 2015.

[171] M. Okuno, V. Couderc, and H.-o. Hamaguchi. Quantitative coherent anti-Stokes Raman scattering microspectroscopy using a nanosecond supercontinuum light source. *Optical Fiber Technology*, 18(5):388–393, 2012.

[172] C. W. Freudiger, W. Min, B. G. Saar, S. Lu, G. R. Holtom, C. He, J. C. Tsai, J. X. Kang, and X. S. Xie. Label-free biomedical imaging with high sensitivity by stimulated Raman scattering microscopy. *Science (New York, N.Y.)*, 322 (5909):1857–61, dec 2008.

[173] W. J. Tipping, M. Lee, A. Serrels, V. G. Brunton, and A. N. Hulme. Stimulated Raman scattering microscopy: an emerging tool for drug discovery. *Chemical Society reviews*, feb 2016.

[174] X. Nan, W. Y. Yang, and X. S. Xie. CARS microscopy lights up lipids in living cells. *Biophotonics International*, 11 (8):44–47, 2004.

[175] A. Zumbusch, W. Langbein, and P. Borri. Nonlinear vibrational microscopy applied to lipid biology. *Progress in lipid research*, 52(4):615–32, oct 2013.

[176] M. Okuno, H. Kano, K. Fujii, K. Bito, S. Naito, P. Leproux, V. Couderc, and H. O. Hamaguchi. Surfactant uptake dynamics in mammalian cells elucidated with quantitative coherent anti-stokes raman scattering microspectroscopy. *PLoS ONE*, 9(4):2–8, 2014.

[177] A. F. Palonpon, J. Ando, H. Yamakoshi, K. Dodo, M. Sodeoka, S. Kawata, and K. Fujita. Raman and SERS microscopy for molecular imaging of live cells. *Nature protocols*, 8(4):677–92, apr 2013.

[178] E. Smith and G. Dent. Surface-Enhanced Raman Scattering and Surface-Enhanced Resonance Raman Scattering. In *Modern Raman Spectroscopy - A Practical Approach*, pages 113–133. John Wiley & Sons, Ltd, Chichester, UK, aug 2005.

[179] P. L. Stiles, J. A. Dieringer, N. C. Shah, and R. P. Van Duyne. Surface-Enhanced Raman Spectroscopy. *Annual Review of Analytical Chemistry*, 1(1):601–626, jul 2008.

[180] J. P. Nolan and D. S. Sebba. Surface-enhanced Raman scattering (SERS) cytometry. *Methods in cell biology*, 102: 515–32, 2011.

[181] J. W. Dobrucki. Fluorescence Microscopy. In *Fluorescence Microscopy*, pages 97–142. Wiley-VCH Verlag GmbH & Co. KGaA, Weinheim, Germany, apr 2013.

[182] C. A. Combs. Fluorescence microscopy: a concise guide to current imaging methods. *Current protocols in neuroscience / editorial board, Jacqueline N. Crawley ... [et al.]*, Chapter 2:Unit2.1, jan 2010.

[183] H. C. Ishikawa-Ankerhold, R. Ankerhold, and G. P. C. Drummen. Advanced Fluorescence Microscopy Techniques—FRAP, FLIP, FLAP, FRET and FLIM. *Molecules*, 17(12):4047–4132, apr 2012.

[184] J. R. Lakowicz, editor. *Principles of Fluorescence Spectroscopy.* Springer US, Boston, MA, 2006. ISBN 978-0-387-31278-1.

[185] A. Jabłoński. Efficiency of Anti-Stokes Fluorescence in Dyes. *Nature*, 131(3319):839–840, jun 1933.

[186] J. W. Lichtman and J.-A. Conchello. Fluorescence microscopy. *Nature Methods*, 2(12):910–919, dec 2005.

[187] G. Drummen. Fluorescent Probes and Fluorescence (Microscopy) Techniques — Illuminating Biological and Biomedical Research. *Molecules*, 17(12):14067–14090, nov 2012.

[188] J. Zhang, R. E. Campbell, A. Y. Ting, and R. Y. Tsien. Creating new fluorescent probes for cell biology. *Nature Reviews Molecular Cell Biology*, 3(12):906–918, dec 2002.

[189] H. Kobayashi, M. Ogawa, R. Alford, P. L. Choyke, and Y. Urano. New Strategies for Fluorescent Probe Design in Medical Diagnostic Imaging. *Chemical Reviews*, 110(5):2620–2640, may 2010.

[190] J. Wu, W. Liu, J. Ge, H. Zhang, P. Wang, I. A. Mikhailov, A. E. Masunov, O. V. Przhonska, J. S. Kim, K. K. L. Cheuk, and B. Z. Tang. New sensing mechanisms for design of fluorescent chemosensors emerging in recent years. *Chemical Society Reviews*, 40(7):3483, 2011.

[191] M. Eisenstein. Helping cells to tell a colorful tale. *Nature Methods*, 3(8):647–655, aug 2006.

[192] T. Suzuki, T. Matsuzaki, H. Hagiwara, T. Aoki, and K. Takata. Recent advances in fluorescent labeling techniques for fluorescence microscopy. *Acta histochemica et cytochemica*, 40(5):131–7, dec 2007.

[193] R. Y. Tsien. The Green Fluorescent Protein. *Annual Review of Biochemistry*, 67(1):509–544, jun 1998.

[194] N. C. Shaner, P. A. Steinbach, and R. Y. Tsien. A guide to choosing fluorescent proteins. *Nature Methods*, 2(12): 905–909, dec 2005.

[195] B. Giepmans, S. Adams, M. Ellisman, and R. Tsien. The Fluorescent Toolbox for Assessing Protein Location and Function. *Science*, 312:217 – 224, 2016.

[196] D. Shakes, D. Miller, and M. Nonet. Immunofluorescence Microscopy. In J. Rothman and A. Singson, editors, *Caenorhabditis Elegans: Cell biology and physiology*, chapter 2, pages 36–62. Elsevier, London, 2012. ISBN 978-0-12-394620-1.

[197] E. C. Jensen. Use of Fluorescent Probes: Their Effect on Cell Biology and Limitations. *The Anatomical Record: Advances in Integrative Anatomy and Evolutionary Biology*, 295(12):2031–2036, dec 2012.

[198] J.-A. Conchello and J. W. Lichtman. Optical sectioning microscopy. *Nature Methods*, 2(12):920–931, dec 2005.

[199] P. Monetta, I. Slavin, N. Romero, and C. Alvarez. Rab1b Interacts with GBF1 and Modulates both ARF1 Dynamics and COPI Association. *Molecular Biology of the Cell*, 18(7):2400–2410, apr 2007.

[200] S. L. Shaw, R. Kamyar, and D. W. Ehrhardt. Sustained Microtubule Treadmilling in Arabidopsis Cortical Arrays. *Science*, 300(5626):1715–1718, jun 2003.

[201] X. Zhang, Y. H. Tee, J. K. Heng, Y. Zhu, X. Hu, F. Margadant, C. Ballestrem, A. Bershadsky, G. Griffiths, and H. Yu. Kinectin-mediated endoplasmic reticulum dynamics supports focal adhesion growth in the cellular lamella. *Journal of Cell Science*, 123(22), 2010.

[202] S. Inoué and T. Inoué. Direct-View High-Speed Confocal Scanner: The CSU-10. In B. Matsumoto, editor, *Methods in Cell Biology*, volume 70, chapter 2, pages 87–127. Elsevier, 2002. ISBN 9780124802773.

[203] R. Gräf, J. Rietdorf, and T. Zimmermann. Live Cell Spinning Disk Microscopy. In J. Rietdorf, editor, *Microscopy Techniques*, pages 57–75. Springer Berlin Heidelberg, may 2005. ISBN 978-3-540-23698-6.

[204] K. N. Fish. Total internal reflection fluorescence (TIRF) microscopy, oct 2009.

[205] D. Toomre and D. J. Manstein. Lighting up the cell surface with evanescent wave microscopy. *Trends in Cell Biology*, 11(7):298–303, 2001.

[206] A. I. McIntosh, B. Yang, S. M. Goldup, M. Watkinson, R. S. Donnan, A. G. Davies, D. A. Ritchie, R. C. Iotti, F. Rossi, H. Yamaguchi, T. Tachiki, K. E. Gray, W. K. Kwok, and U. Welp. Terahertz spectroscopy: a powerful new tool for the chemical sciences? *Chem. Soc. Rev.*, 41(6):2072–2082, 2012.

[207] A. G. Davies, A. D. Burnett, W. Fan, E. H. Linfield, and J. E. Cunningham. Terahertz spectroscopy of explosives and drugs. *Materials Today*, 11(3):18–26, 2008.

[208] G. J. Wilmink, B. L. Ibey, C. L. Roth, R. L. Vincelette, B. D. Rivest, C. B. Horn, J. Bernhard, D. Roberson, and W. P. Roach. Determination of death thresholds and identification of terahertz (THz)-specific gene expression signatures. In E. D. Jansen and R. J. Thomas, editors, *Optical Interactions with Tissues and Cells XXI*, page 75620K, feb 2010.

[209] H. Hoshina, A. Hayashi, N. Miyoshi, F. Miyamaru, and C. Otani. Terahertz pulsed imaging of frozen biological tissues. *Applied Physics Letters*, 94(12):123901, mar 2009.

[210] F. Wahaia, G. Valusis, L. M. Bernardo, A. Almeida, J. A. Moreira, P. C. Lopes, J. Macutkevic, I. Kasalynas, D. Seliuta, R. Adomavicius, R. Henrique, and M. Lopes. Detection of colon cancer by terahertz techniques. *Journal of Molecular Structure*, 1006(1):77–82, 2011.

[211] T. C. Bowman, M. El-Shenawee, and L. K. Campbell. Terahertz Imaging of Excised Breast Tumor Tissue on Paraffin Sections. *IEEE Transactions on Antennas and Propagation*, 63(5):2088–2097, may 2015.

[212] H. Chen, T.-H. Chen, T.-F. Tseng, J.-T. Lu, C.-C. Kuo, S.-C. Fu, W.-J. Lee, Y.-F. Tsai, Y.-Y. Huang, E. Y. Chuang, Y.-J. Hwang, and C.-K. Sun. High-sensitivity in vivo THz transmission imaging of early human breast cancer in a subcutaneous xenograft mouse model. *Optics Express*, 19(22):21552, oct 2011.

[213] P. Tewari, C. P. Kealey, D. B. Bennett, N. Bajwa, K. S. Barnett, R. S. Singh, M. O. Culjat, A. Stojadinovic, W. S. Grundfest, and Z. D. Taylor. In vivo terahertz imaging of rat skin burns. *Journal of Biomedical Optics*, 17(4):040503, 2012.

[214] T. Hasebe, S. Kawabe, H. Matsui, and H. Tabata. Metallic mesh-based terahertz biosensing of single- and double-stranded DNA. *Journal of Applied Physics*, 112(9):094702, nov 2012.

[215] A. Arora, T. Q. Luong, M. Krüger, Y. J. Kim, C.-H. Nam, A. Manz, M. Havenith, J. Winter, M. Tani, and M. Havenith. Terahertz-time domain spectroscopy for the detection of PCR amplified DNA in aqueous solution. *The Analyst*, 137(3):575–579, 2012.

[216] L. Xie, Y. Yao, and Y. Ying. The Application of Terahertz Spectroscopy to Protein Detection: A Review. *Applied Spectroscopy Reviews*, 49(6):448–461, aug 2014.

[217] D.-K. Lee, J.-H. Kang, J.-S. Lee, H.-S. Kim, C. Kim, J. H. Kim, T. Lee, J.-H. Son, Q.-H. Park, and M. Seo. Highly sensitive and selective sugar detection by terahertz nano-antennas. *Scientific reports*, 5:15459, oct 2015.

[218] S. J. Park, J. T. Hong, S. J. Choi, H. S. Kim, W. K. Park, and S. T. Han. Detection of microorganisms using terahertz metamaterials. *Scientific Reports*, 4:358–364, may 2014.

[219] K. Shiraga, Y. Ogawa, T. Suzuki, N. Kondo, A. Irisawa, and M. Imamura. Characterization of Dielectric Responses of Human Cancer Cells in the Terahertz Region. *Journal of Infrared, Millimeter, and Terahertz Waves*, 35(5):493–502, may 2014.

[220] X. Yang, X. Zhao, K. Yang, Y. Liu, Y. Liu, W. Fu, and Y. Luo. Biomedical Applications of Terahertz Spectroscopy and Imaging. *Trends in Biotechnology*, 34(10):810–824, 2016.

[221] M. Grognot and G. Gallot. Quantitative measurement of permeabilization of living cells by terahertz attenuated total reflection. *Applied Physics Letters*, 107(10):103702, sep 2015.

[222] B. Alberts, J. Wilson, and T. Hunt. *Molecular biology of the cell, 5th edition.* Garland Science, New-York, 2008. ISBN 9780815341116.

[223] H. Lodish, A. Berk, S. L. Zipursky, P. Matsudaira, D. Baltimore, and J. Darnell. Biomembranes: Structural Organization and Basic Functions, 2000.

[224] R. B. Gennis. *Biomembranes : Molecular Structure and Function.* Springer New York, 1989. ISBN 1475720653.

[225] M. Edidin. The State of Lipid Rafts: From Model Membranes to Cells. *Annual Review of Biophysics and Biomolecular Structure*, 32(1):257–283, jun 2003.

[226] G. Karp and P. L. Masson. *Biologie cellulaire et moleculaire.* De Boeck, 2010. ISBN 9782804160111.

[227] J. Lombard. Once upon a time the cell membranes: 175 years of cell boundary research. *Biology direct*, 9:32, dec 2014.

[228] J. Singer. Some Early History of Membrane Molecular Biology. *Annual Review of Physiology*, 66(1):1–27, mar 2004.

[229] R. Hooke. *Micrographia, or Some Physiological Descriptions of Minute Bodies Made by Magnifying Glasses.* Royal Society, London, 1665.

[230] M. Schleiden. Beiträge zur Phytogenesis. *Arch Anat Phisio wiss Med*, 1:137–176, 1838.

[231] T. Schwann. *Mikroskopische Untersuchungen über die Uebereinstimmung in der Struktur und dem Wachsthum der Thiere und Pflanzen.* Sander, Berlin, 1. auflage edition, 1839.

[232] C. Nägeli. Zellenkerne, Zellenbildung und Zellenwachsthum bei den Pflanzen. *Z wiss Bot*, 1:37–133, 1844.

[233] N. Pringsheim. *Untersuchungen Über Den Bau Und Die Bindung Der Pflanzenzelle.* Hirschwald, Berlin, 1854.

[234] W. Nernst. Ein osmotischer Versuch. *Zeit phys Chem*, 6:37–40, 1890.

[235] M. Traube. Experimente zur Theorie der Zellenbildung und Endosmose. *Arch Anat Physiol wiss Med*, 1:87–167, 1867.

[236] C. Overton. Über die osmotischen Eigenschaften der lebenden Pflanzen-und Tierzelle. 1895.

[237] R. Höber. Eine Methode, die elektrische Leitfähigkeit im Innern von Zellen zu messen. *Pflugers Arch*, 133:237–253, 1910.

[238] R. Chambers. A micro injection study on the permeability of the starfish egg. *J Gen Physiol*, 5(2):189–193, 1922.

[239] G. B. Chapman and J. Hillier. Electron microscopy of ultra-thin sections of bacteria I. Cellular division in Bacillus cereus. *Journal of bacteriology*, 66(3):362–73, sep 1953.

[240] G. B. Chapman and A. J. Kroll. Electron microscopy of ultrathin sections of Spirillum serpens. *Journal of bacteriology*, 73(1):63–71, jan 1957.

[241] G. B. Chapman. Electron microscopy of ultrathin sections of bacteria. III. Cell wall, cytoplasmic membrane, and nuclear material. *Journal of bacteriology*, 78(1):96–104, jul 1959.

[242] E. Gorter and F. Grendel. ON BIMOLECULAR LAYERS OF LIPOIDS ON THE CHROMOCYTES OF THE BLOOD. *Journal of Experimental Medicine*, 41(4):439–443, mar 1925.

[243] D. F. Waugh and F. O. Schmitt. Investigation of the thickness and ultrastructure of cellular membranes by the analytical leptoscope. *Cold Spring Harbor Symposia on Quantitative Biology*, 8(0):233–241, jan 1940.

[244] J. D. Robertson. New observations on the ultrastructure of the membranes of frog peripheral nerve fibers. *The Journal of biophysical and biochemical cytology*, 3(6):1043–8, nov 1957.

[245] E. Jorpes. The protein component of the erythrocyte membrane or stroma. *The Biochemical journal*, 26(5):1488–503, 1932.

[246] D. Branton and R. Park. *Papers on biological membrane structure.* Little, Brown and Company, Boston, 1968.

[247] J. Lenardt and S. J. Singer. Protein conformation in cell membrane preparations as studied by optical rotatory dispersion and circular dichroism. *Proceedings of the National Academy of Sciences*, 56(6):1828–1835, 1966.

[248] A. H. Maddy and B. R. Malcolm. Protein conformations in the plasma membrane. *Science*, 150(3703):1616–8, dec 1965.

[249] D. Haydon and J. Taylor. The stability and properties of bimolecular lipid leaflets in aqueous solutions. *Journal of Theoretical Biology*, 4(3):281–296, may 1963.

[250] S. J. Singer and G. L. Nicolson. The Fluid Mosaic Model of the Structure of Cell Membranes. *Source: Science, New Series*, 175(4023):720–731, 1972.

[251] L. D. Frye and M. Edidin. The rapid intermixing of cell surface antigens after formation of mouse-human heterokaryons. 7(3):1–9.

[252] D. M. Engelman. Membranes are more mosaic than fluid. *Nature*, 438(7068):578–580, dec 2005.

[253] J. F. Danielli and H. Davson. A contribution to the theory of permeability of thin films. *Journal of Cellular and Comparative Physiology*, 5(4):495–508, feb 1935.

[254] G. M. Cooper. *The cell : a molecular approach.* ASM Press, 1997. ISBN 0878931198.

[255] G. M. Cooper. Cell Membranes. 2000.

[256] R. Brenner. Effect of unsaturated acids on membrane structure and enzyme kinetics. *Progress in Lipid Research*, 23 (2):69–96, 1984.

[257] E. Ikonen. Cellular cholesterol trafficking and compartmentalization. *Nature Reviews Molecular Cell Biology*, 9(2): 125–138, feb 2008.

[258] J. Huang and G. W. Feigenson. A microscopic interaction model of maximum solubility of cholesterol in lipid bilayers. *Biophysical journal*, 76(4):2142–57, apr 1999.

[259] H. M. McConnell and A. Radhakrishnan. Condensed complexes of cholesterol and phospholipids. *Biochimica et Biophysica Acta (BBA) - Biomembranes*, 1610(2):159–173, mar 2003.

[260] G. van Meer, D. R. Voelker, and G. W. Feigenson. Membrane lipids: where they are and how they behave. *Nature Reviews Molecular Cell Biology*, 9(2):112–124, feb 2008.

[261] E. Boekema, B. Hankamer, D. Bald, J. Kruip, J. Nield, A. Boonstra, J. Barber, and M. Rögner. Supramolecular structure of the photosystem II complex from green plants and cyanobacteria. *Proc Natl Acad Sci U S A*, 92(1): 175–179, 1995.

[262] L. Seganti, F. Superti, P. Mastromarino, L. Sinibaldi, and N. Orsi. Role of carbohydrates in cell membrane receptors for vesicular stomatitis virus. *Bollettino dell'Istituto sieroterapico milanese*, 61(4):294–9, 1982.

[263] C. A. Day, L. J. Kraft, M. Kang, and A. K. Kenworthy. Analysis of protein and lipid dynamics using confocal fluorescence recovery after photobleaching (FRAP). *Current protocols in cytometry*, Chapter 2:Unit2.19, oct 2012.

[264] J. M. Berg, J. L. Tymoczko, and L. Stryer. Lipids and Many Membrane Proteins Diffuse Rapidly in the Plane of the Membrane. In J. M. Berg, J. L. Tymoczko, and L. Stryer, editors, *Biochemistry, Fifth Edition*, chapter 12.6. W. H. Freeman, New-york, 2002. ISBN 10: 0-7167-3051-0.

[265] S. Ladha, A. R. Mackie, L. J. Harvey, D. C. Clark, E. J. Lea, M. Brullemans, and H. Duclohier. Lateral diffusion in planar lipid bilayers: a fluorescence recovery after photobleaching investigation of its modulation by lipid composition, cholesterol, or alamethicin content and divalent cations. *Biophysical journal*, 71(3):1364–73, sep 1996.

[266] F. Pincet, V. Adrien, R. Yang, J. Delacotte, J. E. Rothman, W. Urbach, and D. Tareste. FRAP to Characterize Molecular Diffusion and Interaction in Various Membrane Environments. *PloS one*, 11(7):e0158457, 2016.

[267] R. J. Cherry. Rotational and lateral diffusion of membrane proteins. *Biochimica et Biophysica Acta (BBA) - Reviews on Biomembranes*, 559(4):289–327, dec 1979.

[268] M. J. Janiak, D. M. Small, and G. G. Shipley. Temperature and compositional dependence of the structure of hydrated dimyristoyl lecithin. *The Journal of biological chemistry*, 254(13):6068–78, jul 1979.

[269] M. Eeman and M. Deleu. From biological membranes to biomimetic model membranes. *Biotechnology, Agronomy, Society and Environment*, 14(4), 2010.

[270] A. J. Laude and I. A. Prior. Plasma membrane microdomains: Organization, function and trafficking (Review). *Molecular Membrane Biology*, 21(3):193–205, jan 2004.

[271] M. L. Kraft. Plasma membrane organization and function: moving past lipid rafts. *Molecular biology of the cell*, 24 (18):2765–8, sep 2013.

[272] R. M. Steinman, I. S. Mellman, W. A. Muller, and Z. A. Cohn. Endocytosis and the recycling of plasma membrane. *The Journal of cell biology*, 96(1):1–27, jan 1983.

[273] M. Edidin. Lipids on the frontier: a century of cell-membrane bilayers. *Nature Reviews Molecular Cell Biology*, 4(5): 414–418, may 2003.

[274] P. Janmey and P. Kinnunen. Biophysical properties of lipids and dynamic membranes. *Trends in Cell Biology*, 16 (10):538–546, oct 2006.

[275] J. A. F. Op den Kamp. Lipid Asymmetry in Membranes. *Annual Review of Biochemistry*, 48(1):47–71, jun 1979.

[276] H. T. McMahon and J. L. Gallop. Membrane curvature and mechanisms of dynamic cell membrane remodelling. *Nature*, 438(7068):590–6, dec 2005.

[277] J. McCormack and R. Denton. The role of Ca2+ ions in the regulation of intramitochondrial metabolism and energy production in rat heart. *Molecular and Cellular Biochemistry*, 89(2):121–125, sep 1989.

[278] F. Sachs. Mechanical transduction by membrane ion channels: a mini review. *Molecular and Cellular Biochemistry*, 104(1-2):57–60, 1991.

[279] Z. L. Sun, J. C. Wataha, and C. T. Hanks. Effects of metal ions on osteoblast-like cell metabolism and differentiation. *Journal of Biomedical Materials Research*, 34(1):29–37, jan 1997.

[280] Y. Kurachi and A. North. Ion channels: their structure, function and control - an overview. *The Journal of Physiology*, 554(2):245–247, jan 2004.

[281] D. J. Muller, N. Wu, and K. Palczewski. Vertebrate Membrane Proteins: Structure, Function, and Insights from Biophysical Approaches. *Pharmacological Reviews*, 60(1):43–78, mar 2008.

[282] A. Y. Cheung and S. C. de Vries. Membrane trafficking: intracellular highways and country roads. *Plant physiology*, 147(4):1451–3, aug 2008.

[283] L.-G. Wu, E. Hamid, W. Shin, and H.-C. Chiang. Exocytosis and Endocytosis: Modes, Functions, and Coupling Mechanisms. *Annual Review of Physiology*, 76(1):301–331, feb 2014.

[284] E. Shechter. *Biochimie et biophysique des membranes: aspects structuraux et fonctionnels*. 2004.

[285] J. A. Hickman. Apoptosis induced by anticancer drugs. *Cancer and Metastasis Review*, 11(2):121–139, sep 1992.

[286] M. I. Simon, M. P. Strathmann, and N. Gautam. Diversity of G proteins in signal transduction. *Science (New York, N.Y.)*, 252(5007):802–8, may 1991.

[287] P. van der Geer, T. Hunter, and R. A. Lindberg. Receptor Protein-Tyrosine Kinases and Their Signal Transduction Pathways. *Annual Review of Cell Biology*, 10(1):251–337, nov 1994.

[288] K. Simons and D. Toomre. Lipid rafts and signal transduction. *Nature Reviews Molecular Cell Biology*, 1(1):31–39, oct 2000.

[289] E. J. Luna and A. L. Hitt. Cytoskeleton–plasma membrane interactions. *Science (New York, N.Y.)*, 258(5084): 955–64, nov 1992.

[290] S. H. Wright. Generation of resting membrane potential. *AJP: Advances in Physiology Education*, 28(4):139–142, dec 2004.

[291] M. A. Crepalde, A. C. Faria-Campos, and S. V. Campos. Modeling and analysis of cell membrane systems with probabilistic model checking. *BMC Genomics*, 12(Suppl 4):S14, 2011.

[292] B. P. Bean. The action potential in mammalian central neurons. *Nature Reviews Neuroscience*, 8(6):451–465, jun 2007.

[293] S. Sundelacruz, M. Levin, and D. L. Kaplan. Role of Membrane Potential in the Regulation of Cell Proliferation and Differentiation. *Stem Cell Reviews and Reports*, 5(3):231–246, sep 2009.

[294] L. Paterson, B. Agate, M. Comrie, R. Ferguson, T. K. Lake, J. E. Morris, A. E. Carruthers, C. T. A. Brown, W. Sibbett, P. E. Bryant, F. Gunn-Moore, A. C. Riches, and K. Dholakia. Photoporation and cell transfection using a violet diode laser. *Optics Express*, 13(2):595, 2005.

[295] K. Rhodes, I. Clark, M. Zatcoff, T. Eustaquio, K. L. Hoyte, and M. R. Koller. Cellular Laserfection. *Methods in Cell Biology*, 82:309–333, 2007.

[296] A. Bouakaz, A. Zeghimi, and A. A. Doinikov. Sonoporation: Concept and Mechanisms. pages 175–189. Springer International Publishing, 2016.

[297] D. L. Miller, S. V. Pislaru, and J. F. Greenleaf. Sonoporation: Mechanical DNA Delivery by Ultrasonic Cavitation. *Somatic Cell and Molecular Genetics*, 27(1/6):115–134, 2002.

[298] E. F. Fynan, R. G. Webster, D. H. Fuller, J. R. Haynes, J. C. Santoro, and H. L. Robinson. DNA vaccines: protective immunizations by parenteral, mucosal, and gene-gun inoculations. *Proceedings of the National Academy of Sciences of the United States of America*, 90(24):11478–82, dec 1993.

[299] M. Uchida, X. W. Li, P. Mertens, and H. O. Alpar. Transfection by particle bombardment: Delivery of plasmid DNA into mammalian cells using gene gun. *Biochimica et Biophysica Acta (BBA) - General Subjects*, 1790(8):754–764, 2009.

[300] C. Plank, O. Zelphati, and O. Mykhaylyk. Magnetically enhanced nucleic acid delivery. Ten years of magnetofection—Progress and prospects. *Advanced Drug Delivery Reviews*, 63(14):1300–1331, 2011.

[301] F. Scherer, M. Anton, U. Schillinger, J. Henke, C. Bergemann, A. Krü Ger, B. Gänsbacher, and C. Plank. Magnetofection: enhancing and targeting gene delivery by magnetic force in vitro and in vivo. *Gene Therapy*, 9:102–109, 2002.

[302] F. Geinguenaud, E. Guenin, Y. Lalatonne, and L. Motte. Vectorization of Nucleic Acids for Therapeutic Approach: Tutorial Review. *ACS Chemical Biology*, 11(5):1180–1191, may 2016.

[303] R. Stampfli. Reversible electrical breakdown of the excitable membrane of a ranvier node. *Ann. Acad. Brasil Cien.*, 30:57–63, 1958.

[304] A. Sale and W. Hamilton. Effects of high electric fields on microorganisms. I. Killing of bacteria and yeasts. *Biochimica et Biophysica Acta (BBA) - General Subjects*, 148(3):781–788, dec 1967.

[305] W. Hamilton and A. Sale. Effects of high electric fields on microorganisms. II. Mechanism of action of the lethal effect. *Biochimica et Biophysica Acta (BBA) - General Subjects*, 148(3):789–800, dec 1967.

[306] Sale, A and W. Hamilton. Effects of high electric fields on microorganisms. III. Lysis of erythrocytes and protoplasts. *iochimica et Biophysica Acta (BBA) - General Subjects*, 163(1):37–43, aug 1968.

[307] E. Neumann and K. Rosenheck. Permeability changes induced by electric impulses in vesicular membranes. *The Journal of Membrane Biology*, 10(1):279–290, dec 1972.

[308] K. Kinosita and T. Y. Tsong. Formation and resealing of pores of controlled sizes in human erythrocyte membrane. *Nature*, 268(5619):438–41, aug 1977.

[309] E. Neumann, M. Schaefer-Ridder, Y. Wang, and P. H. Hofschneider. Gene transfer into mouse lyoma cells by electroporation in high electric fields. *The EMBO journal*, 1(7):841–5, 1982.

[310] T.-K. Wong and E. Neumann. Electric field mediated gene transfer. *Biochemical and Biophysical Research Communications*, 107(2):584–587, jul 1982.

[311] T. Y. Tsong. Electroporation of cell membranes. *Biophysical journal*, 60(2):297–306, aug 1991.

[312] J. Teissié, N. Eynard, B. Gabriel, and M. Rols. Electropermeabilization of cell membranes. *Advanced Drug Delivery Reviews*, 35(1):3–19, 1999.

[313] U. Zimmermann, U. Friedrich, H. Mussauer, P. Gessner, K. Hamel, and V. Sukhorukov. Electromanipulation of mammalian cells: fundamentals and application. *IEEE Transactions on Plasma Science*, 28(1):72–82, 2000.

[314] C. Chen, S. W. Smye, M. P. Robinson, and J. A. Evans. Membrane electroporation theories: a review. *Medical & Biological Engineering & Computing*, 44(1-2):5–14, mar 2006.

[315] H. P. Schwan. Electrical properties of tissue and cell suspensions. *Advances in biological and medical physics*, 5: 147–209, 1957.

[316] T. Kotnik, F. Bobanović, and D. Miklavcic. Sensitivity of transmembrane voltage induced by applied electric fields—A theoretical analysis. *Bioelectrochemistry and Bioenergetics*, 43(2):285–291, aug 1997.

[317] H. Pauly and H. P. Schwan. Impendance of a suspension of ball-shaped particles with a shell; a model for the dielectric behavior of cell suspensions and protein solutions]. *Zeitschrift fur Naturforschung. Teil B: Chemie, Biochemie, Biophysik, Biologie*, 14B(2):125–31, feb 1959.

[318] B. Alberts, D. Bray, J. Lewis, M. Raff, K. Roberts, J. D. Waston, M. Minskowski, and G. Rolland. Biologie moléculaire de la cellule.

[319] K. Kinosita, I. Ashikawa, N. Saita, H. Yoshimura, H. Itoh, K. Nagayama, A. Ikegami, and A. Ikegami. Electroporation of cell membrane visualized under a pulsed-laser fluorescence microscope. *Biophysical journal*, 53(6):1015–9, jun 1988.

[320] T. Kotnik, G. Pucihar, and D. Miklavcic. Induced transmembrane voltage and its correlation with electroporation-mediated molecular transport. *The Journal of membrane biology*, 236(1):3–13, jul 2010.

[321] J. Teissié and M. P. Rols. An experimental evaluation of the critical potential difference inducing cell membrane electropermeabilization. *Biophysical journal*, 65(1):409–13, jul 1993.

[322] J. Teissie and T. Y. Tsong. Electric field induced transient pores in phospholipid bilayer vesicles. *Biochemistry*, 20 (6):1548–54, mar 1981.

[323] R. O'Neill and L. Tung. Cell-attached patch clamp study of the electropermeabilization of amphibian cardiac cells. *Biophysical Journal*, 59(5):1028–1039, may 1991.

[324] L. H. Wegner, B. Flickinger, C. Eing, T. Berghöfer, P. Hohenberger, W. Frey, and P. Nick. A patch clamp study on the electro-permeabilization of higher plant cells: Supra-physiological voltages induce a high-conductance, K+ selective state of the plasma membrane. *Biochimica et Biophysica Acta (BBA) - Biomembranes*, 1808(6):1728–1736, jun 2011.

[325] J. C. Weaver and Y. Chizmadzhev. Theory of electroporation: A review. *Bioelectrochemistry and Bioenergetics*, 41 (2):135–160, dec 1996.

[326] Z. Vasilkoski, A. T. Esser, T. R. Gowrishankar, and J. C. Weaver. Membrane electroporation: The absolute rate equation and nanosecond time scale pore creation. *Physical Review E*, 74(2):021904, aug 2006.

[327] M. Tarek. Membrane electroporation: a molecular dynamics simulation. *Biophysical journal*, 88(6):4045–4053, 2005.

[328] P. Vernier, Y. Sun, L. Marcu, C. M. Craft, and M. A. Gundersen. Nanosecond pulsed electric fields perturb membrane phospholipids in T lymphoblasts. *FEBS Letters*, 572(1-3):103–108, aug 2004.

[329] M. J. Ziegler and P. T. Vernier. Interface Water Dynamics and Porating Electric Fields for Phospholipid Bilayers. *The Journal of Physical Chemistry B*, 112(43):13588–13596, oct 2008.

[330] Z. A. Levine and P. T. Vernier. Life Cycle of an Electropore: Field-Dependent and Field-Independent Steps in Pore Creation and Annihilation. *The Journal of Membrane Biology*, 236(1):27–36, jul 2010.

[331] L. Delemotte and M. Tarek. Molecular Dynamics Simulations of Lipid Membrane Electroporation. *The Journal of Membrane Biology*, 245(9):531–543, sep 2012.

[332] P. Marracino, F. Castellani, P. T. Vernier, M. Liberti, and F. Apollonio. Geometrical Characterization of an Electropore from Water Positional Fluctuations. *The Journal of Membrane Biology*, pages 1–9, jul 2016.

[333] M. Tokman, J. H. Lee, Z. a. Levine, M.-C. C. Ho, M. E. Colvin, and P. T. Vernier. Electric Field-Driven Water Dipoles: Nanoscale Architecture of Electroporation. *PLoS ONE*, 8(4):e61111, apr 2013.

[334] P. Marracino, M. Liberti, G. D'Inzeo, and F. Apollonio. Water response to intense electric fields: A molecular dynamics study. *Bioelectromagnetics*, 36(5):377–385, may 2015.

[335] M. Casciola, D. Bonhenry, M. Liberti, F. Apollonio, and M. Tarek. A Molecular Dynamic Study of Cholesterol Rich Lipid Membranes: Comparison of Electroporation Protocols. *Bioelectrochemistry*, 2014.

[336] M. Bloom, E. Evans, and O. G. Mouritsen. Physical properties of the fluid lipid-bilayer component of cell membranes: a perspective. *Quarterly reviews of biophysics*, 24(3):293–397, aug 1991.

[337] D. A. Brown and E. London. Structure and Function of Sphingolipid- and Cholesterol-rich Membrane Rafts. *Journal of Biological Chemistry*, 275(23):17221–17224, jun 2000.

[338] R. Dimova, S. Aranda, N. Bezlyepkina, V. Nikolov, K. A. Riske, and R. Lipowsky. A practical guide to giant vesicles. Probing the membrane nanoregime via optical microscopy. *Journal of Physics: Condensed Matter*, 18(28): S1151–S1176, jul 2006.

[339] Y.-H. M. Chan and S. G. Boxer. Model membrane systems and their applications. *Current Opinion in Chemical Biology*, 11(6):581–587, 2007.

[340] K. A. Riske and R. Dimova. Electro-deformation and poration of giant vesicles viewed with high temporal resolution. *Biophysical journal*, 88(2):1143–1155, feb 2005.

[341] T. Portet, C. Mauroy, V. Démery, T. Houles, J.-M. Escoffre, D. S. Dean, and M.-P. Rols. Destabilizing Giant Vesicles with Electric Fields: An Overview of Current Applications. *The Journal of Membrane Biology*, 245(9):555–564, sep 2012.

[342] T. Portet, F. Camps i Febrer, J.-M. Escoffre, C. Favard, M.-P. Rols, and D. S. Dean. Visualization of Membrane Loss during the Shrinkage of Giant Vesicles under Electropulsation. *Biophysical Journal*, 96(10):4109–4121, 2009.

[343] M. Breton, L. Delemotte, A. Silve, L. M. Mir, and M. Tarek. Transport of siRNA through lipid membranes driven by nanosecond electric pulses: an experimental and computational study. *Journal of the American Chemical Society*, 134(34):13938–41, aug 2012.

[344] A. Silve. *Nouveaux dispositifs pour l'application contrôlée d'impulsions électriques nanosecondes et pour la détection de leurs effets sur les cellules . Nouveaux résultats et hypothèses sur les paramètres contrôlant l'électroperméabilisation des cellules biologiqu.* PhD thesis, University Paris-Sud, 2012.

[345] B. Gabriel and J. Teissié. Generation of reactive-oxygen species induced by electropermeabilization of Chinese hamster ovary cells and their consequence on cell viability. *European journal of biochemistry / FEBS*, 223(1):25–33, jul 1994.

[346] O. N. Pakhomova, V. A. Khorokhorina, A. M. Bowman, R. Rodaitė-Riševičienė, G. Saulis, S. Xiao, and A. G. Pakhomov. Oxidative effects of nanosecond pulsed electric field exposure in cells and cell-free media. *Archives of Biochemistry and Biophysics*, 527(1):55–64, nov 2012.

[347] R. Mittler. Oxidative stress, antioxidants and stress tolerance. *Trends in Plant Science*, 7(9):405–410, 2002.

[348] K. Apel and H. Hirt. Reactive Oxygen Species: Metabolism, Oxidative Stress, and Signal Transduction. *Annual Review of Plant Biology*, 55(1):373–399, jun 2004.

[349] E. E. Farmer and M. J. Mueller. ROS-Mediated Lipid Peroxidation and RES-Activated Signaling. *Annual Review of Plant Biology*, 64(1):429–450, apr 2013.

[350] J. M. Gutteridge. Lipid peroxidation and antioxidants as biomarkers of tissue damage. *Clinical chemistry*, 41(12 Pt 2):1819–28, dec 1995.

[351] S. Leutner, A. Eckert, and W. E. Müller. ROS generation, lipid peroxidation and antioxidant enzyme activities in the aging brain. *Journal of Neural Transmission*, 108(8):955–967, sep 2001.

[352] S. Briganti and M. Picardo. Antioxidant activity, lipid peroxidation and skin diseases. What's new. *Journal of the European Academy of Dermatology and Venereology*, 17(6):663–669, nov 2003.

[353] N. Mimica-Duki, N. Simin, E. Svirev, D. Ori, I. Beara, M. Lesjak, and B. Boi. The Effect of Plant Secondary Metabolites on Lipid Peroxidation and Eicosanoid Pathway. In *Lipid Peroxidation*. InTech, aug 2012.

[354] M. Bachar, P. Brunelle, D. P. Tieleman, and A. Rauk. Molecular dynamics simulation of a polyunsaturated lipid bilayer susceptible to lipid peroxidation. *Journal of Physical Chemistry B*, 108(22):7170–7179, 2004.

[355] R. M. Cordeiro. Reactive oxygen species at phospholipid bilayers: Distribution, mobility and permeation. *Biochimica et Biophysica Acta - Biomembranes*, 1838(1 PARTB):438–444, 2014.

[356] J. Wong-Ekkabut, Z. Xu, W. Triampo, I.-M. Tang, D. P. Tieleman, and L. Monticelli. Effect of lipid peroxidation on the properties of lipid bilayers: a molecular dynamics study. *Biophysical Journal*, 93(12):4225–4236, 2007.

[357] J. Van der Paal, E. C. Neyts, C. C. W. Verlackt, and A. Bogaerts. Effect of lipid peroxidation on membrane permeability of cancer and normal cells subjected to oxidative stress. *Chem. Sci.*, 7(1):489–498, 2016.

[358] J. Garrec, A. Monari, X. Assfeld, L. M. Mir, and M. Tarek. Lipid Peroxidation in Membranes: The Peroxyl Radical Does Not "Float". *The Journal of Physical Chemistry Letters*, 5(10):1653–1658, may 2014.

[359] P. T. Vernier, Z. a. Levine, Y. H. Wu, V. Joubert, M. J. Ziegler, L. M. Mir, and D. P. Tieleman. Electroporating fields target oxidatively damaged areas in the cell membrane. *PLoS ONE*, 4(11), 2009.

[360] M. Breton and L. M. Mir. A chemical study of the interaction of electric pulses with a cell model : giant unilamellar vesicles. In *1st World Congress on Electroporation and Pulsed Electric Fields in Biology, Medicine and Food & Environment Technologies*, page 4, 2015.

[361] P. Bonnafous, M.-C. Vernhes, J. Teissié, and B. Gabriel. No Title. 1461(1), dec 1999.

[362] M. Breton, A. Silve, and L. M. Mir. Cell electropulsation: the Membrane Impermeability Rupture Model Reconciles Electroporation and Electropermeabilization. *Submitted*, 2017.

[363] A. Agarwal, I. Zudans, E. A. Weber, J. Olofsson, O. Orwar, and S. G. Weber. Effect of cell size and shape on single-cell electroporation. *Analytical chemistry*, 79(10):3589–96, may 2007.

[364] G. Pucihar, D. Miklavčič, and T. Kotnik. A Time-Dependent Numerical Model of Transmembrane Voltage Inducement and Electroporation of Irregularly Shaped Cells. *IEEE TRANSACTIONS ON BIOMEDICAL ENGINEERING*, 56 (5), 2009.

[365] A. Denzi, C. Merla, C. Palego, F. Apollonio, J. C. M. Hwang, and M. Liberti. Single Cell Microdosimetric Studies Comparing Ideal and Measured Nanosecond Pulsed Electric Fields. In *2013 IEEE MTT-S International Microwave Symposium Digest (MTT)*, pages 1–4. IEEE, jun 2013. ISBN 978-1-4673-6176-7.

[366] A. Denzi, C. Merla, P. Camilleri, A. Paffi, G. D'Inzeo, F. Apollonio, and M. Liberti. Microdosimetric Study for Nanosecond Pulsed Electric Fields on a Cell Circuit Model with Nucleus. *The Journal of Membrane Biology*, 246 (10):761–767, oct 2013.

[367] R. Susil, D. Šemrov, and D. Miklavčič. Electric Field-Induced Transmembrane Potential Depends on Cell Density and Organization. *Electro- and Magnetobiology*, 17(3):391–399, jan 1998.

[368] B. E. Henslee, A. Morss, X. Hu, G. P. Lafyatis, and L. James Lee. Cell-cell proximity effects in multi-cell electroporation. *Biomicrofluidics*, 8(5):052002, sep 2014.

[369] C. S. Djuzenova, V. L. Sukhorukov, G. Klöck, W. M. Arnold, and U. Zimmermann. Effect of electric field pulses on the viability and on the membrane-bound immunoglobulins of LPS-activated murine B-lymphocytes: Correlation with the cell cycle. *Cytometry*, 15(1):35–45, jan 1994.

[370] G. Pucihar, T. Kotnik, J. Teissié, and D. Miklavčič. Electropermeabilization of dense cell suspensions. *European Biophysics Journal*, 36(3):173–185, mar 2007.

[371] M. Golzio, M.-P. Mora, C. Raynaud, C. Delteil, J. Teissié, and M.-P. Rols. Control by Osmotic Pressure of Voltage-Induced Permeabilization and Gene Transfer in Mammalian Cells. *Biophysical Journal*, 74(6):3015–3022, 1998.

[372] S. Romeo, Y.-H. Wu, Z. A. Levine, M. A. Gundersen, and P. T. Vernier. Water influx and cell swelling after nanosecond electropermeabilization. *Biochimica et Biophysica Acta (BBA) - Biomembranes*, 1828(8):1715–1722, 2013.

[373] G. L. Craviso, C. Fisher, I. Chatterjee, and P. Thomas Vernier. Adrenal chromaffin cells do not swell when exposed to nanosecond electric pulses. *Bioelectrochemistry*, 103:98–102, 2015.

[374] M. P. Rols and J. Teissié. Experimental evidence for the involvement of the cytoskeleton in mammalian cell electropermeabilization. *Biochimica et biophysica acta*, 1111(1):45–50, oct 1992.

[375] C. Kanthou, S. Kranjc, G. Sersa, G. Tozer, A. Zupanic, and M. Cemazar. The endothelial cytoskeleton as a target of electroporation-based therapies. *Molecular cancer therapeutics*, 5(12):3145–52, dec 2006.

[376] L. Carr, S. M. Bardet, R. C. Burke, D. Arnaud-Cormos, P. Leveque, and R. P. O'Connor. Calcium-independent disruption of microtubule dynamics by nanosecond pulsed electric fields in U87 human glioblastoma cells. *Scientific Reports*, 7:41267, jan 2017.

[377] H. G. Hansma and J. H. Hoh. Biomolecular Imaging with the Atomic Force Microscope. *Annual Review of Biophysics and Biomolecular Structure*, 23(1):115–140, jun 1994.

[378] D. J. Müller and Y. F. Dufrêne. Atomic force microscopy: a nanoscopic window on the cell surface. *Trends in Cell Biology*, 21(8):461–469, 2011.

[379] L. Chopinet, C. Roduit, M. P. Rols, and E. Dague. Destabilization induced by electropermeabilization analyzed by atomic force microscopy. *Biochimica et Biophysica Acta - Biomembranes*, 1828(9):2223–2229, 2013.

[380] P. L. McNeil and R. A. Steinhardt. Plasma Membrane Disruption: Repair, Prevention, Adaptation. *Annual Review of Cell and Developmental Biology*, 19(1):697–731, nov 2003.

[381] P. L. McNeil and T. Kirchhausen. An emergency response team for membrane repair. *Nature Reviews Molecular Cell Biology*, 6(6):499–505, jun 2005.

[382] R. A. Steinhardt. The Mechanisms of Cell Membrane Repair: A Tutorial Guide to Key Experiments. *Annals of the New York Academy of Sciences*, 1066(1):152–165, dec 2005.

[383] A. Joaquina, A. J. Jimenez, P. Maiuri, J. Lafaurie-janvore, S. Divoux, and M. Piel. ESCRT Machinery Is Required for Plasma Membrane Repair.pdf. 2014.

[384] S. K. Frandsen, A. K. McNeil, I. Novak, P. L. McNeil, and J. Gehl. Difference in Membrane Repair Capacity Between Cancer Cell Lines and a Normal Cell Line. *The Journal of Membrane Biology*, 249(4):569–576, aug 2016.

[385] A. Silve, N. Dorval, T. Schmid, L. L. M. Mir, and B. Attal-Tretout. A wide-field arrangement for single-shot CARS imaging of living cells. *Journal of Raman Spectroscopy*, 43(5):644–650, may 2012.

[386] G. Pucihar, T. Kotnik, D. Miklavčič, and J. Teissié. Kinetics of Transmembrane Transport of Small Molecules into Electropermeabilized Cells. *Biophysical Journal*, 95(6):2837–2848, 2008.

[387] M.-P. Rols and J. Teissié. Electropermeabilization of Mammalian Cells to Macromolecules: Control by Pulse Duration. *Biophysical journal*, 75(3):1415–1423, sep 1998.

[388] K. Schwister and B. Deuticke. Formation and properties of aqueous leaks induced in human erythrocytes by electrical breakdown. *Biochimica et biophysica acta*, 816(2):332–48, jun 1985.

[389] H. Liang, W. J. Purucker, D. A. Stenger, R. T. Kubiniec, and S. W. Hui. Uptake of fluorescence-labeled dextrans by 10T 1/2 fibroblasts following permeation by rectangular and exponential-decay electric field pulses. *BioTechniques*, 6(6):550–2, 554, 556–8, jun 1988.

[390] M. Rols and J. Teissié. Ionic-strength modulation of electrically induced permeabilization and associated fusion of mammalian cells. *European Journal of Biochemistry*, 179(1):109–115, jan 1989.

[391] M.-C. Vernhes, P.-A. Cabanes, and J. Teissie. Chinese hamster ovary cells sensitivity to localized electrical stresses. *Bioelectrochemistry and Bioenergetics*, 48(1):17–25, 1999.

[392] A. Silve, A. Guimerà Brunet, B. Al-Sakere, A. Ivorra, and L. Mir. Comparison of the effects of the repetition rate between microsecond and nanosecond pulses: Electropermeabilization-induced electro-desensitization? *Biochimica et Biophysica Acta (BBA) - General Subjects*, 1840(7):2139–2151, 2014.

[393] O. N. Pakhomova, B. W. Gregory, V. A. Khorokhorina, A. M. Bowman, S. Xiao, and A. G. Pakhomov. Electroporation-induced electrosensitization. *PloS one*, 6(2):e17100, 2011.

[394] O. N. Pakhomova, B. W. Gregory, and A. G. Pakhomov. Facilitation of electroporative drug uptake and cell killing by electrosensitization. *Journal of cellular and molecular medicine*, 17(1):154–9, jan 2013.

[395] J. Dermol, O. N. Pakhomova, S. Xiao, A. G. Pakhomov, and D. Miklavčič. Cell Sensitization is Induced by a Wide Range of Permeabilizing Electric Fields. pages 163–166. Springer Singapore, 2016.

[396] G. Pucihar, L. Mir, and D. Miklavčič. The effect of pulse repetition frequency on the uptake into electropermeabilized cells in vitro with possible applications in electrochemotherapy. *Bioelectrochemistry*, 57(2):167–172, 2002.

[397] T. Kotnik, L. M. Mir, K. Flisar, M. Puc, and D. Miklavčič. Cell membrane electropermeabilization by symmetrical bipolar rectangular pulses: Part I. Increased efficiency of permeabilization. *Bioelectrochemistry*, 54(1):83–90, 2001.

[398] T. Kotnik, D. Miklavčič, and L. M. Mir. Cell membrane electropermeabilization by symmetrical bipolar rectangular pulses: Part II. Reduced electrolytic contamination. *Bioelectrochemistry*, 54(1):91–95, 2001.

[399] C. S. Djuzenova, U. Zimmermann, H. Frank, V. L. Sukhorukov, E. Richter, and G. Fuhr. Effect of medium conductivity and composition on the uptake of propidium iodide into electropermeabilized myeloma cells. *Biochimica et biophysica acta*, 1284(2):143–52, oct 1996.

[400] V. L. Sukhorukov, H. Mussauer, and U. Zimmermann. The effect of electrical deformation forces on the electropermeabilization of erythrocyte membranes in low- and high-conductivity media. *The Journal of membrane biology*, 163 (3):235–45, jun 1998.

[401] G. Pucihar, T. Kotnik, M. Kanduser, and D. Miklavcic. The influence of medium conductivity on electropermeabilization and survival of cells in vitro. *Bioelectrochemistry (Amsterdam, Netherlands)*, 54(2):107–15, nov 2001.

[402] Y. Antov, A. Barbul, H. Mantsur, and R. Korenstein. Electroendocytosis: exposure of cells to pulsed low electric fields enhances adsorption and uptake of macromolecules. *Biophysical journal*, 88(3):2206–23, mar 2005.

[403] E. Ferreira, E. Potier, D. Logeart-Avramoglou, S. Salomskaite-Davalgiene, L. M. Mir, and H. Petite. Optimization of a gene electrotransfer method for mesenchymal stem cell transfection. *Gene therapy*, 15(7):537–44, apr 2008.

[404] A. Ivorra, J. Villemejane, and L. M. Mir. Electrical modeling of the influence of medium conductivity on electroporation. *Physical Chemistry Chemical Physics*, 12(34):10055, 2010.

[405] A. Silve, I. Leray, C. Poignard, and L. M. Mir. Impact of external medium conductivity on cell membrane electropermeabilization by microsecond and nanosecond electric pulses. *Scientific Reports*, 6:19957, feb 2016.

[406] B. J. Wards and D. M. Collins. Electroporation at elevated temperatures substantially improves transformation efficiency of slow-growing mycobacteria. *FEMS Microbiology Letters*, 145(1), 1996.

[407] M. Knaduser, M. Sentjurc, and D. Miklavcic. Cell membrane fluidity at different temperatures in relation to electroporation effectiveness of cell line V79. In *11th Mediterranean Conference on Medical and Biomedical Engineering and Computing 2007*, pages 570–573. Springer Berlin Heidelberg, Berlin, Heidelberg, 2007.

[408] N. I. Lebovka, I. Praporscic, S. Ghnimi, and E. Vorobiev. Temperature enhanced electroporation under the pulsed electric field treatment of food tissue. *Journal of Food Engineering*, 69(2):177–184, 2005.

[409] M. B. Lande, J. M. Donovan, and M. L. Zeidel. The relationship between membrane fluidity and permeabilities to water, solutes, ammonia, and protons. *The Journal of General Physiology*, 106(1), 1995.

[410] M. P. Rols, C. Delteil, G. Serin, and J. Teissié. Temperature effects on electrotransfection of mammalian cells. *Nucleic Acids Research*, 22(3):540, 1994.

[411] K. S. Cole. PERMEABILITY AND IMPERMEABILITY OF CELL MEMBRANES FOR IONS. *Cold Spring Harbor Symposia on Quantitative Biology*, 8(0):110–122, jan 1940.

[412] K. Wang, Y. Zhao, D. Chen, B. Fan, Y. Lu, L. Chen, R. Long, J. Wang, and J. Chen. Specific membrane capacitance, cytoplasm conductivity and instantaneous Young's modulus of single tumour cells. *Scientific Data*, 4, 2017.

[413] T. Kotnik and D. Miklavcic. Second-order model of membrane electric field induced by alternating external electric fields. *IEEE Transactions on Biomedical Engineering*, 47(8):1074–1081, 2000.

[414] T. García-Sánchez, A. Azan, I. Leray, J. Rosell-Ferrer, R. Bragós, and L. M. Mir. Interpulse multifrequency electrical impedance measurements during electroporation of adherent differentiated myotubes. *Bioelectrochemistry (Amsterdam, Netherlands)*, 105:123–35, oct 2015.

[415] A. Ivorra, B. Al-Sakere, B. Rubinsky, and L. M. Mir. In vivo electrical conductivity measurements during and after tumor electroporation: conductivity changes reflect the treatment outcome. *Physics in Medicine and Biology*, 54(19): 5949–5963, oct 2009.

[416] K. H. Schoenbach, B. Y. Hargrave, R. P. Joshi, J. F. Kolb, R. Nuccitelli, E. Stephen, C. J. Osgood, A. G. Pakhomov, M. W. Stacey, J. R. Swanson, J. A. White, S. Xiao, J. Zhang, S. J. Beebe, P. F. Blackmore, and E. Stephen Buescher. Bioelectric Effects of Intense Nanosecond Pulses. *Bioelectrics Publications*, 2007.

[417] M. Behrend, A. Kuthi, Xianyue Gu, P. Vernier, L. Marcu, C. Craft, and M. Gundersen. Pulse generators for pulsed electric field exposure of biological cells and tissues. *IEEE Transactions on Dielectrics and Electrical Insulation*, 10 (5):820–825, oct 2003.

[418] A. Chaney and R. Sundararajan. Simple MOSFET-Based High-Voltage Nanosecond Pulse Circuit. *IEEE Transactions on Plasma Science*, 32(5):1919–1924, oct 2004.

[419] J. F. Kolb, S. Kono, and K. H. Schoenbach. Nanosecond pulsed electric field generators for the study of subcellular effects. *Bioelectromagnetics*, 27(3):172–87, apr 2006.

[420] M. Kenaan, S. El Amari, A. Silve, C. Merla, L. M. Mir, V. Couderc, D. Arnaud-Cormos, and P. Leveque. Characterization of a 50- Ω exposure setup for high-voltage nanosecond pulsed electric field bioexperiments. *IEEE transactions on bio-medical engineering*, 58(1):207–14, jan 2011.

[421] K. H. Schoenbach, S. J. Beebe, and E. S. Buescher. Intracellular effect of ultrashort electrical pulses. *Bioelectromagnetics*, 22(6):440–448, sep 2001.

[422] R. Sundararajan. Nanoelectroporation: a first look. *Methods in molecular biology (Clifton, N.J.)*, 423:109–28, 2008.

[423] R. Sundararajan. Nanosecond Electroporation: Another Look. *Molecular Biotechnology*, 41(1):69–82, jan 2009.

[424] L. Chopinet and M.-P. Rols. Nanosecond electric pulses: A mini-review of the present state of the art. *Bioelectrochemistry*, 2014.

[425] B. T. Napotnik, M. Reberšek, P. T. Vernier, B. Mali, and D. Miklavčič. Effects of high voltage nanosecond electric pulses on eukaryotic cells (in vitro): A systematic review. *Bioelectrochemistry (Amsterdam, Netherlands)*, 110:1–12, aug 2016.

[426] P. T. Vernier, Y. Sun, L. Marcu, S. Salemi, C. M. Craft, and M. A. Gundersen. Calcium bursts induced by nanosecond electric pulses. *Biochemical and Biophysical Research Communications*, 310(2):286–295, 2003.

[427] S. J. Beebe, J. White, P. F. Blackmore, Y. Deng, K. Somers, and K. H. Schoenbach. Diverse Effects of Nanosecond Pulsed Electric Fields on Cells and Tissues. *DNA and Cell Biology*, 22(12):785–796, dec 2003.

[428] G. L. E. Koch. The endoplasmic reticulum and calcium storage. *BioEssays*, 12(11):527–531, nov 1990.

[429] D. G. Nicholls and S. Chalmers. The Integration of Mitochondrial Calcium Transport and Storage. *Journal of Bioenergetics and Biomembranes*, 36(4):277–281, aug 2004.

[430] P. T. Vernier, Y. Sun, M.-T. Chen, M. A. Gundersen, and G. L. Craviso. Nanosecond electric pulse-induced calcium entry into chromaffin cells. 2008.

[431] P. T. Vernier. Mitochondrial membrane permeabilization with nanosecond electric pulses. In *2011 Annual International Conference of the IEEE Engineering in Medicine and Biology Society*, pages 743–745. IEEE, aug 2011. ISBN 978-1-4577-1589-1.

[432] T. B. Napotnik, Y.-H. Wu, M. A. Gundersen, D. Miklavčič, and P. T. Vernier. Nanosecond electric pulses cause mitochondrial membrane permeabilization in Jurkat cells. *Bioelectromagnetics*, 33(3):257–264, apr 2012.

[433] G. L. Craviso, S. Choe, P. Chatterjee, I. Chatterjee, and P. T. Vernier. Nanosecond electric pulses: a novel stimulus for triggering Ca2+ influx into chromaffin cells via voltage-gated Ca2+ channels. *Cellular and molecular neurobiology*, 30(8):1259–65, nov 2010.

[434] D. Beutner, T. Voets, E. Neher, and T. Moser. Calcium Dependence of Exocytosis and Endocytosis at the Cochlear Inner Hair Cell Afferent Synapse. *Neuron*, 29(3):681–690, 2001.

[435] J. K. Jaiswal, N. W. Andrews, and S. M. Simon. Membrane proximal lysosomes are the major vesicles responsible for calcium-dependent exocytosis in nonsecretory cells. *The Journal of Cell Biology*, 159(4), 2002.

[436] P. E. MacDonald, L. Eliasson, and P. Rorsman. Calcium increases endocytotic vesicle size and accelerates membrane fission in insulin-secreting INS-1 cells. *Journal of cell science*, 118(Pt 24):5911–20, dec 2005.

[437] G. L. Thompson, C. C. Roth, D. R. Dalzell, M. Kuipers, and B. L. Ibey. Calcium influx affects intracellular transport and membrane repair following nanosecond pulsed electric field exposure. *Journal of Biomedical Optics*, 19(5):055005, may 2014.

[438] M.-A. de Menorval, F. M. Andre, A. Silve, C. Dalmay, O. Français, B. Le Pioufle, and L. M. Mir. Electric pulses: a flexible tool to manipulate cytosolic calcium concentrations and generate spontaneous-like calcium oscillations in mesenchymal stem cells. *Scientific Reports*, 6:32331, aug 2016.

[439] S. Beebe, P. Fox, L. Rec, K. Somers, R. Stark, and K. Schoenbach. Nanosecond pulsed electric field (nsPEF) effects on cells and tissues: apoptosis induction and tumor growth inhibition. *IEEE Transactions on Plasma Science*, 30(1): 286–292, feb 2002.

[440] S. J. Beebe, P. M. Fox, L. J. Rec, E. L. K. Willis, and K. H. Schoenbach. Nanosecond, high-intensity pulsed electric fields induce apoptosis in human cells. *FASEB journal : official publication of the Federation of American Societies for Experimental Biology*, 17(11):1493–5, aug 2003.

[441] D. Xiao, C. Yao, H. Liu, C. Li, J. Cheng, F. Guo, and L. Tang. Irreversible electroporation and apoptosis in human liver cancer cells induced by nanosecond electric pulses. *Bioelectromagnetics*, 34(7):512–20, oct 2013.

[442] W. E. Ford, W. Ren, P. F. Blackmore, K. H. Schoenbach, and S. J. Beebe. Nanosecond pulsed electric fields stimulate apoptosis without release of pro-apoptotic factors from mitochondria in B16f10 melanoma. *Archives of biochemistry and biophysics*, 497(1-2):82–9, may 2010.

[443] W. Ren and S. J. Beebe. An apoptosis targeted stimulus with nanosecond pulsed electric fields (nsPEFs) in E4 squamous cell carcinoma. *Apoptosis : an international journal on programmed cell death*, 16(4):382–93, apr 2011.

[444] W. Ren, N. M. Sain, and S. J. Beebe. Nanosecond pulsed electric fields (nsPEFs) activate intrinsic caspase-dependent and caspase-independent cell death in Jurkat cells. *Biochemical and biophysical research communications*, 421(4): 808–12, may 2012.

[445] D. Xiao, L. Tang, C. Zeng, J. Wang, X. Luo, C. Yao, and C. Sun. Effect of actin cytoskeleton disruption on electric pulse-induced apoptosis and electroporation in tumour cells. *Cell biology international*, 35(2):99–104, feb 2011.

[446] P. T. Vernier, A. Li, L. Marcu, C. Craft, and M. Gundersen. Ultrashort pulsed electric fields induce membrane phospholipid translocation and caspase activation: differential sensitivities of Jurkat T lymphoblasts and rat Glioma C6 cells. *IEEE Transactions on Dielectrics and Electrical Insulation*, 10(5):795–809, oct 2003.

[447] P. T. Vernier, Y. Sun, L. Marcu, C. M. Craft, and M. A. Gundersen. Nanoelectropulse-Induced Phosphatidylserine Translocation. *Biophysical Journal*, 86(6):4040–4048, 2004.

[448] G. P. Tolstykh, H. T. Beier, C. C. Roth, G. L. Thompson, and B. L. Ibey. 600ns pulse electric field-induced phosphatidylinositol4,5-bisphosphate depletion. *Bioelectrochemistry*, 100:80–87, 2014.

[449] N. Chen, K. H. Schoenbach, J. F. Kolb, R. James Swanson, A. L. Garner, J. Yang, R. P. Joshi, and S. J. Beebe. Leukemic cell intracellular responses to nanosecond electric fields. *Biochemical and biophysical research communications*, 317(2):421–7, apr 2004.

[450] H. Xu, P. D. Nallathamby, and X.-H. N. Xu. Real-time imaging and tuning subcellular structures and membrane transport kinetics of single live cells at nanosecond regime. *The journal of physical chemistry. B*, 113(43):14393–404, oct 2009.

[451] M. Stacey, P. Fox, S. Buescher, and J. Kolb. Nanosecond pulsed electric field induced cytoskeleton, nuclear membrane and telomere damage adversely impact cell survival. *Bioelectrochemistry (Amsterdam, Netherlands)*, 82(2):131–134, oct 2011.

[452] P. T. Vernier, Y. Sun, and M. A. Gundersen. Nanoelectropulse-driven membrane perturbation and small molecule permeabilization. *BMC cell biology*, 7(1):37–53, jan 2006.

[453] S. S. Scarlett, J. A. White, P. F. Blackmore, K. H. Schoenbach, and J. F. Kolb. Regulation of intracellular calcium concentration by nanosecond pulsed electric fields. *Biochimica et biophysica acta*, 1788(5):1168–75, may 2009.

[454] V. Nesin, A. M. Bowman, S. Xiao, and A. G. Pakhomov. Cell permeabilization and inhibition of voltage-gated Ca(2+) and Na(+) channel currents by nanosecond pulsed electric field. *Bioelectromagnetics*, 33(5):394–404, jul 2012.

[455] A. G. Pakhomov, J. F. Kolb, J. A. White, R. P. Joshi, S. Xiao, and K. H. Schoenbach. Long-lasting plasma membrane permeabilization in mammalian cells by nanosecond pulsed electric field (nsPEF). *Bioelectromagnetics*, 28(8):655–663, dec 2007.

[456] A. M. Bowman, O. M. Nesin, O. N. Pakhomova, and A. G. Pakhomov. Analysis of plasma membrane integrity by fluorescent detection of Tl(+) uptake. *The Journal of membrane biology*, 236(1):15–26, jul 2010.

[457] B. L. Ibey, J. C. Ullery, O. N. Pakhomova, C. C. Roth, I. Semenov, H. T. Beier, M. Tarango, S. Xiao, K. H. Schoenbach, and A. G. Pakhomov. Bipolar nanosecond electric pulses are less efficient at electropermeabilization and killing cells than monopolar pulses. 2014.

[458] L. H. Ramirez, S. Orlowski, D. An, G. Bindoula, R. Dzodic, P. Ardouin, C. Bognel, J. Belehradek, J. N. Munck, and L. M. Mir. Electrochemotherapy on liver tumours in rabbits. *British journal of cancer*, 77(12):2104–11, jun 1998.

[459] G. Sersa, M. Cemazar, C. S. Parkins, and D. J. Chaplin. Tumour blood flow changes induced by application of electric pulses. *European journal of cancer (Oxford, England : 1990)*, 35(4):672–7, apr 1999.

[460] J. Gehl, T. Skovsgaard, and L. M. Mir. Vascular reactions to in vivo electroporation: characterization and consequences for drug and gene delivery. *Biochimica et biophysica acta*, 1569(1-3):51–8, jan 2002.

[461] G. Sersa, T. Jarm, T. Kotnik, A. Coer, M. Podkrajsek, M. Sentjurc, D. Miklavcic, M. Kadivec, S. Kranjc, A. Secerov, and M. Cemazar. Vascular disrupting action of electroporation and electrochemotherapy with bleomycin in murine sarcoma. *British journal of cancer*, 98(2):388–98, jan 2008.

[462] B. Rubinsky, J. Edd, and L. Horowitz. Electroporation to interrupt blood flow, 2004.

[463] D. Palanker, A. Vankov, Y. Freyvert, and P. Huie. Pulsed electrical stimulation for control of vasculature: temporary vasoconstriction and permanent thrombosis. *Bioelectromagnetics*, 29(2):100–7, feb 2008.

[464] B. Markelc, G. Sersa, M. Cemazar, N. Henao-Guerrero, and J. Robertson. Differential Mechanisms Associated with Vascular Disrupting Action of Electrochemotherapy: Intravital Microscopy on the Level of Single Normal and Tumor Blood Vessels. 8(3):e59557, mar 2013.

[465] G. Sersa, D. Mikiavcic, M. Cemazar, J. Belehradek, T. Jarm, and L. M. Mir. Electrochemotherapy with CDDP on LPB sarcoma: comparison of the anti-tumor effectiveness in immunocompetent and immunodeficient mice. *Bioelectrochemistry and Bioenergetics*, 43:279–283.

[466] C. Y. Calvet, F. M. André, and L. M. Mir. Dual therapeutic benefit of electroporation-mediated DNA vaccination in vivo. *OncoImmunology*, 3(4):e28540, apr 2014.

[467] L. Mir, C. Roth, S. Orlowski, F. Quintin-Colonna, D. Fradelizi, J. Belehradek, and P. Kourilsky. Systemic Antitumor Effects of Electrochemotherapy Combined with Histoincompatible Cells Secreting Inerluekin-2. *Journal of Immunotherapy*, 17(1):30–38, 1996.

[468] S. Roux, C. Bernat, B. Al-Sakere, F. Ghiringhelli, P. Opolon, A. F. Carpentier, L. Zitvogel, L. M. Mir, and C. Robert. Tumor destruction using electrochemotherapy followed by CpG oligodeoxynucleotide injection induces distant tumor responses. *Cancer Immunology, Immunotherapy*, 57(9):1291–1300, sep 2008.

[469] C. Y. Calvet and L. M. Mir. The promising alliance of anti-cancer electrochemotherapy with immunotherapy. *Cancer and Metastasis Reviews*, 35(2):165–177, mar 2016.

[470] B. Poddevin, S. Orlowski, J. Belehradek, and L. Mir. Very high cytotoxicity of bleomycin introduced into the cytosol of cells in culture. *Biochemical Pharmacology*, 42:S67–S75, dec 1991.

[471] L. M. Mir, S. Orlowski, J. Belehradek, and C. Paoletti. Electrochemotherapy potentiation of antitumour effect of bleomycin by local electric pulses. *European journal of cancer*, 27(1):68–72, jan 1991.

[472] M. Marty, G. Sersa, J. R. Garbay, J. Gehl, C. G. Collins, M. Snoj, V. Billard, P. F. Geertsen, J. O. Larkin, D. Miklavcic, I. Pavlovic, S. M. Paulin-Kosir, M. Cemazar, N. Morsli, D. M. Soden, Z. Rudolf, C. Robert, G. C. O'Sullivan, and L. M. Mir. Electrochemotherapy – An easy, highly effective and safe treatment of cutaneous and subcutaneous metastases: Results of ESOPE (European Standard Operating Procedures of Electrochemotherapy) study. *European Journal of Cancer Supplements*, 4(11):3–13, nov 2006.

[473] O. Tounekti, G. Pron, J. Belehradek, and L. M. Mir. Bleomycin, an apoptosis-mimetic drug that induces two types of cell death depending on the number of molecules internalized. *Cancer research*, 53(22):5462–9, nov 1993.

[474] S. Orlowski, J. Belehradek, C. Paoletti, and L. M. Mir. Transient electropermeabilization of cells in culture. Increase of the cytotoxicity of anticancer drugs. *Biochemical pharmacology*, 37(24):4727–33, dec 1988.

[475] J. Gehl, T. Skovsgaard, and L. M. Mir. Enhancement of cytotoxicity by electropermeabilization: an improved method for screening drugs. *Anti-cancer drugs*, 9(4):319–25, apr 1998.

[476] G. I. Evan and K. H. Vousden. Proliferation, cell cycle and apoptosis in cancer. *Nature*, 411(6835):342–348, may 2001.

[477] J.-M. Escoffre and M.-P. Rols. Electrochemotherapy: Progress and Prospects. *Current Pharmaceutical Design*, 18 (23):3406–3415, aug 2012.

[478] B. Mali, T. Jarm, M. Snoj, G. Sersa, and D. Miklavcic. Antitumor effectiveness of electrochemotherapy: A systematic review and meta-analysis. *European Journal of Surgical Oncology (EJSO)*, 39(1):4–16, jan 2013.

[479] B. Mali, D. Miklavcic, L. G. Campana, M. Cemazar, G. Sersa, M. Snoj, T. Jarm, P. Strojan, D. Miklavcic, G. Sersa, M. Cemazar, M. Snoj, D. Miklavčič, E. Gadzijev, G. Sersa, M. Snoj, and G. Sersa. Tumor size and effectiveness of electrochemotherapy. *Radiology and Oncology*, 47(1):32–41, jan 2013.

[480] M. Ðokic, B. Trotovsek, V. Sojar, D. Stanisavljevic, R. Jansa, P. Popovic, M. Cemazar, D. Miklavcic, N. Pozar, P. Kavcic, A. Tomazic, M. Petric, and G. Sersa. Treatment of Primary Liver Tumors with Electrochemotherapy – Clinical Trial. pages 267–270. Springer, Singapore, 2016.

[481] M. Linnert, B. Agerholm-Larsen, F. Mahmood, H. K. Iversen, and J. Gehl. Treatment of Brain Tumors: Electrochemotherapy. pages 247–259. Springer Netherlands, 2014.

[482] S. Bimonte, M. Leongito, V. Granata, A. Barbieri, V. del Vecchio, M. Falco, A. Nasto, V. Albino, M. Piccirillo, R. Palaia, A. Amore, R. di Giacomo, S. Lastoria, S. V. Setola, R. Fusco, A. Petrillo, and F. Izzo. Electrochemotherapy in pancreatic adenocarcinoma treatment: pre-clinical and clinical studies. *Radiology and Oncology*, 50(1):14–20, 2016.

[483] G. Bianchi, L. Campanacci, M. Ronchetti, and D. Donati. Electrochemotherapy in the Treatment of Bone Metastases: A Phase II Trial. *World Journal of Surgery*, 40(12):3088–3094, dec 2016.

[484] I. Edhemovic, E. Brecelj, A. Ivanecz, G. Gasljevic, M. M. Music, T. Jarm, B. Kos, M. Bosnjak, M. Cemazar, D. Miklavcic, S. Potrc, E. Gadzijev, and G. Sersa. Electrochemotherapy of Colorectal Liver Metastases – Trial Update. pages 263–266. Springer, Singapore, 2016.

[485] A. Groslej, B. Kos, M. Cemazar, J. Urbancic, G. Kragelj, M. Bosnjak, B. VErberic, P. Strojan, D. Miklavčič, and G. Serša. Coupling treatment planning with navigation system: a new technological approach in treatment of head and neck tumors by electrochemotherapy. *BioMedical Engineering OnLine*, 12(3), 2015.

[486] N. Mozzillo, E. Simeone, L. Benedetto, M. Curvietto, D. Giannarelli, G. Gentilcore, R. Camerlingo, M. Capone, G. Madonna, L. Festino, C. Caracò, G. Di Monta, U. Marone, M. Di Marzo, A. M. Grimaldi, S. Mori, G. Ciliberto, and P. A. Ascierto. Assessing a novel immuno-oncology-based combination therapy: Ipilimumab plus electrochemotherapy. *OncoImmunology*, 4(6):e1008842, jun 2015.

[487] M. Brizio, P. Fava, C. Astrua, G. Cavaliere, and P. Savoia. Complete regression of melanoma skin metastases after electrochemotherapy plus ipilimumab treatment: an unusual clinical presentation. *European Journal of Dermatology*, 25(3):271–272, 2017.

[488] N. Somia and I. M. Verma. Gene therapy: trials and tribulations. *Nature Reviews Genetics*, 1(2):91–99, nov 2000.

[489] M. A. Kutzler and D. B. Weiner. DNA vaccines: ready for prime time? *Nature Reviews Genetics*, 9(10):776–788, oct 2008.

[490] S. Šatkauskas, F. André, M. F. Bureau, D. Scherman, D. Miklavčič, and L. M. Mir. Electrophoretic Component of Electric Pulses Determines the Efficacy of In Vivo DNA Electrotransfer. *Human Gene Therapy*, 16(10):1194–1201, oct 2005.

[491] J.-M. Escoffre, T. Portet, L. Wasungu, J. Teissié, D. Dean, and M.-P. Rols. What is (Still not) Known of the Mechanism by Which Electroporation Mediates Gene Transfer and Expression in Cells and Tissues. *Molecular Biotechnology*, 41 (3):286–295, mar 2009.

[492] C. Rosazza, S. H. Meglic, A. Zumbusch, M.-P. Rols, and D. Miklavcic. Gene Electrotransfer: A Mechanistic Perspective. *Current gene therapy*, 16(2):98–129, 2016.

[493] M. Pavlin, M. Kandušer, D. Branton, D. W. Deamer, and D. Scherman. New Insights into the Mechanisms of Gene Electrotransfer – Experimental and Theoretical Analysis. *Scientific Reports*, 5(1):9132, aug 2015.

[494] A. I. Daud, R. C. DeConti, S. Andrews, P. Urbas, A. I. Riker, V. K. Sondak, P. N. Munster, D. M. Sullivan, K. E. Ugen, J. L. Messina, and R. Heller. Phase I trial of interleukin-12 plasmid electroporation in patients with metastatic melanoma. *Journal of clinical oncology : official journal of the American Society of Clinical Oncology*, 26(36): 5896–903, dec 2008.

[495] L. M. Mir. Nucleic acids electrotransfer-based gene therapy (electrogenetherapy): Past, current, and future. *Molecular Biotechnology*, 43(2):167–176, oct 2009.

[496] A. Gothelf and J. Gehl. Gene Electrotransfer to Skin; Review of Existing Literature and Clinical Perspectives. *Current Gene Therapy*, 10(4):287–299, aug 2010.

[497] B. Rubinsky. Irreversible Electroporation in Medicine. *Technology in Cancer Research & Treatment*, 6(4):255–259, aug 2007.

[498] A. Ivorra and B. Rubinsky. Historical Review of Irreversible Electroporation in Medicine. pages 1–21. Springer Berlin Heidelberg, 2010.

[499] R. V. Davalos, S. Bhonsle, and R. E. Neal. Implications and considerations of thermal effects when applying irreversible electroporation tissue ablation therapy. *The Prostate*, 75(10):1114–1118, jul 2015.

[500] M. J. C. van Gemert, P. G. K. Wagstaff, D. M. de Bruin, T. G. van Leeuwen, A. C. van der Wal, M. Heger, and C. W. M. van der Geld. Irreversible electroporation: Just another form of thermal therapy? *The Prostate*, 75(3): 332–335, feb 2015.

[501] A. Golberg and M. L. Yarmush. Nonthermal Irreversible Electroporation: Fundamentals, Applications, and Challenges. *IEEE Transactions on Biomedical Engineering*, 60(3):707–714, mar 2013.

[502] B. Al-Sakere, F. André, C. Bernat, E. Connault, P. Opolon, R. V. Davalos, B. Rubinsky, and L. M. Mir. Tumor ablation with irreversible electroporation. *PloS one*, 2(11):e1135, jan 2007.

[503] K. R. Thomson, W. Cheung, S. J. Ellis, D. Federman, H. Kavnoudias, D. Loader-Oliver, S. Roberts, P. Evans, C. Ball, and A. Haydon. Investigation of the Safety of Irreversible Electroporation in Humans. *Journal of Vascular and Interventional Radiology*, 22(5):611–621, may 2011.

[504] H. J. Scheffer, K. Nielsen, M. C. de Jong, A. A. van Tilborg, J. M. Vieveen, A. R. Bouwman, S. Meijer, C. van Kuijk, P. M. van den Tol, and M. R. Meijerink. Irreversible Electroporation for Nonthermal Tumor Ablation in the Clinical Setting: A Systematic Review of Safety and Efficacy. *Journal of Vascular and Interventional Radiology*, 25 (7):997–1011, jul 2014.

[505] M. Pech, A. Janitzky, J. J. Wendler, C. Strang, S. Blaschke, O. Dudeck, J. Ricke, and U.-B. Liehr. Irreversible Electroporation of Renal Cell Carcinoma: A First-in-Man Phase I Clinical Study. *CardioVascular and Interventional Radiology*, 34(1):132–138, feb 2011.

[506] P. Wagstaff, M. Buijs, W. van den Bos, D. de Bruin, P. Zondervan, J. de la Rosette, and P. Laguna. Irreversible electroporation: state of the art. *OncoTargets and Therapy*, 9:2437, apr 2016.

[507] D. Gross, L. Loew, and W. Webb. Optical imaging of cell membrane potential changes induced by applied electric fields. *Biophysical Journal*, 50(2):339–348, aug 1986.

[508] B. Ehrenberg, D. Farkas, E. Fluhler, Z. Lojewska, and L. Loew. Membrane potential induced by external electric field pulses can be followed with a potentiometric dye. *Biophysical Journal*, 51(5):833–837, may 1987.

[509] D. J. Arndt-Jovin and T. M. Jovin. Fluorescence labeling and microscopy of DNA. *Methods in cell biology*, 30:417–48, 1989.

[510] A. Silve, C. Poignard, M. Sack, R. Straessner, and W. Frey. Study of Transmembrane Voltage Kinetics During 100 us Pulse using Voltage Sensitive Dyes. In *1st World Congress on Electroporation and Pulsed Electric Fields in Biology, Medicine and Food & Environment Technologies*, page 74, 2015.

[511] J. M. Escoffre, E. Bellard, C. Faurie, S. C. Sébaï, M. Golzio, J. Teissié, and M. P. Rols. Membrane disorder and phospholipid scrambling in electropermeabilized and viable cells. *Biochimica et Biophysica Acta - Biomembranes*, 1838(7):1701–1709, 2014.

[512] C. Rosazza, H. Deschout, A. Buntz, K. Braeckmans, M.-P. Rols, and A. Zumbusch. Endocytosis and Endosomal Trafficking of DNA After Gene Electrotransfer In Vitro. *Molecular Therapy—Nucleic Acids*, 5(2):e286, feb 2016.

[513] E. E. Vaughan and D. A. Dean. Intracellular Trafficking of Plasmids during Transfection Is Mediated by Microtubules. *Molecular Therapy*, 13(2):422–428, feb 2006.

[514] C. Rosazza, A. Buntz, T. Rieß, D. Wöll, A. Zumbusch, and M.-P. Rols. Intracellular tracking of single-plasmid DNA particles after delivery by electroporation. *Molecular therapy : the journal of the American Society of Gene Therapy*, 21(12):2217–26, dec 2013.

[515] D. Moreau, C. Lefort, R. Burke, P. Leveque, and R. P. O'Connor. Rhodamine B as an optical thermometer in cells focally exposed to infrared laser light or nanosecond pulsed electric fields. *Biomedical optics express*, 6(10):4105–17, oct 2015.

[516] A. Vitkin. Improving treatment efficacy with biological or biophysical feedback. *SPIE Newsroom*, apr 2012.

[517] B. Markelc, E. Bellard, G. Sersa, S. Pelofy, J. Teissie, A. Coer, M. Golzio, and M. Cemazar. In Vivo Molecular Imaging and Histological Analysis of Changes Induced by Electric Pulses Used for Plasmid DNA Electrotransfer to the Skin: A Study in a Dorsal Window Chamber in Mice. *The Journal of Membrane Biology*, 245(9):545–554, sep 2012.

[518] E. Bellard, B. Markelc, S. Pelofy, F. Le Guerroué, G. Sersa, J. Teissié, M. Cemazar, and M. Golzio. Intravital microscopy at the single vessel level brings new insights of vascular modification mechanisms induced by electropermeabilization. *Journal of Controlled Release*, 163(3):396–403, nov 2012.

[519] T. Berghöfer, C. Eing, B. Flickinger, P. Hohenberger, L. H. Wegner, W. Frey, and P. Nick. Nanosecond electric pulses trigger actin responses in plant cells. *Biochemical and Biophysical Research Communications*, 387(3):590–595, sep 2009.

[520] A. G. Pakhomov, S. Xiao, O. N. Pakhomova, I. Semenov, M. A. Kuipers, and B. L. Ibey. Disassembly of actin structures by nanosecond pulsed electric field is a downstream effect of cell swelling. *Bioelectrochemistry*, 100:88–95, dec 2014.

[521] G. P. Tolstykh, G. L. Thompson, H. T. Beier, Z. A. Steelman, and B. L. Ibey. nsPEF-induced PIP 2 depletion, PLC activity and actin cytoskeletal cortex remodeling are responsible for post-exposure cellular swelling and blebbing. *Biochemistry and Biophysics Reports*, 9:36–41, mar 2017.

[522] M. Wu, F. Yuan, B. Mossop, F. Yuan, and T. Tomov. Membrane Binding of Plasmid DNA and Endocytic Pathways Are Involved in Electrotransfection of Mammalian Cells. *PLoS ONE*, 6(6):e20923, jun 2011.

[523] C. Rosazza, J.-M. Escoffre, A. Zumbusch, and M.-P. Rols. The actin cytoskeleton has an active role in the electrotransfer of plasmid DNA in mammalian cells. *Molecular therapy : the journal of the American Society of Gene Therapy*, 19(5):913–21, may 2011.

[524] D. Zalvidea and E. Claverol-Tinturé. Second Harmonic Generation for time-resolved monitoring of membrane pore dynamics subserving electroporation of neurons. *Biomedical Optics Express*, 2(2):305, jan 2011.

[525] E. K. Moen, B. L. Ibey, and H. T. Beier. Detecting subtle plasma membrane perturbation in living cells using second harmonic generation imaging. *Biophysical journal*, 106(10):L37–40, may 2014.

[526] E. K. Moen, H. T. Beier, G. L. Thompson, A. M. Armani, and B. L. Ibey. Nonlinear imaging of lipid membrane alterations elicited by nanosecond pulsed electric fields. page 93260T. International Society for Optics and Photonics, mar 2015.

[527] E. K. Moen, B. L. Ibey, H. T. Beier, and A. M. Armani. Investigating membrane nanoporation induced by bipolar pulsed electric fields via second harmonic generation. *Applied Physics Letters*, 109(11):113701, sep 2016.

[528] S. M. Bardet, L. Carr, M. Soueid, D. Arnaud-Cormos, P. Leveque, and R. P. O'Connor. Multiphoton imaging reveals that nanosecond pulsed electric fields collapse tumor and normal vascular perfusion in human glioblastoma xenografts. *Scientific reports*, 6:34443, oct 2016.

[529] J. T. Sengel and M. I. Wallace. Imaging the dynamics of individual electropores. *Proceedings of the National Academy of Sciences*, 113(19):5281–5286, 2016.

[530] M. Szabo and M. I. Wallace. Imaging potassium-flux through individual electropores in droplet interface bilayers. *Biochimica et biophysica acta*, 1858(3):613–7, mar 2016.

[531] C. Mauroy, T. Portet, M. Winterhalder, E. Bellard, M. C. Blache, J. Teissié, A. Zumbusch, and M. P. Rols. Giant lipid vesicles under electric field pulses assessed by non invasive imaging. *Bioelectrochemistry*, 87:253–259, 2012.

[532] J. Teissie, M. Golzio, and M. P. Rols. Mechanisms of cell membrane electropermeabilization: a minireview of our present (lack of ?) knowledge. *Biochimica et biophysica acta*, 1724(3):270–280, aug 2005.

[533] S. Unterreitmeier, A. Fuchs, T. Schäffler, R. G. Heym, D. Frishman, and D. Langosch. Phenylalanine promotes interaction of transmembrane domains via GxxxG motifs. *Journal of molecular biology*, 374(3):705–18, nov 2007.

[534] N. C. Maiti, M. M. Apetri, M. G. Zagorski, P. R. Carey, and V. E. Anderson. Raman spectroscopic characterization of secondary structure in natively unfolded proteins: alpha-synuclein. *Journal of the American Chemical Society*, 126 (8):2399–408, mar 2004.

[535] Z. Cournia, T. W. Allen, I. Andricioaei, B. Antonny, D. Baum, G. Brannigan, N.-V. Buchete, J. T. Deckman, L. Delemotte, C. Del Val, R. Friedman, P. Gkeka, H.-C. Hege, J. Hénin, M. A. Kasimova, A. Kolocouris, M. L. Klein, S. Khalid, M. J. Lemieux, N. Lindow, M. Roy, J. Selent, M. Tarek, F. Tofoleanu, S. Vanni, S. Urban, D. J. Wales, J. C. Smith, and A.-N. Bondar. Membrane Protein Structure, Function, and Dynamics: a Perspective from Experiments and Theory. *The Journal of membrane biology*, 248(4):611–40, aug 2015.

[536] M. Dezi, A. Di Cicco, P. Bassereau, and D. Levy. Detergent-mediated incorporation of transmembrane proteins in giant unilamellar vesicles with controlled physiological contents. *Proceedings of the National Academy of Sciences*, 110(18):7276–7281, apr 2013.

[537] S. R. Kirchner, A. Ohlinger, T. Pfeiffer, A. S. Urban, F. D. Stefani, A. Deak, A. a. Lutich, and J. Feldmann. Membrane composition of jetted lipid vesicles: A Raman spectroscopy study. *Journal of Biophotonics*, 5(1):40–46, 2012.

[538] M. Stacey, J. Stickley, P. Fox, V. Statler, K. Schoenbach, S. J. Beebe, and S. Buescher. Differential effects in cells exposed to ultra-short, high intensity electric fields: cell survival, DNA damage, and cell cycle analysis. *Mutation research*, 542(1-2):65–75, dec 2003.

[539] N. Chen, A. L. Garner, G. Chen, Y. Jing, Y. Deng, R. J. Swanson, J. F. Kolb, S. J. Beebe, R. P. Joshi, and K. H. Schoenbach. Nanosecond electric pulses penetrate the nucleus and enhance speckle formation. *Biochemical and Biophysical Research Communications*, 364(2):220–225, 2007.

[540] E. W. Lee, D. Wong, S. V. Prikhodko, A. Perez, C. Tran, C. T. Loh, and S. T. Kee. Electron microscopic demonstration and evaluation of irreversible electroporation-induced nanopores on hepatocyte membranes. *Journal of vascular and interventional radiology : JVIR*, 23(1):107–13, jan 2012.

[541] C. Jiang, R. V. Davalos, and J. C. Bischof. A Review of Basic to Clinical Studies of Irreversible Electroporation Therapy. *IEEE Transactions on Biomedical Engineering*, 62(1):4–20, jan 2015.

[542] M. E. Lacouture, M. J. Anadkat, R.-J. Bensadoun, J. Bryce, A. Chan, J. B. Epstein, B. Eaby-Sandy, and B. A. Murphy. Clinical practice guidelines for the prevention and treatment of EGFR inhibitor-associated dermatologic toxicities. *Supportive Care in Cancer*, 19(8):1079–1095, jun 2011.

[543] Y. Balagula, K. B. Huston, K. J. Busam, M. E. Lacouture, P. B. Chapman, and P. L. Myskowski. Dermatologic side effects associated with the MEK 1/2 inhibitor selumetinib (AZD6244, ARRY-142886). *Investigational New Drugs*, 29(5):1114–1121, 2011.

[544] M. Mandalà, D. Massi, and V. De Giorgi. Cutaneous toxicities of BRAF inhibitors: Clinical and pathological challenges and call to action. *Critical Reviews in Oncology/Hematology*, 88(2):318–337, 2013.

[545] R. Anforth, P. Fernandez-Peñas, and G. V. Long. Cutaneous toxicities of RAF inhibitors. *The Lancet. Oncology*, 14 (1):e11–8, jan 2013.

[546] E. Livingstone, L. Zimmer, J. Vaubel, and D. Schadendorf. BRAF, MEK and KIT inhibitors for melanoma: adverse events and their management. *Chinese Clinical Oncology*, 3(3):29, sep 2014.

[547] V. R. Belum, A. Fischer, J. N. Choi, and M. E. Lacouture. Dermatological Adverse Events from BRAF Inhibitors: A Growing Problem. *Current Oncology Reports*, 15(3):249–259, mar 2013.

[548] C. Zhang, W. Spevak, Y. Zhang, E. A. Burton, Y. Ma, G. Habets, J. Zhang, J. Lin, T. Ewing, B. Matusow, G. Tsang, A. Marimuthu, H. Cho, G. Wu, W. Wang, D. Fong, H. Nguyen, S. Shi, P. Womack, M. Nespi, R. Shellooe, H. Carias, B. Powell, E. Light, L. Sanftner, J. Walters, J. Tsai, B. L. West, G. Visor, H. Rezaei, P. S. Lin, K. Nolop, P. N. Ibrahim, P. Hirth, and G. Bollag. RAF inhibitors that evade paradoxical MAPK pathway activation. *Nature*, 526 (7574):583–586, oct 2015.

[549] H.-b. Liu, Y. Wu, T.-f. Lv, Y.-w. Yao, Y.-y. Xiao, D.-m. Yuan, and Y. Song. Skin rash could predict the response to EGFR tyrosine kinase inhibitor and the prognosis for patients with non-small cell lung cancer: a systematic review and meta-analysis. *PloS one*, 8(1):e55128, jan 2013.

[550] F. Petrelli, K. Borgonovo, M. Cabiddu, V. Lonati, and S. Barni. Relationship between skin rash and outcome in non-small-cell lung cancer patients treated with anti-EGFR tyrosine kinase inhibitors: a literature-based meta-analysis of 24 trials. *Lung cancer (Amsterdam, Netherlands)*, 78(1):8–15, oct 2012.

9

Annexe

9.1 Cell membrane electropulsation: chemical analysis of cell membrane modifications and associated transport mechanisms

Here is reported a book chapter in the framework of the 2017 special issue in "Advances in Anatomy, Embryology and Cell Biology" published by Springers . This special issue is edited by Dr. Julita Kulbacka from the Wroclaw Medical University in Poland. This book chapter focused on cell membrane electropulsation based on chemical analysis of cell membrane modifications and associated transport mechanisms.

Chapter 4

Cell membrane electropulsation: chemical analysis of cell membrane modifications and associated transport mechanisms

Antoine Azan, Florian Gaillièque, Lluis M. Mir[1] and Marie Breton

Abstract

The transport of substances across the cell membrane is complex because the main physiological role of the membrane is the control of the substances that would enter or exit the cells. Life would not be possible without this control. Cell electropulsation corresponds to the delivery of electric pulses to the cells and comprises cell electroporation and cell electropermeabilization. Cell electropulsation allows for the transport of non-permeant molecules across the membrane, bypassing the physiological limitations. In this chapter we discuss the changes occurring in the cell membrane during electroporation or electropermeabilization as they allow to understand which molecules can be transported as well as when and how their transport can occur. Electrophoretic or diffusive transports across the cell membrane can be distinguished. This understanding has a clear impact on the choice of the electrical parameters to be applied to the cells as well as on other aspects of the experimental protocols that have to be set to load the cells with non-permeant molecules.

4.1. Introduction

The cell membrane, also termed plasma membrane, highly regulates all the exchanges between the outside and the inside of the cell. In particular, the cell membrane is a barrier that prevents the unregulated penetration/leakage of molecules of vital importance for the cell physiology, such as all the substrates/products of the cell metabolism, ions, sugars or amino acids. None of these molecules can cross the cell membrane by free diffusion. Other large hydrophilic molecules are also unable to cross the membrane by diffusion. These molecules and the small hydrophilic molecules that are not transported through channels or pumps, are termed “non-permeant” molecules (Silve et al., 2012a); they can only reach certain cell compartments (but neither the cytosol nor the nucleosol) by endocytosis/exocytosis.

To allow the uptake of non-permeant molecules, cell membrane perturbations must be initiated that will transiently rupture the membrane impermeability. One of the most popular and practical way to reversibly permeabilize the cell membrane consists in the application of adequate electric pulses. The term electroporation was first introduced by (Neumann and Katchalsky, 1972) in 1972. The modelization of the phenomenon began almost as early and started with 1D approximations of the membrane (Litster, 1975). The initial basis of analytical models was the Schwan Equation:

---

[1] Lluis M. Mir
Vectorology and Anticancer Therapies, UMR8203, Univ. Paris-Sud, CNRS, Gustave Roussy, Université Paris-Saclay, Villejuif, F-94805, France.
E-mail : Luis.mir@cnrs.fr

$$\Delta\Psi = 3/2.E.R.cos(\theta)$$

(the transmembrane potential $\Delta\Psi$ at a given point on the membrane is equal to the electric field amplitude E times the radius of the cell R times the cosine of the angular coordinate θ).

This equation implies that polarization in the cells occurs at the poles according to the electric field orientation and thus will in priority induce an electrical breakdown of the membrane in these regions.

There are two main mathematical approaches to model the pore formation: either static or dynamic. Older models focused on the static approach as in (Pastushenko and Chizmadzhev, 1982). The other approach, the dynamic one, considers the temporal evolution of the pore density (Krassowska and Filev, 2007). This model links the number of pores to the voltage applied, and then evaluates the evolution of the pore radii. The flaw of this model is that it is highly dependent on the mesh size. Using a fine mesh gives different results from a coarser one. Indeed, with the Krassowka model, small changes in initial non-measurable parameters can result in very different outcomes (Poignard et al., 2016). This can be a consequence of the fact that many initial variables are only approximations, because measuring them, for example the conductivity and permittivity of the membrane or the cytosol, is possible (Wang et al., 2017) but difficult. Indeed, the cytosol is not just a solution of proteins and other biological compounds since the cytoskeleton and the vesicles occupy a large fraction of the cytoplasmic volume. To address this problem, a new model (the Leguèbe model) has been developed which relies on a lower number of variables. Moreover it considers two steps in the pulsing process: the generation of defects (possibly pores) at the poles of the cell membrane, followed by the diffusion of these defects in the cell membrane after the pulses delivery (Leguèbe et al., 2014). The Leguèbe model suggests a two-step approach of electropulsation. The membrane conductance fluctuates between the conductance at rest, the conductance during the pulse for a fully permeabilized membrane and the conductance after the pulse which reflects the long term effect of electroporation, also termed electropermeabilization.

Molecular dynamics (MD) have proven to be helpful to understand the interaction of cells with electric pulses. As far as the electroporation is concerned, MD allow for the study of the membrane structure at a nanoscale level. This computational method enables the simulation of the evolution of the atoms composing the membrane and its surroundings during up to tens of nanoseconds. If the force corresponding to the simulated electric field is high enough, pore generation can occur during the computational time. The process of pore generation is stochastic and simulations often require a high field amplitude. Since each individual molecule is considered in the calculations of the simulation, the region of interest is limited by the number of elements that the computer is able to handle simultaneously. Therefore there are constraints in both the size of the sample considered and the duration of the simulation in order to avoid that running MD simulations are too computationally heavy. In particular, the nanosecond time range of this modelling is limited compared to the time during which the cell remains permeabilized. Nevertheless, in the case of nanosecond pulses, the predictions of the MD have been experimentally validated (Breton et al., 2012). More details of the results provided by these numerical approaches are reported in chapter 1 of this volume.

Another relevant issue concerns the fact that the cell membrane is not the only membrane in the cell that may undergo modifications when the cell is submitted to an electric pulse. If nanosecond pulses are used, the membrane of internal organelles can also be porated (Schoenbach et al., 2001; de Menorval et al., 2016). Such an electroporation of the internal organelles of the cell may allow exchanges of molecules between different internal compartments of the cell, namely between the cytosol and the endoplasmic reticulum or between the cytosol and the mitochondria. Therefore, after exposure to electric pulses, the complexity of the possible transports of molecules must be taken into account.

A further issue is that there is no consensus up to now about the term “electroporation”. Electroporation refers to the generation of pores via Pulsed Electric Fields (PEFs), while the term “electropermeabilization” refers to the generation of defects by PEFs. It is sometimes considered a more suitable term because even after the pores resealing, the cell can remain in a permeabilized state for periods of time that are orders of magnitude longer than the pulses duration. Recently the term “electropulsation” has been proposed to describe the action of submitting cells to electric fields.

In this chapter, we present recent findings that have improved the understanding of the interaction of electric pulses with cell membranes and we address the mechanisms that may underlie the transport of molecules either during or after the pulse delivery.

4.2. Recent experimental data on chemical modifications of membranes submitted to electric pulses

It has been known for a long time that the application of electric pulses to cells induced the appearance of reactive oxygen species (ROS) in the cell medium (Bonnafous et al., 1999). It has also been reported that the addition of antioxidants could reduce the death rate of cells provoked by pulses (Gabriel and Teissié, 1994). Finally, some groups used indirect measurements of phospholipid oxidation by absorbance studies to show that pulses could peroxidize membrane phospholipids (Benov et al., 1994). More recently, mass spectrometry has been used to directly investigate the chemical processes taking place during or after electropulsation at the level of membranes. The study was conducted on a well-known membrane model, the giant unilamellar vesicles (GUVs). These vesicles were constituted of either saturated or unsaturated phospholipids since these lipids are both present in all cell membranes. The mass spectra obtained clearly showed that electric pulses can induce the oxidation of the unsaturated membrane phospholipids. Whatever the duration of the pulses (millisecond, microsecond or nanosecond pulses), unsaturated lipids were oxidized while saturated lipids remained intact. The mass spectra clearly presented a classical oxidation pattern showing peaks corresponding to the addition of oxygen atoms as well as peaks of low masses corresponding to lipids that underwent chain breaks after oxidation. Mechanistic studies conducted on the same GUV model showed that the presence of light or dioxygen could be cofactors in the oxidation (M. Breton et al, submitted). More importantly, the concentration of ROS in the solution increased after pulsing only if unsaturated vesicles were present in the solution. Therefore, the electric pulses should not directly cause ROS generation and lipid peroxidation. It seems more likely that the main effect of the electric pulses is that they facilitate the peroxidation induced by the ROS already present in the solution before pulsing. Finally, the effects of the pulse parameters on the level of lipid oxidation follows the same trend as the effects of the pulse parameters on the level of cell permeability. Indeed, if the duration, the number or the voltage of the pulses are increased, the level of oxidation is increased. This is the case for all kinds of pulses (millipulses, micropulses, nanopulses).

4.3. Cell electropulsation model

Our group proposed a new model which describes both the immediate effects of the pulses during their application to the cells as well as the chemical and physical consequences of the pulses on the cell membranes. One of the basis of this model is that, when a very high electric field is applied on a membrane, non-permeant molecules such as water or ROS can enter the membrane first as water fingers and later as water pores (Tarek, 2005). This model contains two steps: electroporation followed by electropermeabilization. Electroporation happens during and shortly after the application of the pulses.

During this step, pores form and therefore water and ROS can enter the lipophilic area of the membrane where the oxidable lipid chains are. The oxidation of the membrane phospholipids can take place. The membrane is then highly conductive and completely permeable. When the pulse is finished, the pores rapidly close in tens of nanoseconds. The electropermeabilization step initiates. The conductivity of the membrane sharply decreases while the decrease of the membrane permeability is more progressive. However, since some oxidized lipids remain in the membrane until they are removed by membrane repair mechanisms, the conductivity and permeability of the membrane remain slightly higher than their basal level. During the electropermeabilization step, the membrane permeability will depend on the density of the oxidized lipids in the membrane. Right after the end of the pulse, the oxidized lipids are concentrated in the porated area. The density of oxidized lipids is high and the membrane is very permeable. Gradually, the oxidized lipids will diffuse laterally in the membrane. The density of oxidized lipids will decrease and therefore the permeability of the membrane will decrease. A low level of membrane conductivity and permeability will remain until the complete removal of oxidized lipids from the membrane. Cells can renew their membrane lipids by the process of endocytosis/exocytosis which can last for several hours (Ullery et al., 2015). The membrane will hence remain slightly permeable and conductive for a few hours. This model is valid for all kind of pulses ranging from nanosecond to millisecond duration. It presents different kinetics which are consistent with all the previous experimental studies that did not fit with the theories of electroporation or electropermeabilization. According to this model, it seems important to take into account both the physical and the chemical consequences of cell pulsation when studying the transport of molecules inside the cells by electrotransfer.

4.4. Study of the interfacial water around biological samples submitted to electric pulses.

Many groups have studied the water/lipid interface based on vibrational spectroscopy techniques (Bonn et al., 2010; Gruenbaum and Skinner, 2011; Nagata and Mukamel, 2010; Nihonyanagi et al., 2013). It has been reported that the interfacial water molecules are highly organized due to strong hydrogen-bonds close to lipid head groups (Lopez et al., 2004) and to preferential water orientation pointing towards the lipids tails (Chen et al., 2010). CARS microscopy has been used to investigate the orientation of water in the lipid/water interfaces of multilamellar vesicles (Cheng et al., 2003). Teissie and colleagues suggested that this interfacial water could be considered as the first barrier to overcome in order to allow molecules to cross the plasma membrane (Teissie, 2007). Molecular dynamics simulations have revealed that the application of an intense electric field on a lipid membrane disorganizes the interfacial water by creating aqueous pores into the membrane (Tarek, 2005). Water molecules play a key role in the initiation and the stabilization of these aqueous pores (Tieleman, 2004; Ziegler and Vernier, 2008). Due to the dipole moment of water, the water molecules are mainly oriented along the electric field, which contributes to stabilization of these aqueous pores (Tokman et al., 2013). The life-time of these aqueous pores is still under debate in the community (Dehez et al., 2014; Pavlin and Miklavčič, 2008; Ziegler and Vernier, 2008). Nevertheless, it is commonly admitted that the aqueous pores are initiated and collapse within nanoseconds or tens of nanoseconds, respectively, after the beginning and the end of the pulsed electric fields (Delemotte and Tarek, 2012). Due to the nanosecond time-scale and the nanometer size-scale of the electropores, obvious experimental proofs of the presence of the electropores created by the pulsed electric fields are still missing. In an experimental study, we focused on an indirect consequence of the delivery of pulsed electric fields on biological membranes by monitoring the interfacial water thanks to a unique Coherent anti-Stokes Raman Scattering (CARS) microscope (Silve et al., 2012b). The illumination geometry specifically enhances the CARS signal at the interfaces. Thus, CARS spectra of water close to biological samples (DC-3F cells and GUVs) exposed or not to PEFs have been acquired. Two families of water, coined "interfacial water" and "interstitial water", are associated to two different vibrational wavenumber spectra bands. The 3000 – 3230 cm^{-1} and 3300 – 3450 cm^{-1} bands are known to be associated, respectively, to the interfacial water and the interstitial water (Gruenbaum and Skinner, 2011). Our results show that the CARS intensity ratio between these two families is highly affected by the pulsed electric field delivery. The interstitial water becomes predominant in the water vibrational spectrum after the PEFs treatment. The differences in the spectra of GUVs before and after the pulsed electric field treatments are larger than those of the spectra of DC-3F cells. We associate this result with the absence of proteins in the membrane of GUVs. Indeed, the presence of proteins contributes to the reduction of the interfacial water/lipid signal. This study reports the first experimental proof of the effect of pulsed electric fields on the water and especially the water/lipid interface of biological samples. More experiments still have to be performed in order to improve the understanding of the underlying mechanisms of the electropermeabilization process such as the determination of a dose effect relationship or the application of different types of electric pulses.

4.5. Biochemical characterization of live cells exposed to pulsed electric fields.

As reported in the previous section, mass spectrometry studies have demonstrated the chemical modification of phospholipids induced by the delivery of PEFs on GUVs. In order to assess the effect of pulsed electric fields on the biochemical composition of cells, confocal Raman microspectroscopy was used to acquire the Raman signature of live cells exposed or not to classical electric pulses parameters: 8 pulses, 100 µs duration, 1000 V/cm field magnitude and 1 Hz repetition rate. Confocal Raman microspectroscopy is a label-free and non-invasive optical technique which provides detailed information about the molecular composition of the samples, especially about the proteins, lipids and DNA contents of the cells. This instrumentation technique has reached a mature state since the discovery in 1928 of the physical underlying mechanism by Sir Raman (Raman, 1928). It has been commonly used to characterize cells (Downes et al., 2011), drug delivery systems (Smith et al., 2015) or to perform biomedical diagnoses (Kong et al., 2015). Major modifications in the Raman signatures of live cells were noticed when comparing the pulsed group to the control group when performing the acquisition in a cytoplasmic area (Figure 4.1). Especially, the vibrational modes of phenylalanine (621, 1003, 1033 and 1607 cm^{-1}), Amide I (1658 cm^{-1}) and lipids (1448 cm^{-1}) were highly impacted by the delivery of pulsed electric fields (figures 4.1.A and 4.1.B) (Azan et al, 2017). Phenylalanine is a nonpolar and hydrophobic amino-acid present in many transmembrane domains (Unterreitmeier et al., 2007). It has been demonstrated that the 1658 cm^{-1} Raman band is a biomarker of the secondary structure of proteins (Maiti et al., 2004). Our results experimentally confirm for the first time the effects of electric pulses on proteins (Azan et al., 2017) that were predicted by a numerical model showing the unfolding of proteins under an intense electric field (Cournia et al., 2015). When the Raman signatures of pulsed and non-pulsed cells were acquired at the nucleus location, vibrational models associated to DNA were also impacted by the pulsed electric fields (Figures 4.1.C and 4.1.D). This result is in agreement with previous studies reporting that DNA is sensitive to the ROS generated in the culture medium by the delivery of electric pulses (Gabriel and Teissié, 1994; Pakhomova et al., 2012; Wiseman and Halliwell, 1996).

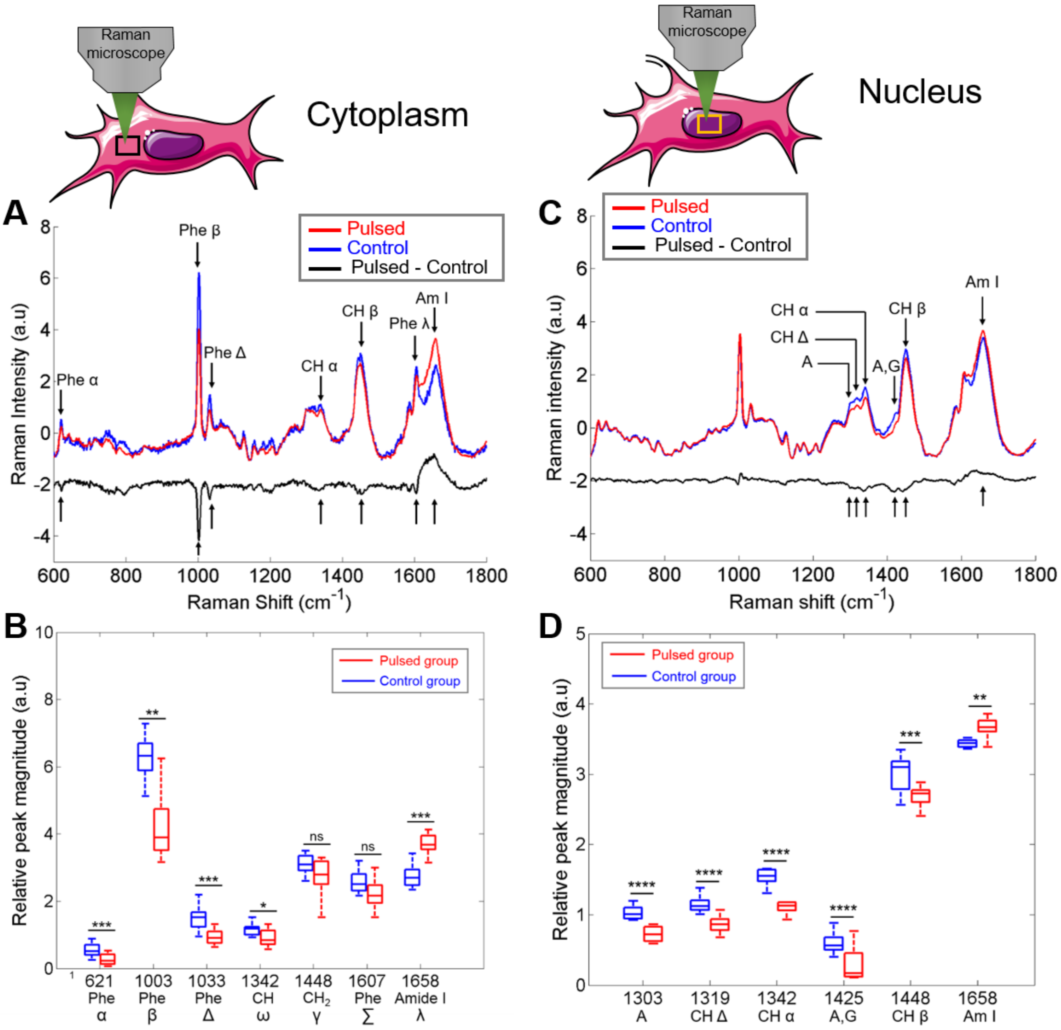

Fig. 4.1. Effect of the delivery of electric pulses on the Raman signatures of live cells at the cytoplasm (A-B) and the nucleus (C-D) locations. A – Mean Raman signatures of control and pulsed cells acquired at the cytoplasm. The differential spectrum (pulsed minus control) is displayed with a vertical offset for more clarity. B – Statistical analysis of the magnitude of 7 critical bands. C – Mean Raman signatures of control and pulsed cells acquired at the nucleus. The differential spectrum (pulsed minus control) is displayed with a vertical offset for more clarity. D – Statistical analysis of the magnitude of 6 critical bands. The electric pulses parameters were fixed to 8 pulses, 100 µs duration, 1000 V/cm field magnitude and 1 Hz repetition rate. Statistics were conducted with a Student's t-test (ns: non-statistically significant, *: p-value < 5%, **: p-value < 1%, ***: p-value < 0.1%, ****: p-value < 0.01%). Adapted from Azan et al., 2017.

4.6. Transport phenomena

Under the context of the theories and facts developed in the previous sections of this chapter, it is essential to distinguish the various transport possibilities that may occur across the membrane at the various steps of the electropulsation process. Here we will consider transports mechanisms under electropulsation conditions that preserve cells viability. Indeed, in the case of irreversible electroporation, when the membrane cannot fully recover its initial impermeability (one of the definitions of the “irreversible electroporation”), all molecules, sooner or later, will be able to freely cross the cell membrane.

Under normal conditions, in the absence of any physical or chemical perturbation, the membrane is impermeable to the non-permeant molecules, that is to all the molecules that are not actively transported across the membrane and that cannot diffuse through the membrane (mainly through the lipid bilayer) because of their size and physico-chemical characteristics. All the metabolically important small molecules (like sugars, amino acids, dipeptides, iron, osmotically important ions such as sodium or potassium, second messengers like calcium ions) do not freely cross the membrane: their transport is highly regulated. No large molecule can cross the plasma membrane, except the molecules that can generate pores in the membrane or affect the membrane structure (like the chains of the vegetal toxins responsible for the internalization of the catalytic chains of the same toxins, or like the cell penetrating peptides such as those derived from TAT or melittin) (Salomone et al., 2014).

When an electric pulse is delivered to cells, and as soon as the cell enters the first step of the membrane destabilization caused by the electric pulse, that is the “electroporation” step, non-permeant molecules can start crossing the membrane (Figure 4.2). They can cross either by diffusion through the aqueous pores created in the membrane, or by electrophoresis. Indeed, because of the presence of the electric field, charged molecules will be efficiently pulled through the membrane. For highly charged molecules, or, better to say, for molecules possessing a high ratio of charges per mass, this transport can be very efficient even for ultrashort pulses as demonstrated by (Breton et al., 2012). In 10 ns, one pulse of 10 ns and 5.8 kV/cm was sufficient to permeabilize the membrane of GUVs and to introduce siRNAs inside the GUVs. Limited diffusive transport also occurs, but at a low level, for several reasons. The first one is that the duration of the pulses, and therefore the half-life of the electropores, is always very short to preserve the cells viability. The second one is that this diffusion will only occur through the electropores, that is, through a small area of the cell surface, which will restrict the flux of molecules across the membrane. The third one is that, unless there is a huge concentration gradient between the outside and the inside of the cell, the number of molecules transported through a small area during an extremely short time (Fick’s law) will be very small, and thus not easily detectable. Nevertheless, this transport exists and could be shown using GUVs prepared with a non-oxidable lipid, for example the DSPC that is a fully saturated phospholipid. Because GUVs are just a phantom of a cell, they can be pulsed many times without the restrictions imposed by viability preservation. Because the lipids of these DSPC GUVs cannot be oxidized, even if pores form during the pulse delivery, the membrane recovers its full integrity when the pores close. DSPC GUVs prepared in 240 mM sucrose (sucrose inside the GUVs) and diluted in 260 mM glucose (glucose outside the GUVs) show a strong optical contrast. Two minutes after one single pulse, or a very limited number of pulses, no change in this contrast is observed (while GUVs prepared with an unsaturated oxidable lipid will already lose this contrast, see next paragraph). However, after the delivery of a high number of long pulses (for example of 5 ms duration), a loss in contrast is detected: it reflects the exchange of glucose and sucrose across the electropores generated during the pulse delivery. The cumulated duration of the pulse and the large concentration gradients of the two sugars allow for a sufficient mass transport of the sugar molecules across the membrane, and therefore the contrast loss, even if sugars are neutral, non-charged molecules. Thus, not only the electrophoretic transport can occur through the pores during the pulses delivery, but also the diffusive transport.

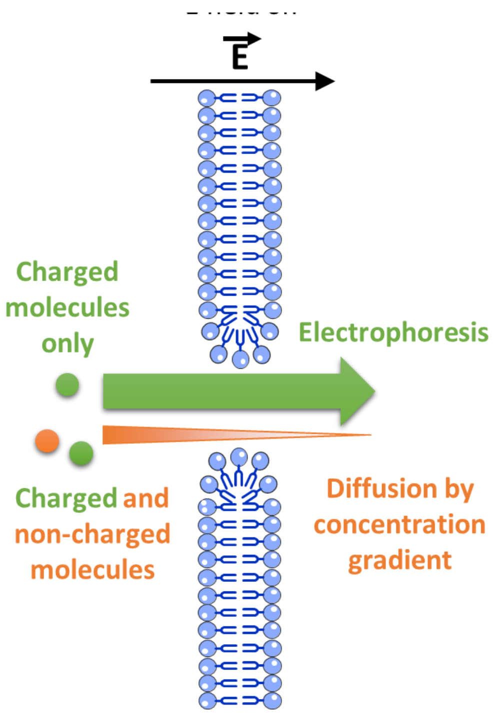

Fig. 4.2. Scheme presenting the transport of molecules during the electroporation step. The electric field is present. The duration of this step is directly related to the duration of the electric pulse and so it ranges from a few nanoseconds to milliseconds. Charged molecules are mostly pulled through the membrane by electrophoresis. Limited diffusive transport also occurs for both charged and non-charged molecules.

After the pulse, and after the rapid closure of the electropores, the cells remain permeabilized for some time, in the seconds to minutes range (Figure 4.3). No electrophoretic transport driven by an external electric field can occur since the electric pulses have ended. The contribution of a transmembrane potential difference across the electropermeabilized membrane has been evoked by Dr T. Vernier and his colleagues, and is under study: the electric field across the membrane could indeed favor or not favor the passage of charged species, as a function of the sign of the charge(s) of these molecules. However, with respect to the "electroporation" step, the "electropermeabilized" state is characterized by the massive transport of charged or non-charged non-permeant molecules across the membrane. One of the main reasons is the duration of the "electropermeabilized" state: seconds or minutes, as already mentioned. These durations are several orders of magnitude longer that the pulse duration, even in the case of the longest pulses, the msPEF. The duration of the permeabilized state is the consequence of the lipids oxidation, since it is well-known that a membrane containing oxidized lipids (Wong-Ekkabut et al., 2007, Vernier et al., 2009), Rems et al., 2016) is a "leaky" membrane. The coefficient of diffusion through an oxidized membrane can be orders of magnitude larger than the coefficient of diffusion through a native, non-oxidized membrane (Rems et al., 2016). This explains why the optical contrast of a GUV prepared using an unsaturated lipid is lost two minutes after the delivery of a single pulse or very small number of pulses: sugars could cross the membrane during the two minutes, a time extremely long with respect to the pulse duration. This diffusive transport is, of course, not constant during the duration of the electropermeabilized state. There are probably two reasons why very large molecules have to be present in the pulsing medium at the time of the pulse delivery: 1) in the case of highly charged molecules, such as long nucleic acid that are too large to move through diffusive processes, to benefit from the electrophoretic transport and to at least initiate the contact with the membrane; 2) in the case of large non-charged molecules such as large proteins, to find regions with a very large density of oxidized lipids, therefore to find regions with very large diffusive capacities. It is important to recall that DNA fragments of up to 150 kbp or proteins of 150 kDa, which were complete antibodies (Bobinnec et al., 1998) have been transported inside the cells by electropulsation. According to our model, and in particular according to the lateral diffusion of the lipids that will "dilute" the oxidized lipids generated in the areas where electropores were formed, the density of the modified lipids and hence the diffusion capabilities will progressively decrease, which will progressively restrict the diffusion of the molecules as a function of their size. The kinetics of such a progressive restriction in the molecule transport have been analyzed in the case of the anticancer drug bleomycin (Silve et al., 2012a). In another respect, the total number of molecules transported (independently of the external concentration, and thus of the gradient of the concentration across the membrane) is directly related to the size of the molecules transported, under identical pulsation conditions and using the same cells to evaluate these transports (Mir, 2008).

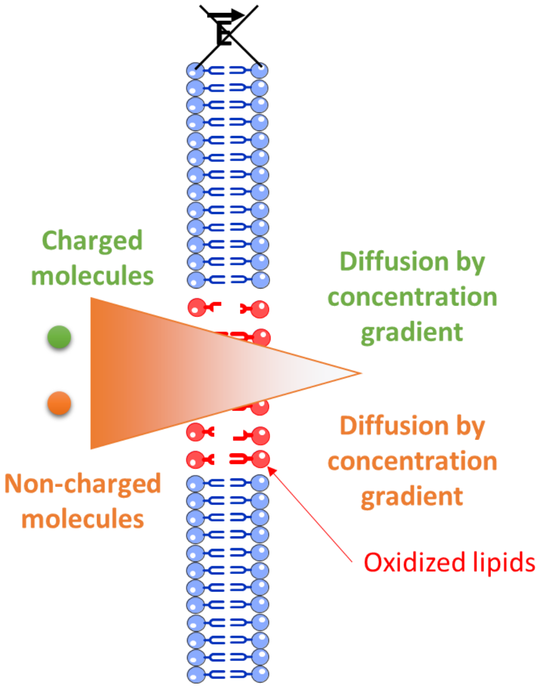

Fig. 4.3. Scheme presenting the transport of molecules during the electropermeabilization step. There is no electric field. This step has a long duration ranging from seconds to hours. The membrane is leaky because it contains oxidized phospholipids. Charged and non-charged molecules can be massively transported by diffusion if a concentration gradient is present.

In conclusion, the properties of the molecules transport across the electropulsed membranes are in agreement with the membrane impermeability rupture model. During the electroporation phase the electrophoretic transport of non-permeant molecules across the electropulsed membrane is more effective than the diffusive transport, while in the electropermeabilization phase, the diffusive transport will be the most efficient one.

References

Azan, A., Untereiner, V., Gobinet, C., Sockalingum, G.D., Breton, M., Piot, O., and Mir, L.M. (2017). Demonstration of the Protein Involvement in Cell Electropermeabilization using Confocal Raman Microspectroscopy. Sci. Rep. *7*, 297–306.

Benov, L.C., Antonov, P.A., and Ribarov, S.R. (1994). Oxidative Damage of the Membrane Lipids after Electroporation. Gen. Physiol. Biophys *13*, 85–97.

Bobinnec, Y., Khodjakov, A., Mir, L.M., Rieder, C.L., Eddé, B., and Bornens, M. (1998). Centriole disassembly in vivo and its effect on centrosome structure and function in vertebrate cells. J. Cell Biol. *143*, 1575–1589.

Bonn, M., Bakker, H.J., Ghosh, A., Yamamoto, S., Sovago, M., and Campen, R.K. (2010). Structural Inhomogeneity of Interfacial Water at Lipid Monolayers Revealed by Surface-Specific Vibrational Pump−Probe Spectroscopy. J. Am. Chem. Soc. *132*, 14971–14978.

Bonnafous, P., Vernhes, M., Teissié, J., and Gabriel, B. (1999). The generation of reactive-oxygen species associated with long-lasting pulse-induced electropermeabilisation of mammalian cells is based on a non-destructive alteration of the plasma membrane. Biochim. Biophys. Acta *1461*, 123–134.

Breton, M., Delemotte, L., Silve, A., Mir, L.M., and Tarek, M. (2012). Transport of siRNA through Lipid Membranes Driven by Nanosecond Electric Pulses: An Experimental and Computational Study. J. Am. Chem. Soc. *134*, 13938–13941.

Chen, X., Hua, W., Huang, Z., and Allen, H.C. (2010). Interfacial Water Structure Associated with Phospholipid Membranes Studied by Phase-Sensitive Vibrational Sum Frequency Generation Spectroscopy. J. Am. Chem. Soc. *132*, 11336–11342.

Cheng, J.-X., Pautot, S., Weitz, D. a, and Xie, X.S. (2003). Ordering of water molecules between phospholipid bilayers visualized by coherent anti-Stokes Raman scattering microscopy. Proc. Natl. Acad. Sci. U. S. A. *100*, 9826–9830.

Cournia, Z., Allen, T.W., Andricioaei, I., Antonny, B., Baum, D., Brannigan, G., Buchete, N.-V., Deckman, J.T., Delemotte, L., Del Val, C., et al. (2015). Membrane Protein Structure, Function, and Dynamics: a Perspective from Experiments and Theory. J. Membr. Biol. *248*, 611–640.

Dehez, F., Delemotte, L., Kramar, P., Miklavčič, D., and Tarek, M. (2014). Evidence of Conducting Hydrophobic Nanopores Across Membranes in Response to an Electric Field. J. Phys. Chem. C *118*, 6752–6757.

Delemotte, L., and Tarek, M. (2012). Molecular Dynamics Simulations of Lipid Membrane Electroporation. J. Membr. Biol. *245*, 531–543.

Downes, A., Mouras, R., Bagnaninchi, P., and Elfick, A. (2011). Raman spectroscopy and CARS microscopy of stem cells and their derivatives. J. Raman Spectrosc. *42*, 1864–1870.

Gabriel, B., and Teissié, J. (1994). Generation of reactive-oxygen species induced by electropermeabilization of Chinese hamster ovary cells and their consequence on cell viability. Eur J Biochem *223*, 25–33.

Gruenbaum, S.M., and Skinner, J.L. (2011). Vibrational spectroscopy of water in hydrated lipid multi-bilayers. I. Infrared spectra and ultrafast pump-probe observables. J. Chem. Phys. *135*, 34–36.

Kong, K., Kendall, C., Stone, N., and Notingher, I. (2015). Raman spectroscopy for medical diagnostics - From in-vitro biofluid assays to in-vivo cancer detection. Adv. Drug Deliv. Rev. *89*, 121–134.

Krassowska, W., and Filev, P.D. (2007). Modeling electroporation in a single cell. Biophys. J. *92*, 404–417.

Leguèbe, M., Silve, A., Mir, L.M., and Poignard, C. (2014). Conducting and permeable states of cell membrane submitted to high voltage pulses: Mathematical and numerical studies validated by the experiments. J. Theor. Biol. *360*, 83–94.

Litster, J.D. (1975). Stability of lipid bilayers and red blood cell membranes. Phys. Lett. A *53*, 193–194.

Lopez, C.F., Lopez, C.F., Nielsen, S.O., Klein, M.L., and Moore, P.B. (2004). Hydrogen bonding structure and dynamics of water at the dimyristoylphosphatidylcholine lipid bilayer surface from a molecular dynamics simulation. J. PHYS. CHEM. B *108*, 6603--6610.

Maiti, N.C., Apetri, M.M., Zagorski, M.G., Carey, P.R., and Anderson, V.E. (2004). Raman spectroscopic characterization of secondary structure in natively unfolded proteins: alpha-synuclein. J. Am. Chem. Soc. *126*, 2399–2408.

de Menorval, M.-A., Andre, F.M., Silve, A., Dalmay, C., Français, O., Le Pioufle, B., and Mir, L.M. (2016). Electric pulses: a flexible tool to manipulate cytosolic calcium concentrations and generate spontaneous-like calcium oscillations in mesenchymal stem cells. Sci. Rep. *6*, 32331.

Mir, L.M. (2008). Application of electroporation gene therapy: past, current, and future. Methods Mol. Biol. *423*, 3–17.

Nagata, Y., and Mukamel, S. (2010). Vibrational sum-frequency generation spectroscopy at the water/lipid interface: molecular dynamics simulation study. J Am Chem Soc *132*, 6434–6442.

Neumann, E., and Katchalsky, A. (1972). Long-lived conformation changes induced by electric impulses in biopolymers. Proc. Natl. Acad. Sci. U. S. A. *69*, 993–997.

Nihonyanagi, S., Mondal, J.A., Yamaguchi, S., and Tahara, T. (2013). Structure and Dynamics of Interfacial Water Studied by Heterodyne-Detected Vibrational Sum-Frequency Generation. Annu. Rev. Phys. Chem. *64*, 579–603.

Pakhomova, O.N., Khorokhorina, V.A., Bowman, A.M., Rodaitė-Riševičienė, R., Saulis, G., Xiao, S., and Pakhomov, A.G. (2012). Oxidative effects of nanosecond pulsed electric field exposure in cells and cell-free media. Arch. Biochem. Biophys. *527*, 55–64.

Pastushenko, V.F., and Chizmadzhev, Y.A. (1982). Stabilization of Conducting Pores in BLM by Electric Current. Gen. Physiol. Biophys *1*, 43–52.

Pavlin, M., and Miklavčič, D. (2008). Theoretical and experimental analysis of conductivity, ion diffusion and molecular transport during cell electroporation — Relation between short-lived and long-lived pores. Bioelectrochemistry *74*, 38–46.

Poignard, C., Silve, A., and Wegner, L. (2016). Different Approaches used in Modeling of Cell Membrane Electroporation.

Raman, C.V. V (1928). A new radiation. Indian J. Phys. *2*, 387–398.

Rems, L., Tarek, M., Casciola, M., and Miklavčič, D. (2016). Properties of lipid electropores II: Comparison of continuum-level modeling of pore conductance to molecular dynamics simulations. Bioelectrochemistry *112*, 112–124.

Salomone, F., Breton, M., Leray, I., Cardarelli, F., Boccardi, C., Bonhenry, D., Tarek, M., Mir, L.M., and Beltram, F. (2014). High-Yield Nontoxic Gene Transfer through Conjugation of the CM $_{18}$ -Tat $_{11}$ Chimeric Peptide with Nanosecond Electric Pulses. Mol. Pharm. *11*, 2466–2474.

Schoenbach, K.H., Beebe, S.J., and Buescher, E.S. (2001). Intracellular effect of ultrashort electrical pulses. Bioelectromagnetics *22*, 440–448.

Silve, A., Leray, I., and Mir, L.M. (2012a). Demonstration of cell membrane permeabilization to medium-sized molecules caused by a single 10 ns electric pulse. Bioelectrochemistry *87*, 260–264.

Silve, A., Dorval, N., Schmid, T., Mir, L.M., and Attal-Tretout, B. (2012b). A wide-field arrangement for single-shot CARS imaging of living cells. J. Raman Spectrosc. *43*, 644–650.

Smith, G.P.S., McGoverin, C.M., Fraser, S.J., and Gordon, K.C. (2015). Raman imaging of drug delivery systems. Adv. Drug Deliv. Rev. *89*, 21–41.

Tarek, M. (2005). Membrane electroporation: a molecular dynamics simulation. Biophys J *88*, 4045–4053.

Teissie, J. (2007). Biophysical effects of electric fields on membrane water interfaces: a mini review. Eur. Biophys. J. *36*, 967–972.

Tieleman, D.P. (2004). The molecular basis of electroporation. BMC Biochem. *5*.

Tokman, M., Lee, J.H., Levine, Z. a., Ho, M.-C.C., Colvin, M.E., and Vernier, P.T. (2013). Electric Field-Driven Water Dipoles: Nanoscale Architecture of Electroporation. PLoS One *8*, e61111.

Ullery, J.C., Tarango, M., Roth, C.C., and Ibey, B.L. (2015). Activation of autophagy in response to nanosecond pulsed electric field exposure. Biochem. Biophys. Res. Commun. *458*, 411–417.

Unterreitmeier, S., Fuchs, A., Schäffler, T., Heym, R.G., Frishman, D., and Langosch, D. (2007). Phenylalanine promotes interaction of transmembrane domains via GxxxG motifs. J. Mol. Biol. *374*, 705–718.

Vernier, P.T., Levine, Z.A., Wu, Y.-H., Joubert, V., Ziegler, M.J., Mir, L.M., and Tieleman, D.P. (2009). Electroporating Fields Target Oxidatively Damaged Areas in the Cell Membrane. PLoS One *4*, e7966.

Wang, K., Zhao, Y., Chen, D., Fan, B., Lu, Y., Chen, L., Long, R., Wang, J., and Chen, J. (2017). Specific membrane capacitance, cytoplasm conductivity and instantaneous Young’s modulus of single tumour cells. Sci. Data *4*, 170015.

Wiseman, H., and Halliwell, B. (1996). Damage to DNA by reactive oxygen and nitrogen species: role in inflammatory disease and progression to cancer. Biochem. J. *313 (Pt 1*, 17–29.

Wong-Ekkabut, J., Xu, Z.T., Triampo, W., Tang, I.M., Tieleman, D.P., and Monticelli, L. (2007). Effect of lipid peroxidation on the properties of lipid bilayers: A molecular dynamics study. Biophys. J. *93*, 4225–4236.

Ziegler, M.J., and Vernier, P.T. (2008). Interface Water Dynamics and Porating Electric Fields for Phospholipid Bilayers. J. Phys. Chem. B *112*, 13588–13596.

universite PARIS-SACLAY

ÉCOLE DOCTORALE
Innovation thérapeutique :
du fondamental à l'appliqué

Titre : Nouveaux biomarqueurs de l'électroperméabilisation cellulaire *in vitro* et des toxicités cutanées chez des patients atteints de cancer utilisant des techniques optiques non-invasives et sans marquage (microspectroscopie Raman et microscopie terahertz)

Mots clés : Electroperméabilisation ; microspectroscopy Raman ; microscopie terahertz ; toxicité cutanée ; thérapies anticancéreuses ciblées

Résumé : Les champs électriques impulsionnels sont connus pour induire la perméabilisation de la membrane plasmique des cellules. Ce doctorat vise à étudier les modifications chimiques de cellules vivantes exposées à des champs électriques impulsionnels grâce à des méthodes optiques non-invasives et sans marquage : la microspectroscopie Raman confocale et la microscopie terahertz.

Nos résultats ont montré que la signature Raman est un biomarqueur précis de l'état d'électroperméabilisation des cellules avec une modification significative des lipides et des protéines. Les expériences de microscopie de terahertz ont montré une fuite des protéines des cellules électroperméabilisées.

En tant que projet parallèle de ce doctorat, une recherche clinique a été réalisée afin d'étudier la toxicité cutanée induite chez les patients traités par des thérapies anticancéreuses ciblées. Bien que l'efficacité de ces thérapies ne soit pas discutée, de nombreux graves effets cutanées secondaires sont associés. Dans cette étude, nous avons étudié l'opportunité de prédire l'apparition de la toxicité cutanée au moyen de la microspectroscopie Raman confocale réalisée sur la peau des patients. Nous avons réussi à déterminer un nouveau biomarqueur pharmacodynamique spécifique de la toxicité cutanée grâce aux signatures Raman de la peau des patients; alors que l'évaluation dermatologique ou histologique n'a détecté aucune modification.

Title : New biomarkers of *in vitro* cell electropermeabilization and of skin toxicities in cancer patients using non-invasive and label-free optical techniques (Raman microspectroscopy and terahertz microscopy)

Keywords : Electropermeabilization; Raman microspectroscopy; terahertz microscopy, skin toxicity, targeted anticancer therapies

Abstract : Pulsed electric fields are known to induce the permeabilization of the plasma membrane of cells. This doctorate aims to investigate the chemical modifications of live cells exposed to pulsed electric fields thanks to non-invasive and label-free optical methods: confocal Raman microspectroscopy and terahertz microscopy.

Our results demonstrate that the Raman signature is an accurate biomarker of the electropermeabilization states of cells with significantly modifications of lipids and proteins. Finally, terahertz microscopy experiments show protein leakage from electropermeabilized cells.

As a side project of this doctorate, a unique clinical research has been performed in order to investigate the cutaneous toxicity induced in patients under targeted anticancer therapies. Although the efficiency of these therapies has not to be discussed, many severe cutaneous side effects are associated. In this study, we investigate the opportunity to predict the apparition of skin toxicity by means of confocal Raman microspectroscopy. We succedded to determine a novel and specific pharmacodynamic biomarker for skin toxicity based on the Raman signatures of the patient's skin, whereas dermatological or histological evaluation did not detect any modifications.

Université Paris-Saclay
Espace Technologique / Immeuble Discovery
Route de l'Orme aux Merisiers RD 128 / 91190 Saint-Aubin, France